Volume 74, issue 4, 15 September 2007
This issue completes volume 74
ISSN 0272-7714

ELSEVIER

ESTUARINE COASTAL AND SHELF SCIENCE

in association with
the Estuarine and Coastal Sciences Association

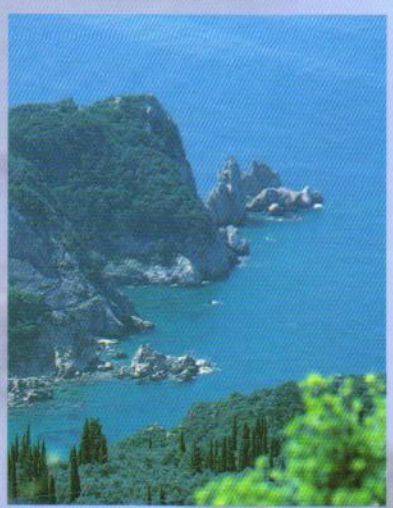

Special Issue

Timescale- and tracer-based methods for understanding the results of complex marine models

Eric Deleersnijder and Eric J.M. Delhez
(Guest Editors)

Table of Contents

Available online at www.sciencedirect.com
ScienceDirect
Estuarine, Coastal and Shelf Science 74 (2007) v–vii
ESTUARINE COASTAL AND SHELF SCIENCE
www.elsevier.com/locate/ecss

Editorial

Timescale- and tracer-based methods for understanding the results of complex marine models

The famous mathematician John von Neumann once wrote:

The sciences do not try to explain, they hardly even try to interpret, they mainly make models. By a model is meant a mathematical construct which, with the addition of certain verbal interpretations, describes observed phenomena. The justification of such a mathematical construct is solely and precisely that it is expected to work.

Though von Neumann was instrumental in designing the first programmable computers, he apparently did not envision that the implementation of mathematical models on powerful computers would produce so huge an amount of real numbers that making sense of them, i.e. producing verbal interpretations of them, would become a real challenge.

To understand the challenge that modellers are nowadays faced with, consider a numerical model of a marine region based on grid of 100×100 points on the horizontal, and 20 points on each vertical, i.e. a total of 2×10^5 grid points, which is far from exceptional. Now assume that there are 20 variables to be computed at every grid point, i.e. velocity components, temperature, salinity, turbulence closure variables, ecological variables, etc. Therefore, 4×10^6 discrete variables will be updated at every time step. Assuming that the latter is of the order of 2 min and that a one-year simulation is to be performed, the numerical model will produce about 10^{12} real numbers. Making sense of such a huge amount of information requires specific post-processing strategies presenting the model results in a format that is amenable to analysis.

Though computer graphics is widely used – and rightly so – it is not the ultimate solution to the problem. A standard computer screen encompasses about 10^6 pixels. Assuming that each pixel is associated with one real number, then one would need to display 10^6 pictures occupying the entire screen to "view" all of the results produced by the model. This is not feasible either. At most, one could perhaps display and analyse 10^2 pictures or sequences of pictures. This amounts to examining only 0.01% of all the real numbers produced by the computer during the numerical simulation. One could argue that the results displayed are sufficiently well chosen that analysing them is sufficient to work out valid interpretations of the results. This argument is, at best, dubious, as we have seen that having recourse to computer graphics may lead to disregarding as much as 99.99% of the model results!

Clearly, post-processing methods that do not leave aside most of the results are needed. Statistical methods are a relevant way of reducing the amount of information to be submitted to the human brain. Equally valid are approaches resorting to – real or artificial – tracers (England and Maier-Reimer, 2001; Delhez et al., 2004a) and associated timescales, i.e. age, residence time, transit time, etc. These techniques are holistic in that they take advantage of most, if not all, of the results. Another advantage of the latter techniques is that they provide a direct quantitative insight into the dynamics and rate of functioning of the system (e.g. Delhez et al., 2004c). Such diagnostics are a first step towards the understanding of model results. This turns out to be very valuable in an interdisciplinary environment or in a management perspective.

Strictly speaking, only two timescales, i.e. the age and the residence time, are often sufficient to characterize the motions of tracers, constituents of seawater or groups of constituents – including the water itself. The age of a particle is the time that has elapsed since this particle left the region in which the age is assumed to be zero, whereas its residence time is the time needed to reach the region in which the residence is prescribed to be zero (Bolin and Rodhe, 1973; Zimmerman, 1976; Takeoka, 1984). In most cases, it is not possible to estimate these timescales in a thorough way by means of field data alone. For instance, evaluating the residence time as the ratio of the volume of the domain of interest to an outgoing flux is a crude approximation that is valid only for a steady state flow in an infinitely well-mixed domain. Another illustrative example pertains to radio ages, i.e. ages obtained by using the decay of a radioactive tracer as a clock to measure the elapsed time. Such ages have been used to measure ventilation rate in deep ocean basins or transit time in shallow seas, but the faster the decay of the radioactive tracer used the poorer the approximation of the correct water age (Delhez et al., 2003).

Over the last decade, theoretical research aimed at establishing partial differential equations from which the age and the residence time may be obtained at any time and position (Delhez et al., 1999; Holzer and Hall, 2000; Deleersnijder et al., 2001; Khatiwala et al., 2001; Waugh and Hall, 2002). These equations can now be solved along with the model

0272-7714/$ - see front matter
doi:10.1016/j.ecss.2007.05.007

equations, leading to timescales that are correct up to numerical errors and, hence, outdo the – usually crude – approximations obtained from field data that were frequently resorted to in the past. Such diagnostic tools are also very flexible; they can be tailored to address any particular aspect of the dynamics.

As field data cannot be used to validate timescales estimated numerically, how can the latter be validated? No direct validation is possible. However, since timescales are obtained by solving equations similar to those from which tracer concentrations are predicted, the accuracy of timescale calculations may be thought to be of the same order as that of the tracer concentrations. In other words, though there is no direct validation of timescale estimates, there are indirect ones, through the assessment of the tracer transport calculations.

Timescales and tracer concentrations may be computed in the Lagrangian formalism. Several examples thereof are given in this special issue (Döös and Engvist, Sandery and Kämpf, Wijeratne and Rydberg). Lagrangian methods are appealing as they are much superior to their Eulerian counterparts in the representation of advection. However, the simulation of diffusion processes by means of random walks is not straightforward when the diffusivity tensor is not diagonal and the eddy coefficient exhibit large space variations (Thomson et al., 1997; LaBolle et al., 2000; Spivakovskaya et al., in press). In this respect, further research is needed.

Most of the papers resort to the Eulerian formalism, which can also pose specific numerical problems. For instance, Naifar et al. address the issue of guaranteeing that the velocity remains divergence free in every type of discretization. On the other hand, a number of articles are concerned with the water renewal of semi-enclosed domains. Using the results of a three-dimensional model, Huang evaluates the flushing time as the ratio of a volume to a flux. Abdelrhman resorts to a simple tidal prism approach and investigates the connection between physical timescales and ecological processes in an embayment. Estimates of the so-called local e-flushing time are obtained by Migon et al. from three-dimensional model results, allowing them to show the existence of a significant correlation between hydrodynamic timescales and metal concentrations measured in the lagoon of Nouméa, New Caledonia. For the latter, Torreton et al. resort to three-dimensional hydrodynamic simulations to test the statistical relationship between flushing indices and *in situ* biological and chemical measurements.

The other contributions use the formalism of CART, the Constituent-oriented Age and Residence time Theory (www.climate.be/CART). The latter provides general equations for calculating at any time and position the age of every constituent of seawater (e.g. Delhez et al., 1999; Deleersnijder et al., 2001), or every group of constituents, including seawater itself (Deleersnijder et al., 2002). An adjoint model approach to the residence time is also available in CART (e.g. Delhez et al., 2004b). Mercier and Delhez study sediment transport in the Belgian coastal zone. To do so, resuspension and transport sediment ages are computed, providing new insights into the issues under consideration. Beckers et al. resort to a multi-facetted approach to understand the transport of dissolved trace metals in the Gulf of Cadiz. River waters entering the domain are considered as passive tracers whose ages are estimated. Then, the incoming tracer fluxes are inferred from a combination of numerical results and field data. Treating water masses as passive tracers was also achieved by Gustfasson and Bendtsen, Meier, Shen and Wang and White and Deleersnijder. These studies focus on water renewal processes. There is no doubt that a general theory thereof is now needed. The latter could emerge from a generalization of the work of Gourgue et al., in which the water initially present in the domain and the different renewing water masses are considered to be passive tracers. Additional diagnoses are provided by computing the residence time of the former and the ages of the latter.

This special issue shows the potential of tracer-based methods for helping in the interpretation of the results of complex marine models. The papers illustrate the wide range of length scales, timescales and fields of application in which diagnostic tools can be used. A wide variety of approaches have also been suggested. In particular, the usefulness of treating water masses as passive tracers has been confirmed.

The guest editors wish to express their gratitude to the authors who contributed articles to the present special issue and to the reviewers for useful suggestions.

Acknowledgements

ED and EJMD are a Research Associate and an honorary Research Associate, respectively, with the Belgian National Fund for Scientific Research (FNRS).

References

Bolin, B., Rodhe, H., 1973. A note on the concepts of age distribution and transit time in natural reservoirs. Tellus 25, 58–62.

Deleersnijder, E., Campin, J.-M., Delhez, E.J.M., 2001. The concept of age in marine modelling: I. Theory and preliminary model results. Journal of Marine Systems 28, 229–267.

Deleersnijder, E., Mouchet, A., Delhez, E.J.M., Beckers, J.-M., 2002. Transient behaviour of water ages in the World Ocean. Mathematical and Computer Modelling 36, 121–127.

Delhez, E.J.M., Campin, J.-M., Hirst, A.C., Deleersnijder, E., 1999. Toward a general theory of the age in ocean modelling. Ocean Modelling 1, 17–27.

Delhez, E.J.M., Deleersnijder, E., Mouchet, A., Beckers, J.-M., 2003. A note on the age of radioactive tracers. Journal of Marine Systems 38, 277–286.

Delhez, E.J.M., Deleersnijder, E., Rixen, M., 2004a. Tracer methods in geophysical fluid dynamics. Proceedings of the 34th International Liège Colloquium on Ocean Dynamics (Liège, Belgium, May 6–10 2002). Journal of Marine Systems 48, 1–193 (special issue).

Delhez, E.J.M., Heemink, A.W., Deleersnijder, E., 2004b. Residence time in a semi-enclosed domain from the solution of an adjoint problem. Estuarine, Coastal and Shelf Science 61, 691–702.

Delhez, E.J.M., Lacroix, G., Deleersnijder, E., 2004c. The age as a diagnostic of the dynamics of marine ecosystem models. Ocean Dynamics 54, 221–231.

England, M.H., Maier-Reimer, E., 2001. Using chemical tracers to assess ocean models. Reviews of Geophysics 39, 29–70.

Holzer, M., Hall, T.M., 2000. Transit-time and tracer-age distribution in geophysical flows. Journal of the Atmospheric Sciences 57, 3539–3558.

Khatiwala, S., Visbeck, M., Schlosser, P., 2001. Age tracers in an ocean GCM. Deep Sea Research I: Oceanographic Research Papers 48, 1423–1441.

LaBolle, E.M., Quastel, J., Fogg, G.E., Gravner, J., 2000. Diffusion processes in composite porous media and their numerical integration by random walks: generalized stochastic differential equations with discontinuous coefficients. Water Resources Research 36, 651–662.

Spivakovskaya, D., Heemink, A.W., Deleersnijder, E. Lagrangian modelling of multi-dimensional advection–diffusion with space-varying diffusivities: theory and idealized test cases. Ocean Dynamics, in press. doi:10.1007/s10236-007-0102-9.

Takeoka, H., 1984. Fundamental concepts of exchange and transport time scales in a coastal sea. Continental Shelf Research 3, 311–326.

Thomson, D.J., Physick, W.L., Maryon, R.H., 1997. Treatment of interfaces in random walk dispersion models. Journal of Applied Meteorology 36, 1284–1295.

Waugh, D.W., Hall, T.M., 2002. Age of stratospheric air: theory, observations, and models. Reviews of Geophysics 40 (4), 1010. doi:10.1029/2000RG000101.

Zimmerman, J.T.F., 1976. Mixing and flushing of tidal embayments in the western Dutch Wadden Sea – part I: distribution of salinity and calculation of mixing time scales. Netherlands Journal of Sea Research 10, 149–191.

Eric Deleersnijder
Université catholique de Louvain, G. Lemaître Institute of Astronomy and Geophysics (ASTR) and Centre for Systems Engineering and Applied Mechanics (CESAME), Bâtiment Euler, 4 Avenue G. Lemaître, B-1348 Louvain-la-Neuve, Belgium
E-mail address: ericd@uclouvain.be

Eric J.M. Delhez
Université de Liège, Département d'aérospatiale et mécanique, Bâtiment B37, 12 Grande Traverse, B-4000 Liège 1, Belgium

7 May 2007

Available online 25 June 2007

Available online at www.sciencedirect.com
ScienceDirect
Estuarine, Coastal and Shelf Science 74 (2007) 585–598
ESTUARINE COASTAL AND SHELF SCIENCE
www.elsevier.com/locate/ecss

Determining the age of water and long-term transport timescale of the Chesapeake Bay

Jian Shen*, Harry V. Wang

Virginia Institute of Marine Science, College of William and Mary, Gloucester Point, VA 23063, USA

Received 29 March 2006; accepted 9 May 2007
Available online 20 July 2007

Abstract

The concept of age of water (AW) is applied to the Chesapeake Bay to investigate the long-term transport properties for dissolved substances. A real-time calibrated hydrodynamic Chesapeake Bay model in 3 Dimensions (CH3D), employing a boundary-fitted curvilinear grid, is used for the study. The long-term transport properties, represented by AW, are investigated under the conditions of low river inflow of 1995 and high river inflow of 1996, as well as for constant mean inflows. The influences of freshwater, density-induced circulation, and wind-induced transport on age distribution have been investigated. Model results show that river inflows, wind stress, and density-induced circulation play important roles in controlling the long-term transport in the Bay. The model results shows that it requires 120–300 days for a marked change in the characteristics of the pollutant source discharged into the Bay from the Susquehanna River to affect significantly the conditions near the mouth under different hydrodynamic conditions. An increase of river discharge results in increases of downstream residual current and gravitational circulation, and thus reduces AW. The density-induced circulation contributes to the transport substantially. The dissolved substances discharged into the Bay are transported out of the Bay more rapidly when the estuary becomes more stratified. Southeasterly and southwesterly winds have strong impacts on the transport compared to the northeasterly and northwesterly winds. The former increases lateral and vertical mixing significantly. Consequently, the gravitational circulation is reduced and the transport time is increased by 50%. The model results provide useful information for understanding the long-term transport processes in the Bay.

Keywords: water age; long-term transport; density-induced circulation; wind-induced circulation; three-dimensional model; Chesapeake Bay

1. Introduction

Many estuaries and coastal seas have become more eutrophic over the past few decades as anthropogenic inputs of nutrients increase (Carpenter et al., 1998; Nixon, 1995; Kemp et al., 2005). Both the amount of the nutrients discharged into estuaries and the nutrient retention time contribute to the eutrophic conditions of estuaries. In fact, it has been suggested that the retention time is a key parameter that controls nutrient budgets (Boynton et al., 1995). To provide better management of nutrient inputs and improve health of aquatic systems, three-dimensional water quality models have been extensively used to study nutrient budgets and eutrophication processes in estuaries (Cerco and Meyers, 2000; Park et al., 2005). Whereas these models are rather complex in terms of biochemical processes, the success of their predictions depends greatly on the long-term transport processes of nutrients and phytoplankton simulated by hydrodynamic transport models. Traditionally, the accurate predictions of a hydrodynamic model rely on the model calibration and verification based on limited time series data recorded at fixed locations. The long-term transport processes are difficult to assess. Characteristics of the transport processes for a dissolved substance depend primarily on the low-frequency residual flow that depends on the interactions among density field, river flow, wind, and the non-linear rectification of the periodic tides in a given estuary. Therefore, it is difficult to separate and quantify the influences of different mechanisms on the long-term

* Corresponding author at: Virginia Institute of Marine Science, Department of Physical Sciences, PO Box 1346, Gloucester Point, VA 23062, USA.
E-mail address: shen@vims.edu (J. Shen).

0272-7714/$ - see front matter © 2007 Elsevier Ltd. All rights reserved.
doi:10.1016/j.ecss.2007.05.017

transport. To understand the underlying dynamics contributing to the transport properties of an estuary, transport timescales, such as flushing time, residence time, and water age, have been used to quantify the overall dynamic conditions of the model system.

Although timescales such as flushing time and mean residence time have often been used to estimate the overall retention time for a waterbody, the steady-state approach does not account for spatial and temporal variations in a large estuary. The retention times in deep channels and shallow areas vary substantially for a complex estuary. It is desirable to know the spatial distribution pattern of the retention time and its temporal variation. In fact, the retention time for a dissolved substance at a given location can be quantified by the use of the concept of age of water (AW). The concept of age of a water parcel has been used as a timescale to quantify pollutant transport in lagoons, estuaries, and oceans (Bolin and Rodhe, 1973; Zimmerman, 1976; Takeoka, 1984; Delhez et al., 1999; Deleersnijder et al., 2001). Zimmerman (1976) applied the age concept to the Dutch Wadden Sea and introduced 'residence time' as the time it takes for a water parcel to leave the domain of interest. The residence time is not a constant timescale. Recent studies have further advanced the theory. Delhez et al. (2004) introduced a general methodology to compute the residence time. Based on Zimmerman's definition, the age is a complement of the residence time. It is the time elapsed since the water parcel under consideration exited the region in which its age is prescribed to be zero. Age defined in this study is the time elapsed since the parcel under consideration departed the region in which its age is prescribed to be zero, or particularly, the time elapsed since a water particle is discharged from the headwater of an estuary. In our case, the age is zero at the headwater of an estuary and the age at any given location is representative of the time elapsed for a dissolved substance to be transported from its source to that location.

Delhez et al. (1999) introduced age theory based on the advection-diffusion of a tracer and provide a general methodology to compute age using a numerical model. Deleersnijder et al. (2001) simulated the age of technetium-99 released from the La Hague nuclear fuel reprocessing plant in the English Channel successfully using a 3-D model. Beckers et al. (2001) studied the properties of age fluid dynamics in a homogeneous environment. Shen and Haas (2004) investigated the AW distribution in the York River estuary using numerical model experiments. This recently developed age concept provides a sound methodology to quantify transport characteristics of dissolved substances over a Eulerian coordinate framework. This allows for the estimation of transport time to be presented as a spatial variable and reveals detailed transit time information for transport in a complex estuary.

In an idealized geometry with uniform flow, AW has been proven to resemble symmetric patterns (Beckers et al., 2001). For a large estuary, such as Chesapeake Bay, estuarine hydrodynamics is far from ideal in that it possesses complicated geometry in three dimensions, has different mixing regimes, and is driven by multiple forcings: tide, wind, and river discharge. In all, the transport and mixing properties and forcing mechanisms of the Bay are temporally and spatially non-uniform. By investigating the variation of transport timescales under different hydrodynamic conditions, one is able to diagnose the contributions of underlying dynamic processes. The main objective of this study is to investigate the influences of hydrological conditions, surface wind stress, and density-induced circulation on the transport timescale of dissolved substances in the Chesapeake Bay. We are interested in determining the transport property using artificial tracers and to what extent they can be interpreted. The investigations were conducted through a series of model simulations and numerical model experiments.

2. Study area

This study focuses on transport properties of dissolved substances in the Chesapeake Bay. The Chesapeake Bay, located along the Eastern Coast of the United States, is one of the largest estuaries in the world and it is one of the world's most complex coastal plain estuaries. Fig. 1 shows the location of the Chesapeake Bay. The Bay spans approximately 320 km between its mouth adjacent to the Atlantic Ocean near Norfolk, Virginia, and its head near the Susquehanna River entrance. The Bay is comprised of many tributaries and numerous interconnected embayments, marshes, islands, and channels. The major tributaries along the Western Shore of the Bay include the

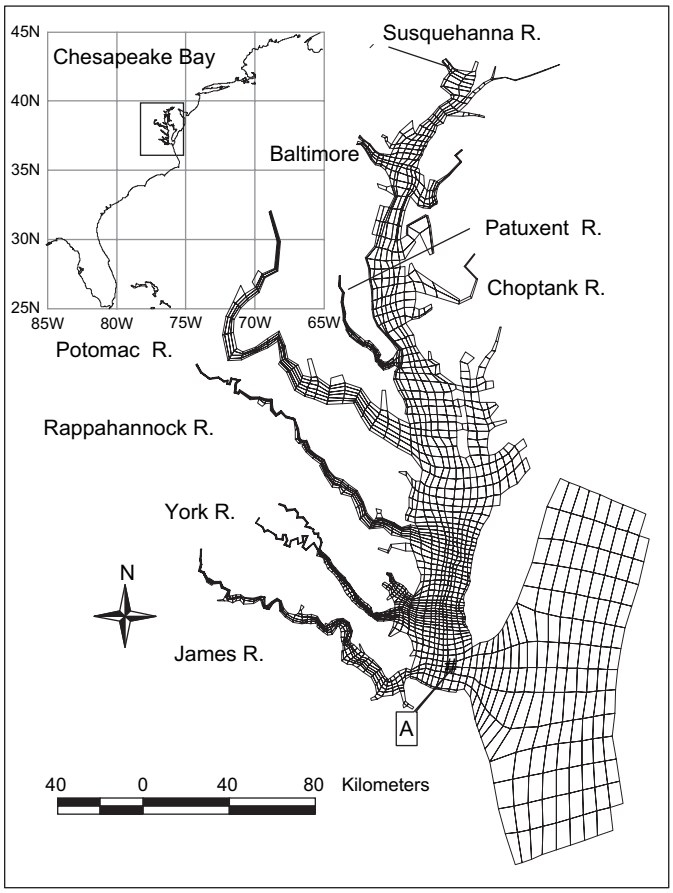

Fig. 1. Map and model grid of the Chesapeake Bay.

James, York, Rappahannock, Potomac, and Patuxent Rivers, and the Choptank River is along the Eastern Shore.

The Chesapeake Bay is a partially mixed estuary (Pritchard, 1952). The mean water depth is about 6.46 m (Schubel and Pritchard, 1986) and the mean tidal range at the mouth is 0.78 m. The tide in the Bay is dominated by the M_2 constituent. The tidal wave requires more than 13 h traveling from the mouth of the Bay to its head. Therefore, two high tides can simultaneously exist within the Bay (Wang, 1979). The M_2 amplitude decreases from the Bay mouth towards its main stem and then increases northward. Two virtual amphidromic points are located near the Potomac River mouth and Annapolis, MD (Hicks, 1964; Fisher, 1987).

The largest freshwater discharge is from the Susquehanna River, which accounts for nearly half of the total freshwater input (Schubel and Pritchard, 1986), followed by the Potomac, James, Rappahannock, York, Patuxent, and Choptank Rivers. The daily discharge varies substantially from year to year. A typical total flow discharged into the Bay from these seven rivers is shown in Fig. 2. This total flow is based on data collected at United States Geological Survey (USGS) gage stations (Stations 01578310, 01646580, 0203500, 01668000, 0167300, 01674500, and 0159440) near the headwaters of the tributaries. The total discharges from these tributaries during the years of 1995 and 1996 are 1323 $m^3 s^{-1}$ and 3033 $m^3 s^{-1}$, which can considered as a representative of long-term low and high flow conditions of 1387 $m^3 s^{-1}$ and 3729 $m^3 s^{-1}$ (Cerco and Cole, 1994), respectively.

Winds are generally episodic with dominant periods of 6–8 days and 2–3 days. In the middle of the Bay, near the mouth of the Patuxent River, the energy peaks at 8 and 3.5 days (Wang, 1979). In the upper and middle reaches of the Bay, northwesterly winds dominate in winter months from November to February. However, these winds are often disrupted by southerly wind events lasting several days during summer (Xu et al., 2002).

3. Methods

3.1. Three-dimensional circulation model

A hydrodynamic model in 3 Dimensions (CH3D), operating over a curvilinear boundary-fitted grid, was used for this study. The model was developed by Sheng (1986) and was subsequently modified extensively by the US Waterway Experiment Station (WES) for application to the Chesapeake Bay (Johnson et al., 1991b; Wang and Chapman, 1995). The model simulates circulation induced by density and topography differences as well as tidal and wind-driven flows, and spatial and temporal distributions of salinity, temperature, and conservative tracers. Model details can be found in Sheng (1986) and Johnson et al. (1991a).

Fig. 1 shows the model grid. Boundary-fitted grid cells, allowing for a better representation of the complex shorelines, were used for the model domain. To ensure that long-term stratification in the deep channels is maintained, the z-coordinate is used in the vertical. The modeling domain includes a portion of the Atlantic Ocean out to depths of 30.49 m. There are 2129 computational cells in the horizontal plane of the model grid with cell lengths varying from approximately 1 km (in tributaries) to 5 km (over the continental shelf). There are up to 20 layers in the vertical with each layer being 1.52 m thick, except for the top layer, which varies with the tide.

The Chesapeake Bay model was developed in 1991 and refined in 2002 (Johnson et al., 1991b; Cerco and Meyers, 2000; Cerco et al., 2002). The model was forced at its open boundary at the mouth by tide, salinity, and temperature. The model was calibrated and verified for tide, salinity, and temperature using data collected from 1984 to 1994. For a detailed description of model calibration and verification, the reader is referred to Cerco and Meyers (2000), Wang and Johnson (2000), and Cerco et al. (2002).

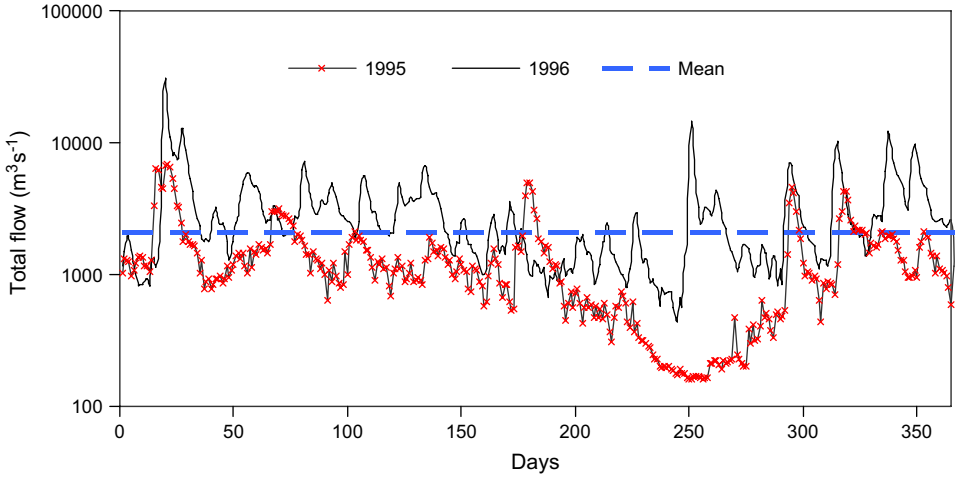

Fig. 2. Total freshwater inflows from major tributaries (Solid line is high flow condition of 1996, line with × is low flow condition of 1995, and dashed line is mean flow.)

3.2. Age of water calculation

Several methods have been introduced for computing the age of water parcels (Bolin and Rodhe, 1973; Zimmerman, 1976; Takeoka, 1984). Delhez et al. (1999) provide a general methodology for using numerical models to compute spatially varying age distributions in a real estuarine environment based on a tracer and age concentrations. Assuming that there is only one tracer discharged into the estuary and no other sources and sinks of the tracer within the estuary, the transport equations for calculating the tracer and the age concentrations can be written as follows (Delhez et al., 1999):

$$\frac{\partial c(t,\vec{x})}{\partial t}+\nabla(uc(t,\vec{x})-K\nabla c(t,\vec{x}))=0 \tag{1}$$

$$\frac{\partial \alpha(t,\vec{x})}{\partial t}+\nabla(u\alpha(t,\vec{x})-K\nabla \alpha(t,\vec{x}))=c(t,\vec{x}) \tag{2}$$

where c is the tracer concentration, α is the age concentration, u is the velocity field, K is the diffusivity tensor, t is time, and $\vec{x}$ is distance. The mean age "a" then can be calculated as follows:

$$a(t,\vec{x})=\frac{\alpha(t,\vec{x})}{c(t,\vec{x})} \tag{3}$$

Eqs. (1) through (3) were used to compute the age of water parcels using CH3D with specified initial and boundary conditions.

3.3. Model setup and model experiments

AW distribution is a function of tide, freshwater discharge, salinity, and wind in estuaries, and it varies with time and space. In order to estimate AW variations under different hydrodynamic conditions, we conducted several model simulations under different flow and wind conditions. A summary of the forcing conditions used for each model simulation is listed in Table 1.

Cases 1 and 2 used 1995 and 1996 observed flow rates obtained at USGS gauging stations near the headwaters of seven tributaries, namely, the Susquehanna, Potomac, James, Rappahannock, York, Patuxent, and Choptank Rivers. The 1995 and 1996 flows are selected as representative flows of low and high discharges. The salinity and temperature boundary conditions were specified using bi-weekly observations near the mouth while the tidal forcing at the mouth was obtained from the results of the ADCIRC model, a large domain model (Wang and Johnson, 2000). The ADCIRC model generates results for a large domain, including the Caribbean, Gulf of Mexico, the East Coast of the United States, and Chesapeake Bay. Hourly wind data (speed and direction) obtained from the upper, middle, and lower Bay regions (Baltimore-Washington International Airport, Patuxent River Naval Air Station, and Norfolk International Airport) were used to force the model at the surface. A linear interpolation method was used to obtain wind speed and direction between these three stations. The occurrences of north and south wind components are almost 50% and the wind speeds for north and south directions are compatible for these two years. Equilibrium temperatures and surface heat transfer coefficients computed from meteorological temperatures at the Patuxent River Naval Air Station were used to compute heat exchange at the surface for the temperature simulation (Edinger et al., 1974). Each model simulation started with initial conditions of salinity and temperature obtained from the end of the previous year's simulation. The model setup is the same as the model setup used for the hydrodynamic model calibration previously. A passive tracer released continuously along with the freshwater discharge with a constant concentration of one unit at the entrance of the Susquehanna River started at 1:00 am on the 6th day after the model simulation began, allowing a 5-day spinup period.

Table 1
A summary of forcing conditions used in the model simulations

Simulation	Flow	Wind	Tide	Salinity	Temperature
Case 1	1995 observed flow (mean flow = 1323 $m^3 s^{-1}$)	1995 observation	1995 observation	1995 observation	1995 observation
Case 2	1996 observed flow (mean flow = 3033 $m^3 s^{-1}$)	1996 observation	1996 observation	1996 observation	1996 observation
Case 3	Constant mean flow (flow = 2052 $m^3 s^{-1}$)	No wind	1996 observation	1996 observation	1996 observation
Case 4	Constant high flow (flow = 3282 $m^3 s^{-1}$)	No wind	1996 observation	1996 observation	1996 observation
Case 5	Constant mean flow of 2052 $m^3 s^{-1}$	1996 observation	1996 observation	1996 observation	1996 observation
Case 6	Constant mean flow of 2052 $m^3 s^{-1}$	NE and NW components of 1996 observed wind	1996 observation	1996 observation	1996 observation
Case 7	Constant mean flow of 2052 $m^3 s^{-1}$	SE and SW components of 1996 observed wind	1996 observation	1996 observation	1996 observation
Tributary simulation 1	1995 real-time flow	1995 observation	1995 observation	1995 observation	1995 observation
Tributary simulation 2	1996 real-time flow	1995 observation	1995 observation	1995 observation	1995 observation

Eqs. (1)–(3) were used to compute the AW. The offshore open boundary condition near the mouth for the tracer was set to zero. Since the ocean side open boundary has been extended far away from the Bay mouth, the influence of the specification of the open boundary condition on the interior tracer concentration is negligible. Each model was run for three years using observed forcing cyclically (i.e., time-varying forcing time series used for the second and third years was identical to that used for the first year) in order to reach a dynamic equilibrium condition. For other cases of model simulation, the model configurations were the same as for Case 2, except that different constant flows and wind forcing were used. For offshore boundary conditions, the observed time series data of 1996 were used, including salinity, tide, and temperature. For model simulations for tributaries, the configurations were the same as for Cases 1 and 2, except that the tracer was released continuously from the headwater of each tributary. A 5-min timestep was used for the model simulations.

4. Results

4.1. Age of water of the Bay

AW varies with time and space depending on the variations of freshwater discharges and other forcing conditions. Fig. 3a shows the time series of the surface AW at Station A near the mouth (see Fig. 1) for the model simulation under 1995 and 1996 conditions (Cases 1 and 2). The model was run for three years. The results of the last 1.5 years (i.e., between Day 552 and Day 1100) is shown in the figure. This was after a transient period allowing water discharged from the headwater of the Bay to reach downstream. It can be seen that the age varies with time. The age varies from 150 to 320 days with an average age of 230 days (Days 552–1100) under the 1995 condition. The age varies from 120 to 240 days with an average age of 168 days under the 1996 condition. The age varies by more than 100 days under both the 1995 and 1996 conditions, whereas the age varies drastically under the 1995 dynamic condition.

AW at any location can be used to represent the average time elapsed for water parcels to be transported to that location from the entrance of the Susquehanna River under average conditions. It should be noted that the age is not the time necessary for a single particle to reach the location examined from its release point, but rather should be interpreted as the time needed for a marked change in the characteristics of the source to affect significantly the conditions at this point (Delhez and Carabin, 2001). The spatial age distribution varies depending on the variations of the dynamic conditions during the modeling period. Fig. 4 shows the spatial age distributions at Days 772 and 752 during the simulation period, respectively, for the 1995 and 1996 conditions. These two days were selected as representative of the maximum and minimum age distributions under different hydrodynamic conditions during the simulation period. It can be seen that the surface age near the mouth is approximately 310 and 140 days under 1995 and 1996 conditions, respectively. The surface age can differ by more than 170 days under different dynamic conditions.

The pattern of the spatial age distribution also varies with the change of the forcing condition. The surface age distribution shows a tongue-shaped pattern with low age in the middle

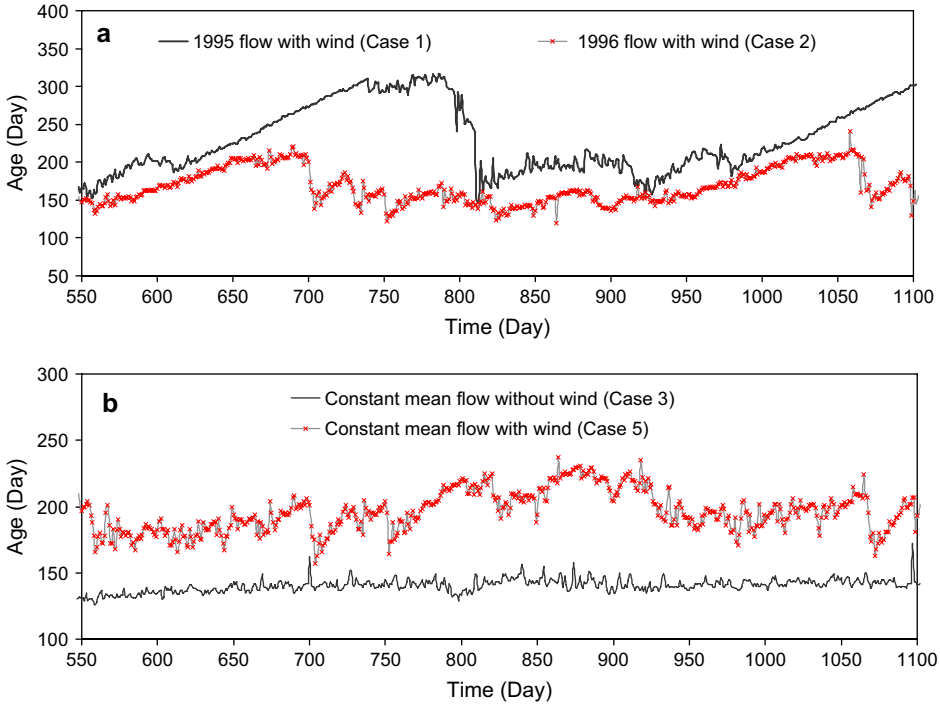

Fig. 3. Time series distribution of age of water near the Bay mouth at Station A. Top panel (a) is results of Cases 1 and 2. (Solid line is Case 1 with observed 1995 flow and wind, thin line with × is Case 2 with observed 1996 flow and wind). Bottom panel (b) is results of Cases 3 and 5 (solid line is Case 3 with long-term mean flow and without wind, and thin line with × is Case 5 with long-term mean flow and real-time 1996 wind).

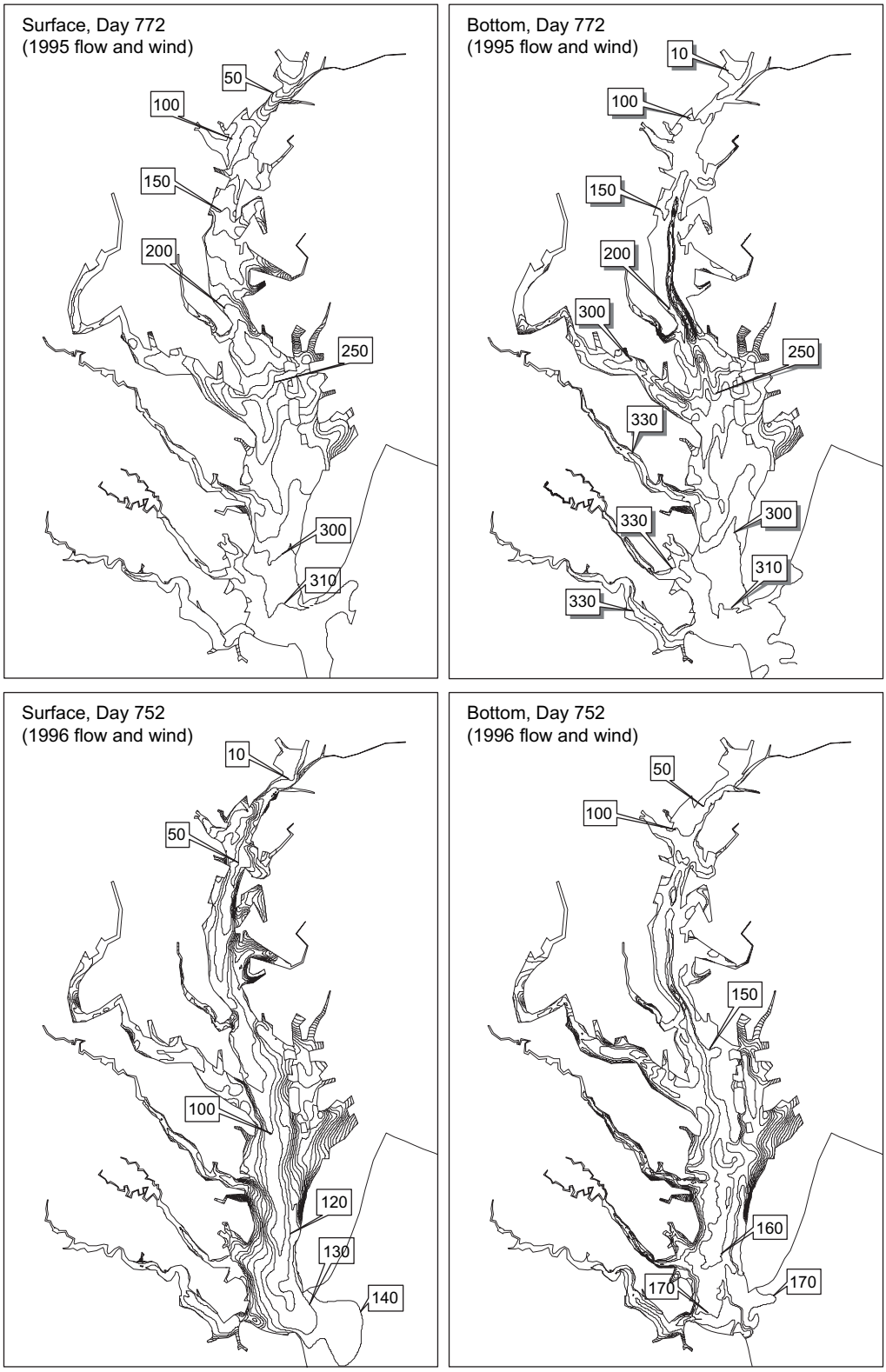

Fig. 4. Distribution of age of water at the surface and the bottom at Day 772 and Day 752, respectively, for the 1995 and 1996 conditions. (Left panel shows water age at the surface and the right panel shows the water age at the bottom. Contour intervals are 10–50 days.)

of the Bay and relatively high age in shallow areas adjacent to the shoreline at Day 752 in Case 2 (Fig. 4). Although the model grid resolution is not fine enough to reveal detailed lateral variation, the result suggests that materials are transported out of the estuary more rapidly in the middle of the channel under the 1996 condition when the flow rate is high. This tongue-shaped pattern resembles the general surface residual current distribution with large residual current in the middle

of the channel and low residual current at the shallow areas adjacent to the deep channel (Hood et al., 1999). This pattern of residual current distribution is expected to be more pronounced under the high flow condition. However, the tongue-shaped pattern disappears at Day 772 in Case 1 and the lateral age variations decrease. This suggests that the influences of wind and other factors become more pronounced under the low flow condition in addition to decreasing the stratification as the flow rate decreases.

As freshwater inflow changes, it results in the change of estuary stratification, which in turn affect the age. The competing influences of river flow and turbulent mixing in an estuary create a time-mean circulation that causes fresher water outflow near the surface and saltier inflow near the bottom (Pritchard, 1952). This pattern of residual flow is referred to as gravitational circulation. It is expected that the vertical age distribution varies as estuarine stratification changes. However, wind can either enhance the stratification or increase vertical mixing to reduce stratification depending on the wind direction. Fig. 5 shows the vertical age distribution at Days 772 and 752 along the main stem of the Bay from the headwater to the mouth of the Bay for Cases 1 and 2. The vertical age distribution shows that the age is homogeneous vertically to the depth above 12 m in Case 1 and the layered distributions only occur in the deep channel. However, the vertical age distribution of Case 2 differs from that of Case 1 significantly. The pattern of vertical age distribution resembles the pattern of salinity stratification with low age at the surface and high age at the bottom. The age difference between the surface and the bottom is more than 60 days in the deep channel. The variations of the age distribution are consistent with the density distributions (not shown), which are caused by gravitational circulation. Therefore, the age difference between the surface and the bottom increases as river inflow increases. It appears that the age difference between the surface and the bottom reduces at the lower Bay regions comparing it to the middle Bay regions, presumably due to the decrease of water depth and increase of wind-induced mixing. Although the age ''stratification'' pattern is observed in the James River estuary (Shen and Lin, 2006), the ''stratification'' effect is noticeably intensified in the main channel of the Bay. The results suggest that the gravitational circulation is quite significant in the Bay, especially in the deep channels under the high flow condition. The freshwater discharge from the Susquehanna River moves more rapidly out of the mouth as the stratification increases.

4.2. Age of water of major tributaries

The model simulations were also conducted for four major tributaries, namely the Potomac, Rappahannock, York, and James Rivers. AW were calculated by releasing a tracer along with freshwater continuously from the fall line of each tributary. For the York River, the tracers ware released continuously from two tributaries, the Mattaponi and Pamunkey Rivers, simultaneously at the headwaters of these tributaries upstream of the York River. The model configurations are the same as for Cases 1 and 2, except that the tracers are released at the fall line of each tributary. For each tributary, the model was executed twice under the 1995 and 1996 conditions, respectively. The vertical mean ages along the middle of the channel of each tributary at Day 772 and Day 752 are shown in Fig. 6. These results correspond to the maximum and minimum

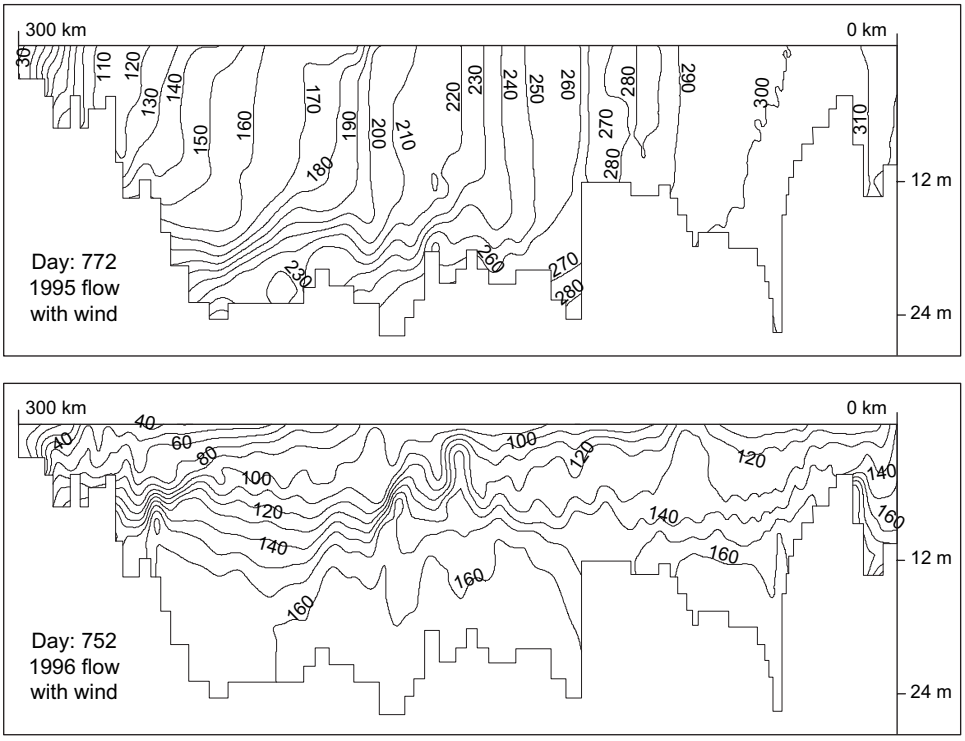

Fig. 5. Vertical distributions of age of water at Day 772 and Day 752, respectively, for the 1995 and 1996 conditions.

ages during the model simulation period. Because the vertically averaged ages are plotted and the depths at different locations are different, the age values at some locations may exceed the values at locations immediately downstream if depths at these downstream locations are much shallower and the age at the bottom is less than that at the upstream. The age at the mouth is higher at each tributary under the low flow condition than the age under the high flow condition. For the 1995 and 1996 conditions, it can be seen that it requires approximately 108 and 50 days, respectively, for a water parcel to be transported from the headwater to the mouth of the James River, whereas it takes 214 and 106 days, respectively, to travel to the mouth of the Potomac River. For the York River, the ages at the mouth are approximately 136 and 62 days, respectively, for the 1995 and 1996 conditions. The ages are higher than the ages computed based on the constant flow conditions by Shen and Haas (2004), which were 100 and 55 days, respectively, for mean and high flows. The differences can be attributed to the variations of discharge and other forcing conditions. The current model results are within the same range, although different models have been used. The results show that the James River has the shortest age at the mouth among the three Virginia estuaries, namely the James, York, and Rappahannock Rivers. The results also agree with the characteristics of residual current in these three estuaries, for which the James River has the strongest residual current (Kuo and Neilson, 1987).

4.3. Influences of discharge

The characteristics of long-term transport processes for a dissolved substance depend primarily on the low frequency and mean motions of the water in an estuary, which is a function of freshwater discharge, tide, wind, and estuarine gravitational circulation. The freshwater variation is one of the dominant factors controlling the transport processes. The river flow with low density sets the basic stratification, which is then mixed vertically either by the growth of the tidal bottom boundary layer or by shear instability (Nunes Vaz et al., 1989; MacCready, 1999). The strength of density-induced circulation plays a critical role in long-term transport.

To test the influence of freshwater discharge on age distribution, Cases 3 and 4, two model simulations with different constant freshwater discharges (see Table 1), were conducted. The constant mean flows of 1200 $m^3 s^{-1}$ and 2430 $m^3 s^{-1}$ discharged from the Susquehanna River were used for Cases 3 and 4, respectively. The flows correspond to the long-term mean and 90th percentile flows of the USGS station (Station 01578310) at the downstream end of the Susquehanna River. Total flow discharged into the Bay from other tributaries is 852 $m^3 s^{-1}$ for both Cases. The total flow of Case 4 increases about 60%. Both model simulations were forced by salinity and tide at the offshore open boundary using 1996 observed data. No wind forcing was applied.

Figs. 7a,b shows the surface age distributions under the mean and high flow conditions at Day 752 during the model simulation period. The age decreases as freshwater discharge increases. The 100-day contour is located above the Potomac River mouth under mean flow condition. It moves to the mouth of the Rappahannock River under the high flow condition. The surface age at the mouth is approximately 140 days and 115 days, respectively. The surface age is reduced by

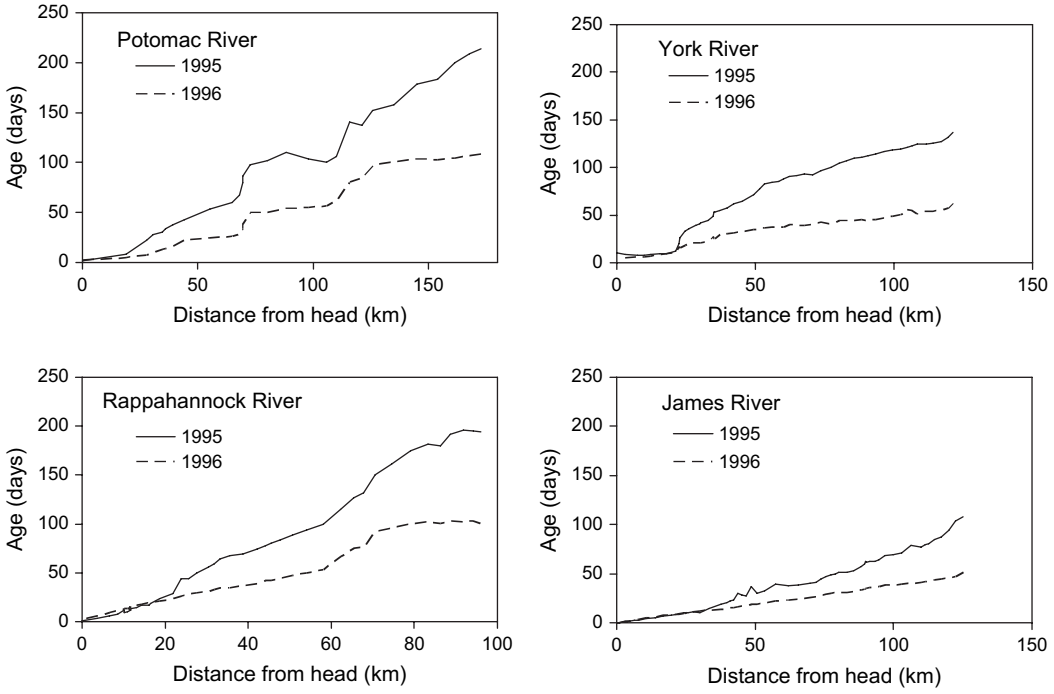

Fig. 6. Distribution of the vertical mean age of water of four major tributaries of the Chesapeake Bay in 1995 and 1996.

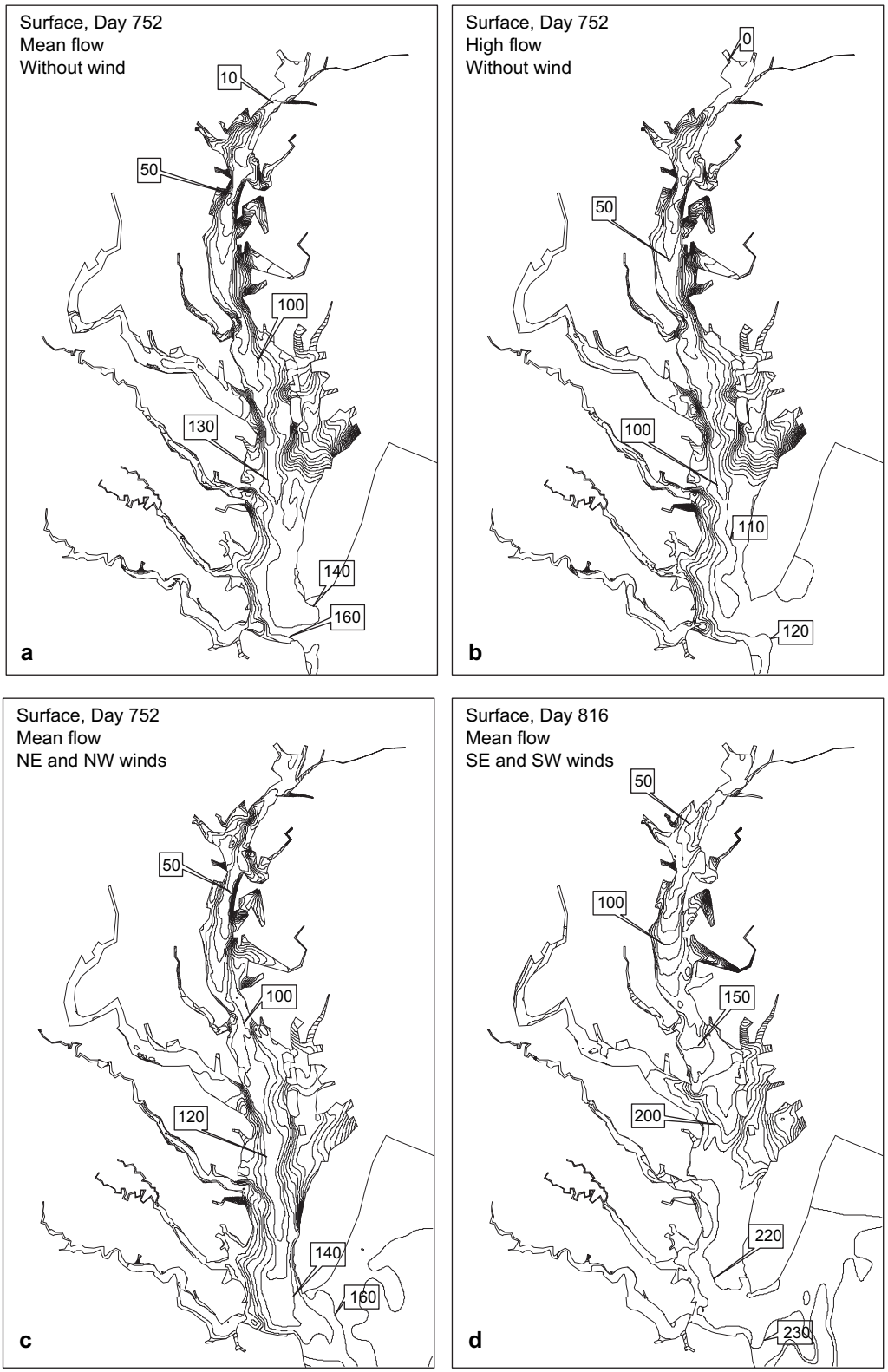

Fig. 7. Distribution of surface age of water under different conditions ((a) is mean-flow without wind (Case 3); (b) is high-flow without wind (Case 4); (c) is mean-flow with NE-NW winds (Case 6); and (d) is mean-flow with SE-SW wind (Case 7)).

approximately 25 days (approximately 18%) at the mouth under the high flow condition. In both cases, the age differences at the mouth between the surface and bottom are less than 9 days.

The mean freshwater residence time (or flushing time) is often used to represent the overall flushing ability of the Bay. Nixon et al. (1996) estimated that the freshwater residence time of the Bay is 7.8 months (248 days). Kemp et al. (2005)

estimated that the mean residence time of the Bay is 90–180 days. The flushing time (T_f) of an estuary can be estimated as:

$$T_f = \frac{fV}{Q} \tag{4}$$

where Q is river inflow and f is the mean fractional freshwater concentration in the estuary, given by:

$$f = \frac{1}{V}\int \frac{S_0 - S}{S_0}\mathrm{dv} \tag{5}$$

where S_0 and S are the sea water salinity and the salinity in the estuary, and V is the volume of the waterbody. Using the surface area of Chesapeake Bay as $11{,}542 \times 10^6$ m^2, a mean depth of 6.8 m (Nixon et al., 1996; Dettmann, 2001), a mean flow of 2052 m^3 s^{-1}, and a high flow of 3282 m^3 s^{-1}, the estimated fractions of freshwater are approximately 0.33 and 0.36, respectively, under the mean flow and high flow conditions based on the model results if S_0 is 34 psu. The estimated flushing times are 140 days and 96 days, respectively. The estimated values are very close to the vertical mean ages at the mouth, which are 145 and 117 days, respectively.

4.4. Influences of offshore boundary conditions

The influence of offshore boundary conditions, i.e., the variation of salinity and tide, can be investigated by examining the time series of age distribution under constant flow rates without wind. Case 3 computed age under a constant mean flow of 2052 m^3 s^{-1} without wind. An example of time series of surface age distribution at Station A near the mouth for Case 3 is shown in Fig. 3b (bottom panel). The age varies from 126 to 172 days. The mean age is 140 days with a standard deviation of 4.7 days. A similar model simulation was conducted with mean high flow (Case 4). The surface age varies from 101 days to 143 days with a mean age of 113 days (not shown in figure). Because a constant flow rate is used for the model simulation and no wind forcing is applied to the surface, the age variation can be attributed to the variations of tide and salinity at the offshore. It can be seen that the age variations are less than 15 days most of the time, except for a couple of spikes that occurred during the simulation period in general.

4.5. Influence of wind

The model results of mean flow shows that the age decreases substantially for most of the time without wind forcing compared to the results under the 1996 condition. This occurred even though the 1996 freshwater discharge was higher than the long-term mean flow for most of the period. This suggests that wind plays an important role on the age distribution. The influence of wind on estuarine circulation has been recognized for many years (Officer, 1976; Wang, 1979). In a shallow estuary, the residence time can vary by more than a factor of three in response to variations in wind-induced flushing (Geyer, 1997). Officer (1976) provides a classic analytic solution for the density-induced estuarine circulation. The result suggests that the estuarine gravitational circulation depends on the wind direction. The downstream wind will enhance the circulation, while the upstream wind has the tendency to reduce the stratification. Scully et al. (2005) reported that wind plays an important role in straining the along-channel density field and also showed evidence for wind mixing resulting in a significant reduction in the vertical density stratification.

To investigate the influence of wind-induced transport, three model experiments (Cases 5, 6, and 7 with different wind forcings) were conducted under the constant mean flow condition. For these simulations, the model configuration is the same as that for Case 2, except that different wind stresses were applied at the surface (Table 1). For Case 5, the observed 1996 wind data obtained from three stations (Baltimore, Patuxent River Naval Air Station, and Norfolk International Airport) were used to force the model. For Cases 6 and 7, only the northeasterly and northwesterly wind components and southeasterly and southwesterly wind components, respectively (i.e., those obtained from the 1996 observed data). Fig. 8 shows the time series of wind distribution at Patuxent River Naval Air Station. Wind directions alternate from SE-SW to NE-NW during the year. The frequency of occurrence of the north and south wind components is nearly 50% during the year. The magnitudes of SE-SW winds are similar to those of NE-NW winds. An example of time series of surface age at Station A near the Bay with the wind forcing for Case 5 is shown in Fig. 3 for comparison. Compared to the age distribution resulting from the simulation without wind forcing, the age varies dramatically from 157 to 230 days with a mean age of 196 days. The averaged surface age increases more than 40 days. It shows that the influence of wind on age is very significant in the Bay.

The influence of the wind on spatial and temporal age distribution depends on both the magnitude and direction of the wind. Figs. 7c,d show the model results of surface age distributions with different wind forcing components. With the NE-NW wind forcing, the age distribution is very similar to the age distribution without wind forcing (Fig. 7a). The result seems different from the classical theory based on a simple uniform channel. It indicates that the wind impact on transport is more complex in an estuary with spatially varying bathymetry. Since the axis of the estuary does not align in the north-south direction, the lateral influence cannot be neglected, even if only applying a downstream wind forcing. The surface age distribution at Day 816 with SE-SW winds is shown in Fig. 7d, which corresponds to the maximum surface age during the model simulation period. The surface age at the mouth is 230 days. The age increases 90 days compared to the age distribution without wind forcing. It appears that the upstream wind plays a dominant role in controlling the long-term transport under the 1996 condition.

It is expected that both the magnitude and direction of the wind forcing will affect the estuarine stratification, thus affecting the age. Fig. 9 shows the vertical age distribution along the main stem of the Bay. It can be seen that the age becomes

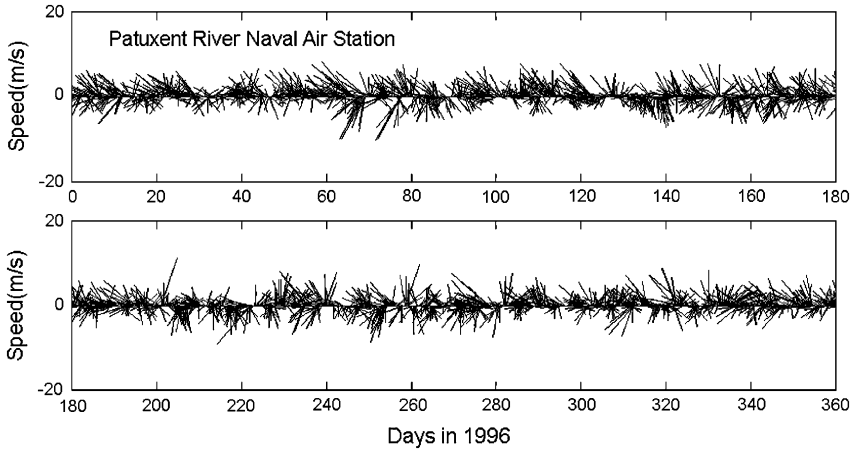

Fig. 8. The 1996 wind vector distribution at Patuxent River Naval Air Station.

more homogeneous vertically in the lower Bay when the model is forced by SE-SW winds. In the middle region of the Bay, the vertical mixing extends to a depth of 12 m when the model is forced by SE-SW wind. The upstream wind causes strong lateral and vertical mixing. Consequently, the gravitational circulation is reduced, thereby increasing the transport time. In contrast, the Bay becomes more stratified when applying NE-NW winds. The development of the strong gravitational circulation results in freshwater being transported out of the Bay more rapidly. The results are consistent with the impact of wind on salinity distribution simulation reported by Li et al. (2005). They also found that wind is critical for modeling salinity stratification correctly in the Bay.

One phenomenon that cannot be examined in detail is how much influence on wind is contributed from Ekman transport caused by remote offshore wind. Wang (1979) shows that the sub-tidal water level fluctuation in the lower portions of the Bay was strongly controlled by the remote winds. Could this partially explain why AW changes more rapidly in the lower Bay with the wind forcing? This issue remains to be resolved, but is beyond the scope of this paper.

5. Discussion

5.1. Transport in upper Bay and lower Bay

By examining the age distribution resulting from simulations of the 1995 and 1996 conditions, we note that the transport time, represented by age, in the regions above the Patuxent River exceeds that in the regions below the Patuxent

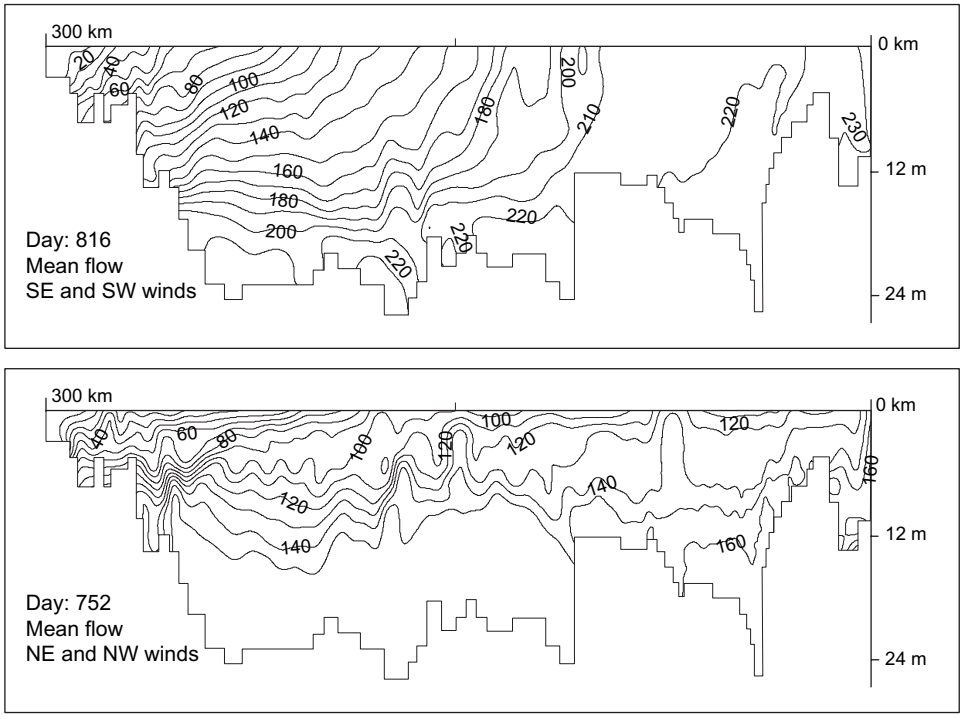

Fig. 9. Vertical distributions of age of water at Day 816 and Day 752, respectively, for SE-SW and NE-NW winds.

River. For example, it requires approximately 210 and 80 days, respectively, for a water parcel to be transported from the headwater of the Bay to the mouth of the Patuxent River at the surface for Cases 1 and 2. This contrasts with only 100 and 50 days that are required for a water parcel to be transported from the Patuxent River mouth to the mouth of the Bay at the surface for Cases 1 and 2, respectively, although the distances are almost identical (Fig. 4). The cause of this is complex and a number of factors can possibly contribute to the difference, including change of channel geometry, fetch, and difference of wind patterns.

It is noteworthy that the ages at the mouth of Patuxent River are 80 and 60 days, respectively, for Cases 3 and 4 under constant mean and high flow conditions without wind forcing. The age differences between the Patuxent River and the mouth of the Bay are 60 and 55 days, respectively, for the mean and high flows. The difference is reduced under the mean flow condition. Under the high flow condition, the age difference is almost the same. Although the total flow discharged from tributaries other than Susquehanna River is less that 41%, it might contribute to the reduced age of the water in the lower Bay. A sensitivity model run was conducted by setting the inflows to the Potomac, Rappahannock, York, and James Rivers to zero under the constant mean flow condition without wind. The model results show that the age at the mouth increases approximately 10 days. Therefore, the freshwater from the Virginia tributaries are not a dominant factor for reducing AW.

The contribution of wind-induced transport on age distribution becomes evident upon examining the model results with wind forcing (Figs. 7c,d). It can be seen that the age differences between the headwater of the Bay to the mouth of the Patuxent River and from Patuxent River mouth to the Bay mouth are 90 and 50 days, respectively, when the model is forced by NE-NW winds. These differences are 140 and 85 days, respectively, when the model is forced by SE-SW winds. When applying SE-SW winds, the age difference between upper and lower portions of the Bay increases. In both cases, the age differences in the upper and lower portions of the Bay increase compared to the model results without wind forcing. It appears that the age changes more rapidly in the lower portion of the Bay with wind forcing. This suggests that wind-induced circulation and mixing contributes to the difference of age distributions in the lower and upper portions of the Bay.

5.2. Interpretation of surface chlorophyll-a spatial distribution.

The metric of water age could be useful in the interpretation of spatial patterns of phytoplankton distribution. Because natural waters are open systems that receive both inflow of matter and energy from external systems, changing physical conditions can act as a driving force controlling transport and retention of any substances. To quantitatively describe the interactions between physical, chemical, and biological processes, one must first consider the relevant temporal and spatial transport scales (Nihoul, 1981; Giller et al., 1992; Mann and Lazier, 1996). The water age calculation thus can be a tool to provide the retention timescale associated with spatial locations for the diagnosis of bio-geo-chemical processes. For example, the annual cycle of phytoplankton in the Bay is dominated by a spring "bloom" that constitutes the highest biomass for the year. There is a strong interest in being able to predict this event, either by direct measurement or use of the numerical model. However, the spring chlorophyll maximum is very difficult to predict in terms of its timing, position, and magnitude of its peak because this requires that all conditions including nutrient (C, N, P, S) concentrations, light, temperature, and physical conditions be satisfied at a given time and location. In the Chesapeake Bay, Bay-wide chlorophyll-a concentrations measured by aircraft are available in 1995 and 1996 (Chesapeake Bay Remote Sensing Program: http://www.cbrsp.org) (Harding et al., 2001). This offers an opportunity to compare the large-scale surface chlorophyll patterns of the transport timescale for the dry year (1995) and the wet year (1996) simultaneously. From chlorophyll-a spatial distributions in May 22, 1995, and 1996, we can recognize that the location of the major bloom for 1995 is significantly further upstream than that of 1996. Given that the spring freshet started about January 29 for 1995 and February 1 for 1996, it took approximately 110 days to encounter the major spring blooms for both years. Based on our model simulation, it is estimated that peak nutrient inputs associated with the freshwater pulse should occur somewhere just downstream of Baltimore Harbor in 1995 while the peak nutrient inputs should occur between the Choptank River and south of the Patuxent River mouth in 1996. This suggests that the 1995 spring bloom should occur approximately 70 km upstream from that of 1996. In a more rigorous analysis, the concentration field of the nutrients should also be considered in conjunction with the mean water age calculation, since it may not require a significant amount of nutrients to stimulate the bloom when it is constrained to limiting conditions. The transport timescale provides the underlying dynamics that may partially account for the location of these bloom events.

6. Conclusions

The concept of age of water is applied to the Chesapeake Bay to assess the long-term transport timescales. The age calculation was formulated with the intention to provide spatial distributions of transport characteristics in a numerical model simulation whereby both advective and diffusive processes are taken into account. The characteristics of transport and mixing of a dissolved pollutant depend primarily on low frequency and mean motions of water. Freshwater input, density-induced circulation, and surface wind stress play important roles in controlling the long-term transport in the estuary. The model results have shown that the age varies drastically under different dynamic conditions. The age at the Bay mouth can vary from 120 days to more than 300 days, respectively, under high flow conditions without wind and under low flow conditions with strong upstream winds. The density-driven

circulation is one of the dominant factors that enhance the transport. The freshwater discharged into the Bay will be transported out of the Bay much faster when the estuary becomes more stratified. The southwesterly or southeasterly wind has the tendency to increase both lateral and vertical mixing and to reduce gravitational circulation and, thus, to reduce the transport of freshwater out of the Bay. The transport time can increase 50% when the estuary is forced by the upstream wind components. In contrast, the downstream wind has limited impact on overall transport under the 1996 hydrodynamic condition.

The model results suggest that using a conservative artificial tracer in a three-dimensional observed model provides a quantitative measure of the mean long-term transport timescale of the Chesapeake Bay. The age of tracer provides an adequate methodology to assess the long-term accumulative effect caused by variations of river inflows, stratification, and wind forcing. With the use of the age of tracer as an indicator, the characteristics of long-term transport in the Bay can be quantified.

Acknowledgements

The authors wish to thank three anonymous referees for their valuable comments. The author J. Shen was partially supported by the State Key Laboratory of Estuarine and Coastal Research, East China Normal University (SKLEC No.200602) for this study. We thank our colleague Mr. Mac Sisson for his comments and editing. This is contribution number 2843 from the Virginia Institute of Marine Science, School of Marine Science, College of William and Mary, Virginia.

References

Beckers, J.M., Delhez, E., Deleersnijder, E., 2001. Some properties of generalized age-distribution equations in fluid dynamics. Journal of Applied Mathematics 61 (5), 1526–1544.

Bolin, B., Rodhe, H., 1973. A note on the concepts of age distribution and transit time in natural reservoirs. Tellus 25, 58–63.

Boynton, W.R., Garber, J.H., Summers, R., Kemp, W.M., 1995. Inputs, transformations, and transport of nitrogen and phosphorus in Chesapeake Bay and selected tributaries. Estuaries 18, 285–314.

Carpenter, S.R., Caraco, N.F., Correll, D.L., Howarth, R.W., Sharpley, A.N., Smith, V.H., 1998. Nonpoint pollution of surface waters with phosphorus and nitrogen. Ecological Application 8, 559–568.

Cerco, C.F., Cole, T.M., 1994. Three-Dimensional Eutrophication Model of Chesapeake Bay; Vol. 1, Main report. U.S. Army Corps of Engineers Waterways Experiment Station, Vicksburg, MS, 658 pp.

Cerco, C.F., Meyers, M., 2000. Tributary refinements to Chesapeake Bay model. Journal of Environmental Engineering 126 (2), 164–174.

Cerco, C.F., Johnson, B.H., Wang, H.V., 2002. Tributary Refinements to the Chesapeake Bay Model. ERDC TR-02–4. U.S. Army Engineer Research and Development Center, Vicksburg, MS.

Deleersnijder, E., Campin, J.M., Delhez, E.J.M., 2001. The concept of age in marine modeling, I. Theory and preliminary model results. Journal of Marine Systems 28, 229–267.

Delhez, E.J.M., Carabin, G., 2001. Integrated modeling of the Belgian coastal zone. Estuarine, Coastal and Shelf Science 53, 477–491.

Delhez, E.J.M., Campin, J.-M., Hirst, A.C., Deleersnijder, E., 1999. Toward a general theory of the age in ocean modeling. Ocean Modelling 1, 17–27.

Delhez, E.J.M., Heemink, A.W., Deleersnijder, E., 2004. Residence time in a semi-enclosed domain from the solution of an adjoint problem. Estuarine, Coastal and Shelf Science 61, 691–702.

Dettmann, E.H., 2001. Effect of water residence time on annual export and denitrification of nitrogen in estuaries: a model analysis. Estuaries 24 (4), 481–490.

Edinger, J.E., Brady, D.F., Geyer, J.G. 1974. Heat Exchange and Transport in the Environment. Report 14, EPRI Publication No. 74-049-00-3, Prepared of Electric Power Research Institute, Palo Alto, CA.

Fisher, C.W., 1987. Tidal Circulation in Chesapeake Bay. Dissertation. Old Dominion University, Norfolk, VA, 273 pp.

Geyer, W.R., 1997. Influence of wind on dynamics and flushing of shallow estuaries. Estuarine, Coastal and Shelf Science 44, 713–722.

Giller, P.S., Hildrew, A.G., Raffaelli, D.G., 1992. Aquatic Ecology: Scale, Pattern, and Process. The 34th Symposium of British Ecological Society with American Society of Limnology and Oceanography. University College, Cork, 649 pp.

Harding Jr., L.W., Miller, M.E., Swift, R.N., Wright, C.W., 2001. Aircraft remote sensing. In: Steele, J., Thorpe, S., Turekian, K. (Eds.), Encyclopedia of Ocean Sciences. Academic Press, London, UK, pp. 113–122.

Hicks, S.D., 1964. Tidal wave characteristics of Chesapeake Bay. Chesapeake Science 5, 103–113.

Hood, R.R., Wang, H.V., Purcell, J.E., Houde, E.D., Harding, L.W., 1999. Modeling Particles and pelagic organisms in Chesapeake Bay: convergent features control plankton distributions. Journal of Geophysical Research 104 (C1), 1223–1243.

Johnson, B.H., Heath, R.E., Hsieh, B.B., Kim, K.W., Butler, H.L., 1991a. Development and Verification of a Three-Dimensional Numerical Hydrodynamic, Salinity, and Temperature Model of Chesapeake Bay; Vol. 1, Main Text and Appendix D, Technical Report HL-91–7, U.S. Army Engineer Waterways Experiment Station, Vicksburg, MS.

Johnson, B.H., Heath, R.E., Hsieh, B.B., Kim, K.W., Butler, H.L., 1991b. Validation of three-dimensional hydrodynamic model of Chesapeake Bay. Journal of Hydraulic Engineering, ASCE 119, 2–20.

Kemp, W.M., Boynton, W.R., Adolf, J.E., Boesch, D.F., Boicourt, W.C., Brush, G., Cornwell, J.C., Fisher, T.R., Gilbert, P.M., Hagy, J.D., Harding, L.W., Houde, E.D., Kimmel, D.G., Miller, W.D., Newell, R.I.E., Roman, M.R., Smith, E.M., Stevenson, J.C., 2005. Eutrophication of Chesapeake Bay: historical trends and ecological interactions. Marine Ecology Progress Series 303 (21), 1–29.

Kuo, A.Y., Neilson, B.J., 1987. Hypoxia and salinity in Virginia estuaries. Estuaries 10 (4), 277–283.

Li, M., Zhong, L., Boicourt, W.C., 2005. Simulations of Chesapeake Bay estuary: sensitivity to turbulence mixing parameterizations and comparison with observations. Journal of Geophysical Research 110 (C12), C12004. doi:10.1029/2004JC002585.

MacCready, P., 1999. Estuarine adjustment to changes in river flow and tidal mixing. Journal of Physical Oceanography 29, 708–726.

Mann, K.H., Lazier, J.R.N., 1996. Dynamics of Marine Ecosystems: Biological-Physical Interactions in the Oceans, second ed. Blackwell Scientific Publication, Boston, pp. 466.

Nihoul, J.C.J., 1981. Marine hydrodynamics at ecological scales. In: Nihoul, J.C.J. (Ed.), Ecohydrodynamics: Proceedings of the 12th International Liege Colloquium on Ocean Hydrodynamics. Elsevier/North-Holland, Scientific Pub. Co., Amsterdam.

Nixon, S.W., 1995. Coastal marine eutrophication: a definition, social causes, and future consequences. Ophelia 41, 199–219.

Nixon, S.W., Ammerman, J.W., Atkinson, L.P., Berounsky, V.M., Billen, G., Boicourt, W.C., Boynton, W.R., Church, T.M., DiToro, D.M., Elmgren, R., Garber, J.H., Giblin, A.E., Jahnke, R.A., Owens, N.J.P., Pilson, M.E.Q., Seitzinger, S.P., 1996. The fate of nitrogen and phosphorus at the land-sea margin of the North Atlantic Ocean. Biogeochemistry 35, 141–180.

Nunes Vaz, R.A., Lennon, G.W., deSilva Samarasinghe, J.R., 1989. The negative role of turbulence in estuarine mass transport. Estuarine, Coastal and Shelf Science 28, 5465–5480.

Officer, C.B., 1976. Physical Oceanography of Estuaries (and Associated Coastal Waters). Wiley, New York.

Park, K., Jung, H.-S., Kim, H.-S., Ahn, S., 2005. Three-dimensional hydrodynamic-eutrophication model (HEM-3D): application to Kwang-Yang Bay, Korea. Marine Environmental Research 60, 171–193.

Pritchard, D.W., 1952. Salinity distribution and circulation in the Chesapeake Bay estuarine system. Journal Marine Research 11, 106–123.

Schubel, J., Pritchard, W., 1986. Responses of upper Chesapeake Bay to variations in discharge of Susquehanna River. Estuaries 9, 236–249.

Scully, M.E., Friedrichs, C., Brubaker, J., 2005. Control of estuarine stratification and mixing by wind-induced straining of the estuarine density field. Estuaries 28 (3), 321–326.

Shen, J., Haas, L., 2004. Calculating age and residence time in the tidal York River using three-dimensional model experiments. Estuarine, Coastal and Shelf Science 61, 449–461.

Shen, J., Lin, J., 2006. Modeling study of the influences of tide and stratification on age of water in the tidal James River. Coastal and Shelf Science 68 (1–2), 101–112.

Sheng, Y.P., 1986. A Three-Dimensional Mathematical Model of Coastal, Estuarine, and Lake Currents Using a Boundary-Fitted Grid. Report No. 585, A.R.A.P. Group of Titan Systems, New Jersey, Princeton, NJ.

Takeoka, H., 1984. Fundamental concepts of exchange and transport time scales in a coastal sea. Continental Shelf Research 3 (3), 322–326.

Wang, D.-P., 1979. Subtidal sea level variations in the Chesapeake Bay and relations to atmospheric forcing. Journal of Geographic Research 9, 413–421.

Wang, H.V., Chapman, R.S., 1995. Application of vertical turbulence closure schemes in the Chesapeake Bay circulation model – a comparative study. In: Spaulding, M., Cheng, R.T. (Eds.), Estuarine and Coastal Modeling, pp. 283–297. New York, ASCE, 730 pp.

Wang, H.V., Johnson, B., 2000. Validation and application of the second generation three dimensional hydrodynamic model of Chesapeake Bay. Water Quality and Ecosystem Modeling 1 (1), 51–90.

Xu, J., Chao, S., Hood, R.R., Wang, H., Boicourt, W.C., 2002. Assimilating high-resolution salinity data into a model of a partially mixed estuary. Journal of Geophysical Research 107, (C7), 1–14.

Zimmerman, J.T.F., 1976. Mixing and flushing of tidal embayments in the Western Dutch Wadden Sea, Part I: distribution of salinity and calculation of mixing time scales. Netherlands Journal of Sea Research 10, 149–191.

Available online at www.sciencedirect.com
ScienceDirect
Estuarine, Coastal and Shelf Science 74 (2007) 599–609
ESTUARINE COASTAL AND SHELF SCIENCE
www.elsevier.com/locate/ecss

Comparison of high spatial resolution trace metal distributions with model simulations for surface waters of the Gulf of Cadiz

J.M. Beckers [a,*], E.P. Achterberg [b], Ch. Braungardt [c]

[a] University of Liège, Sart-Tilman B5, B-4000 Liège, Belgium
[b] National Oceanography Centre, Southampton, University of Southampton, European Way, Waterfront Campus, Southampton, SO14 3ZH, UK
[c] School of Earth, Ocean and Environmental Sciences, University of Plymouth, Plymouth, PL4 8AA, UK

Received 20 September 2006; accepted 20 December 2006
Available online 8 March 2007

Abstract

A multidisciplinary study in the Gulf of Cadiz is revisited, using additional diagnostic modelling tools. The dissolved trace metal (Cu, Ni, Zn, Co) distributions in the Gulf of Cadiz are analysed using modelled tracer evolutions, field observations and the concept of tracer ages. This study shows that a significant part of the observed metal distributions can be explained by the metal inputs of three river systems (Guadiana, Rio Tinto and Odiel, Guadalquivir) discharging into the Gulf of Cadiz, while the remainder of the signal is most likely associated with the benthic metal remobilisation along the shelf of this coastal region.

Keywords: trace metals; tracers; Gulf of Cadiz; model

1. Introduction

In June 1997 and October 1998, surveys were carried out in the Gulf of Cadiz (Fig. 1), organized within the multidisciplinary project TOROS (Tinto-Odiel-River-Ocean Study). The surveys were designed to study the trace metal and nutrient biogeochemistry in the coastal waters influenced by the discharges of the rivers Guadiana, Tinto, Odiel and Guadalquivir which drain parts of the southern Iberian Peninsula. The freshwater discharges of the rivers in this region are relatively minor, but their metal loads are strongly enhanced. Indeed, the Tinto-Odiel, Guadiana and Guadalquivir rivers drain the largest sulphide mineralisation in the world (Leistel et al., 1998), and weathering and mining activities have led to extremely high metal concentrations and acidity (pH <3) in the rivers. The Gulf of Cadiz is responsible for 5–10% of fish and shellfish catches of Spain and Portugal, and hence it is of great importance to further our understanding of trace metal biogeochemistry in this coastal region and assess the potential influences of metals on ecosystem functioning. The TOROS project has produced a number of publications on its findings in recent years (Elbaz-Poulichet et al., 2000, 2001a,b,c; Leblanc et al., 2000; Braungardt et al., 2003; Achterberg et al., 2003), which showed that metals are only partly removed in the Tinto and Odiel rivers (Braungardt et al., 2003), the rivers have an important regional impact, and the river signals can be detected in the waters flowing eastwards through the Straits of Gibraltar (Elbaz-Poulichet et al., 2001c). The river systems hence have a wider importance and the findings from the TOROS project can help to explain the enhanced trace metal concentrations previously observed in surface waters of the Mediterranean Sea (Boyle et al., 1985).

The application of high spatial and temporal resolution ship-board dissolved trace metal measurements in the Gulf of Cadiz has provided some of the first highly detailed coastal trace metal distributions (Achterberg et al., 1999). The complex nature of the metal distributions apparent in the Gulf of Cadiz (see below) is strongly related to the various sources

* Corresponding author.
E-mail address: jm.beckers@ulg.ac.be (J.M. Beckers).

0272-7714/$ - see front matter © 2007 Elsevier Ltd. All rights reserved.
doi:10.1016/j.ecss.2006.12.020

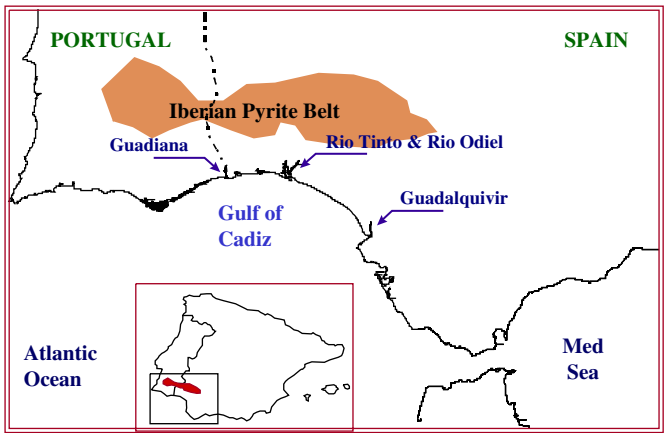

Fig. 1. Gulf of Cadiz and part of the Western Mediterranean Sea, with the locations of the mouths of the rivers (Guadiana, Rio Tinto and Odiel, Guadalquivir) draining the Iberian Pyrite Belt.

(riverine and benthic), which exhibit different strengths. However, to further our understanding of the importance of the various trace metal sources in the Gulf of Cadiz, and the behaviour of the different metals, we need to apply novel modelling approaches.

We will address this issue in this publication by using the high resolution TOROS dissolved trace metal data set and the modelling tools developed within the project, with the addition of the novel diagnostic tool "age" (CART, Constituent-oriented Age and Residence time Theory), the theory of which has been developed in recent years (Deleersnijder et al., 2001, 2002, 2006; Delhez and Deleersnijder, 2002; Delhez et al., 2003). This multi-facetted approach will allow us to identify typical time scales affecting metals within the river plumes and aid our understanding of the different biogeochemical behaviours of the metals. Therefore the aim of this work is, through a combination of high spatial resolution field data (Section 2) and novel modelling approaches (Sections 3 and 4), to elucidate trace metal inputs and behaviour in the Gulf of Cadiz (Sections 5 and 6).

2. High spatial resolution dissolved trace metal distributions in the Gulf of Cadiz

High spatial resolution data for dissolved Cu, Ni, Zn and Co were obtained in the Gulf of Cadiz on-board the research vessel Garcia del Cid during cruises in June 1997 (T2) and October 1998 (T4). Continuous underway sampling at ca. 2 m depth was carried out using a fish towed from a crane on the Garcia del Cid (Braungardt et al., 1998). A high volume peristaltic pump transported the water through braided PVC tubing into a continuous filtration system (WCN cellulose nitrate membrane filter, diameter 47 mm, pore size 0.45 μm, Whatman) and the filtrate was carried by a second peristaltic pump through PTFE tubing to an in-line UV digestion unit employed to destroy dissolved organic matter and surfactants that may interfere with the voltammetric analysis of metals (Braungardt et al., 1998). All tubing and filter membranes were acid cleaned prior to use. The pre-treated sample was pumped into two fully automated electrochemical analysers for the determination of Zn/Cu and Ni/Co, respectively. On-line trace metal analysis was carried out using square wave adsorptive cathodic stripping voltammetry, with a method adapted from (Achterberg and Van den Berg, 1994). The limits of detection (LOD) for the multi-elemental on-line determination of Zn/Cu and Ni/Co were $LOD_{Co} = 0.24$ nM, $LOD_{Zn} = 0.81$ nM, $LOD_{Cu} = 0.48$ nM and $LOD_{Ni} = 0.21$ nM. Analyses of certified reference waters for total dissolved Zn, Cu, Ni and Co showed good agreement with certified values for estuarine water (SLEW-2) and coastal seawater (CASS-3). Further details of the automated ship-board measurements are given in Braungardt et al. (1998).

The surveys with the Garcia del Cid covered the shelf and slope area of the Gulf of Cadiz between the Guadalquivir in the east and the Guadiana in the west (Fig. 1). The survey in June 1997 yielded ca. 380 high quality (i.e. >LOD) surface water measurements for dissolved Cu and Ni, and ca. 120 for dissolved Zn and Co. In October 1998 data comprised of ca. 390 values for dissolved Zn and Cu, and ca. 580 for dissolved Ni.

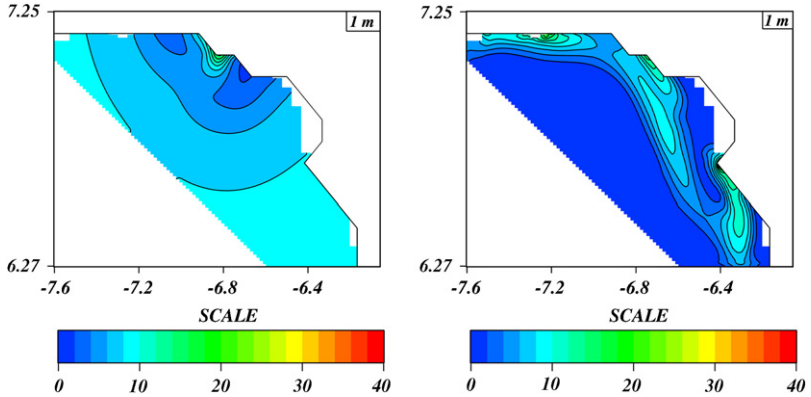

Fig. 2. Co distribution from field data (left panel) and best model fit of the three river sources (right panel) for cruise T2; concentrations in nM.

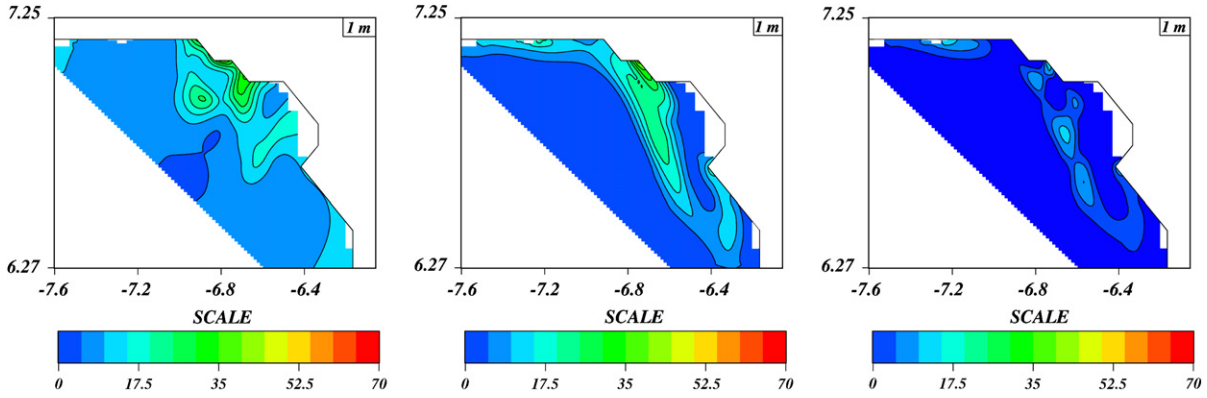

Fig. 3. Cu cruise T2; concentrations in nM.

The cruise data were gridded by a method equivalent to objective analysis (Rixen et al., 2000). Using this approach dissolved trace metal fields for surface waters were obtained that were directly comparable with results from modelling activities. The fields (such as in Fig. 2) were also used to infer discharge concentrations at the river mouths. These concentrations characterize the waters that enter the Gulf of Cadiz and are not necessarily those measured in the freshwater region of the rivers (e.g. (Elbaz-Poulichet et al., 2001a)), because of important metal removal in the high salinity region of estuaries. The TOROS project observed for example extremely enhanced metal concentrations in the freshwater regions of the Tinto and Odiel rivers (up to 11 mM Fe, 2.6 mM Zn, 860 μM Cu, 17 μM Ni, 40 μM Co) as a result of the acid mine drainage from past mining activities in the Iberian Pyrite Belt. During mixing of river with seawater in the estuary, the neutralisation of pH values and the increase in salinity resulted in the partial removal of metals from solution (ca. 76% for Zn, 64% for Cu, 45% for Co and 12% for Ni) through adsorption, coagulation and flocculation processes (Braungardt et al., 2003), with subsequent metal deposition in the estuarine sediments. These processes were largely complete at salinity >33.5 and pH >7.5, above which conservative dissolved metal behaviour was observed in the lower estuary and coastal plume, where the particulate metal concentrations constituted ca. 10% Zn and Ni, 40% Cu and 5% Co of total metal in the water column (Braungardt et al., 2003).

Relatively low net water volumes and high metal concentrations are discharged from the Tinto-Odiel river system, resulting in a distinct metal plume with a small salinity difference relative to the ambient coastal waters (Figs. 2–8). In contrast, the river plume of the Guadalquivir carried a strong low salinity signal coupled with elevated trace metal concentrations. Conservative behaviour of dissolved Zn, Cu and Ni in surface waters was observed along a transect from the mouth of the Guadalquivir in a south-southwesterly direction into the Gulf of Cadiz during the T2, but not the T4 survey (Figs. 2–8). Depth profiles indicated that mobilisation from the bottom sediments could contribute to the dissolved metal concentrations in the Gulf of Cadiz, in particular for Cu and Zn within the Tinto-Odiel plume and off-shore locations (Fig. 9), and during T4 also within the plume of the Guadalquivir. Nickel and Co showed less enrichment in bottom waters compared to mid-column concentrations, indicating a lower potential for sediment-induced increases in their dissolved concentrations.

3. Hydrodynamic model

The hydrodynamic model to which tracer dispersion models are coupled is based on the primitive equation model

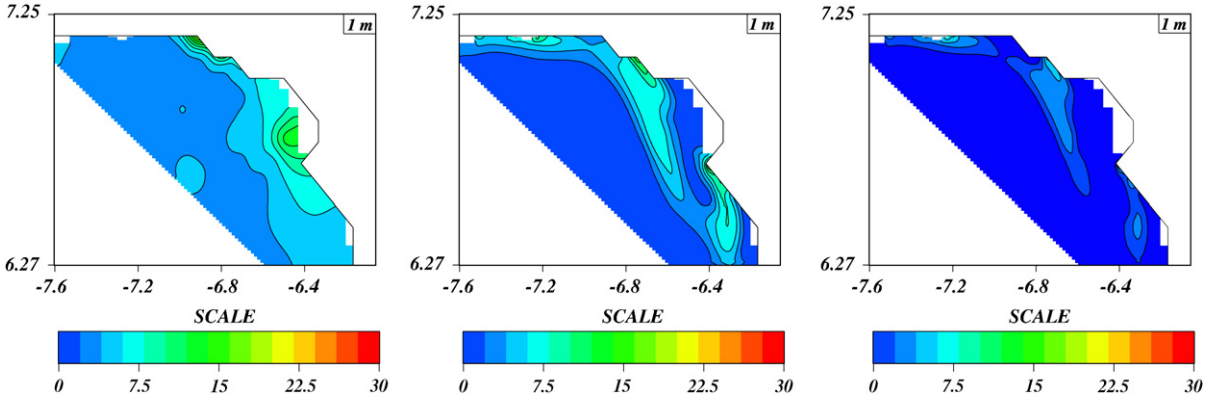

Fig. 4. Ni cruise T2; concentrations in nM.

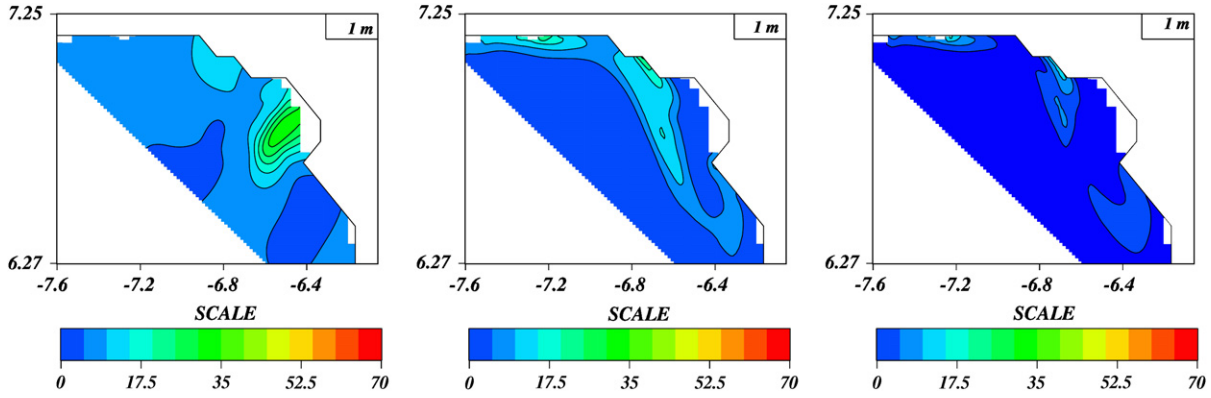

Fig. 5. Zn cruise T2; concentrations in nM.

applied to the Mediterranean Sea (Beckers, 1991). As the Gulf of Cadiz is influenced by both the Atlantic Ocean and the Mediterranean Sea, a nested-model approach was implemented for the version of the Gulf of Cadiz (Nomérange, 1998; Elbaz-Poulichet et al., 2001c). The model is a 3D primitive-equation model discretised by a finite volume method on an Arakawa C-grid, well suited for high-resolution models including tracer dynamics. As advection dominates the conservative tracer evolution, particular attention was paid to the advection scheme, which features a total variation diminishing (TVD) approach ensuring positive defined tracers and numerical conservation, yet maintaining frontal structures. For the dynamical parts, the model relies on standard Boussinesq and hydrostatic approximations and a turbulent kinetic energy turbulence closure. Of specific interest for the present study is the two-way nesting with a 1.3 km grid-size model of the Gulf of Cadiz embedded into a 4 km grid-size model of the Atlantic Ocean and Mediterranean Sea regions in the vicinity of the Strait of Gibraltar (Fig. 10).

The model is forced at the air–sea interface by ECMWF surface fluxes including wind stress, heat flux and evaporation. At the lateral open boundaries of the large-scale model, relaxation towards climatology is performed. Also initialization is taken from climatology, here the MODB data base (Brasseur et al., 1996; Rixen et al., 2000). With respect to the climatology, a 1 year spin up was applied to take care of the specific conditions for 1997, relative to average conditions.

Three river discharges were added to the model. To distinguish the different origins, we use three different passive tracers, called C_1, C_2 and C_3, one for each of the three river systems, respectively Guadiana, Guadalquivir and Tinto-Odiel. The annual mean water discharges are 157 m^3/s for Guadiana, 200 m^3/s for Guadalquivir and 15 m^3/s for the Tinto-Odiel rivers.

The tracer evolutions are governed by an advection–diffusion equation. The advection process is modelled using the horizontal velocity $\boldsymbol{u}$ of the hydrodynamic model, its vertical velocity u_3 and, when necessary a sediment-bent u hic velocity (w_i, negative when metal removal occurred). Turbulence is taken into account through the vertical diffusion coefficient $\tilde{\lambda}$ depending on the model turbulent kinetic energy, while the horizontal diffusion F_i is a simple subgrid scale parameterization with a very low horizontal laplacian diffusion.

$$\frac{\partial C_i}{\partial t} + \nabla\cdot(\boldsymbol{u}C_i) + \frac{\partial u_3 C_i}{\partial x_3} + \frac{\partial w_i C_i}{\partial x_3} = Q_i + F_i + \frac{\partial}{\partial x_3}\left[\tilde{\lambda}\frac{\partial C_i}{\partial x_3}\right] \qquad (1)$$

For passive (i.e. conservative) tracers, the source term Q_i is zero within the domain. Because the equation is linear in the absence of internal sources, we can work with normalized

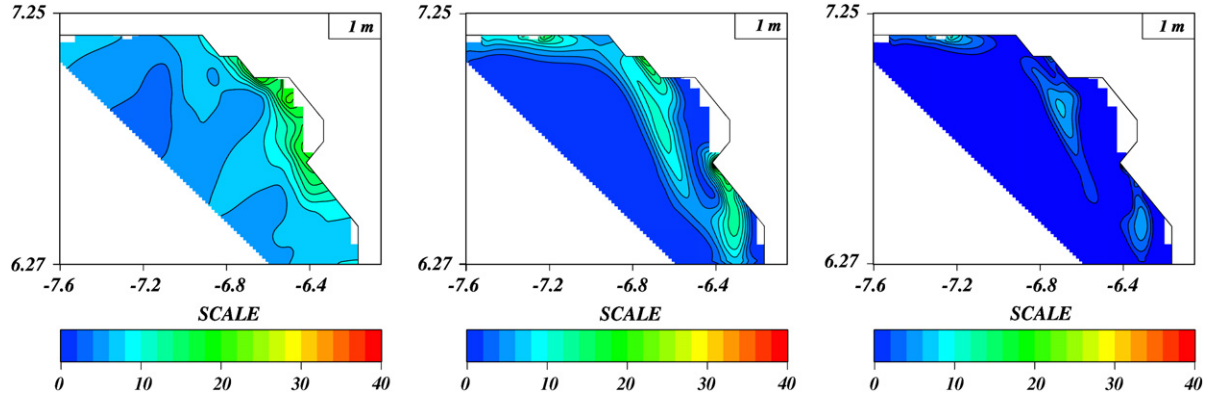

Fig. 6. Cu cruise T4; concentrations in nM.

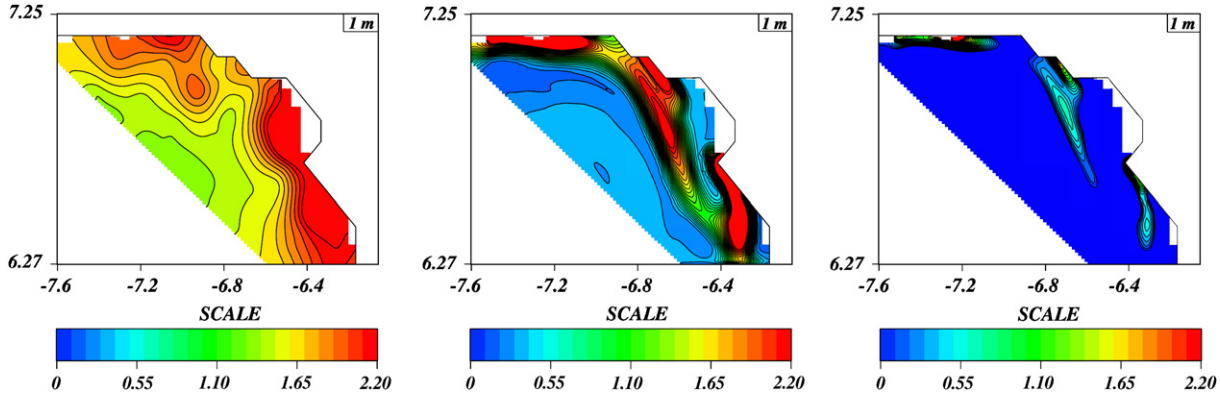

Fig. 7. Ni cruise T4; concentrations in nM.

values of the concentrations. Here we normalized by the (unknown) concentration at the point where river waters are becoming oceanic. Hence tracer C_1 is only released at the Guadiana outflow with a unit concentration, C_2 is only released in Guadalquivir and C_3 only in the Tinto-Odiel location, also with unit values.

Below we will use these tracer fields to determine the actual river concentrations that would lead to tracer concentrations which best fit the observed field data.

In addition to metal supply due to river discharges, a fourth numerical tracer called ''sediments'' was added, initially present only at the bottom of the water column in the model. This will allow us to identify regions of benthic metal supply which are assumed to contribute to the enhanced metal concentrations in the Gulf of Cadiz shelf waters (van Geen et al., 1991).

The definition of these numerical tracers was guided by the requirement in the TOROS project to quantify fluxes that are difficult to measure in the field. In particular the benthic trace metal supply in the Gulf of Cadiz and the dilution of Tinto-Odiel and other river discharges before entering Mediterranean were a concern. With the help of the model simulations (Fig. 11), the circulation revealed the advection and dispersion of the river discharges towards the Straits of Gibraltar, occurring predominantly along the shelf-break in a south-easterly direction (Fig. 12). Furthermore, the sediment tracer (Fig. 13) indicated a benthic metal supply in the shelf region. The model simulations also indicated large scale northward circulations in the open sea.

The dilution of metal-rich river discharges is clearly discernable in the model simulations (Fig. 14), which nevertheless show enriched waters flowing into the Western Mediterranean.

4. Validation and diagnostic tools

One of the recurrent tasks in modelling studies is the validation of model results and a thorough diagnosis of model outputs. As a result of the large output produced by models, appropriate diagnostic tools have become a necessary part of models. Standard statistical tools are of course applicable (rms, correlations, principle component analysis, trends analysis, etc.), but in some instances additional model equations can aid with our understanding of model behaviour. Among the latter possibilities (in addition to the addition of passive tracers to depict flow patterns, as used in this study), the age theory (Deleersnijder et al., 2002; Delhez et al., 2004a) provides an elegant framework to analyse ages of tracers within the model domain, where the age is set to zero at a given location (e.g. the inflow). The theory requires the calculation of the evolution of a tracer as in Eq. (1) to which we add an equation for the so-called age-concentration α_i

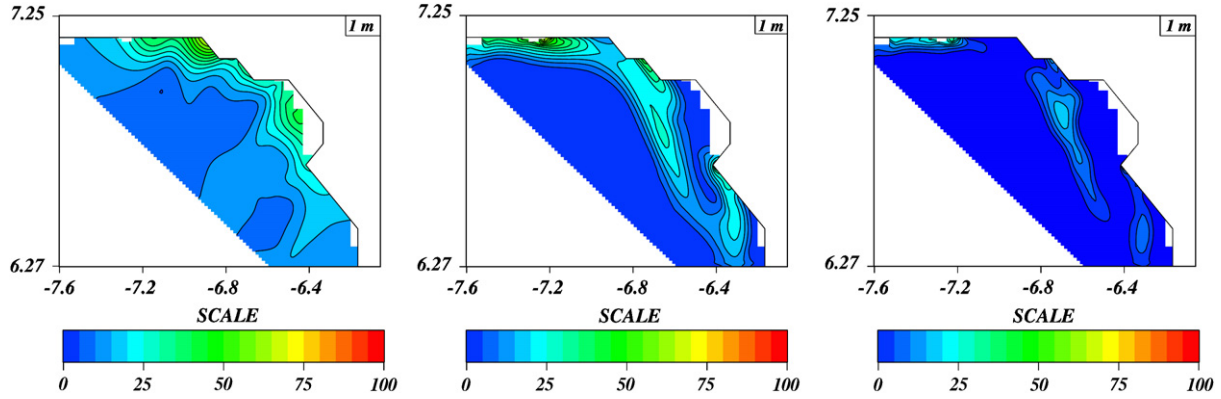

Fig. 8. Zn cruise T4; concentrations in nM.

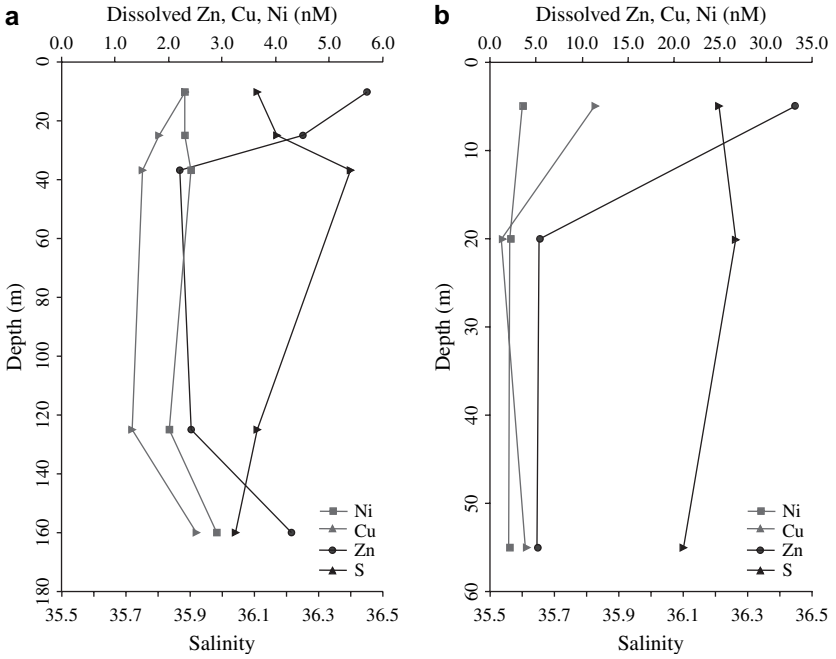

Fig. 9. (a) Depth profile of dissolved Cu, Ni and Zn at a station in central part of Gulf of Cadiz (at 36°52.80′ N, 6°59.94′ W). (b). Depth profile of dissolved Cu, Ni and Zn in plume of river Gualquivir, south of river mouth (at 36°24.33′ N, 6°25.26′ W). Samples for dissolved trace metals were collected using trace metal clean Go-Flo bottles and analysed using electrothermal atomic absorption spectrometry following solvent extraction (Elbaz-Poulichet et al., 2001b).

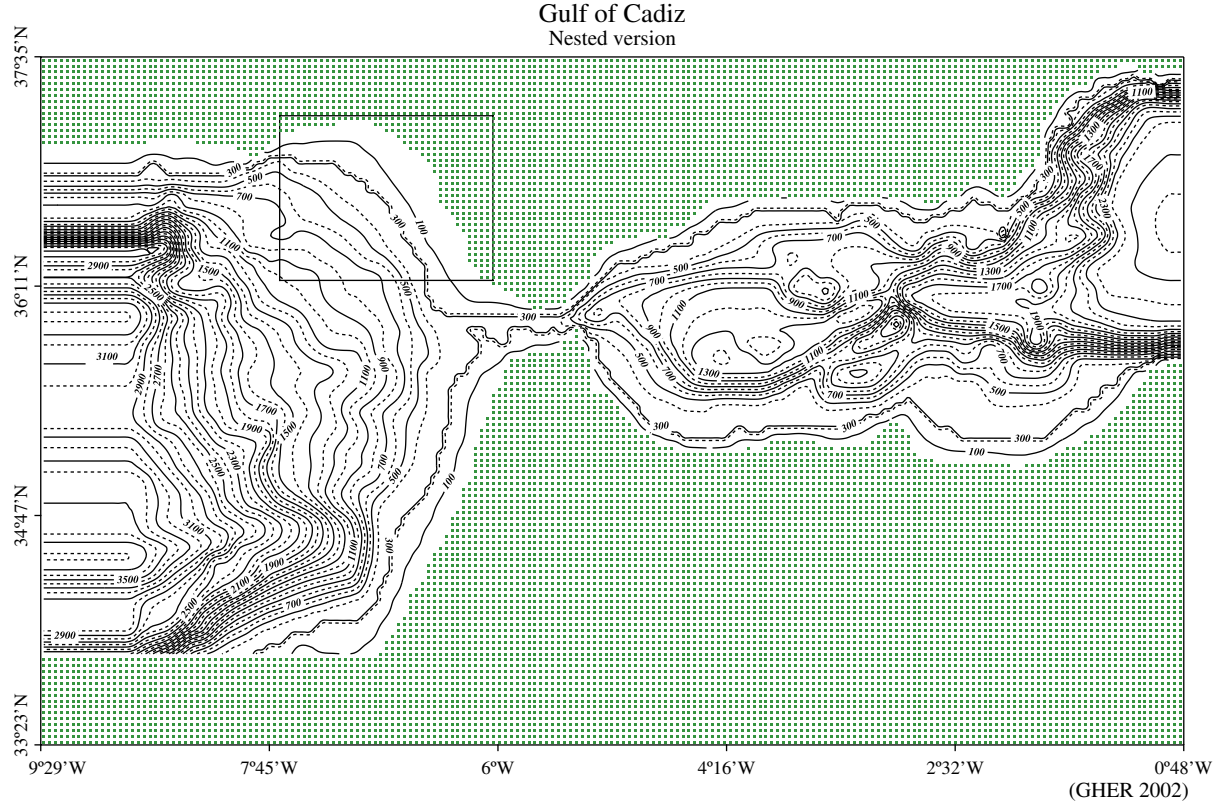

Fig. 10. Gulf of Cadiz nested model with coarse resolution model grid and location of the nested model. Isolines represent depth contours of the topography, with a shelf in the region of interest.

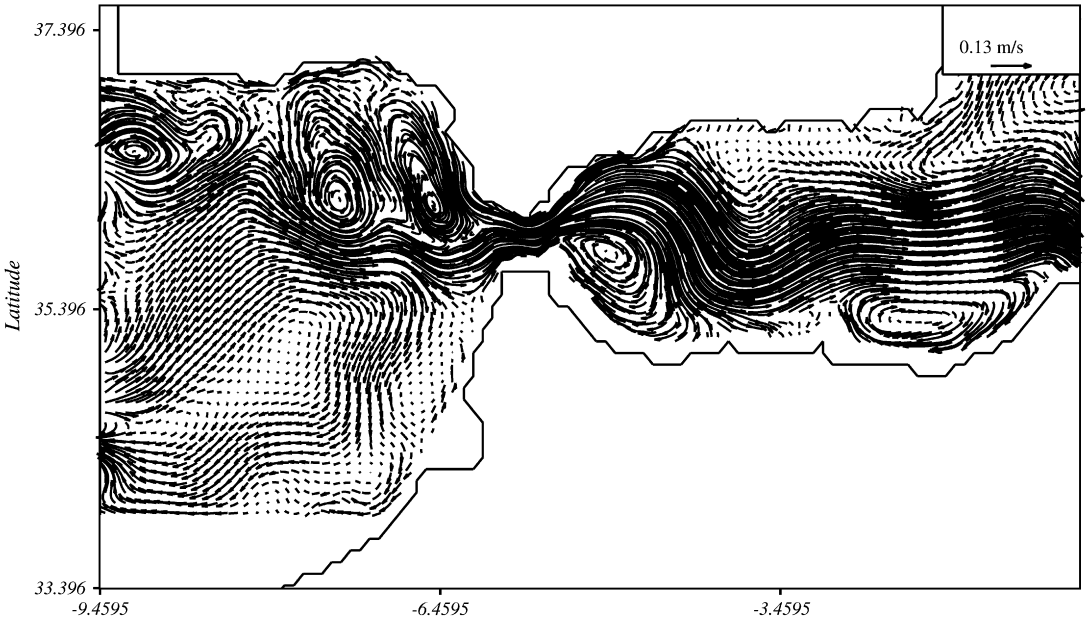

Fig. 11. Model simulation of circulation in the Gulf of Cadiz and Western Mediterranean at 10 m depth.

$$\frac{\partial \alpha_i}{\partial t} + \nabla \cdot (\boldsymbol{u}\alpha_i) + \frac{\partial u_3 \alpha_i}{\partial x_3} + \frac{\partial w_i \alpha_i}{\partial x_3} = C_i + \frac{\partial}{\partial x_3}\left[\tilde{\lambda}\frac{\partial \alpha_i}{\partial x_3}\right] \tag{2}$$

For simplicity of the presentation, we considered a conservative tracer with a negligible horizontal diffusion. Then the age a_i of the tracer C_i can be calculated at any location and any moment as

$$a_i = \frac{\alpha_i}{C_i} \tag{3}$$

This quantity provides a direct interpretation of the time a tracer has spent in the domain, subject to mixing with water parcels of different ages and is particularly useful to asses the time scales of biogeochemical cycling of trace metals (Delhez et al., 2004b). Here, we will of course impose for each tracer a zero-age boundary condition at the corresponding river mouth, so that the age field in a given position will reflect the time it took to move from the river to this position.

Interestingly, the age calculations (Fig. 15) indicate the different time scales of the plume displacements. In particular, the age within the plume can be used to interpret biogeochemical processes occurring within the plume, since it allows us to quantify the time passed since the river water was injected into the coastal water. Also recirculations across the open boundary (resolved by the bidirectional nesting) show the different plume structures and water ages associated with each river. The time scales within the plumes are of the order of months.

5. Tracer simulations and observations

The simulations of the fate of river or benthic supplied passive tracers provided information about the dilution

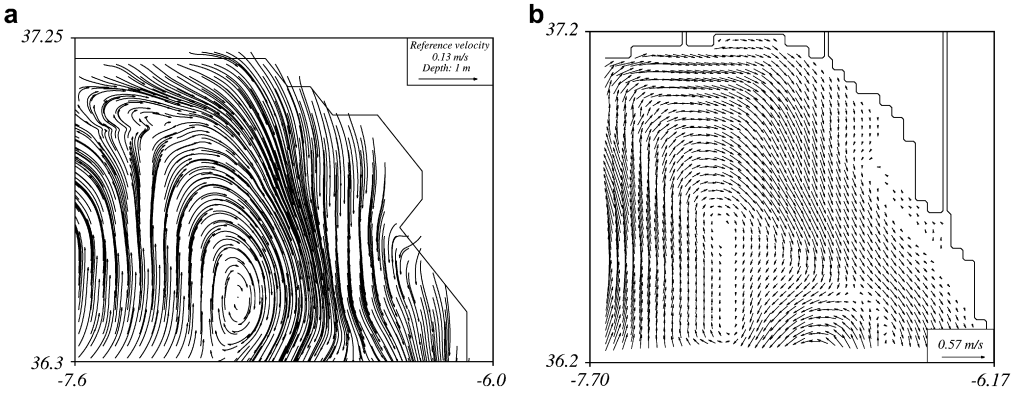

Fig. 12. Snapshots of circulation modelled in the Gulf of Cadiz with the nested model at surface (a) and 20 m (b) depth. In (b), the positions of the river discharges have been added schematically.

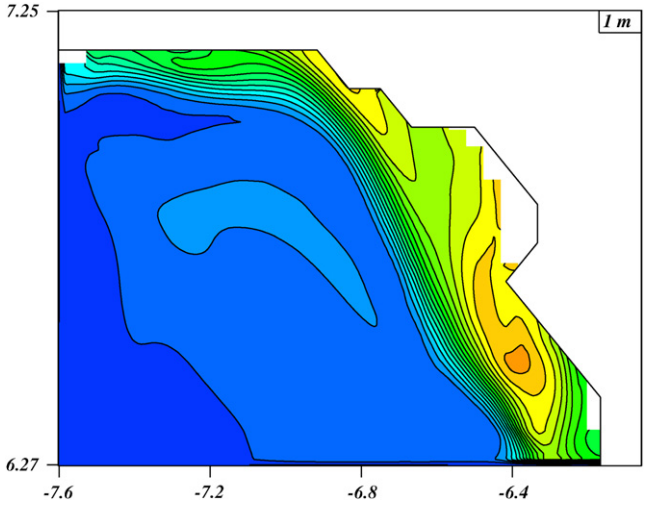

Fig. 13. Sediment tracer showing benthic metal supply to surface waters through use of a tracer released at the bottom of water column (arbitrary units, from zero values (blue) to highest values (red)).

factors and probable benthic supply regions. However, because of the normalization, the approach did not allow for a direct comparison with the observed trace metal fields. Furthermore, the metal concentrations in the river discharges at the point of entering the coastal waters were not well defined. Therefore we have utilised the trace metal distributions from field surveys for two purposes: (i) to estimate the concentrations in the river discharges at the mouths of the rivers (upon entry in coastal waters) and hence the spatial distribution of the trace metals from field surveys by simple superposition, (ii) to compare the simulated fields with the observed fields. The difference between the two fields will provide an indication of the influence of the river discharges on the trace metal distributions and the existence of additional trace metal sources or sinks.

For a given trace metal, the mathematical challenge was to obtain three values w_i of the river discharge concentrations that provided a spatial field $w_1C_1 + w_2C_2 + w_3C_3$ that was as close as possible to the observed field C. In other words the difference $C - (w_1C_1 + w_2C_2 + w_3C_3)$ should be as small as possible. If we take as a measure (the norm $|\ |$) of the difference the root mean square value, we perform a least square fit analysis, which can be readily solved. The least square fit analysis provides the three values w_1, w_2 and w_3 (objective (i)) and we use these to calculate the misfit between the modelled and observed distributions (objective (ii)):

$$\epsilon = w_1C_1 + w_2C_2 + w_3C_3 - C$$

This misfit is a spatial field, a local positive value indicating a missing sink in the model and a local negative value a missing source. We can provide a global measure of the misfit by comparing the norm of the misfit to the norm of the observed field

$$r = \frac{|\epsilon|^2}{|C|^2}$$

This measures thus the fraction of the signal that is not explained by the modelled fields combining the three river sources. The least square fit results for the different surveys and trace metals are provided in Table 1.

Note that we also can calculate the age of the best fit:

$$a = \frac{w_1\alpha_1 + w_2\alpha_2 + w_3\alpha_3}{w_1C_1 + w_2C_2 + w_3C_3} \tag{4}$$

which is of interest in case a radiotracer is discharged from a riverine source and this would allow us to tag water masses in terms of age.

6. Discussion

The model achieved a good overall fit to the observed dissolved metal data, and indicates that the three rivers constituted the dominant sources of metals to the coastal zone. The calculated source concentrations are within a factor of 2–3 for Cu, Ni and Zn of observed values at river mouths (data not shown), supporting the strength of the model. However, the river source strength of Co is overestimated by

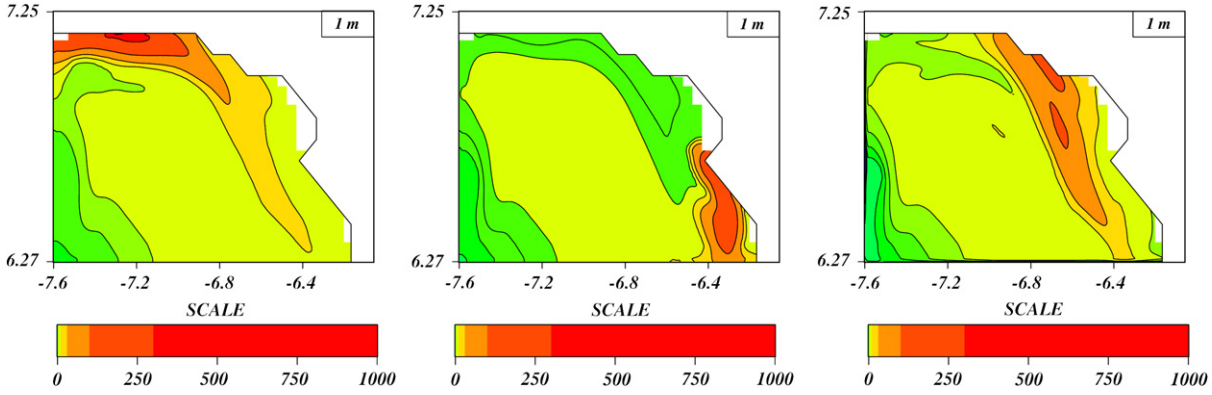

Fig. 14. Relative concentrations (compared to the input values in ‰) of non-reactive tracers originating from the three rivers Guadiana (C_1), Guadalquivir (C_2) and Tinto-Odiel (C_3) (from left to right).

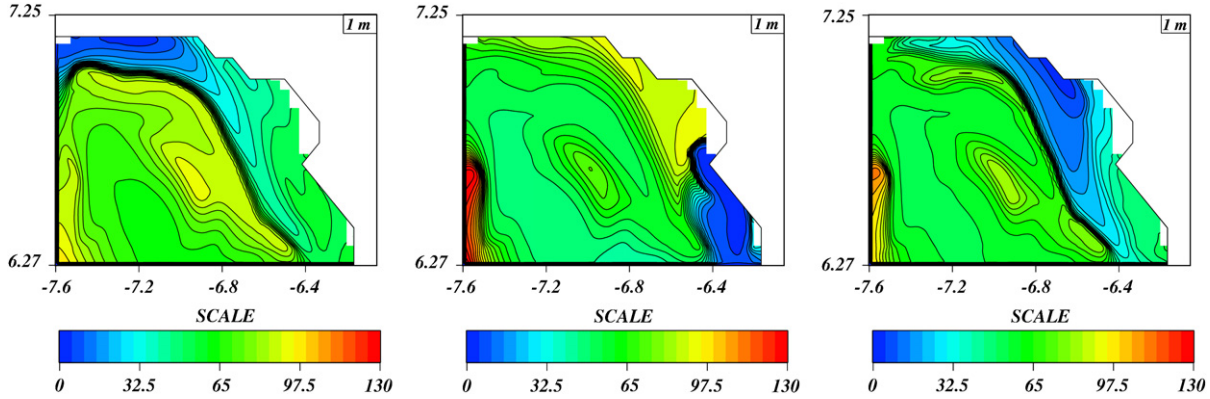

Fig. 15. River-discharge ages for the three rivers Guadiana (C_1), Guadalquivir (C_2) and Tinto-Odiel (C_3) (from left to right). Maximum values are 100, 133 and 111 days for the three tracers.

a factor of ca. 5 in all rivers, which may be the result of patchiness in the field data (see below).

Through comparison of the gridded observed data with the model fits and the calculated errors, a number of observations regarding the metal behaviour in the Gulf of Cadiz can be made. For example, some of the error calculations indicate a missing source of Cu, Zn and Ni in the plume regions of the Tinto-Odiel and/or Guadalquivir estuaries (e.g. Figs. 5, 8 for Zn), as well as for Co in the outer Gulf of Cadiz (Fig. 16). Fig. 13 shows the modelled benthic tracer distribution in coastal waters at 1 m depth resulting from benthic supplies. Zones of highest benthic tracer concentrations coincided with river plume distributions, and previous studies have shown enhanced metal concentrations in bottom sediment of the Gulf of Cadiz (Palanques et al., 1995; Morillo et al., 2004). Moreover, depth profiles (e.g. Fig. 9a) of dissolved metals in the Gulf of Cadiz showed enhanced bottom water concentrations and hence indicated the mobilisation of metals from the sediments. Therefore, the mobilisation of metals from sediments through diffusive processes and resuspension could at least partially account for the missing sources identified by the model error calculations. Another potential source for dissolved metals may arise from particulate suspended material supplied by the river systems, which has not been included in the model calculations. In the Tinto-Odiel plume region, the model fit suggests a missing sink for Zn (T2), Cu (T2), Ni (T4) and Co (T2) (Figs. 3, 5, 7, 16), indicating the removal of metals from solution, for example through adsorption onto particles or uptake by phytoplankton. Although this explanation seems to contradict our suggestion that river derived sediment particles act as a source of metals to the water column (see above), the supply of oceanic ''clean'' suspended matter (biogenic or lithogenic) to the Gulf of Cadiz has not been taken into consideration in the model and could potentially act as a sink for metals. Furthermore, the model fit indicates Co addition during T4 and Ni removal during T2 in the outer Gulf of Cadiz. The tracer age calculations provided an additional tool for geochemical interpretations. For example, important missing sinks were observed for Co and these were most important in regions of low Co age (compare Figs. 17 and 16), suggesting that active removal of Co occurred at young Co ages while the older Co concentrations were related to a missing source, which correlated well with benthic sources. Cobalt is a reactive element with rapid removal onto particles in oxygenated waters and supply from sediments through redox driven benthic diffusion. The behaviour of Co in aquatic systems is strongly related to Fe (Achterberg et al., 1997; Braungardt et al., 2003) which has a strong redox driven geochemistry. These observations show that the model simulations aid with scrutinising the dissolved metal behaviour in different regions of the coastal zone and confirm the interpretation of the observed survey data, which showed non-conservative metal behaviour in surface waters for large parts of our study area.

Important limitations of the comparisons between field data and model simulations need to be taken into account. For example, the plume region of the Guadiana estuary was located at the margin of the cruise coverage for the observed data, and the mouth of this river was only passed at distance by the ship. Therefore, the gridding procedure underestimated the dissolved surface water concentrations at the mouth of this river, resulting in a missing sink as indicated by the error calculation. Further gaps in the observed data contributed to the misfit of the model. During the T2 cruise, Zn measurements were not carried out near the mouth of the Rio Tinto/Odiel, and Co data was missing near the Guadalquivir estuary. This resulted in the underestimation of

Table 1
Values of river discharge concentrations w_i (in nmol/l) for cruises T2 and T4 for Co, Cu, Zn and Ni. The parameter r is the unexplained percentage of the variance by the model

	w_1	w_2	w_3	r
T2Co	34	58	76	54
T2Cu	42	58	214	31
T2Ni	20	43	67	45
T2Zn	49	33	129	55
T4Cu	32	71	96	43
T4Ni	10	15	19	45
T4Zn	132	114	218	41

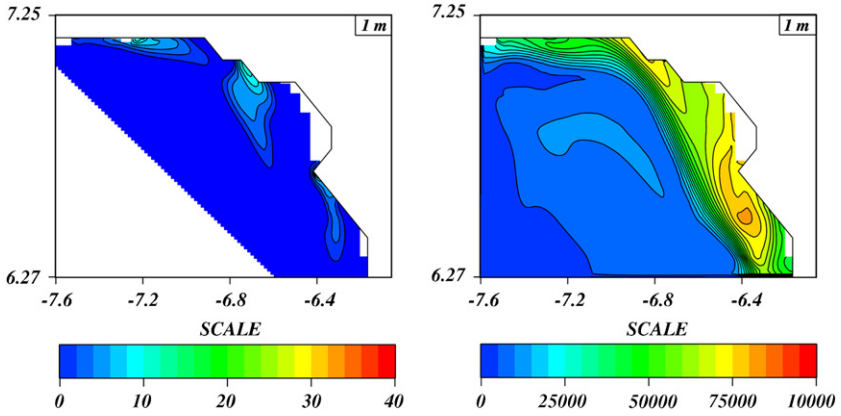

Fig. 16. Co misfit (left panel) sediment tracer (right panel).

observed Zn and Co concentrations during the gridding in the respective areas, and accounts, at least in part, for the missing sink suggested by the model fit error.

On the other hand, the data coverage close inshore was better during the T4 than the T2 cruise. As a result, the model fit was generally better for T4, emphasizing the importance of high-resolution monitoring for detailed data interpretation.

It is important not to over-interpret the model fits by analysing small scale details resulting from the different shapes of observed and modelled plume dispersions. Nevertheless, important differences occurred between the survey and model plume dispersions which highlight potential requirements for further model efforts. While the model shape of the Guadiana plume appears to replicate the observed ones well, the observed plume of the Tinto-Odiel and Guadalquivir estuary deviate from the model in three ways. (i) The Tinto-Odiel plume is dispersed to the northwest and during T2 also to the south of the river mouth, probably the result of tidal excursion, which was not considered in the model, and/or the lack of spatial resolution of the ECMWF atmospheric forcing. (ii) The Tinto-Odiel plume travels closely inshore, this is in particular shown in the field data for the T4 cruise, while the model plume is detached from the coast and does enter the bay to the southeast of the estuary. (iii) The Guadalquivir plume protrudes further into the Gulf of Cadiz for the observed survey data of both cruises, while the model suggests that it remains closer to the headland and extends almost due south. Depth profiles obtained during the T2 cruise in June 1997, after a prolonged period without rainfall, showed a clear surface layer of lower salinity waters with elevated metal concentrations, compared to mid-column waters (see Fig. 9b). This confirms the observations from high-resolution monitoring that the river plumes are dispersed over a wider area further into the outer Gulf of Cadiz than the model suggests. These discrepancies result in calculated model errors which suggest missing metal sources and sinks that may be artefacts of the model shape, rather than the result of geochemical processes affecting metal distributions.

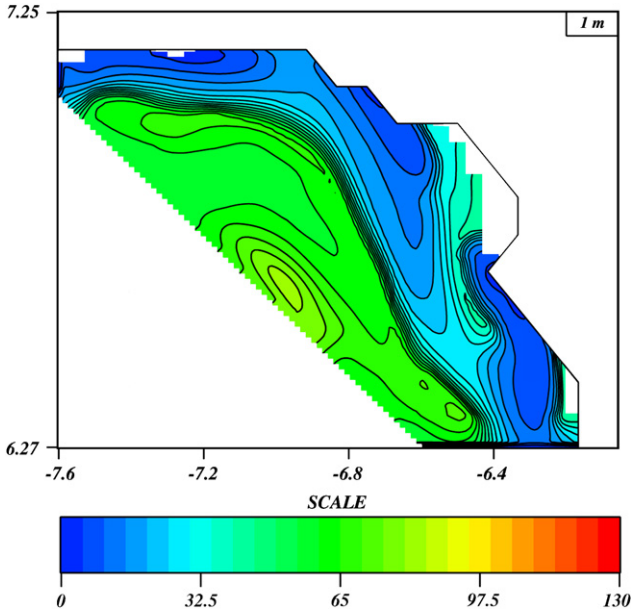

Fig. 17. Age of combined sources (in days).

7. Conclusions

The exercise of combining high resolution trace metal data, hydrodynamic models and diagnostic tools was effective in terms of interpreting observed trace metal distributions using a dispersion model of river discharges. A least square fit method allowed us to calculate metal concentrations in the outflows of the river systems that matched the observed values closely. The spatial distribution of the fit itself allowed us to identify regions of missing sources and sinks. The missing sources were most likely related to benthic inputs, and the missing sinks were mostly apparent for young tracers, suggesting still active removal mechanisms. The results however need to be subjected to an analysis of errors in the plume positions that we observed. Sensitivity analysis in terms of river discharge variability (e.g. effects of flow discharges), tidal excursions and resolution of atmospheric forcings could provide the required information to enhance the match between the observed and model metal distributions.

Acknowledgements

The European Union is acknowledged for funding the TOROS project (ENV4-CT96-0217). All TOROS project partners contributed in some form to this paper. The National Fund for Scientific Research, Belgium, is acknowledged for the financing of a supercomputer. The contribution of dissolved trace metal profiles by Dr Nick Morley is gratefully acknowledged. Eric Delhez and Eric Deleersnijder are acknowledged for their patience whilst waiting for our contribution. This is MARE publication MARE0101.

References

Achterberg, E., Braungardt, C., Herzl, V., Millward, G., 2003. Metal behaviour in an estuary polluted by acid mine drainage: the role of particulate matter. Environmental Pollution 121, 283–292.

Achterberg, E., Elbaz-Poulichet, F., Morley, N., Braungardt, C., 1999. Impact of Los Frailes mine spill on riverine, estuarine and coastal waters in southern Spain. Water Research 33, 3387–3394.

Achterberg, E.P., Van den Berg, C.M.G., 1994. Automated voltammetric system for shipboard determination of metal speciation in sea water. Analytica Chimica Acta 284, 463–471.

Achterberg, E.P., Van den Berg, C.M.G., Boussemart, M., Davison, W., 1997. Speciation and cycling of trace metals in Esthwaite Water, a productive English lake with seasonal deep-water anoxia. Geochimica et Cosmochimica Acta 61, 5233–5253.

Beckers, J.-M., 1991. Application of a 3D model to the Western Mediterranean. Journal of Marine Systems 1, 315–332.

Boyle, E., Chapnick, S., Bai, X., Spivack, A., 1985. Trace metal enrichments in the Mediterranean Sea. Earth and Planetary Science Letters 74, 405–419.

Brasseur, P., Beckers, J.-M., Brankart, J.-M., Schoenauen, R., 1996. Seasonal temperature and salinity fields in the Mediterranean Sea: climatological analyses of a historical data set. Deep Sea Research 43, 159–192.

Braungardt, C., Achterberg, E., Elbaz-Poulichet, F., Morley, N., 2003. Metal biogeochemistry in an acidic mine polluted estuarine system in southwest Spain. Applied Geochemistry 18, 1757–1871.

Braungardt, C., Achterberg, E.P., Nimmo, M., 1998. On-line voltammetric monitoring of dissolved Cu and Ni in the Gulf of Cadiz, south-west Spain. Analytica Chimica Acta 377, 205–215.

Deleersnijder, E., Beckers, J.-M., Delhez, E., 2006. The residence time of settling particles in the surface mixed layer. Environmental Fluid Dynamics 6, 25–42.

Deleersnijder, E., Campin, J.-M., Delhez, E., 2001. The concept of age in marine modelling: I. Theory and preliminary model results. Journal of Marine Systems 28, 229–267.

Deleersnijder, E., Mouchet, A., Delhez, E., Beckers, J.-M., 2002. Transient behaviour of water ages in the World Ocean. Mathematical and Computer Modelling 36, 121–127.

Delhez, E., Deleersnijder, E., 2002. The concept of age in marine modelling: II. Concentration distribution function in the English Channel and the North Sea. Journal of Marine Systems 31, 279–297.

Delhez, E., Deleersnijder, E., Mouchet, A., Beckers, J.-M., 2003. A note on the age of radioactive tracers. Journal of Marine Systems 38, 277–286.

Delhez, E., Heemink, A., Deleersnijder, E., 2004a. Residence time in a semi-enclosed domain from the solution of an adjoint problem. Estuarine, Coastal and Shelf Science 61, 691–702.

Delhez, E., Lacroix, G., Deleersnijder, E., 2004b. The age as a diagnostic of the dynamics of marine ecosystem models. Ocean Dynamics 54, 221–231.

Elbaz-Poulichet, F., Braungardt, C., Achterberg, E., Morley, N., Cossa, D., Beckers, J.-M., Nomerange, P., Cruzado, A., Leblanc, M., 2001a. Metal biogeochemistry in the Tinto-Odiel rivers (southern Spain) and in the Gulf of Cadiz. A synthesis of the results of TOROS project. Continental Shelf Research 21, 1961–1973.

Elbaz-Poulichet, F., Dupuy, C., Cruzado, A., Velasquez, Z., Achterberg, E., Braungardt, C., 2000. Influence of sorption processes by Fe oxides and algal uptake on Arsenic and Phosphate cycle in an acidic estuary (Tinto rivers, Spain). Water Research 34, 3222–3230.

Elbaz-Poulichet, F., Guieu, C., Morley, N., 2001b. A reassessment of trace metal budgets in the Western Mediterranean Sea. Marine Pollution Bulletin 42, 623–627.

Elbaz-Poulichet, F., Morley, N., Beckers, J.-M., Nomerange, P., 2001c. Metal fluxes through the strait of Gibraltar: the influence of the Tinto and Odiel rivers (SW Spain). Marine Chemistry 73, 193–213.

van Geen, L., Boyle, E., Moore, W., 1991. Trace metal enrichments in the Gulf of Cadiz. Geochimica Cosmochimica Acta 55, 2173–2192.

Leblanc, M., Morales, J., Borrego, J., Elbaz-Poulichet, F., 2000. 4,500-year-old mining pollution in southwestern Spain: long-term implications for modern mining pollution. Economic Geology 95, 655–662.

Leistel, J., Marcoux, E., Thieblemont, D., Quesada, C., Sanchez, A., Almodovar, G., Pascual, E., Saez, R., 1998. The volcanic-hosted massive sulphide deposits of the Iberian Pyrite Belt. Mineralium Deposita 33, 2–30.

Morillo, J., Usero, J., Gracia, I., 2004. Heavy metal distribution in marine sediments from the southwest coast of Spain. Chemosphere 55, 431–442.

Nomérange, P., 1998. Implementation of a nesting procedure in the GHER 3D model. Application in the Gulf of Cadiz. In: Proceedings of the third MMARIE Annual Meeting.

Palanques, A., Diaz, J.I., Farran, M., 1995. Contamination of heavy metals in the suspended and surface sediment of the Gulf of Cadiz (Spain): the role of sources, currents, pathways and sinks. Oceanologica Acta 18, 469–477.

Rixen, M., Beckers, J.-M., Brankart, J.-M., Brasseur, P., 2000. A numerically efficient data analysis method with error map generation. Ocean Modelling 2, 45–60.

Available online at www.sciencedirect.com
ScienceDirect
Estuarine, Coastal and Shelf Science 74 (2007) 610–627
ESTUARINE COASTAL AND SHELF SCIENCE
www.elsevier.com/locate/ecss

Modeling the pathways and ages of inflowing salt- and freshwater in the Baltic Sea

H.E. Markus Meier*

Swedish Meteorological and Hydrological Institute, Rossby Centre, 60176 Norrköping, Sweden

Received 25 September 2006; accepted 9 May 2007
Available online 16 July 2007

Abstract

A three-dimensional, eddy-permitting ocean circulation model with implemented bottom boundary layer model and flux-corrected transport scheme is used to calculate the pathways and ages of various water masses in the Baltic Sea. The agreement between simulated and observed temperature and salinity profiles of the period 1980–2004 is satisfactory. Especially the renewal of the deep water in the Baltic proper by gravity-driven dense bottom flows is better simulated than in previous versions of the model. Based upon these model results details of the mean circulation are analyzed. For instance, it is found that after the major Baltic inflow in January 2003 saline water passing the Słupsk Furrow flows directly towards northeast along the eastern slope of the Hoburg Channel. However, after the baroclinic summer inflow in August/September 2002 the deep water flow spreads along the southwestern slope of the Gdansk Basin. Further, the model results show that the patterns of mean vertical advective fluxes across the halocline that close the large-scale vertical circulation are rather patchy. Mainly within distinct areas are particles of the saline inflow water advected vertically from the deep water into the surface layer. To analyze the time scales of the circulation mean ages of various water masses are calculated. It is found that at the sea surface of the Bornholm Basin, Gotland Basin, Bothnian Sea, and Bothnian Bay the mean ages associated to inflowing water from Kattegat amount to 26–30, 28–34, 34–38, and 38–42 years, respectively. Largest mean sea surface ages of more than 30 years associated to the freshwater of the rivers are found in the central Gotland Basin and Belt Sea. At the bottom the mean ages are largest in the western Gotland Basin and amount to more than 36 years. In the Baltic proper vertical gradients of ages associated to the freshwater inflow are smaller than in the case of inflowing saltwater from Kattegat indicating an efficient recirculation of freshwater in the Baltic Sea.

Keywords: Baltic Sea; numerical modeling; circulation; passive tracer; age of water masses

1. Introduction

The Baltic Sea is a strongly stratified semi-enclosed basin. Its horizontal and vertical salinity gradients are the result of the large freshwater supply from rivers and net precipitation and of the reduced water exchange with the world ocean (Fig. 1). The climate of the 20th century is characterized by an average salinity of about 7.4 (calculated from climatological data by Janssen et al., 1999) and a freshwater supply including river runoff and net precipitation of about 16,100 $m^3 s^{-1}$ (calculated from reconstructed hydrological and atmospheric data by Cyberski and Wroblewski, 2000 and Kauker and Meier, 2003, respectively; see Meier and Kauker, 2003). Applying the well-known Knudsen formulae (Knudsen, 1900) with surface and bottom layer salinities of 8.7 and 17.4, respectively, the in- and outflows of the Baltic Sea amount to 16,100 $m^3 s^{-1}$ and 32,200 $m^3 s^{-1}$, respectively.

In several earlier studies the mean horizontal and vertical circulations of the Baltic Sea and its variability were studied (e.g., Sarkisyan et al., 1975; Stigebrandt, 1987; Kõuts and Omstedt, 1993; Elken, 1996; Lehmann and Hinrichsen, 2000; Lehmann et al., 2002; Meier and Kauker, 2003; Andrejev et al., 2004a,b; Döös et al., 2004; Meier, 2005; Myrberg and

* Present address: Swedish Meteorological and Hydrological Institute, Division of Oceanography, Research Department, 60176 Norrköping, Sweden.
E-mail address: markus.meier@smhi.se

0272-7714/$ - see front matter © 2007 Elsevier Ltd. All rights reserved.
doi:10.1016/j.ecss.2007.05.019

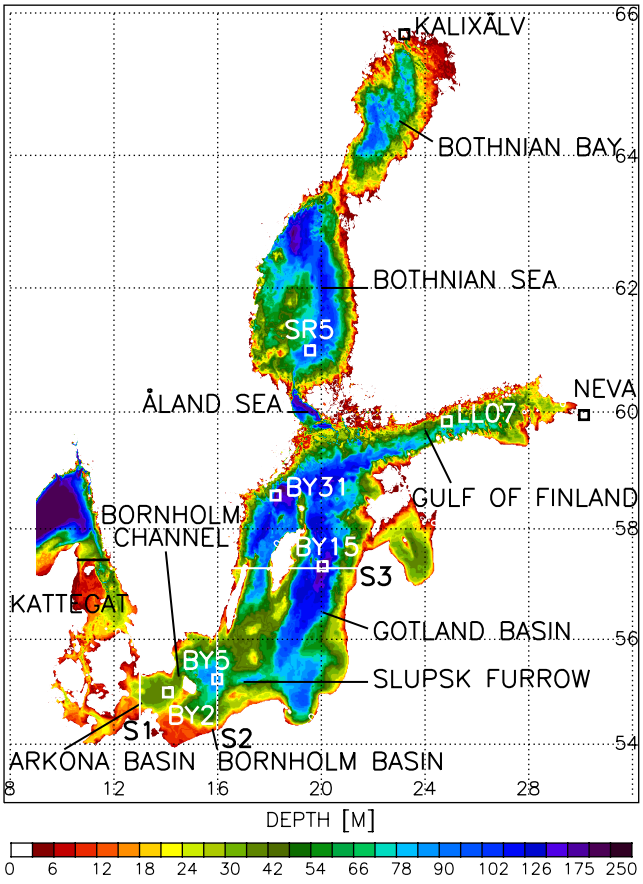

Fig. 1. Bottom topography of the Baltic Sea. The domain of the Rossby Centre Ocean model (RCO) is limited with open boundaries in the northern Kattegat (black line). In addition, the monitoring stations at Arkona Deep (BY2), Bornholm Deep (BY5), Gotland Deep (BY15), Landsort Deep (BY31), in the Gulf of Finland (LL07), and in the Bothnian Sea (SR5), cross-sections (S1–S3, white lines), and the mouths of the rivers Neva and Kalixälv are depicted.

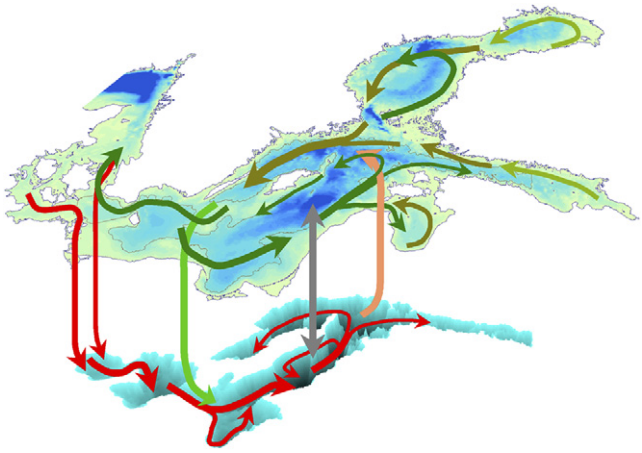

Fig. 2. Schematic view of the large-scale circulation in the Baltic Sea (taken from Elken and Matthäus, in press). Green and red arrows denote the surface and bottom layer circulation, respectively. The light green and beige arrows show entrainment. The gray arrow denotes diffusion.

Andrejev, 2006). The large-scale horizontal circulation of the subbasins is characterized by cyclonic gyres as a result of the interplay between earth rotation and depth variations on time scales larger than the inertial period (Fig. 2). Lehmann et al. (2002) showed that the horizontal circulation can be described by a depth-integrated vorticity equation omitting bottom friction and wind stress curl.

The vertical circulation is driven by the inflow of high-saline water from the Kattegat (Stigebrandt, 1987). The bottom water in the deep subbasins is usually only replaced after large gale-forced events, so-called Major Baltic Inflows (MBIs, e.g., Matthäus and Franck, 1992; Fischer and Matthäus, 1996). The likelihood that these events occur is highest during the winter season. The typical forcing of these events consists of a sequence of easterly winds lasting for about 20 days followed by strong to very strong westerly winds of similar duration (Lass and Matthäus, 1996). However, small and medium-strength inflows are important as well since they have the potential to renew intermediate layers of the Baltic proper halocline (Feistel et al., 2006). During the past two decades the frequency of large barotropic inflows (mainly in winter) has decreased and the frequency of medium-intensity baroclinic inflows (observed in summer) has increased (Mohrholz et al., 2006).

During all kinds of inflow events the high-saline water spills over the shallow sills of the Baltic Sea entrance area (i.e. Drogden and Darss sills, see Fig. 1) into the Arkona Basin and Bornholm Basin (Fig. 2). In addition to the entrance area, the Słupsk Sill and the Słupsk Furrow are important locations for the transformation of water masses (Piechura and Beszczyńska-Möller, 2003). Passing the Słupsk Furrow, both gravity-driven dense bottom flows and sub-surface cyclonic eddies, which are eroded laterally by thermohaline intrusions, renew the deep water of the eastern Gotland Basin (Zhurbas and Paka, 1999). Saline water passing the Słupsk Furrow may flow either towards northeast along the eastern slope of the Hoburg Channel or may spread along the southwestern slope of the Gdansk Basin (Elken, 1996; see Fig. 2). From the Gotland Deep the saline flow continues via the Northern Deep either into the northwestern Gotland Basin with the deepest location of the entire Baltic close to the Swedish coast (Landsort Deep) or into the Gulf of Finland (Fig. 2). The sill between the Åland Sea and the Baltic proper prevents the northward propagation of the deep water flow. It is assumed that the Bothnian Sea is renewed mainly by inflowing surface water from the Baltic proper (Marmefelt and Omstedt, 1993). On the way from the Kattegat into the Landsort Deep the inflowing dense water is diluted due to entrainment. For that distance, Kõuts and Omstedt (1993) estimated a total entrainment factor of 4. What is known today about the processes important for the renewal of the Baltic Sea deep water is summarized in a recent review by Meier et al. (2006).

Although the circulation of the Baltic Sea has been studied intensively, there are still many open questions connected to pathways and average ages of inflowing salt- and freshwater in various subbasins. The unknown pathway of saltwater plumes in the southern Gotland Basin was mentioned already. It is also not clear where the upwelling of the deep water flow occurs closing the large-scale Baltic conveyor belt (Döös

et al., 2004) and what are the governing processes. The role of topographically stirred upwelling, diapycnical mixing caused by breaking internal waves, and the entrainment of the deep water into the moving surface water in the Baltic proper is not well understood.

Due to the large temporal and spatial variability the investigation of the mean large-scale circulation of the Baltic Sea is only with the help of models possible. To analyze the complex model results both Lagrangian and Eulerian methods were applied. For instance, Döös et al. (2004) calculated from three-dimensional circulation model results residence times of various simulated Baltic water masses using Lagrangian particles released either at the sills in the Baltic entrance area or at the mouth of the river Neva. Döös et al. (2004) found that the time evolution of the residence of the Neva water in the Baltic is very similar to the water for the entire Baltic (including particles released at both the sills and at the Neva river mouth) with e-folding time scales of 26–29 years. Similar studies based upon trajectories were performed for the Gulf of Riga and Gdansk Bay (Jönsson et al., 2004), and for the Gulf of Finland (Jönsson, 2005). In the latter study the Lagrangian formalism has also been used to calculate overturning stream-functions for different water masses.

The Lagrangian method based upon trajectories of particles has the disadvantage that subgrid-scale mixing is not included. For the results of the analysis, especially vertical turbulent mixing might be important on longer time scales. As the circulation models utilized so far are only eddy-permitting, the results might also be affected by the horizontal mixing parameterizing mesoscale eddies.

Analysis methods using Eulerian tracers do not have this limitation. (However, note that for estuaries like the Baltic Sea the importance of the differences between the two methods is not clear yet.) An example is the concept of age distribution and transit time (Bolin and Rodhe, 1973) which has been applied to Himmerfjärden Estuary (Engqvist, 1996), the Gulf of Finland (Andrejev et al., 2004b), the Gulf of Bothnia (Myrberg and Andrejev, 2006), and the entire Baltic (Meier, 2005). In these studies a passive tracer was added to the model variables to characterize the average age of sea water in the reservoir with prescribed values at the lateral open boundaries or at the sea surface. For instance, Meier (2005) found for the period 1903–1998 mean ages of the bottom water of 1 year at Bornholm Deep, 5 years at Gotland Deep, and 7 years at Landsort Deep. For the whole Baltic a maximum age of about 11 years appeared in the bottom water at Landsort Deep. In his study the age of sea water is the time elapsed since a water particle left the sea surface. If the age of the inflowing water at the source regions (i.e. the lateral open boundaries towards the Baltic proper and the river mouths) is set to zero, Andrejev et al. (2004b) and Myrberg and Andrejev (2006) found maximum water ages of around 2 years in the Gulf of Finland and of around 7.4 years in the Gulf of Bothnia, respectively. These studies have in common that the age of sea water is estimated from the equation of the age of pure water (Deleersnijder et al., 2001). Hence, it is not possible to distinguish between different water masses.

In the present study a high-resolution simulation for 1980–2004 was performed using an eddy-permitting three-dimensional circulation model. In the model various water masses were marked with passive tracers and the associated ages of the specific water masses were calculated. The aim is to better understand the large-scale circulation and related time scales.

The paper is organized as follows. The circulation model, the numerical experiment, the analysis method, and investigated water masses are described in Sections 2.1–2.4, respectively. In Section 3, firstly model results of temperature and salinity are compared with observations (Section 3.1). Secondly, the simulated mean circulation above and below the halocline is presented (Section 3.2). Thirdly, pathways of specific water masses marked with passive tracers are analyzed (Section 3.3). Fourthly, mean ages associated to selected water masses are calculated and discussed (Section 3.4). In Section 4, the results are compared with previous publications. The paper ends with conclusions (Section 5).

2. Methods

2.1. Model description

In this study a new version of the Rossby Centre Ocean model (RCO) (Meier et al., 2003) was used to perform a multi-year long, high-resolution simulation for the Baltic Sea. RCO is a Bryan–Cox–Semtner primitive equation circulation model with a free surface (Killworth et al., 1991) and open boundary conditions (Stevens, 1991) in the northern Kattegat (Fig. 1). It is coupled to a Hibler-type sea ice model (Hibler, 1979) with elastic–viscous–plastic rheology (Hunke and Dukowicz, 1997). Subgrid-scale mixing is parameterized using a turbulence closure scheme of the k–ε type with flux boundary conditions to include the effect of a turbulence enhanced layer due to breaking surface gravity waves and a parameterization for breaking internal waves (Meier, 2001). The deep water mixing is assumed to be inversely proportional to Brunt–Väisälä frequency with a proportionality factor $\alpha = 1 \times 10^{-7}\ \mathrm{m^2\,s^{-2}}$. This value is in good agreement with results from dissipation measurements in the eastern Gotland Basin (Lass et al., 2003). Lass et al. (2003) found the best fit to their data using $\alpha = 0.87 \times 10^{-7}\ \mathrm{m^2\,s^{-2}}$.

The model domain covers the Baltic Sea including Kattegat (Fig. 1). In the present study, RCO was used with a horizontal resolution of two nautical miles and with 41 vertical levels with layer thicknesses between 3 and 12 m. Minimum and maximum depths amount to 6 and 250 m corresponding to 2 and 41 levels, respectively.

As the layer thicknesses of the vertical grid are too large to resolve the bottom boundary layer (BBL) accurately, a BBL model is embedded to allow the direct communication between bottom boxes of the step-like topography (Beckmann and Döscher, 1997). The BBL model helps to improve the simulation of gravity-driven dense bottom flows (Meier et al., 2004). In this study a bottom drag coefficient of $c_\mathrm{d} = 1.1 \times 10^{-3}$ is used.

Test experiments showed that in long simulations the modified SPLIT-QUICK advection scheme (Webb et al., 1998) which was earlier embedded within RCO does not guarantee numerical stability of passive tracers released at point sources. SPLIT-QUICK is of third order accuracy but does not preserve monotonicity. At large gradients overshooting due to numerical dispersion is observed. Hence, in this study a flux-corrected, monotonicity preserving transport (FCT) scheme following Gerdes et al. (1991) is embedded. In the simulation for 1980–2004 (see Section 2.2) no explicit horizontal diffusion is applied.

Summarizing, in the model version of this study (HR2) explicitly prescribed deep water mixing is two times larger, horizontal diffusion is significantly smaller, and gravity-driven dense bottom flows are less diffusive (due to the BBL model) compared to the earlier version by Meier et al. (2003) (HR0). In Section 3.1, the new model results are compared to observations. To investigate the impact of various subgrid-scale parameterizations three model versions are compared: HR0, HR1, and HR2. HR1 is similar to HR2 but instead of FCT SPLIT-QUICK together with a background harmonic diffusion of $A_H = 10\ m^2\ s^{-1}$ is used. In addition, the vertical mixing schemes differ. Instead of the k–ε model a k model with an algebraic relation for the turbulent length scale is used (Meier and Kauker, 2002). However, the differences between the k–ε model and the k model do not affect the presented results.

2.2. Simulation 1980–2004

A model simulation for 1980–2004 is performed. RCO is started from rest on 26 May 1980 with initial temperature and salinity observations from May 1980. At the open boundary in the northern Kattegat hourly sea level observations from the Swedish tide gauge station Ringhals are prescribed. In case of inflow, temperature and salinity at the open boundary are relaxed towards observed climatological mean data. In case of outflow, a radiation condition is utilized (Stevens, 1991). Also the freshwater inflows of the 29 largest rivers of the Baltic catchment area are considered. Monthly mean discharges are calculated from a large-scale hydrological model (Graham, 1999). The atmospheric forcing is derived from three-hourly gridded observations of sea level pressure, geostrophic wind components, 2 m air temperature, 2 m relative humidity, precipitation, and total cloud cover. For details of the model experiment the reader is referred to Meier et al. (2003).

2.3. Age concept

To track specific water masses concentrations of passive tracers and associated age concentrations are calculated following previous studies (e.g., Delhez et al., 1999; Deleersnijder et al., 2001). At time t and location $\vec{r}$, the concentration of a tracer, $C(t,\vec{r})$, would obey the following equation:

$$\frac{\partial C}{\partial t} + \nabla\cdot\left(\vec{v}C - K\cdot\nabla C\right) = 0 \qquad (1)$$

where $\vec{v}$ is the water velocity and K denotes the diffusivity tensor. The age concentration, $\alpha(t,\vec{r})$, of the water mass under study is the solution of:

$$\frac{\partial \alpha}{\partial t} + \nabla\cdot\left(\vec{v}\alpha - K\cdot\nabla\alpha\right) = C \qquad (2)$$

Finally, the age is then given as the ratio $a(t,\vec{r}) = \alpha(t,\vec{r})/C(t,\vec{r})$. For further details of the concept of age in marine modeling the reader is referred to Deleersnijder et al. (2001).

The initial tracer and age concentrations are set to zero. At the open boundary in Kattegat the same radiation conditions as used within RCO for temperature and salinity are utilized. In case of inflow, at the open boundary the concentrations of the tracers and associated ages are relaxed to zero, with a time scale of one day. At the sea surface no flux boundary conditions are used.

2.4. Selected water masses

The sources of the following water masses are marked with passive tracers:

(1) inflowing water at the Darss and Drogden sills independently of salinity;
(2) water at the section S1 across the Arkona Basin (see Fig. 1) with salinities more than 17;
(3) warm intermediate water at section S2 across the Bornholm Basin (see Fig. 1) with salinities between 8.95 and 14.3 and with temperatures more than 11 °C;
(4) inflowing freshwater from the river Neva into the Gulf of Finland (see Fig. 1);
(5) inflowing freshwater from the river Kalixälv into the Bothnian Bay (see Fig. 1); and
(6) inflowing freshwater from all rivers.

Each tracer obeys its own transport equation. Inflowing water crossing the shallow sills in the Baltic entrance area is the source of the first tracer. The second tracer marks only the high-saline inflows with salinities more than 17. If an event is defined as MBI, the salinity is more than 17 (Fischer and Matthäus, 1996). This criterion is a necessary condition but not a sufficient one because also the duration of an event determines the classification as an MBI. The third tracer marks the warm intermediate water within the halocline of the Bornholm Sea. This water is generated by small and medium-intensity baroclinic inflows that occur during summer. The criteria used to characterize these inflows follow Mohrholz et al. (2006). Further, the freshwater flows of the largest and the third largest rivers that discharge into the Baltic, Neva and Kalixälv, are marked with tracers. Their annual mean flows amount to $2584\ m^3\ s^{-1}$ and $749\ m^3\ s^{-1}$, respectively (Bergström and Carlsson, 1994). Finally, the freshwater of all rivers is the source of the last tracer considered. For 1980–2004 the total annual mean flow amounts to $14{,}800\ m^3\ s^{-1}$.

On 26 May 1980 the tracer and age concentrations were set to zero. As at the end of the almost 25-year long simulation in

December 2004 the tracer concentrations are not in steady-state, a 96-year spin-up experiment was performed with four times repeated atmospheric and hydrological forcing. The aim was to calculate quasi steady-state age distributions based upon the climate variability for 1980–2004.

To visualize the pathways of inflowing saltwater after the MBI event in January 2003 (Feistel et al., 2003a) and after the baroclinic summer inflow in August/September 2002 (Feistel et al., 2003b) a shorter experiment was performed starting with zero tracer and age concentrations on 7th September 2001 but with corresponding initial conditions for temperature, salinity, sea level, and current velocity from the long simulation for 1980–2004.

3. Results

3.1. Comparison of model results and observations

In Figs. 3–5 salinity and temperature as function of time and depth and associated median profiles for the period May 1980–December 2004 at selected monitoring stations are shown. The hydrography at each of these monitoring stations characterizes the conditions of the corresponding subbasin. In Table 1 model errors of median temperature and salinity profiles at six selected stations (see Fig. 1) are listed.

The temporal and spatial variability of temperature and salinity is well reproduced by the model. Most of the observed large and medium-strength saltwater inflows happen also in the model (Fig. 3). Due to the reduced frequency of large inflows during the 1980s, the salinity of the lower layer decreased in all subbasins (Fig. 3). Actually this stagnation period started already after the strong MBI in 1975/1976 (not shown). MBIs in January 1993, September 1997 (following the definition by Matthäus, 2006), and January 2003 terminated the exceptionally long stagnation period and renewed together with medium-strength inflows the deep water of the Baltic proper. At the end of the simulation period in December 2004, the salinity at BY15 is in 200 m depth even higher than at the beginning of the integration in May 1980 in correspondence with observations (Feistel et al., 2006). Such large changes of the hydrography are simulated satisfactorily while the vertical two-layer structure is preserved. However, especially at Gotland Deep the simulated halocline is too shallow and the sea surface salinity in the Gotland Basin is overestimated (Figs. 3 and 5). Consequently, salinity in the Bothnian Sea is also overestimated because the deep water of the Bothnian Sea is renewed with inflowing surface water from the Gotland Basin. Nevertheless, the model reproduces salinity gradients from north to south as well as from the surface to the bottom (Fig. 5). Due to the implementation of the BBL the simulation of saltwater inflows into the deep water of the Bornholm Basin has significantly improved (Fig. 3) compared to earlier versions of the model (Meier et al., 2003; their Fig. 8).

Also for temperature satisfactory results are found (Figs. 4 and 5). However, there is a tendency of overestimated sea surface temperatures (SSTs) during summer in the southern subbasins. Although the seasonal cycle is well captured by the model, the depth of the summer thermocline is slightly underestimated (Fig. 4).

Temperature variations within and below the halocline indicate that during baroclinic inflows occurring mainly in summer warm water penetrates into the Bornholm Basin (Fig. 4) and even further into the eastern Gotland Basin (not shown here, the summer inflow in August/September 2002 was analyzed by Meier et al., 2004). Annual temperature maxima and minima within the halocline at Bornholm Deep (salinities in the range between 8.95 and 14.3) are shown in Fig. 6. As in summer SSTs are overestimated in the model, simulated temperature maxima in the intermediate winter water (caused by lateral inflows) are overestimated as well. Nevertheless, in case of temperature extrema the correlations between model results and observations are satisfactory.

In general, model errors of specific median temperature and salinity profiles are lesser than 1 °C and 1, respectively (Table 1). Overall median temperatures in all model versions are overestimated indicating either systematic biases of the atmospheric forcing or of the heat flux parameterizations used in RCO (Meier, 2002). The biases of median salinity are negative in HR0 and positive in HR1 and HR2. It is impossible here to draw a conclusion about the causes because the experiment HR0 was carried out only for the stagnation period until 1993. In HR1 and HR2 the renewal of the deep water in the Bornholm Basin is improved due to the BBL model. However, simultaneously the halocline in the eastern Gotland Basin is lifted up resulting in an overestimated salinity averaged for the entire Baltic. This deficit of the present model version seems to be independent of the numerical advection scheme and of the details of the vertical turbulence parameterization used. Further investigations are still necessary to improve RCO. However, the performance is regarded as sufficiently good to analyze the large-scale circulation on decadal time scales.

3.2. Mean circulation

Based on six-hourly snapshots the mean circulation for 1981–2004 is calculated. As the Baltic Sea is a two-layered estuary approximately, volume transports above and below the halocline are calculated. Per definition the halocline is located at the depth of the maximum of the first derivative of salinity as function of depth. In case of an almost vertically homogenous water column the halocline depth is close to the water depth. However, the conceptual two-layer model works only accurately in those areas with a perennial halocline. For instance, in the shallow entrance areas the water column is often well-mixed. In these cases either inflow or outflow might happen depending on the barotropic forcing. As in these cases the thickness of the upper layer transport is equal to the water depth and the thickness of the lower layer transport is negligible, the calculated total mean Baltic outflow from the upper layer is underestimated. Consequently even the total mean Baltic inflow into the lower layer is underestimated due to volume conservation. Nevertheless, in RCO the mean deep water

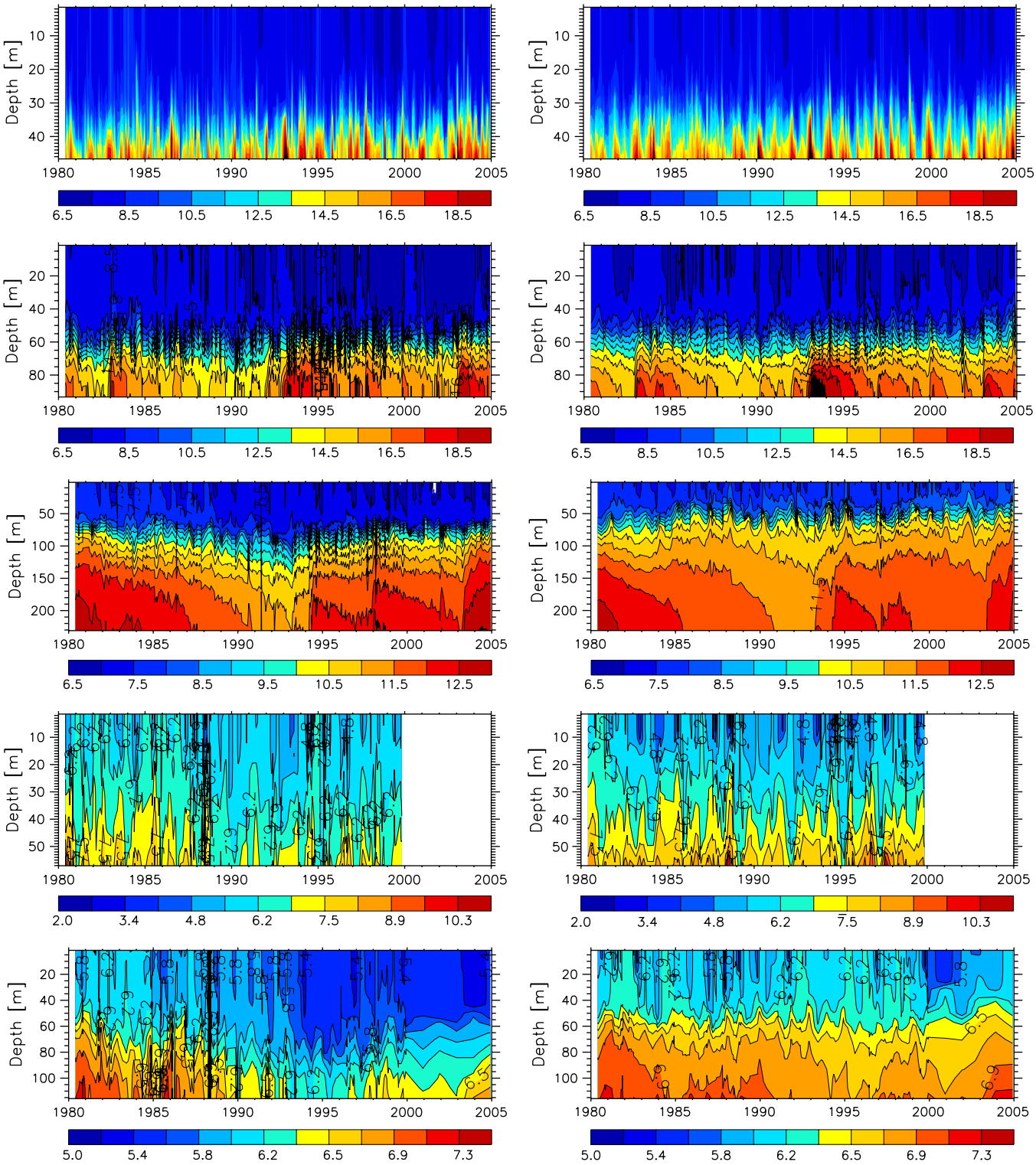

Fig. 3. Salinity as function of time and depth for 1980–2004 at the monitoring stations Arkona Deep (BY2, first row), Bornholm Deep (BY5, second row), Gotland Deep (BY15, third row), Gulf of Finland (LL07, fourth row), and Bothnian Sea (SR5, fifth row): observations (left panels) and results of the Rossby Centre Ocean model, RCO (right panels). Note the different color bars for different stations.

flow is simulated in close agreement with observations (Meier and Kauker, 2003).

In the northeastern Gotland Basin and in the Gdansk Basin maximum annual mean halocline depths of 68 and 75 m are found, respectively (Fig. 7). In the deep region including Gotland Deep a possibly artificial 'dome' of the halocline is found. This would explain the results shown in Figs. 3 and 5.

Especially in the western Gotland Basin, in the Bothnian Sea, and in the Bothnian Bay halocline depths vary considerably during the seasons. In general, the halocline is deeper in

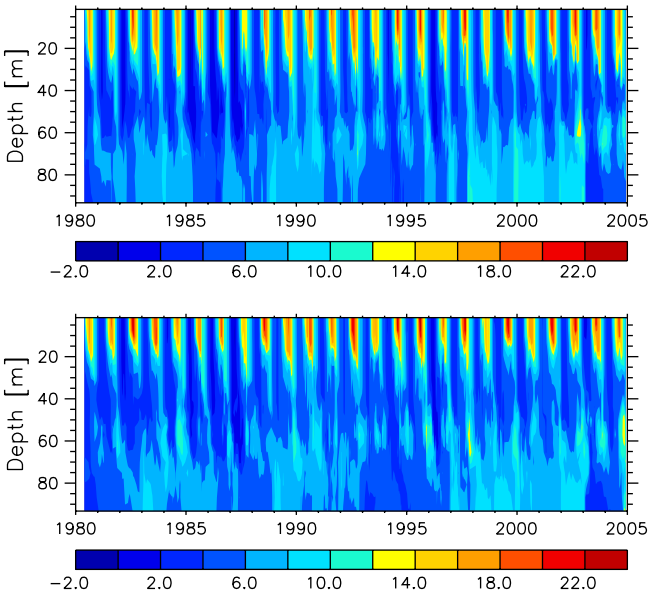

Fig. 4. Observed (upper panel) and simulated (lower panel) temperature (in °C) as function of time and depth for 1980–2004 at the monitoring station Bornholm Deep (BY5).

winter and spring than in summer and autumn (not shown). Maximum differences between the halocline depths in spring and autumn amount to 36 m (Fig. 7). In winter the largest halocline depths of the year of more than 83 m in the Northern Basin (close to the entrance into the Gulf of Finland) are calculated (not shown).

The mean transports both above and below the halocline show pronounced cyclonic gyres in the Baltic proper and in the Bothnian Sea (Figs. 8 and 9) with high persistencies (Fig. 10). Especially in the eastern Gotland Basin high transports flowing around the Gotland Deep area are found. Strength and persistence of the transports and currents (not shown) in the Gulf of Finland, the Gulf of Riga, and the northern Bothnian Bay are smaller compared to the Baltic proper indicating possibly the impact of sea ice during the winter season.

Close to the Swedish coast a relatively intensive flow within the upper layer from the western Gotland Basin into the Bornholm Basin and Arkona Basin is found (Fig. 8). The main flow crosses the central Arkona Basin and bifurcates north of Rügen island. One branch leaves the Baltic at the Darss Sill and continues through the Belt Sea and the Great Belt. The other branch recirculates and forms a cyclonic gyre in the Arkona Basin. A smaller but still significant flow follows the Swedish coast into the Öresund and Kattegat.

In the lower layer the flow follows the bathymetry, from the Darss Sill into the Arkona Basin and further towards Bornholm Channel passing Rügen island and the northern side of the Adlergrund (Fig. 9). The deep water flow continues further towards Bornholm Deep and into the Słupsk Furrow with large persistency (Fig. 10). Leaving the Słupsk Furrow the main flow spreads along the southwestern slope of the Gdansk Basin and surrounds this basin close to the coast. However, a weaker and more diffusive flow separates from the main flow within the Gdansk Basin and propagates directly towards northeast along the eastern slope of the Hoburg Channel. Along the western slope of the Hoburg Channel the mean flow is directed southward. Details of the pathway of the inflowing saltwater in the Gdansk Basin and in the eastern Gotland Basin are discussed further in the next section.

3.3. Pathways of water masses

To visualize the pathways of selected water masses several passive tracers have been used. One of them marks the inflowing saltwater at section S1 in the Arkona Basin (Fig. 1) with salinities more than 17 (Section 2.4). The tracer concentration was set to zero on 7th September 2001, well before the MBI in January 2003. Maps of the propagation of the gravity-driven dense water clearly show that after leaving the Słupsk Furrow part of the plume flows towards northeast along the eastern slope of the Hoburg Channel and another part spreads along the southwestern slope of the Gdansk Basin (Fig. 11). Following the slope of the bathymetry the plume flows further into the deepest part of the eastern Gotland Basin. In addition, at the basin-wide section S3 across the Gotland Basin (Fig. 1) a smaller, second concentration maximum within the halocline at about 50–100 m depth is found (Fig. 11). This signal is caused from a previous, smaller inflow (not MBI) when high-saline water (with salinities more than 17 in the Arkona Basin) is diluted on its way from the sills in the entrance area towards Gotland Deep. The depth of the core of the intrusion within the halocline coincides with the maximum of the horizontally integrated volume transport across section S3 (Meier and Kauker, 2003).

In summer 2002 an exceptional warm inflow event was observed at Darss Sill (Feistel et al., 2003b; Mohrholz et al., 2006). Summer inflows are driven by baroclinic pressure gradients during calm wind conditions when in the Belt Sea and in the Arkona Basin the mixing of the inflowing water with the ambient water is reduced. As a consequence, warm and saline water masses are sandwiched into the halocline of the Bornholm Basin and could be traced even at Gotland Deep because the associated temperatures are higher than those of the surrounding water. Warm inflows in September 1997, October 2001, August 2002, and August 2003 had a considerable impact on the water temperature at 200 m depth in the eastern Gotland Basin which increased to more than 6 °C (Feistel et al., 2006; their Fig. 1).

Maps of concentrations of the tracer marking warm intermediate water at section S2 in the Bornholm Basin (Fig. 1) with salinities between 8.95 and 14.3 and with temperatures more than 11 °C show that the saline water of the event in August 2002 flows after the Słupsk Furrow only towards southwest following the slope in Gdansk Basin (Fig. 12). The Gdansk Basin plays the role of a buffer zone for the inflow water before spreading further towards Gotland Deep. The core of the flow intersects section S3 in about 80 m depth (Fig. 12). These results suggest that the path of the inflowing water in Gdansk Basin depends on the salinity of the flow. In

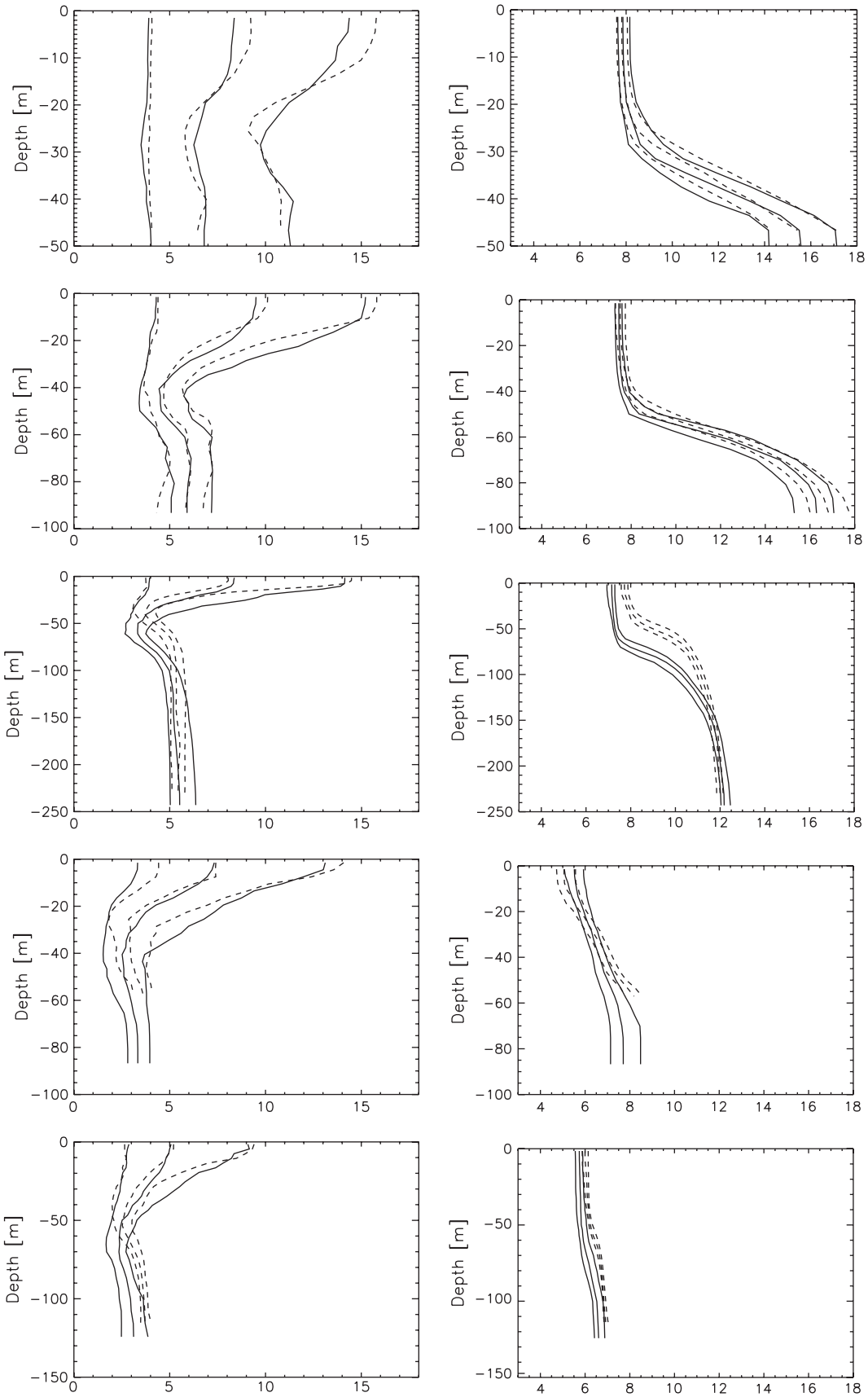

Fig. 5. Observed (solid) and simulated (dashed) median, first and third quartile profiles for temperature (in °C, left panels) and salinity (right panels) for the period May 1980–December 2004 at BY2 (first row), BY5 (second row), BY15 (third row), LL07 (fourth row), and SR5 (fifth row). The locations of the monitoring stations are shown in Fig. 1.

Table 1
Model errors of median temperature (T) and salinity (S) profiles for three RCO versions (see Section 2.1): HR0 (1980–1993, Meier et al., 2003), HR1 (1980–2003), and HR2 (1980–2004, this study). Sum denotes the error of all profiles except LL07. (N = number of observed profiles, ME = mean error, and RMSE = root mean square error)

Basin	N	ME T (°C)			RMSE T (°C)			ME S			RMSE S		
		HR0	HR1	HR2	HR0	HR1	HR2	HR0	HR1	HR2	HR0	HR1	HR2
BY2	539	0.64	0.17	−0.00	0.81	0.48	0.54	−0.07	0.13	0.15	0.34	0.35	0.37
BY5	558	−0.07	0.10	−0.05	1.15	0.57	0.47	−0.67	0.37	0.27	0.96	0.52	0.34
BY15	435	−0.04	0.42	0.09	0.59	0.95	0.79	−0.21	0.86	0.87	0.29	1.07	1.16
BY31	167	0.11	0.48	0.29	0.43	0.60	0.45	0.00	0.83	0.82	0.21	0.91	0.87
LL07	258	–	−0.23	0.08	–	0.65	0.46	–	−0.04	0.08	–	0.64	0.43
SR5	192	−0.21	0.33	0.12	0.29	0.49	0.52	−0.52	0.18	0.37	0.53	0.19	0.38
Sum	1891	0.43	1.50	0.53	1.61	1.43	1.27	−1.47	2.37	2.48	1.20	1.55	1.58

March 2003 the induced circulation at the Farö Deep is more pronounced than in the eastern Gotland Basin.

Also the pathways of the tracers marking freshwater of the rivers Neva and Kalixälv have been studied. From the mouth of the river Neva the freshwater is spreading close to the Finnish coast into the northern Gotland Basin and further southward close to the Swedish east coast (not shown). Thereafter the tracer follows the large-scale cyclonic gyre within the Gotland Basin. From the mouth of the river Kalixälv the freshwater is spreading along the Swedish east coast southward (not shown). The tracer results confirm the sketch of the vertical circulation in Fig. 2. For instance, the first signal of the Kalixälv tracer in the Gulf of Finland is found in the lower layer. After the arrival in the Gulf of Finland the upper layer is slowly filled with the tracer due to vertical advection and diffusion whereas lateral advection into the upper layer is negligible.

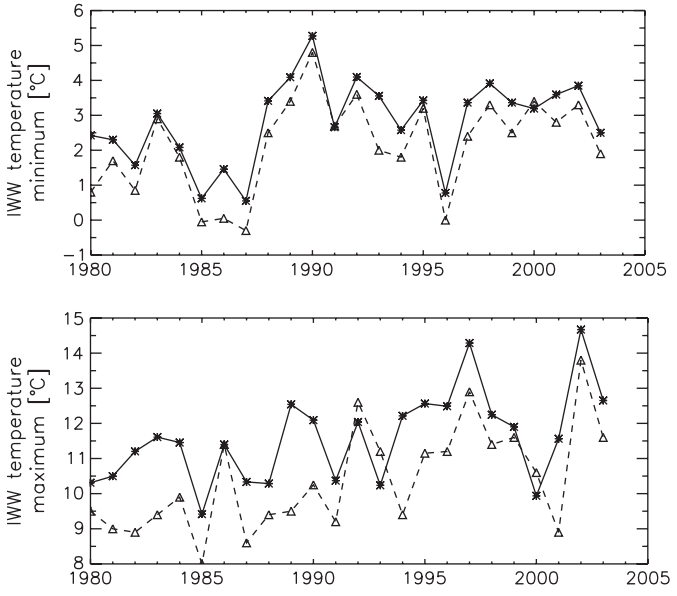

Fig. 6. Annual temperature minimum (upper panel) and maximum (lower panel) (in °C) in the intermediate winter water at Bornholm Deep (BY5): model results (solid lines) and observed temperature minimum and maximum (dashed line). The data are taken from Mohrholz et al. (2006).

An important question is: where is the inflowing saltwater coming up. In Fig. 13 the 24-year mean vertical flux across the halocline of the tracer associated with inflowing water with salinities more than 17 is shown. Note, that at the end of the 48-year long simulation the tracer distribution is not in steady-state (Section 3.4). This explains why the vertical fluxes in the Bothnian Bay are much smaller than in the Gotland Basin.

In general, the vertical fluxes are scattered and no larger region with only one sign is found (Fig. 13). However, large negative fluxes from the upper into the lower layer are found in wide areas of the Arkona Basin and in the Słupsk Furrow indicating entrainment (Fig. 13). Also in downwelling regions at the slopes of the eastern Gotland Basin and of the eastern Bothnian Sea the fluxes are mainly negative.

Relatively large, positive fluxes from the lower into the upper layer are found at the western and eastern slopes of the Słupsk Furrow, at the western slope of the eastern Gotland Basin, in the central part of the eastern Gotland Basin, in the Northern Basin north of Gotland island, and at the western coast of Gotland close to Visby (just to name a few pronounced locations shown in Fig. 13). The patterns of the vertical tracer fluxes are highly significant and resemble the patterns of vertical velocity at the sea surface (Myrberg and Andrejev, 2003).

When saline waters enter the Baltic, the halocline is lifted up. Due to mixing the halocline is eroded and is sinking back to the original depth after some time. From Fig. 13 it is concluded that in the mean the vertical movement is not spatially uniform. There are distinct areas of upward and downward advective (and connected diffusive) tracer fluxes across the halocline where the large-scale vertical circulation is closed.

3.4. Mean ages

The evolutions of the tracer masses marking the inflowing water at the Darss and Drogden sills (case 1, see Section 2.4) integrated for various subbasins above and below the halocline suggest that after 96 years of spin-up the tracer is almost in steady-state in all subbasins (Fig. 14). An averaging interval of about 5 years is sufficient to ensure stable results.

In the deep subbasins like the eastern and northwestern Gotland Basin and in the Bothnian Sea the tracer mass is in

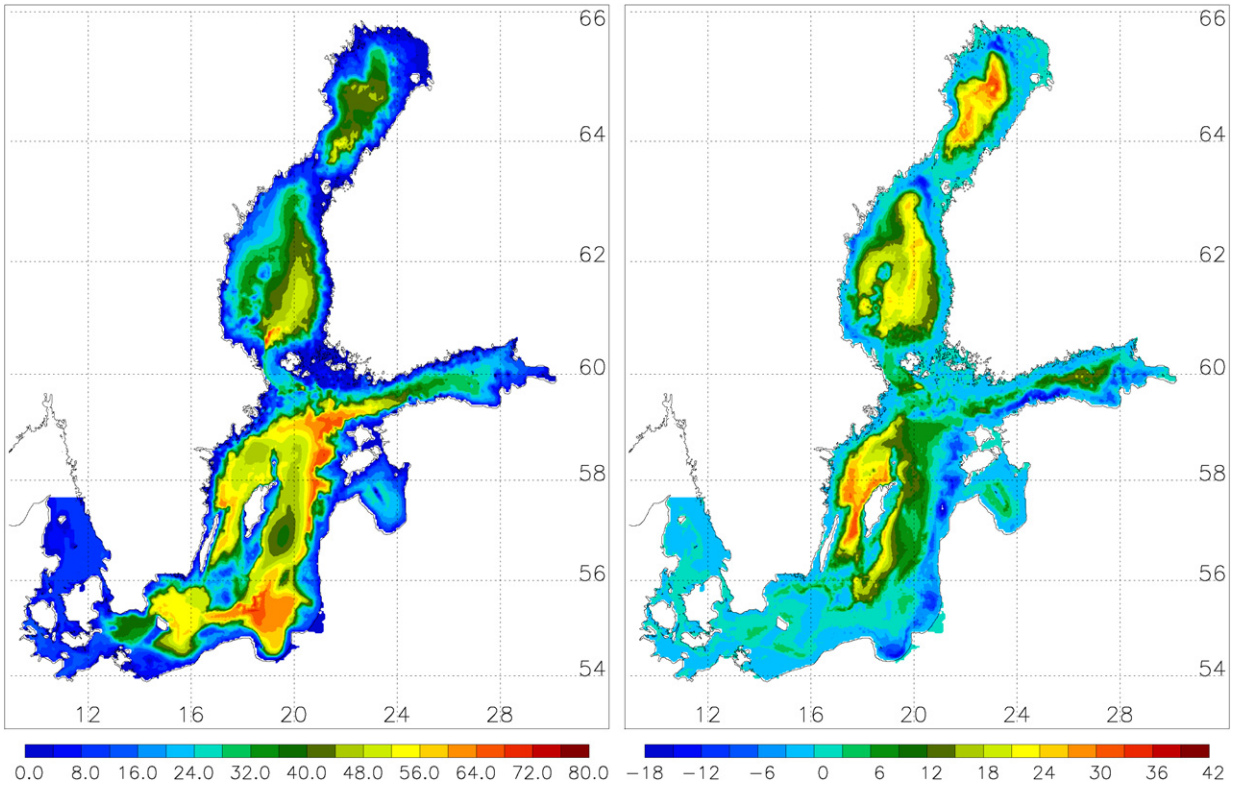

Fig. 7. Halocline depths (in m) for 1981–2004: annual mean (left panel) and difference between spring and autumn means characterizing the seasonal variation (right panel).

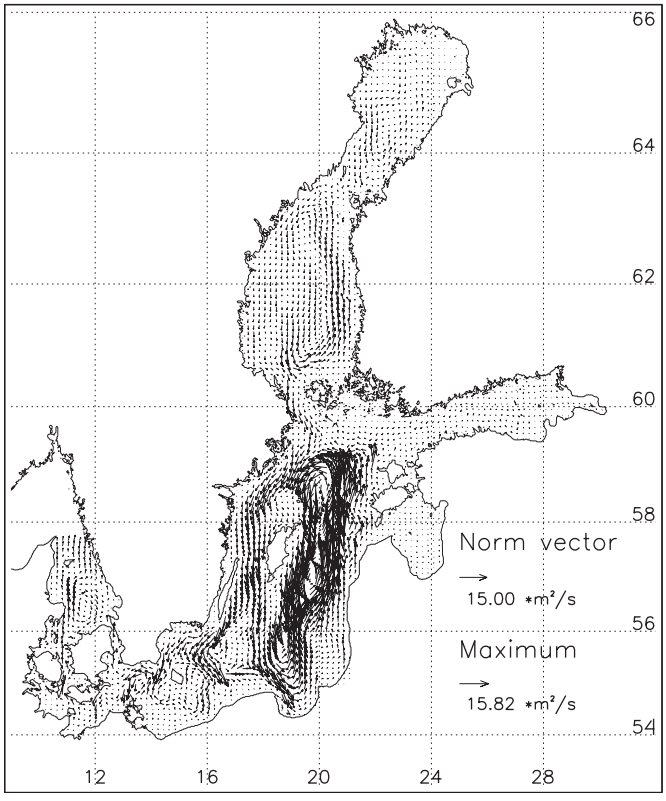

Fig. 8. Annual mean transport per unit length (in $m^2\,s^{-1}$) for 1981–2004 above the halocline. Only vectors at every third gridpoint of the model are shown.

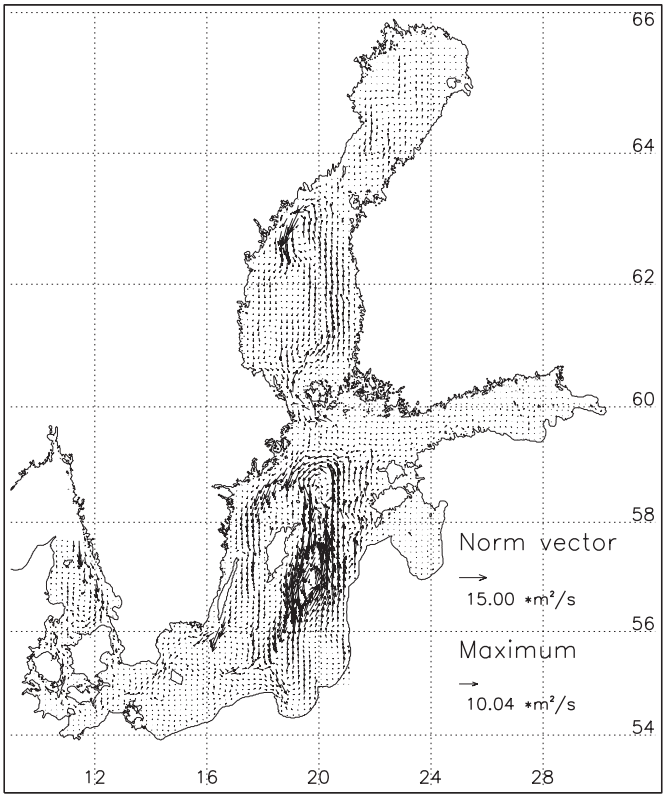

Fig. 9. As Fig. 8 but transport below the halocline.

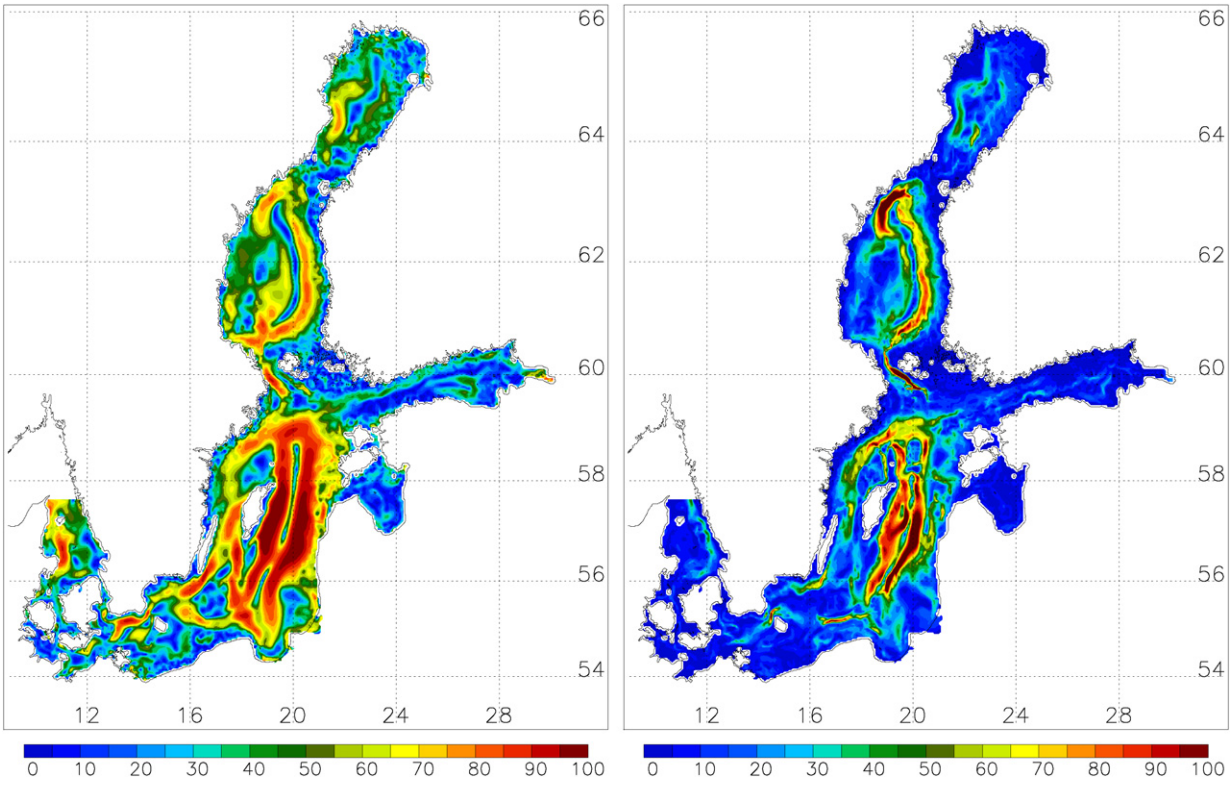

Fig. 10. Persistency (in %) of the mean transport above (left panel) and below (right panel) the halocline for 1981–2004. For the definition of persistency the reader is referred to Lehmann and Hinrichsen (2000).

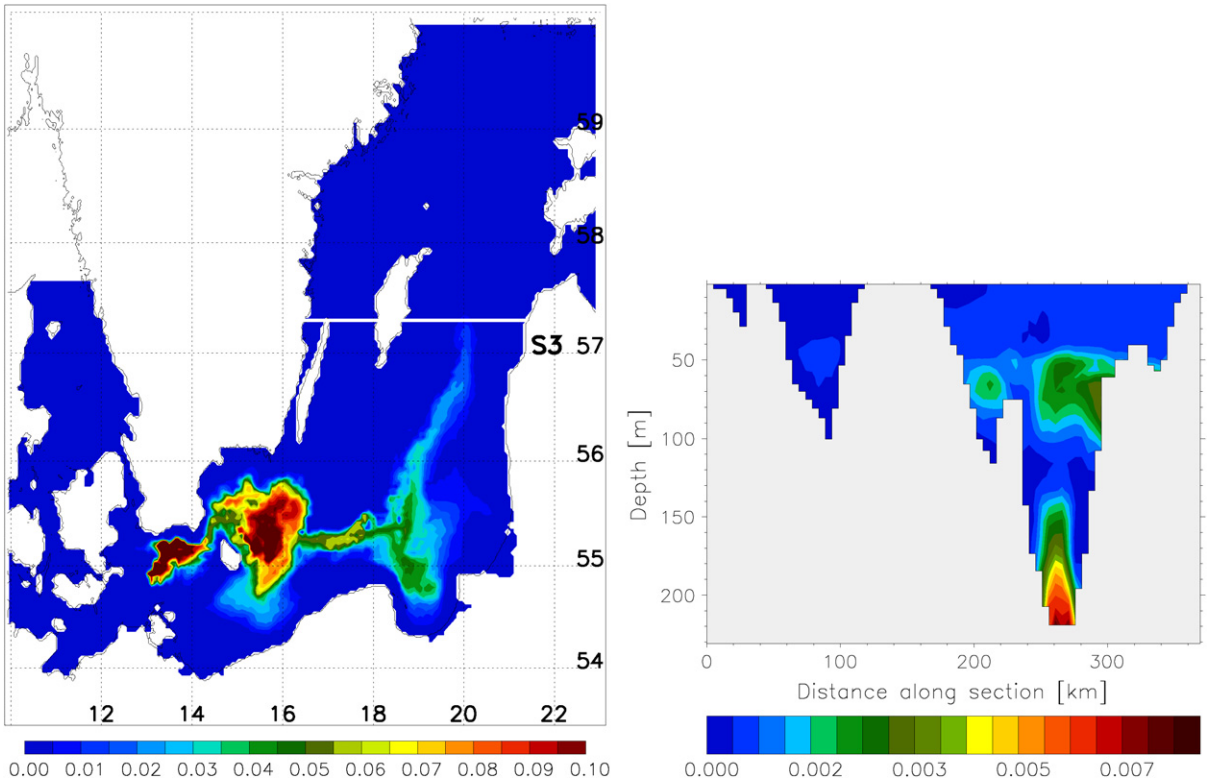

Fig. 11. Monthly mean tracer concentration in May 2003 marking inflowing saltwater in the Arkona Basin with salinities more than 17 at the surface with a salinity of 17 (left panel) and at a longitudinal section across the Gotland Basin (right panel). The location of the section is shown as white line in the left panel. If the salinity in the water column is less than 17, the tracer concentration at the bottom is depicted. The results were taken from an experiment when the tracer was initialized on 7th September 2001.

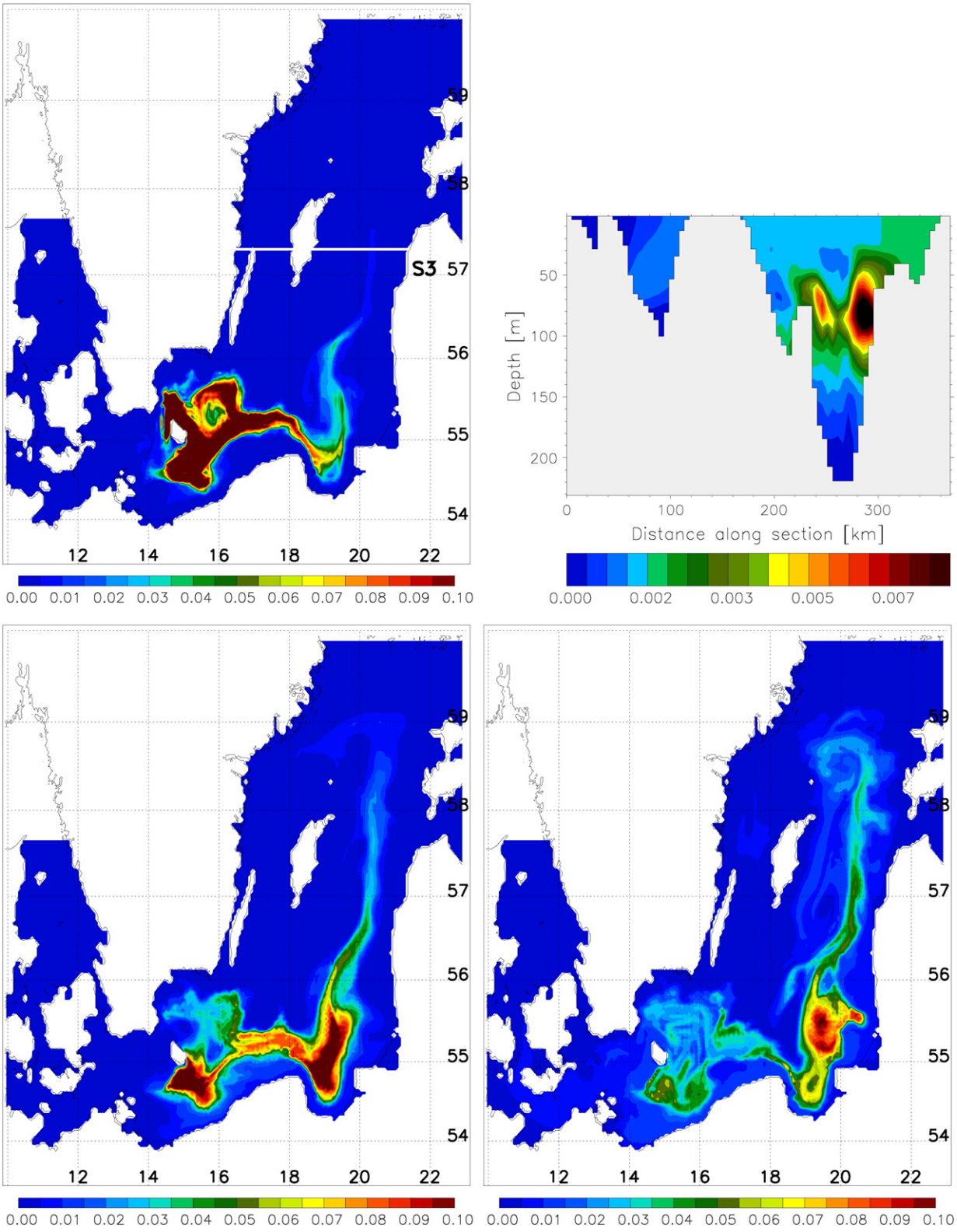

Fig. 12. Monthly mean tracer concentration in November 2002 marking warm intermediate water in the Bornholm Sea with salinities between 8.95 and 14.3 and with temperatures more than 11 °C at the surface with a salinity of 9 (upper left panel) and at a longitudinal section across the Gotland Sea (upper right panel). The location of the section is shown as white line in the upper left panel. If the salinity in the water column is less than 9, the tracer concentration at the bottom is depicted. The lower panels show the corresponding tracer concentration in January 2003 (lower left panel) and March 2003 (lower right panel). The results were taken from an experiment when the tracer was initialized on 7th September 2001.

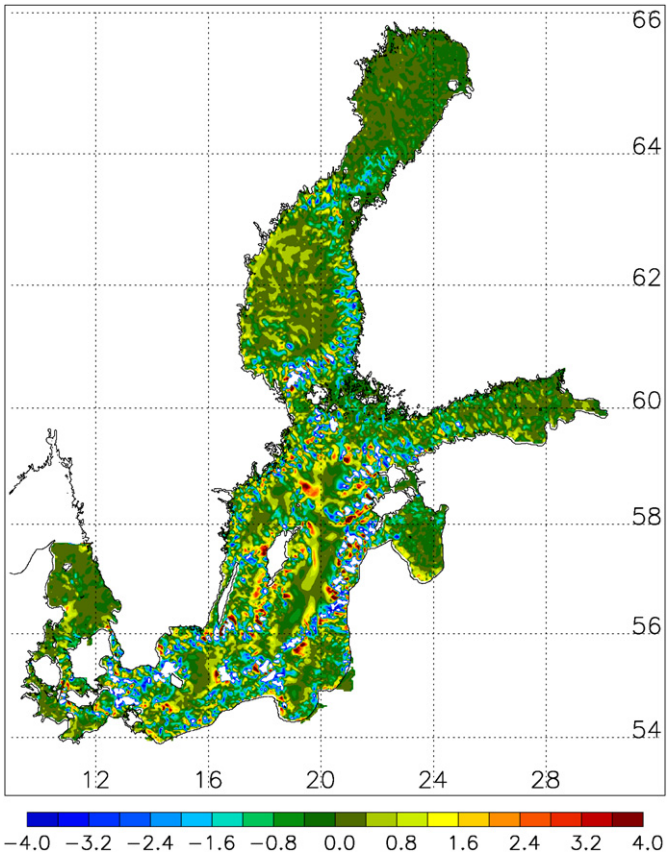

Fig. 13. Twenty-four-year mean vertical mass flux (in 10^3 kg s^{-1}) across the halocline of the tracer marking inflowing saltwater in the Arkona Sea with salinities more than 17. Upward fluxes are counted positive and fluxes lesser than -4×10^3 kg s^{-1} are depicted in white. The results were taken from an experiment with spin-up using the same atmospheric and hydrological forcing fields for 1981–2004 repeated two times. The tracer was initialized on 26th May 1980. The average was calculated for the whole second cycle.

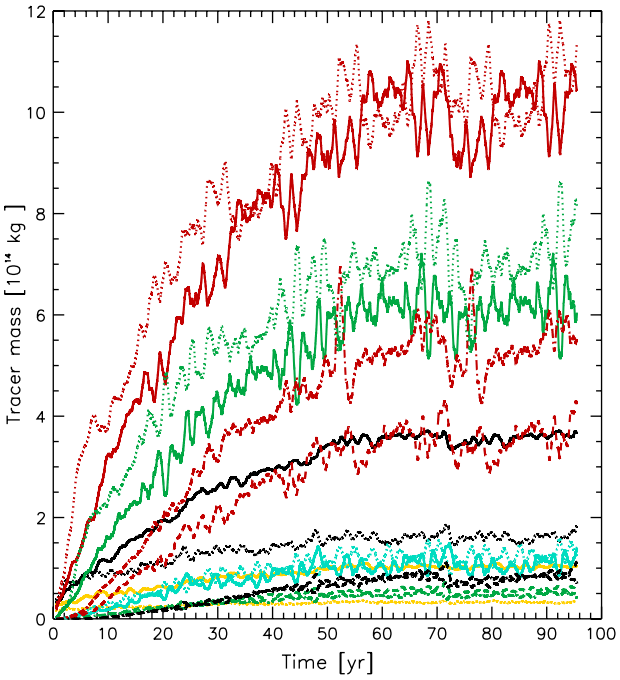

Fig. 14. Evolution of tracer mass (in 10^{14} kg) in various subbasins during the 96-year spin-up. The tracer marks inflowing water at the Darss and Drogden sills of all salinities. The tracer was initialized on 26th May 1980. The curves denote the 4-year running mean integrated tracer masses above and below the halocline in the Arkona Basin (yellow solid and dotted lines), in the Bornholm Basin (black solid and dotted lines), in the eastern Gotland Basin (red solid and dotted lines), in the northwestern Gotland Basin (green solid and dotted lines), in the Gulf of Finland (blue solid and dotted lines), in the Gulf of Riga (green dashed and dash-dotted lines), in the Bothnian Sea (red dashed and dash-dotted lines), and in the Bothnian Bay (black dashed and dash-dotted lines).

the lower layer larger than in the upper layer. This is also true for the Arkona Basin and the Bornholm Basin during the first 4 years. Thereafter the tracer mass of the upper layer is getting larger in these subbasins.

The tracer marking freshwater from all rivers (case 6) is also approximately in steady-state at the end of the 96-year long spin-up simulation although the required time scale is significantly larger than in the case of the tracer marking inflowing water from Kattegat (Fig. 15). In all subbasins the tracer masses of the upper layers are larger than those of the lower layers. An exception is the Bothnian Sea. After about 10 years the tracer mass of the lower layer is larger indicating an intense vertical recirculation of freshwater in the Gulf of Bothnia.

The evolutions of the tracer masses marking the freshwater from the river Neva (case 4) indicate that in the eastern and northwestern Gotland Basin and in the Bothnian Sea a steady-state has not been achieved (not shown). This is not astonishing as the turnover time of the Neva freshwater in the Baltic Sea with a total volume of 21,500 km^3 considering an inflow of 2584 m^3 s^{-1} amounts to 264 years approximately. Hence, the calculated ages are only lower limits of the ages in steady-state and are not depicted. In the Gulf of Finland, most of the changes in the upper and lower layers occur during the first 10 years approximately.

Also the tracers marking freshwater from Kalixälv (case 5) and high-saline inflows (case 2) are not in steady-state after about 100 years of integration whereas the tracer marking warm summer inflows (case 3) is in steady-state approximately (not shown).

In Figs. 16 and 17 5-year mean ages at the end of the 96-year spin-up experiment in three different depths are shown. The associated tracers mark either inflowing water at the Darss Sill and at the Drogden Sill (Fig. 16) or freshwater from all rivers (Fig. 17). In the first case of inflowing water from Kattegat there are pronounced vertical and horizontal age gradients between the lower and the upper layers and between the Baltic entrance area and the Bothnian Bay in the north, respectively (Fig. 16). At the sea surface of the Belt Sea and the Bothnian Bay minimum and maximum ages are smaller than 14 and larger than 40 years, respectively. In the bottom layer of the Arkona Basin minimum ages are even smaller than 10 years. The halocline separates the water masses of the two layers that have in the Gotland Basin associated ages smaller or larger than about 26 years.

In the case of the tracer marking freshwater from all rivers (case 6) the vertical age gradients in the Gotland Basin are

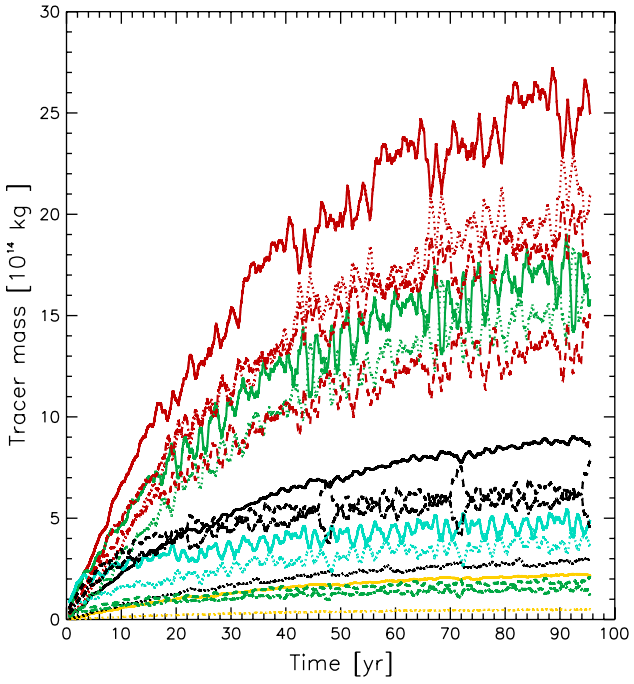

Fig. 15. As Fig. 14 but the tracer marks freshwater from all rivers.

much smaller than in the case of inflowing water from Kattegat (Fig. 17). At the sea surface largest mean ages of more than 30 years are found in the central Gotland Basin and Belt Sea. Very young water is only found in narrow areas close to the coast and close to river mouths. At the bottom the mean ages are largest in the western Gotland Basin and amount to more than 36 years. On the horizontal surface at the depth of the halocline ages are rather homogeneously distributed in the Baltic proper in contrast to ages associated to inflowing water from Kattegat that are characterized by large gradients on the pathway between the entrance sills and the deepest parts of the Baltic (Fig. 16).

Mean ages associated to freshwater from the river Neva (case 4) amount at the sea surface of the Gotland Basin and western Baltic Sea to about 32 years (not shown). Largest gradients are found in the Gulf of Finland. Between the mouth of the river Neva and the Northern Basin the ages vary between 0 and more than 30 years. The sea surface map also indicates that a significant amount of the freshwater from Neva flows through the Archipelago Sea northward into the coastal regions of the eastern Bothnian Sea. At the sea surface largest ages of more than 38 years are found in the Bothnian Bay. At the bottom the largest age gradients are found between the eastern and northern coastal regions and the central parts of the Gulf of Finland (not shown). Within a sharp coastal jet the freshwater from Neva is transported close to the Finnish coast eastward into the Northern Basin. In the bottom layer largest ages of more than 38 years are found in the northern Bothnian Bay and in the northwestern Gotland Basin.

The horizontal sea surface map of mean ages associated to freshwater from the river Kalixälv (case 5) is characterized by a strong north–south gradient with sharp fronts between the Bothnian Bay and the Bothnian Sea and between the Bothnian Sea and the Gotland Basin (not shown). In the eastern Gotland Basin, the western Baltic and the Kattegat mean ages are in the range between 38 and 40 years. Largest ages of more than 40 years are found in the Gulf of Finland and in the Gulf of Riga.

Horizontal distributions of mean ages associated to high-saline inflows (case 2) and associated to warm summer inflows (case 3) are rather similar than shown in Fig. 16 although the ages are generally larger. At the sea surface of the eastern Gotland Basin mean ages between 32 and 34 years (case 2) and between 30 and 32 years are found (case 3). Note that the mean ages associated to high-saline inflows (case 2) and to freshwater from the particular rivers Neva (case 4) and Kalixälv (case 5) are only lower limits of the ages in steady-state as mentioned before.

It is interesting to note that the vertical age differences across the halocline are much larger in case of inflowing deep water than in case of spreading juvenile freshwater (Figs. 16 and 17). This finding suggests that in the model the downward tracer flux across the halocline caused by the entrainment of the surface water into the deep water flow is balanced by the upward tracer flux due to the interplay of vertical advection and diffusion. Consequently, the upward tracer flux caused by the entrainment of the deep water into the surface layer flow is less important. If the upward and downward entrainment fluxes would balance each other, the problem would be symmetric and the vertical tracer gradient would be the same in the two cases when the tracer is injected into the freshwater of the upper layer or into the saltwater of the lower layer.

4. Discussion

In this study passive tracers have been used to track various water masses. The overall aim was to analyze the large-scale circulation on short (advective) and long (approaching steady-state) time scales in more detail. As the simulation period of less than 25 years is rather short compared to typical turnover times, a 96-year long spin-up experiment with four times repeated atmospheric and hydrological forcing was performed to calculate the ages of selected water masses in steady-state. These ages are governed by the climate variability of the period 1980–2004. It would be interesting to calculate also the ages related to the inflow variability during other periods when more MBIs were observed (e.g. in the 1950/1960s). However, such investigations are beyond the scope of this study.

The applied method of repeating time slices has the disadvantage that the stratification changes slightly with each cycle (towards higher salinities) because the atmospheric and hydrological forcing functions are not periodic. However, the salinities at the beginning of the integration in May 1980 and at the end of 2004 are relatively similar. Hence, the impact of the overall drift is assumed to be minor. During each cycle the main features of the hydrography are preserved (not shown).

As mentioned in Section 1 the large-scale circulation was assessed earlier. Lehmann and Hinrichsen (2000) and Lehmann et al. (2002) found similar cyclonic gyres for the surface and for the barotropic circulation as in our study. Also the

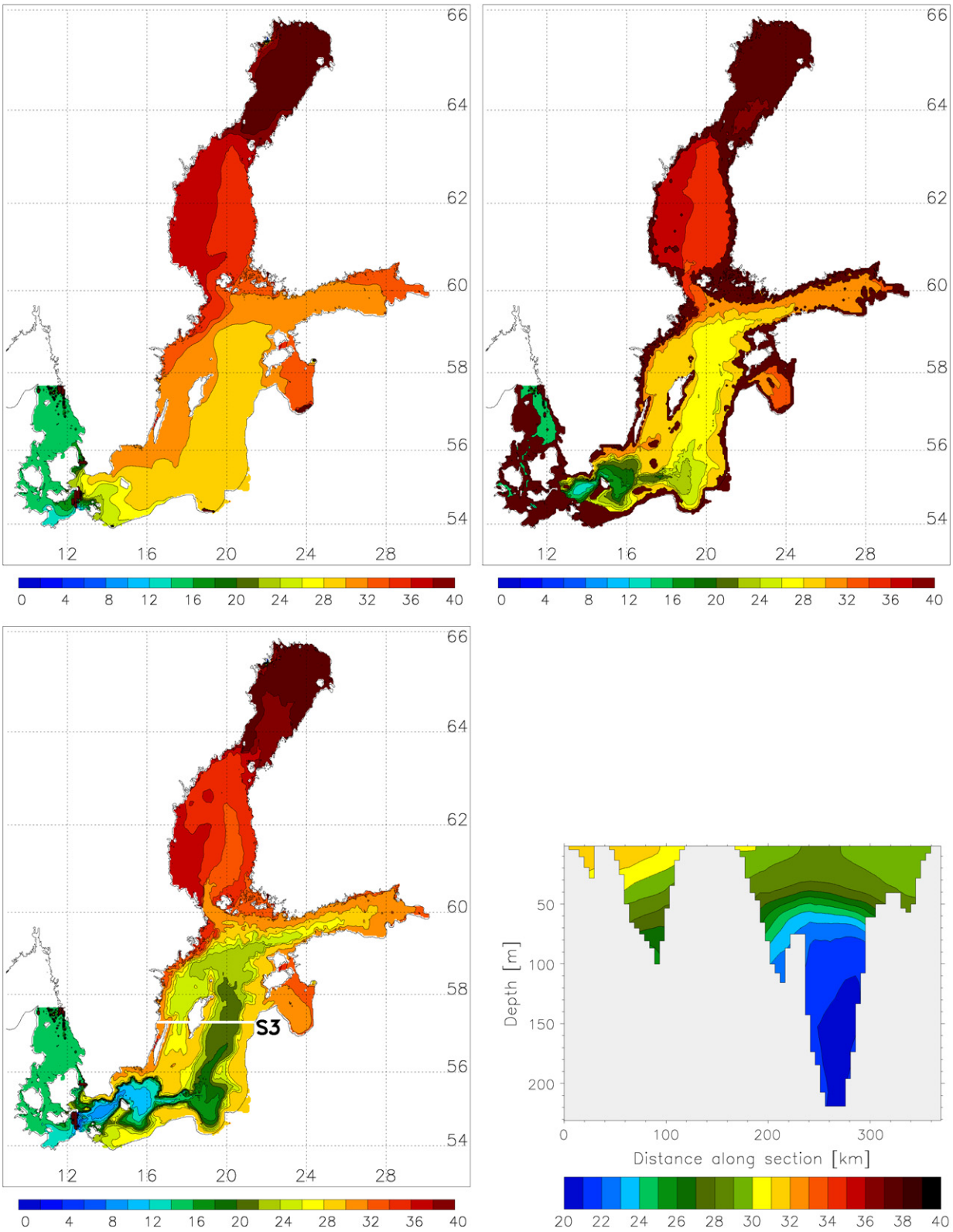

Fig. 16. Mean age (in years) for the last 5 years of the 96-year spin-up associated to the tracer marking inflowing water at the Darss and Drogden sills. The figures depict ages at the sea surface (upper left panel), at the halocline depth (upper right panel), at the surface with a salinity of 17 (lower left panel), and at the longitudinal section S3 across the Gotland Basin (lower right panel). The location of the section is shown as white line in the lower left panel. Note the different color bars. In the upper right panel mean ages are not depicted in shallow areas without a perennial halocline, where the conceptual two-layer model does not apply (see Section 3.2). Per arbitrary definition these areas (in brown) are characterized by a water depth less than 22.5 m. Is the salinity in the water column below 17 the associated surface is set equal to the water depth. Hence, the lower left panel shows bottom ages in most of the Baltic interior.

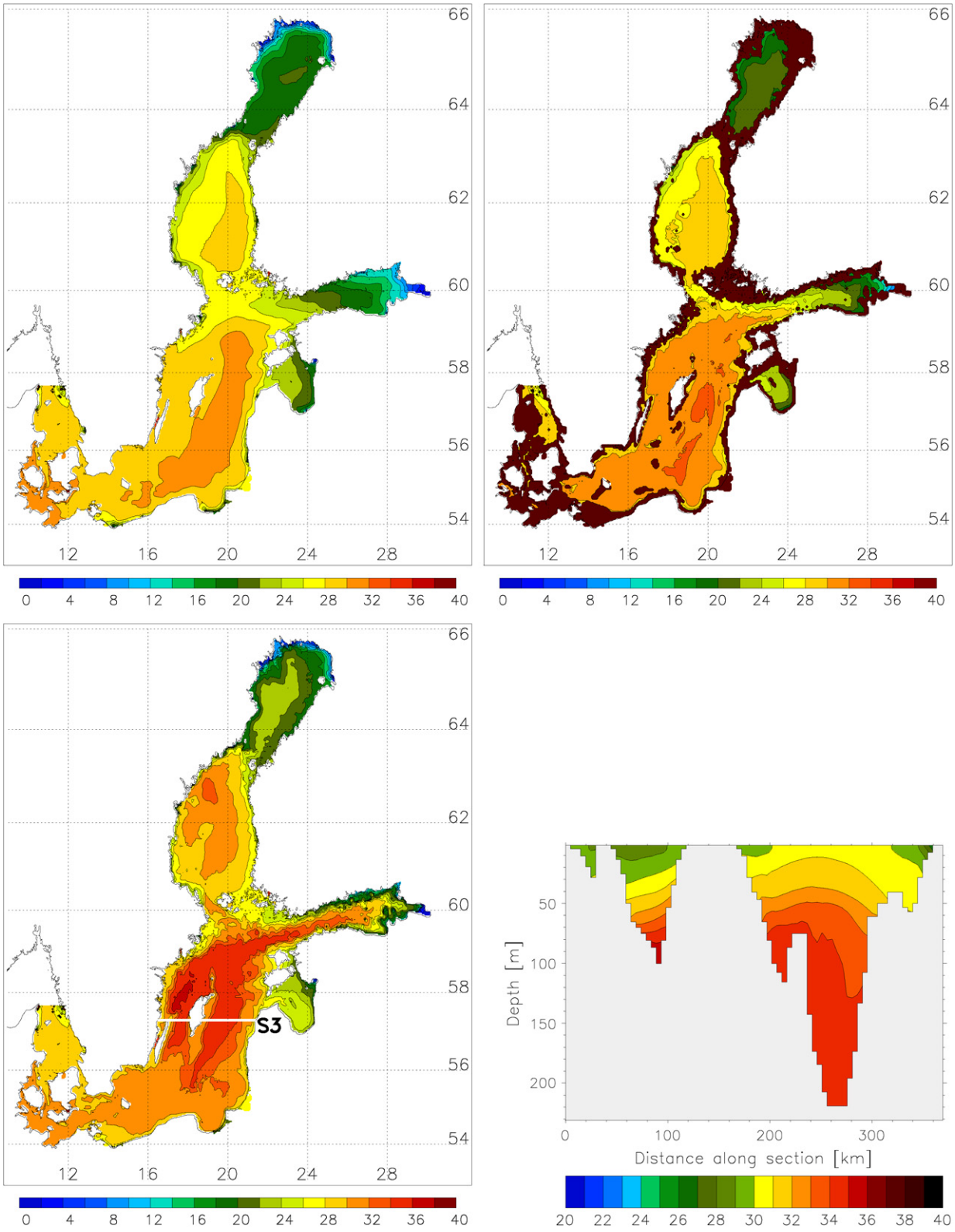

Fig. 17. As Fig. 16 but the ages are associated to the tracer marking freshwater from all rivers.

results for the Gulf of Finland by Andrejev et al. (2004a) and for the Bothnian Sea and Bothnian Bay by Myrberg and Andrejev (2006) resemble our findings. However, there might be differences in details. For instance, the persistency of the sea surface circulation in the Bothnian Sea and Bothnian Bay is in this study larger compared to the results by Myrberg and Andrejev (2006) (not shown). An explanation might be the use of the k-ε turbulence model with flux boundary conditions to include the effect of a turbulence enhanced layer due to breaking surface gravity waves. However, the exact reasons

for the different results are unknown. In none of the previous studies the large-scale pattern of the deep water flow on long time scales was investigated.

5. Conclusions

The main conclusions of this study are as follows.

1. The implementation of the BBL model improves simulations of the multi-annual variability in the Baltic Sea.
2. The implementation of the FCT advection scheme enables the investigation of the pathways and ages of Baltic water masses generated at spatially limited sources on long time scales (e.g., the calculation of ages in steady-state).
3. The calculation of ages of inflowing water from the Kattegat in steady-state requires at least 100-year simulations because maximum ages of more than 40 years are found in the Bothnian Bay. The method of repeated integration of a time slice with atmospheric and hydrological forcing from the period 1980 to 2004 allows the calculation of plausible age distributions.
4. From simulated ages in steady-state it is concluded that the downward flux across the halocline caused by the entrainment of the surface water into the deep water flow can only be balanced by the upward advective and diffusive fluxes. Thus, studies of passive tracers and associated ages help to understand the physical processes important for the large-scale vertical circulation in the Baltic Sea.

Acknowledgments

The model simulations were performed on the climate computing resource 'Tornado' operated by the National Supercomputer Centre at Linköping University. Tornado is funded with a grant from the Knut and Alice Wallenberg foundation. Philip Axe is acknowledged for providing CTD data from the Oceanographic Data Centre for BALTEX (ODCB) at the Swedish Meteorological and Hydrological Institute. I would like to acknowledge the two reviewers for their constructive comments.

References

Andrejev, O., Myrberg, K., Lundberg, P.A., 2004a. Mean circulation and water exchange in the Gulf of Finland – a study based on three-dimensional modelling. Boreal Environment Research 9, 1–16.

Andrejev, O., Myrberg, K., Lundberg, P.A., 2004b. Age and renewal time of water masses in a semi-enclosed basin – application to the Gulf of Finland. Tellus 56A, 548–558.

Beckmann, A., Döscher, R., 1997. A method for improved representation of dense water spreading over topography in geopotential-coordinate models. Journal of Physical Oceanography 27, 581–591.

Bergström, S., Carlsson, B., 1994. River runoff to the Baltic Sea: 1950–1990. Ambio 23, 280–287.

Bolin, B., Rodhe, H., 1973. A note on the concepts of age distribution and transit time in natural reservoirs. Tellus 25, 58–62.

Cyberski, J., Wroblewski, A., 2000. Riverine water inflows and the Baltic Sea water volume 1901–1990. Hydrology and Earth System Sciences 4, 1–11.

Deleersnijder, E., Campin, J.-M., Delhez, E.J.M., 2001. The concept of age in marine modelling: I. Theory and preliminary results. Journal of Marine Systems 28, 229–267.

Delhez, E.J.M., Campin, J.-M., Hirst, A.C., Deleersnijder, E., 1999. Toward a general theory of the age in ocean modelling. Ocean Modelling 1, 17–27.

Döös, K., Meier, H.E.M., Döscher, R., 2004. The Baltic haline conveyor belt or the overturning circulation and mixing in the Baltic. Ambio 33, 258–262.

Elken, J., 1996. Deep Water Overflow, Circulation and Vertical Exchange in the Baltic Proper. Report Series No. 6. Estonian Marine Institute, Tallinn, Estonia, 91 pp.

Elken, J., Matthäus, W. Baltic Sea oceanography. In: von Storch, H. (Ed.), BALTEX Assessment of Climate Change for the Baltic Sea Basin (BACC). Annex A.1.1, Springer, Berlin, in press.

Engqvist, A., 1996. Long-term nutrient balances in the eutrophication of the Himmerfjärden estuary. Estuarine, Coastal and Shelf Science 42, 483–507.

Feistel, R., Nausch, G., Matthäus, W., Hagen, E., 2003a. Temporal and spatial evolution of the Baltic deep water renewal in spring 2003. Oceanologia 45, 623–642.

Feistel, R., Nausch, G., Mohrholz, V., Łysiak-Pastuszak, E., Seifert, T., Matthäus, W., Krüger, S., Sehested-Hansen, I., 2003b. Warm waters of summer 2002 in the deep Baltic Proper. Oceanologia 45, 571–592.

Feistel, R., Nausch, G., Hagen, E., 2006. Unusual inflow activity 2002/3 and varying deep-water properties. Oceanologia 48 (S), 21–35.

Fischer, H., Matthäus, W., 1996. The importance of the Drogden Sill in the Sound for major Baltic inflows. Journal of Marine Systems 9, 137–157.

Gerdes, R., Köberle, C., Willebrand, J., 1991. The influence of numerical advection schemes on the results of ocean general circulation models. Climate Dynamics 5, 211–226.

Graham, P.L., 1999. Modeling runoff to the Baltic Sea. Ambio 27, 328–334.

Hibler, W.D., 1979. A dynamic thermodynamic sea ice model. Journal of Physical Oceanography 9, 817–846.

Hunke, E.C., Dukowicz, J.K., 1997. An elastic–viscous–plastic model for sea ice dynamics. Journal of Physical Oceanography 27, 1849–1867.

Janssen, F., Schrum, C., Backhaus, J., 1999. A climatological dataset of temperature and salinity for the North Sea and the Baltic Sea. Deutsche Hydrographische Zeitung 9 (Suppl.), 245 pp.

Jönsson, B., 2005. Using Lagrangian Trajectories to Study Mixing in a Gradually Varying Estuary. DM Report No. 93. Department of Meteorology, Stockholm University, Stockholm, Sweden.

Jönsson, B., Lundberg, P.A., Döös, K., 2004. Baltic sub-basin turnover times examined using the Rossby Centre Ocean model. Ambio 33 (4–5), 257–260.

Kõuts, T., Omstedt, A., 1993. Deep water exchange in the Baltic Proper. Tellus 45A, 311–324.

Kauker, F., Meier, H.E.M., 2003. Modeling decadal variability of the Baltic Sea: 1. Reconstructing atmospheric surface data for the period 1902–1998. Journal of Geophysical Research 108 (C8), 3267. doi:10.1029/2003JC001797.

Killworth, P., Stainforth, D., Webb, D., Paterson, S., 1991. The development of a free-surface Bryan–Cox–Semtner ocean model. Journal of Physical Oceanography 21, 1333–1348.

Knudsen, M., 1900. Ein hydrographischer Lehrsatz. Annalen der Hydrographie und maritimen Meteorologie 28, 316–320 (in German).

Lass, H.-U., Matthäus, W., 1996. On temporal wind variations forcing salt water inflows into the Baltic Sea. Tellus 48A, 663–671.

Lass, H.-U., Prandke, H., Liljebladh, B., 2003. Dissipation in the Baltic proper during winter stratification. Journal of Geophysical Research 108 (C6), 3187. doi:10.1029/2002JC001401.

Lehmann, A., Hinrichsen, H.-H., 2000. On the wind driven and thermohaline circulation of the Baltic Sea. Physics and Chemistry of the Earth 25 (B), 183–189.

Lehmann, A., Krauss, W., Hinrichsen, H.-H., 2002. Effects of remote and local atmospheric forcing on circulation and upwelling in the Baltic Sea. Tellus 54A, 299–316.

Marmefelt, E., Omstedt, A., 1993. Deep water properties in the Gulf of Bothnia. Continental Shelf Research 13, 169–187.

Matthäus, W., 2006. The History of Investigation of Salt Water Inflows into the Baltic Sea – From the Early Beginning to Recent Results.

Meereswissenschaftliche Berichte No. 65. Institut für Ostseeforschung Warnemünde, Rostock-Warnemünde, Germany, pp. 1–73.

Matthäus, W., Franck, H., 1992. Characteristics of major Baltic inflows – a statistical analysis. Continental Shelf Research 12, 1375–1400.

Meier, H.E.M., 2001. On the parameterization of mixing in three-dimensional Baltic Sea models. Journal of Geophysical Research 106, 30997–31016.

Meier, H.E.M., 2002. Regional ocean climate simulations with a 3D ice-ocean model for the Baltic Sea. Part 1: model experiments and results for temperature and salinity. Climate Dynamics 19, 237–253.

Meier, H.E.M., 2005. Modeling the age of Baltic Sea water masses: quantification and steady state sensitivity experiments. Journal of Geophysical Research 110, C02006. doi:10.1029/2004JC002607.

Meier, H.E.M., Kauker, F., 2002. Simulating Baltic Sea Climate for the Period 1902–1998 with the Rossby Centre Coupled Ice-Ocean Model. Reports Oceanography No. 30. Swedish Meteorological and Hydrological Institute, SE-60176 Norrköping, Sweden, 111 pp.

Meier, H.E.M., Kauker, F., 2003. Modeling decadal variability of the Baltic Sea: 2. Role of freshwater inflow and large-scale atmospheric circulation for salinity. Journal of Geophysical Research 108 (C11), 3368. doi:10.1029/2003JC001799.

Meier, H.E.M., Döscher, R., Faxén, T., 2003. A multiprocessor coupled ice-ocean model for the Baltic Sea: application to salt inflow. Journal of Geophysical Research 108 (C8), 3273. doi:10.1029/2000JC000521.

Meier, H.E.M., Döscher, R., Broman, B., Piechura, J., 2004. The major Baltic inflow in January 2003 and preconditioning by smaller inflows in summer/autumn 2002: a model study. Oceanologia 46, 557–579.

Meier, H.E.M., Feistel, R., Piechura, J., Arneborg, L., Burchard, H., Fiekas, V., Golenko, N., Kuzmina, N., Mohrholz, V., Nohr, C., Paka, V.T., Sellschopp, J., Stips, A., Zhurbas, V., 2006. Ventilation of the Baltic Sea deep water: a brief review of present knowledge from observations and models. Oceanologia 48 (S), 133–164.

Mohrholz, V., Dutz, J., Kraus, G., 2006. The impacts of exceptionally warm summer inflow events on the environmental conditions in the Bornholm Basin. Journal of Marine Systems 60, 285–301.

Myrberg, K., Andrejev, O., 2003. Main upwelling regions in the Baltic Sea – a statistical analysis based on three-dimensional modeling. Boreal Environmental Research 8, 97–112.

Myrberg, K., Andrejev, O., 2006. Modelling of the circulation, water exchange and water age properties of the Gulf of Bothnia. Oceanologia 48 (S), 55–74.

Piechura, J., Beszczyńska-Möller, A., 2003. Inflow waters in the deep regions of the southern Baltic Sea – transport and transformations. Oceanologia 45, 593–621.

Sarkisyan, A.S., Staskwiecz, A., Koalik, Z., 1975. Diagnostic computations of the summer circulation in the Baltic Sea. Oceanologia 15, 653–656.

Stevens, D.P., 1991. The open boundary condition in the United Kingdom Fine-resolution Antarctic Model. Journal of Physical Oceanography 21, 1494–1499.

Stigebrandt, A., 1987. A model of the vertical circulation of the Baltic deep water. Journal of Physical Oceanography 17, 1772–1785.

Webb, D.J., de Cuevas, B.A., Richmond, C.S., 1998. Improved advection schemes for ocean models. Journal of Atmospheric and Oceanic Technology 15, 1171–1187.

Zhurbas, V.M., Paka, V.T., 1999. What drives thermohaline intrusions in the Baltic Sea. Journal of Marine Systems 21, 229–241.

Available online at www.sciencedirect.com
ScienceDirect
Estuarine, Coastal and Shelf Science 74 (2007) 628–640
ESTUARINE COASTAL AND SHELF SCIENCE
www.elsevier.com/locate/ecss

Toward a generic method for studying water renewal, with application to the epilimnion of Lake Tanganyika

Olivier Gourgue [a,*], Eric Deleersnijder [b,a], Laurent White [a,b]

[a] Centre for Systems Engineering and Applied Mechanics (CESAME), Université catholique de Louvain 4, Avenue Georges Lemaître, B-1348 Louvain-la-Neuve, Belgium
[b] Georges Lemaître Institute of Astronomy and Geophysics (ASTR), Université catholique de Louvain 2, Chemin du Cyclotron, B-1348 Louvain-la-Neuve, Belgium

Received 10 August 2006; accepted 9 May 2007
Available online 26 June 2007

Abstract

We present a method, based on the concept of age and residence time, to study the water renewal in a semi-enclosed domain. We split the water of this domain into different water types. The initial water is the water initially present in the semi-enclosed domain. The renewing water is defined as the water entering the domain of interest. Several renewing water types may be considered depending on their origin. We present the equations for computing the age and the residence time of a certain water type. These timescales are of use to understand the rate at which the water renewal takes place. Computing these timescales can be achieved at an acceptable extra computer cost.

The above-mentioned method is applied to study the renewal of epilimnion (i.e. the surface layer) water in Lake Tanganyika. We have built a finite element reduced-gravity model modified to take into account the water exchange between the epilimnion and the hypolimnion (i.e. the bottom layer), the water supply from precipitation and incoming rivers, and the water loss from evaporation and the only outgoing river. With our water renewal diagnoses, we show that the only significant process in the renewal of epilimnion water in Lake Tanganyika is the water exchange between the epilimnion and the hypolimnion, other phenomena being negligible.

Keywords: water renewal; age; residence time; Lake Tanganyika; reduced-gravity model; finite elements

1. Introduction

In semi-enclosed aquatic domains, most of the biomass, nutrients, contaminants, dissolved gasses and suspended particles are exchanged with their surrounding environment. Therefore, it is essential to understand hydrodynamic processes that transport water and its constituents. A first-order description of transport may be expressed as ‘‘age’’ and ‘‘residence time’’, which we conceive as timescales of the water renewal of the semi-enclosed domain (Monsen et al., 2002). Several studies have been made about the water renewal in a semi-enclosed domain, using different definitions of renewal timescales to quantify the time that water remains inside the domain. Bolin and Rodhe (1973) defined the theoretical concepts of age and residence time, followed by Zimmerman (1976, 1988) who used the residence time to study the hydrodynamics of estuaries. Takeoka (1984) used the age and the residence time to study the water exchange in a coastal sea. Deleersnijder et al. (1997) and Tartinville et al. (1997) resorted to the residence time to study the transport of water and tracer from the Mururoa Lagoon to the Pacific Ocean. Braunschweig et al. (2003) defined different renewal timescales that were helpful to understand the hydrodynamics of the Tagus Estuary.

This article presents a method for studying water renewal that is based on the idea that the water can be viewed as a mixture of different water types. The latter are treated as passive tracers (Cox, 1989; Hirst, 1999; Goosse et al., 2001; White and Deleersnijder, 2007). The initial water is the water initially

* Corresponding author.
E-mail address: gourgue@mema.ucl.ac.be (O. Gourgue).

0272-7714/$ - see front matter © 2007 Elsevier Ltd. All rights reserved.
doi:10.1016/j.ecss.2007.05.009

present in the domain of interest. The renewing water is the water entering the domain. We may define different renewing water types, depending on their origin. To quantify the rate at which water is renewed, we will estimate the residence time of the initial water and the age of the renewing water, in accordance with CART (Constituent-oriented Age and Residence time Theory, http://www.climate.be/CART).

The age of a water parcel is defined to be the time elapsed since this water parcel left the region in which its age is prescribed to be zero (Bolin and Rodhe, 1973; Takeoka, 1984; Delhez et al., 1999; Deleersnijder et al., 2001). The age is thus an interesting timescale for the different renewing water types. Furthermore, it only requires to solve well-known advection-diffusion equations (Delhez et al., 1999; Deleersnijder et al., 2001) to obtain a local renewal timescale, depending on space and time. The concept of age is very useful to quantify the time spent by renewing water parcels into the domain. But, by definition, the age of initial water parcels will always be the time elapsed since the initial instant. That is why we use the residence time for the initial water, but only for this water type. The residence time of a water parcel in a water body is defined as the time taken by this water parcel to leave the water body (Bolin and Rodhe, 1973; Takeoka, 1984; Delhez et al., 2004; Delhez, 2006). There are two different approaches to compute the residence time. We can compute the residence time from the solution of an adjoint problem (Delhez et al., 2004). However, it is not easy to implement but it provides a local residence time, depending on space and time. We can also compute the residence time by means of a direct approach that is easier to implement (it only requires to solve advection-diffusion equations) but too expensive to get the same results as those of the adjoint problem. That is because the direct approach merely provides a global mean residence time, as an integral over space and time. A compromise can be achieved by dividing the semi-enclosed domain into a small number of regions. The mean residence time is then computed for each region. Moreover the mean residence time may be computed for a small number of different initial times. We have decided to adopt this approach.

The method that we use to study the water renewal in a semi-enclosed domain is as follows. First, we define the different water types: the initial water and several renewing water types. Second, we compute the evolution of their concentration field. Then we compute the evolution of the renewing water age field. Finally, we divide the domain into different regions and we compute, for each region and for several initial times, the mean residence time of the initial water in this region. This approach requires no important additional numerical development once a hydrodynamic model of the problem is set up. These concepts are applied herein to the epilimnion (i.e. the surface layer) of Lake Tanganyika. Note that this paper is just an illustration of a general theory to study the water renewal in semi-enclosed domains.

The present article is organized as follows. Section 2 describes the two-dimensional hydrodynamic model (Section 2.1) and the equations for the concentration of the different water types, the equations for the age of the different renewing water types and the equations for the residence time of the initial water (Section 2.2), as well as the numerical methods used to model them (Section 2.3). In Section 3, we present our results and we conclude with Section 4.

2. Model description

Lake Tanganyika is situated on the east of central Africa, and is shared by four developing countries: Democratic Republic of Congo, Burundi, Tanzania and Zambia (Fig. 1). It lies between 3°20′ to 8°45′ S and 29°05′ to 31°15′ E. It is about 650 km long and 50 km wide on average. The mean depth of the lake is around 570 m, with a maximum depth of 1470 m. Thermal stratification in the lake is well marked so that we can define two distinct layers: the epilimnion and the hypolimnion. This two-layer regime is ubiquitous within the lake. The epilimnion is the surface layer and is composed of relatively warm (24–28 °C), oxygenated water. The hypolimnion is the bottom layer and is composed of colder (23.5 °C), anoxic water. These two main layers are separated by a thin layer where temperature variations are more important, the thermocline. Overall, the thermocline lies deeper in the north than in the south with a mean depth of 50 m over the entire lake (Coulter and Spigel, 1991; Naithani et al., 2003). The region undergoes two main seasons: the dry season (approximately from May to August), characterized by strong winds blowing northwestward along the main axis of the lake, and the wet season (approximately from September to April), when the winds are generally weaker (Coulter and Spigel, 1991). During the dry season, the wind stress pushes the warmer epilimnion water away from the southern end of the

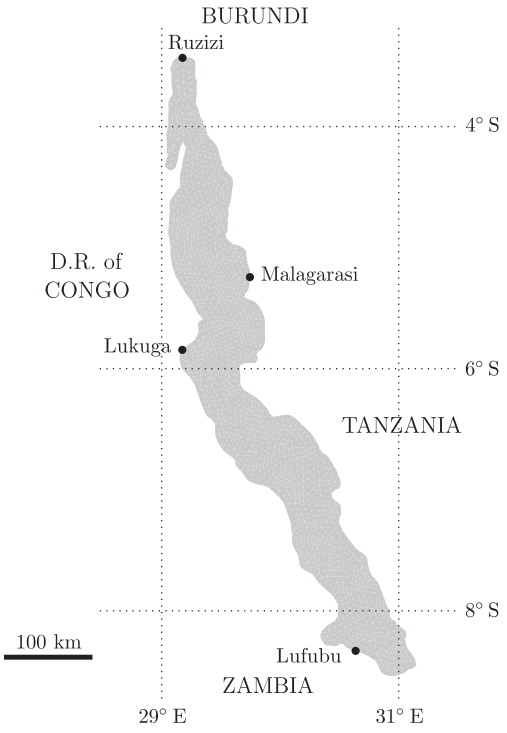

Fig. 1. Map of Lake Tanganyika, indicating the four neighboring countries and the mouth of the most important rivers (Lukuga is the only outgoing river of the lake).

lake toward the northern end. Upwelling occurs to replace the loss of water at the south and the epilimnion water accumulated at the north is pulled downward by gravity. The thermocline is then tilted downward toward the north and may totally disappear in the south. At the end of the dry season, when the southeasterly winds stop, the epilimnion and the hypolimnion slide over each other, and the thermocline oscillates to reach a new equilibrium. These waves get reflected at the lake boundaries and gradually transform into standing wave patterns, called internal seiches. By December, the thermocline reaches its mean level (around 50 m) but still oscillates throughout the wet season until the beginning of the next dry season and the onset of the southeasterly winds (Coulter and Spigel, 1991; Naithani et al., 2003). These observations have already been reproduced by a finite difference model (Naithani et al., 2002; Naithani et al., 2003; Naithani et al., 2004; Naithani and Deleersnijder, 2004). Similar results were obtained by means of the reduced-gravity finite element model used herein, so that there is no need for a detailed discussion of its validity in the present article.

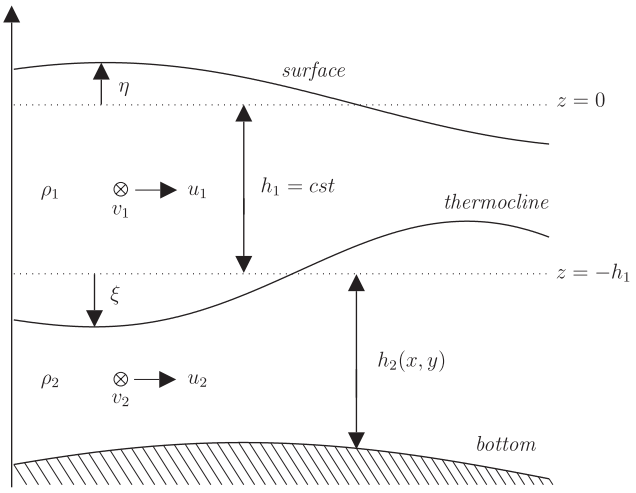

Fig. 2. The parameters and variables of a two-layer model: η is the upward displacement of the surface, ξ is the downward displacement of the thermocline, ρ_i is the density of the ith layer, u_i and v_i are the depth-integrated velocity components of the ith layer in the x and y directions, h_1 is the undisturbed thickness of the top layer, or the mean thermocline depth, and h_2 is the distance between the mean thermocline depth and the bottom.

2.1. The hydrodynamic model

It has already been shown that the two-dimensional reduced-gravity model is able to produce rather good results on the hydrodynamics of Lake Tanganyika (Naithani et al., 2002; Naithani et al., 2003; Naithani et al., 2004; Naithani and Deleersnijder, 2004). By using a reduced-gravity model, we assume that the density stratification is much more important in determining the internal oscillations than the underlying bottom topography. In Lake Tanganyika, it is appropriate to have recourse to such a model since stratification is present all year round and the epilimnion thickness is much smaller than that of the hypolimnion one (Coulter and Spigel, 1991; Naithani et al., 2003).

The reduced-gravity model consists of two layers of different constant temperatures and densities (Fig. 2). Here, we also assume that the temperature is constant inside these two layers. The shallow water equations are applied to both layers and two important hypotheses are made. First, the surface layer thickness ($H_1 = h_1 + \eta + \xi$) is considered to be much smaller than that of the bottom layer thickness ($H_2 = h_2 - \xi$), supposed to be infinitely thick. Second, the displacement of the free surface is assumed to be much smaller than that of the thermocline. These two hypotheses are well verified in Lake Tanganyika. This leads us to the equations of the reduced-gravity model (Naithani et al., 2003; Naithani et al., 2004) from which the velocity in the epilimnion and the downward displacement of the thermocline may be obtained:

$$\frac{\partial \xi}{\partial t} + \boldsymbol{\nabla}\cdot(H\boldsymbol{u}) = 0, \tag{1}$$

$$\frac{\partial}{\partial t}(H\boldsymbol{u}) + \boldsymbol{\nabla}\cdot(H\boldsymbol{u}\boldsymbol{u}) + f\boldsymbol{e}_z \times (H\boldsymbol{u}) = -(\epsilon g)H(\boldsymbol{\nabla}\xi) + \boldsymbol{\nabla}\cdot\Big(H\boldsymbol{A}\cdot(\boldsymbol{\nabla}\boldsymbol{u})\Big) + \frac{\boldsymbol{\tau}}{\rho}, \tag{2}$$

where we have dropped the subscripts "1" relative to the surface layer because we only deal with this layer. The variables are ξ, the downward displacement of the thermocline, and $\boldsymbol{u} = (u, v)$, the epilimnion depth-integrated velocity vector (the y direction is chosen to be along the main axis of the lake); f is the Coriolis parameter, ϵg is the reduced gravity, where g is the gravitational acceleration and $\epsilon = (\rho_2 - \rho_1)/\rho_2$ is the relative density difference ranging from 6.3×10^{-4} to 9.06×10^{-4} (Naithani et al., 2003); $\boldsymbol{A}$ is the eddy viscosity tensor which is diagonal and positive, $\boldsymbol{\tau} = (\tau_x, \tau_y)$ is the surface wind stress, and ρ is the constant water density in the surface layer. To compute the surface wind stress, we use the data collected every 6 h at Mpulungu (at the south end of the lake in Zambia) from 1st April 1993 to 31st March 1994 (Fig. 3a, b) during the FAO/FINNIDA project "Research for the Management of the Fisheries on Lake Tanganyika". We see that the wind stress is indeed more important along the main axis of the lake (the y direction) and that it is definitely stronger during the dry season.

The classical reduced-gravity model Eqs. (1) and (2) do not take the different water exchanges into account. We want to add the effects of the water exchanges between the epilimnion and the hypolimnion, the effects of precipitation and evaporation, and the effects of the three most important incoming rivers (Malagarasi, Ruzizi and Lufubu) and the only outgoing river (Lukuga) (Fig. 1). The mouths of these rivers are assumed to be too narrow to be resolved explicitly by the model. Therefore, the rivers are modelled by means of source/sink terms that are zero over most of the domain. Then, Eq. (1) becomes:

$$\frac{\partial \xi}{\partial t} + \boldsymbol{\nabla}\cdot(H\boldsymbol{u}) = w + q_{\mathrm{p}} + q_{\mathrm{v}} + q_{\mathrm{r}}, \tag{3}$$

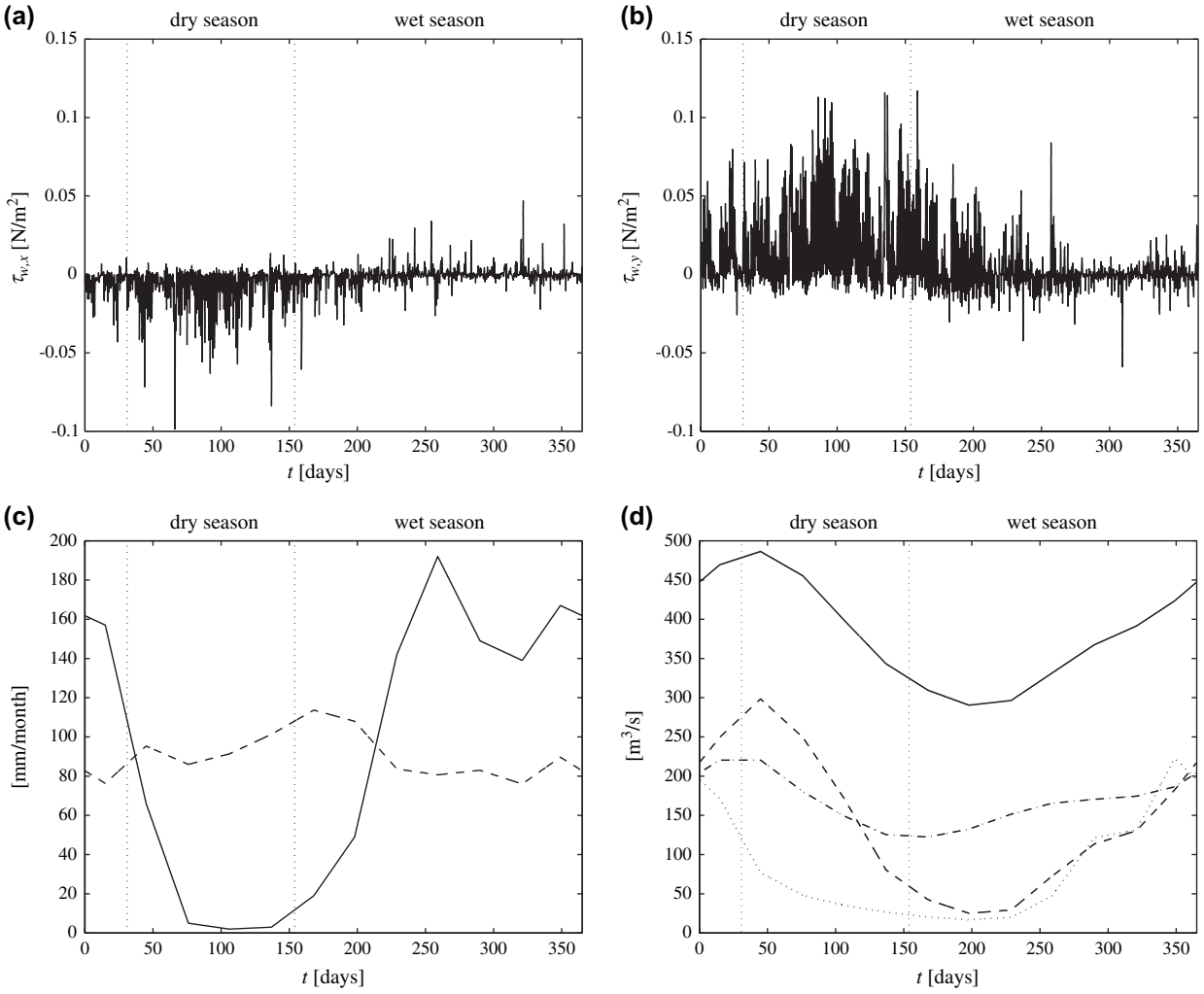

Fig. 3. The various model forcings. (a, b) Wind stress in the x and y directions, respectively, measured at Mpulungu in Zambia, every 6 h from 1st April 1993 to 31st March 1994. (c) Absolute value of the monthly lake-averaged water fluxes due to precipitation (solid) and due to evaporation (dashed) (Bergonzini, 1998). These water fluxes are always positive and negative, respectively. (d) Monthly water flow of the most important rivers: Malagarasi (dashed), Ruzizi (dash-dotted) and Lufubu (dotted) are incoming rivers, Lukuga (solid) is an outgoing river (Bergonzini, 1998).

where w is the entrainment velocity (i.e. the water flux crossing the thermocline) which is positive when hypolimnion water is entrained by turbulent processes into the epilimnion and negative otherwise, q_p is the water flux due to precipitation (always positive), q_v is the water flux due to evaporation (always negative), and q_r is the water flux due to rivers which is positive wherever a river brings water to the epilimnion and negative otherwise. These four functions have the dimension of a velocity. Assuming that only the water leaving the epilimnion carries non-negligible momentum, Eq. (2) becomes:

$$\frac{\partial}{\partial t}(H\boldsymbol{u})+\boldsymbol{\nabla}\cdot(H\boldsymbol{u}\boldsymbol{u})+f\boldsymbol{e}_z\times(H\boldsymbol{u}) = -(\epsilon g)H(\boldsymbol{\nabla}\xi)+\boldsymbol{\nabla}\cdot\left(H\boldsymbol{A}\cdot(\boldsymbol{\nabla}\boldsymbol{u})\right)+\frac{\boldsymbol{\tau}}{\rho}+\left(w^-+q_v+q_r^-\right)\boldsymbol{u}, \quad (4)$$

where the last term is the momentum flux leaving the epilimnion, w^- and q_r^- denoting the negative part of w and q_r, respectively. The negative and positive parts of any function ψ are identified herein by superscripts "−" and "+", respectively, with $\psi^{\pm}=(\psi\pm|\psi|)/2$. And since q_p is always positive and q_v is always negative, we have $q_p^+=q_p$, $q_p^-=0$, $q_v^+=0$ and $q_v^-=q_v$, explaining the last term in the right-hand side of Eq. (4).

To compute the entrainment velocity w we use the following parameterization (Naithani et al., 2007):

$$w=\sqrt{\frac{3}{20}}\frac{\sqrt{\tau_x^2+\tau_y^2}}{\rho\sqrt{(\epsilon g)H}}-w_d-\frac{\xi}{T_r}, \quad (5)$$

where the first term is the entrainment term inspired by Price (1979) and w_d is the detrainment velocity defined such that annual mean of the epilimnion volume remains approximately constant. There are large uncertainties in the parameterization of entrainment and detrainment. As a consequence, to avoid occasional occurrence of spurious values of ξ, a relaxation term (ξ/T_r) is needed, which slowly nudges the epilimnion thickness toward its equilibrium position. The relaxation

timescale T_r is sufficiently long so that the relaxation term is generally much smaller than the entrainment and detrainment terms. For the problem studied in this paper, we used $w_d \simeq 10^{-5}$ m/s and $T_r = 45$ days. As can be seen in Eq. (5), the entrainment velocity depends on the wind stress and the epilimnion thickness. But it is more sensitive to wind stress. The water renewal from hypolimnion to epilimnion ($w > 0$) occurs in the region where H (or ξ) is small but overall during important wind stress periods, i.e. during the dry season.

To compute the water fluxes due to precipitation, evaporation and rivers, we use monthly data collected by Bergonzini (1998) (Fig. 3c, d). The first two water fluxes are distributed uniformly over the surface of the lake. But the water flux due to a given river is distributed as a hyperbolic tangent decreasing with the distance from the mouth of this river. The characteristic lengthscale of the hyperbolic tangent is 3 km. Note that we had to slightly adjust the evaporation data in order to keep the annual mean of the epilimnion volume constant.

We concede that the treatment of rivers as sink/source terms is unusual. But their flow is about 10^2 m^3/s and the flow crossing the thermocline is about 10^5 m^3/s. Therefore, the rivers carry negligible momentum throughout the lake compared with the water exchange between the epilimnion and the hypolimnion. It may not be true near the mouth of a river. But to take this local effect into account, we would have to make a drastic refinement of the mesh near the mouth of the four rivers. That would be useless since the river momentum is negligible.

The boundary conditions associated with Eqs. (3) and (4) are presented in Appendix A.

2.2. Water renewal diagnoses

Different water types have to be traced in order to study the renewal of epilimnion water in Lake Tanganyika. We first define the initial water (with the subscript "i") as the water initially in the epilimnion. We then define several renewing water types: the hypolimnion water ("h") is the water entering the epilimnion from hypolimnion, the precipitation water ("p") is the water entering the epilimnion from precipitation, and the river water ("r") is the water entering the epilimnion from incoming rivers. We compute the concentration and the age of all of these water types. But the age is not a useful renewal timescale for the initial water because it is equal to the elapsed time. That is why we also compute the residence time for this water type.

2.2.1. Concentration

The concentration of every water type is denoted $C_s(t,\boldsymbol{x})$, where the subscript "s" can be equal to "i", "h", "p" or "r" for initial, hypolimnion, precipitation or river water, respectively. The following notations are of some use:

$$C_{\mathrm{tot}}(t,\boldsymbol{x}) = C_{\mathrm{i}}(t,\boldsymbol{x}) + C_{\mathrm{h}}(t,\boldsymbol{x}) + C_{\mathrm{p}}(t,\boldsymbol{x}) + C_{\mathrm{r}}(t,\boldsymbol{x}), \tag{6}$$

$$C_{\mathrm{rw}}(t,\boldsymbol{x}) = C_{\mathrm{h}}(t,\boldsymbol{x}) + C_{\mathrm{p}}(t,\boldsymbol{x}) + C_{\mathrm{r}}(t,\boldsymbol{x}), \tag{7}$$

where $C_{\mathrm{tot}}(t,\boldsymbol{x})$ is the total concentration (i.e. the water concentration) and $C_{\mathrm{rw}}(t,\boldsymbol{x})$ is the renewing water concentration.

The equations governing the concentration of any water type can be cast into the following generic conservative form:

$$\frac{\partial}{\partial t}(HC_s) + \boldsymbol{\nabla}\cdot(H\boldsymbol{u}C_s) = \sigma_s + \boldsymbol{\nabla}\cdot\Big(H\boldsymbol{K}\cdot(\boldsymbol{\nabla}C_s)\Big), \quad s = \mathrm{i,h,p,r}, \tag{8}$$

where $\boldsymbol{K}$ is the diffusivity tensor which must be symmetric and positive definite and σ_s is the source/sink term which takes on different values according to the water type:

$$\sigma_{\mathrm{i}} = \big(w^- + q_{\mathrm{v}} + q_{\mathrm{r}}^-\big)C_{\mathrm{i}}, \tag{9}$$

$$\sigma_{\mathrm{h}} = w^+ + \big(w^- + q_{\mathrm{v}} + q_{\mathrm{r}}^-\big)C_{\mathrm{h}}, \tag{10}$$

$$\sigma_{\mathrm{p}} = q_{\mathrm{p}} + \big(w^- + q_{\mathrm{v}} + q_{\mathrm{r}}^-\big)C_{\mathrm{p}}, \tag{11}$$

$$\sigma_{\mathrm{r}} = q_{\mathrm{r}}^+ + \big(w^- + q_{\mathrm{v}} + q_{\mathrm{r}}^-\big)C_{\mathrm{r}}. \tag{12}$$

The initial conditions are:

$$C_{\mathrm{i}}(0,\boldsymbol{x}) = 1, \quad C_{\mathrm{h}}(0,\boldsymbol{x}) = C_{\mathrm{p}}(0,\boldsymbol{x}) = C_{\mathrm{r}}(0,\boldsymbol{x}) = 0, \tag{13}$$

and the boundary conditions are presented in Appendix A.

Common sense has it that the following properties must be satisfied:

$$0 \le C_s(t,\boldsymbol{x}) \le 1, \quad s = \mathrm{i,h,p,r}, \tag{14}$$

$$C_{\mathrm{tot}}(t,\boldsymbol{x}) = 1, \tag{15}$$

$$\lim_{t\to\infty} C_{\mathrm{i}}(t,\boldsymbol{x}) = 0, \tag{16}$$

$$\lim_{t\to\infty} C_{\mathrm{rw}}(t,\boldsymbol{x}) = 1. \tag{17}$$

We demonstrate that properties (14)–(17) hold true in Appendix B.

Let us now define $\overline{C}_s$ the global mean concentration of the water type "s" as:

$$\overline{C}_s(t) = \frac{\displaystyle\int_{\Omega} H(t,\boldsymbol{x})C_s(t,\boldsymbol{x})\mathrm{d}\boldsymbol{x}}{\displaystyle\int_{\Omega} H(t,\boldsymbol{x})\mathrm{d}\boldsymbol{x}}, \qquad s = \mathrm{i,h,p,r}, \tag{18}$$

where Ω is the domain of interest (i.e. the lake surface since we work with a two-dimensional model). Then, if we divide Ω into different regions $\Omega_1, \ldots, \Omega_n$, we may also define, $\overline{C}_{s,j}$, the mean concentration of the water type "s" from the region j as:

$$\overline{C}_{s,j}(t) = \frac{\displaystyle\int_{\Omega_j} H(t,\boldsymbol{x})C_s(t,\boldsymbol{x})\mathrm{d}\boldsymbol{x}}{\displaystyle\int_{\Omega_j} H(t,\boldsymbol{x})\mathrm{d}\boldsymbol{x}}, \quad s = \mathrm{i,h,p,r};\ j = 1,\ldots,n. \tag{19}$$

2.2.2. Age

As introduced in Section 1, the age of a water parcel is defined to be the time elapsed since this water parcel left the -region in which its age is prescribed to be zero (Bolin and Rodhe, 1973; Takeoka, 1984; Delhez et al., 1999; Deleersnijder et al., 2001).

Let us define the age concentration and the age of every water type as $\alpha_s(t,\boldsymbol{x})$ and $a_s(t,\boldsymbol{x})$, respectively. They are linked together as follows (Delhez et al., 1999; Deleersnijder et al., 2001):

$$a_s(t,\boldsymbol{x}) = \frac{\alpha_s(t,\boldsymbol{x})}{C_s(t,\boldsymbol{x})}, \quad s = \mathrm{i,h,p,r}. \tag{20}$$

Assuming that the age of a water parcel is zero at the moment it enters the epilimnion and that every water parcel leaves the epilimnion *along with its age*, then the equations governing the evolution of the age concentration of every water type can be cast into the following generic conservative form:

$$\frac{\partial}{\partial t}(H\alpha_s) + \boldsymbol{\nabla}\cdot(H\boldsymbol{u}\alpha_s) = HC_s + \left(w^- + q_\mathrm{v} + q_\mathrm{r}^-\right)\alpha_s + \boldsymbol{\nabla}\cdot\left(H\boldsymbol{K}\cdot(\boldsymbol{\nabla}\alpha_s)\right), \; s=\mathrm{i,h,p,r}. \tag{21}$$

The initial conditions are:

$$\alpha_s(0,\boldsymbol{x}) = 0, \quad s = \mathrm{i,h,p,r}, \tag{22}$$

and the boundary conditions are presented in Appendix A.

We claim that the following property must be satisfied:

$$0 \le a_s(t,\boldsymbol{x}) \le t, \quad s = \mathrm{i,h,p,r}. \tag{23}$$

And because the initial water can only leave the domain of interest (i.e. there is no source of *new* initial water), its age should be equal to the elapsed time:

$$a_\mathrm{i}(t,\boldsymbol{x}) = t. \tag{24}$$

Properties (23) and (24) are demonstrated in Appendix C.

Let us now define $\overline{a}_s$ the global mean age of the water type "s" as:

$$\overline{a}_s(t) = \frac{\overline{\alpha}_s(t)}{\overline{C}_s(t)}, \quad s = \mathrm{i,h,p,r}, \tag{25}$$

where $\overline{\alpha}_s$ is the global mean age concentration of the water type "s", and is defined as:

$$\overline{\alpha}_s(t) = \frac{\int_\Omega H(t,\boldsymbol{x})\alpha_s(t,\boldsymbol{x})\mathrm{d}\boldsymbol{x}}{\int_\Omega H(t,\boldsymbol{x})\mathrm{d}\boldsymbol{x}}, \quad s = \mathrm{i,h,p,r}, \tag{26}$$

where Ω is the domain of interest. Then, if we divide Ω into different regions $\Omega_1,\ldots,\Omega_n$, we may also define, $\overline{a}_{s,j}$, the mean age of the water type "s" from the region j as:

$$\overline{a}_{s,j}(t) = \frac{\overline{\alpha}_{s,j}(t)}{\overline{C}_{s,j}(t)}, \quad s = \mathrm{i,h,p,r}; \; j = 1,\ldots,n. \tag{27}$$

where $\overline{\alpha}_{s,j}$ is the mean age concentration of the water type "s" from the region j, and is defined as:

$$\overline{\alpha}_{s,j}(t) = \frac{\int_{\Omega_j} H(t,\boldsymbol{x})\alpha_s(t,\boldsymbol{x})\mathrm{d}\boldsymbol{x}}{\int_{\Omega_j} H(t,\boldsymbol{x})\mathrm{d}\boldsymbol{x}}, \quad s = \mathrm{i,h,p,r}; \; j = 1,\ldots,n. \tag{28}$$

2.2.3. Residence time

A partial differential problem has been established for estimating the age of the different renewing water types, which is the time that has elapsed since entering the epilimnion. The solutions to this problem are well behaved, i.e. the age of every renewing water type is larger than zero and smaller than that of the elapsed time. The age of the initial water appears as the solution to a similar partial differential problem and is equal to the elapsed time, which makes it uninteresting. The age of the initial water is equal to the elapsed time because the initial water can only leave the domain of interest. Therefore, it would be more relevant to focus on the time needed for the initial water to leave this domain. To that end, the residence time is a proper diagnosis, because, as introduced in Section 1, the residence time of a water parcel in a water body is defined as the time taken by this water parcel to leave the water body (Bolin and Rodhe, 1973; Takeoka, 1984; Delhez, 2006; Delhez and Deleersnijder, 2006).

To compute mean residence times from different regions of the lake, we first have to divide the domain Ω into n different regions $\Omega_1,\ldots,\Omega_n$. Then we can define n different initial water types, i.e. the initial water from region 1,…, the initial water from region n. The concentration of the initial water from region j is denoted as $\theta_j(t,\boldsymbol{x})$. The equation governing the concentration of initial water from region j is the same as that of the concentration of initial water, i.e. Eq. (8) with $s = \mathrm{i}$, and thus can be cast into the following generic conservative form:

$$\frac{\partial}{\partial t}(H\theta_j) + \boldsymbol{\nabla}\cdot(H\boldsymbol{u}\theta_j) = \left(w^- + q_\mathrm{v} + q_\mathrm{r}^-\right)\theta_j + \boldsymbol{\nabla}\cdot\left(H\boldsymbol{K}\cdot(\boldsymbol{\nabla}\theta_j)\right), \quad j = 1,\ldots,n. \tag{29}$$

The equation governing the initial water from region j and its boundary condition (see Appendix A) are the same for each region j. The only difference lies in the initial condition:

$$\theta_j(t_0,\boldsymbol{x}\in\Omega_j) = 1 \;\text{ and }\; \theta_j(t_0,\boldsymbol{x}\in\Omega\backslash\Omega_j) = 0, \; j = 1,\ldots,n. \tag{30}$$

Finally, we can compute the mean residence time of the initial water from region j at time t_0 as:

$$\overline{\Theta}_j(t_0) = \frac{\int_{t_0}^{\infty}\int_\Omega H(t,\boldsymbol{x})\theta_j(t,\boldsymbol{x})\mathrm{d}\boldsymbol{x}\,\mathrm{d}t}{\int_\Omega H(t_0,\boldsymbol{x})\theta_j(t_0,\boldsymbol{x})\mathrm{d}\boldsymbol{x}}, \quad j = 1,\ldots,n. \tag{31}$$

That is the time taken by a water parcel initially in region j to leave the epilimnion. That is why the surface integrals must extend on the entire lake surface Ω.

Note that if $n = 1$, expression (31) yields the global mean residence time of initial water at time t_0:

$$\overline{\Theta}(t_0) = \frac{\int_{t_0}^{\infty} \int_{\Omega} H(t,\boldsymbol{x}) C_{\mathrm{i}}(t,\boldsymbol{x}) \mathrm{d}\boldsymbol{x}\, \mathrm{d}t}{\int_{\Omega} H(t_0,\boldsymbol{x}) C_{\mathrm{i}}(t_0,\boldsymbol{x}) \mathrm{d}\boldsymbol{x}}. \tag{32}$$

It should be pointed out that we have an additional system of equations to solve for each region and for each initial time. For this study we have defined three regions (from south to north) and 12 initial times (the beginning of each month). We thus had to solve $3 \times 12 = 36$ additional systems of equations at each time step. This is a very important amount compared with the two systems for the hydrodynamic model (to compute ξ and $\boldsymbol{u}$), the four systems to compute the concentration of the different water types (C_{i}, C_{h}, C_{p} and C_{r}), and the three systems to compute the age concentration (and thus the age) of the different renewing water types (α_{h}, α_{p} and α_{r}). The mean residence time is thus very expensive compared with the age and it is moreover much less accurate since it is a global variable.

2.3. Numerical implementation

The finite element method is used to discretize both the hydrodynamic model equations and the concentration and age concentration equations. We have discretized the non-conservative form of these equations on the mesh displayed in Fig. 4.

For the hydrodynamic model, we use the finite element model SLIM (Second-generation Louvain-la-Neuve Ice-ocean Model, http://www.climate.be/SLIM) which is essentially built upon the work by Hanert et al. (2004, 2005) for the shallow water equations. The elevation and velocity variables are approximated by linear conforming (P_1) and linear non-conforming (P_1^{NC}) shape functions, respectively. Therefore, the elevation nodes are situated at the vertices of each element of the mesh, and the velocity nodes at the middle of their edges. To enhance robustness, advection terms are computed with an upwind-biased scheme (Hanert et al., 2004).

For the equations of concentration (8) and (29) and age concentration (21), given that they are very similar to those of momentum conservation (4), we use a similar method. That makes our approach very interesting: we do not have to implement a completely new model to compute ages and mean residence times once the hydrodynamic model is built. Therefore, the concentration and age concentration variables are approximated by linear non-conforming shape functions (P_1^{NC}) and their nodes are situated at the middle of the edges of each element of the mesh. We also compute an upwind-biased scheme to compute advection terms (Hanert et al., 2004).

The solution technique is sequential. At each time step, we first compute the elevation field ξ, then we compute simultaneously the horizontal depth-integrated velocity fields u and v, next we compute the different concentration fields and finally the different age concentration fields. The mean residence times are only computed at the end of the simulation because we have to integrate in time from t_0 for a sufficiently long time. By sufficiently long time, we mean the time to allow θ_j to be much smaller than 1 throughout the lake. In this study we compute these equations over a period of 3 years.

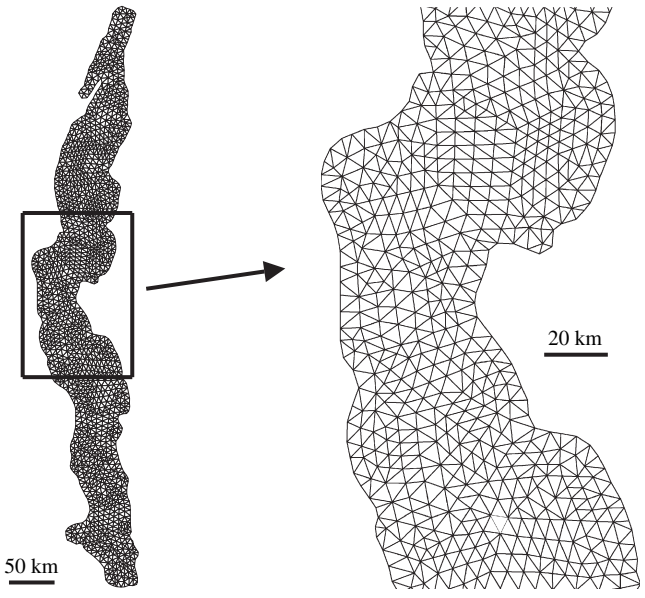

Fig. 4. Unstructured mesh of Lake Tanganyika used for the simulations of this paper. There are 2997 triangular elements. The mean mesh size is about 5 km.

3. Results

First, a 4-year run of the hydrodynamic model was carried out to get the regime solution. Then, a 4-year run was carried out to compute both the concentration and the age distribution of the different water types. Finally, 12 runs were carried out to compute the mean residence time with different initial times. We used homogeneous constant eddy viscosity and diffusivity tensors, which means that $\boldsymbol{A}$ and $\boldsymbol{K}$ are diagonal identity tensors multiplied by a constant $A = 3\ \mathrm{m}^2/\mathrm{s}$ and $K = 10\ \mathrm{m}^2/\mathrm{s}$, respectively. The time step is 12 min.

Before analyzing the renewal of the epilimnion water, we take a brief look at its hydrodynamic cycle. The epilimnion volume budget varies with the supply and the loss of water from hypolimnion, precipitation, evaporation and rivers. Fig. 5a shows the evolution of the global mean epilimnion thickness:

$$\overline{H}(t) = \frac{\int_{\Omega} H(t,\boldsymbol{x}) \mathrm{d}\boldsymbol{x}}{\int_{\Omega} \mathrm{d}\boldsymbol{x}}, \tag{33}$$

which is proportional to the epilimnion volume. It grows from the beginning of the cycle (1st April) to approximately the end of the dry season (end of August). Then it decreases to reach

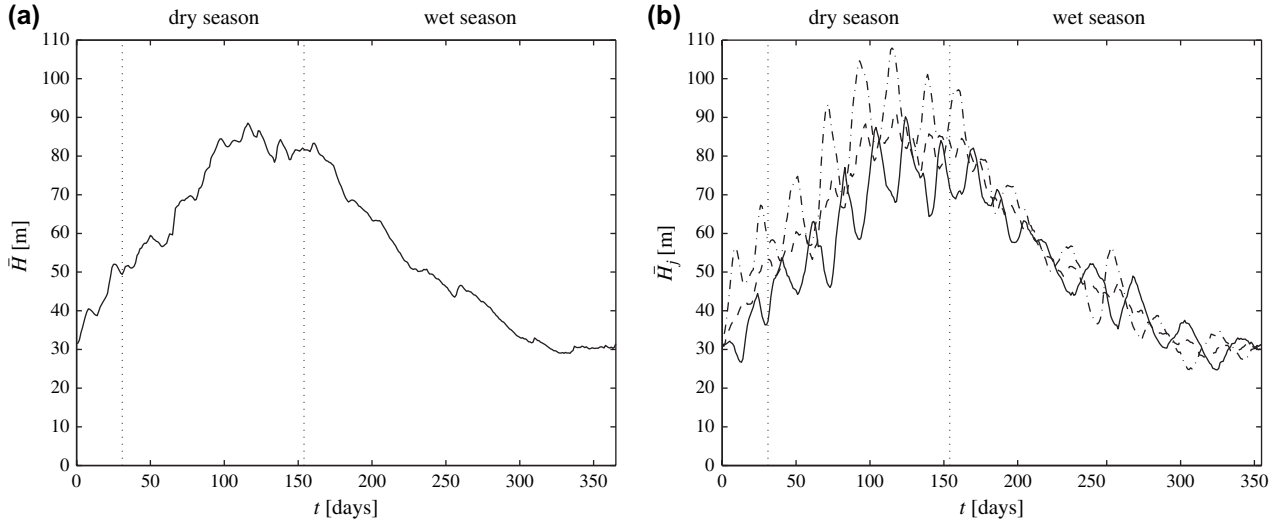

Fig. 5. (a) Evolution of the global mean epilimnion thickness, $\overline{H}$, at regime state. (b) Evolution of the mean epilimnion thickness $\overline{H}_j$ ($j = 1, 2, 3$ from south to north) in the south (solid), in the center (dashed) and in the north (dash-dotted), at regime state.

its minimum value at the end of the cycle (end of March). It is approximately the same shape as the wind stress cycle on Fig. 3b, which is the most important factor of the exchange of water between the epilimnion and the hypolimnion. We may thus expect that this latter phenomenon be more important than the three others considered (precipitation, evaporation and rivers).

Fig. 5b shows the evolution of the mean epilimnion thickness from different regions:

$$\overline{H}_j(t) = \frac{\displaystyle\int_{\Omega_j} H(t,\boldsymbol{x})\mathrm{d}\boldsymbol{x}}{\displaystyle\int_{\Omega_j} \mathrm{d}\boldsymbol{x}}, \quad j = 1,2,3. \tag{34}$$

In this paper, we always divide the domain into three regions, $j = 1, 2, 3$ referring to the south, the center and the north of the lake, respectively. We see that the mean epilimnion thickness is greater in the north than in the south, especially during the dry season. This is due to the important wind stress along the main direction of the lake during this season. The epilimnion water is pushed from south to north where it accumulates. Following Eq. (5), the water supply from hypolimnion to epilimnion is more important in the south. This is why we may expect the age of the hypolimnion water to be smaller in the south than in the north. This would be caused by a larger supply of *new* hypolimnion water in the south, making it *younger*. On the other hand, the water loss from epilimnion to hypolimnion is more important in the north. This is why we may expect the residence time of the initial water to be smaller in the north than in the south.

We see in Fig. 6a that the global mean concentrations of precipitation water and river water never exceed 2% and 0.5%, respectively. Thus, we have:

$$\overline{C}_{\mathrm{rw}} = \overline{C}_{\mathrm{h}} + \overline{C}_{\mathrm{p}} + \overline{C}_{\mathrm{r}} \simeq \overline{C}_{\mathrm{h}}. \tag{35}$$

As expected, while the renewing water replaces the initial water, the global mean initial water concentration $\overline{C}_{\mathrm{i}}$ decreases toward 0, and the global mean renewing water concentration $\overline{C}_{\mathrm{rw}} \simeq \overline{C}_{\mathrm{h}}$ increases toward 1. These trends are well marked during the dry season, when the winds are stronger and thus when the supply of hypolimnion water is more important. It is worth stressing that it takes only 1 year to replace 90% of the initial water. Fig. 6b shows that the renewing water concentration is larger in the south than in the north. That is because the supply of hypolimnion water is more important in this region. We see the same features in Movie 1 (available online). The renewing water concentration increases everywhere in the lake, but faster during the dry season and also faster in the south than in the north of the lake. This confirms that the water exchange between the epilimnion and the hypolimnion seems to be the only important process driving the renewal of epilimnion water in Lake Tanganyika.

We see in Fig. 7a that the global mean hypolimnion water age increases at the beginning of the simulation. But just before the second dry season, it begins to decrease. That is because the wind stress begins to be significant (see Fig. 3). The supply of *new* hypolimnion water is important at this moment and hypolimnion water in the epilimnion becomes *younger*. Then, around the end of the dry season, the global mean hypolimnion water age begins to increase again, until the next rise of the wind stress, and so on. It is the same process for the global mean age of precipitation water and river water, except that the most important supply of *new* renewing water occurs during the wet season for these water types. We also see in this figure that the global mean ages of precipitation water and river water are on the same order of the global mean initial water age:

$$\overline{a}_{\mathrm{h}} \sim \overline{a}_p \sim \overline{a}_{\mathrm{r}}, \tag{36}$$

Since $\overline{a}_s = \overline{\alpha}_s / \overline{C}_s$ and because $\overline{C}_{\mathrm{p}}$ and $\overline{C}_{\mathrm{r}}$ are very small compared with $\overline{C}_{\mathrm{h}}$, Eq. (36) implies that $\overline{\alpha}_{\mathrm{p}}$ and $\overline{\alpha}_{\mathrm{r}}$ are also

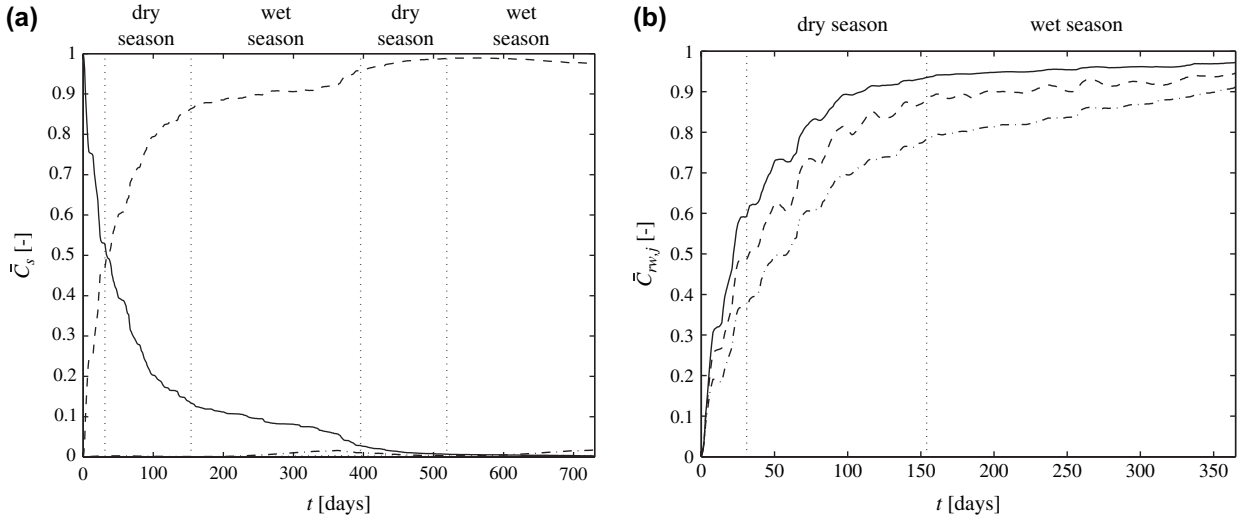

Fig. 6. (a) Evolution of the global mean initial (solid), hypolimnion (dashed), precipitation (dash-dotted) and river (dotted) water concentrations $\overline{C}_s$ ($s = \mathrm{i}, \mathrm{h}, \mathrm{p}, \mathrm{r}$), during the first 2 years. (b) Evolution of the mean renewing water concentration $\overline{C}_{\mathrm{rw},j}$ ($j = 1, 2, 3$ from south to north) in the south (solid), in the center (dashed) and in the north (dash-dotted), during the first year.

very small compared with $\overline{\alpha}_\mathrm{h}$. Following the definition of the age, we have:

$$\overline{a}_\mathrm{rw} = \frac{\overline{\alpha}_\mathrm{rw}}{\overline{C}_\mathrm{rw}} = \frac{\overline{\alpha}_\mathrm{h} + \overline{\alpha}_\mathrm{p} + \overline{\alpha}_\mathrm{r}}{\overline{C}_\mathrm{h} + \overline{C}_\mathrm{p} + \overline{C}_\mathrm{r}} \simeq \frac{\overline{\alpha}_\mathrm{h}}{\overline{C}_\mathrm{h}} = \overline{a}_\mathrm{h}, \tag{37}$$

That is what we see in Fig. 8. This is another confirmation that the water exchange between the epilimnion and the hypolimnion seems to be the only important process driving the renewal of epilimnion water in Lake Tanganyika. Fig. 7b shows, as expected, that the renewing water age is less important in the south than in the north. That is because the mean epilimnion thickness is smaller in the south, which implies, following Eq. (5), that a more significant supply of *new* hypolimnion water occurs in the south. We see the same features in Movie 2 (available online). The renewing water age decreases everywhere in the lake from the beginning of the year until the end of the dry season. It then increases until the end of the year. But the renewing water is always *younger* in the south than in the north of the lake.

Now, consider the residence time. The latter depends on the value of $(w^- + q_\mathrm{v} + q_\mathrm{r}^-)$, the water flux leaving the epilimnion. Since $w^- \sim 10^{-5}$ m/s, $q_\mathrm{v} \sim 10^{-8}$ m/s and q_r^- is zero almost everywhere, we may assume that the residence time only depends on the value of w^-. Once again, it confirms that the renewal of epilimnion water in Lake Tanganyika is largely dominated by the water exchange between the epilimnion and the hypolimnion. The residence time increases when $|w^-| = 0$, i.e. when water stays into the epilimnion, and it decreases when $|w^-| > 0$, i.e. when water leaves the epilimnion.

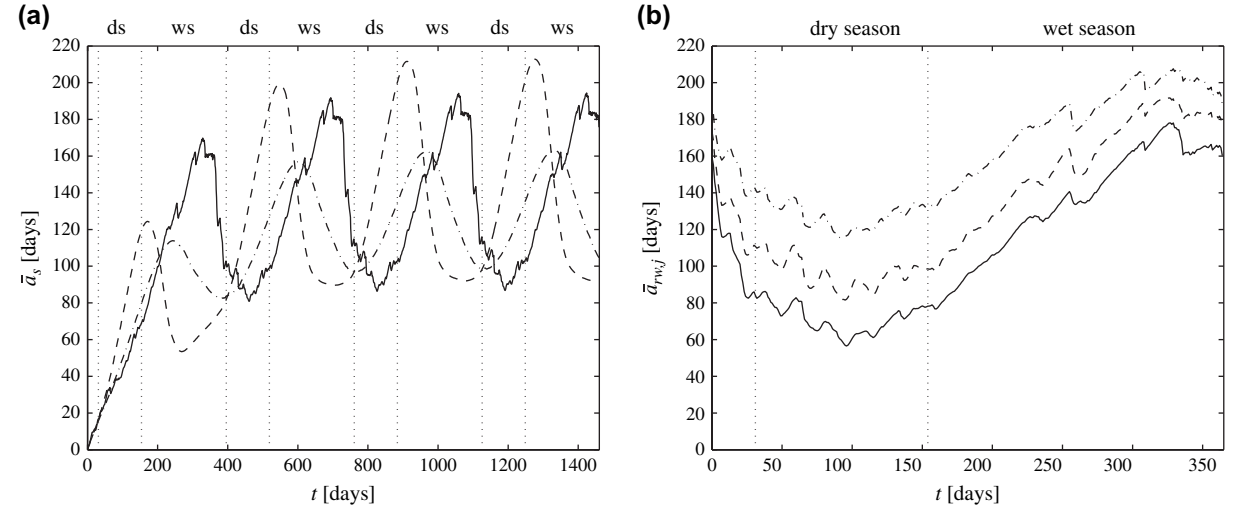

Fig. 7. (a) Evolution of the global mean hypolimnion (solid), precipitation (dashed) and river (dash-dotted) water ages $\overline{a}_s$ ($s = \mathrm{h}, \mathrm{p}, \mathrm{r}$), during the first 4 years. (b) Evolution of the mean renewing water age in the south (solid), in the center (dashed) and in the north (dash-dotted) $\overline{a}_{\mathrm{rw},j}$ ($j = 1, 2, 3$ from south to north), at regime state.

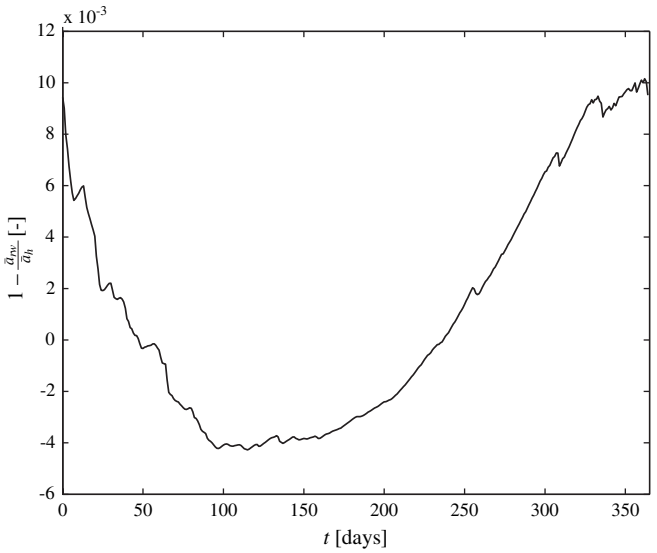

Fig. 8. Evolution of the relative difference between the global mean renewing water age and the global mean hypolimnion water age, at equilibrium state.

The first term of Eq. (5) is always positive, but is on the same order of magnitude as the second one, by definition of the detrainment velocity w_d. So, to have $|w^-| > 0$, the relaxation term (ξ/T_r) has to be important. Thus, overall, the residence time depends on the value of ξ, i.e. the value of the epilimnion thickness H: the residence time increases or decreases when the epilimnion is thin or thick, respectively. That explains why the evolution of the global mean residence time (Fig. 9a) seems to be inversely proportional to the global mean epilimnion thickness (Fig. 5), and why, as expected, the mean residence time is larger in the south than in the north (Fig. 9b). Coulter and Spigel (1991) find a residence time of about 1 year, defining it as the mass of a certain nutrient present in the epilimnion dividing by the rate of addition of this nutrient in the epilimnion. Following our more accurate definition, the residence time is much smaller. The mean residence time of the initial water integrated over the whole year is equal to 127 days.

4. Conclusion

We have suggested a theoretical method based on the concepts of age and residence time to study the renewal of epilimnion water in Lake Tanganyika. This method is easy to implement when the hydrodynamic model is already set up and it may be easily adapted to the water renewal of a more general (even three-dimensional) semi-enclosed domain. Moreover, the method presented to compute the age and the residence time uses all the information of the solution obtained by the hydrodynamic model. The goal is always to separate the water of the domain into different water types: the initial water and the various renewing water types. We then compute the age of the different renewing water types and the residence time of the initial water.

This method allowed us to show that the effects of precipitation, evaporation and river input are negligible in the renewal of epilimnion water in Lake Tanganyika. The only significant effect is the water exchange by turbulent processes between the epilimnion and the hypolimnion. Moreover we showed that it takes only 1 year to replace about 90% of the water in the epilimnion by water from hypolimnion. This is particularly important considering that the hypolimnion contains the major part of the nutrients but is also anoxic. The residence time of the water in the epilimnion is indeed equal to 127 days on average.

Because the water exchange between the epilimnion and the hypolimnion depends on the wind stress and the epilimnion thickness, these two parameters regulate the water renewal. The renewing water age decreases when the water exchange from hypolimnion to epilimnion is important, i.e. when the wind stress is important. That is why the renewing water age decreases during the dry season and increases during the wet season. Moreover, the water exchange from hypolimnion to

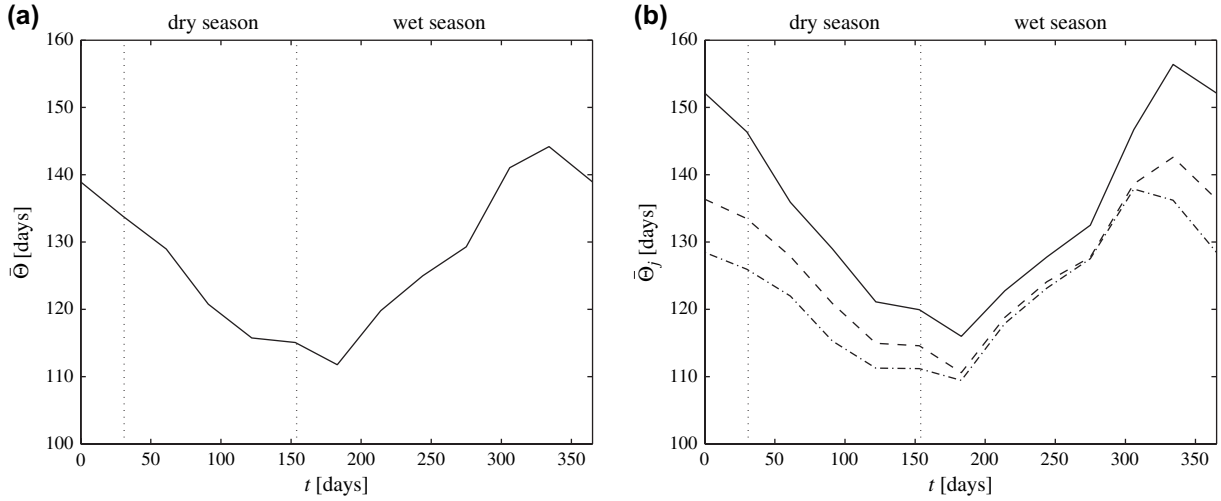

Fig. 9. (a) Evolution of the global mean initial water residence time $\overline{\Theta}$. (b) Evolution of the mean initial water residence time in the south (solid), in the center (dashed) and in the north (dash-dotted) $\overline{\Theta}_j$ ($j = 1, 2, 3$ from south to north).

epilimnion is particularly important where the epilimnion is thin, leading to a smaller renewing water age in the south than in the north. The initial water residence time decreases when the water exchange from epilimnion to hypolimnion is important. We have shown in Section 3 that this water exchange is roughly inversely proportional to the epilimnion thickness. Hence the initial water residence time decreases during the dry season (when the epilimnion thickness increases) and increases during the wet season (when the epilimnion thickness decreases). Finally, since the epilimnion is always the thinnest in the south, the initial water residence time is systematically larger there.

The next steps of this work will be to build a three-dimensional model of Lake Tanganyika including the epilimnion and the hypolimnion. It will allow us to study the water exchange between these two layers without the parameterization (5).

Acknowledgements

Eric Deleersnijder and Laurent White are a Research Associate and a Research Fellow, respectively, with the Belgian National Fund for Scientific Research (FNRS). The present study was carried out within the scope of the project "A second-generation model of the ocean system", which is funded by the Communauté Française de Belgique, as Actions de Recherche Concertées, under contract ARC 04/09-316. This work is a contribution to the construction of SLIM, the Second-generation Louvain-la-Neuve Ice-ocean Model (http://www.climate.be/SLIM). The authors are indebted to Jaya Naithani for useful discussions. The authors are also indebted to Laurent Alleman for pointing to the work of Laurent Bergonzini on the precipitation, evaporation and river fluxes. Finally, the present study is linked to the CLIMFISH project (Climate change impact on the sustainable use of Lake Tanganyika fisheries), funded by the STEREO program of the Belgian Federal Science Policy and the framework agreement between DGCD (the Belgian Development Cooperation) and the Royal Museum for Central Africa (RMCA).

Appendix A. Boundary conditions

Since the rivers are taken into account by means of source/sink terms, the boundary of the domain of interest (Γ) can be assumed to be impermeable to both advective and diffusive matter fluxes. Therefore, if $\boldsymbol{n}$ denotes the outward unit normal to the boundary, and u_t is the velocity component tangential to the boundary, the boundary conditions associated with Eqs. (3), (4), (8), (21) and (29), respectively, are as follows:

$$[\boldsymbol{u}\cdot\boldsymbol{n}]_{x\in\Gamma} = 0, \tag{38}$$

$$[H\boldsymbol{n}\cdot\boldsymbol{A}\cdot(\boldsymbol{\nabla}u_t)]_{x\in\Gamma} = 0, \tag{39}$$

$$[H\boldsymbol{n}\cdot\boldsymbol{K}\cdot(\boldsymbol{\nabla}C_s)]_{x\in\Gamma} = 0, \quad s=\mathrm{i,h,p,r}, \tag{40}$$

$$[H\boldsymbol{n}\cdot\boldsymbol{K}\cdot(\boldsymbol{\nabla}\alpha_s)]_{x\in\Gamma} = 0, \quad s=\mathrm{i,h,p,r}, \tag{41}$$

$$[H\boldsymbol{n}\cdot\boldsymbol{K}\cdot(\boldsymbol{\nabla}\theta_j)]_{x\in\Gamma} = 0, \quad j=1,\ldots,n. \tag{42}$$

Appendix B. Concentration properties

We want to demonstrate that properties (14)–(17) hold true.

By adding the equations governing the concentration of each water type, the equation satisfied by the water concentration C_{tot} is readily seen to be:

$$\frac{\partial}{\partial t}(HC_{\mathrm{tot}}) + \boldsymbol{\nabla}\cdot(H\boldsymbol{u}C_{\mathrm{tot}}) = \left(w^+ + q_{\mathrm{p}} + q_{\mathrm{r}}^+\right) + \left(w^- + q_{\mathrm{v}} + q_{\mathrm{r}}^-\right)C_{\mathrm{tot}} + \boldsymbol{\nabla}\cdot\left(H\boldsymbol{K}\cdot(\boldsymbol{\nabla}C_{\mathrm{tot}})\right). \tag{43}$$

Taking into account continuity Eq. (3), the boundary conditions (38) and (40) and the initial conditions (13), the solution of Eq. (43) is:

$$C_{\mathrm{tot}}(t,\boldsymbol{x}) = 1. \tag{44}$$

Therefore, property (15) holds true.

If Ω represents the domain of interest (i.e. the lake surface), elementary manipulations of Eq. (8) applied to the initial water and the continuity Eq. (3) yield:

$$\frac{\partial}{\partial t}\int_\Omega HC_{\mathrm{i}}^2\,\mathrm{d}\boldsymbol{x} = -\int_\Omega\Big(\left(|w| + q_{\mathrm{p}} - q_{\mathrm{v}} + |q_{\mathrm{r}}|\right)C_{\mathrm{i}}^2 + 2H(\boldsymbol{\nabla}C_{\mathrm{i}})\cdot\boldsymbol{K}\cdot(\boldsymbol{\nabla}C_{\mathrm{i}})\Big)\mathrm{d}\boldsymbol{x}. \tag{45}$$

As $\boldsymbol{K}$ is positive definite, q_{p} is positive and q_{v} is negative, the integrand in the right-hand side member of Eq. (45) is positive unless C_{i} is zero at every location of the domain of interest. As a result, the integral over Ω of (HC_{i}^2), which is a measure of the magnitude of the initial water concentration, will decrease until the initial water concentration is zero at every point. Therefore, property (16) holds true.

Eqs. (6) and (7) and properties (15) and (16) imply that property (17) holds true, which is trivial.

Demonstrating that property (14) holds true is equivalent to show that the concentration C_s and the overshooting of the concentration $\widehat{C}_s = 1 - C_s$ are positive, or that their negative parts are zero, i.e.:

$$C_s^-(t,\boldsymbol{x}) = 0, \quad s=\mathrm{i,h,p,r}, \tag{46}$$

$$\widehat{C}_s^-(t,\boldsymbol{x}) = 0, \quad s=\mathrm{i,h,p,r}. \tag{47}$$

Intricate manipulations of Eqs. (8) and (3) are needed to show that the negative part of every concentration C_s obeys an expression of the form:

$$\frac{\partial}{\partial t}\int_\Omega H\left(C_s^-\right)^2\mathrm{d}\boldsymbol{x} = -\int_\Omega\Big(\omega\left(C_s^-\right)\left|C_s^-\right| + 2H\left(\boldsymbol{\nabla}C_s^-\right)\cdot\boldsymbol{K}\cdot\left(\boldsymbol{\nabla}C_s^-\right)\Big)\mathrm{d}\boldsymbol{x}, \quad s=\mathrm{i,h,p,r}. \tag{48}$$

Table 1
Values of $\omega\,(C_s^-)$ and $\omega(\widehat{C}_s^-)$ from Eqs. (48) and (49), respectively, depending on the water type

	$\omega\,(C_s^-)$	$\omega(\widehat{C}_s^-)$
$s=\mathrm{i}$	$(\lvert w\rvert+q_\mathrm{p}-q_\mathrm{v}+\lvert q_\mathrm{r}\rvert)\lvert C_\mathrm{i}^-\rvert$	$(\lvert w\rvert+q_\mathrm{p}-q_\mathrm{v}+\lvert q_\mathrm{r}\rvert)\lvert C_\mathrm{i}^-\rvert+2\left(w^++q_\mathrm{p}+q_\mathrm{r}^+\right)$
$s=\mathrm{h}$	$(\lvert w\rvert+q_\mathrm{p}-q_\mathrm{v}+\lvert q_\mathrm{r}\rvert)\lvert C_\mathrm{h}^-\rvert+2w^+$	$(\lvert w\rvert+q_\mathrm{p}-q_\mathrm{v}+\lvert q_\mathrm{r}\rvert)\lvert C_\mathrm{h}^-\rvert+2\left(q_\mathrm{p}+q_\mathrm{r}^+\right)$
$s=\mathrm{p}$	$(\lvert w\rvert+q_\mathrm{p}-q_\mathrm{v}+\lvert q_\mathrm{r}\rvert)\lvert C_\mathrm{p}^-\rvert+2q_\mathrm{p}^+$	$(\lvert w\rvert+q_\mathrm{p}-q_\mathrm{v}+\lvert q_\mathrm{r}\rvert)\lvert C_\mathrm{p}^-\rvert+2\left(w^++q_\mathrm{r}^+\right)$
$s=\mathrm{r}$	$(\lvert w\rvert+q_\mathrm{p}-q_\mathrm{v}+\lvert q_\mathrm{r}\rvert)\lvert C_\mathrm{r}^-\rvert+2q_\mathrm{r}^+$	$(\lvert w\rvert+q_\mathrm{p}-q_\mathrm{v}+\lvert q_\mathrm{r}\rvert)\lvert C_\mathrm{r}^-\rvert+2\left(w^++q_\mathrm{p}\right)$

A similar expression holds valid for the negative part of $\widehat{C}_s$, i.e.:

$$\frac{\partial}{\partial t}\int_\Omega H(\widehat{C}_s^-)^2\mathrm{d}\boldsymbol{x}=-\int_\Omega\Big(\omega(\widehat{C}_s^-)\big|\widehat{C}_s^-\big|+2H(\boldsymbol{\nabla}\widehat{C}_s^-)\cdot\boldsymbol{K}\cdot(\boldsymbol{\nabla}\widehat{C}_s^-)\Big)\mathrm{d}\boldsymbol{x},\quad s=\mathrm{i},\mathrm{h},\mathrm{p},\mathrm{r}. \tag{49}$$

The Table 1 provides $\omega(C_s^-)$ and $\omega(\widehat{C}_s^-)$.

Clearly, the integrands in the right-hand side of Eqs. (48) and (49) are positive, unless C_s^- and $\widehat{C}_s^-$ are zero at every point. As a consequence, the measures of the undershootings and the overshootings of the different water type concentrations cannot increase. But, at the initial time, they are already zero, by virtue of the initial conditions (13). Thus, C_s^- and $\widehat{C}_s^-$ will be zero at any time and location, implying that property (14) holds true.

Appendix C. Age properties

We want to demonstrate that properties (23) and (24) hold valid.

Using the equation of the initial water concentration, i.e. Eq. (8) with $s=i$, it is readily seen that $\alpha_\mathrm{i}=C_\mathrm{i}t$ is the solution of the partial differential problem of Eqs. (21) and (22). Therefore, property (24) holds true.

Since property (24) holds true, the age of the initial water satisfies the property (23) for $s=i$. But for the sake of generality and completeness, the demonstration below will keep dealing with the initial water.

Since the different water type concentrations C_s are positive, showing the validity of property (23) is equivalent to showing that the age concentration α_s and the overshooting of the age concentration $\widehat{\alpha}_s=C_st-\alpha_s$ are positive, or that their negative parts are zero, i.e.

$$\alpha_s^-(t,\boldsymbol{x})=0,\quad s=\mathrm{i},\mathrm{h},\mathrm{p},\mathrm{r}, \tag{50}$$

$$\widehat{\alpha}_s^-(t,\boldsymbol{x})=0,\quad s=\mathrm{i},\mathrm{h},\mathrm{p},\mathrm{r}. \tag{51}$$

Table 2
Values of $\omega\,(\alpha_s^-)$ and $\omega(\widehat{\alpha}_s^-)$ from Eqs. (52) and (53), respectively, depending on the water type

	$\omega\,(\alpha_s^-)$	$\omega(\widehat{\alpha}_s^-)$
$s=\mathrm{i}$	$(\lvert w\rvert+q_\mathrm{p}-q_\mathrm{v}+\lvert q_\mathrm{r}\rvert)\lvert\alpha_\mathrm{i}^-\rvert+2HC_\mathrm{i}$	$(\lvert w\rvert+q_\mathrm{p}-q_\mathrm{v}+\lvert q_\mathrm{r}\rvert)\lvert\alpha_\mathrm{i}^-\rvert$
$s=\mathrm{h}$	$(\lvert w\rvert+q_\mathrm{p}-q_\mathrm{v}+\lvert q_\mathrm{r}\rvert)\lvert\alpha_\mathrm{h}^-\rvert+2HC_\mathrm{h}$	$(\lvert w\rvert+q_\mathrm{p}-q_\mathrm{v}+\lvert q_\mathrm{r}\rvert)\lvert\alpha_\mathrm{h}^-\rvert+2w^+t$
$s=\mathrm{p}$	$(\lvert w\rvert+q_\mathrm{p}-q_\mathrm{v}+\lvert q_\mathrm{r}\rvert)\lvert\alpha_\mathrm{p}^-\rvert+2HC_\mathrm{p}$	$(\lvert w\rvert+q_\mathrm{p}-q_\mathrm{v}+\lvert q_\mathrm{r}\rvert)\lvert\alpha_\mathrm{p}^-\rvert+2q_\mathrm{p}t$
$s=\mathrm{r}$	$(\lvert w\rvert+q_\mathrm{p}-q_\mathrm{v}+\lvert q_\mathrm{r}\rvert)\lvert\alpha_\mathrm{r}^-\rvert+2HC_\mathrm{r}$	$(\lvert w\rvert+q_\mathrm{p}-q_\mathrm{v}+\lvert q_\mathrm{r}\rvert)\lvert\alpha_\mathrm{r}^-\rvert+2q_\mathrm{r}^+t$

Intricate manipulations of Eqs. (21) and (3) are needed to show that the negative parts of every age concentration α_s obeys an expression of the form:

$$\frac{\partial}{\partial t}\int_\Omega H(\alpha_s^-)^2\mathrm{d}\boldsymbol{x}=-\int_\Omega\Big(\omega(\alpha_s^-)\big|\alpha_s^-\big|+2H(\boldsymbol{\nabla}\alpha_s^-)\cdot\boldsymbol{K}\cdot(\boldsymbol{\nabla}\alpha_s^-)\Big)\mathrm{d}\boldsymbol{x},\quad s=\mathrm{i},\mathrm{h},\mathrm{p},\mathrm{r}. \tag{52}$$

A similar expression holds valid for the negative part of $\widehat{\alpha}_s$, i.e.:

$$\frac{\partial}{\partial t}\int_\Omega H(\widehat{\alpha}_s^-)^2\mathrm{d}\boldsymbol{x}=-\int_\Omega\Big(\omega(\widehat{\alpha}_s^-)|\widehat{\alpha}_S^-|+2H(\boldsymbol{\nabla}\widehat{\alpha}_s^-)\cdot\boldsymbol{K}\cdot(\boldsymbol{\nabla}\widehat{\alpha}_s^-)\Big)\mathrm{d}\boldsymbol{x},\quad s=\mathrm{i},\mathrm{h},\mathrm{p},\mathrm{r}. \tag{53}$$

The Table 2 provides $\omega(\alpha_s^-)$ and $\omega(\widehat{\alpha}_s^-)$.

Clearly, the integrands in the right-hand side of Eqs. (52) and (53) are positive, unless α_s^- and $\widehat{\alpha}_s^-$ are zero at every point. As a consequence, the measures of the undershootings and the overshootings of the different water type age concentrations cannot increase. But, at the initial time, they are already zero, by virtue of the initial conditions (22). Thus, α_s^- and $\widehat{\alpha}_s^-$ will be zero at any time and location, implying that property (23) holds true.

Appendix D. Supplementary data

Supplementary data associated with this article can be found, in the online version, at doi:10.1016/j.ecss.2007.05.009.

References

Bergonzini, L., 1998. Bilans hydriques de lacs (Kivu, Tanganyika, Rukwa et Nyassa) du rift est-africain. Musée royal de l'Afrique centrale, Tervuren, Belgique (Chapter 2).

Bolin, B., Rodhe, H., 1973. A note on the concepts of age distribution and transit time in natural reservoirs. Tellus 25, 58–62.

Braunschweig, F., Martins, F., Chambel, P., Neves, R., 2003. A methodology to estimate renewal timescales in estuaries: the Tagus Estuary case. Ocean Dynamics 53 (3), 137–145.

Coulter, G.W., Spigel, R.H., 1991. Hydrodynamics. In: Coulter, G.W. (Ed.), Lake Tanganyika and Its Life. Oxford University Press, New York, USA, pp. 49–75.

Cox, M.D., 1989. An idealized model of the world ocean. Part I: the global-scale water masses. Journal of Physical Oceanography 19 (11), 1730–1752.

Deleersnijder, E., Campin, J.-M., Delhez, E.J.M., 2001. The concept of age in marine modeling: I. Theory and preliminary model results. Journal of Marine Systems 28 (3–4), 229–267.

Deleersnijder, E., Tartinville, B., Rancher, J., 1997. A simple model of the tracer flux from the Mururoa Lagoon to the Pacific. Applied Mathematics Letters 10 (5), 13–17.

Delhez, E.J.M., Campin, J.-M., Hirst, A.C., Deleersnijder, E., 1999. Toward a general theory of the age in ocean modelling. Ocean Modelling 1 (1), 17–27.

Delhez, E.J.M., Deleersnijder, E., 2006. The boundary layer of the residence time field. Ocean Dynamics 56 (2), 139–150.

Delhez, E.J.M., Heemink, A.W., Deleersnijder, E., 2004. Residence time in a semi-enclosed domain from the solution of an adjoint problem. Estuarine, Coastal and Shelf Science 61 (4), 691–702.

Delhez, E.J.M., 2006. Transient residence and exposure times. Ocean Science 2 (1), 1–9.

Goosse, H., Campin, J.-M., Tartinville, B., 2001. The sources of Antarctic bottom water in a global ice-ocean model. Ocean Modelling 3 (1–2), 51–65.

Hanert, E., Le Roux, D.Y., Legat, V., Deleersnijder, E., 2004. Advection schemes for unstructured grid ocean modelling. Ocean Modelling 7 (1–2), 39–58.

Hanert, E., Le Roux, D.Y., Legat, V., Deleersnijder, E., 2005. An efficient Eulerian finite element method for the shallow water equations. Ocean Modelling 10 (1–2), 115–136.

Hirst, A.C., 1999. Determination of water component age in ocean models: application to the fate of North Atlantic deep water. Ocean Modelling 1 (2–4), 81–94.

Monsen, N.E., Cloern, J.E., Lucas, L.V., Monismith, S.G., 2002. A comment on the use of flushing time, residence time, and age as transport time. Limnology and Oceanography 47 (5), 1545–1553.

Naithani, J., Darchambeau, F., Deleersnijder, E., Descy, J.-P., Wolanski, E., 2007. Study of the nutrient and plankton dynamics in Lake Tanganyika using a reduced-gravity model. Ecological Modelling 200 (1–2), 225–233.

Naithani, J., Deleersnijder, E., Plisnier, P.-D., Legrand, S., 2004. Preliminary results of a reduced-gravity model of the wind-induced oscillations of the thermocline in Lake Tanganyika. In: Demarée, G., De Dapper, M., Alexandre, J. (Eds.), Second International Conference on Tropical Climatology, Meteorology and Hydrology, pp. 27–40.

Naithani, J., Deleersnijder, E., Plisnier, P.-D., 2002. Origin of intraseasonal variability in Lake Tanganyika. Geophysical Research Letters 29 (23), 2093. doi:10.1029/2002GL015843.

Naithani, J., Deleersnijder, E., Plisnier, P.-D., 2003. Analysis of wind-induced thermocline oscillations of Lake Tanganyika. Environmental Fluid Mechanics 3 (1), 23–39.

Naithani, J., Deleersnijder, E., 2004. Are there internal Kelvin waves in Lake Tanganyika? Geophysical Research Letters 31, L06303. doi:10.1029/2003GL019156.

Price, J.F., 1979. On the scaling of stress-driven entrainment experiments. Journal of Fluid Mechanics 90 (3), 509–529.

Takeoka, H., 1984. Fundamental concepts of exchange and transport timescales in a coastal sea. Continental Shelf Research 3 (3), 311–326.

Tartinville, B., Deleersnijder, E., Rancher, J., 1997. The water residence time in the Mururoa atoll lagoon: sensitivity analysis of a three-dimensional model. Coral Reefs 16 (3), 193–203.

White, L., Deleersnijder, E., 2007. Diagnoses of vertical transport in a three-dimensional finite-element model of the tidal circulation around an island. Estuarine. Coastal and Shelf Science 74 (4), 735–749.

Zimmerman, J.T.F., 1976. Mixing and flushing of tidal embayments in the Western Dutch Wadden Sea. Part I: distribution of salinity and calculation of mixing timescales. Netherlands Journal of Sea Research 10 (2), 149–191.

Zimmerman, J.T.F., 1988. Estuarine residence times. In: Kjerfve, B. (Ed.), Hydrodynamics of Estuaries, vol. 1, pp. 75–84.

Available online at www.sciencedirect.com
ScienceDirect
Estuarine, Coastal and Shelf Science 74 (2007) 641–654
ESTUARINE COASTAL AND SHELF SCIENCE
www.elsevier.com/locate/ecss

Elucidating the dynamics and mixing agents of a shallow fjord through age tracer modelling

Karin E. Gustafsson*, Jørgen Bendtsen

National Environmental Research Institute, University of Aarhus, Frederiksborgvej 399, P.O. Box 358, 4000 Roskilde, Denmark

Received 8 June 2006; accepted 9 May 2007
Available online 5 July 2007

Abstract

The mixing agents and their role in the dynamics of a shallow fjord are elucidated through an Eulerian implementation of artificial tracers in a three-dimensional hydrodynamic model. The time scales of vertical mixing in this shallow estuary are short, and the artificial tracers are utilized in order to reveal information not detectable in the temperature or salinity fields. The fjord's response to external forcing is investigated through a series of model experiments in which we quantify vertical mixing, transport time scales of fresh water runoff and estuarine circulation in relation to external forcing.

Using age tracers released at surface and bottom, we quantify the time scales of downward mixing of surface water and upward mixing of bottom water. Wind is shown to be the major agent for vertical mixing at nearly all depth levels in the fjord, whereas the tide or external sea level forcing is a minor agent and only occasionally more important just close to the bottom. The time scale of vertical mixing of surface water to the bottom or ventilation time scale of bottom water is estimated to be in the range 0.7 h to 9.0 days, with an average age of 2.7 days for the year 2004.

The fjord receives fresh water from two streams entering the innermost part of the fjord, and the distribution and age of this water are studied using both ageing and conservative tracers. The salinity variations outside this fjord are large, and in contrast to the salinity, the artificial tracers provide a straight forward analysis of river water content. The ageing tracer is used to estimate transport time scales of river water (i.e. the time elapsed since the water left the river mouth). In May 2004, the typical age of river water leaving the fjord mouth is 5 days. As the major vertical mixing agent is wind, it controls the estuarine circulation and export of river water. When the wind stress is set to zero, the vertical mixing is reduced and the vertical salinity stratification is increased, and the river water can be effectively exported out of the fjord.

We also analyse the river tracer fields and salinity field in relation to along estuary winds in order to detect signs of wind-induced straining of the along estuary density gradient. We find that events of down estuary winds are primarily associated with a reduced along estuary salinity gradient due to increased surface salinity in the innermost part of the fjord, and with an overall decrease in vertical stratification and river water content at the surface. Thus, our results show no apparent signs of wind-induced straining in this shallow fjord but instead they indicate increased levels of vertical mixing or upwelling during down estuary wind events.

Keywords: tracers; modelling; vertical mixing; mixing processes; boundary layers; estuarine dynamics; age tracer

1. Introduction

In shallow systems, time scales of vertical mixing are short and the turbulent surface and bottom boundary layers may overlap. Due to the intermittent absence of vertical gradients of salinity and temperature, the magnitude of vertical mixing is, however, difficult to detect via these parameters. Instead, artificial age tracers may be added to a hydrodynamic model in order to quantify the vertical mixing on short time scales ranging from hours to days (Bendtsen et al., 2006). Several studies discuss the concept of age for estimating time scales for transport and mixing of water and dissolved substances (e.g. Bolin and Rodhe, 1973; Zimmermann, 1976; Stuiver et al., 1983; Takeoka, 1984; Thiele and Sarmiento, 1990; Delhez et al.,

* Corresponding author.
E-mail address: kgu@dmu.dk (K.E. Gustafsson).

0272-7714/$ - see front matter © 2007 Elsevier Ltd. All rights reserved.
doi:10.1016/j.ecss.2007.05.023

1999; Deleersnijder et al., 2001), and artificial age tracers have been introduced in hydrodynamic models in studies of coastal and open seas (e.g. Gustafsson, 2000; Delhez and Carabin, 2001; Delhez and Deleersnijder, 2002), fjord estuaries (e.g. Engqvist, 1996) and river estuaries (e.g. Shen and Haas, 2004; Shen and Lin, 2006).

The shallow Danish estuary ''Horsens Fjord'' has a mean depth of only 2.9 m. The vertical stratification in the fjord is primarily associated with large variations in salinity outside the fjord in addition to buoyancy input to the fjord in the form of river discharge. Due to the shallowness of this fjord, the vertical mixing is related to the turbulent boundary layer dynamics on short time scales. The vertical mixing in the surface boundary layer is associated with surface forcing due to wind, and intermittent wind bursts may ventilate the water column down to a few meters depth (e.g. Bendtsen et al., 2006). The bottom boundary layer dynamics is related to bottom friction and vertical shear caused by barotropic flow components. These are normally associated with tides, but can also be due to wind surge effects. The dynamics and estuarine exchange flow are regulated by the vertical mixing. In order to analyse the general dynamics of the fjord in relation to the major mixing agents, we introduce various types of artificial tracers in a three-dimensional hydrodynamic model of the fjord and study the fjord's response to external forcing (e.g. tides and winds) through a sensitivity study. By analysing the vertical distribution of age tracers released at bottom or surface, we quantify the vertical mixing in the fjord in relation to external forcing.

The vertical mixing and horizontal transport of river water containing dissolved substances and nutrients have implications on the water quality parameters and the biogeochemical cycling and retention of nutrients discharged to the fjord (e.g. Stedmon et al., 2006). The export of river water and estuarine exchange may be controlled by several factors. Winds and tides provide energy for vertical mixing, but may also contribute to increased stratification due to straining of along estuary gradients (Simpson et al., 1990; Scully et al., 2005). The amount of fresh water discharge also plays a role in regulating the wind and tidally induced mixing and estuarine exchange flow through its effect on vertical stratification (e.g. Shen and Lin, 2006; Bendtsen et al., 2007).

Due to the variable conditions outside Horsens Fjord, estimates of river water content in the fjord via salinity are, however, dependent on a correct account for the inflows of water of much varying salinity. By releasing artificial river tracers in a hydrodynamic model of the fjord, we may detect and quantify the distribution and transport time scales of river water in the fjord. The river water content is analysed by marking the river runoff with a conservative (i.e. not ageing) reference tracer where the resulting tracer field is directly proportional to the distribution of river water in the fjord, in similar to what could be told from the salinity field if salinity was to be constant at the open boundary. In addition, an age tracer is added to the river water in order to analyse the transport time scales and estuarine circulation in relation to external forcing.

In Section 2.1, we introduce the reader to Horsens Fjord. This is followed by a presentation of the hydrodynamic model of the fjord (Section 2.2), and the implementation of artificial age tracers (Section 2.3). The sensitivity study is outlined in Section 2.4. Results are presented and discussed in Section 3, and the paper is concluded by a short summary (Section 4).

2. Model simulations

2.1. Horsens Fjord

Horsens Fjord is located on the east coast of Jutland, Denmark (Fig. 1). It is about 10 km long and 5 km wide and has a volume of 0.132 km^3. The mean depth of the fjord is 2.9 m, and the deepest part of the fjord is a narrow ship route channel of 6 m depth which goes from the entrance area of the fjord to Horsens Harbour in the western innermost part of the fjord. The major fresh water sources are the two streams, Hansted Å and Bygholm Å, both located in the innermost western part of the fjord. The drainage areas for these two streams constitute 290 km^2 or 70% of the total drainage area for Horsens Fjord. The average discharge during 2004 is 2.1 m^3/s for Bygholm Å and 1.9 m^3/s for Hansted Å. The fjord has been monitored as a part of the Danish National Monitoring Programme during the last decade where two stations inside the fjord and one station outside the fjord have been visited about once a week. The measurements of salinity at these stations in 2004 are shown in Fig. 2. Station 5790 is 4 m deep and is situated in the inner western part of the fjord on the flank of the 6 m deep ship route channel, and the 17 m deep station 6489 is located in the entrance area of the fjord. Station 6883 is located about 10 km outside the fjord. The fjord enters Kattegat Sea, which consists of the transition zone between the Baltic Sea and North Sea. The advection of water masses from the Baltic Sea estuary is regulated by the large-scale atmospheric conditions and water level in the Baltic Sea–North Sea system and is associated with large differences in salinity in the Kattegat Sea (Fig. 2c). This may lead to inflows to Horsens Fjord of much varying salinity. In addition, the deepest waters of the fjord are well ventilated (Fig. 2b) as the fjord does not have a sill in the entrance area. Instead, there is a deep passage in the form of a narrow and long submarine channel which stretches from the fjord mouth towards the open sea, through the otherwise rather shallow coastal area outside the fjord. The deep passage has a maximum depth of 22 m.

2.2. The hydrodynamic model

A three-dimensional primitive equation model based on the COHERENS model (Luyten et al., 1999) is used for hydrodynamic simulations of the fjord system during the year 2004. The model solves the hydrodynamic equations on a Cartesian C-grid and a vertical sigma coordinate system. This implies a fixed number of vertical grid levels over the whole model domain, and we use 15 layers with an equidistant spacing of the layers in the vertical. The horizontal grid is equidistant with

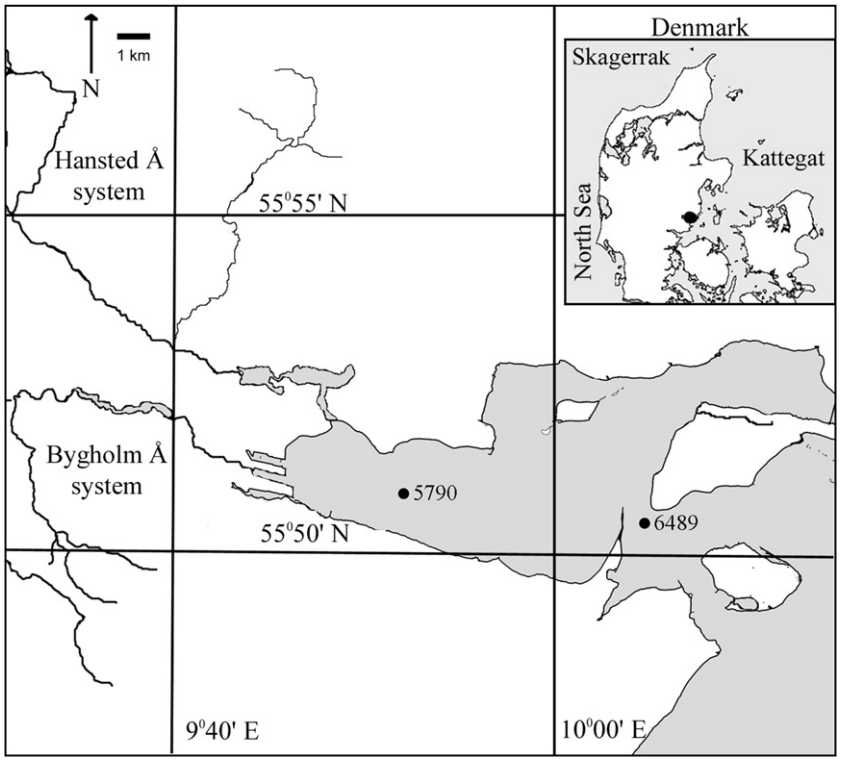

Fig. 1. Horsens Fjord with the monitoring station 5790 in the innermost part of the fjord and station 6489 at the mouth of the fjord. Station 6883 (not shown) is located outside the fjord in Kattegat near the eastern border of the figure. The two major fresh water suppliers, Hansted Å and Bygholm Å, enter the innermost part of the fjord close to Horsens City and Horsens Harbour.

a grid size of 250 m. Vertical mixing is parameterised by a k–epsilon turbulence closure scheme.

The model is driven by hourly meteorological records of wind, temperature, cloudiness, pressure and relative humidity generated by an operational weather forecast model (Brandt et al., 2001). As the atmospheric model has a coarser resolution than the model domain, records from one point in the atmospheric model are used for forcing the model. We chose the

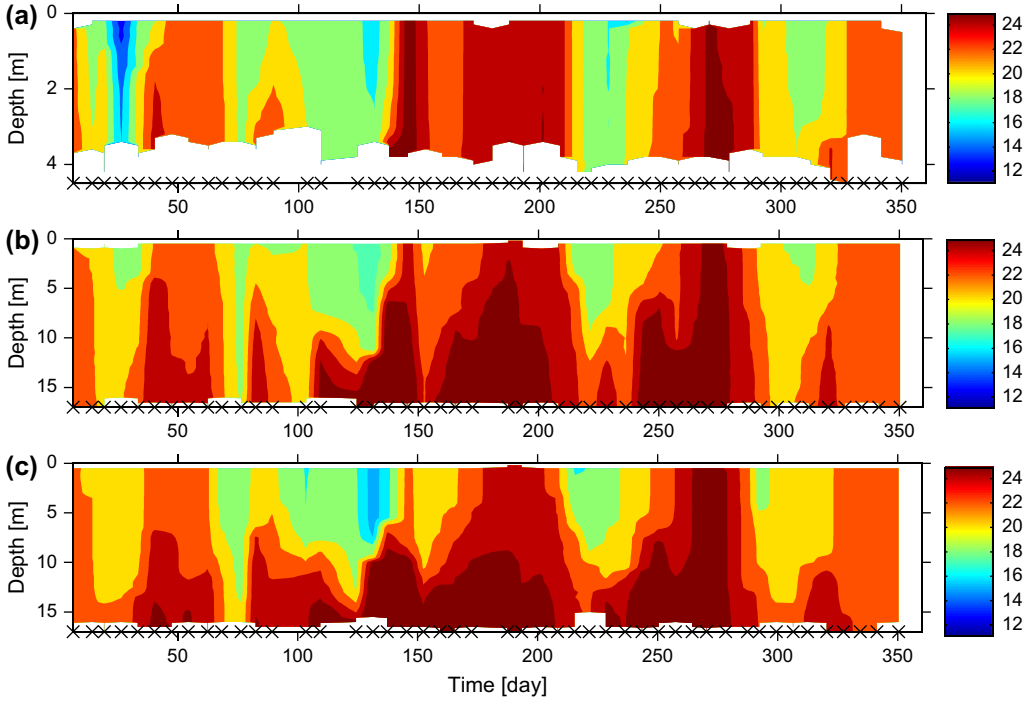

Fig. 2. Observed salinity at station 5790 (a) at the innermost part of the fjord, station 6489 (b) at the mouth of the fjord, and station 6883 (c) outside the fjord. The times of observations are shown as crosses.

land point in the atmospheric model which is closest to the observational site 5790 in the fjord. Open boundary conditions of salinity and temperature are taken from CTD measurements at station 6883 in the Kattegat Sea. Salinity and temperature were measured at station 6883 about once a week during 2004. Observations are linearly interpolated in time and in the vertical and the horizontally uniform model boundary conditions of salinity and temperature are updated once a day. We use daily means of discharge from the two streams, Hansted Å and Bygholm Å. The hydrodynamic model has a free surface and the model is forced with the sea surface level at the open boundary. For this purpose we use data from the nearest sea level recorder at the harbour of Juelsminde which is located by the coast about 10 km south of the model domain. The sea surface level is measured every 20 min and is linearly interpolated in time. The horizontally uniform model boundary conditions of water level are updated every 15 min. The deep and narrow submarine channel stretching from the fjord mouth to the open sea is in a north west–south east direction. We have therefore rotated the bathymetry 49 degrees anticlockwise so that the high saline water can be transported across the deepest model grid cells, and we have reproduced the channel by setting the depth of a series of cells from the open sea to the fjord mouth to 20.0 m. The wind direction of meteorological records has been rotated accordingly. The model grid and bathymetry are shown in Fig. 3.

2.3. Implementation of artificial age tracers

Two different age tracers are used in the hydrodynamic model simulations for quantifying the time scales associated with vertical mixing: a "surface age tracer" which describes the age and downward mixing of surface water (i.e. surface boundary layer dynamics), and a "bottom age tracer" which is utilised to quantify the upward mixing of bottom water (i.e. bottom boundary layer dynamics). We also study the distribution and time scales of spreading of fresh water from the two major rivers considering both conservative and ageing river water tracers.

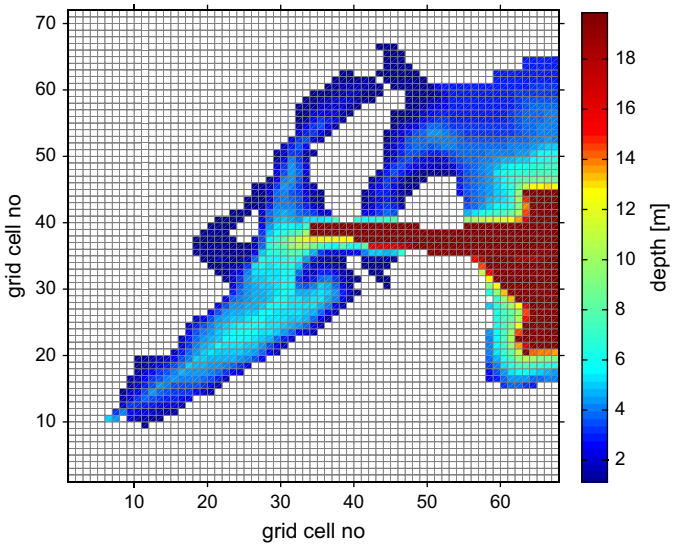

Fig. 3. The model domain, together with the computational grid and bathymetry (rotated 49 degrees anticlockwise). The horizontal grid spacing is 250 m. The colour scale shows depth in units of metre.

The evolution of a tracer concentration $c(t,\boldsymbol{x})$ and age concentration $\alpha(t,\boldsymbol{x})$ can be described from the transport equation as

$$\frac{\partial c(t,\boldsymbol{x})}{\partial t} + \nabla\cdot(\boldsymbol{u}c(t,\boldsymbol{x}) - \boldsymbol{K}\cdot\nabla c(t,\boldsymbol{x})) = 0 \tag{1}$$

$$\frac{\partial \alpha(t,\boldsymbol{x})}{\partial t} + \nabla\cdot(\boldsymbol{u}\alpha(t,\boldsymbol{x}) - \boldsymbol{K}\cdot\nabla \alpha(t,\boldsymbol{x})) = c(t,\boldsymbol{x}) \tag{2}$$

where $\boldsymbol{u}$ is the velocity field, $\boldsymbol{K}$ is the diffusivity tensor, t is the time and $\boldsymbol{x}$ is the spatial coordinate (e.g. Delhez et al., 1999). The age $a(t,\boldsymbol{x})$ can be calculated in an Eulerian model through successive computations of tracer concentration and age concentration, and the age is thereafter evaluated as

$$a(t,\boldsymbol{x}) = \frac{\alpha(t,\boldsymbol{x})}{c(t,\boldsymbol{x})} \tag{3}$$

However, if there is no mixing with water not originating from the source (e.g. from an open boundary), the only constituent is the water from the source itself (i.e. $c\sim 1$), and the age concentration of the water is almost equal to its age (i.e. $\alpha\sim a$), which means the age can be directly evaluated (i.e. not via computations of the age concentration) as

$$\frac{\partial a(t,\boldsymbol{x})}{\partial t} + \nabla\cdot(\boldsymbol{u}a(t,\boldsymbol{x}) - \boldsymbol{K}\cdot\nabla a(t,\boldsymbol{x})) = 1 \tag{4}$$

The term on the RHS of Eqs. (1), (2) and (4) expresses the source or sink of the tracer concentration, age concentration and age, respectively. In Eq. (1), this term is zero and the tracer concentration can only be modified by advective fluxes from surrounding waters or by diffusive fluxes. Eq. (1) can thus be used directly to study the concentration of a "conservative tracer". In Eq. (4), the term on the RHS expresses the dimensionless growth of the age of a water parcel, and as it equals one, the age of a water parcel will increase in proportion to the time step itself and due to the diffusive and advective age flux from the surrounding waters. The age will thus reflect the transport time scale or time elapsed since the tracer left a source region in which a is set to zero. In Eqs. (2)–(3), account is taken for dilution with water not originating from the tracer source. The term on the RHS of Eq. (2) expresses the ageing of the fraction of the water parcel which constitutes the tracer. Thus, it is equal to one if 100% of the water parcel originates from the tracer source and Eq. (4) can then be used directly instead of Eqs. (1)–(3).

For the river age tracer, the dilution with water not originating from the river is significant, and we use Eqs. (1)–(3) to compute tracer concentration and age. For the bottom and surface tracer experiments, c is assumed to be close to 1, and we calculate the age directly according to Eq. (4). $\boldsymbol{u}$, $\boldsymbol{K}$, t and $\boldsymbol{x}$ are given by the hydrodynamic model simulation, and the tracers are implemented in a coupled mode. The tracers and boundary conditions are further presented in the following two sections.

2.3.1. Surface and bottom tracers

For the purpose of estimating vertical mixing and boundary layer dynamics we use two age tracers and study their different age fields. The surface age tracer a_s reflects the time elapsed since the water was in contact with the surface, corresponding to the boundary condition $a_s(t,x,y,z=0)=0$ at the surface. A zero gradient condition is applied at the bottom ($z=-h$). The opposite is applied for the bottom age tracer a_b with the boundary condition $a_b(t,x,y,z=-h)=0$ at the bottom and a zero gradient condition at the surface. The bottom tracer is thus suitable for describing time scales related to the upward mixing of bottom water and for evaluating the average age of or time elapsed since water at different depths was in contact with bottom. Since we analyse the surface and bottom tracer age at a station in the shallow inner part of the fjord, the time scales of vertical mixing are short, and the tracer concentration can be assumed to be close to one (i.e. the concentration of water which never has been in contact with sea surface or bottom, respectively, is low). It should be noted that we apply a zero gradient condition at the open boundary towards the sea, meaning that there is no exchange across the open boundary. Under these circumstances, we consider the usage of Eq. (4) a reasonable approximation. The effects of water depth on the ages computed in the surface boundary layer are further analysed in Bendtsen et al. (2006). The mean age of the surface and bottom tracers will evolve along the vertical as a result of the integrated mixing history on time scales on the order of the time it takes to vertically mix the whole water column. Thus, the tracer age will also be a meaningful measure of the mixing resolved onto time scales relevant for benthic pelagic coupling and ecological parameters such as oxygen and nutrient supply.

2.3.2. River tracers

We also use tracers in order to study the spreading of river water in the fjord. The river water is marked by adding a conservative "reference tracer" c_{ref} to the fresh water discharge from Bygholm Å and Hansted Å. As they both enter the innermost western part of the fjord close to each other, we consider them as one tracer source. River runoff is specified in terms of a flux boundary condition with a vertically constant flow at the river mouth with the condition $c_{ref}\ (t)=1$ for inflowing river water. At the open sea boundary, an upwind condition is applied where $c_{ref}\ (t)=0$ for inflowing water. The reference tracer thus varies between 1 and 0 and represents the fraction of river water. It shows the relative distribution of river water in the fjord, in similar to what could be told from the salinity field if salinity was to be constant outside the fjord. In addition, we calculate the age concentration α_r of river water in order to determine its age a_r (by using α_r and c_{ref} in Eqs. (1)–(3)). The vertically constant boundary condition at the river mouth is now set to $\alpha_r(t)=0$ for the inflowing river water. At the open sea boundary, we apply a zero gradient condition.

The river tracer age a_r reflects the time elapsed since the river water entered the fjord. However, in waters far away from the source (or little affected by the source), the age will not be a representative measure of the transport time scale as the tracer concentration reaches very small values (cf. Eq. (3)).

2.4. Sensitivity study of external forcing

In order to make quantitative estimates of the mixing agents and their role in the dynamics of the fjord, we perform a sensitivity study of the fjord's response to external forcing on the open boundaries. We therefore analyse the artificial tracer distributions in four sensitivity experiments (see Table 1). In case I, corresponding to the reference case, the model is forced with observed water level at the open boundary and surface fluxes from the meteorological forcing fields. In case II, the wind stress is set to zero in order to detect the effect of wind-induced vertical mixing and circulation. In case III, the fjord's response to external sea level or tidal forcing is investigated. The sea surface elevations at the open sea boundary are therefore set to zero. Finally, we run a case IV where both external sea level and wind stress are set to zero so that the only forcing is via gradients in salinity or temperature caused by the open boundary conditions, sensible or radiant heat fluxes at sea surface and river runoff.

3. Results and discussion

3.1. Hydrodynamic model

Fig. 4 shows time series of modelled and observed sea level, temperature and salinity. The salinity and temperature are shown for the whole simulation year, whereas the sea level is shown for a shorter period for clarity. The model solution of the amplitude and phase of sea level (Fig. 4a) are in accordance with observations from Horsens Harbour located in the innermost western part of the fjord. Observations of temperature and salinity are from station 5790 in the inner part of the fjord (see Fig. 1). This station is only 4 m deep, and the observed bottom temperature ranges from 1.4 °C in January to 22.5 °C in August, and as indicated in Fig. 4b there is almost no thermal stratification at this station. The model solution of salinity (Fig. 4c) shows a large variability in surface salinity, indicating that the station is affected by the fresh water plumes from the two nearby rivers. The observations show almost no vertical stratification at this station and we speculate that the observations might not cover the near surface salinity variations in the thin 0.5–1 m deep surface layer. The average of the observed salinity at or above 1 m depth during the year is 21.5, whereas the average modelled salinity at 0.8 m depth is 17.0. The average observed salinity at or below 3.5 m depth

Table 1
Model forcing in the four experiments of the sensitivity study

Case	Wind	Water level	Comment
I	+	+	Reference (normal)
II	−	+	No wind stress
III	+	−	No external sea level forcing
IV	−	−	No wind stress and no external sea level forcing

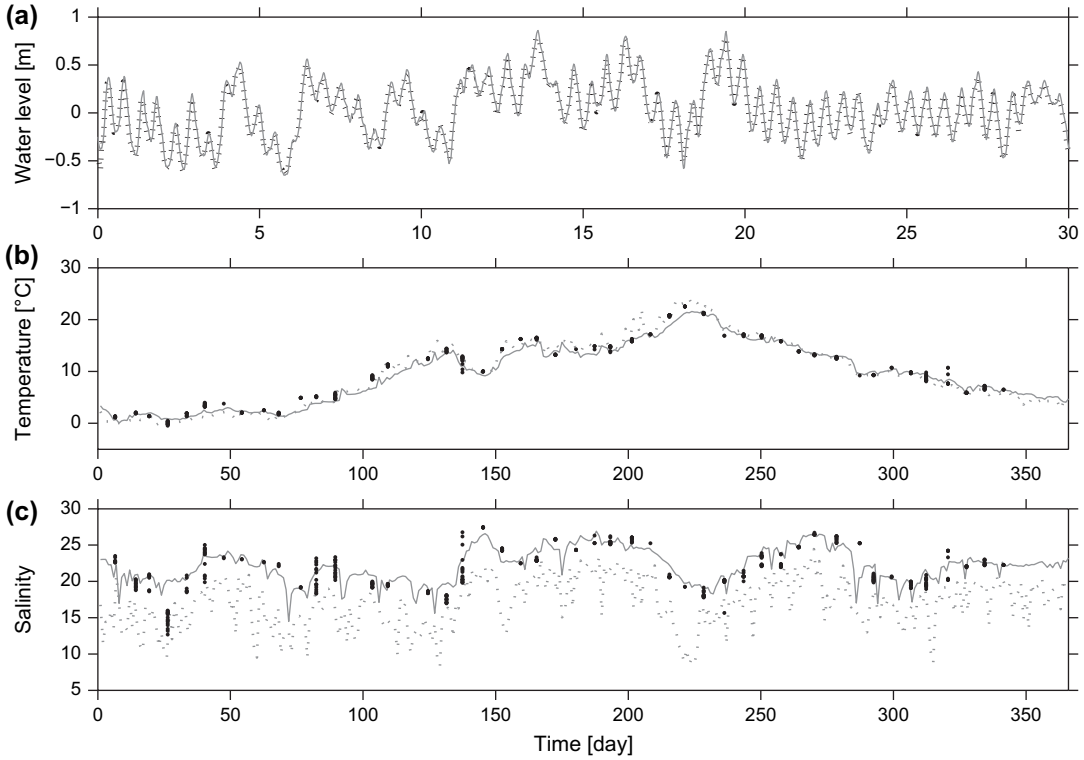

Fig. 4. Modelled and observed water level (a), temperature (b) and salinity (c) for 2004. The observed (black dashed) and modelled (grey solid) water levels are from Horsens Harbour in the innermost western part of the fjord, and are shown for January 2004 only for clarity. Observations of temperature and salinity are from the inner part of the fjord at station 5790. The stratification at this shallow station is weak and the entire sets of observations (at all depths) are displayed (black dots). The grey dotted and solid lines are the model results at surface and bottom, respectively.

(down to bottom at 4.0 m) is 22.7, and the average modelled salinity at 3.9 m depth is 22.1. The modelled and observed salinity are also shown as contour plots in Fig. 5 for both station 5790 and the 17.0-m deep station 6489 by the fjord entrance area. Also at station 6489 the model simulations show fresh water near surface which cannot be seen in the observations. The model solution also displays a variability in the salinity field, which is of a higher frequency than the observational frequency (the times of observations are shown as crosses along the *x*-axis of Fig. 5a and c). Apart from the near surface variability in salinity, there is a good agreement between model and observations at both station 5790 and station 6489 showing that the model is able to reproduce the saline inflows and following intrusions to the innermost part of the fjord.

3.2. Vertical mixing agents

In the two upper panels of Fig. 6, time series of the surface and bottom tracer age at station 5790 are shown. The surface tracer age at bottom (top panel of Fig. 6) reflects the time elapsed since bottom water was in contact with the surface. In the normal reference case (case I), the age varies between 0.7 h and 9.0 days during the year and the average age is 2.7 days. Without external sea level forcing (case III), the average age of the surface tracer at bottom is slightly increased (with about 0.3 days) to 3.0 days, whereas without wind (case II), the mean age is increased significantly with 9.3 days to 12.0 days. The mixing by tides is thus significantly lower than the mixing by winds. The results show clearly that the local wind has the largest effect on the surface tracer age and is the major agent causing downward vertical mixing of surface water at this station. In panel three, the cubed wind (corresponding to the performed work) is shown, and in the last panel, we display the vertical salinity stratification determined as the difference in salinity between bottom and surface. One can see that the work performed by wind causes large variations in the salinity stratification and age on short time scales. The maximum surface tracer age of 9.0 days occurs at day 220 during a period of relatively calm winds and increased levels of stratification. Correspondingly, low ages can be seen, for example, during a period prior to day 150 with modest but persistent wind forcing and decreased levels of stratification.

In panel two of Fig. 6, time series of the bottom tracer age at surface are shown. The age is now a measure for the time scales of upward mixing of bottom water. The pattern is similar to the surface tracer with large variations and spikes in age related to the wind-driven surface boundary layer dynamics. The bottom tracer age varies between 1.3 h and 11.8 days, and the average age during the year is 6.8 days. The average age increases to 18.6 days when wind is turned off (case II) and to 7.3 days when tides are turned off (case III). The wind is thus the major vertical mixing agent also for the bottom tracer. The difference between average surface and bottom tracer ages indicates an asymmetry between the time scales of downward mixing of

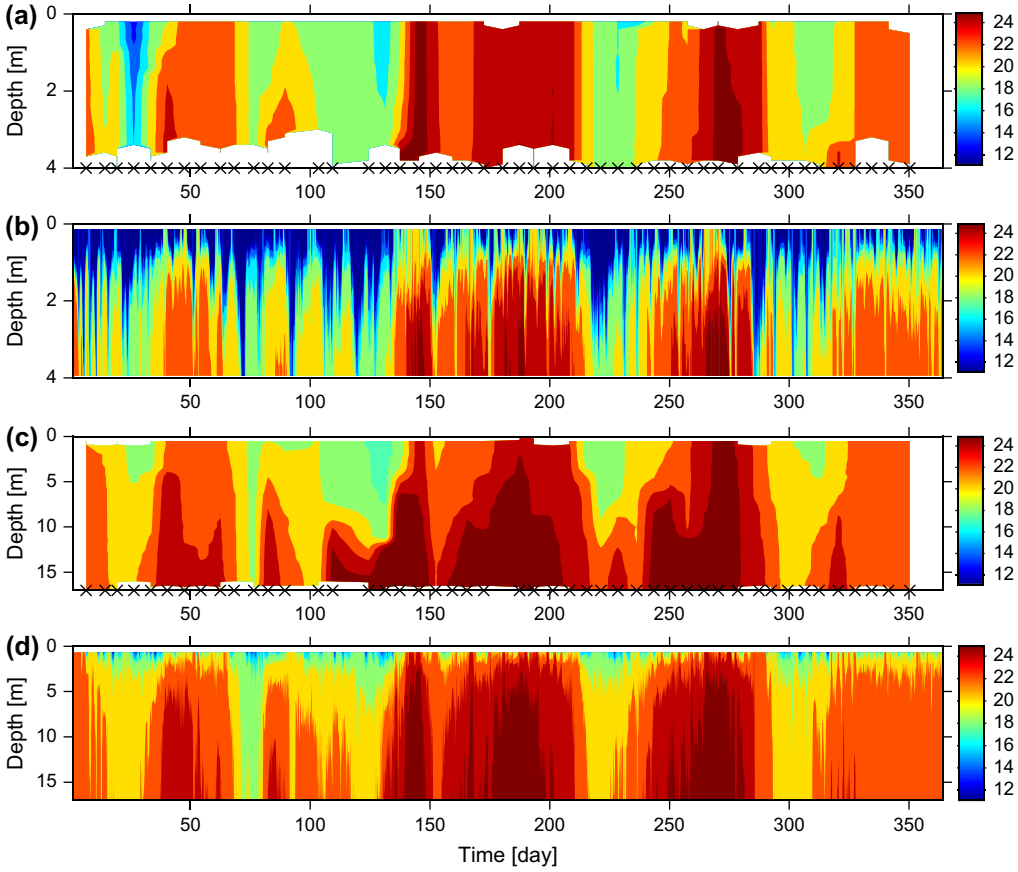

Fig. 5. Observed (a) and modelled (b) salinity at station 5790, and observed (c) and modelled (d) salinity at station 6489. The times of observations are shown as crosses along the *x*-axis of (a) and (c). Modelled fields are sampled every 0.25 days.

surface water and upward mixing of bottom water, related to the different spatial and temporal scales of the wind-driven surface boundary layer and tidally driven bottom boundary layer.

The variation in the surface and bottom tracer age seen in case II without wind should not be related to variations in tidal mixing, but to forcing via gradients in salinity or temperature caused by the open boundary conditions, sensible or radiant heat fluxes at sea surface and river runoff. To clarify this, we ran the model without both wind and tidal forcing (case IV, Fig. 6). We note that the age in both cases II and IV somewhat resembles the salinity stratification in case IV. It can be shown that the salinity stratification in case IV also is similar to the salinity at the open boundary (see e.g. Fig. 2 or bottom salinity for case I in Fig. 4 which also resembles the salinity at the open boundary). This indicates that the age in cases II and IV is reflecting the density-driven circulation caused by salinity variations outside the fjord. In case IV, the variation in age is larger than in case II, as consistent with the tidal mixing present in case II, and during several periods (e.g. day 0–25, day 50–75 or day 190–225) the surface tracer age in case IV increases by about 1 day per day showing that there is only a small downward mixing or movement of surface water. The same pattern can be seen for the bottom tracer age at the surface. However, the amplitude of the variations is smaller as the bottom tracer age increases somewhat slower during these periods. This is a consequence of the density-driven estuarine circulation of the fjord driven by density variations at the open boundary and fresh water supply. The density-driven estuarine circulation implies a general upward movement of the water resulting in lower bottom tracer ages at the surface compared to surface tracer ages at the bottom (Fig. 6, case IV). The estuarine circulation and response to vertical mixing agents are further analysed in relation to the river tracers in Section 3.3.

Fig. 7a and b displays the occurrence of surface and bottom tracer ages at three depth levels (surface, mid-depth and bottom) at station 5790. The age is sampled four times daily during the whole year and binned into different age intervals. The figures show how the age increases with distance from the source, and that the surface tracer covers a narrow age range at surface and the bottom tracer covers a narrow range of ages at bottom. The variance of the age distribution thus reflects periods with different mixing intensities throughout the year as well as mixing with surrounding waters (see also Deleersnijder et al., 2001).

As expected, the lowest depth contains the highest number of occasions of low surface tracer ages (top panel Fig. 7a). Further down the water column, the surface tracer age is displaced towards higher ages. Cases I and III are quite similar with only a slight displacement towards higher ages in case III, showing that tidal mixing has a minor effect on the surface

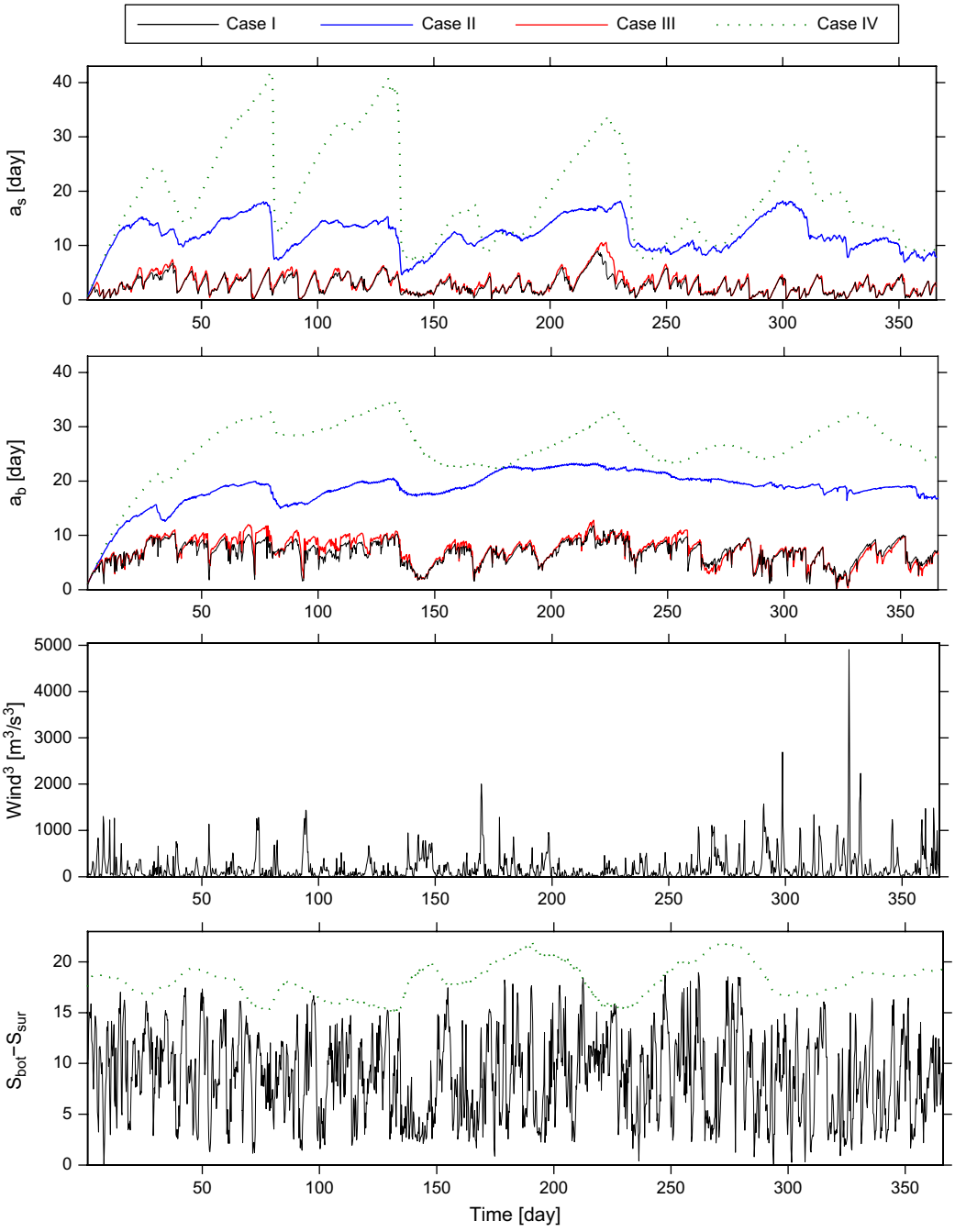

Fig. 6. Time series of surface tracer age (top panel) at bottom, and of bottom tracer age (second panel) at surface at station 5790 and for cases I–IV. Panel three shows the cubed wind, and the last panel shows the modelled stratification in salinity for case I (black) and case IV (green) computed as the difference between the bottom and surface salinity at station 5790.

tracer age. Case II is clearly distributed around high ages with a median of 7.1 at mid-depth (middle panel). Thus, it is also here apparent that the wind has the largest influence on surface tracer ages all the way from surface to bottom.

The distribution of the bottom tracer (Fig. 7b) shows that the bottom tracer ages are slightly affected by tides, so that the age distributions of cases I and III are similar with a slight displacement towards higher ages for case III without tides. The wind does have the largest impact also on the bottom tracer ages. Without wind (case II) the median is displaced towards higher ages than in case III except for the deepest level where the simulation without tides show a somewhat larger displacement towards higher ages, showing tides are of importance for the vertical mixing close to bottom. Thus, the local wind has the largest impact on both surface and bottom tracer ages at nearly all depths.

3.3. River water export and estuarine dynamics in relation to external forcing

In this fjord, where variations in salinity to a large extent are due to variations in salinity outside the fjord, a reference

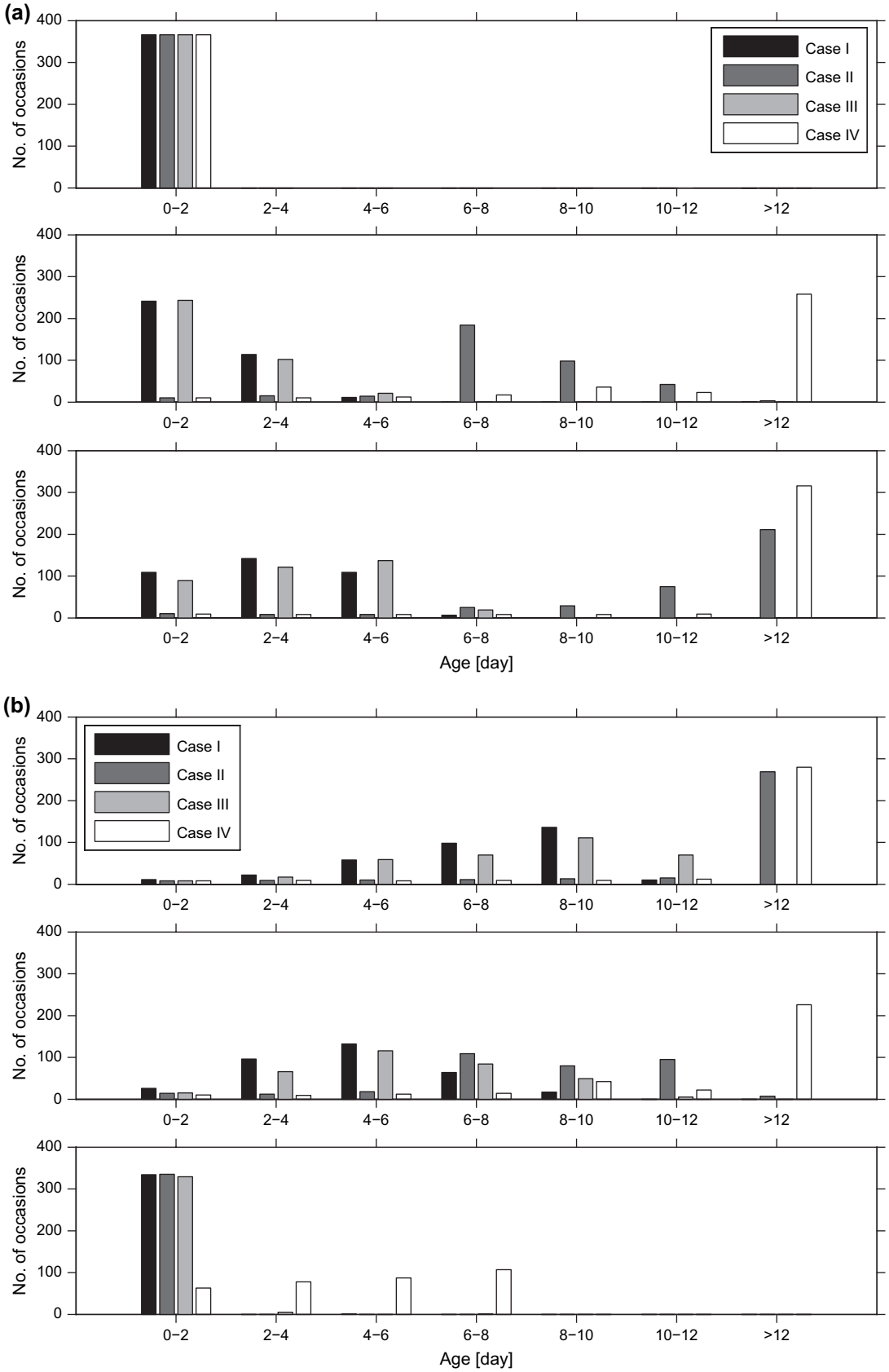

Fig. 7. (a) Distribution of surface tracer ages on age intervals. The surface tracer ages are sampled from the model at station 5790 every 6 h during 2004. The top panel is for 0.4 m depth, the middle panel is for 2.0 m depth and the lower panel is for 4.0 m depth (bottom layer of model). (b) Distribution of bottom tracer ages on age intervals. The bottom tracer ages are sampled from the model at station 5790 every 6 h during 2004. The top panel is for 0.1 m depth, the middle panel is for 2.0 m depth and the lower panel for 3.7 m depth.

tracer is of particular help in the analysis of the distribution and age of river water. Salinity, reference tracer and age fields are shown in Fig. 8 (for surface) and Fig. 9 (for bottom). We ran the model with river tracers from January to May and analyse the results averaged over the period 1–15 May (the period is arbitrarily chosen). The reference tracer distribution in Fig. 8 shows the extent of the fresh water plume from the runoff, and at the mouth of the fjord, the reference tracer concentration decreases rapidly towards sea. The low reference tracer concentration outside the fjord causes the ages computed from the ratio of age concentration to reference tracer concentration to become relatively large, and we have chosen to cut-off the age colour scale of Figs. 8 and 9 at 30 days. Inside the fjord, the age distribution reveals spatial differences in the river water age. The age of river water reaching the mouth is typically about 5 days during this period, whereas the age in the more isolated north-eastern bay reaches values above 20 days.

The different cases indicate the dynamics caused by wind versus external sea level forcing during the period. If wind is turned off (case II) the average surface salinity and river water age at surface decrease, due to a reduced vertical mixing and an increased stratification, and the fresh water runoff can be effectively exported in a surface layer without being vertically mixed with waters from below. This is also seen from the increased reference tracer concentration at the surface and the reduced reference tracer concentration at the bottom. These results are relevant for this fjord where wind is the major vertical mixing agent. For example, in the tidal James River estuary Shen and Lin (2006) found that the difference in river tracer age between surface and bottom is increased during neap tide in comparison with the spring tide. Contrary to this, it is almost exclusively the wind that controls the export of river water in Horsens Fjord through its effect on vertical stratification.

When external sea level forcing is turned off (case III) there is a minor decrease in the salinity distribution and a minor increase in the reference tracer distribution both at the bottom and at the surface. The age distributions are similar to case I. Thus, even though sea level forcing causes a large barotropic exchange with the open sea, it has a limited influence on the vertical mixing in the fjord interior.

We have also analysed the salinity and river tracer results in relation to down estuary winds in order to detect signs of wind-induced straining of the along density gradient. Through

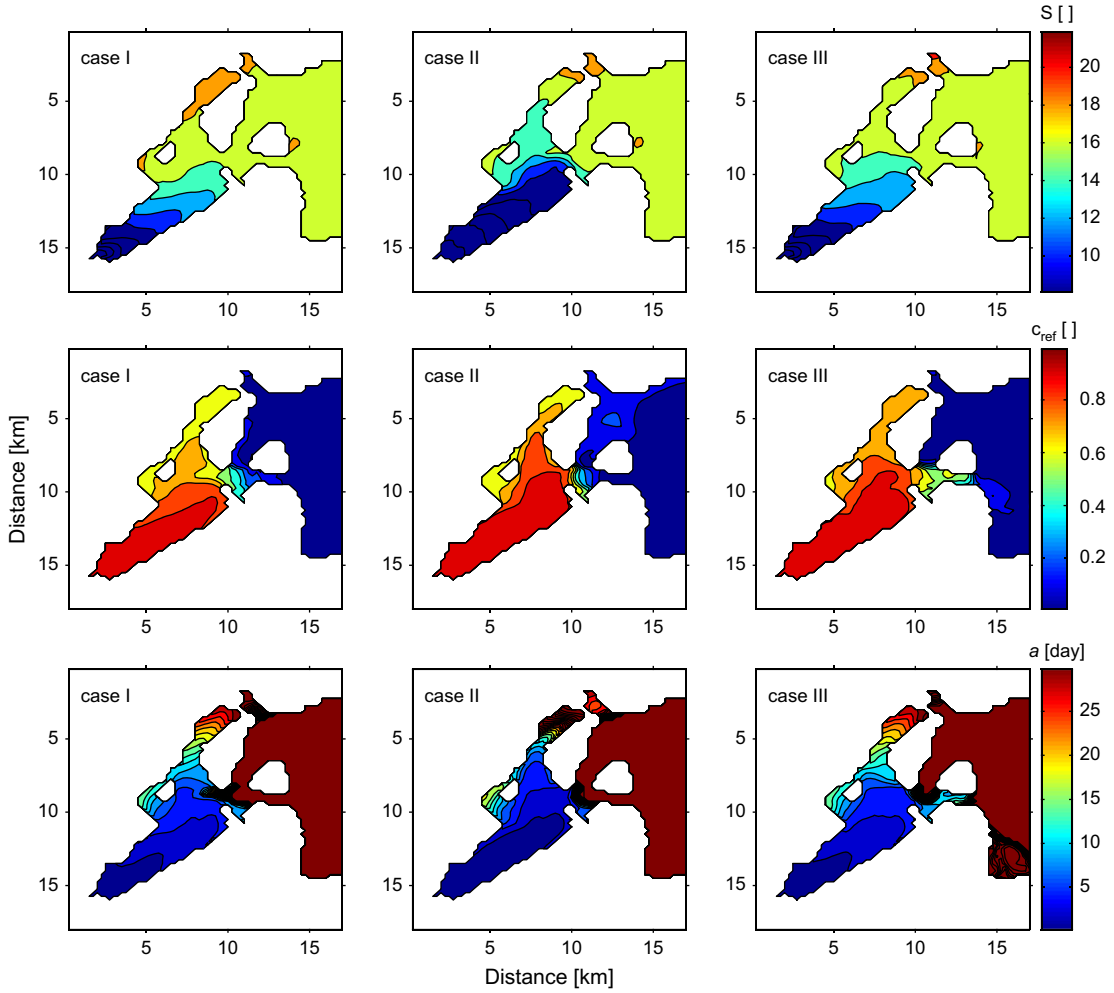

Fig. 8. Average salinity (top panels), river reference tracer (middle panels) and age (lower panels) in the surface layer for the period 1–15 May 2004 and model simulation case I (left), case II (middle) and case III (right).

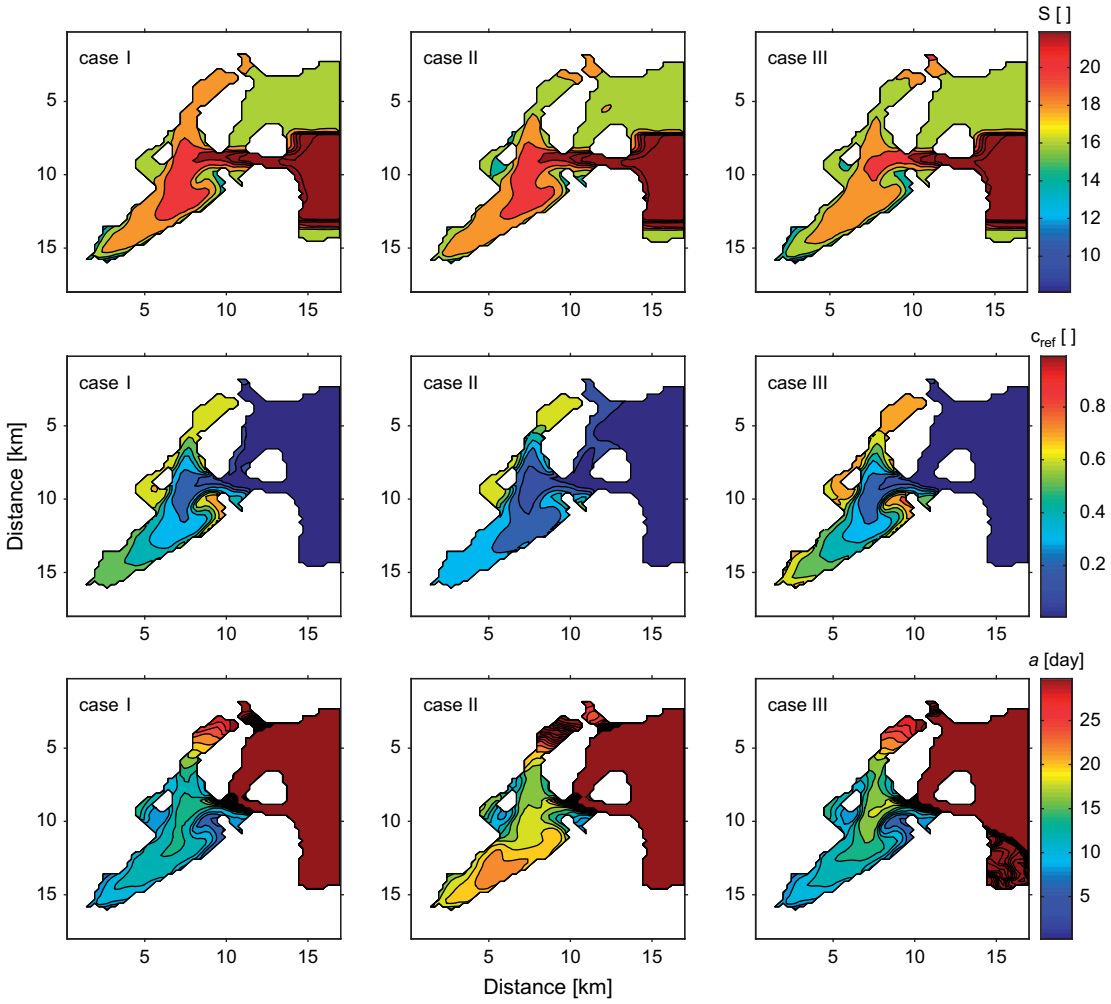

Fig. 9. The same as in Fig. 8 but for the bottom layer of the model.

observations in the partially mixed estuary of the York River, Scully et al. (2005) demonstrate that down estuary winds may increase vertical stratification by straining of the along estuary density gradient, which in turn may dampen vertical mixing. They suggest that winds may not only provide energy for vertical mixing, but may also play an even more important role in controlling the efficiency of wind and tidal mixing through straining of the along density gradient.

At station 5790, events of down estuary winds (as given by $W_x > 0$) are apparently correlated with increased river tracer age at surface, see Fig. 10. For clarity, we display the results for one month only, and we have arbitrarily chosen February. In turn, the occurrences of high ages correlate with reduced reference tracer concentration in surface and increased surface salinity, showing increased mixing with water originating from outside the fjord. The response is similar near the mouth of the fjord at station 6489 where down estuary wind events are generally associated with increased age and decreased reference tracer concentration. Thus, we detect no obvious signs of down estuary wind straining. The down estuary wind events do correlate with reduced along estuary salinity gradients in surface (data not shown), which could in principle be a sign of straining. However, the decrease in the along estuary gradient is mainly due to an increase in surface salinity at station 5790, and *not* due to decreased surface salinity at station 6489 (the along estuary salinity gradient nearly mirrors the surface salinity at 5790). Thus, our results imply that down estuary winds may, or even particularly do, increase the vertical mixing or cause upwelling in the inner part of the fjord. As pointed out by Scully et al. (2005), there is likely a fundamental difference in the response of shallow estuaries versus partially mixed estuaries. Our results are more in line with the results by Geyer (1997), who study two shallow estuaries and find that down estuary winds enhance the surface outflow and correlate with reduced along estuary gradients and an overall decrease in vertical stratification.

In this paper, we have concentrated on the usage of tracers for analysing physical processes. For example, the surface tracer study presented here shows that time scales of vertical mixing in the shallow part of the fjord are short and in the order of hours or days. On such short time scales, the surface tracer age is also a useful tool in estimating the magnitude of benthic pelagic coupling which is amplified during mixing events where the surface and bottom boundary layers overlap.

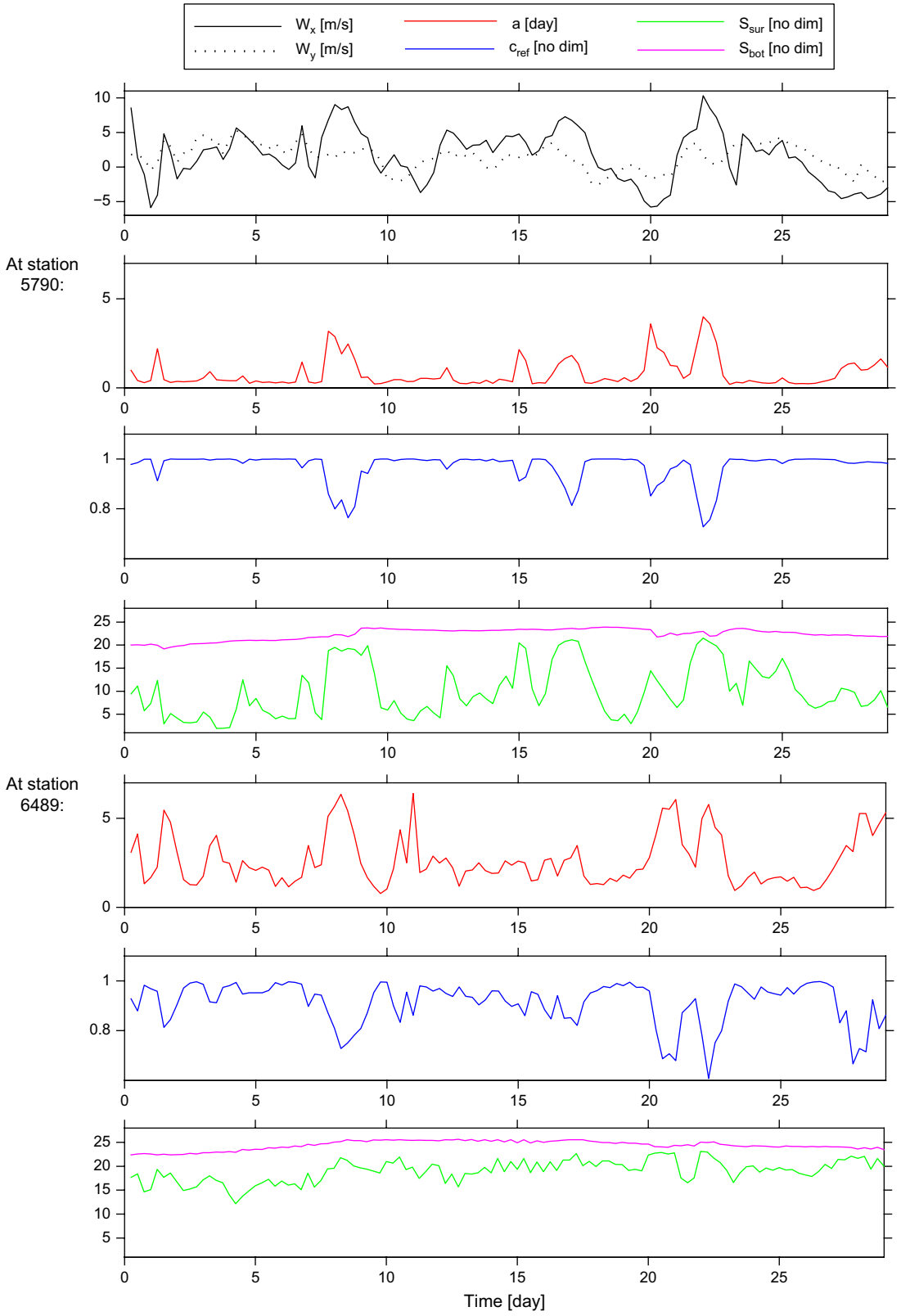

Fig. 10. Wind magnitude in the x- and y-direction (top panel) during February 2004, where down estuary winds are associated with mainly $W_x > 0$ (see Fig. 3 for the alignment of the fjord). The y component of the wind is in general smaller than the x component, and the prevailing wind direction is $W_x > 0$. The following three panels are model results from the inner part of the fjord (station 5790) of river water age at surface, reference tracer concentration c_{ref} at surface and salinity at surface S_{sur} and bottom S_{bot}. The last three panels show the corresponding time series at station 6489 at the mouth of the fjord.

In Horsens Fjord, the benthic filtrators (mussels) have the potential of filtering the water column about three times a day, but their phytoplankton grazing potential cannot be fully used unless there is downward vertical mixing of phytoplankton rich surface water. This suggests that there is a correlation between phytoplankton biomass and surface tracer age for low values of the surface tracer age, and that the benthic biomass is regulated by the vertical mixing on short time scales (e.g. Petersen, 2004; Kristensen et al., 2005).

4. Conclusions

By the use of artificial age tracers in a hydrodynamic model of Horsens Fjord, it is possible to reveal information on mixing and circulation not detectable in the temperature or salinity fields. Using various types of tracers in a sensitivity study of the fjord's response to external forcing, we identify and quantify the mixing agents and elucidate their role in the dynamics of the fjord.

The model experiments were carried out for the year 2004 and reveal that wind is the major mixing agent at nearly all depth levels of this relatively shallow fjord. An analysis of the bottom and surface tracer ages shows that the time scale for vertical mixing at a 4.0-m deep station ranges from less than 1 h to a few days. The average surface tracer age at the bottom is 2.7 days, and the average age of the bottom tracer at the surface is 6.8 days. Without wind stress, the corresponding ages are 12.0 days and 18.6 days, respectively. Tides or external sea level forcing is a minor mixing agent compared to the wind, but does have an effect on the vertical mixing and might be of importance close to bottom and during periods of calm winds.

The simulations with tracer marked river water show the concentration and age of river water in the fjord. In contrast to salinity, the reference concentration directly shows the distribution of river water in the fjord, and the fresh water plumes are easily identified. In the first half of May, the average age of river water near the fjord mouth is 5 days at the surface. However, temporal and spatial variations inside the fjord are large. As the wind is the major mixing agent of this fjord, it is also important in regulating the baroclinic exchange flow and estuarine circulation. If wind stress is turned off, the reduced vertical mixing and increased vertical stratification allow for an effective transport of fresh water out of the system. This is confirmed through an increased river water concentration in surface and decreased river water concentration at bottom, together with reduced river water age in surface and increased river water age at bottom. This should also be the case during periods of calm winds. The tide plays a minor role in the vertical mixing, but when external sea level forcing is set to zero, the average salinity in the fjord is somewhat reduced and the river water concentration is slightly increased. Thus, even though sea level forcing causes a large barotropic exchange with the open sea, it has a limited influence on the vertical mixing in the fjord interior.

An analysis of the response of this shallow fjord to along estuary wind shows no signs of down estuary wind-induced straining. Instead, we find that events of down estuary winds can be associated with a reduced along estuary salinity gradient due to increased surface salinity in the innermost part of the fjord, and with an overall decrease in vertical stratification and river water content in surface, indicating increased levels of vertical mixing or upwelling in the inner part of the fjord during down estuary wind events.

Acknowledgements

We thank Torben Vang for providing data for the model set up, and Jørgen Brandt and Jesper Christensen for providing the atmospheric forcing fields.

References

Bendtsen, J., Gustafsson, K.E., Petersen, J.K., 2006. Modelling vertical mixing in the surface boundary layer using artificial age tracers. Journal of Marine Systems 60, 115–128.

Bendtsen, J., Gustafsson, K.E., Rysgaard, S., Vang, T., 2007. Physical conditions, dynamics and model simulations during the ice-free period of the Young Sound/Tyrolerfjord system. In: Rysgaard, S., Glud, R.N. (Eds.), Carbon Cycling in Arctic Marine Ecosystems: Case Study Young Sound. Bioscience vol. 58, 46–59. Meddr. Grønland.

Bolin, B., Rodhe, H., 1973. A note on the concepts of age distribution and transit time in natural reservoirs. Tellus 25, 58–62.

Brandt, J., Christensen, J.H., Frohn, L.M., Palmgren, F., Berkowicz, R., Zlatev, Z., 2001. Operational air pollution forecasts from European to local scale. Atmospheric Environment 35 (Suppl. 1), S91–S98.

Deleersnijder, E., Campin, J.M., Delhez, E.J.M., 2001. The concept of age in marine modelling I. Theory and preliminary model results. Journal of Marine Systems 28, 229–267.

Delhez, É.J.M., Carabin, G., 2001. Integrated modelling of the Belgian coastal zone. Estuarine, Coastal and Shelf Science 53, 477–491.

Delhez, É.J.M., Deleersnijder, E., 2002. The concept of age in marine modelling II. Concentration distribution function in the English Channel and the North Sea. Journal of Marine Systems 31, 279–297.

Delhez, É.J.M., Campin, J.M., Hirst, A.C., Deleersnijder, É., 1999. Toward a general theory of the age in ocean modelling. Ocean Modelling 1, 17–27.

Engqvist, A., 1996. Long-term nutrient balances in the eutrophication of the Himmelfjärden estuary. Estuarine, Coastal and Shelf Science 42, 483–507.

Geyer, W.R., 1997. Influence of wind on dynamics and flushing of shallow estuaries. Estuarine, Coastal and Shelf Science 44, 713–722.

Gustafsson, B.G., 2000. Time-dependent modeling of the Baltic entrance area. 1. Quantification of circulation and residence times in the Kattegat and the Straits of the Baltic Sill. Estuaries 23, 231–252.

Kristensen, L.D., Becker, R.W., Sennels, R.H., Schwærter, S., Vang, T., 2005. Kystvande 2004 Fokusrapport (in Danish). Teknik og Miljø, Vejle Amt, ISBN 87-7750-908-0, 24 pp.

Luyten, P.J., Jones, J.E., Proctor, R., Tabor, A., Tett, P., Wild-Allen, K., 1999. COHERENS – A Coupled Hydrodynamical–Ecological Model for Regional and Shelf Seas: User Documentation. MUMM Report. Management Unit of the Mathematical Models of the North Sea, 914 pp.

Petersen, J.K., 2004. Grazing on pelagic primary production – the role of benthic suspension feeders in estuaries. In: Nielsen, S.L., Banta, G.T., Pedersen, M.F. (Eds.), Estuarine Nutrient Cycling: The Influence of Primary Producers. Kluwer Academic Publishers, P.O Box 17, 3300 AA Dordrecht, The Netherlands, pp. 129–152.

Scully, M.E., Friedrichs, C., Brubaker, J., 2005. Control of estuarine stratification and mixing by wind-induced straining of the estuarine density field. Estuaries 28, 321–326.

Shen, J., Haas, L., 2004. Calculating age and residence time in the tidal York River using three-dimensional model experiments. Estuarine, Coastal and Shelf Science 61, 449–461.

Shen, J., Lin, J., 2006. Modeling study of the influences of tide and stratification on age of water in the tidal James River. Estuarine, Coastal and Shelf Science 68, 101–112.

Simpson, J.H., Brown, J., Matthews, J., Allen, G., 1990. Tidal straining, density currents, and stirring in the control of estuarine stratification. Estuaries 13, 125–132.

Stedmon, C.A., Markager, S., Søndergaard, M., Vang, T., Laubel, A., Borch, N.H., Windelin, A., 2006. Dissolved organic matter (DOM) export to a temperate estuary: seasonal variations and implications of land use. Estuaries and Coasts 29 (3), 388–400.

Stuiver, M., Quay, P., Ostlund, H., 1983. Abyssal water carbon-14 distribution and the age of the world oceans. Science 219, 849–851.

Takeoka, H., 1984. Fundamental concepts of exchange and transport time scales in a coastal sea. Continental Shelf Research 3, 322–326.

Thiele, G., Sarmiento, J., 1990. Tracer dating and ocean ventilation. Journal of Geophysical Research 95, 9377–9391.

Zimmermann, J.T.F., 1976. Mixing and flushing of tidal embayments in the Western Dutch Wadden Sea, Part I: distribution of salinity and calculation of mixing time scales. Netherlands Journal of Sea Research 10, 149–191.

Available online at www.sciencedirect.com
ScienceDirect
Estuarine, Coastal and Shelf Science 74 (2007) 655–669
ESTUARINE COASTAL AND SHELF SCIENCE
www.elsevier.com/locate/ecss

Diagnoses of vertical transport in a three-dimensional finite element model of the tidal circulation around an island

Laurent White [a,b,*], Eric Deleersnijder [a,b]

[a] Centre for Systems Engineering and Applied Mechanics (CESAME), Université catholique de Louvain, 4, Avenue G. Lemaître, B-1348 Louvain-la-Neuve, Belgium
[b] G. Lemaître Institute of Astronomy and Geophysics (ASTR), Université catholique de Louvain, 2, chemin du Cyclotron, B-1348 Louvain-la-Neuve, Belgium

Received 10 May 2006; accepted 28 July 2006
Available online 14 September 2006

Abstract

A three-dimensional finite element model is used to investigate the formation of shallow-water eddies in the wake of Rattray Island (Great Barrier Reef, Australia). Field measurements and visual observations show that stable eddies develop in the lee of the island at rising and falling tides. The water turbidity downstream of the island suggests the existence of strong upwelling that would be responsible for carrying bed sediments up to the sea surface. We first propose to look at the upwelling velocity and then use the theory of the age to diagnose vertical transport. The water age is defined as the time elapsed since particles of water left the sea bottom, where the age is prescribed to be zero. Two versions of this diagnosis are considered. Although the model predicts upwelling within the eddies, it is not sufficiently intense to account for vertical transport throughout the water column during the life span of the eddies. As mesh resolution increases, this upwelling does not intensify. However, strong upwelling is then resolved off the island's tips, which is confirmed by the results obtained with the age. This study also shows that the finite element method, together with unstructured meshes, performs well for representing three-dimensional flow past an island.

Keywords: age; upwelling; unstructured mesh; finite element method; island wake; Rattray Island

1. Introduction

In shallow coastal regions, flow disturbances caused by topographical features, such as islands, headlands, reefs and narrow passages, can have strong effects on marine ecosystems. Topographically generated circulation affects the distribution of sediments and can significantly influence the local dispersal of pelagic organisms (Hamner and Hauri, 1981; Wolanski and Hamner, 1988; Wolanski et al., 1988; Wolanski, 1994; Coutis and Middleton, 1999, 2002). As pointed out by Wolanski et al. (1984), this has important implications in the location of fisheries and waste outfalls. Due to the presence of islands and reefs, oncoming currents separate and, as water is stripped away at the surface, it is replaced by upwelled water (Hamner and Hauri, 1981). Upwelled water is generally enriched with nutrients, which may locally alter the biotic diversity (Wolanski et al., 1988). Depending on flow characteristics and island geometry, stable or unstable eddies may develop in the island wake (Wolanski et al., 1984; Pattiaratchi et al., 1986; Ingram and Chu, 1987; Wolanski et al., 1996). These eddies may have a local impact on the ecosystem because of secondary circulation, enhanced turbulence and upwelling (Hamner and Hauri, 1981; Wolanski and Hamner, 1988; Wolanski et al., 1988).

Of particular concern are the shallow-water eddies generated in the wakes of islands by oscillating tidal flows. By shallow water, it is meant here that the ratio of the water depth to the island width (facing the current) is much less than one. Shallow-water flows are characterized by dominant bottom friction, which has important consequences onto their

* Corresponding author. Centre for Systems Engineering and Applied Mechanics (CESAME), Université catholique de Louvain, 4, Avenue G. Lemaître, B-1348 Louvain-la-Neuve, Belgium.
E-mail address: lwhite@mema.ucl.ac.be (L. White).

0272-7714/$ - see front matter © 2006 Elsevier Ltd. All rights reserved.
doi:10.1016/j.ecss.2006.07.014

dynamics (Ingram and Chu, 1987; Tomczak, 1988). Unsteadiness of tidal flows was shown to play a crucial role in the formation of eddies (Black and Gay, 1987). To take into account bottom friction in the description of the island wake dynamics, Wolanski et al. (1984) suggested to use the ''island wake parameter'' P rather than the usual Reynolds number prevailing in the description of two-dimensional wake flows. Pattiaratchi et al. (1986) confirmed this concept with laboratory and field experiments. The island wake parameter P is defined as the ratio of nonlinear acceleration to bottom friction. For $P < 1$, no wake is present. For $P \simeq 1$, two stable eddies form in the lee of the island and remain attached while for increasing values of P, instabilities occur in the wake, following by eddy shedding. In this paper, we will focus on the case $P \simeq 1$ for which eddies essentially result from a balance between radial pressure gradient and centrifugal effect due to flow curvature. Near the bottom, the azimuthal velocity decreases because of bottom friction. However, a constant pressure gradient is maintained throughout the water column. Therefore, the balance breaks down near the seabed, leading to flow convergence towards the center of the eddy and upwelling within the water column.

Among shallow-water islands for which stable tidal eddies are observed, Rattray Island (Great Barrier Reef, Northeast Australia) has been the focus of many studies in the past two decades (Wolanski et al., 1984; Falconer et al., 1986; Black and Gay, 1987; Wolanski and Hamner, 1988; Deleersnijder et al., 1992; Wolanski et al., 1996, 2003). Rattray Island is 1.5 km long and lies in well-mixed water approximately 25 m deep. The currents are dominated by the tides, whose ellipses are strongly polarized and essentially oriented from northwest to southeast. The island was subject to an extensive field survey in 1982 (Wolanski et al., 1984). Twenty-six current meters were deployed in four transects in the wake of the island during flood tide and made clear the existence of a clockwise-rotating eddy extending across the wake. No measurements were made at falling tide but aerial photographs suggested the presence of two counter-rotating eddies. Aerial photographs also showed turbid water in the wake both at rising and falling tides, suggesting upwelling capable of carrying bed sediments upwards. While two-dimensional numerical models are able to faithfully represent depth-averaged features (e.g., Falconer et al., 1986; Black and Gay, 1987), only three-dimensional models can account for vertical motion. There have been only a few attempts in the past at analyzing vertical motion in shallow-water island wakes. Deleersnijder et al. (1992) utilized a 200-m horizontal resolution finite-difference model to compute the three-dimensional velocity field in the vicinity of Rattray Island. Although upwelling was predicted within the bulk of the eddies, its intensity was too low to account for vertical transport across the entire water column during the lifetime of the eddies. It was put forward that the model used a resolution that was too low to accurately represent velocity gradients (and hence divergence). Wolanski et al. (1996) used the same model as that by Deleersnijder et al. (1992) with an additional parameterization to account for the impact of the free shear layer extending downstream from the tips of the island. Later on, Alaee et al. (2004) also used a three-dimensional finite-difference model but they focused on upwelling at the tips of an idealized elliptic island. The main difference between the work by Alaee et al. (2004) and the previous one is that Alaee et al. (2004) worked with flow regimes for which no eddies were generated.

In this paper, we wish to continue along the path set out by Deleersnijder et al. (1992) with two crucial improvements. The first one is concerned with the numerical method, as we use a three-dimensional finite element model. The finite element method (FEM) allows for conveniently using unstructured meshes, whose resolution may vary and increase within regions of interest to attain higher accuracy. In addition, the ability of unstructured meshes to conform to complex coastlines is attractive. The FEM has been successfully utilized in the past for the modeling of coastal flows and oceanic processes (e.g., Walters, 1992; Lynch et al., 1996; Le Roux et al., 2000; Hanert et al., 2005b; Pietrzak et al., 2005; White et al., 2006) and its popularity within the ocean modeling community is likely to grow in the future. With the FEM, we will be able to increase the mesh resolution around the island and in the wake, and analyze the sensitivity of upwelling intensity on resolution. The second improvement is achieved by using a more sophisticated diagnosis of vertical transport. By looking at the upwelling velocity, Deleersnijder et al. (1992) considered vertical transport due to advection only. However, because vertical transport is a combination of advective and diffusive effects, we need a diagnosis that is able to account for both. The concept of the age may be used for that purpose. It is presented in detail by Delhez et al. (1999), Deleersnijder et al. (2001) and Delhez and Deleersnijder (2002). It is a component of CART (Constituent-oriented Age and Residence time Theory, http://www.climate.be/CART). The age of a particle of seawater is defined as the time elapsed since the particle under consideration left the region in which the age is prescribed to be zero. In the theory of the age, all classical advection–diffusion operators are accounted for. By prescribing the age of all particles lying on the seabed to be zero, we may track the time needed for those particles to reach the sea surface. The main goal of this paper is to determine whether the eddies are partly or fully responsible for the vertical transport of bed sediments. Thus, we would like to answer the following question: How much time is required for particles of a non-buoyant, passive tracer to travel from the seabed to the sea surface?

This paper is organized as follows. Section 2 describes the three-dimensional hydrodynamic model together with its implementation with the FEM. In Section 3, two different diagnoses of vertical transport using the age are laid out. Results are presented in Section 4 and we conclude with Section 5.

2. Model description

In this section, the underlying physical assumptions are outlined. The equations, the domain of interest and the boundary conditions are presented. The finite element method is briefly explained. Because of the limited extent of the region of

interest, the *f*-plane approximation is made. As pointed out by Wolanski et al. (1984), Rattray Island lies in well-mixed water with very little contrast of salinity and temperature. Therefore, a constant density is assumed throughout the domain. Finally, we work within the scope of the hydrostatic approximation. The currents around Rattray Island being dominated by tidal forcing, we neglect wind stress. All these assumptions were made by Deleersnijder et al. (1992) and we deliberately decide to work within the same framework to be able to assess whether or not coarse mesh resolution was responsible for underestimating the upwelling velocity.

Let $\boldsymbol{v}=(u,v,w)$ be the velocity, $\boldsymbol{u}=(u,v)$ be the horizontal components of $\boldsymbol{v}$ and η be the free-surface elevation with respect to the constant reference height $z=0$ taken to be the mean sea level. We will distinguish between the three-dimensional gradient operator $\boldsymbol{\nabla}$ and the horizontal gradient operator $\boldsymbol{\nabla}_{\mathrm{h}}$, affecting only the horizontal components of a vector. Under the aforementioned assumptions, the horizontal momentum equation is:

$$\frac{\partial \boldsymbol{u}}{\partial t}+(\boldsymbol{v}\cdot\boldsymbol{\nabla})\boldsymbol{u}+f\widehat{e}_z\wedge\boldsymbol{u}=-g\boldsymbol{\nabla}_{\mathrm{h}}\eta+\frac{\partial}{\partial z}\left(\nu_z\frac{\partial \boldsymbol{u}}{\partial z}\right)+\boldsymbol{D}, \tag{1}$$

where f is the constant Coriolis parameter taken at a latitude of -20°, $\widehat{e}_z$ is the upward-pointing unit vector, g is the gravitational acceleration and ν_z is the vertical eddy viscosity coefficient. Horizontal momentum diffusion is parameterized by $\boldsymbol{D}$. Eq. (1) is complemented with the usual continuity and free-surface equations, which are not reproduced here. As was done by Deleersnijder et al. (1992) and directly inspired by Fischer et al. (1979), a simple turbulence closure is considered for which the vertical eddy viscosity ν_z is given by:

$$\nu_z=\kappa u^*(h+z)\left(1-\delta\frac{h+z}{H}\right), \tag{2}$$

where κ is the von Karman constant, u^* is the bottom friction velocity (the square root of the norm of the bottom stress divided by the water density) and δ is an adjustable parameter, taken to be 0.6 in all numerical experiments. The horizontal eddy viscosity term $\boldsymbol{D}$ is:

$$\boldsymbol{D}=\frac{\partial}{\partial x}\left(\nu_{\mathrm{h}}\frac{\partial \boldsymbol{u}}{\partial x}\right)+\frac{\partial}{\partial y}\left(\nu_{\mathrm{h}}\frac{\partial \boldsymbol{u}}{\partial y}\right),$$

where ν_{h} is computed via a Smagorinsky scheme (Smagorinsky, 1963):

$$\nu_{\mathrm{h}}=c_{\mathrm{s}}\Delta^2\left[\frac{\partial\overline{u}}{\partial x}\frac{\partial\overline{u}}{\partial x}+0.5\left(\frac{\partial\overline{u}}{\partial y}+\frac{\partial\overline{v}}{\partial x}\right)^2+\frac{\partial\overline{v}}{\partial y}\frac{\partial\overline{v}}{\partial y}\right]^{1/2}, \tag{3}$$

in which c_{s} is a constant and Δ is a measure of the local mesh size. For triangular meshes, Δ^2 is taken to be the surface area of the local triangle (Akin et al., 2003). In expression (3), the overbar denotes depth-averaged quantities, as suggested by Lynch et al. (1996).

Because the tidal ellipses are strongly polarized (Wolanski et al., 1984), we take the *y*-axis of the domain to be parallel to the major axis of the tidal ellipses, namely oriented from southeast to northwest as depicted in Fig. 1. In so doing, we may assume the side boundaries to be impermeable to the flow so that only the southeast and northwest boundaries — hereafter referred to as lower and upper boundaries, respectively — remain open. Using available field measurements, the depth-averaged normal velocity and the elevation are imposed at both the lower and upper boundaries by prescribing the incoming characteristic variable $\overline{u}_{\mathrm{n}}-\eta\sqrt{g/h}$, where $\overline{u}_{\mathrm{n}}$ is the depth-averaged normal velocity. The phase lag between both boundaries is less than 20 min and is neglected in the model. At the bottom, a slip condition is imposed on the horizontal velocity and the bottom stress $\boldsymbol{\tau}$ is parameterized by the following logarithmic law:

$$\begin{aligned}\boldsymbol{\tau}(x,y,\xi_{\mathrm{b}})&=\left[\nu_z\frac{\partial \boldsymbol{u}}{\partial z}\right]_{z=-\mathrm{h}}\\&=\left[\frac{\kappa}{\ln(\xi_{\mathrm{b}}/\xi_0)}\right]^2\|\boldsymbol{u}_{\mathrm{b}}(x,y,\xi_{\mathrm{b}})\|\boldsymbol{u}_{\mathrm{b}}(x,y,\xi_{\mathrm{b}}),\end{aligned} \tag{4}$$

in which ξ_{b} is the distance to the seabed where the appropriate bottom velocity $\boldsymbol{u}_{\mathrm{b}}$ is defined and $\xi_0=5\times10^{-3}$ m is the roughness length (Black and Gay, 1987).

The three-dimensional finite element model SLIM (Second-generation Louvain-la-Neuve Ice-ocean Model, http://www.climate.be/SLIM) is used. The detailed implementation is described by White et al. (in preparation). The model is essentially built upon the work by Hanert et al. (2005a) and Hanert et al. (2005b) for its two-dimensional structure. The three-dimensional space discretization is based upon downward extrusion of two-dimensional triangular meshes and column splitting into prisms. The location of horizontal and vertical velocity nodes is shown in Fig. 1. All nodes are free to move in the vertical. This allows for tracking the free surface and for dynamical mesh redistribution and refinement in the vertical following a scheme based e.g., on a posteriori error estimates, as proposed by Hanert et al. (2006). The latter, however, is not yet implemented. The solution technique is sequential. We first solve the equations for the depth-averaged velocity and the elevation. All linear terms are semi-implicit in time, which permits to circumvent the stability constraint due to the propagation of inertia-gravity waves. The mesh geometry is updated with the new elevation field. We then solve for the full three-dimensional horizontal velocity by alternating at each time step between u and v so that the Coriolis force does not produce nor dissipate energy. The vertical velocity is computed after correction of the full horizontal velocity by the depth-averaged velocity. The same time step is used for both modes.

Because the last velocity node lies on the seabed, the bottom stress (4) is computed by using the mean value of the last two velocity nodes. The distance to the seabed ξ_{b} is calculated accordingly. The constant c_{s} used in the parameterization of the horizontal momentum diffusion coefficient, Eq. (3), typically lies in the range 0.1–0.3. It is slightly larger than the value recommended by Smagorinsky (1963) but on the same

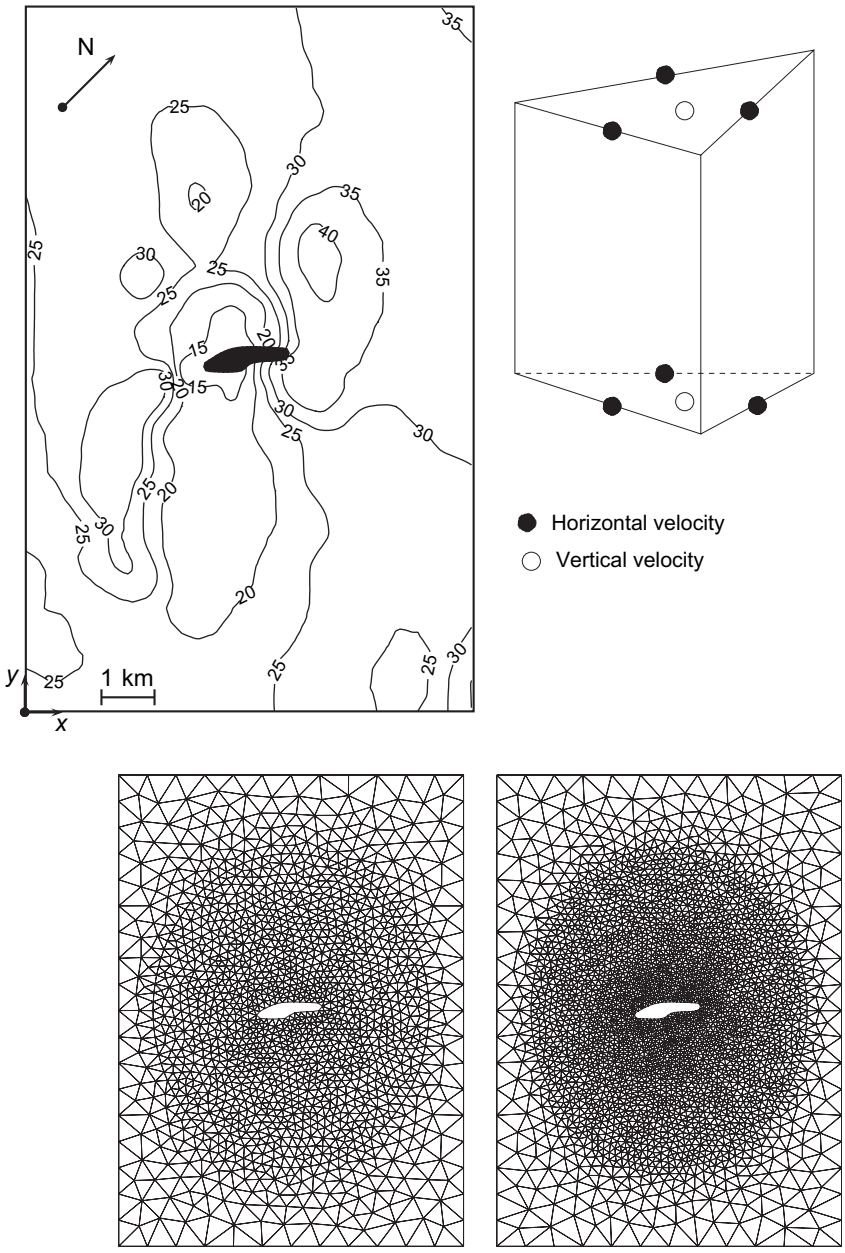

Fig. 1. Top left: domain of interest with bathymetry in meters (Rattray Island is the black area at the center). Top right: basic prismatic element used to interpolate both components of the horizontal velocity (non-conforming linear in the horizontal and linear in the vertical) and the vertical velocity (constant in the horizontal and linear in the vertical). Bottom: unstructured meshes used to simulate the flow around Rattray Island. The mesh on the left contains 3024 triangles and has a resolution of 140 m around the island. The mesh on the right contains 6096 triangles and has a resolution of 85 m in the vicinity of the island. This is to be compared with the 200-m resolution used by Deleersnijder et al. (1992) and Wolanski et al. (2003). Note that uniform refinement over the whole domain would quadruple the number of triangles. Local refinement avoids this drawback.

order as that used in usual finite element models such as that of Lynch et al. (1996). In our model, this choice leads to peak values in the horizontal eddy viscosity ν_h of less than 1 m^2/s when the flow is the swiftest in the wake of the island. This is in agreement with a value of 0.5 m^2/s estimated by Wolanski et al. (1984) in the field. The value of ν_h attains 2–3 m^2/s off the island's tips due to flow curvature and acceleration. However, this effect is strongly localized. To enhance robustness, advection terms are computed with an upwind-biased scheme, following the method by Hanert et al. (2005a). Although the scheme is somewhat numerically dissipative, the amount of dissipation only damps out unresolved (or poorly resolved) scales with little effect on the main solution. Examples of unstructured meshes used for numerical experiments are shown in Fig. 1.

3. Diagnoses of vertical transport

As model resolution increases over time, so does the amount of output data and the difficulty of having a relevant

and unbiased view of the results. A few cuts through a three-dimensional domain at some selected timesteps to display one variable gives quite a poor rendition of an otherwise N-dimensional problem. In this paper, we focus on vertical transport and three relevant diagnoses are presented.

3.1. The upwelling velocity

Deleersnijder et al. (1992) looked at the advective vertical transport by resorting to the upwelling velocity (Deleersnijder, 1989, 1994). The latter is devoid of topographic effects and is entirely due to intrinsic upwelling mechanisms. Placing ourselves in a sigma-coordinate system (terrain-following coordinates), the upwelling velocity is that component of the vertical velocity that causes a relative change in the vertical position within the water column. This should be differentiated from the topography-induced component that is only nonzero because of the nonflat bathymetry and free surface. The value of the upwelling velocities modeled by Deleersnijder et al. (1992) peaked at 10^{-3} m/s at mid-depth within the eddies, which is more than twice smaller than the value needed for a water particle having this velocity to travel across the entire water column during the life span of the eddies. This argument rests on the assumption that the intensity of the eddies is strong enough during about 2–3 h. The reason put forward for the underestimation was the grid coarseness.

3.2. The age

Despite its simplicity – this is a postprocessing step and no computation is involved – the main drawback of the upwelling velocity is that it does not account for all processes responsible for vertical transport and it gives an instantaneous snapshot of the dynamics. The theory of the age is a holistic approach (Delhez et al., 1999; Deleersnijder et al., 2001; Delhez and Deleersnijder, 2002). That is, the age is a diagnosis that accounts for advective and diffusive transport and depends on all model results. The question that we want to answer is: How much time is required for particles of a non-buoyant, passive tracer to travel from the seabed to the sea surface? The theory presented by Deleersnijder et al. (2001) allows for computing the mean age of particles since they left the region where the age is set to zero. It is not uncommon to regard water masses as passive tracers (Cox, 1989; Hirst, 1999; Goosse et al., 2001). In that respect, the concentration of the passive tracer is interpreted as the concentration of the water mass under consideration. In our situation, we trace the bottom water, that is the water that has touched the seabed.

We shall define two types of age. The first age is defined as the arithmetic average of the times that have elapsed since the particles left the seabed for the last time. The age of a water particle keeps increasing as long as it does not touch the seabed again. Once a water particle touches the seabed, its age is reset to zero. The second age is defined to be the time needed to travel from the seabed to the sea surface. Similarly to the first type of age, the age of a water particle is reset to zero when it touches the seabed. However, once the water particle touches the sea surface, it is disregarded until it touches the seabed again. This key difference between both types of age is illustrated in Fig. 2. From now on, all variables associated with the type of age i will have a subscript i. The ages will be referred to as age 1 and age 2.

To compute the age, we have to solve advection–diffusion equations for the bottom water concentration C_i and the age concentration α_i. Once those two variables are known, the age a_i is given as the ratio of the age concentration to the water concentration:

$$a_i = \frac{\alpha_i}{C_i} \quad (i = 1, 2). \tag{5}$$

The water concentration C_i is solution to (Delhez et al., 1999):

$$\frac{\partial C_i}{\partial t} + \nabla \cdot (\boldsymbol{v} C_i) = \frac{\partial}{\partial z}\left(K_z \frac{\partial C_i}{\partial z}\right) + D \quad (i = 1, 2), \tag{6}$$

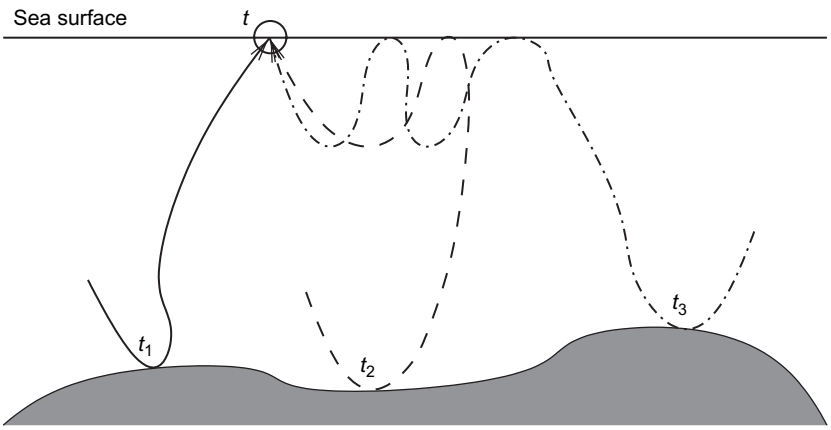

Fig. 2. A water sample containing three water particles is taken at the sea surface at time t. Each particle has a different history, as illustrated by their trajectories. For the first type of age, the age keeps increasing as long as the particle does not touch the seabed again. Therefore, the first age is $a_1 = [(t - t_1) + (t - t_2) + (t - t_3)]/3$. For the second age, the particle is disregarded when it touches the sea surface. Therefore, only the first particle need be accounted for: $a_2 = (t - t_1)$.

where K_z is the vertical eddy diffusivity coefficient and D parameterizes turbulent horizontal diffusivity with a Smagorinsky scheme similar to Eq. (3) The age concentration α_i obeys the following equation (Delhez et al., 1999):

$$\frac{\partial \alpha_i}{\partial t} + \nabla \cdot (\boldsymbol{v}\alpha_i) = C_i + \frac{\partial}{\partial z}\left(K_z \frac{\partial \alpha_i}{\partial z}\right) + D \quad (i = 1, 2), \tag{7}$$

where the water concentration C_i is the so-called aging term. Note that the water concentration varies between 0 and 1. Boundary conditions are yet to be prescribed to close the system. Because the vertical eddy diffusivity at the bottom is zero, it is convenient to introduce a bottom roughness length ξ_b. This is similar to the roughness length introduced for the computation of the bottom stress, see Eq. (4). We may similarly define a surface roughness length ξ_s. The bottom and surface boundary conditions will be enforced at $z_b = -h + \xi_b$ and $z_s = \eta - \xi_s$. At sea bottom, the water concentration is 1 and the age concentration is 0 for both ages:

$$[C_i]_{z=z_b} = 1 \text{ and } [\alpha_i]_{z=z_b} = 0 \quad (i = 1, 2), \tag{8}$$

which translates the fact that we want to track water particles that leave the seabed with the age reset to 0. At the sea surface, we have to distinguish between age 1 and age 2. Since the free surface is impermeable to the first age, we have:

$$\left[K_z \frac{\partial C_1}{\partial z}\right]_{z=z_s} = 0 \text{ and } \left[K_z \frac{\partial \alpha_1}{\partial z}\right]_{z=z_s} = 0, \tag{9}$$

which means that age 1 keeps increasing even when water particles touch the free surface. For the second age, we have to implement the fact that once a particle touches the surface, it is disregarded. In other terms, the water concentration is zero at the surface:

$$[C_2]_{z=z_s} = 0. \tag{10}$$

Finally, in order to avoid infinite values of age 2 at the surface, Eq. (5) requires to have:

$$[\alpha_2]_{z=z_s} = 0. \tag{11}$$

The conditions applied on lateral boundaries depend on whether they are closed or open. Along closed boundaries, a no-flux condition is enforced on the water and age concentrations. At outflow open boundaries, both the water and age concentrations are advected out of the domain. At inflow open boundaries, incoming water and age concentrations must be prescribed to compute the advective flux. The incoming water (age) concentration is taken to be the mean outgoing water (age) concentration. In other terms, the incoming age is prescribed to be the mean outgoing age, leading to periodic boundary conditions on the age in the mean sense. This is based on the hypothesis that horizontal age contrasts appear close to the island and that homogeneity prevails far away from it.

At this point, two remarks can be formulated:

(1) we will take the vertical eddy diffusivity coefficient K_z to be equal to the vertical eddy viscosity coefficient ν_z. In other words, the Prandtl number – which is the ratio of viscosity to diffusivity – is assumed to be equal to one. This hypothesis is generally accepted for unstratified fluids and it therefore applies to Rattray Island (Munk and Anderson, 1948);
(2) the computation of age 2 at the surface implies to evaluate an indeterminate limit of type 0/0. We have to make sure that the limit exists.

3.3. A one-dimensional water-column model

A simplified one-dimensional water-column model is very useful to gain additional insight into both types of age. It will also give indications as to the difficulties lying ahead of us in the numerical resolution, and in particular those pertaining to the boundary conditions. Steady state and horizontal uniformity are assumed for all variables. Since the horizontal components of the velocity field are deemed horizontally homogeneous, the vertical component must be constant everywhere in the water column to satisfy the continuity equation. Because of the impermeability of the seabed, the vertical component of the velocity must therefore vanish throughout the water column. Only vertical diffusivity remains. To simplify calculations, we assume that the domain extends from $z = 0$ to $z = H$. The origin of the z-axis coincides with the seabed and no longer with the mean sea level. The vertical eddy diffusivity is given by:

$$K_z = \kappa u^* z\left(1 - \delta \frac{z}{H}\right). \tag{12}$$

It follows that the bottom and surface boundary conditions are enforced at $z_b = \xi_b$ and $z_s = H - \xi_s$. The differential problem (6)–(11) simplifies to:

$$\frac{\mathrm{d}}{\mathrm{d}z}\left(K_z \frac{\mathrm{d}C_i}{\mathrm{d}z}\right) = 0 \text{ and } \frac{\mathrm{d}}{\mathrm{d}z}\left(K_z \frac{\mathrm{d}\alpha_i}{\mathrm{d}z}\right) + C_i = 0 \quad (i = 1, 2), \tag{13}$$

subject to the boundary conditions:

$$C_1(z_b) = 1, \left[K_z \frac{\partial C_1}{\partial z}\right]_{z=z_s} = 0, \quad \alpha_1(z_b) = 0, \left[K_z \frac{\partial \alpha_1}{\partial z}\right]_{z=z_s} = 0,$$
$$C_2(z_b) = 1, C_2(z_s) = 0, \quad \alpha_2(z_b) = 0, \alpha_2(z_s) = 0. \tag{14}$$

The problem (13) and (14) can be nondimensionalized. Dimensionless variables – denoted by primes – are defined by:

$$(z', z'_b, z'_s, \xi'_b, \xi'_s) = (z, z_b, z_s, \xi_b, \xi_s)/H, \; K'_z = K_z/\overline{K}_z,$$
$$C'_i = C_i, \; \alpha'_i = \alpha_i \overline{K}_z / H^2,$$

where $z'_s = 1 - \xi'_s$ and $\overline{K}_z$ is the depth-average of K_z defined by Eq. (12). The dimensionless diffusivity coefficient is:

$$K'_z = \frac{6}{3 - 2\delta} z'(1 - \delta z'). \tag{15}$$

Henceforth, only dimensionless variables will be used and we may omit the primes. All notations remain the same and the problem to solve is still referenced by Eqs. (13) and (14). The analytical solution to Eqs. (13) and (14) – whose development is given in the Appendix – is shown in Fig. 3. These exact solutions feature three important aspects:

(1) age 1 is about seven times larger than age 2 at the surface. This suggests that age 2 will not be influenced by the lateral boundaries as much as age 1 in the vicinity of the island. Assuming a depth-average eddy diffusivity of 0.05 m^2/s and a typical depth of 20 m around the island, age 1 is on the order of 5 h while age 2 is on the order of 45 min. Since tidal flow is reversing approximately every 6 h, age 1 has barely the time to fully develop during a half tidal cycle while this is not a concern for age 2. We have to keep that in mind when designing open boundary conditions on the age;
(2) both ages feature a logarithmic bottom layer whose length scale is on the order of the bottom roughness length. Unless we choose vertical increments to resolve the bottom layers – which is infeasible in practice – something will have to be done to account for them;
(3) the definition of age 2 at the surface gave rise to an indeterminate limit of type 0/0. This limit exists, as is shown in the Appendix.

3.4. Numerical resolution of the water-column model

The presence of a logarithmic bottom layer in the age profile makes it more challenging to solve numerically. We propose here to compare three finite element discretizations in the vertical for the resolution of the age concentration. We will focus on age 1. In this paper, we do not aim at giving a detailed overview of the finite element method. Therefore, each discretization method will be covered conceptually without delving into technical details.

The first discretization is based on approximating the exact solution by a piecewise linear field. That is, the water column is divided into N elements with $N+1$ nodes, the bottommost lying at $z=z_b$ and the topmost coinciding with the free surface at $z=z_s$. The field is interpolated with linear polynomials between nodes. The second discretization is based upon the extended finite element method (Moes et al., 1999). The latter consists in enriching a few bottom nodes with a global logarithmic function $\ln(z/z_b)$. In so doing, we actually increase the number of degrees of freedom. Within the bottom elements adjacent to the selected enriched nodes, we add an enriched field to the piecewise linear field. The enriched field is made up of a piecewise linear field modulated by the global logarithmic function. The third discretization consists in substituting the linear shape functions for logarithmic shape functions within the bottommost element (Hanert, personal communication). Instead of approximating the exact field by a linear polynomial, we approximate it with a linear combination of logarithmic functions.

A comparison between all three discretizations is shown in Fig. 4. Clearly, the first discretization – the usual piecewise linear interpolation – fails at decently representing the exact solution. The second discretization – enriching a few bottom nodes – yields a very accurate approximation. Unfortunately, the tridiagonal structure of the linear system is lost and a very high-order quadrature rule is required to achieve this level of accuracy (typically more than 20 Gauss points). This proved to be too expensive in three dimensions even though more Gauss points could be used near the bottom by dividing out the bottommost element into non-uniform subelements in which a low-order quadrature rule could be used. With the third discretization, an accurate solution is obtained while the tridiagonal structure of the matrix is preserved and a low-order (5 Gauss points) quadrature rule suffices. This is the employed method to compute the solutions to all age-related advection–diffusion equations.

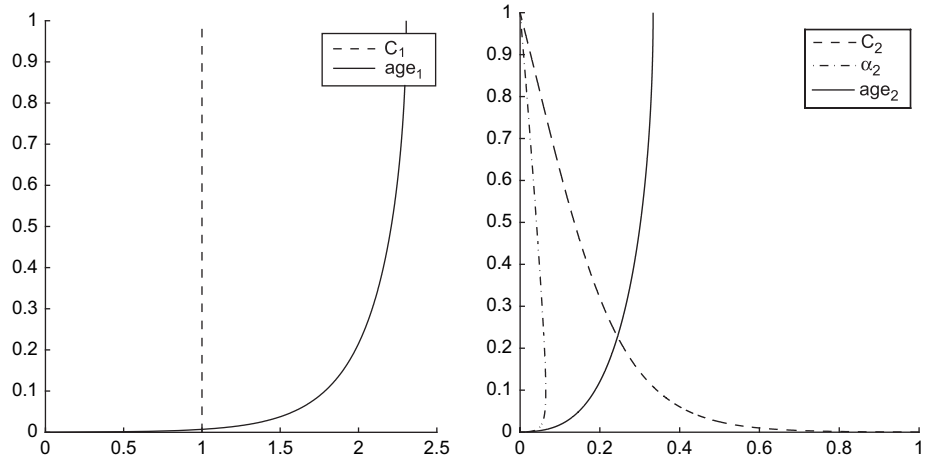

Fig. 3. Exact solutions to nondimensionalized problem Eqs. (13) and (14) with $\delta=0.6$, $H=20$ m and $\xi_b=\xi_s=5\times10^{-3}$ m. At the surface ($z=z_s$), age 1 is about seven times larger than age 2. For age 1, since the water concentration is 1 across the entire domain, the age concentration is equal to the age. Notice also the logarithmic bottom layers and the finite value of age 2 at the surface (the limit was indeterminate).

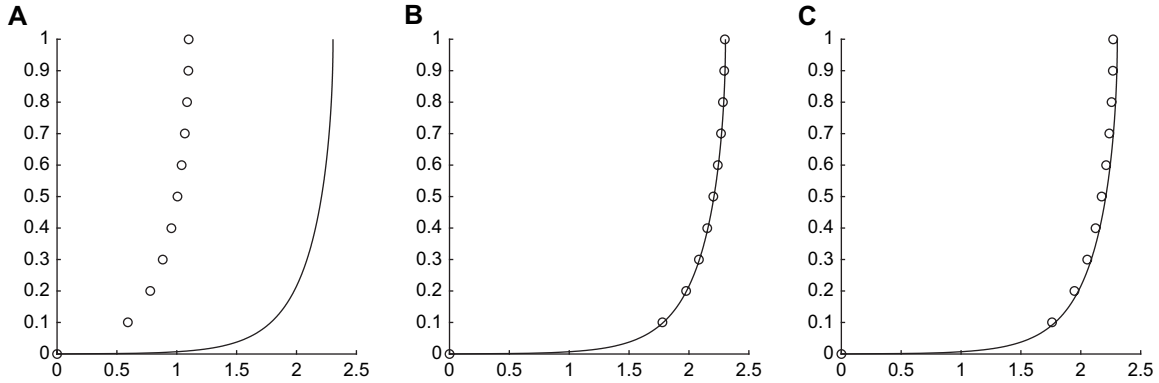

Fig. 4. Numerical resolution of the water-column model for age 1 with 10 elements. In all panels, the solid line is the exact solution while the numerical approximation is represented by the circles. (A) Piecewise linear approximation. (B) Piecewise linear approximation with enrichment of the two bottom nodes with a global logarithmic function. (C) Discretization for which the linear shape functions are substituted for logarithmic shape functions within the bottommost element. In all other elements, linear shape functions are used. The third discretization yields the best quality-price ratio.

4. Results and discussion

A 5-day run was carried out on each mesh displayed in Fig. 1. In the vertical, 10 and 16 layers were used for the coarse and the fine mesh, respectively. The Smagorinsky constant c_s is 0.1 for the coarse mesh and 0.3 for the fine mesh. These values were chosen to remain as close as possible to the estimate of the horizontal eddy viscosity coefficient by Wolanski et al. (1984). However, the total amount of dissipation (physical and numerical) is larger for the coarse mesh. This is due to the artificial dissipation introduced by the upwind-biased advection scheme. This artificial dissipation is dependent on the mesh size. Although not required, the same time step of 15 s was used for both meshes so that the sole effect of spatial discretization was taken into account. To ensure that a regime solution is attained, the results are presented after 3 days. We first show the results on the upwelling velocity and then proceed with the age. In the subsequent discussion, the northern (southern) island's tip will be referred to as the right (left) tip.

4.1. The upwelling velocity

The upwelling velocity on each mesh is shown at two different times during falling tide in Fig. 5. Note that the upwelling velocity is taken at mid-depth, as was done by Deleersnijder et al. (1992). Panels B–C in Fig. 5 show the upwelling velocity during falling tide when the free-stream speed is maximum at about 0.5 m/s. Though the distribution of upwelling and downwelling zones is quite similar for both meshes, two important differences are observed. First, for the coarse mesh (panel B), the upwelling velocity field is quite noisy, contrary to that obtained with the fine mesh. Second, for the latter (panel C), a small-scale intense upwelling zone (4 mm/s) is resolved off the right tip of the island (see the white patch). This upwelling zone remains unresolved with the coarse mesh. Snapshots E–F are taken at the end of falling tide, shortly before tide reversal. The free-stream speed is about 0.1 m/s. The results for both meshes are very similar because only larger-scale features persist. Aside from these detailed differences and similarities, a few general remarks may be formulated regarding the upwelling velocity:

(1) in all snapshots, the upwelling velocity within the eddies is about 1 mm/s. This is particularly clear on the right panels in Fig. 5E–F, where the eddies are well formed and still intense shortly before tide reversal. Because those eddies typically start to develop when the tidal velocity is maximum and die off after tide reversal, their life span is roughly 3 h. Therefore, a distance of 10 m could at best be traveled by water particles motioned by the upwelling velocity and leaving the seabed at the onset of the eddy formation. Since the depth around the island is about 20 m, the predicted upwelling is not sufficiently intense to carry bottom water up to the sea surface during the eddies lifetime.
(2) the mesh resolution does not significantly modify the upwelling intensity within the eddies. The orders of magnitude obtained in this study are in line with those predicted by Deleersnijder et al. (1992).
(3) some smaller-scale features, such as the intense upwelling zone off the right island's tip shown in Fig. 5C, are not resolved by the coarse mesh. Note that increasing the mesh resolution up to 65 m confirms the presence of those small-scale features (not shown). Upwelling is also predicted off the left tip of the island for the fine mesh. Deleersnijder et al. (1992) also reported upwelling off the right island's tip but the intensity was much smaller (about 1 mm/s) than our predictions.

4.2. The age

The surface age for age 1 and age 2 obtained with the fine mesh is shown in Fig. 6 at two different times during rising tide and in Fig. 7 at two different times during falling tide. Experiments on extended meshes (in the free-stream direction) have been made to assess the sensitivity of the predicted age on the distance at which boundary conditions are imposed. In all cases, the predicted age remains within a few percent of that computed with the original mesh (not shown). Hence, the

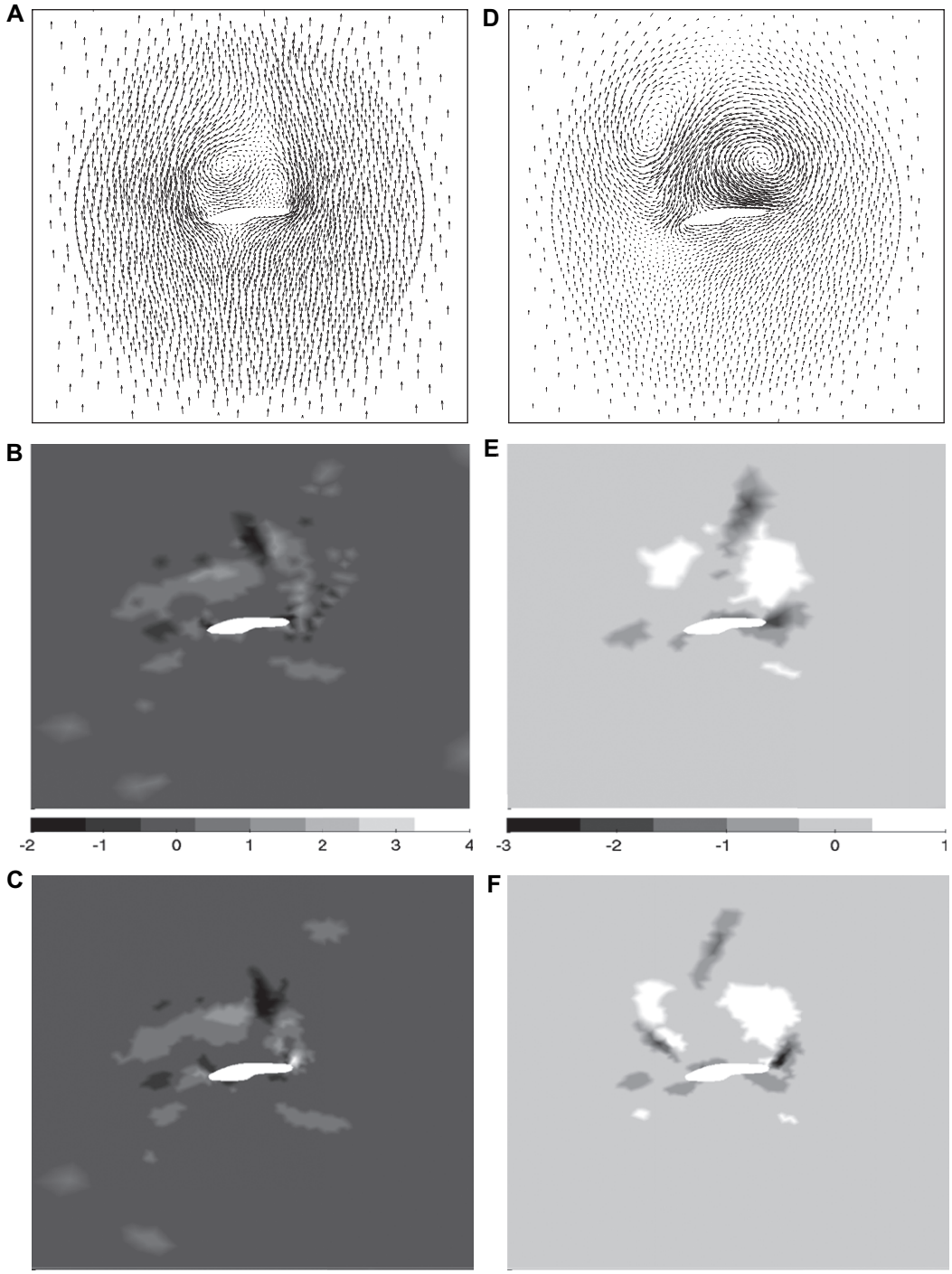

Fig. 5. Upwelling velocity at mid-depth (mm/s) during falling tide. Each column shows (from top to bottom): the depth-averaged velocity field on the fine mesh, the upwelling velocity for the coarse mesh and the upwelling velocity for the fine mesh. Snapshot times correspond to: (A–C) December 2 at 15h00 at peak ebb velocity. (D–F) December 2 at 18h20 at the end of falling tide, shortly before tide reversal.

boundaries are located far enough from the island. At the onset of the simulation, the water concentration is prescribed to be the solution of the water-column model presented in the previous section. The initial age concentration is zero. For age 1, the water concentration is never computed and remains equal to one throughout the domain and at all time. For age 2, both the water and age concentrations are computed.

Let us first concentrate on age 1, which is shown on panels B and E of each figure. See also Movie 1 (available online) showing age 1 at the surface during a full tidal cycle. A striking feature is visible in Figs. 6B and 7B, where bottom water (the darker elongated patches) emanates off the island's tips. This water is less than 1 h old at both tips. The fact that the age of the bottom water is roughly the same off both island's

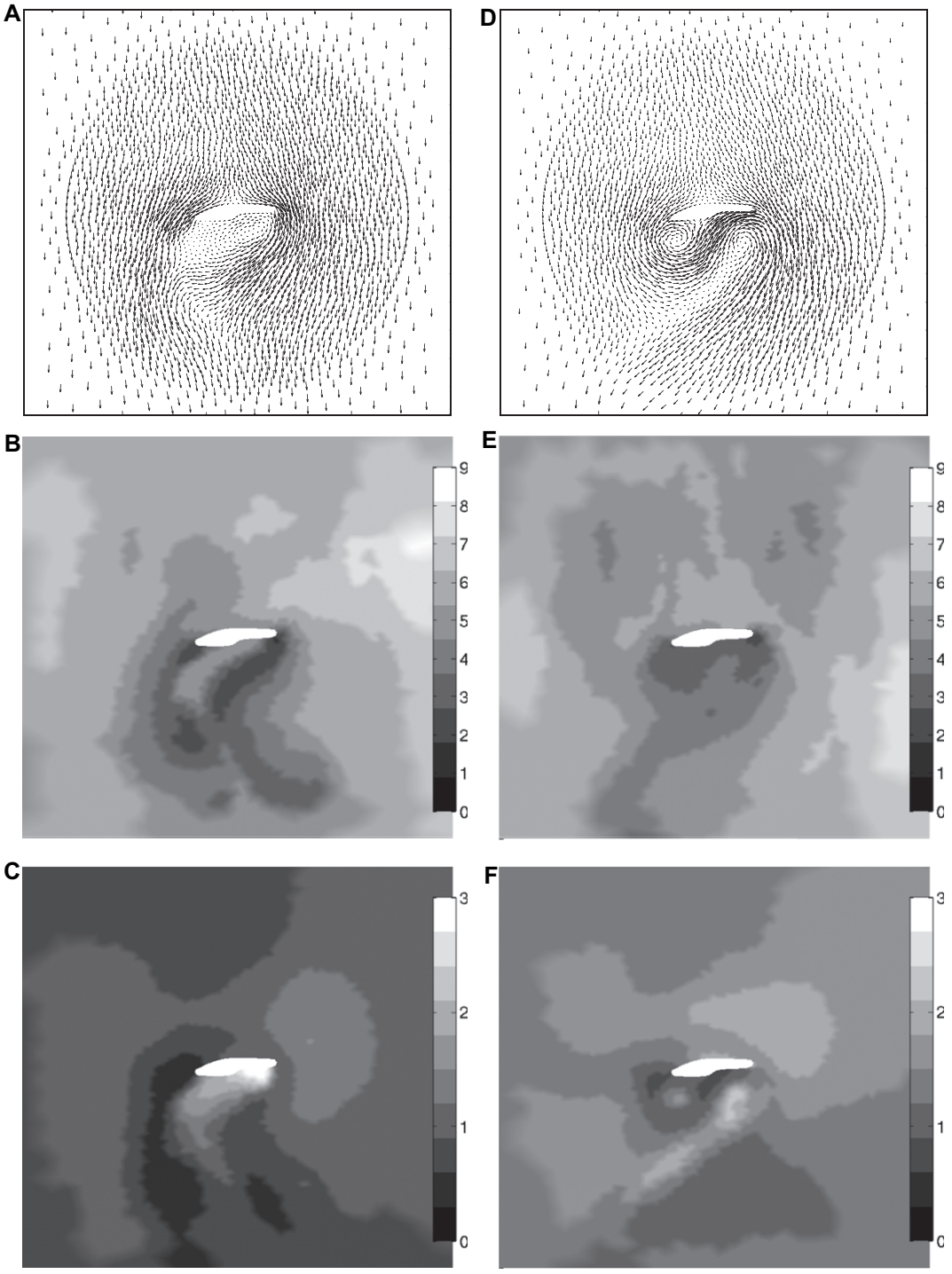

Fig. 6. Surface age in hours for the fine mesh during rising tide. Each column shows (from top to bottom): depth-averaged velocity field, surface age 1 and surface age 2. Snapshot times correspond to: A–C. December 1 at 8h00 at peak flood velocity. D–F. December 1 at 10h40 at the end of rising tide, shortly before tide reversal.

tips can be explained by the depth difference. Off the right tip, the depth is about 30 m while off the left tip, it is about 15 m. However, upwelling on the right is found to be at least twice as intense as that on the left, which could explain the resulting symmetry. When the tide keeps rising, some of the bottom water recirculates within the island's wake while the rest is advected downstream. At the end of rising tide, age 1 is about 2–3 h downstream of the island, as shown in Fig. 6E. Finally, at the end of falling tide, the age varies between 3 and 4 h with a few exceptions of younger water located near the centers of both eddies. The age of these patches is about 2 h. This is shown in Fig. 7E. Since the age of bottom water within the island's wake shortly before tide reversal is roughly 3 h, it could be hypothesized that this water mainly originates from the island's tips when the free-stream speed is large enough to initiate upwelling.

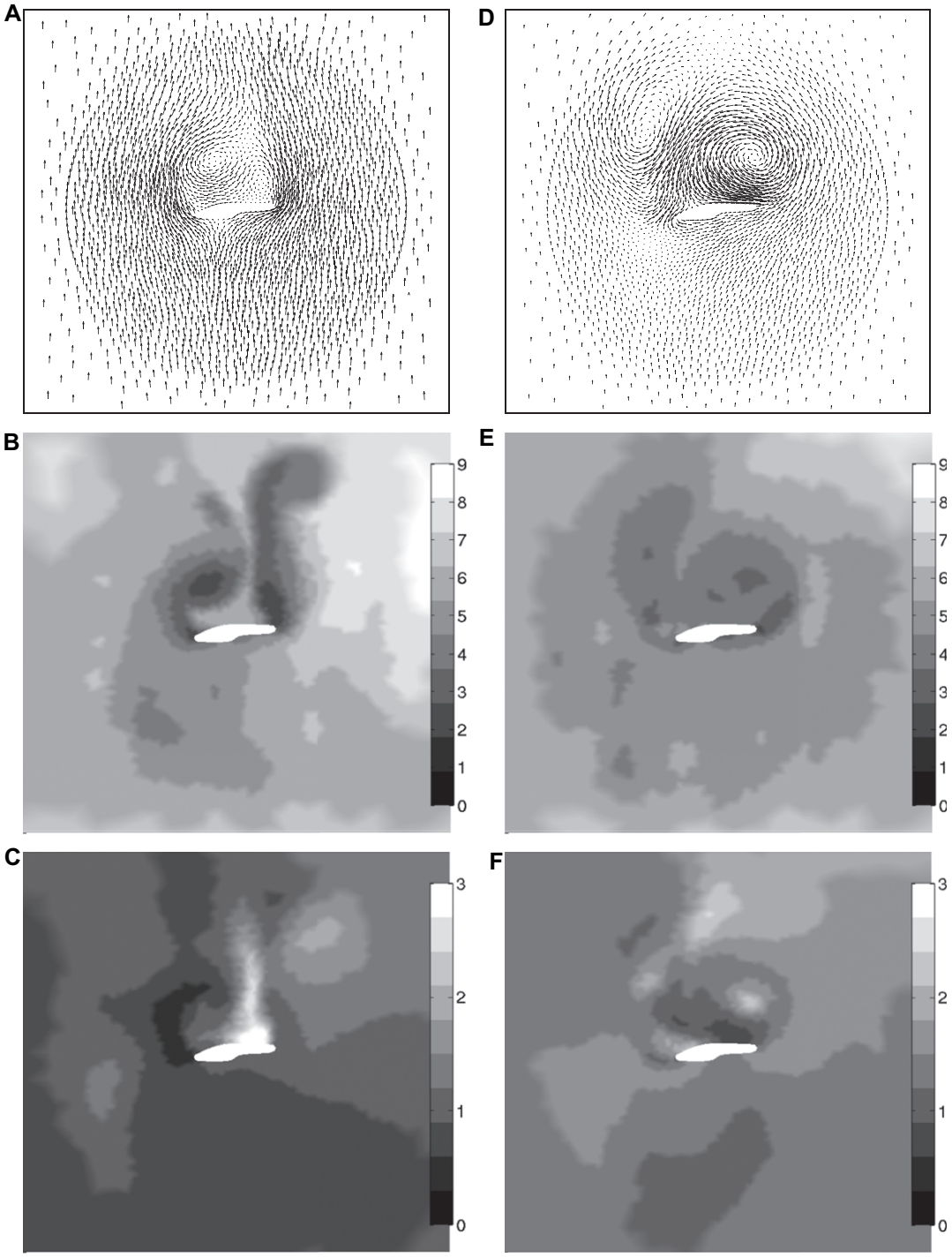

Fig. 7. Surface age in hours for the fine mesh during falling tide. Each column shows (from top to bottom): depth-averaged velocity field, surface age 1 and surface age 2. Snapshot times correspond to: A–C. December 2 at 15h00 at peak flood velocity. D–F. December 2 at 18h20 at the end of rising tide, very shortly before tide reversal.

The interpretation of age 2 at the surface is more delicate. Although not as definite as for age 1, we may also discern young patches originating from the island's tips in Figs. 6C and 7C. See also Movie 2 (available online) showing age 2 at the surface during a full tidal cycle. Along the downstream edge of the island, a patch of older water is visible (lighter patch). These patches coincide with regions of very low horizontal velocity, as can be seen on the right panels showing the depth-averaged velocity field. Because of less intense circulation, vertical diffusion decreases, which has a direct impact on the age. Finally, shortly before tide reversal, age 2 behaves rather counter-intuitively. The surface age pattern seems to be opposite to that for age 1 (see Figs. 6F and 7F). The largest values of the surface age is found around the centers of the eddies where the upwelling velocity is the largest. This is very clear for the left-hand side eddy in Fig. 6F and the

right-hand side eddy in Fig. 7F. This behavior motivates the following investigation regarding the effect of vertical advection on the age within eddies.

4.3. The effect of vertical advection

The water-column model previously presented included vertical diffusion only. Although incomplete, it allowed for grasping important features in the age such as the logarithmic bottom layer and the quantitative differences between both types of age. We now wish to go one step further by adding the effect of vertical advection. In this case, it is incorrect to assume horizontal homogeneity in the horizontal velocity, for otherwise the vertical velocity would be zero. Since we are primarily interested in the vertical transport within eddies, we will instead formulate the problem in cylindrical coordinates (r, θ, z). The eddy is rotating about the z-axis and is supposed to be axisymmetrical. The corresponding velocity components are (v_r, v_θ, w). The domain of interest is a thin cylinder extending from the bottom to the top and whose radius r_0 is such that $0 < r_0 < \epsilon$, with $\epsilon \ll 1$. In cylindrical coordinates, the advection term of the advection–diffusion equation for a scalar ϕ is:

$$\nabla \cdot (\boldsymbol{v}\phi) = v_r \frac{\partial \phi}{\partial r} + v_\theta \frac{1}{r}\frac{\partial \phi}{\partial \theta} + w\frac{\partial \phi}{\partial z}, \tag{16}$$

using the fact that $\nabla \cdot \boldsymbol{v} = 0$. Because the problem is axisymmetrical, we have $\partial\phi/\partial r = 0$ at $r = 0$. It can also be contended that $\partial\phi/\partial r$ is arbitrarily small as ϵ approaches 0. Therefore, the first term in the right-hand side of Eq. (16) is neglected everywhere in the water column, provided that v_r remains finite. For small values of r_0, the azimuthal component, v_θ, can be linearized to $v_\theta \simeq kr$ (for some constant k). Hence, the second term of the right-hand side of Eq. (16) reduces to $k\,\partial\phi/\partial\theta$, which vanishes because ϕ is independent of θ. Thus, only vertical advection remains, that is $\nabla \cdot (\boldsymbol{v}\phi) = w\,\partial\phi/\partial z$. Although less legitimate, we will also neglect the effects of horizontal diffusion. Note that, for the continuity equation to be satisfied, v_r must depend on z. This is so because the continuity equation reduces to $\nabla \cdot \boldsymbol{v} = v_r/r + \partial w/\partial z$ within the thin cylinder. With vertical advection, the differential problem (13) becomes:

$$w(z)\frac{dC_i}{dz} = \frac{d}{dz}\left(K_z \frac{dC_i}{dz}\right) \text{ and}$$
$$w(z)\frac{d\alpha_i}{dz} = \frac{d}{dz}\left(K_z \frac{d\alpha_i}{dz}\right) + C_i \quad (i = 1, 2), \tag{17}$$

subject to the same boundary conditions (14). The vertical velocity must vanish at $z = 0$ and $z = H$. We will assume a parabolic profile for which the maximum speed w_0 is reached at mid-depth:

$$w(z) = \frac{4w_0}{H^2} z(H - z). \tag{18}$$

This expression is inspired by the fact that the upwelling velocity typically vanishes at the bottom and the surface while it reaches its maximum somewhere near mid-depth. The nondimensional version of Eq. (18) is:

$$w'(z') = 4z'(1 - z'),$$

so that nondimensionalization of Eq. (17) gives rise to:

$$Pe\, w(z)\frac{dC_i}{dz} = \frac{d}{dz}\left(K_z \frac{dC_i}{dz}\right) \text{ and}$$
$$Pe\, w(z)\frac{d\alpha_i}{dz} = \frac{d}{dz}\left(K_z \frac{d\alpha_i}{dz}\right) + C_i, \quad (i = 1, 2), \tag{19}$$

where all variables are dimensionless and primes are again omitted. The Peclet number $Pe = w_0 H/\overline{K}_z$ measures the importance of advective transport relative to diffusive transport. The differential problem (19), subject to boundary conditions (14), is not amenable to analytical solutions when $Pe \neq 0$. Numerical solutions are therefore sought and for each value of $Pe \neq 0$, the surface age – that is, the age at $z = z_s$ – is compared with the surface age computed with $Pe = 0$. The objective is to investigate the relative effect that advection has on the surface age. The results are reported in Fig. 8 for age 2 only.

The behavior pertaining to the latter is counter-intuitive. When there is downward advection ($Pe < 0$), the surface age decreases. For a range of positive Peclet numbers ($0 < Pe < Pe^*$), the surface age increases while for $Pe > Pe^*$, the surface age decreases. To shed light on this behavior, let us take the situation in which we have a moderately intense upward advective transport (say $Pe = 1$). In this case, the water concentration C_2 reaches higher values within the water column due to advection. This, in turn, brings about an increase in the age concentration α_2 because the aging term in the equation for α_2 increases. There is, however, a counter-balancing effect due to the upward advection of smaller values of α_2 coming from the seabed. The net effect is an increase in α_2. When computing the ratio α_2/C_2, both the numerator and the denominator have increased but the former has done so by a larger factor, leading to an increase in the surface age. The same reasoning applies to the situation in which $Pe < 0$. Finally, for values of Pe larger than Pe^*, advective transport of low values of α_2 overcomes the aging process, caused by the fact that saturation takes place for C_2, which gets close to 1 and does not increase any more.

Within the eddies, the numerical model predicts upwelling at an intensity of 0.001 m/s and an average vertical eddy diffusivity coefficient of about 0.02 m^2/s. Taking a depth of 20 m leads to a Peclet number of 1 while the critical Peclet number for this situation is around 6.5. We thus fall in the range for which positive vertical advection contributes to increase the surface age at the center of the eddies.

Finally, it should be stressed that the threshold Peclet number Pe^* depends itself on the dimensionless number ξ_b/H, namely the ratio of the bottom roughness length to the water-column height. This dependence is shown for age 2 in Fig. 8 for three different values of ξ_b/H, where it can be seen that the threshold Peclet number Pe^* increases as ξ_b/H decreases. The chosen values

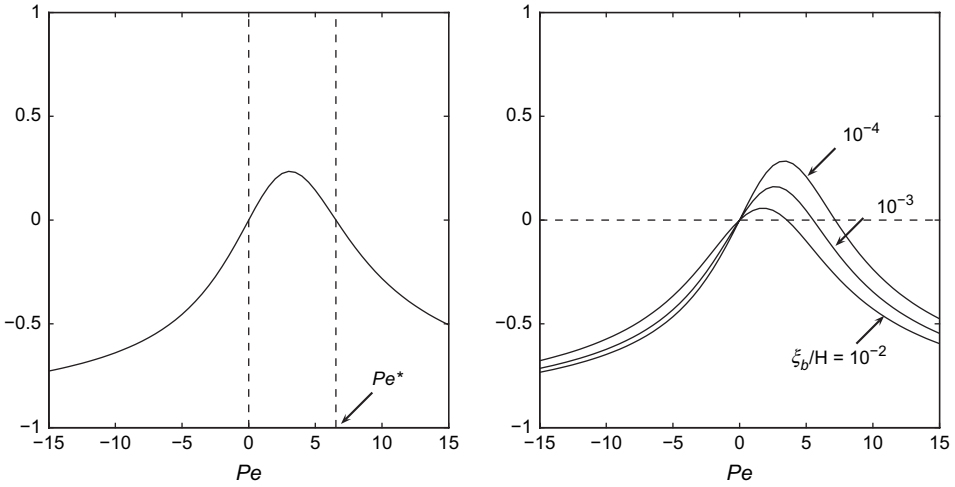

Fig. 8. Left: relative deviation of surface age 2 from the reference surface age (obtained for $Pe = 0$) as a function of the Peclet number for $\xi_b = \xi_s = 5 \times 10^{-3}$ m, $H = 20$ m and $\delta = 0.6$. Negative (positive) Peclet numbers indicate downward (upward) advection. Age 2 features a counter-intuitive behavior by showing a decrease when $Pe < 0$ and an increase when $0 < Pe < Pe^*$, where Pe^* is a threshold Peclet number. For $Pe > Pe^*$, a decrease in the surface age 2 is observed. Right: relative deviation of surface age 2 from the reference surface age (obtained for $Pe = 0$), for three different values of ξ_b/H. As ξ_b/H decreases, the critical Peclet number $Pe^* > 0$ at which the surface age starts decreasing reaches higher values.

of ξ_b/H have a negligible impact on the deviations of the surface age 1, which are not shown here.

5. Conclusions

The use of unstructured meshes together with the finite element method proves to be effective at representing the three-dimensional tidal flow past an island. In particular, higher mesh resolution in the vicinity of the island allows for capturing smaller-scale processes, such as intense upwelling off the island's tips, which cannot be resolved with coarse meshes.

The theory of the age was used to design two sophisticated diagnoses of vertical transport. Age 1 was defined as the time elapsed since water particles left the seabed while age 2 was defined as the time required for water particles to travel from the seabed to the sea surface. A simple water-column model was employed to compare both ages and to investigate the boundary conditions. The logarithmic boundary layer, present for both ages, was successfully resolved numerically with a modified finite element method.

The pattern of age 1 at the surface confirms the presence of intense upwelling off the island's tips. Most importantly, the value of age 1 at the surface, downstream of the island and shortly before tide reversal, suggests that the water at the surface originate from the tips of the island and recirculate within the wake. The role of the age in explaining this circulation pattern is crucial as the latter could not readily be proposed by a simple look at the upwelling velocity. Furthermore, this flow description is somewhat in contradiction with the sketch proposed by Wolanski and Hamner (1988), in which upwelling only takes place within the eddies. The results presented in this work motivate further research toward a better understanding of the three-dimensional flow circulation around shallow-water islands.

The pattern pertaining to age 2 also exhibits upwelling off the island's tips. However, within the eddies where upwelling velocity is the largest, the surface age increases. This counter-intuitive behavior was validated by a simplified water-column model including both advection and diffusion. Nevertheless, at this stage, the effect of advection upon age 2 remains physically not well understood. Drawing conclusions based on age 2 is not straightfoward and, undoubtedly, requires additional effort.

The age-based diagnoses considered in this work rely upon tracking water masses. In so doing, we do not take into account the weight and buoyancy of the sediments. The next version of the model should also include a higher-order turbulence closure such as Mellor–Yamada level 2.5 and an adequate parameterization of the free shear layer. Another improvement would consist in relaxing the slip condition on the horizontal velocity at the bottom. As was done to compute the age, we could impose the horizontal velocity to vanish at the bottom and use logarithmic shape functions within the bottommost element.

Finally, as we tend to use higher-resolution meshes, we could resolve smaller-scale processes for which the hydrostatic approximation might be invalidated. In particular, with a local mesh size of roughly 5 m, the free shear layer could be resolved with a non-hydrostatic model. Therefore, a more faithful rendition of the physical processes around shallow-water islands could be achieved by using a non-hydrostatic model. Nevertheless, the size of the eddies and the fact that they are well represented by two-dimensional models indicate that for those, the hydrostatic approximation remains valid.

Acknowledgements

Laurent White and Eric Deleersnijder are a Research fellow and a Research associate, respectively, with the Belgian National Fund for Scientific Research (FNRS). The present study was carried out within the scope of the project ''A second-generation model of the ocean system'', which is funded by the

Communauté Française de Belgique, as *Actions de Recherche Concertées*, under contract ARC 04/09-316. This work is a contribution to the construction of SLIM, the Second-generation Louvain-la-Neuve Ice-ocean Model (http://www.climate.be/SLIM). The authors are indebted to Eric Wolanski for very useful comments he provided during the preparation of this manuscript.

Appendix A. Exact solution to the water-column model

The exact solution to problem (13) and (14) is developed herein. The water concentration C_1 for the first type of age obeys the following nondimensional differential problem:

$$\begin{cases} \dfrac{\partial}{\partial z}\left(K_z\dfrac{\partial C_1}{\partial z}\right)=0 \\ C_1(z_\mathrm{b})=1 \text{ and } \left[K_z\dfrac{\partial C_1}{\partial z}\right]_{z=z_\mathrm{s}}=0. \end{cases}$$

Note that K_z has the following form:

$$K_z=\frac{6}{3-2\delta}z(1-\delta z).$$

It is readily seen that the solution is $C_1(z)=1$. It follows that the age concentration α_1 satisfies the problem:

$$\begin{cases} \dfrac{\partial}{\partial z}\left(K_z\dfrac{\partial \alpha_1}{\partial z}\right)+1=0 \\ \alpha_1(z_\mathrm{b})=0 \text{ and } \left[K_z\dfrac{\partial \alpha_1}{\partial z}\right]_{z=z_\mathrm{s}}=0. \end{cases}$$

After twice integrating and using the boundary conditions, we obtain:

$$\alpha_1(z)=\frac{3-2\delta}{6}\left\{\ln\left(\frac{z}{z_\mathrm{b}}\right)+\left(\frac{1-\delta}{\delta}\right)\ln\left(\frac{1-\delta z}{1-\delta z_\mathrm{b}}\right)-(1-z_\mathrm{s})\ln\left[\frac{z(1-\delta z_\mathrm{b})}{z_\mathrm{b}(1-\delta z)}\right]\right\},$$

which, using the fact that $1-z_\mathrm{s}\ll 1$, can be approximated by:

$$\alpha_1(z)\simeq\frac{3-2\delta}{6}\left[\ln\left(\frac{z}{z_\mathrm{b}}\right)+\left(\frac{1-\delta}{\delta}\right)\ln\left(\frac{1-\delta z}{1-\delta z_\mathrm{b}}\right)\right].$$

The water concentration C_2 for the second type of age obeys the following differential problem:

$$\begin{cases} \dfrac{\partial}{\partial z}\left(K_z\dfrac{\partial C_2}{\partial z}\right)=0 \\ C_2(z_\mathrm{b})=1 \text{ and } C_2(z_\mathrm{s})=0. \end{cases}$$

Twice integrating and using the boundary conditions yields:

$$C_2(z)=\frac{\lambda(z_\mathrm{s})-\lambda(z)}{\lambda(z_\mathrm{s})},$$

where:

$$\lambda(z)=\int_{z_\mathrm{b}}^{z}\frac{1}{K_z(t)}\mathrm{d}t=\frac{(3-2\delta)}{6}\ln\left[\frac{z(1-\delta z_\mathrm{b})}{z_\mathrm{b}(1-\delta z)}\right].$$

Finally, the age concentration α_2 is solution to:

$$\begin{cases} \dfrac{\partial}{\partial z}\left(K_z\dfrac{\partial \alpha_2}{\partial z}\right)+C_2(z)=0 \\ \alpha_2(z_\mathrm{b})=0 \text{ and } \alpha_2(z_\mathrm{s})=0, \end{cases}$$

which yields:

$$\alpha_2(z)=\frac{\mu(z_\mathrm{s})\lambda(z)-\lambda(z_\mathrm{s})\mu(z)}{\lambda(z_\mathrm{s})},$$

where:

$$\mu(z)=\int_{z_\mathrm{b}}^{z}\frac{1}{K_z(\xi)}\left(\int_{z_\mathrm{b}}^{\xi}\frac{\lambda(z_\mathrm{s})-\lambda(t)}{\lambda(z_\mathrm{s})}\,\mathrm{d}t\right)\mathrm{d}\xi. \tag{A1}$$

An expression for age 2 can be arrived at by computing the ratio of $\alpha_2(z)$ to $C_2(z)$, namely:

$$a_2(z)=\frac{\mu(z_\mathrm{s})\lambda(z)-\lambda(z_\mathrm{s})\mu(z)}{\lambda(z_\mathrm{s})-\lambda(z)}.$$

At $z=z_\mathrm{s}$, the above expression equals an indeterminate ratio of type 0/0. The limit when z goes to z_s exists and can be computed by using L'Hospital's rule. We obtain:

$$\begin{aligned} a_2(z_\mathrm{s}) &= \lim_{z\to z_\mathrm{s}} a_2(z) \\ &= \lambda(z_\mathrm{s})(z_\mathrm{s}-z_\mathrm{b})-\mu(z_\mathrm{s})-\int_{z_\mathrm{b}}^{z_\mathrm{s}}\lambda(\xi)\mathrm{d}\xi. \end{aligned}$$

A closed form may be obtained for $\mu(z)$ by evaluating Eq. (A1):

$$\mu(z)=\frac{(3-2\delta)}{6}\left\{z_\mathrm{b}\ln\left[\frac{z_\mathrm{b}(1-\delta z)}{z(1-\delta z_\mathrm{b})}\right]-\frac{1}{\delta}\ln\left(\frac{1-\delta z}{1-\delta z_\mathrm{b}}\right)\right\}-\frac{(3-2\delta)}{6\delta}\times\left\{\frac{2\mathrm{Li}_2(1-\delta z)-2\mathrm{Li}_2(1-\delta z_\mathrm{b})+\ln\left(\delta^2 z z_\mathrm{b}\right)\ln\left(\dfrac{1-\delta z}{1-\delta z_\mathrm{b}}\right)}{\ln\left[\dfrac{z_\mathrm{s}(1-\delta z_\mathrm{b})}{z_\mathrm{b}(1-\delta z_\mathrm{s})}\right]}\right\},$$

where Li_2 is the dilogarithm function defined as:

$$\mathrm{Li}_2(z)=-\int_0^z\frac{\ln(1-\xi)}{\xi}\mathrm{d}\xi=\sum_{k=1}^{\infty}\frac{z^k}{k^2}.$$

Assuming that $z_\mathrm{b}\ll 1$ and $z_\mathrm{s}\simeq 1$, the above expression for μ can be simplified to:

$$\mu(z)\simeq\frac{(3-2\delta)}{6\delta}\left[\frac{2\mathrm{Li}_2(1-\delta z)-\dfrac{\pi^2}{3}+\ln(1-\delta z)\ln\left(\dfrac{\delta^2 z}{1-\delta z_\mathrm{s}}\right)}{\ln(z_\mathrm{b}(1-\delta z_\mathrm{s}))}\right]$$

where the following approximation was used: $\mathrm{Li}_2(1-\delta z_b) \simeq \mathrm{Li}_2(1) = \pi^2/6$.

Appendix B. Supplementary data

Supplementary data associated with this article can be found, in the online version, at doi:10.1016/j.ecss.2006.07.014.

References

Akin, J.E., Tezduyar, T., Ungor, M., Mittal, S., 2003. Stabilization parameters and Smagorinsky turbulence model. Journal of Applied Mechanics 70 (1), 1–9.

Alaee, M.J., Ivey, G., Pattiaratchi, C., 2004. Secondary circulation induced by flow curvature and Coriolis effects around headlands and islands. Ocean Dynamics 54, 27–38.

Black, K.P., Gay, S.L., 1987. Eddy formation in unsteady flows. Journal of Geophysical Research 92 (C9), 9514–9522.

Coutis, P.F., Middleton, J.H., 1999. Flow-topography interaction in the vicinity of an isolated, deep ocean island. Deep-Sea Research Part I Oceanographic Research Papers 46, 1633–1652.

Coutis, P.F., Middleton, J.H., 2002. The physical and biological impact of a small island wake in the deep ocean. Deep-Sea Research Part I Oceanographic Research Papers 49, 1341–1361.

Cox, M.D., 1989. An idealized model of the world ocean. Part I: the global-scale water masses. Journal of Physical Oceanography 19, 1730–1752.

Deleersnijder, E., 1989. Upwelling and upsloping in three-dimensional marine models. Applied Mathematical Modelling 13, 462–467.

Deleersnijder, E., 1994. An analysis of the vertical velocity field computed by a three-dimensional model in the region of the Bering Strait. Tellus 46A, 134–148.

Deleersnijder, E., Norro, A., Wolanski, E., 1992. A three-dimensional model of the water circulation around an island in shallow water. Continental Shelf Research 12 (7/8), 891–906.

Deleersnijder, E., Campin, J.-M., Delhez, E.J.M., 2001. The concept of age in marine modelling: I. Theory and preliminary results. Journal of Marine Systems 28, 229–267.

Delhez, E.J.M., Deleersnijder, E., 2002. The concept of age in marine modelling: II. Concentration distribution function in the English Channel and the North Sea. Journal of Marine Systems 31, 279–297.

Delhez, E.J.M., Campin, J.-M., Hirst, A.C., Deleersnijder, E., 1999. Toward a general theory of the age in ocean modelling. Ocean Modelling 1, 17–27.

Falconer, R.A., Wolanski, E., Mardapitta-Hadjipandeli, L., 1986. Modeling tidal circulation in an island's wake. Journal of Waterway, Port, Coastal and Ocean Engineering 112, 234–254.

Fischer, H.B., List, E.Y., Koh, R.C.Y., Imberger, J., Brooks, N.H., 1979. Mixing in Inland and Coastal Waters. Academic Press, New York.

Goosse, H., Campin, J.-M., Tartinville, B., 2001. The sources of Antarctic bottom water in a global ice-ocean model. Ocean Modelling 3, 51–65.

Hamner, W.M., Hauri, I.R., 1981. Effects of island mass: water flow and plankton pattern around a reef in the Great Barrier Reef lagoon, Australia. Limnology and Oceanography 26 (6), 1084–1102.

Hanert, E., Le Roux, D.Y., Legat, V., Deleersnijder, E., 2005a. Advection schemes for unstructured grid ocean modelling. Ocean Modelling 7, 39–58.

Hanert, E., Le Roux, D.Y., Legat, V., Deleersnijder, E., 2005b. An efficient Eulerian finite element method for the shallow water equations. Ocean Modelling 10, 115–136.

Hanert, E., Deleersnijder, E., Legat, V., 2006. An adaptive finite element water column model using the Mellor–Yamada level 2.5 turbulence closure scheme. Ocean Modelling 12, 205–223.

Hirst, A.C., 1999. Determination of water component age in ocean models: application to the fate of North Atlantic Deep Water. Ocean Modelling 1, 81–94.

Ingram, R.G., Chu, V.H., 1987. Flow around islands in Ruppert Bay: an investigation of the bottom friction effect. Journal of Geophysical Research 92 (C13), 14,521–14,533.

Le Roux, D.Y., Lin, C.A., Staniforth, A., 2000. A semi-implicit semi-lagrangian finite element shallow-water ocean model. Monthly Weather Review 128, 1384–1401.

Lynch, D.R., Ip, J.T.C., Naimie, C.E., Werner, F.E., 1996. Comprehensive coastal circulation model with application to the Gulf of Maine. Continental Shelf Research 16, 875–906.

Moes, N., Dolbow, J., Belytschko, T., 1999. A finite element method for crack growth without remeshing. International Journal for Numerical Methods in Engineering 46, 131–150.

Munk, W.H., Anderson, E.R., 1948. Notes on a theory of the thermocline. Journal of Marine Research 3, 276–295.

Pattiaratchi, C., James, A., Collins, M., 1986. Island wakes and headland eddies: a comparison between remotely sensed data and laboratory experiments. Journal of Geophysical Research 92 (C1), 783–794.

Pietrzak, J., Deleersnijder, E., Schröter, J., 2005. The second international workshop on unstructured mesh numerical modelling of coastal, shelf and ocean flows. Ocean Modelling 10, 1–252 (Special issue).

Smagorinsky, J., 1963. General circulation experiments with the primitive equations. 1 The basic experiment. Monthly Weather Review 91 (5), 99–165.

Tomczak, M., 1988. Island wakes in deep and shallow water. Journal of Geophysical Research 93 (C5), 5153–5154.

Walters, R.A., 1992. A three-dimensional, finite element model for coastal and estuarine circulation. Continental Shelf Research 25, 83–102.

White, L., Beckers, J.-M., Deleernijder, E., Legat, V., 2006. Comparison between free-surface and rigid-lid finite element models of barotropic instabilities. Ocean Dynamics 56, 86–103. doi:10.1007/s10236-006-0059-0.

White, L., Deleernijder, E., Legat, V. Three-dimensional finite element marine modeling, in preparation.

Wolanski, E., 1994. Physical Oceanographic Processes of the Great Barrier Reef. CRC Marine Science Series. CRC Press.

Wolanski, E., Hamner, W.M., 1988. Topographically controlled fronts in the ocean and their biological influence. Science 241 (4862), 177–181.

Wolanski, E., Imberger, J., Heron, M.L., 1984. Island wakes in shallow coastal waters. Journal of Geophysical Research 89 (C6), 10,553–10,569.

Wolanski, E., Drew, E., Abel, K.M., O'Brien, J., 1988. Tidal jets, nutrient upwelling and their influence on the productivity of the alga Halimeda in the Ribbon Reefs, Great Barrier Reef. Estuarine, Coastal and Shelf Science 26 (2), 169–201.

Wolanski, E., Asaeda, T., Tanaka, A., Deleersnijder, E., 1996. Three-dimensional island wakes in the field, laboratory experiments and numerical models. Continental Shelf Research 16 (11), 1437–1452.

Wolanski, E., Brinkman, R., Spagnol, S., McAllister, F., Steinberg, C., Skirving, W., Deleersnijder, E., 2003. Merging scales in models of water circulation: perspectives from the Great Barrier Reef. In: Lakhan, V.C. (Ed.), Advances in Coastal Modeling. Elsevier Oceanography Series, vol. 67. Elsevier Science, pp. 411–429 (Chapter 15).

Available online at www.sciencedirect.com
ScienceDirect
Estuarine, Coastal and Shelf Science 74 (2007) 670–683
ESTUARINE COASTAL AND SHELF SCIENCE
www.elsevier.com/locate/ecss

Diagnosis of the sediment transport in the Belgian Coastal Zone

C. Mercier*, E.J.M. Delhez

Université de Liège, Modélisation et Méthodes Mathématiques, Aerospatiale et mecanique, Sart-Tilman B37, B-4000 Liège, Belgium

Received 14 August 2006; accepted 9 May 2007
Available online 5 July 2007

Abstract

Estimating the age of particles in marine environment constitutes an invaluable tool to understand the interactions between complex flows and sediment dynamics, particularly in highly energetic coastal areas such as the Belgian Coastal Zone (Southern Bight in the North Sea). To this end, the Constituent Age and Residence time Theory – CART – introduced by Delhez, E.J.M., Campin, J.-M., Hirst, A.C., Deleersnijder, E. [1999a. Toward a general theory of the age in ocean modelling. Ocean Modelling 1, 17–27] for passive water constituents is extended to describe the sediment dynamics. It is then used in combination with a three-dimensional coupled hydrodynamic-sediment transport model to investigate sediment processes in the Belgian Coastal Zone focusing on two complementary aspects of the sediment dynamics: the internal sediment motion and redistribution within the Belgian coast; and the horizontal transport.

Keywords: Belgian Coastal Zone; sediment transport; age; model

1. Introduction

During recent years, scientists and engineers involved in coastal water management have developed an increasing interest in sediment transport modelling which is motivated by its significant economical and ecological impacts.

The movement of cohesive sediments can cause siltation of navigation waterways, harbours and coastal environments. Expensive dredging activities are carried out regularly to maintain the maritime access routes to the Belgian coastal ports. According to Van den Eynde (2004), 10 million tons of dry material are dredged each year in the Belgian Coastal Zone (BCZ). Most of this material is disposed of in the sea and can therefore be transported back to the coast at a later time, with the need to dredge it again. Since sediments are polluted to varying degrees, the associated recirculation from the dumping site might also lead to the dispersion of polluted material over large areas.

The transport of cohesive sediments is also highly relevant for the water quality. Because of the cohesive properties of fine sediments, nutrients, heavy metals and organic contaminants are transported preferentially in an adsorbed state (Holt and James, 1999) and therefore tend to bind to the sediments. The adsorption of these pollutants is a function of the grain size (Lumborg, 2004) and other environmental factors. When sediments are stirred up, adsorbed nutrients and pollutants are released into the water column and can impact significantly the ecological balance of shallow areas (Liu et al., 2002b). The accumulation of substantial amounts of nutrients, for instance, will lead to eutrophication. In coastal waters, the amount of material in suspension (affected by dredging activities and sand/gravel exploitation) influences the turbidity, controls the penetration of light in the water column and influence therefore the primary production (Morris and Howarth, 1998). The transport and accumulation of fine-grained sediments are thus major factors when pollution of the marine environment is to be assessed.

In this paper, only the cohesive sediments with a grain size smaller than 62.5 μm are considered. This material is generally referred to as mud. It is a mixture of water, different

* Corresponding author.
E-mail address: c.mercier@ulg.ac.be (C. Mercier).

0272-7714/$ - see front matter © 2007 Elsevier Ltd. All rights reserved.
doi:10.1016/j.ecss.2007.05.010

clay minerals (mainly illite, montmorillonite and kaolinite), organic matter, and small amount of sand and silt (Berlamont et al., 1993). Consequently, mud is much more difficult to characterize than sand which can be fully characterized by its grain size distribution (e.g. Fredsøe, 1993) and its dynamics is quite complex. The most important mechanism involved in cohesive sediment transport is the hydrodynamic action which advects sediments, generates the force needed to erode the seabed and also affects the flocculation and the break-up of flocs through turbulence. Cohesive sediments also differ from non-cohesive ones because of two major processes: flocculation and consolidation of cohesive deposits with compaction of the sediments. Flocs are formed by the collision and aggregation of individual particles and can significantly modify the sediments' settling velocity. When flocs reach the seabed, they form a dense fluid–mud layer with a fragile structure that gradually collapses under its increasing weight as deposition occurs. The interstitial pore water is then expelled and the weight of the mud layer is progressively supported by inter-particle reaction forces. This process is known as self-weighted consolidation (Teisson et al., 1993). If a time scale of the order of the tidal period is chosen to focus on the mechanisms and movements of sediments in response to wind forcing and tides, the longer time scale of the consolidation process (due to the small pore dimensions) make this process of secondary importance (Cancino and Neves, 1999; Kuhrts et al., 2004) and changes in sediment properties of the sea floor can thus be neglected.

In the past, due to computer limitations, cohesive sediment transport was generally modelled by means of depth-integrated models (e.g. Mulder and Udink, 1991; McManus and Prandle, 1997; Yu et al., 1998; Liu et al., 2002b; Fettweis and Van den Eynde, 2003; Van den Eynde, 2004). While such 2D models are still used for many practical engineering applications, it must be recognized that sediment transport is a true 3D problem. Even without strong vertical density gradient, the settling velocity and the water–bottom interactions generate vertical gradients of suspended sediment concentration. Moreover, the actual deposition rate depends on the near-bed concentration while 2D models only give access to the depth-average concentration; assumptions must be made to relate the depth-integrated concentration to the near-bed value. These usually assume the instantaneous adjustment of the vertical profile of the sediment concentration profile to the equilibrium state (Lin and Falconer, 1996). Such an hypothesis is of course questionable in energetic coastal areas where flow conditions change rapidly and where 3D approaches are therefore physically more appropriate (Gerritsen et al., 2000, 2001; de Kok et al., 2001).

The transport of sediments in a tidal environment is usually very complex and difficult to describe. The net sediment transport arises from the tidal asymmetry: while pollutants and sediments can be transported by tidal currents at the scale of the tidal excursion, i.e. around 10 km in the BCZ, the net transport is generally much smaller and time scale of the bottom evolution should be expected to be much larger than tidal periods (Delhez, 1996a; Cancino and Neves, 1999; Delhez and Carabin, 2001). The usual (Eulerian or Lagrangian) residual current field, computed over several tidal cycles or a period of time long enough to smooth out mesoscale features, cannot, however, be used to characterize this transport because, in the mean time, the vertical profile of the sediment concentration varies with the evolving turbulence conditions and with the intermittent deposition and resuspension events occurring at a variety of time scales ranging from the dominant tidal period to a period of few days, characteristic of short term wind events and storms and to that of the spring–neap oscillations.

The present paper aims at the development of a diagnosis technique to understand the sediment transport in the Belgian Coastal Zone. The paper is organized as follows. Section 2 gives a brief outline of hydrodynamics and sedimentology of the BCZ. In Sections 3 and 4, fundamentals and calibration of the 3D hydrodynamic and cohesive sediment transport model are detailed. Next, in Section 5, some results are discussed and finally, in Section 6, the general age theory introduced in Delhez et al. (1999a) and Deleersnijder et al. (2001) is applied to understand and describe the transport of sediments.

2. Studied area

The Belgian Coastal Zone is a part of the Southern Bight of the North Sea comprised between 2°20′E and 3°20′E, and between 51°05′N and 51°40′N. It covers approximately 3600 km^2. The bathymetry is shallow and irregular (a mean depth of about 20 m and a maximum of 35 m). The area is also characterized by a complex system of sand banks parallel to the coast, some of which emerge from the water at very low tides. The modelled area and its bathymetry are presented in Fig. 1.

The hydrodynamics of the Belgian Coastal Zone is dominated by the tides and by the prevailing winds and waves' conditions.

The winds and thus waves are mainly from southwest or from northeast (Van den Eynde, 2004). They usually are under 5 Bft and their fluctuations evolve at time scales of 5–7 days (Nihoul and Hecq, 1984).

The tidal signal is semi-diurnal and slightly asymmetrical. At Oostende, the amplitudes of the M_2 and S_2 components reach, respectively, 1.8 m and 0.7 m (Delhez and Carabin, 2001). Along the coasts, the tidal currents, generally oriented parallel to the coast, can exceed 1 m/s at spring tide. The Atlantic tides and the storms reaching the Belgian shallow waters dissipate large amounts of energy, ensuring an intense mixing of the water column during the entire year (Delhez, 1996b) and the resuspension and vertical redistribution of bottom sediments. Because of the low freshwater discharge (mean value around 120 m^3/s) and of the strong mixing, there is no permanent haline stratification associated with the plume of the Scheldt river.

In response to the interactions of the tidal currents with the bathymetry, the plume of the Scheldt river first turns left along the Belgian coast before moving offshore. It is then progressively swept along by the general circulation flowing northward from the Dover Strait into the North Sea. This results

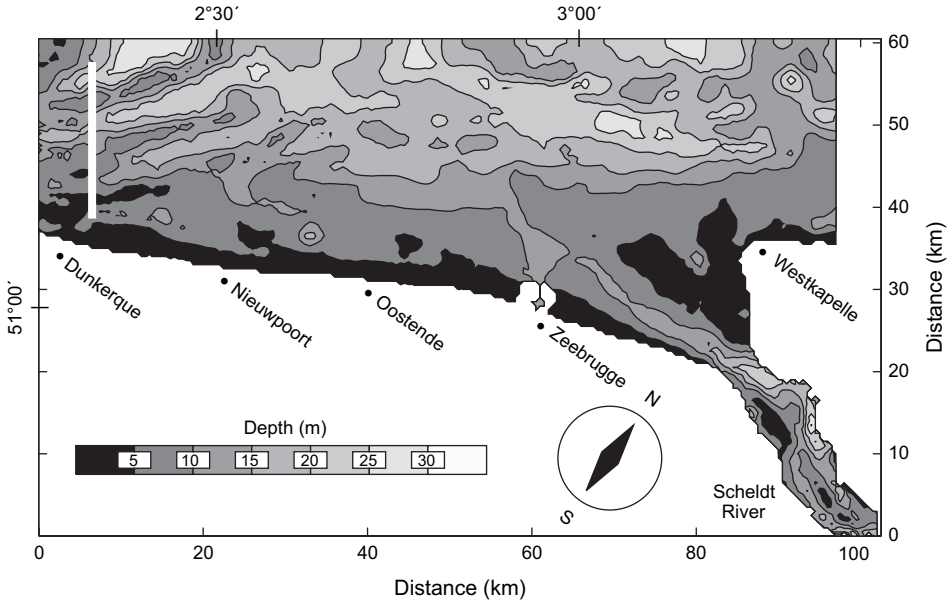

Fig. 1. Bathymetry of the Belgian Coastal Zone (axis labels indicate distance in kilometer, depth is in meters). The white line is the source region considered in the horizontal transport study in Section 6.

in a clockwise residual gyre characteristic of the BCZ (Nihoul and Hecq, 1984; Delhez and Carabin, 2001).

In the southern North Sea, intensive sediment movements and associated sediment transport occur frequently, owing to wind-induced currents, tides and wave action. The sediment distribution in the BCZ is influenced by the presence of the many large sand banks which form the complex BCZ's bathymetry. The sediments can be divided into different classes with different density, mineralogical compositions, grain sizes, organic contents, etc. They mainly consist of fine to medium size particles with a general fining trend to the northeast (Van der Molen, 2002). Medium grain size sediments (>400 μm) are found where the water depth is larger than 12 m. Close to the coast, between Oostende and the Westerschelde estuary, large mud fields are found with concentrations of Suspended Particular Matter (SPM) larger than a few hundreds of mg/l (Fettweis and Van den Eynde, 2003). According to Van den Eynde (2004), the presence of these mud fields is partly correlated with the high turbidity zones between Oostende and Zeebrugge, and in the mouth of the Westerschelde.

3. Hydrodynamic model

The general characteristics of the high-resolution hydrodynamic model of the BCZ are common to those of the general form of the GHER model (GeoHydrodynamics and Environment Research laboratory, University of Liège; e.g. Nihoul et al., 1989; Delhez and Martin, 1992). The model offers a three-dimensional view of the marine hydrodynamics and is formulated in the so-called σ-coordinate system to follow the bathymetry as closely as possible and to avoid the rigid lid approximation for the movement of the free surface (Phillips, 1957; Blumberg and Mellor, 1983). It is also non-linear and baroclinic with the computation of temperature and salinity as prognostic variables. The model includes a refined and robust turbulent closure scheme based on the three-dimensional evolution equation for the turbulent kinetic energy per unit mass and on an algebraic parametric expression of the mixing length taking into account the surface wind induced activity and the stratification (e.g. Nihoul et al., 1989; Delhez et al., 1999b). This approach is particularly well suited to shallow shelf seas where the vertical structure of turbulence is not too complex and sound empirical formulae are available for the mixing length. The state variables are thus the free surface elevation, three components of the velocity vector, temperature and salinity, turbulent kinetic energy and mixing length.

The discretization is based on the FBTCS method, i.e. Forward Backward on Time and Centered Space (Beckers and Deleersnijder, 1993). The equations are solved by a finite volume method based on an Arakawa C grid (Arakawa and Lamb, 1977), using a mode-splitting technique to handle the fast surface gravity waves (Madala and Piacsek, 1977; Blumberg and Mellor, 1987). Vertical advection and turbulent diffusion are treated semi-implicitly. A TVD advection scheme (i.e. Total Variation Diminishing) with Superbee limiter is used for the advection of scalar quantities (Sweby, 1984; James, 1996). The model has an horizontal resolution of 500×500 m and uses 10 unequally spaced vertical σ-levels with enhanced resolution near the surface and the bottom. The mesh is roughly aligned with the Belgian coast for a better representation of the coastline and allows a good description of the river mouth. The model also includes a drying and flooding algorithm to cope with the shallow sand banks (a grid point is considered to be dry when the local water height decreases below a threshold value of 5 cm).

The local hydrodynamic model is forced with six-hourly NCEP wind stress, air pressure and heat fluxes (computed

from solar radiation, cloud cover, air temperature and humidity, and sea surface temperature). These meteorological data were extracted from the NCEP/NCAR reanalysis of surface data from NOAA/CDC[1] The precipitation flux is assumed to balance the evaporation. The forcing data at the open boundaries, i.e. water level, temperature and salinity, are obtained from a large scale 3D hydrodynamic model covering the whole North-western European Continental Shelf with a grid size of $10' \times 10'$ and 10 vertical σ-levels. This large scale model has the same characteristics as the local model, is forced with the same meteorological data and nine principal tidal components at its own open boundaries. The output of the large scale model are interpolated in time and space and prescribed to the local model using a radiation open boundary condition.

Note that the current implementation does not include any feed-back from the small scale BCZ model on the shelf model. Also, owing to the moderate concentration of suspended sediments (a few hundreds of mg/l), the influence of sediment particles on the density field is neglected in the hydrodynamic model.

4. Cohesive sediment transport model

The distribution of suspended sediments in the water column (grain size <62.5 μm) is described by means of the concentration fields C^i of four classes of sediments. Basically, grain size is the main motivation to differentiate the four classes. More generally, however, the different sediment classes are introduced to take into account the variability of the dynamic properties (sedimentation velocity, erosion and deposition thresholds, etc.) of the suspended sediments.

The concentration of each type of sediment varies according to

$$\frac{\partial C^i}{\partial t} + \nabla \cdot \left[(\mathbf{v} + \mathbf{w}_s^i) C^i \right] = \nabla \cdot \left(\mathbf{K} \cdot \nabla C^i \right) \tag{1}$$

where t is the time [s], $\mathbf{v}$ is the full 3D current velocity (including the Stokes' Drift) [m s^{-1}], $\mathbf{w}_s^i = -w_s^i \mathbf{e}_z$ is the apparent settling velocity for particle class i [m/s], $\mathbf{e}_z$ axis is vertical upwards, $\mathbf{K}$ is the diffusion tensor [m^2/s] and ∇ is the differential operator nabla. The velocity field and the diffusion coefficients are provided by the hydrodynamic module.

Suspended sediments are allowed to settle on the bottom and to be re-entrained into suspension. Ignoring bed load transport, the mass per unit area C_s^i of the sediment of type i that is lying on the bottom varies therefore, according to

$$\frac{\partial C_s^i}{\partial t} = F_{sed}^i - F_{ero}^i \tag{2}$$

where F_{ero}^i and F_{sed}^i are the corresponding erosion and sedimentation fluxes per unit area. Eqs. (1) and (2) are coupled through these fluxes which also appear in the boundary condition of Eq. (1)

$$\left[(\mathbf{v} + \mathbf{w}_s^i) C^i - \mathbf{K} \cdot \nabla C^i \right] \cdot \mathbf{n} = F_{sed}^i - F_{ero}^i \tag{3}$$

where $\mathbf{n}$ denotes the unit downward normal at the bottom.

The four state variables C_s^i describe the amount of sediments on the bottom that is available for erosion. These sediments are assumed to be easily remobilised (see Section 4.3) by bottom shear stress. In addition, a consolidated parent layer is assumed to exist underneath. This parent layer accounts for local sources of sediments.

4.1. The settling velocity

A priori, the settling velocity $\mathbf{w}_s^i$ depends on the vertical shear and on the gravitational forces through many factors such as the density of the individual particle in flocs, the floc porosity (both influencing the gravitational forces), the form of the individual particle/floc, the organic content, the mineralogic composition, the suspended sediment concentration, and some physico-chemical properties of the fluid such as turbulence (affecting aggregation and break-up of flocs), temperature, and ionic composition (Berlamont et al., 1993).

For instance, many studies were carried out to investigate the dependence of $\mathbf{w}_s^i$ on the suspended sediment concentration (e.g. Mehta, 1989; Winterwerp, 2002; You, 2004) leading to the identification of three different settling regimes according to the suspended concentration: (1) the free settling (concentration below 0.4 g/l), when the settling velocity does not depend on the suspended sediment concentration (2) the enhanced settling (concentration comprised between 0.4 and 2.0 g/l), characterized by an increase of the probability of flocculation with suspended concentration, particularly in saline environments, and (3) the hindered settling (concentration above 2.0 g/l) where the settling velocity rapidly decreases due to break-up of flocs, flocs mutual hindrance and interactions between the flows around adjacent ones that tend to increase upward friction (Teisson et al., 1993; Cancino and Neves, 1999; Liu et al., 2002b). According to Berlamont et al. (1993), settling velocities of cohesive particles aggregates met in nature are of the order of 0.01–10 mm/s.

Because of the difficulty to find appropriate values of the site specific parameters needed in formulations that take into account flocculation effects (e.g. Cancino and Neves, 1999; Lumborg and Windelin, 2003; You, 2004), the settling velocity of cohesive sediments is usually directly calculated from Stokes' law (Estournel et al., 1997; Holt and James, 1999; Jiang et al., 2000; Liu et al., 2002b; Fettweis and Van den Eynde, 2003; Van den Eynde, 2004, etc.). In this model, the problem is avoided by the definition of the sediments' classes in terms of the settling velocity itself. In other words, the four sediment classes provide a rough description of the distribution of settling velocities of the sediments. Table 1 shows the different values considered. The average particle size for each class is only indicative.

[1] http://www.cdc.noaa.gov/cdc/reanalysis.

Table 1
Settling velocities w_s^i for the different sediment classes considered

Size class	Average particle sizes [μm]	Settling velocities	
		[mm/s]	[m/h]
I	2	0.005	0.018
II	6	0.05	0.18
III	10	0.1	0.36
IV	35	1	3.6

4.2. The deposition model

The process of deposition of cohesive sediment depends on a combination of several factors including size, settling velocity and cohesion of the single settling particle or of the slightly or strongly bounded aggregates/flocs (Teisson et al., 1993). Deposition is controlled by turbulent processes near the seabed: flocs that are strong enough to resist the bed shear stresses will settle to the seabed while others will be broken into two or more smaller units and re-entrained into suspension by the hydrodynamic lift forces.

In this paper, as in many other studies (e.g. Teisson et al., 1993; Cancino and Neves, 1999; Holt and James, 1999; Hayter and Gu, 2001; Ribbe and Holloway, 2001; Liu et al., 2002a,b; Fettweis and Van den Eynde, 2003; Lumborg and Windelin, 2003; Lumborg, 2004; Pandoe and Edge, 2004; Periáñez, 2005, etc.), the deposition model follows the direction given by Krone (1962)

$$F_{\text{sed}}^i = w_{\text{d}}^i P_{\text{sed}}^i C_{\text{b}}^i \tag{4}$$

where the subscript b means 'just above the seabed', w_{d}^i is the deposition velocity [m/s] and P_{sed}^i is the sedimentation threshold which depends on the critical shear stress for sedimentation τ_{crd}^i [Pa] according to

$$P_{\text{sed}}^i = \begin{cases} \left(1 - \dfrac{\tau_{\text{b}}}{\tau_{\text{crd}}^i}\right) & \text{if } \tau_{\text{b}} < \tau_{\text{crd}}^i \\ 0 & \text{if } \tau_{\text{b}} \geq \tau_{\text{crd}}^i \end{cases} \tag{5}$$

where τ_{b} is the bottom stress [Pa]. P_{sed}^i can be regarded as a probability of deposition: a particle reaching the seabed has a probability of remaining there comprised between 0 and 1 as the bottom shear stress varies between its upper limit for deposition and zero. Note that the deposition velocity w_{d}^i is generally equivalent to the settling velocity w_{s}^i. However, for the smallest particles, w_{d}^i may be larger than w_{s}^i because of Brownian motion, diffusion or aggregation at sea–water interface (Sanford and Halka, 1993). When w_{d}^i is constant, Eq. (4) represents the deposition flux only in the case of low suspended sediment concentration (Sanford and Halka, 1993; Van den Eynde, 2004).

The critical shear stress for deposition is a fundamental characteristic of sediments depending mainly on the particles/flocs' grain size. If the sediment grain size is uniform, all sediments will remain in suspension above this critical shear stress. For inhomogeneous sediment size, however, the larger or heavier flocs will deposit for shear stresses above the critical value. In situ measurement of the critical shear stress for deposition is a very difficult task (Berlamont et al., 1993). As a consequence, τ_{crd}^i is usually used as a calibration parameter and fixed to a constant value for each sediment classes (e.g. Liu et al., 2002a,b; Lumborg and Windelin, 2003; Lumborg, 2004, etc.) keeping in mind that bigger flocs have a higher probability to remain on the seabed than smaller particles.

According to Berlamont et al. (1993), τ_{crd} is usually in the range of 0.05–0.2 Pa. For inhomogeneous sediments, some larger aggregates will generally begin to deposit at higher shear stresses in the range of 0.1–1 Pa. Krone (1962) mentions critical shear stress for deposition in the range 0.06–0.078 Pa. In their model study of the North Sea, Lumborg and Pejrup (2005) report values between 0.05 and 0.3 Pa. Holt and James (1999) while Periáñez (2005) use a value of 0.10 Pa for all their sediment classes. In their study of the mud transport in the BCZ, Fettweis and Van den Eynde (2003) use a value of 0.5 Pa. Since the critical stress is likely to vary in space, reflecting the nature and composition of the sediments, the value of 0.5 Pa used by Fettweis and Van den Eynde (2003) is assumed to be representative of the Belgian Coastal Zone and is therefore used for our four sediment classes.

4.3. The erosion model

The process of erosion of cohesive sediments is driven by shear but also depends on electrochemical forces and on a large number of parameters including the mineral composition and organic content, the biological and geochemical processes, the composition of pore water and eroding fluids, and consolidation and time-related histories of the bed.

A lot of formulations of the erosion flux can be found in the literature (e.g. Sanford and Maa, 2001; Aberle et al., 2004). Assuming that the critical shear stress for erosion τ_{cre} [Pa] does not change with depth within the sediment layer, several authors (e.g. Whitehouse et al., 2000; Ribbe and Holloway, 2001; Kuhrts et al., 2004; Pandoe and Edge, 2004; Van den Eynde, 2004, etc.) use the erosion rate formulation proposed by Partheniades (1965)

$$F_{\text{ero}} = \begin{cases} M\left(\dfrac{\tau_{\text{b}}}{\tau_{\text{cre}}} - 1\right)^n & \text{if } \tau_{\text{b}} > \tau_{\text{cre}} \\ 0 & \text{if } \tau_{\text{b}} \leq \tau_{\text{cre}} \end{cases} \tag{6}$$

where τ_{b} is the bottom shear stress [Pa], M is an empirical erosion parameter and where n represents the strength of erosion (usually set to unity). The erosion rate is then not only independent of the suspended sediment concentration in the eroding current, but also of the sediment concentration available on the bottom.

When multiple sediment classes are used, the erosion rate for each sediment type should depend on the actual sediment composition. Following many authors (Cancino and Neves, 1999; Holt and James, 1999; Liu et al., 2002a,b; Fettweis and Van den Eynde, 2003; Periáñez, 2005, etc.), the modified

formulation proposed by Ariathurai (1974) is therefore used in the model

$$F^i_{\text{ero}} = \begin{cases} M^i f^i \left(\dfrac{\tau_b}{\tau^i_{\text{cre}}} - 1 \right) & \text{if } \tau_b > \tau^i_{\text{cre}} \\ 0 & \text{if } \tau_b \le \tau^i_{\text{cre}} \end{cases} \tag{7}$$

where M^i and τ^i_{cre} denote, respectively, the erosion parameter and the critical erosion stress for sediment type i, and f_i represents the fraction of particles of class i available on the bottom, i.e.

$$f^i = \frac{C^i_s}{\sum_j C^j_s} \tag{8}$$

Note that Eq. (7) does not take into account the layering of the bottom sediments which would imply that sediments are eroded in reversed order of their deposition. In Eq. (7), perfect mixing of the bottom sediments is assumed.

The erosion constant M^i depends on physico-chemical characteristics of the bottom sediment (class, density, organic content, mineralogic composition, etc.). In North Sea, for sediment with a diameter between 2 and 35 μm, Holt and James (1999) used a value of 0.04 gm^2/s^2. In the Western Scheldt, Mulder and Udink (1991) used 0.05 gm^2/s^2. In Fettweis and Van den Eynde (2003), the erosion constant is set to 0.12 gm^2/s^2. As a compromise, a value of 0.08 gm^2/s^2 is used for all sediment classes in this study.

Typical values for critical shear stress for erosion of soft muds measured in laboratory tests are in the range 0.1–2 Pa (Berlamont et al., 1993). Parchure and Mehta (1985) report values between 0.04 and 0.62 Pa based on soft dredged cohesive sediments analyzed in the laboratory. Values within this range are often applied in modelling studies (e.g. Holt and James, 1999; Ribbe and Holloway, 2001; Fettweis and Van den Eynde, 2003; Lumborg, 2004; Pandoe and Edge, 2004; Van den Eynde, 2004; Lumborg and Pejrup, 2005, etc.). In this work, since only mud is considered and consolidation of the bottom is neglected in the upper sediment layer, τ_{cre} is set to the constant high value of 0.5 Pa which is in the range of value usually used for mud in North Sea (Holt and James, 1999; Fettweis and Van den Eynde, 2003; Van den Eynde, 2004). The sand–mud interactions, the fluidization, liquefaction and changing material parameters of sediments are neglected in the present paper.

The above formulation of the erosion flux and the associated constants apply to the resuspension of freshly deposited sediments described by the C^i_s. For the erosion rate of the consolidated parent layer, Eq. (7) is used with some adaptations. First, erosion of the parent layer only occurs when the upper non-consolidated layer is completely eroded. Then, a much larger critical shear stress of 2.0 Pa is used to take into account the nature of the parent layer. Finally, the mud content of the parent layer is prescribed as a spatially varying field. The value of the critical shear stress and the spatial distributions of the mud content of the parent layer are identical to those used by Fettweis and Van den Eynde (2003).

4.4. The bottom shear stress

The cohesive sediment transport model used the local bottom shear stress τ_b [Pa] as the governing factor to compute resuspension and deposition fluxes. Following Fettweis and Van den Eynde (2003), the bottom stress in this study is calculated under the combined effect of waves and currents using Bijker's (1966) formula

$$\tau_b = \tau_c \left[1 + 0.5 \left(\frac{c}{\sqrt{2g}} \sqrt{f_w} \frac{u_b}{u_c} \right)^2 \right] \tag{9}$$

where τ_c is the bottom stress due to currents [Pa], g is the acceleration due to gravity [m/s^2], u_c is the current velocity [m/s], u_b is the orbital wave velocity [m/s] at the bottom, f_w is the wave friction factor and c is evaluated using (Van den Eynde and Ozer, 1993)

$$c = 77.5 + 14.18 \min \left(\frac{u_c}{u_b}, 0.67 \right) \tag{10}$$

The calculation of τ_c is performed using a quadratic law based on the assumption of a logarithmic bottom boundary layer (Blumberg and Mellor, 1987)

$$\tau_c = \max \left\{ (C_d)_{\min}, \left[\frac{\kappa}{\ln\left(\frac{z_b}{z_0}\right)} \right]^2 \right\} \rho u_c^2 \tag{11}$$

where u_c is the current velocity calculated at a height z_b within the logarithmic boundary layer, z_0 is the roughness length and $(C_d)_{\min}$ is the drag coefficient when z_b is outside the boundary layer. The data needed to evaluate f_w and u_b are those obtained by the MU-WAVE model for the calculation of the wave environment in the BCZ (Van den Eynde, 1992; Van den Eynde and Ozer, 1993).

4.5. Boundary condition

While the hydrodynamic module takes its boundary conditions from the large scale shelf model, boundary conditions for the sediment module must be derived from available data because sediment dynamics is not simulated at the larger scale.

The flux of suspended matter through the Strait of Dover represents the dominant input of mud in the area with a yearly average SPM flux into the BCZ model of 15.4×10^6 t/yr (see Fettweis and Van den Eynde, 2003). Assuming that the four sediment classes account evenly for this flux, this figure translates into an average concentration of sediments in the incoming Channel water of 1.25 mg/l for the four sediment classes.

At the NW and NE open boundaries, the incoming flux is computed by relaxing the boundary concentration towards zero with a time scale of an hour. This is a reasonable assumption for the offshore NW boundary since this coincide roughly with a streamline of the general circulation from the English Channel to the Southern Bight of the North Sea. At the NE, the assumption amounts to ignoring the possible inputs of SPM from the Rhine plume.

Sediments are allowed to be advected out of the computational domain through all its open boundaries.

5. Results

The simulations start on the 15th of January 1993 and run for 43 days. At the initial time, the hydrodynamic fields are dynamically adjusted and the concentration of the sediments in the non-consolidated layer is assumed to be zero. The sediment model is then run for 13 days to ensure a proper initialization. The results shown below are representative of the last 30 days of the simulation.

The spatial distribution of the suspended matter in the BCZ is shown in Fig. 2 for spring and neap conditions. These distributions are in good agreement with the measurements presented by Fettweis and Van den Eynde (2003) and the results obtained by these authors using a coarser resolution depth-integrated model.

The SPM distribution reflects the different mud origins. While the flux of suspended matter through the Strait of Dover represents the dominant input of mud in the area, the distribution is characterized by a local maximum offshore Zeebrugge and along the coast up to Dunkerque. Low values of the bottom stress (below 0.5 Pa) are found in this region and allow the accumulation of mud in the bottom layer. Since the parent layer is also enriched in mud around Zeebrugge (the mud content of the parent bed is as high as 40% in this region), the occasional erosion of this layer is responsible for the SPM maximum seen in Fig. 2.

The magnitude of the local SPM maximum and its lateral extension vary of course with the spring/neap cycle. On account of the increased bottom stress, significant concentrations

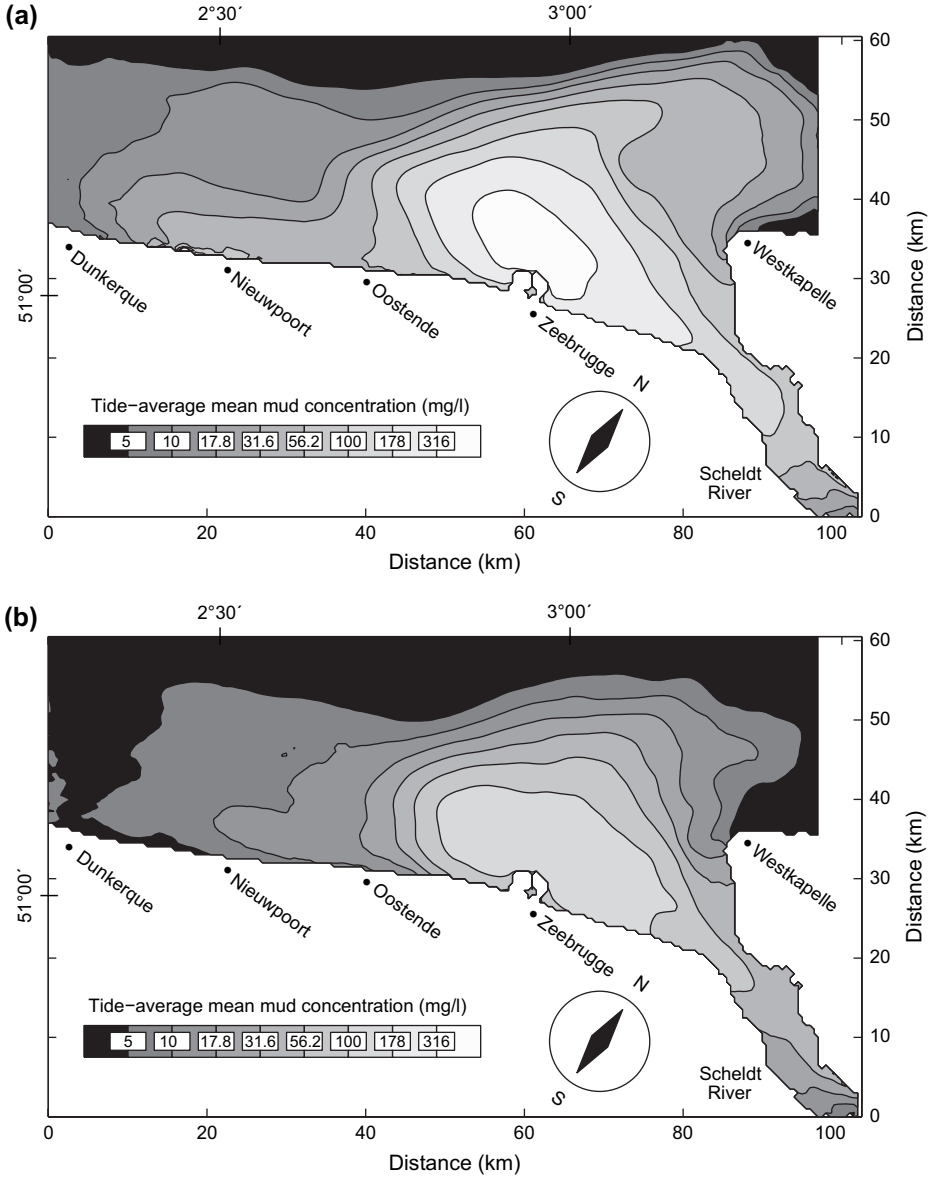

Fig. 2. Tide-average of depth integrated suspended particulate matter concentrations [mg/l] during (a) a spring tide of 5th February and (b) a neap tide of 31st January 1993.

of SPM are found along the western part of the coast (around Oostende and Nieuwpoort) under spring conditions. The plume also extends deeper in the Westerschelde than under neap conditions (Fig. 2).

The bottom stress (not shown) induced under the combined effects of waves and currents reaches its highest values on the shallow sides of the sand banks offshore Dunkerque and Nieuwpoort (the Flemish Banks) and at the entrance of the Scheldt estuary. The percentage of mud in the parent layer in these areas is, however, very small so that these do not contribute significantly to the local increase of SPM concentration.

Unfortunately, the data about the SPM distribution in the BCZ are scarce and do not allow any extensive quantitative validation of the model results. While obviously frustrating, the qualitative comparison with previous studies shows that our results are at least compatible with the current understanding of the sediments' dynamics in the area.

6. Diagnosis of sediment dynamics

The Constituent-oriented Age and Residence time Theory – CART (Delhez et al., 1999a; Deleersnijder et al., 2001) can be used to get a deeper understanding of the sediment dynamics in the Belgian Coastal Zone.

According to CART, the age of a particle is defined as the time elapsed since a given origin that can be regarded as the 'birth' of the particle and that can be freely set to match the particular objectives of the study. In essence, the computation procedure amounts to attach a clock to each particle and reset this clock at an appropriate time. The time shown by the clock at a later time is called the age of the particle. In most applications, the time origin differs from one particle to the other. This is the case, for instance, when the concept of age is used to quantify the time elapsed since the particle had contact with the surface or the time since a particle entered a particular control domain (Delhez et al., 1999a). Note that while the age is a Lagrangian concept which is defined for each particle, CART provides a Eulerian description of the mean age and is therefore directly applicable to diagnose tracers dynamics and hydrodynamic models formulated in an Eulerian framework.

Since CART was originally formulated for dissolved tracer, we show first how the theory can be extended to describe the dynamics of suspended matter that can settle on the bottom and be resuspended at a later time. We demonstrate then how the degree of freedom associated with the choice of the birth date of the particles can be used to highlight two complementary aspects of the sediment dynamics, namely resuspension and horizontal transport.

In a first approach, we use the concept of age to study the duration of the resuspension–deposition events. To this end, we define the age of a particle as the time elapsed since that particle was eroded from the bottom layer. In other words, the age is defined as the time elapsed since the particle last contact with the sediment layer. Hereafter, the age defined in this way is called 'resuspension age'.

As explained above, the suspended sediments in the water column is a mixture of mud advected through the Strait of Dover and mud resuspended from the bottom (non-consolidated or parent) layers in the computational domain. Obviously, only the resuspension age of the suspended sediments of the second group can be computed (since the 'birth' of other particles is not explicitly described in the model). Because the dynamics of mud is not linear (through the erosion term), the suspended sediments of the two origins must, however, be simulated simultaneously. Therefore, the appropriate procedure is to introduce new state variables $\tilde{C}^i$ and $\tilde{C}^i_s$ measuring the water column and bottom concentrations of sediments of the four classes that are actually resuspended in the BCZ in the time-window of the simulation. These variables satisfy similar differential equations as the total mud concentrations but ignoring any lateral input at the open boundaries (the concentration is set to zero at inflow open boundaries). The sedimentation and erosion fluxes $\tilde{F}^i_{\text{sed}}$ and $\tilde{F}^i_{\text{ero}}$ of the sediments marked in this way are computed by multiplying the total sedimentation and erosion fluxes by the fraction of the concentration of the marked sediment with respect to the total concentration, i.e.

$$\tilde{F}^i_{\text{sed}} = \frac{\tilde{C}^i}{C^i} F^i_{\text{sed}}, \qquad \tilde{F}^i_{\text{ero}} = \frac{\tilde{C}^i_s}{C^i_s} F^i_{\text{ero}} \tag{12}$$

To describe and understand the resuspension age of the marked sediments, the concept of the concentration distribution function is central in CART (Delhez et al., 1999a; Deleersnijder et al., 2001; Delhez and Deleersnijder, 2002). The idea behind this concept is that the particles that are present at a given location at a given time have different histories and bear therefore different ages. The concentration distribution function describes the distribution of the ages of these particles. For each of the four classes of marked sediments, one will have

$$\tilde{C}^i(t,\mathbf{x}) = \int_0^\infty \tilde{c}^i(t,\mathbf{x},\tau)\mathrm{d}\tau \tag{13}$$

where $\tilde{c}^i(t,\mathbf{x},\tau)$ is the corresponding concentration distribution function such that $\tilde{c}^i(t,\mathbf{x},\tau)\mathrm{d}\tau$ represents the contribution of the material with an age between τ and $\tau+\mathrm{d}\tau$ to the total concentration of marked sediments at time t and location $\mathbf{x}$.

While the concentration distribution function completely describes the distribution of the particles along the age axis, it is generally sufficient to determine the mean age $a^i(t,\mathbf{x})$ (to simplify the notation, the ˜ is not used but is implicit for age related quantities) of every marked constituent, i.e.

$$a^i(t,\mathbf{x}) = \frac{\alpha^i(t,\mathbf{x})}{\tilde{C}^i(t,\mathbf{x})} \tag{14}$$

where

$$\alpha^i(t,\mathbf{x}) = \int_0^\infty \tau\tilde{c}^i(t,\mathbf{x},\tau)\mathrm{d}\tau \tag{15}$$

The purpose of the introduction of the so-called age concentration α^i is that this is an additive quantity for which a budget can be computed. Using the procedure described in

Delhez et al. (1999a) and Deleersnijder et al. (2001), the budget of α^i translates into the evolution equation

$$\frac{\partial \alpha^i}{\partial t} + \nabla \cdot \left[(\mathbf{v} + \mathbf{w}_s^i)\alpha^i \right] = \tilde{C}^i + \nabla \cdot \left(\mathbf{K} \cdot \nabla \alpha^i \right) \tag{16}$$

The mean resuspension age of the marked suspended matter can be computed by solving Eq. (16) with the bottom boundary condition

$$\left[(\mathbf{v} + \mathbf{w}_s^i)\alpha^i - \mathbf{K} \cdot \nabla \alpha^i \right] \cdot \mathbf{n} = F^i_{\alpha,\mathrm{sed}} \tag{17}$$

where the age concentration sedimentation flux $F^i_{\alpha,\mathrm{sed}}$ is parameterized according to

$$F^i_{\alpha,\mathrm{sed}} = \begin{cases} \alpha^i_b w^i_d \left(1 - \dfrac{\tau_b}{\tau^i_{crd}} \right) & \text{if } \tau_b < \tau^i_{crd} \\ 0 & \text{if } \tau_b \geq \tau^i_{crd} \end{cases} \tag{18}$$

where α^i_b is the age concentration at the bottom of the water column. This formulation assumes that the material settles on the bottom 'with its age' and that the probability to settle does not depend on the age. It is the boundary condition Eq. (17) that really defines the resuspension age. Indeed, the comparison of Eq. (17) with Eq. (3) shows that the resuspension/erosion flux of age $F^i_{\alpha,\mathrm{ero}}$ is zero, i.e. that resuspension does not contribute to the increase of the age content of the water column. This implies that the resuspension age of the material lying in the bottom layers is zero and that the ageing process of the particles starts when these are eroded to the water column.

Snapshots of the (depth-averaged) resuspension age taken at the same tidal phase (1 h before low tide) on the 14th and 27th of February 1993 are shown in Figs. 3 and 4. To avoid entering into too many details, only the results for the sediments of class I (finer sediment) and IV (coarser sediment) are discussed. Contours of the resuspension age are plotted only where the concentration of marked sediments is significant.

Because of their very small settling velocity (0.005 mm/s), the dynamics of sediments of class I is only weakly influenced by sedimentation and the distribution of the resuspension age mainly reflects the origin of the material and its advection by the residual circulation. On the 2/14 snapshot, which is taken at the end of a period of calm weather conditions (see Fig. 5), the youngest material (<5 days) is found around Zeebrugge and along the coastline up to Dunkerque (Fig. 4a). Because of the relatively weak mean bottom stresses in these areas, mud can indeed accumulate on the bottom during part of the tidal cycle and be resuspended at a later time. As a result, the mean age of the suspended sediments is small in these areas which appear as sources of sediments for the BCZ.

The fine sediments that are eroded from coastal areas are progressively advected offshore by the general circulation. The resuspension age distribution reflects both the direction of this offshore motion and the timescale at which it occurs. Fig. 4a clearly shows the effect of the residual gyre which characterizes the general circulation in the BCZ (Nihoul and Hecq, 1984; Delhez and Carabin, 2001). Following the general anti-cyclonic motion, the resuspension age increases from less than 5 days at the coast to about 13 days in the centre of the gyre.

The 2/27 results (see Fig. 3) come after a period of stronger winds. These winds are responsible for a complete collapse of the residual gyre structure. The suspended sediments are also efficiently flushed-out of the area. The age of the oldest material does not exceed 10 days anymore. Quite counterintuitively, the youngest material (age below 5 days) also disappear; this is because the much higher turbulence levels and bottom stress do not allow the fine material to settle on the bottom. As a result of the modified hydrodynamic conditions, the (marked) fine sediments are confined to small areas around Zeebrugge and the Scheldt estuary and their mean age is larger in calm weather conditions.

The coarser sediments of class IV have a completely different dynamics (Fig. 5); their larger settling velocity results in a much larger effect of sedimentation on their dynamics and spatial distribution. Since turbulence is very high in the BCZ, even the large settling velocity of sediments of class IV is relatively ineffective at counteracting the vertical homogenization of the water column induced by turbulence. The vertical distribution of these sediments shows only a 10% increase of the concentration above the sea bottom (whereas the profiles are perfectly homogeneous for sediments in class I). However, since the settling velocity of the sediments of class I and IV is in a ratio of 1:200, the deposition flux on the bottom is in the same ratio for the two sediment classes and the dynamics of the sediments of class IV is strongly influenced by successive settling and resuspension episodes. As a result, the mean age of these sediments is everywhere smaller than 3 days in both calm and strong wind conditions. At most coastal locations, the mean age is even smaller than 0.5 days meaning that the SPM dynamics strongly interacts with the tidal cycle and transient wind and wave events.

After calm weather conditions (Fig. 5a), the smallest resuspension ages are also found along the coast between Dunkerque and Zeebrugge, in the shallow part of the Westerschelde and around Westkapelle. In general, however, the sediments of class IV do not reach the coastline between Zeebrugge and Nieuwpoort. The stronger winds have a weaker influence on sediments of class IV than on the finer sediments (Fig. 5b). Roughly speaking, the age distribution reflects the local bathymetry. The modification of the horizontal circulation plays a minor part since the coarse sediments concentrate at the bottom of the water column where the horizontal currents are weaker.

Using a different choice for the birth date of the particles, the age can be used to quantify the transport rate of mud across the BCZ. The point is that, because of the occurrence of intermittent sedimentation/resuspension events, the residual transport of suspended matter cannot be described by means of the usual residual velocity field. In fact, the description would require a Lagrangian residual velocity field that is computed by following the particle along its movement, including the resting phase on the bottom, the resuspension events and the vertical motion in the water column. While such a Lagrangian approach is feasible to compute the path of the sediment particles using random walk models, it is not appropriate to synthesize or describe the complex movements of the sediments

by means of a single Lagrangian residual velocity field. The concept of age can be used to circumvent this difficulty. To this end, the age of a particle can be defined as the time elapsed since that particle passed through a source region S. In the simulations, this source region is defined as a single line which is drawn perpendicular to the coast (see Fig. 1). The mean age at a downstream location measures the average time taken by the suspended sediment parcel to travel from the source region to the observation point. Hereafter, the age computed in that way is called 'transport age'. It should be noticed that deposition events influence the transport age since the virtual clock that is attached to each particle keeps running when the parcel is lying on the bottom.

Obviously, the transport age makes sense only for the particles that moved through the source region at a previous time. Therefore, it is also necessary to mark these particles as done for the resuspension age. Using the same notations for the concentrations of the marked sediments $\tilde{C}^i$ and $\tilde{C}^i_s$, but with different interpretations, the new marking procedure is described by the requirement that

$$\tilde{C}^i = C^i, \qquad \tilde{C}^i_s = C^i_s \quad \text{in } S \tag{19}$$

As above, the flux of marked sediments is assumed to be zero at inflowing open boundaries and the sedimentation and erosion fluxes are computed according to Eq. (12).

A budget of the age concentration of the marked sediments leads again to Eq. (16). This equation is now coupled to the corresponding equation for the age concentration in the sediment layer. Introducing the mean transport age of the marked fractions of the freshly deposited sediments of each class

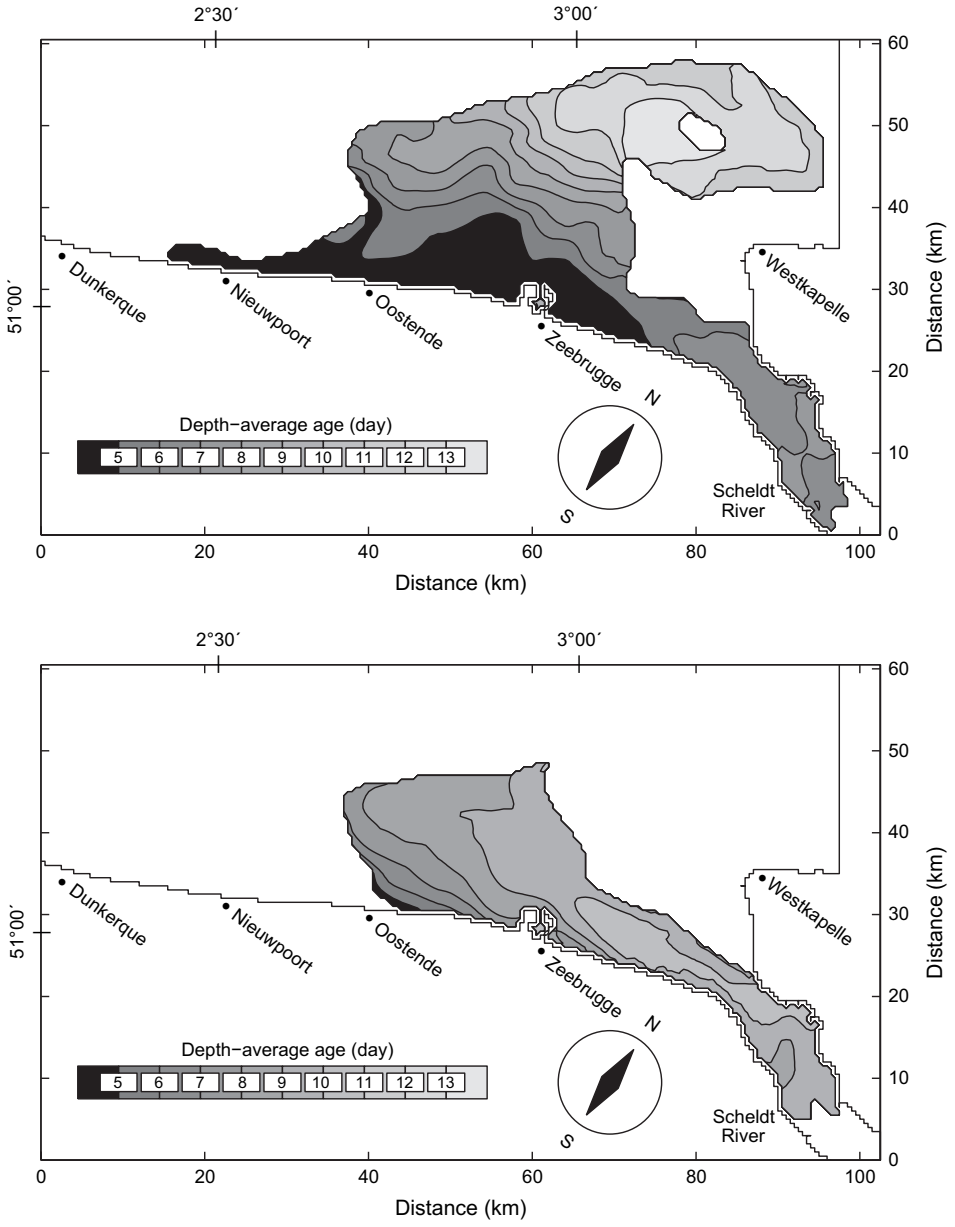

Fig. 3. Depth-average mean resuspension age (day) of sediment from class I on 14th February 1993 at 12 h (top panel) and on 27th February 1993 at 14 h (bottom panel).

$$a_s^i(t,\mathbf{x}) = \frac{\alpha_s^i(t,\mathbf{x})}{\tilde{C}_s^i(t,\mathbf{x})} \tag{20}$$

one has indeed

$$\frac{\partial \alpha_s^i}{\partial t} = \tilde{C}_s^i + F^i_{\alpha,\mathrm{sed}} - F^i_{\alpha,\mathrm{ero}} \tag{21}$$

where $F^i_{\alpha,\mathrm{sed}}$ and $F^i_{\alpha,\mathrm{ero}}$ denote the age concentration fluxes corresponding to the sedimentation and the erosion fluxes. These fluxes account for the exchange of age content between the water column and the bottom layer and couple Eqs. (16) and (21) through the bottom boundary condition

$$\left[(\mathbf{v}+\mathbf{w}_s^i)\alpha^i - \mathbf{K}\cdot\nabla\alpha^i\right]\cdot\mathbf{n} = F^i_{\alpha,\mathrm{sed}} - F^i_{\alpha,\mathrm{ero}} \tag{22}$$

Appropriate parameterisations of the sedimentation and erosion fluxes $F^i_{\alpha,\mathrm{sed}}$ and $F^i_{\alpha,\mathrm{ero}}$ of the age concentrations of the marked sediments can be obtained under the natural assumption that the marked material behaves exactly in the same way as the total suspended matter and that the particles settle on the bottom or are put back in the water column with their age. One has

$$F^i_{\alpha,\mathrm{ero}} = a_s^i \tilde{F}^i_{\mathrm{ero}} = \frac{\alpha_s^i}{C_s^i} F^i_{\mathrm{ero}} \tag{23}$$

and

$$F^i_{\alpha,\mathrm{sed}} = a_b^i \tilde{F}^i_{\mathrm{sed}} = \frac{\alpha_b^i}{C_b^i} F^i_{\mathrm{ero}} \tag{24}$$

where a_b^i and α_b^i denote, respectively, the mean age and the age concentration of the marked sediment at the bottom of the water column.

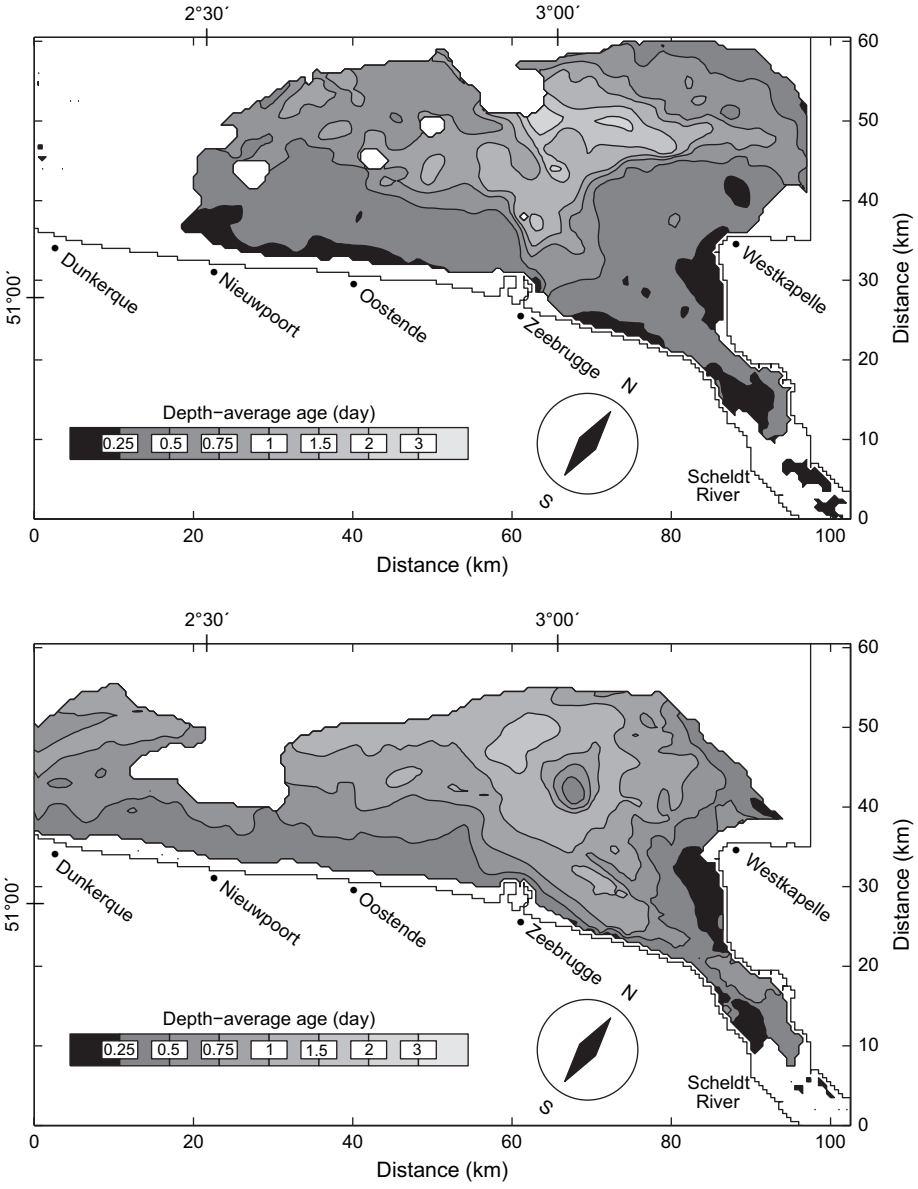

Fig. 4. Depth-average mean resuspension age (day) of sediment from class IV on 14th February 1993 at 12 h (top panel) and on 27th February 1993 at 14 h (bottom panel).

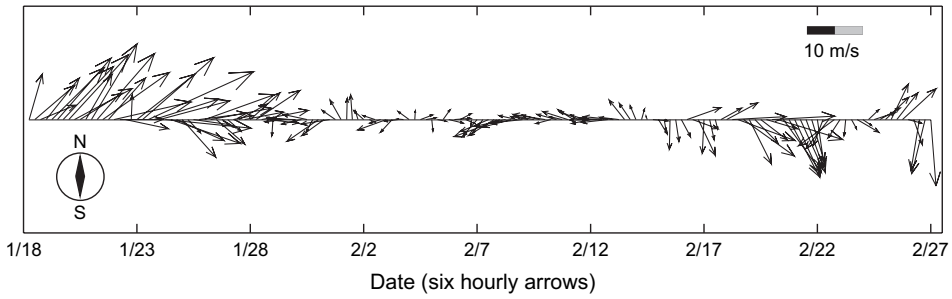

Fig. 5. Wind vectors during the simulation period.

The transport ages computed for sediments of class I and IV on the 27th of February 1993 are shown in Fig. 6.

From Dunkerque to Oostende and at offshore locations, the transport of both types of sediments occur at similar rates: the mean transport age of the material offshore Zeebrugge reaches about 15 days for both sediment types. Differences appear for more coastal waters around Zeebrugge and in the Scheldt estuary. The transport of Channel material into the Scheldt

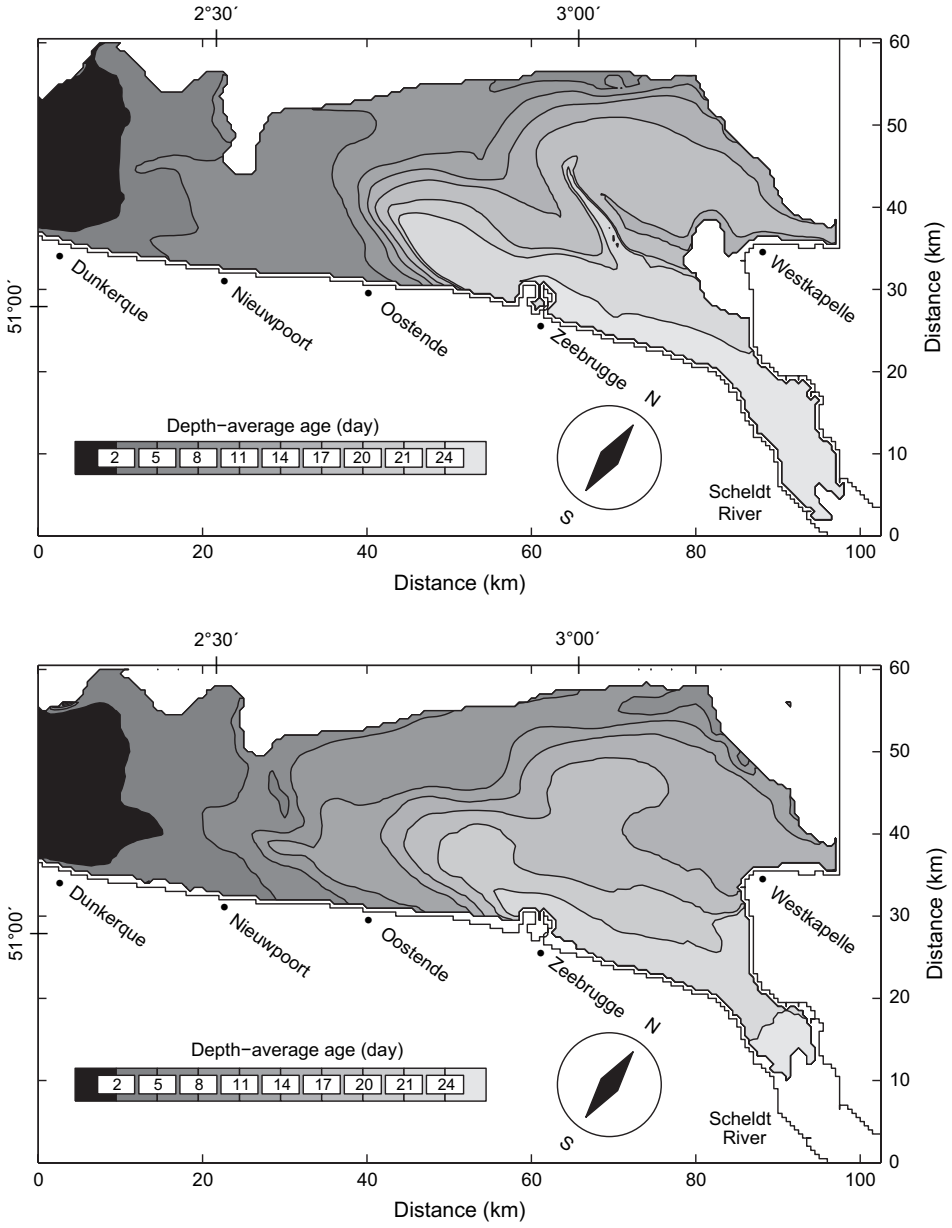

Fig. 6. Depth-average mean transport age (day) of sediment from class I (top panel) and class IV (bottom panel) on the 27th February 1993 (14 h).

estuary seems less efficient for fine sediments than for coarse sediments with transport age of, respectively, about 25 days and 21 days. Similarly, fine sediments from the English Channel hardly influence the shallow areas around Westkapelle while coarse grain mud with a transport age of 25–20 days (from the chosen origin) is found at these locations.

The different behaviors and transport routes/rates of the two types of sediments considered here are related to complex interactions between the vertical motions in the water column (and the settling on the bottom) and the horizontal circulation. For instance, the higher transport age of sediments of type I around Zeebrugge and the larger horizontal gradient between Zeebrugge and Oostende are clearly related to the fact that the incoming SPM flux from the source region has to face the adverse residual circulation flowing from the Scheldt along the coast towards Oostende. Since sediments of class I behave more like dissolved tracer, their movements towards Zeebrugge strongly rely on (moderately slow) diffusion. For class IV sediments, the differential advection between ebb and flood with possible deposition–resuspension events constitutes a more efficient mechanism to transport SPM against the residual flow.

7. Conclusions

Both the resuspension and horizontal transport of sediments can be studied using the Constituent-oriented Age and Residence time Theory. The application of this theory allows the computation of the transport rates of mud in the coastal zone as a function of the characteristics of the sediments.

The different transport routes and transport rates of the different sediment classes are likely to play a significant part in the transport of attached pollutants. For instance, while cadmium and copper tend to exhibit an inverse relationship with salinity, suggesting that these heavy metals behave like dissolved tracer, the more 'particle reactive' mercury becomes rapidly associated with particulate matter. The resulting transport rate and dispersion of mercury in the coastal environment will therefore be strongly affected by its partition between sediments of the different size classes considered here. Future work will therefore be devoted to the characterization of the transport of sediments and its influence on the spreading of contaminants.

Acknowledgements

E.J.M. Delhez is an Honorary Research Associate with the Belgian National Fund for Scientific Research (F.N.R.S.). Dries Van den Eynde is thanked for providing the wave data. Part of this work was supported by the French Community of Belgium (RACE, ARC-05/10-333). This is MARE publication n° 111.

References

Aberle, J., Nikora, V., Walters, R., 2004. Effects of bed material properties on cohesive sediment erosion. Marine Geology 207, 83–93.

Arakawa, A., Lamb, V.R., 1977. Computational design of the basic dynamical processes of the UCLA general circulation model. Methods in Computational Physics 17, 173–265.

Ariathurai, C.R., 1974. A Finite Element Model for Sediment Transport in Estuaries. Ph.D. thesis, University of California, Davis, CA.

Beckers, J.-M., Deleersnijder, E., 1993. Stability of a FBTCS scheme applied to the propagation of shallow-water inertia-gravity waves on various space grids. Journal of Computational Physics 108, 95–104.

Berlamont, J., Ockenden, M., Toorman, E., Winterwerp, J., 1993. The characterisation of cohesive sediment properties. Coastal Engineering 21, 105–128.

Bijker, E.W., 1966. The increase of bed shear in a current due to wave motion. In: Proceedings of the 10th Conference on Coastal Engineering, Tokyo, pp. 746–765.

Blumberg, A.F., Mellor, G.L., 1983. Diagnostic and prognostic numerical calculation studies of the south atlantic bight. Journal of Geophysical Research 88, 4579–4592.

Blumberg, A.F., Mellor, G.L., 1987. A description of a three-dimensional coastal ocean circulation model. In: Heaps, N. (Ed.), Three-dimensional Coastal Ocean Models, Coastal and Estuarine Science, vol. 4. American Geophysical Union, Washington DC, pp. 1–16.

Cancino, L., Neves, R., 1999. Hydrodynamic and sediment suspension modelling in estuarine systems. Part I: description of the numerical models. Journal of Marine Systems 22, 105–116.

Deleersnijder, E., Campin, J.-M., Delhez, E.J.M., 2001. The concept of age in marine modelling: I. Theory and preliminary model results. Journal of Marine Systems 28, 229–267.

Delhez, E.J.M., Martin, G., 1992. Preliminary results of 3-D baroclinic numerical models of the mesoscale and macroscale circulations on the North-western European Continental Shelf. Journal of Marine Systems 3, 423–440.

Delhez, E.J.M., 1996a. Reconnaissance of the general circulation of the North-western European continental shelf by means of a three-dimensional turbulent closure model. Earth-Science Reviews 41, 3–29.

Delhez, E.J.M., 1996b. On the residual advection of passive constituents. Journal of Marine Systems 8, 147–169.

Delhez, E.J.M., Campin, J.-M., Hirst, A.C., Deleersnijder, E., 1999a. Toward a general theory of the age in ocean modelling. Ocean Modelling 1, 17–27.

Delhez, E.J.M., Grégoire, M., Nihoul, J.C.J., Beckers, J.-M., 1999b. Dissection of the GHER turbulent closure scheme. Journal of Marine Systems 21, 379–397.

Delhez, E.J.M., Carabin, G., 2001. Integrated modelling of the Belgian Coastal Zone. Estuarine, Coastal and Shelf Science 53, 477–491.

Delhez, E.J.M., Deleersnijder, E., 2002. The concept of age in marine modelling: II. Concentration distribution function in the English Channel and the North Sea. Journal of Marine Systems 31, 279–297.

Estournel, C., Kondrachoff, V., Marsaleix, P., Vehil, R., 1997. The plume of the Rhone: numerical simulation and remote sensing. Continental Shelf Research 17, 899–924.

Fettweis, M., Van den Eynde, D., 2003. The mud deposits and the high turbidity in the Belgian–Dutch coastal zone, southern bight of the North Sea. Continental Shelf Research 23, 669–691.

Fredsøe, J., 1993. Modelling of non-cohesive sediment transport processes in the marine environment. Coastal Engineering 21, 71–103.

Gerritsen, H., Vos, R.J., van der Kaaij, T., Laneand, A., Boon, J.G., 2000. Suspended sediment modelling in a shelf sea (North Sea). Coastal Engineering 41, 317–352.

Gerritsen, H., Boon, J.G., van der Kaaij, T., Vos, R.J., 2001. Integrated modelling of suspended matter in the North Sea. Estuarine, Coastal and Shelf Science 53, 581–594.

Hayter, E.J., Gu, R., 2001. Prediction of contaminated sediment transport in the Maurice River-union Lake, New Jersey, USA. In: McAnally, W.H., Mehta, A.J. (Eds.), Coastal and Estuarine Fine Sediment Processes. Elsevier, Amsterdam, pp. 439–458.

Holt, J.T., James, I.D., 1999. A simulation of the southern North Sea in comparison with measurements from the North Sea project part 2 suspended particulate matter. Continental Shelf Research 19, 1617–1642.

James, I.D., 1996. Advection schemes for shelf sea models. Journal of Marine Systems 8, 237–254.

Jiang, W., Pohlmann, T., Sündermann, J., Feng, S., 2000. A modelling study of SPM transport in the Bohai sea. Journal of Marine Systems 24, 175–200.

de Kok, J.M., de Valk, C., van Kester, J.H.Th.M., de Goede, E., Uittenbogaard, R.E., 2001. Salinity and temperature stratification in the Rhine plume. Estuarine, Coastal and Shelf Science 53, 467–475.

Krone, R.B., 1962. Flume Studies of the Transport of Sediment in Estuarial Shoaling Processes. Final Report. Hydraulic Engineering Laboratory And Sanitary Engineering Research Laboratory, University of California, Berkeley.

Kuhrts, C., Fennel, W., Seifert, T., 2004. Model studies of transport of sedimentary material in the western Baltic. Journal of Marine Systems 52, 167–190.

Lin, B., Falconer, R.A., 1996. Numerical modelling of three-dimensional suspended sediment for estuarine and coastal waters. Journal of Hydraulic Research, IAHR 34, 533–556.

Liu, J.T., Chao, S.-Y., Hsu, R.T., 2002a. Numerical modelling study of sediment dispersal by a river plume. Continental Shelf Research 22, 1745–1773.

Liu, W.-C., Hsu, M.-H., Kuo, A.Y., 2002b. Modelling of hydrodynamics and cohesive sediment transport in Tanshui river estuarine system, Taiwan. Marine Pollution Bulletin 44, 1076–1088.

Lumborg, U., Windelin, A., 2003. Hydrography and cohesive sediment modelling: application to the RømøDyb tidal area. Journal of Marine Systems 38, 287–303.

Lumborg, U., 2004. Modelling the deposition, erosion and flux of cohesive sediment through Øresund. Journal of Marine Systems 56, 179–193.

Lumborg, U., Pejrup, M., 2005. Modelling of cohesive sediment transport in a tidal lagoon–an annual budget. Marine Geology 218, 1–16.

Madala, R.V., Piacsek, S.A., 1977. A semi-implicit numerical model for baroclinic oceans. Journal of Computational Physics 23, 167–178.

McManus, J.P., Prandle, D., 1997. Development of a model to reproduce observed suspended sediment distributions in the southern North Sea using principal component analysis and multiple linear regression. Continental Shelf Research 17, 761–778.

Mehta, A.J., 1989. On estuarine cohesive sediment suspension behavior. Journal of Geographical Research 94 (C10), 14303–14314.

Morris, A.W., Howarth, M.J., 1998. Bed stress induced sediment resuspension (SERE 88/89). Continental Shelf Research 18, 1203–1213.

Mulder, H.P.J., Udink, C., 1991. Modelling of cohesive sediment transport. A case study: the western Scheldt estuary. In: Edge, B.L. (Ed.), Proceedings of the 22nd International Conference on Coastal Engineering. American Society of Civil Engineers, New York, pp. 3012–3023.

Nihoul, J.C.J., Hecq, J.-H., 1984. Influence of the residual circulation on the physico-chemical characteristics of water masses and the dynamics of ecosystems in the Belgian Coastal Zone. Continental Shelf Research 3, 167–174.

Nihoul, J.C.J., Deleersnijder, E., Djenidi, S., 1989. Modelling the general circulation of shelf seas by 3D $k-\varepsilon$ models. Earth-Science Reviews 26, 163–189.

Pandoe, W.W., Edge, B.L., 2004. Cohesive sediment transport in the 3D-hydrodynamic-baroclinic circulation model: study case for idealized tidal inlet. Ocean Engineering 31, 2227–2252.

Parchure, T.M., Mehta, A.J., 1985. Erosion of soft cohesive sediment deposits. Journal of Hydraulic Engineering 111, 1308–1326.

Partheniades, E., 1965. Erosion and deposition of cohesive soils. Journal of the Hydraulics Division Proceedings of the ASCE 91 (HY1), 105–139.

Periáñez, R., 2005. Modelling the transport of suspended particulate matter by the Rhone river plume (France). Implications for pollutant dispersion. Environmental Pollution 133, 351–364.

Phillips, N.A., 1957. A coordinate system having some special advantages for numerical forecasting. Journal of Meteorology 14, 184–185.

Ribbe, J., Holloway, P., 2001. A model of suspended sediment transport by internal tides. Continental Shelf Research 21, 395–422.

Sanford, L.P., Halka, J.P., 1993. Assessing the paradigm of mutually exclusive erosion and deposition of mud, with examples from upper Chesapeake Bay. Marine Geology 114, 37–57.

Sanford, L.P., Maa, J.P.-Y., 2001. A unified erosion formulation for fine sediments. Marine Geology 179, 9–23.

Sweby, P.K., 1984. High resolution schemes using flux limiters for hyperbolic conservation laws. SIAM Journal on Numerical Analysis 21, 995–1011.

Teisson, C., Ockenden, M., Le Hir, P., Kranenburg, C., Hamm, L., 1993. Cohesive sediment transport processes. Coastal Engineering 21, 129–162.

Van den Eynde, D., 1992. MU-WAVE: an operational wave forecasting system for the Belgian coast. In: Proceedings of the Third International Workshop on Wave Hindcasting and Forecasting, May 19–22, Montreal, Canada. Atmospheric Environment Service, Downsview, Ontario, Canada, pp. 313–324.

Van den Eynde, D., Ozer, J., 1993. Sediment-trend-analyse: calculation of the sediment transport by the use of a mathematical model. In: Report BMM/STA/TR01 Study Executed in Charge of HAECON. Management Unit of the North Sea Mathematical Model, Brussels, pp. 76 (in Dutch).

Van den Eynde, D., 2004. Interpretation of tracer experiments with fine-grained dredging material at the Belgian continental shelf by the use of numerical models. Journal of Marine Systems 48, 171–189.

Van der Molen, J., 2002. The influence of tides, wind and waves on the net sand transport in the North Sea. Continental Shelf Research 22, 2739–2762.

Whitehouse, R.J.S., Soulsby, R.L., Roberts, W., Mitchener, H.J., 2000. Dynamics of Estuarine Muds. HR Wallingford Limited and Thomas Telford Limited, pp. 210.

Winterwerp, J.C., 2002. On the flocculation and settling velocity of estuarine mud. Continental Shelf Research 22, 1339–1360.

You, Z.-J., 2004. The effect of suspended sediment concentration on the settling velocity of cohesive sediment in quiescent water. Ocean Engineering 31, 1955–1965.

Yu, C., Berlamont, J., Embrechts, H., Roose, D., 1998. Modelling coastal sediment transport on a parallel computer. Physics and Chemistry of the Earth 23, 497–504.

Available online at www.sciencedirect.com
ScienceDirect
Estuarine, Coastal and Shelf Science 74 (2007) 684–696
ESTUARINE COASTAL AND SHELF SCIENCE
www.elsevier.com/locate/ecss

Transport timescales for identifying seasonal variation in Bass Strait, south-eastern Australia

Paul A. Sandery [a,b,*], Jochen Kämpf [a]

[a] School of Chemistry, Physics and Earth Sciences, Flinders University Adelaide–Australia, GPO Box 2100, Adelaide, SA 5001, Australia
[b] Marine and Ocean Forecasting Group, Bureau of Meteorology, GPO Box 1289, Melbourne, Vic. 3001, Australia

Received 19 April 2006; accepted 9 May 2007
Available online 19 July 2007

Abstract

A three-dimensional σ-coordinate ocean model with realistic forcing is used to derive and compare flushing time, residence time and water age distributions in Bass Strait, a broad shallow shelf sea in south-eastern Australia which exhibits seasonal variation in water mass properties and circulation. Results illustrate flushing out of most old water occurs each winter–spring period and the circulation in summer increases age of remnant older water in the Strait. A correlation between water age and salinity is found in winter which is the result of advective "erosion" of the interior water mass. The presence of an area in the south-eastern part of the interior with low flushing is suggested to result from a number of physical factors including the presence of quasi-stationary eddies which entrain age, leading to relatively older water residing there.

Keywords: water age; flushing time; residence time; water mass; tracers

1. Introduction

Hydrodynamic models are routinely used to predict flushing of water bodies or dispersion of toxic materials, such as those introduced by oil spills or outfalls, which may expose ecosystems to contamination. Methods include the use of transport timescales such as flushing times, residence times and more recently water age. With these methods, variation of water mass or variation of individual constituents which comprise seawater, such as pure water, suspended matter, dissolved gases and solids, pollutants, contaminants and biota can be studied.

Transport timescales in general provide summaries of advective and diffusive transport processes and can be used to highlight variability in the distribution of important properties critical to marine ecosystems and climate such as temperature, salinity, chlorophyll *a*, macro- and micronutrients and dissolved O_2 and CO_2. Many case studies exist where transport timescales have been used to trace water mass and estimate ventilation rates in the deep ocean (England, 1995; Karstensen and Tomczak, 1998; Hirst, 1999; Deleersnijder et al., 2002) or to investigate circulation in semi-enclosed seas and estuaries (Oliviera and Baptista, 1997; Walker, 1999; Delhez and Deleersnijder, 2002; Monsen et al., 2002; Sadrinasab and Kämpf, 2004; Sandery and Kämpf, 2005).

Timescale measurements can be made using either a Lagrangian or an Eulerian tracer in a numerical model and found using arbitrary boundaries which delimit a control region of interest. There are advantages and disadvantages to both which are discussed in Section 2.2. The placement of the boundaries to define a region of interest is an arbitrary choice, and will influence absolute values of the timescales. To some extent, the timescale distributions in the system are relative by nature and similar patterns will be seen regardless of the location of the boundary.

Flushing time of a volume of seawater is usually the time taken for most or all of the constituents to be overturned or replaced with water from outside the volume (Takeoka,

* Corresponding author. Present address: Marine and Ocean Forecasting Group, Bureau of Meteorology, GPO Box 1289, Melbourne, Vic. 3001, Australia.
E-mail address: p.sandery@bom.gov.au (P.A. Sandery).

0272-7714/$ - see front matter © 2007 Elsevier Ltd. All rights reserved.
doi:10.1016/j.ecss.2007.05.011

1984; Zimmerman, 1988; Monsen et al., 2002; Sadrinasab and Kämpf, 2004). The e-folding flushing time is typically used as an estimate of the mean flushing time (Delhez et al., 2004). This is defined as the time taken for tracer concentration to drop to $1/e$ of its initial concentration. This definition used in a number of previous studies (Walker, 1999; Monsen et al., 2002; Sandery and Kämpf, 2005) and adhered to in this study. Local flushing times for sub-volumes of a control region can only be defined with respect to the control region itself. The scale of smallest sub-volumes within the region of interest is also somewhat arbitrary and influences the resolution of the timescale distribution. This scale is best defined at model grid resolution.

Residence time can be defined as the time taken for a water parcel or introduced material to leave a region (Takeoka, 1984; Delhez et al., 2004; Delhez, 2006). Material can be introduced to the region by either point or diffuse sources. Residence time and flushing time are the same in the integral sense, i.e. when distributions are summed and averaged over an entire volume. If tracer concentration decreases with time according to $m(t) = m(0)e^{-t/\tau f}$, where m is tracer mass, t is time and τ_f is flushing time, then mean flushing time is equal to mean residence time (Delhez et al., 2004). While integral timescales are useful for comparing and classifying different systems, their relevance is limited to steady state cases with strong mixing and they potentially misrepresent transport processes (Oliviera and Baptista, 1997). The distribution of a timescale, or its local variation, within a region of interest provides additional information, and can be used to determine the ''advection–diffusion'' climate of the system (Monsen et al., 2002). This may be more important from an ecological point of view.

Age is a property of each constituent and can be used to trace movements and variations of constituents within (or away from) a region of interest. The age of a constituent or water parcel can be defined as the time since it entered the region or was last exposed to the region (England, 1995; Karstensen and Tomczak, 1998; Delhez et al., 1999; Hirst, 1999; Deleersnijder et al., 2001, 2002; Delhez and Deleersnijder, 2002; Monsen et al., 2002; Deleersnijder and Delhez, 2004; Hall and Haine, 2004). Deleersnijder et al. (2001) derive an age concentration function which accounts for advection, diffusion, production and destruction of constituents. Production and destruction can be ignored when considering the age of the pure water fraction of seawater laterally transported into the region of interest. In this case water age is governed only by advection and diffusion and can be described by the following Eulerian age equation:

$$\frac{\partial A}{\partial t} = K_{\mathrm{H}}\nabla^2 A + K_{\mathrm{V}}\frac{\partial^2 A}{\partial z^2} - A(\nabla \cdot V) + S_{\mathrm{A}}$$

where A is age, t is time, K_{H} and K_{V} are horizontal and vertical turbulent diffusivity coefficients, S_{A} is a source term equal to unity. V is a three-dimensional velocity vector and ∇ is the gradient operator. The limitation of using such an equation is that age distribution in a control volume cannot properly be accounted for. Solutions would only be able to represent statistical averages. In this study we use a novel alternative approach and derive a time-varying age distribution with a simple method using Lagrangian particles.

All constituents in a region have different ages according to the time they enter the region (or were last exposed to the region) through some boundary to that region. Age is both a property of the constituent and a function of its pathway. The spatial age distribution in a control region can be used to identify age-fronts, which may delimit different water masses. By examining the time varying spatial age distribution in a control region, the sources and sinks of the control region can be identified and the question of where the oldest water resides in the control region becomes answerable.

In steady state flow, local or integral transport timescales could be assessed by single release of a tracer concentration field with even distribution in the region of interest, at any time, provided a suitable period is allowed for the turnover of the mass or volume of the system. To understand variation in a non-stationary system, such as one which exhibits seasonal variation, the use of release time dependent tracer concentration fields is required (Oliviera and Baptista, 1997). In this case, tracer should be released at appropriate time intervals. This is similar to prescribing a suitable sampling frequency. For example, seasonal variation in flushing could be captured by release of independent tracer fields in the region of interest at monthly to quarterly intervals.

In general, differences that occur between timescales stem from their definitions, which imply different initial and boundary conditions. Differences may be better understood by considering which statistics form part of the respective timescale distributions. Neither material entering, leaving or outside the control region is part of the age distribution in the control region. Only material leaving a control region forms the residence time distribution, that entering or inside is not part of it (Takeoka, 1984). Flushing time distribution is similar to residence time distribution in this sense because it cannot be found until flushing times for all sub-volumes of a control region are obtained.

1.1. Background physical characteristics

Bass Strait is a broad, relatively shallow shelf-sea connecting the southeast Indian Ocean in the west with the Tasman Sea in the east and is located between Tasmania and Victoria in Australia (Fig. 1). The Strait's mean depth is between 50–70 m and abyssal depths on either side are around 5 km. Oceanic margins are characterised by shelf-break and continental slope incised by submarine canyons. Entrances to the Strait feature sills and island groups. The centralised basin has maximum average depth of around 100 m. The Strait has a reputation for large complex swell patterns, high winds and strong tidal currents (Jones, 1980).

A confluence of different water masses occurs in the region, which influences ecological processes and water mass in Bass Strait (Fig. 2). The East Australian Current (EAC) is a western boundary current which transports between minimum of 7 Sv and maximum of 16 Sv in winter and summer, respectively, southwards between 23°S and 43°S off eastern Australia

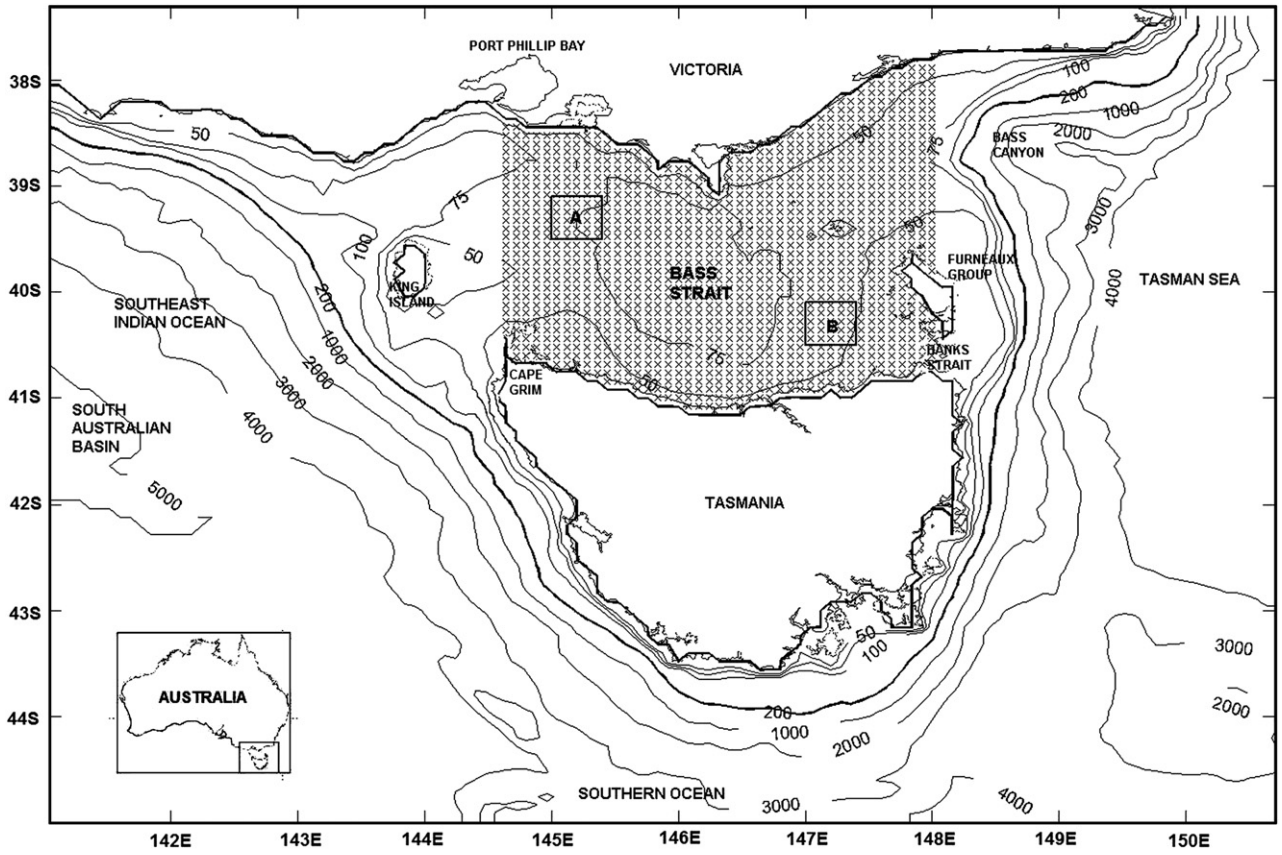

Fig. 1. Model domain and bathymetry (model is limited to maximum 1000 m depth). Model coastline (heavier line) shown to illustrate fitting of model to the region. Area within Bass Strait marked with crosses at model grid resolution is arbitrarily defined control region of interest for transport timescales. Areas A and B are used to illustrate age distributions at different times of year. Coastline and bathymetric data source: Geoscience Australia, 2002.

(Ridgway and Godfrey, 1997) (1 Sverdrup (Sv) = 10^6 m^3 s^{-1}). There may be periodic intrusions into north-eastern Bass Strait (Newell, 1960); however, this is not well documented. For at least 6 months of the year, around the austral winter season, the South Australian Current (SAC) moves relatively saltier-warmer water eastward along the southern Australian shelf from the Great Australian Bight to western Bass Strait. This current bifurcates near 39°S, 143°E with one extension

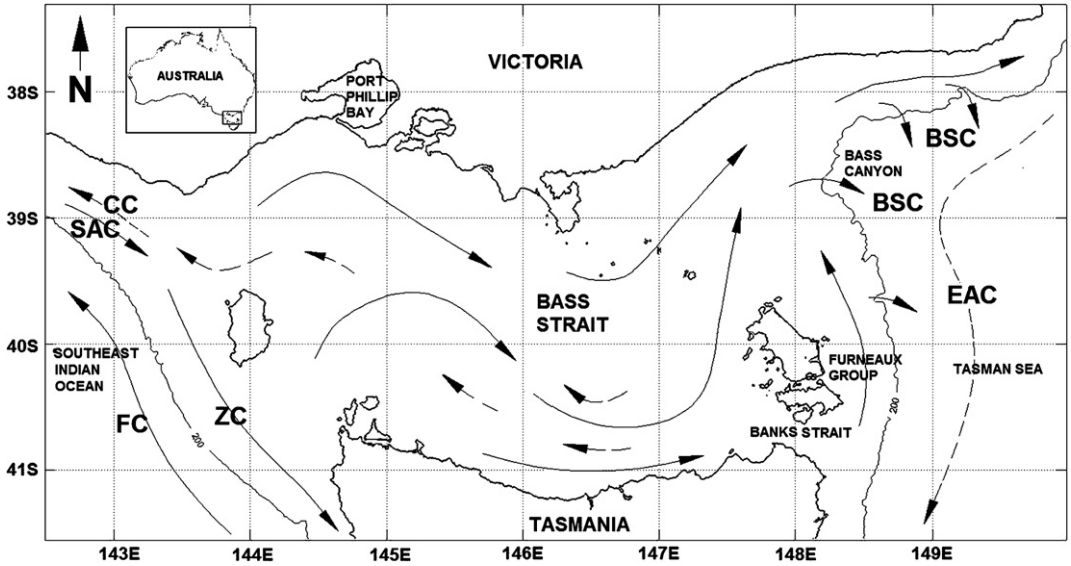

Fig. 2. Schematic representation of currents in region. Dashed arrows denote summer currents. Shelf break depth (200 m isobath) is indicated. Bathymetric data source: Geoscience Australia, 2002. Adapted and modified from the following: EAC, East Australian Current (Ridgway and Godfrey, 1997); SAC, South Australian Current (Ridgway and Condie, 2004); ZC, Zeehan Current (Baines et al., 1983); FC, Flinders Current (Bye, 1983; Middleton and Cirano, 2002); CC, summer Coastal Current (Kämpf et al., 2004).

moving into Bass Strait and one becoming the Zeehan Current (ZC) off western Tasmania. The ZC is about 40 km wide and 50 m deep and transports about 1 Sv (Baines et al., 1983). This is a small part of the longest known coastal current system, a seasonal linkage of the Leeuwin, South-Australian and Zeehan Currents, beginning on the northwest shelf of Australia and finishing off eastern Tasmania (Ridgway and Condie, 2004). The Flinders Current (FC) transports fresher-cooler water, from the surface to depths of ~800 m along the continental slope, in a northwest direction from off western Tasmania as far west as Cape Leeuwin in Western Australia (Bye, 1983; Middleton and Cirano, 2002). The coastal current (CC) is part of a summer coastal upwelling system, resulting from regular south-easterly winds (Kämpf et al., 2004), and is associated with low sea-level anomalies, at this time of year, along parts of the southern shelf of Australia.

In winter, dense water forms in the Strait and flows down the eastern continental slope to depths of between 300–400 m. This density current is known as the Bass Strait Cascade (BSC) (Boland, 1971; Godfrey et al., 1980; Tomczak, 1985, 1987; Gibbs et al., 1991; Luick et al., 1994).

Currents within Bass Strait are primarily driven by tides, winds, incident continental shelf waves and density driven flows (Brodie and Radok, 1970; Fandry, 1982, 1983; Baines and Fandry, 1983; Baines et al., 1983; McIntosh and Bennett, 1984; Fandry et al., 1985; Middleton and Viera, 1991; Hannah, 1992; Middleton and Black, 1994; Sandery and Kämpf, 2005). These phenomena work sea level anomalies at either end of the channel, causing pressure gradients. The external Rossby radius is of the order of the Strait width (250–300 km) and geostrophy plays a significant part in the production of currents in the Strait. Residual throughflow is governed mainly by mean sea levels at the western and eastern entrances. On average, a summer current system may be present in the Strait for up to ~1/3 of the year brought about by mean southerly winds but this is unclear and not well documented (Gibbs et al., 1986; Tomczak, 1987). For the remainder of the year mean westerly winds drive zonal eastward residual throughflow. The extent and influence of currents and water masses varies seasonally and inter-annually. Water mass properties in the Strait are influenced by local air-sea heat-salt/freshwater fluxes and properties carried by inflow mostly from the west (Tomczak, 1985, 1987; Herzfeld and Tomczak, 1997). Shallow regions surrounding the island groups and in the Strait entrances are usually well mixed vertically throughout the year. Waters in the deeper interior are well mixed vertically for up to 6 months of the year (Baines and Fandry, 1983; Gibbs et al., 1986). Stratification has seasonal variation over a large part of the interior. In summer, a shallow warmer (by up to 4 °C) surface mixed layer up to 30–40 m deep may be present. Wind-stress controls levels of vertical mixing in the interior, where tidal influence is small, and affects seasonal onsets and breakdowns of stratification.

The aim of this study is to derive and compare flushing time, residence time and age distributions for Bass Strait, from realistic model simulations, to gain an understanding of seasonal variation of residual circulation and hydrographic properties. The bathymetry of the region and the extent of the model domain is shown in Fig. 1. An arbitrarily chosen control region of interest for finding timescale distributions is indicated with crosses at model horizontal grid resolution. Model coastline (heavier line) is plotted to illustrate how the model fits within the region. Two areas A and B, which are 5×5 horizontal grid cells are used to illustrate age distributions at different times of year.

2. Methods

2.1. Model description

In this study we use COHERENS, a coupled hydrodynamic and ecological model for regional and shelf seas (Luyten et al., 1999). This has been developed into a regional model for south-eastern Australia and Bass Strait. COHERENS is a three-dimensional primitive equation σ-coordinate finite-difference numerical model which is coupled to biological, optical and sediment transport modules. Only the hydrodynamic aspect of the model is used here. The model has been extensively tested and used in estuarine and regional case studies (Umgiesser et al., 2002; Marinov et al., 2006). The model is public domain and a full description with sensitivity studies and test cases can be found in Luyten et al. (1999). The model is configured in the following way to resolve physical processes characteristic of the region. The model uses a spherical Arakawa C grid with variable Coriolis parameter. Sub-grid scale horizontal turbulent diffusion of momentum, heat, salt and Eulerian tracer is parameterized using the Smagorinsky formulation which accounts for current shear and horizontal grid scale. Advection of momentum and scalar quantities is found using a Total Variation Diminishing scheme with Superbee limiter for regions with strong current shear (Luyten et al., 1999). This method has been found to be stable over long simulations (40 years) (Sadrinasab and Kämpf, 2004). Vertical turbulent diffusion is parameterised with the $\kappa - \varepsilon$ (mixing length – dissipation rate) second order turbulence closure scheme which employs an implicit time scheme. The model uses the general equation of state of seawater defined by the Joint Panel on Oceanographic Tables and Standards (UNESCO, 1981). Bathymetric data was acquired from the 0.01 degree resolution *Geoscience Australia Bathymetry and Topography Grid* (2002). This was interpolated onto a 0.08 degree grid, which is the horizontal resolution of the model. The bathymetry was smoothed so that slopes were less than or equal to 0.1. This assists in satisfying hydrostatic consistency and minimising pressure gradient errors (Haney, 1990). The model grid has 128 x 96 x 5 grid points in the λ, φ, and σ directions respectively. Here λ refers to longitude, φ to latitude and σ to vertical sigma level. Five vertical sigma levels was a compromise to maximise model efficiency with relatively fine lateral resolution and long simulation times. Shorter simulations with 20 sigma levels yielded similar results (not shown). Reference λ and φ are 141°E and 45°S, which define the bottom left corner of the model domain (Fig. 1). The model has a minimum depth of 20 m and

a maximum depth of 1000 m. Bottom friction is calculated based on a roughness length of 8 mm. The model uses a two-dimensional barotropic mode time step of 30 s, which satisfies the Courant–Friedrichs–Lewy condition, and a three-dimensional baroclinic mode time step of 300 s. A simulation of 2 years in length is carried out, starting 1 January. A suitable period for determining the length of a flushing/residence time simulation is a period about twice the length of the flushing/residence timescale itself (Deleersnijder et al., 2001; Delhez and Deleersnijder, 2002). Two years simulation time is sufficient to find the flushing/residence times of the tracer/particles released towards end of the first year.

The initial density field and time-dependent three-dimensional open boundary profiles are established using the *CSIRO Climatological Atlas of Regional Seas* (CARS) atlas (Dunn and Ridgway, 2002; Ridgway et al., 2001). Incoming water mass properties are defined at every model time step using CARS annual and semi-annual harmonics. Atmospheric forcing data supplied to the model consists of spatially varying surface wind stress, relative humidities, precipitation and air temperatures from *NCEP reanalysis* monthly long-term means (Kalnay et al., 1996). NCEP reanalysis data is provided on a global $2.5^\circ \times 2.5^\circ$ horizontal grid and represents the period 1968–1998. NCEP monthly long-term mean wind speed (which differs in magnitude from NCEP monthly long-term mean wind components) is used to force the latent and sensible heat fluxes. Fractional cloud cover was obtained from the *Arctic Ocean Model Intercomparison Project* (AOMIP) which provides long-term mean cloudiness ratio on a global $1.1^\circ \times 1.1^\circ$ horizontal grid. This was used in this study as it was the only available information of this type at the time the experiments and model were designed. The atmospheric forcing fields were temporally linearly interpolated at each time step in the model from month to month over the annual cycle. Two dimensional open-sea boundary forcing consisted of prescribed tidal sea-level amplitude and phase, for the M_2, S_2, O_1 and K_1 constituents, based on data from the *Australian National Tidal Centre* (NTC). Open boundaries are set a significant distance from the Strait to minimise their influence. Additional boundary forcing is added to generate a SAC and EAC because these are not generated in the model domain. This is in the form of a residual seasonally varying exponentially shaped sea surface which satisfies the external Rossby radius of deformation (Luyten et al., 1999). For the SAC an annual rise and fall in residual sea level at the northern end of the western open boundary from 0 cm in summer to 12 cm in winter is prescribed. For the EAC an annual fall and rise from 20 cm in summer to 0 cm in winter at the north-eastern open boundary corner is prescribed. Model tuning and verification was carried out by harmonic analysis of the tides and comparison of mean model salinities and temperatures with the CARS atlas.

2.2. Calculation of relevant transport timescales

To find distributions of flushing times, residence times and water age, we place a control region (Fig. 1) in the model. The same control region is applied irrespective of timescales or frames of reference. Eulerian tracer concentration fields are used for flushing times and Lagrangian particles are used for age and residence times. The number of particles used is 10,000. The use of particles requires a significant source population be continually available at the control region's open boundaries. Also, many need to be present in the control region at any moment for representations of the age or residence time distributions with statistical significance. One important difference between the two frames of reference is parameterisation of sub-grid scale mixing. Diffusion in the Lagrangian method is modelled using a Monte-Carlo or random walk method where particles are subjected to random motion with variance $\sigma^2 = 2K\Delta t$ where K is local diffusivity and Δt *is* model time step (Maier-Reimer and Sündermann, 1982). The Eulerian method models diffusion processes using the Smagorinsky scheme for sub-grid scale parameterization of horizontal turbulence. The Eulerian scheme contains finite-difference advection-diffusion conservation equations for transport of conservative tracer. If tracer is initialised at unit concentration at all cells in the model control region, then the tracer concentration field represents all mass in the volume of the control region. Change in concentration in a local cell represents change in mass with respect to the control region. Accompanying this change is an equal amount of mass leaving and new mass entering the control region. The Eulerian method offers advantages in terms of being a computationally efficient statistical representation of the mass distribution. Lagrangian tracers offer advantages over this approach if suitable amounts of particles are utilised. Computational effort is directed to areas where particles are concentrated, allowing sources and sinks to be represented and sharp fronts to be resolved (Luyten et al., 1999). The Eulerian finite difference method uses the resolution defined by the grid and is usually a coarser resolution than that needed to resolve frontal structures. This approach introduces smoothing of frontal structures and numerical dispersion into the solution.

The Lagrangian particle tracking scheme uses a recycling method which keeps the same original number of particles (10,000) in the model domain. Particles that leave the model domain are reinitialised at random locations at the sea surface in areas where the maximum depth is less than 200 m, inside and outside the control region. This generates a steady rain of source particles over the shelf in the model. This is useful because the circulation organises source particles from open boundaries to be concentrated in certain locations and there exists a need to continually introduce source material in areas where low concentrations exist, otherwise these areas would not be sampled often enough. The particles that rain on the control region are only used for residence times so that local cells in the control region have as many measurements as possible. Particles that rain on the control region are not used for age, even though they could be if we were considering age of constituents entering through the air-sea interface. Instead we are interested in age of external water mass coming into the control region through its open boundaries. Having suitable quantities of particles continually recycled through the system

is important for attempting to obtain statistically significant residence time and age measurements. Flushing time, residence time and age distributions are three-dimensional but have been depth-averaged in the analysis.

2.3. Flushing time

To calculate e-folding flushing times we use 12 different three-dimensional Eulerian tracer concentration fields. Each tracer field has a different release time which is at the beginning of each month during the first year of the simulation. All tracer concentration fields are initialised at unit concentration, in the control region shown in Fig. 1. Flushing times are calculated for each model grid cell in the control region. The 12 different tracer concentration fields produce 12 different flushing time distributions. Annual mean flushing times are calculated from the 12 different flushing time distributions. For summer mean flushing times we use tracer concentration fields released in December, January and February. For winter mean flushing times tracer concentration fields released during June, July and August are used.

2.4. Residence time

Residence times are found by measuring the time taken for particles emanating from sub-volumes or local cells to leave the control region. Particles already in the system which enter local cells laterally are used as well as particles that are randomly introduced into the local cells. Here, each local cell is defined to be each model horizontal grid scale water column. A distribution of residence times for each water column is found by re-running the loop of particle trajectories for every water column. Annual mean residence times for each water column are found by running through the full two year simulation of particle trajectories for each water column. The average of each distribution is the residence time that is gridded to produce an Eulerian map. Residence times dependent on release time either in the summer months or winter months are found by only tagging particles emanating from each water column in the respective seasons. Residence times are removed from the analysis if less than 25 samples per local cell are obtained.

2.5. Water age

Finding age distribution in the control region requires open boundaries act like sensors that turn on timers associated with new particles entering. Particles that leave the control region are not used for age. If particles re-enter they are considered new again. It is not possible to estimate initial ages of particles inside the control region, so it is necessary to ‘‘spin-up’’ the age distribution over the first part of the simulation. A spatial distribution is formed when there are many particles broadly distributed in the control region, however it is eventually lost if source particles are not available. Age distribution is mapped by gridding particle ages with respect to their irregular locations. The time varying age distribution is followed at every particle trajectory time step, which is every 24 h. The age distribution in the system takes about 6 months to spin up and is in constant transition, so seasonal mean age distributions for the final year of the simulation are presented.

3. Results and discussion

3.1. Tides, seasonal cycle of hydrographic properties and general circulation

Harmonic analysis of two years of model sea-level data was carried out to find the co-tidal amplitudes and phases for the M_2, O_2, S_1 and K_1 tides (Fig. 3). These are in agreement with NTC values (not shown) and previous studies (McIntosh and Bennett, 1984; Fandry et al., 1985). Relative errors are between 3–8%. The model resolves the characteristic M_2 standing wave and the locations of virtual amphidromic points, which are key features of the tides in the region.

Seasonal cycles of mean surface and bottom σ-layer temperature and salinity (averaged over the control region) predicted by the model are in reasonable agreement with corresponding mean CARS atlas values (Fig. 4), despite inherent uncertainties in both model and atlas data. Ten year model simulations carried out with the same configuration show that the second year of the simulation is close to steady state.

Model currents resulting from wind driven, tidal driven and remotely forced sea-level forcing are in close agreement with previous studies (Fandry, 1982, 1983; McIntosh and Bennett, 1984; Fandry et al., 1985; Middleton and Viera, 1991; Hannah, 1992; Middleton and Black, 1994).

Summer and winter depth-averaged salinity and current fields are presented in Fig. 5a and b. Salinity in summer reflects relatively high evaporation in northern Bass Strait, driven by model latent heat fluxes. This continues in the simulation in autumn and the salinity anomaly spreads further southward (not shown). In areas in the Strait Passages, such as in Banks Strait and north of the Furneaux Group, relatively strong vertical and horizontal tidal mixing acts to lower salinities. The salinity distribution in winter is a result of advective ‘‘erosion’’ of the field produced in summer by lateral transport into the region. Interestingly, the model predicts that the saltiest water in summer is in northern Bass Strait whereas the saltiest water in winter is in south-eastern Bass Strait.

3.2. Annual mean transport timescale distributions

The differences in transport timescale distributions can be accounted for by their different definitions, resolutions and parameterisations of mixing. It is emphasised that these transport timescales are different ways of viewing the same residual advection and diffusion for the 2-year simulation. Frequency distributions of all sampled ages, flushing times and residence times measured in the simulation are given in Fig. 6.

Annual mean and depth-averaged flushing time distribution (Fig. 7a) compares well with the annual age distribution (Fig. 7g). The oldest water on average is suggested by these results to reside in the south-eastern quadrant of the control

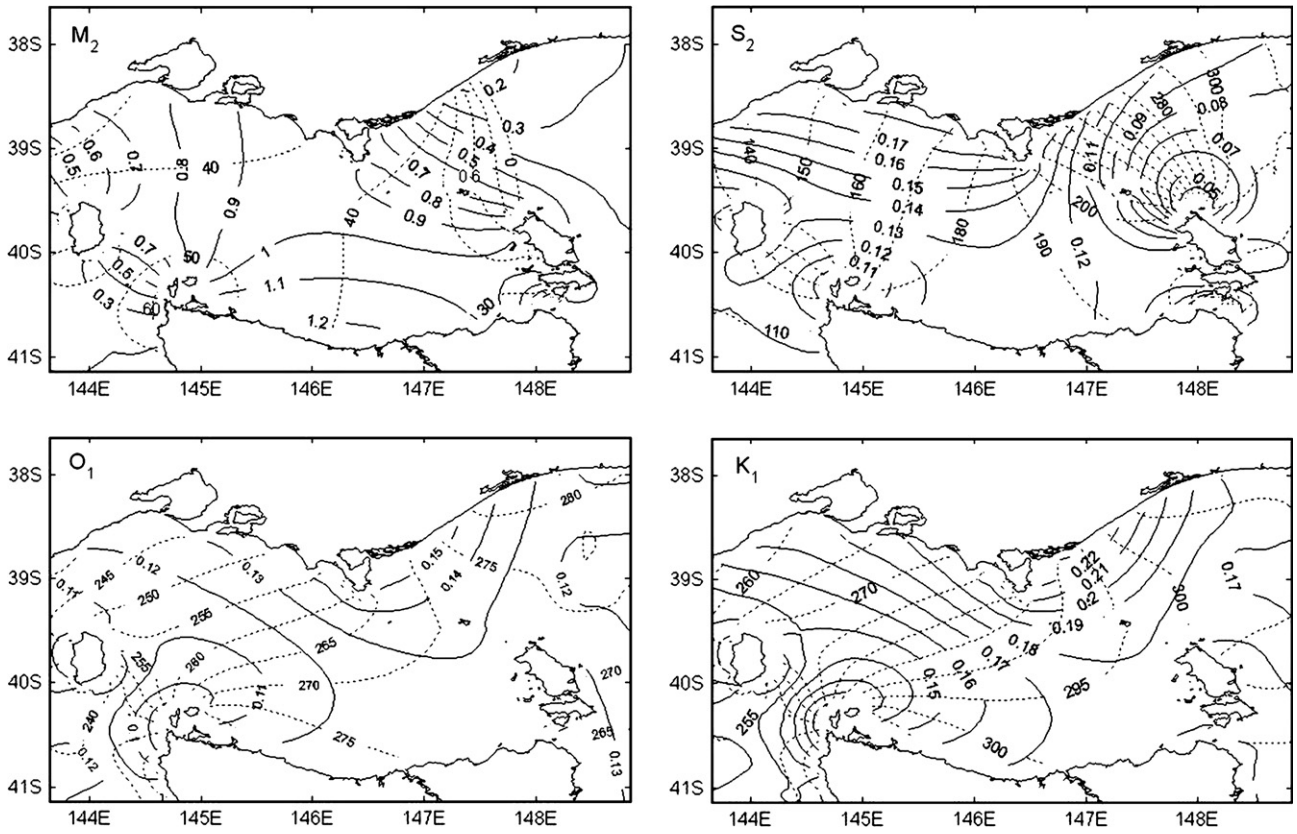

Fig. 3. Co-amplitudes (m) and co-phases (degrees relative to UTC) for modelled M_2, S_2, O_1 and K_1 tidal constituents.

region. Annual mean age and flushing time distributions suggest that transport is larger through the north-western boundary of the control region than the south-western boundary. Annual mean residence time distribution (Fig. 7d) suggests that water leaving from the western side and along the northern Tasmanian coastline has the longest residence times in the system.

All annual mean transport timescale distributions indicate that the model generates transport that is generally eastward. Transport through the Strait is along a pathway from the main source in the north-western corner to the main sink in the north-eastern corner. Whilst moving through, a proportion of water coming in from the west goes southeast into a region of older age and longer flushing times, before it is moved northwards and out of the region towards the east. In this region there is a tendency for quasi-stationary eddies to develop and recirculate water mass. The presence of these eddies are where long age or flushing times can coincide with long residence times. Longer flushing times and residence times adjacent the northern Tasmanian coastline are a signature of the westward movement of waters from these locations in the summer period. Longer local flushing times and shorter local

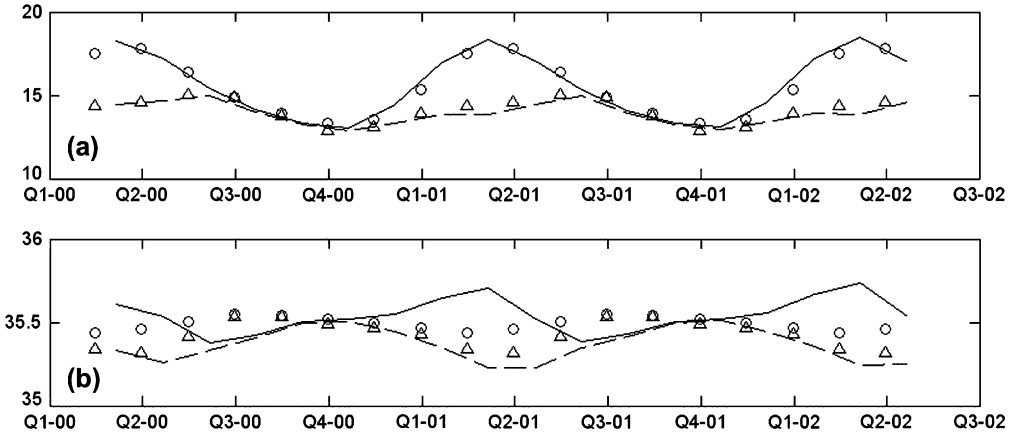

Fig. 4. Weekly averages of model and CARS atlas (a) temperature (°C) and (b) salinity (psu) spatially averaged over the control region. Solid lines are model surface σ-layer and dashed lines are model bottom σ-layer, circles denote atlas surface σ-layer and triangles atlas bottom σ-layer.

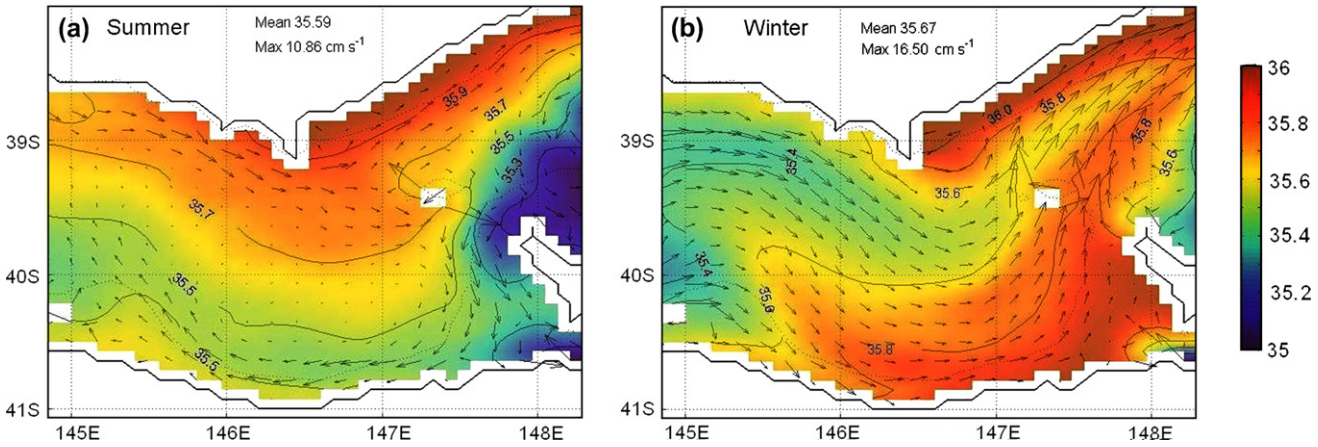

Fig. 5. Mean depth-averaged salinity (psu) and depth-averaged currents (cm s^{-1}) for (a) summer and (b) winter. Maximum depth-averaged current speed corresponds to longest vector shown.

residence times at the eastern side, and the contrary at the western side, is what would be expected with residual eastward transport through the region. Maximum annual and depth-averaged flushing time is ~255 days, residence time is ~228 days and age is ~252 days. The similarities between annual average age and flushing time distributions suggest that the two tend towards each other over time. Flushing times presented here are longer (~10–30 days) than those given in Sandery and Kämpf (2005). This is because the latter focused on conservative estimates of the flushing times using a high mean wind scenario in a winter to spring period, rather than investigating the full annual cycle in a climate-averaged sense.

3.3. Seasonal variations of transport timescale distributions

Summer and winter mean age distributions for the second year of the simulation are shown in Fig. 7h and i, respectively. Relatively older water mass is present during summer, in the southern area of the Strait interior. Through autumn this older water mass moves east. Winter mean age distribution shows that the older water mass then moves towards the north-east. Some of this mass forms the Bass Strait Cascade, which is remote from the control region. Through spring old water still leaves in a similar manner to the way it does in winter, however remnants not flushed out in this period become trapped in eddies. The model results suggest these remnants end up remaining in the interior throughout the next summer and are not flushed out until the next winter–spring period. Lateral transport of water mass from the west is largest in winter which is when correlation of age with salinity is highest.

Summer and winter mean flushing time distributions are shown in Fig. 7b and c. Flushing time distributions are spatially smoother than age distributions due to the different methods used to derive them. Flushing time distributions, based on different tracer release times, reflect the circulation that occurs in the period between release time and flushing time. A flushing time distribution captures relative tracer age through time. If the flushing timescale is close to semi-annual in a seasonally varying system, as in this case, flushing times in particular areas derived from tracer fields released during winter will depend on the summer circulation and flushing times from tracer fields released during summer will depend on the winter circulation. Main source areas at the western side appear as intrusions indicated by low flushing times (~50 days). The source in the northwest is more predominate. In winter months the western side of the control region exhibits shorter flushing times. Seasonal variation in the

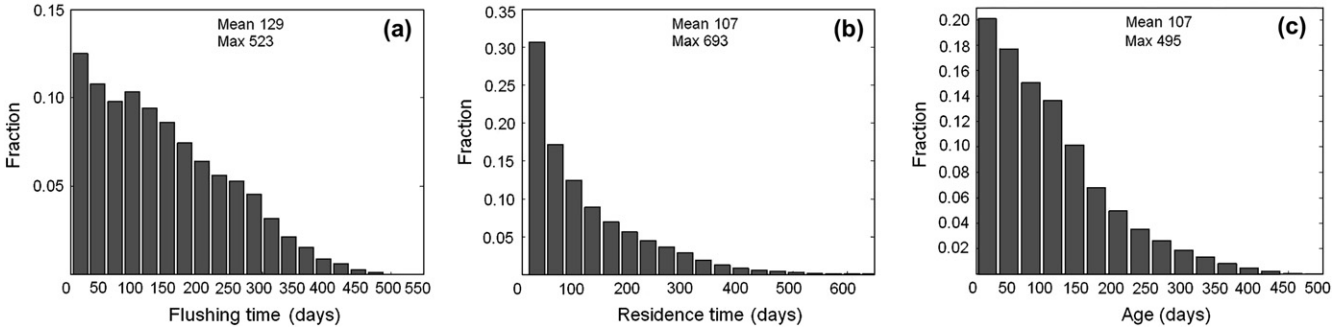

Fig. 6. Frequency distribution of all sampled (a) flushing times, (b) residence times and (c) ages. Flushing times were sampled from around 76,000 measurements and residence times from around 738,000 measurements. At any time, between approximately 750 and 2000 thousand particles are present in the control region and used for age. The number of particles in the control region varied seasonally with minimum in July and maximum in February.

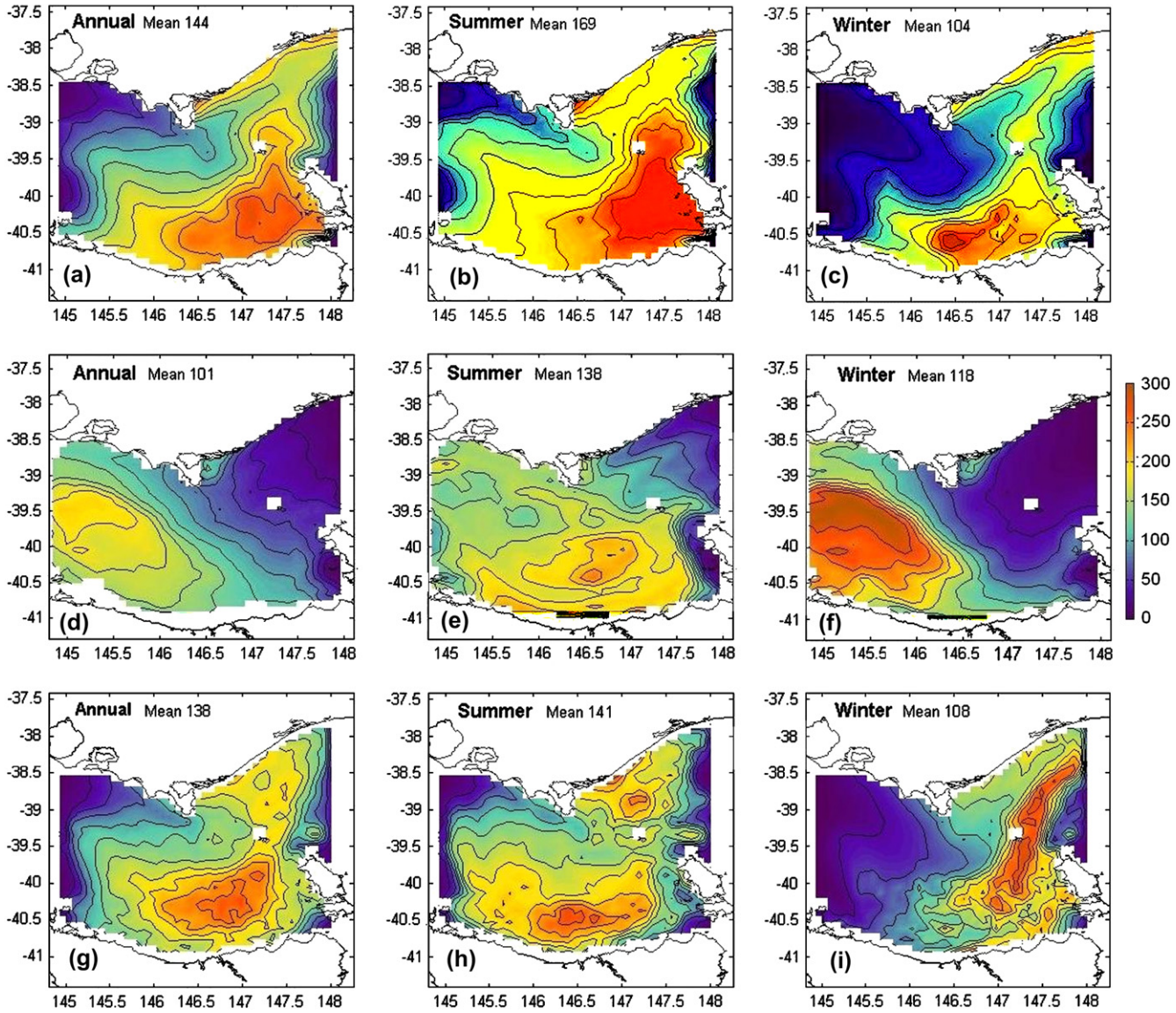

Fig. 7. Mean flushing time distributions (a) annual, (b) summer and (c) winter. Mean residence time distributions (d) annual, (e) summer and (f) winter. Mean age distributions (g) annual, (h) summer and (i) winter. All timescales are derived from three-dimensional distributions but are shown as depth-averaged and in units of days.

transport within the Strait is evident. The flushing time patterns for winter are characteristic of winter–spring flushing (Sandery and Kämpf, 2005). Flushing time patterns for summer reveal a transition to a different state where relatively longer flushing times exist in the central-southern part of the interior. This is because climate-average winds are southerly for about 2–3 months during the austral summer period and drive a periodic westward transport. This residual westward transport carries water mass present in the south-eastern side in late spring back to the western side. Flushing of the ''summer water mass'' is not possible until the following winter–spring period.

First impressions of residence time distributions in Bass Strait dependent on release time in either summer or winter are given in Fig. 7e and f, respectively. Distinctly different distributions are found, which highlight seasonal variation in the model circulation.

For similar reasons given regarding flushing times, residence times dependent on release time are subject to the circulation in the period ahead of release time. A significant amount of particles released in winter months will be subject to the summer circulation and particles released in summer months the winter circulation, however, this depends on the actual residence time for a particular local area. Particles introduced into local areas in summer in central-southern Bass Strait generally have residence times of the order of 6 months (Fig. 7e) suggesting the winter circulation eventually removes them from the system. A large area of long residence times of the order of 10 months is found in western Bass Strait, in the lee of King Island (Fig. 7f). Particles leaving this area in winter months are drawn into the south-eastern area and experience the summer circulation thereby increasing the time they spend in the region. Particles released in summer months in western Bass Strait experience the winter circulation resulting

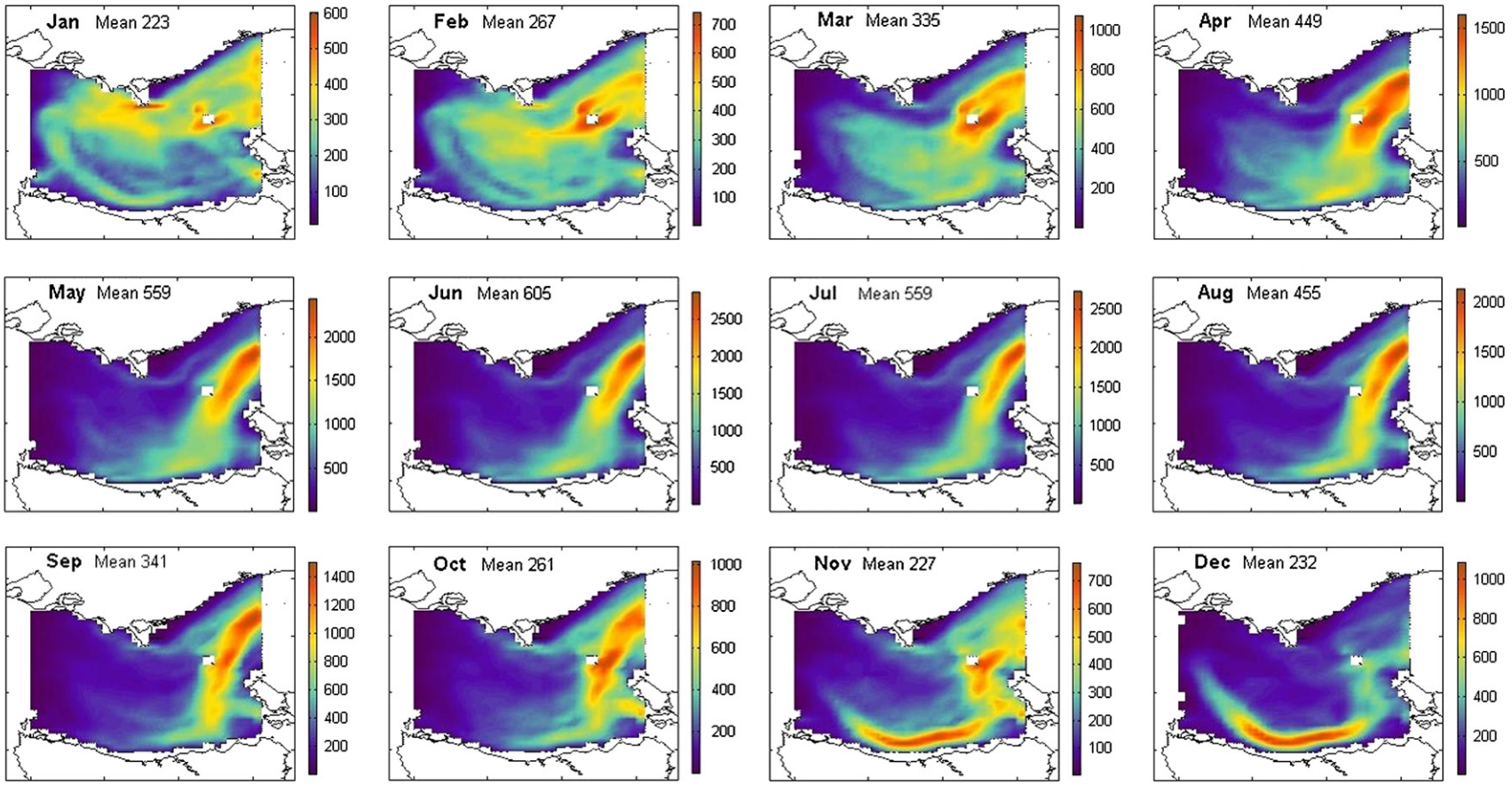

Fig. 8. Monthly mean depth-averaged number of residence time measurements per model horizontal grid cell. Note that colour scales are different.

in relatively lower residence times than particles released in winter.

These residence times, however, have some deficiency in resolving this variation in some locations because of the way the circulation concentrates particles leading to smaller numbers of measurements being made in certain cells. Ideally, the same large amounts should be used for each location. Since particles that flow into local cells are the main source of residence time measurements, the distribution of the number of measurements indicates how particles are concentrated by transport in the system. To illustrate this, monthly mean distributions of the number of residence time measurements per grid cell, which are depth-averaged, are given in Fig. 8. The areas where larger numbers of residence time measurements are sampled are flow corridors. The winter corridor extends from south-eastern Bass Strait to Bass Canyon and is associated with the flushing out of older water at this time of year. A late-spring/early-summer corridor can be clearly seen in southern Bass Strait parallel to the northern Tasmanian coastline. This is associated with a westward flow at this time of year in the model circulation.

Water mass properties in Banks Strait are significantly influenced by tidal stirring (Baines and Fandry, 1983). The model has strong tidal mixing fronts around Banks Strait, which can be seen clearly in the summer-mean salinity distribution. The salinity (and temperature) is generally lower here (and in other parts of the Strait passages), due to strong vertical mixing induced by horizontal currents. The timescale distributions also exhibit fronts on the western side of Banks Strait, highlighting limited exchanges of water mass properties between this area and areas further west. The results suggest residual throughflow in Banks Strait is limited and export of most Strait water occurs between the Furneaux Group and mainland Australia. The relatively long flushing times in the south-eastern areas occur because of the forcing of tides in Banks Strait, the location of the Furneaux Group, the overall eastward residual flow and geostrophic and topographic control of the circulation. The latter two mechanisms are well documented (Fandry, 1981, 1982, 1983; Baines et al., 1991; Middleton and Viera, 1991; Hannah, 1992; Middleton and Black, 1994).

Summer and winter examples of age distributions in areas A and B (locations given in Fig. 1) are given in Fig. 9. Age data is from the second year of the simulation. In summer, the age distribution in area A suggests an age mixture containing young and old water up to 235 days. A large proportion has age between 75–125 days. Area B in summer generally contains older water than area A, with a peak at around 160 days. No water with age less than 75 days is detected. The age distribution in area A in winter shows the presence of mainly young water with age between 20 and 100 days; however, small proportions of remnant older water (up to ~300 days) are captured. In winter, area B has the largest proportion of old water of all the distributions with a significant fraction having age between 280 and 420 days. These results support the idea that the oldest water resides in the vicinity of area B in winter. In this period a large fraction of new water is brought in from the west near area A. This is balanced by an export flux from the system, to the north-east, of similar proportion, which leaves in late winter and early spring. It is most likely that this export flux contains a significant proportion of the oldest Strait water because the large portion of oldest water is not detected in areas A or B in summer.

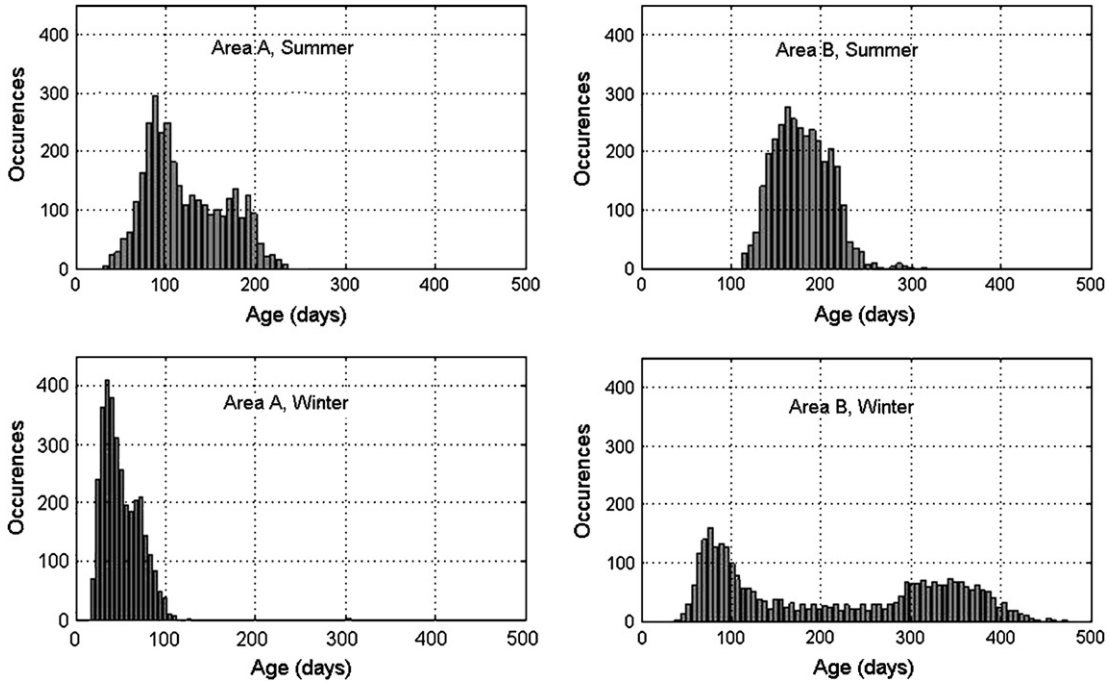

Fig. 9. Summer and winter age distribution histograms for areas A and B.

4. Conclusions

A variety of conservative and time-dependent transport timescale methods were employed and distributions were derived and compared in a realistic simulation of seasonal scale circulation in Bass Strait. Flushing time and water age distributions were entirely related to lateral advection and diffusion of water mass across the predetermined control region's open boundaries. Residence time distributions were also related to this and additionally to source material being introduced inside the control region. Each timescale captured a different view of processes occurring in the same circulation. The results showed that flushing time distributions, in the case of an oceanic strait, are closely related to age distributions despite the use of different methods in their derivation. The results suggest that, due to eastward residual throughflow and topographic and geostrophic influence on currents in the region, an area of relatively long flushing times and average water age ($\sim$200–250 days) exists in south-eastern Bass Strait.

It was shown that by including time dependence in these methods, seasonal variability in circulation could be detected. The interpretation of flushing time and residence time distributions in this context is complicated because it is determined by the circulation in the period between release of tracer and the timescale itself and is locally dependent. The results, however, assist in the interpretation of flushing time and residence time distributions in the case of an oceanic strait. Residence and flushing time distributions were shown to have distinctly different spatial distributions in an oceanic strait in the case where advection is important. Here, long residence times coincided with short flushing times on the western side and the converse on the eastern side.

The time-varying age distribution of water mass in the simulation was derived from a novel approach using Lagrangian particles. This showed that the summer circulation increased the age of water mass, not flushed in the winter–spring period by moving remnant older water at the eastern side to the west along the northern Tasmanian coast. The largest fraction of young water was seen to be brought in from the west during each winter–spring period. This was accompanied by the largest fraction of old water moving out towards the north-east.

The age of water in the Strait has implications for water mass transformation by air-sea exchanges. Old water is likely to have relatively higher salinity and therefore increased density upon winter cooling. The older water mass is hypothesised to form part of the Bass Strait Cascade which is observed as positive salinity anomalies in the western Tasman Sea between depths of 200 and 500 m.

In future studies, water age could be used to trace the export of Bass Strait Water into the Tasman Sea and the Bass Strait Cascade. Age distributions of various individual constituents important to ecological systems, such as dissolved gases and suspended particulate matter, would provide useful insights into their nature. New water is also added by precipitation, which could also be considered. Another important area to investigate is the relationship between water mass age and regional marine ecosystems. The methods used in this study could be applied to investigate characteristics of other regional and local marine systems.

Acknowledgements

We thank the editors and reviewers for their interest in this article and for providing the opportunity for the work to be published. We wish to acknowledge Matthias Tomczak and Scott Condie for their support of this work. We also thank Patrick Luyten and the co-authors of COHERENS. Data used in the study was provided by CSIRO Marine and Atmospheric Research, the National Tidal Centre, the Australian Bureau of Meteorology, NOAA/PMEL and Geoscience Australia. Simulations were carried out using computing facilities at SAPAC, the South Australian Partnership for Advanced Computing.

References

Baines, P.G., Fandry, C.B., 1983. Annual cycle of the density field in Bass Strait. Australian Journal of Marine and Freshwater Research 34, 143–153.

Baines, P.G., Edwards, R.J., Fandry, C.B., 1983. Observations of a new baroclinic current along the western continental slope of Bass Strait. Australian Journal of Marine and Freshwater Research 34, 155–157.

Baines, P.G., Hubbert, G., Power, S., 1991. Fluid transport through Bass Strait. Continental Shelf Research 11, 269–293.

Boland, F.M., 1971. Temperature-salinity anomalies at depths between 200 m and 800 m in the Tasman Sea. Australian Journal of Marine and Freshwater Research 22, 55–62.

Brodie, R., Radok, R., 1970. Tides, Weather and Surface Drift in Bass Strait. Horace Lamb Centre for Oceanographic Research, Flinders University of South Australia, p. 35.

Bye, J.T., 1983. The general circulation in a dissipative basin with longshore wind stresses. Journal of Physical Oceanography 13, 1553–1563.

Deleersnijder, E., Delhez, E.J.M., 2004. Symmetry and asymmetry of water ages in a one-dimensional flow. Journal of Marine Systems 48, 61–66.

Deleersnijder, E., Campin, J.M., Delhez, E.J.M., 2001. The concept of age in marine modelling I. Theory and preliminary modelling results. Journal of Marine Systems 28, 229–267.

Deleersnijder, E., Mouchet, A., Delhez, E.J.M., Beckers, J.M., 2002. Transient behaviour of water ages in the world ocean. Mathematical and Computer Modelling 36, 121–127.

Delhez, E.J.M., 2006. Transient residence and exposure times. Ocean Science 2, 1–9.

Delhez, E.J.M., Deleersnijder, E., 2002. The concept of age in marine modelling II. Concentration distribution function in the English channel and the North Sea. Journal of Marine Systems 31, 279–297.

Delhez, E.J.M., Campin, J.M., Hirst, A.C., Deleersnijder, E., 1999. Toward a general theory of the age in ocean modelling. Ocean Modelling 1, 17–27.

Delhez, E.J.M., Heemink, A.W., Deleersnijder, E., 2004. Residence time in a semi-enclosed domain from the solution of an adjoint problem. Estuarine, Coastal and Shelf Science 61, 691–702.

Dunn, J.R., Ridgway, K.R., 2002. Mapping ocean properties in regions of complex topography. Deep Sea Research Part I: Oceanographic Research 49 (3), 591–604.

England, M.H., 1995. The age of water and ventilation timescales in a global ocean model. Journal of Physical Oceanography 25, 2756–2777.

Fandry, C.B., 1981. Development of a numerical model of tidal and wind driven circulation in Bass Strait. Australian Journal of Marine and Freshwater Research 32, 9–21.

Fandry, C.B., 1982. A numerical model of the wind-driven transient motion in Bass Strait. Journal of Geophysical Research 87 (C1), 499–517.

Fandry, C.B., 1983. Model for the three-dimensional structure of wind-driven and tidal circulation in Bass Strait. Australian Journal of Marine and Freshwater Research 34, 121–141.

Fandry, C.B., Hubbert, G.D., McIntosh, P.C., 1985. Comparison of predictions of a numerical model and observations of tides in Bass Strait. Australian Journal of Marine and Freshwater Research 36 (6), 727–752.

Geoscience Australia, 2002. Australian Bathymetry and Topography Grid. ANZCW0703004301.

Gibbs, C.F., Arnott, G.H., Longmore, A.R., Marchant, J.W., 1991. Nutrient and plankton distribution near a shelf break front in the region of the Bass Strait Cascade. Australian Journal of Marine and Freshwater Research 42, 201–217.

Gibbs, C.F., Tomczak, M.J., Longmore, A.R., 1986. The nutrient regime of Bass Strait. Australian Journal of Marine and Freshwater Research 37, 451–466.

Godfrey, S.J., Jones, I.S.F., Garrey, J., Maxwell, H., Scott, B.D., 1980. On the winter cascade from Bass Strait into the Tasman Sea. Australian Journal of Marine and Freshwater Research 31, 275–286.

Hall, T., Haine, T.W.N., 2004. Tracer age symmetry in advective-diffusive flows. Journal of Marine Systems 48, 51–59.

Haney, R.L., 1990. On the pressure gradient force over steep topography in sigma coordinate ocean models. Journal of Physical Oceanography 21, 610–619.

Hannah, C.G., 1992. Geostrophic control with wind forcing: application to Bass Strait. Journal of Physical Oceanography 22, 1596–1599.

Herzfeld, M., Tomczak, M., 1997. Numerical modelling of sea surface temperature and circulation in the Great Australian Bight. Progress in Oceanography 39, 29–78.

Hirst, A.C., 1999. Determination of water component age in ocean models: application to the fate of North Atlantic Deep Water. Ocean Modelling 1, 81–94.

Jones, I.S.F., 1980. Tidal and wind-driven currents in Bass Strait. Australian Journal of Marine and Freshwater Research 31, 109–117.

Kalnay, E., et al., 1996. The NCEP/NCAR 40-year reanalysis project. Bulletin of the American Meteorological Society 77, 437–471.

Kämpf, J., Doubell, M., Griffin, D., Matthews, R.L., Ward, T.M., 2004. Evidence of large seasonal coastal upwelling system along the southern shelf of Australia. Geophysical Research Letters 31, 1–4.

Karstensen, J., Tomczak, M., 1998. Age determination of mixed water masses using CFC and oxygen data. Journal of Geophysical Research 103 (C9), 18599–18609.

Luick, J.L., Kase, R., Tomczak, M., 1994. On the formation and spreading of the Bass Strait cascade. Continental Shelf Research 14, 385–399.

Luyten, P.J. et al., 1999. COHERENS—A Coupled Hydrodynamical-Ecological Model for Regional and Shelf Seas: User Documentation., Management Unit of the Mathematical Models of the North Sea.

Maier-Reimer, E., Sündermann, J., 1982. On Tracer Methods in Computational Hydrodynamics. Engineering Application of Computational Hydraulics. Pitman Advanced Publ. Program, Boston. 1.

Marinov, D., Norro, A., Zaldivar, J.-M., 2006. Application of COHERENS model for hydrodynamic investigation of Sacca di Goro coastal lagoon (Italian Adriatic Sea shore). Ecological Modelling 193, 52–68.

McIntosh, P.C., Bennett, A.F., 1984. Open ocean modelling as an inverse problem: M2 tides in Bass Strait. Journal of Physical Oceanography 14, 601–614.

Middleton, J.F., Black, K.P., 1994. The low frequency circulation in and around Bass Strait: a numerical study. Continental Shelf Research 14, 1495–1521.

Middleton, J.F., Cirano, M., 2002. A northern boundary current along Australia's southern shelves: the Flinders Current. Journal of Geophysical Research 107.

Middleton, J.F., Viera, F., 1991. The forcing of low frequency motions within Bass Strait. Journal of Physical Oceanography 21, 695–708.

Monsen, N.E., Cloem, J.E., Lucas, L.V., Monismith, S.G., 2002. A comment on the use of flushing time, residence time, and age as transport time scales. Limnology and Oceanography 47 (5), 1545–1553.

Newell, B.S., 1960. Hydrology of south-eastern Australian waters: Bass Strait and New South Wales tuna fishing area. CSIRO Australian Division of Fisheries and Oceanography.

Oliviera, A., Baptista, A.M., 1997. Diagnostic modeling of residence times in estuaries. Water Resources Research 33, 1935–1946.

Ridgway, K.R., Condie, S.A., 2004. The 5500-km-long boundary flow off western and southern Australia. Journal of Geophysical Research 109.

Ridgway, K.R., Godfrey, J.S., 1997. Seasonal cycle of the East Australian Current. Journal of Geophysical Research 102 (C10), 22,921–22,936.

Ridgway, K.R., Dunn, J.R., Wilkin, J.L., 2001. Ocean interpolation by 4-dimensional weighted least squares—application to the waters around Australasia. Journal of Atmospheric and Oceanic Technology 19, 1357–1375.

Sadrinasab, M., Kämpf, J., 2004. Three-dimensional flushing times in the Persian Gulf. Geophysical Research Letters 31 (L24301). doi:10.1029/2004GL020425.

Sandery, P.A., Kämpf, J., 2005. Winter-spring flushing of Bass Strait, south-eastern Australia, a numerical modelling study. Estuarine, Coastal and Shelf Science 63, 23–31.

Takeoka, H., 1984. Fundamental concepts of exchange and transport time scales in a coastal sea. Continental Shelf Research 3, 311–326.

Tomczak, M.J., 1985. The Bass Strait water cascade during winter 1981. Continental Shelf Research 4, 255–278.

Tomczak, M.J., 1987. The Bass Strait water cascade during summer 1981–1982. Continental Shelf Research 7, 561–572.

Umgiesser, G., Luyten, P.J., Carniel, S., 2002. Exploring the thermal cycle of the Northern North Sea area using a 3-D circulation model: the example of PROVESS NSS station. Journal of Sea Research 48, 271–286.

UNESCO, 1981. Tenth report of the joint panel on oceanographic tables and standards, UNESCO Technical Papers in Marine Science No. 36, UNESCO, Paris.

Walker, S.J., 1999. Coupled hydrodynamic and transport models of Port Phillip Bay, a semi-enclosed bay in south-eastern Australia. Australian Journal of Marine and Freshwater Research 50, 469–481.

Zimmerman, J.T.F., 1988. Estuarine residence times. In: Kjerfv, B. (Ed.), Hydrodynamics of Estuaries, vol. 1. CRC Press, Boca Raton, FL, pp. 75–84.

Available online at www.sciencedirect.com
ScienceDirect
Estuarine, Coastal and Shelf Science 74 (2007) 697–708
ESTUARINE COASTAL AND SHELF SCIENCE
www.elsevier.com/locate/ecss

Modelling and observations of tidal wave propagation, circulation and residence times in Puttalam Lagoon, Sri Lanka

E.M.S. Wijeratne [a,*], L. Rydberg [b]

[a] Oceanography Division, NARA, Crow Island, Mattakkuliya, Colombo 15, Sri Lanka
[b] Department of Oceanography, Earth Sciences Centre, University of Gothenburg, PO Box 460, SE 40530 Gothenburg, Sweden

Received 23 June 2006; accepted 9 May 2007
Available online 10 July 2007

Abstract

Tidal measurements and a depth-averaged 2D model are used to examine wave progression and circulation in a long, shallow, micro-tidal lagoon in Sri Lanka. Ranges and phase lags for different tidal constituents are used to calibrate the model. A single drag coefficient, $C_d = 0.0032$, gives almost perfect agreement with data. Current measurements are used for validation of the model. The lagoon tide consists of a combination of progressive and standing waves, where progressive waves dominate in the outer part and standing waves in the inner. A Lagrangian based particle-tracking method is developed to study tidally and wind induced residence times. If tides were the only factor affecting the residual circulation, the residence time inside the narrowest section would be approximately 100 days. Steady winds (of typical monsoon average) decrease the residence times to 60–90 days. Estuarine forcing due to net freshwater supply is not modelled (due to lack of reliable runoff data), but independent, long-term salinity observations and calculations based on volume and salt conservation during periods of negligible freshwater supply (the lagoon is seasonally hypersaline) indicate residence times ranging from 40 to 80 days. Model derived residence times based on tides alone represent a minimum exchange. Even weak forcing, through winds, excess evaporation or freshwater supply efficiently reduces residence times.

Keywords: residence time; water exchange; tidal model; Puttalam Lagoon; Sri Lanka

1. Introduction

1.1. Puttalam Lagoon

Puttalam Lagoon on the west coast of Sri Lanka (Fig. 1) offers excellent conditions for testing tidal models on residual circulation and water exchange. The lagoon is very shallow (1.7 m) and long enough (45 km) to develop well-defined differences in tidal range and salinity. Spring tidal range decreases from more than 50 cm at the entrance to about 20 cm at the head (Wijeratne et al., 1995). During dry seasons, the salinity in the inner end may reach 50 psu (Jayasiri et al., 1998), whereas the overall mean salinity varies from 32 to 42 psu on a seasonal basis (Arulananthan et al., 1995). These rather extreme variations are due to high evaporation in combination with a seasonally variable rainfall, typical of the Indian Ocean monsoon circulation. In this paper, we are presenting data on tides and current measurements, from various positions in the estuary. These are used to calibrate and validate a 2D tidal model. The model is used to examine tidally- and wind-driven residual circulation and residence times. The results are compared with independent calculations of residence times, based on volume and salt conservation (Arulananthan et al., 1995; Arulananthan, 2004).

1.2. Estuarine forcing and residual circulation

Oceanic tides, net freshwater fluxes and winds interact with local topography and (in larger areas) Earth's rotation, to

* Corresponding author.
E-mail addresses: wijeratne.e@nara.ac.lk (E.M.S. Wijeratne), lary@oce.gu.se (L. Rydberg).

0272-7714/$ - see front matter © 2007 Elsevier Ltd. All rights reserved.
doi:10.1016/j.ecss.2007.05.012

Nomenclature

C_a	drag coefficient at the sea surface (2.7×10^{-3})
C_d	drag coefficient at the bottom
D	total depth
f	Coriolis parameter
g	gravitational acceleration
L, L_f	lagoon length, frictional length scale
T_p	tidal period
W_x	wind speed in x-direction $= W \cos\theta$, where θ is the wind direction rel. to the x-axis
W_y	wind speed in y-direction $= W \sin\theta$
U, V	are the depth-averaged velocities in the x- and y-directions
ε	η_0/D, an aspect ratio
η	sea level
η_o	tidal amplitude
ρ_a	density of air ($\sim$1.29 kg/m^3)
ρ_o	density of sea water (1025 kg/m^3)
$\tau_x^b, \tau_y^b, \tau_x^w, \tau_y^w$	bottom and wind stress in x- and y-directions, respectively.

produce a long-term mean residual circulation in estuaries and lagoons. Sub-tidal barotropic and baroclinic motions in the ocean, driven by large-scale winds, are also important but mainly in deeper estuaries (e.g. Samuelsson and Stigebrandt, 1996; Liungman et al., 2001; Souto et al., 2003). Predictions of the residual circulation, including adherent water exchange and residence times have occupied the scientific community during the last 50 years (e.g. Stommel and Farmer, 1953; Hansen and Rattray, 1965; Prandle, 1985; Nunes-Vaz et al., 1990; Li and Valle-Levinson, 1999; Li and O'Donnell, 2005), but is still a major challenge (Simpson et al., 2005). A majority of authors treat the interaction between tides and freshwater (buoyancy) forcing, fewer (i.e. Geyer, 1997; Scully et al., 2005) the direct forcing by wind. In Puttalam Lagoon, we expect the (small) but strongly variable net freshwater flux to exert large influence on residual circulation and residence times, but also, because of the shallowness of the lagoon that local winds are of importance. Negative or positive fluxes are both likely to increase circulation and reduce residence times. Maximum residence times are expected to appear when net freshwater flux (and wind forcing) is zero. A model, which correctly predicts tidally induced residual circulation, alone will also indicate maximum residence times.

1.3. Tidal response in shallow estuaries

The tidally induced residual circulation is directly related to the nature of the tidal co-oscillation. We expect a diminutive residual circulation in bays with standing tides, but a more efficient circulation where the tide is progressive, typical for shallow bays with tidal asymmetries (e.g. Signell and Butman, 1992). Moreover, the tidal wave motion is often subjected to frictional effects (e.g. Le Blond, 1978) and the tide appears as damped progressive waves. Robinson et al. (1983) investigated the Fleet, a long and shallow lagoon on the south coast of England. In this lagoon, total extinction of the tide occurs before the tidal wave reaches the head. In the Fleet, wave propagation is purely progressive. The frictional length scale, used by Műnchow and Garvine (1991), $L_f = (gD^2T_p^2/\varepsilon C_d)^{1/3}$ (for definitions, see list of symbols) is shorter than the length of the lagoon, L. Even in Puttalam Lagoon, $L_f < L$ ($L_f \approx 30$ km) but the aspect ratio $\varepsilon = \eta_0/D$ is smaller (0.06) than in the Fleet. Thus, complete extinction does not occur (Wijeratne et al., 1995). Instead, the lagoon tide appears as a combination of incident and reflected waves, both of which are subjected to friction. A detailed description of this interaction is found in Bowers and Lennon (1990), discussing tidal propagation in Spencer Gulf, Australia.

1.4. Residence times and water exchange

The residence time may be defined as the time it takes for a particular water parcel to leave a water body through its inlet. Then, for an individual parcel, it depends on the location and the time of release (i.e. Luff and Pohlmann, 1995). This is how we use it here. Sometimes, similar quantities, such as the "age of the water", defined as the time it takes for a water parcel to reach from the entrance (i.e. Björk et al., 2000), or the head (Shen and Lin, 2006) to a particular location within the estuary, are also used.

If, on the other hand, the residence time is interpreted as an average, and not refers to individual water parcels, it may be expressed as $T_r = V/q_i$, where V is the volume of the water body and q_i is the water exchange (the sum of net freshwater supply and exchange with the open sea). Here, water exchange is determined from volume and salt conservation (Wolanski, 1986; Officer and Kester, 1991), while T_r is the time it takes to remove $(1-e^{-1})$ of the volume of the water from the water body. An equally distributed tracer with an initial concentration, C_i will decay exponentially according to $C = C_i e^{-t/T_r}$. The residence time, T_r, as defined here is similar to flushing-time as it is used by Bolin and Rodhe (1973) and to turnover-time, as it is used by Prandle (1984). For steady state solutions, the average residence time should be same, whatever approach is used, presuming that it refers to the same water mass.

In this article we compare our calculations of residence times for individual parcels (based on Lagrangian tracking) with estimates of T_r from volume and salt budgets.

We employ a non-linear 2D model which is used to predict tides and tidal currents (Wijeratne, 2003). For calibration and validation we use tidal and current meter data from various sites in the lagoon. The Lagrangian particle-tracking method is added to calculate residence times due to tides and winds with the aim to improve earlier overall estimates of residence times. Study area and hydrography are presented in Ch 2, tide gauge and current meter data in Ch 3. A summary of results from tidal observations (harmonic analysis, etc.) is given in Ch 4. Ch 5 presents the model including calibration and validation runs. Ch 6–7 shows results from calculations of

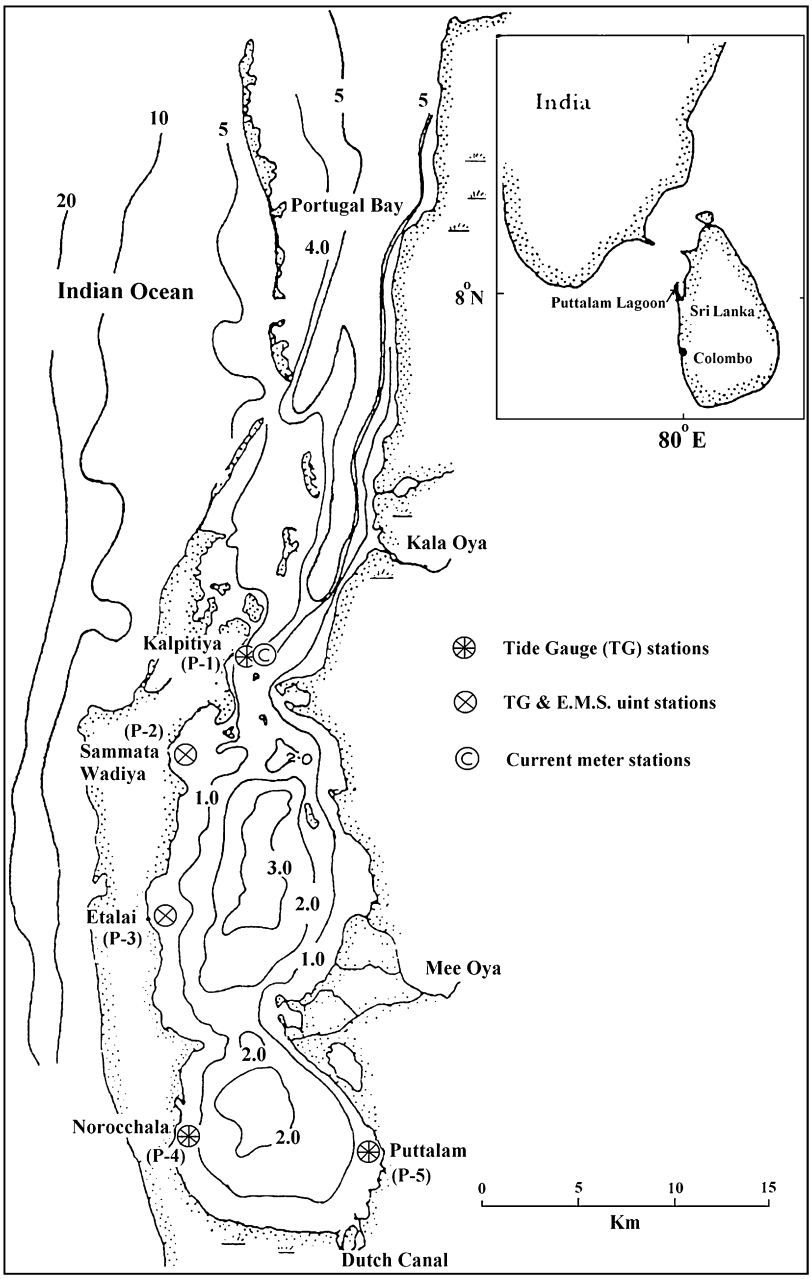

Fig. 1. Map of Puttalam Lagoon showing station net and bathymetry.

currents and residence times due to tides and winds. Ch 8 finally discusses the results, particularly, in relation to earlier estimates on T_r based on salinity observations.

2. The study area

Puttalam Lagoon (Fig. 1), on the west coast of Sri Lanka, is separated from the ocean by a long, permanent sand bar, which opens up in its northern end. The surface area and mean depth inside Kalpitiya are 225 km^2 and 1.7 m, respectively (at MSL).

Tides on the west coast of Sri Lanka are mixed semidiurnal, with a spring tidal range of 0.56 m, and small N–S variations. In Puttalam Lagoon, the horizontal mean, spring tidal range is about half that of the oceanic tide (Wijeratne et al., 1995).

The winds over Sri Lanka are monsoon dominated, with the SW Monsoon (SWM) blowing from June to September, and the NE Monsoon (NEM) blowing from December to March. Mean winds are 5–6 m s^{-1}during the peak monsoon periods, but the NEM is weaker on the west coast (Arulananthan, 2004). During NEM, local winds on the west coast are often dominated by a diurnal land–sea breeze (Wijeratne, 2003).

River discharge is dominated by the rivers Kala Oya and Mee Oya, including a smaller contribution from the Dutch Canal (Fig. 1). In the 1970s mean river discharge were 20 and 8 m^3 s^{-1}, respectively, with strong seasonal variations (Amarasinghe et al., 1999) and maximum runoff from November to February. Because of security problems, more recent runoff data are not available. Mean annual rainfall in the

Puttalam area is 1200 mm and potential evaporation 1800 mm (Arulananthan et al., 1995), corresponding to 12 and 18 $m^3 s^{-1}$ for the lagoon surface area inside Kalpitiya.

Arulananthan et al. (1995) carried out a 3-year study (1990–1992) consisting of almost monthly salinity observations throughout the lagoon. Seasonality in rainfall, runoff and evaporation was found to create large variations in salinity, with a seasonal range of about 10 psu (32–42 psu), and strong hypersalinity during dry periods (Fig. 2). Comparing salinity data from 1961 to 1962 with data from 1990 to 1992 indicated that the river discharge had decreased considerably ($>10\ m^3 s^{-1}$), most likely due to increased water use for irrigation. Residence times for the waters inside Kalpitiya, T_r based on volume and salt conservation, were calculated using data from drought periods with low or non-existing river runoff (as indicated in Fig. 2). Four periods gave residence times between 33 and 67 days (Arulananthan, 2004). Regarding the fact that some freshwater could have been added from Kala Oya, even after long periods of drought, the residence times were conservatively estimated between 40 and 80 days (Arulananthan, 2004).

3. Instrumentation and field campaign

Water level measurements were undertaken from February to June 1996, using three recording tide gauges of type Micro Tide (Coastal Leasing). The instruments are equipped with a strain gauge, which measures the total pressure with an accuracy corresponding to 1.5 cm of water. The resolution is 0.5 cm. The tide gauges were deployed at five different stations (see Fig. 1), during three different campaign periods (I–III). One tide gauge was deployed at Kalpitiya (Stn P-1). It was kept in the same position during the entire campaign. The other tide gauges were moved around between Sammatawadiya (Stn P-2), Etalai (Stn P-3), Norocchalai (Stn P-4) and Puttalam (Stn P-5). Fig. 3, which shows sea level data from all deployments, also indicates how the instruments were grouped together during Period I–III.

Current measurements were carried out from 1 March to 12 April at Kalpitiya (Stn C; Fig. 1), using a recording current meter of type SD-6000 (Sensor data). It was deployed to about mid-depth at a total depth of approximately 2 m. However, the location was not quite suitable. For security reasons the instrument had to be deployed too close to the shore, whereas both directions and velocities were somewhat affected by the local topography.

4. Tidal and current measurements

A detailed analysis of sea level and current measurements from the field campaigns is given in Wijeratne (2003). Here we show some basic results from this work, the core of which will be used for calibration and validation of the tidal model.

Raw data from the tide gauges were corrected for variations in daily mean air pressure and also for relatively large contributions from atmospheric tides (i.e. S_1), the ranges of which are 2–4 cm (see Wijeratne, 2003). Corrected sea level data from all stations and periods are shown in Fig. 3.

The sea level data were examined for maximum ranges and for phase lags in relation to Kalpitiya (Stn P-1). Results, shown in Table 1, indicate that the maximum range, defined as the largest difference (at spring) between a maximum and the next minimum, is similar at the head (Stns P-4 and P-5) and at the mid-lagoon (Stn P-3), approximately 0.28 m, but nearly 50% larger at Stn P-1 (0.39 m). The phase lags (Table 1) show that the tidal wave progression is slow from Stn P-1 to P-3 but fast from Stn P-3 to the head (Stn P-4/P-5), and thus that the tide is more progressive in the outer end and more of standing nature further in. Ebb periods are also slightly longer than flood periods, with a maximum asymmetry at Stn P-2, which is located in the shallowest part of the lagoon. Data from Table 1 also show that the low water phase lags are somewhat larger than high water, indicating a finite amplitude effect on the wave progression (Friedrichs and Aubrey, 1988). Another noteworthy result is that maximum ranges during Period III are all somewhat smaller

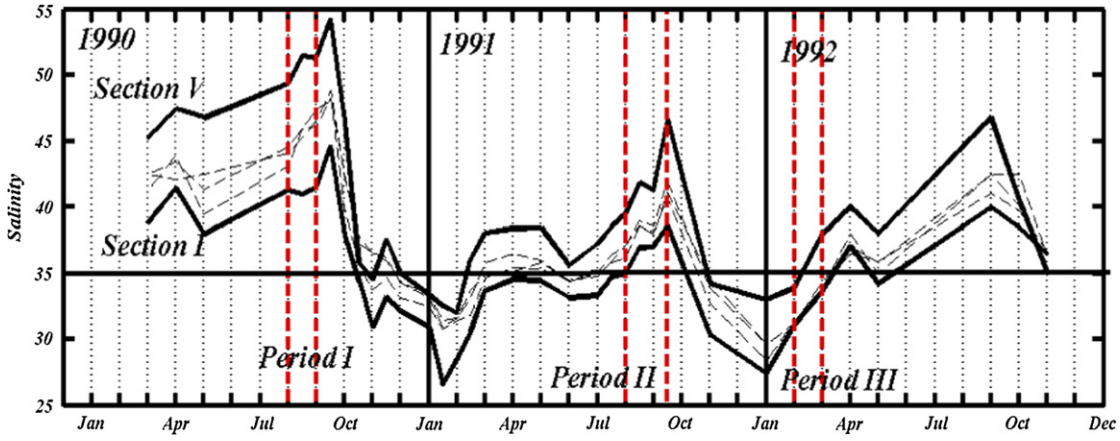

Fig. 2. Horizontal mean salinity development in Puttalam Lagoon 1990–1992; Section I data are composite of two stations at Kalpitiya, Section V data are composite of three stations in the Puttalam Basin (from Arulananthan, 2004). Hatched lines refer to stations in between. Periods I–II indicate two of those for which residence times were calculated.

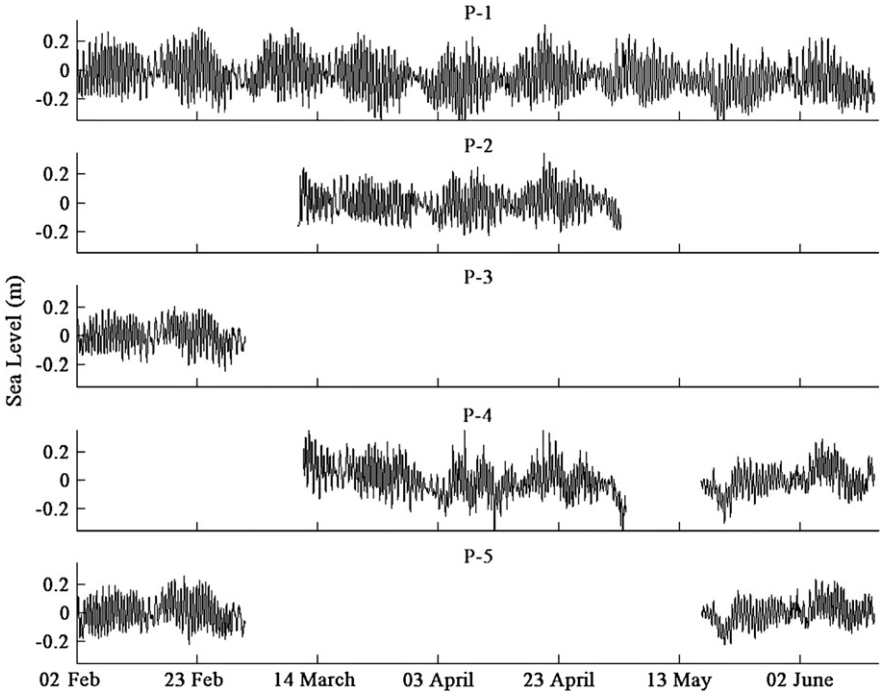

Fig. 3. Tide gauge data from Stns P-1 to P-5. For positions of stations, see Fig. 1. Period I (2 Feb–2 March), Period II (11 March–3 May) and Period III (16 May–15 June). The series are individually levelled to zero, and there is no general reference level.

than the values obtained for Periods I and II. The maximum range at Stn P-1 during Period II is about 0.43 m, as compared to 0.34 m during Period III. The phase lags are also larger during Period III, compared to Periods I and II. Lesser tidal ranges and larger phase lags during Period III indicate a more efficient frictional damping. This is most likely due to a decrease in the mean sea level of 15 cm from Period II to III. The seasonal range in Sri Lankan waters is typically 25 cm, with a major decrease of approximately 15 cm from April to June (Wijeratne, 2003).

Harmonic analysis applied to tide gauge data are shown in Tables 2 and 3. From Table 2, which also includes data from model calibration runs, we see that the spring tidal range on the coast is 0.56 m and the neap range is 0.13 m (Wijeratne, 2003), whereas the horizontal mean spring tidal range in the lagoon, inside Kalpitiya is 0.30 m, and the average neap tidal range 0.05 m, only. A comparison of amplitudes and phase lags between stations for the main constituents (M_2, S_2, K_1 and O_1) corroborates the aforementioned character of the lagoon tide. The phase lags, in addition, show that the progression of semidiurnal tides is slower than that of the diurnal (Table 2): for M_2 the phase lag is 100° (3.5 h) from Kalpitiya to the head, for K_1 is less than 30° (<2 h). The phase lag for S_2 from Kalpitiya to Stn P-3 is 70° but only 55° from the middle to the head of the lagoon. For K_1, the corresponding values are 50° and 10°, respectively.

Table 1
Tidal characteristics of sea level data from Stns P-1 to P-5

Station no.	Maximum sea level range (m)	Average sea level range (m)	Average flood period (h)	Average ebb period (h)	Phase lag in relation to Stn P-1 (h)			
					Spring		Neap	
					High (h)	Low (h)	High (h)	Low (h)
Period I								
P-1	0.38	0.23	6.14	6.21	–	–	–	–
P-3	0.28	0.18	6.30	6.32	2.05	2.25	2.17	2.40
P-5	0.30	0.18	6.16	6.18	3.40	3.55	3.14	3.17
Period II								
P-1	0.43	0.22	6.17	6.24	–	–	–	–
P-2	0.37	0.17	6.05	6.31	1.12	1.39	1.23	1.54
P-4	0.33	0.17	6.17	6.29	3.57	3.64	3.35	4.01
Period III								
P-1	0.34	0.20	6.19	6.21	–	–	–	–
P-4	0.25	0.13	6.17	6.20	3.46	3.71	3.90	4.49
P-5	0.24	0.13	6.17	6.21	3.48	3.71	4.00	4.86

Table 2
Harmonic analysis results, from observations and model runs. Tidal amplitude, a_η [m] and phase angle, g_η [degrees relative to local time] for major semidiurnal and diurnal constituents. The analysis was run with 11 constituents including N_2 and five shallow water components. Open sea data are from Colombo tide gauge (Wijeratne, 2003)

Stn		M_2		S_2		K_1		O_1		M_f	
		a_η	g_η	a_η	g_η	a_η	g_η	a_η	g_η	a_η	g_η
Open sea		0.18	045	0.11	092	0.09	043	0.04	058		
P-1	Observation	0.12	090	0.07	152	0.06	060	0.03	081	0.010	202
	Model	0.12	090	0.07	155	0.06	070	0.03	085		
P-2	Observation	0.09	127	0.05	190	0.05	102	0.02	092	0.013	163
	Model	0.09	130	0.05	195	0.05	105	0.02	100		
P-3	Observation	0.07	148	0.05	221	0.05	110	0.02	110	0.038	338
	Model	0.07	145	0.05	223	0.05	118	0.02	115		
P-4	Observation	0.08	189	0.07	272	0.05	120	0.02	137	0.030	113
	Model	0.08	187	0.07	274	0.05	140	0.02	135		
P-5	Observation	0.08	200	0.07	280	0.07	127	0.02	166	0.034	183
	Model	0.08	190	0.07	275	0.06	142	0.02	138		

The lagoon tide is mixed, semidiurnal with a form factor at Kalpitiya of $F = 0.42$ (Table 3). The form factor increases slightly towards the head, indicating that semidiurnal tides are more rapidly damped than the diurnal. The phase age at Kalpitiya is 60 h, compared to 38 h at the mouth (Wijeratne, 2003) but nearly 100 h at the head. It indicates a fortnightly variability, due to frictional set-up of mean sea level during spring and a few days thereafter (see Section 8). The fortnightly component, M_f, has a range of 2 cm at Kalpitiya (Table 2), increasing to between 6 and 7 cm at the head. Otherwise, the shallow water components are small, with a maximum range of 2 cm (not shown, but taken into account when running harmonic analysis).

Harmonic analysis was carried out also on the current measurements from Kalpitiya (Stn C). These results are shown in Table 4. As mentioned, the velocity measurements were affected by the proximity to the shore and up to 20% lower than continuity would require (Wijeratne, 2003). However, the positioning had no apparent effect on the phase lag. As seen from Table 3, the spring velocity range is 25 cm s^{-1}, the neap velocity range 3 cm s^{-1}. Semidiurnal velocities, as expected, are six to seven times higher than diurnal.

5. The tidal model

The numerical model was formulated for solving the 2D barotropic shallow water equations using a semi-implicit algorithm (Kowalik and Murty, 1993). The discretisation is shown in Appendix 1.

Table 3
Summary of tidal characteristics from Puttalam Lagoon (degree sign is shown for phase angles)

Tidal characteristics	Stn				
	P-1	P-2	P-3	P-4	P-5
Spring tidal range ($2[M_2 + S_2]$)	0.38	0.27	0.24	0.31	0.30
Mean tidal range ($2.2\ M_2$)	0.26	0.20	0.15	0.18	0.18
Neap tidal range ($2[M_2 - S_2]$)	0.09	0.07	0.04	0.01	0.02
Phase age ($0.98[S_2^\circ - M_2^\circ]$) (h)	60	62	71	81	113
Form factor ($F = [K_1 + O_1]/[M_2 + S_2]$)	0.42	0.51	0.59	0.43	0.58

5.1. Formulation

$$\frac{\partial U}{\partial t} + U\frac{\partial U}{\partial x} + V\frac{\partial U}{\partial y} - fV = -g\frac{\partial \eta}{\partial x} + \frac{1}{\rho_o}\frac{\tau_x^w - \tau_x^b}{D} \quad (1)$$

$$\frac{\partial U}{\partial t} + U\frac{\partial U}{\partial x} + V\frac{\partial U}{\partial y} - fV = -g\frac{\partial \eta}{\partial x} + \frac{1}{\rho_o}\frac{\tau_y^w - \tau_y^b}{D} \quad (2)$$

$$\frac{\partial \eta}{\partial t} + \frac{\partial (DU)}{\partial x} + \frac{\partial (DV)}{\partial y} = 0 \quad (3)$$

Here U and V are the depth-averaged velocities in the x- and y-directions, respectively, D is the depth, t is time, f is the Coriolis parameter, ρ_o is the water density, η is sea level and g is gravitational acceleration. τ_x^b and τ_y^b are the bottom stresses in the x- and y-directions and τ_x^w and τ_y^w, respectively. Bottom and wind stresses are expressed through a quadratic relationship (see e.g. Dronkers, 1969); $\tau_x^b = \rho_o C_d U (U^2 + V^2)^{1/2}$ and $\tau_y^b = \rho_o C_d V (U^2 + V^2)^{1/2}$, where C_d is the bottom drag coefficient and $\tau_x^w = \rho_a C_a W_x (W_x^2 + W_y^2)^{1/2}$ and $\tau_y^w = \rho_a C_a W_y (W_x^2 + W_y^2)^{1/2}$ and C_a is the wind drag coefficient. Boundary conditions used for the above equations were taken as $x = 0$; $\eta = \eta_0(t)$ with zero fluxes through coastal boundaries. The initial conditions are $t = 0$; $\eta = U = V = 0$.

Table 4
Amplitudes and phases based on harmonic analysis of current observations at Kalpitiya, Stn P-1, Period II, 1996 (phase angles refer to local time)

Constituent	Amplitude (a_v) (m s^{-1})	Phase angle (g_v) (degrees)
M_2	0.128	071
K_1	0.020	305
S_2	0.114	125
O_1	0.015	015

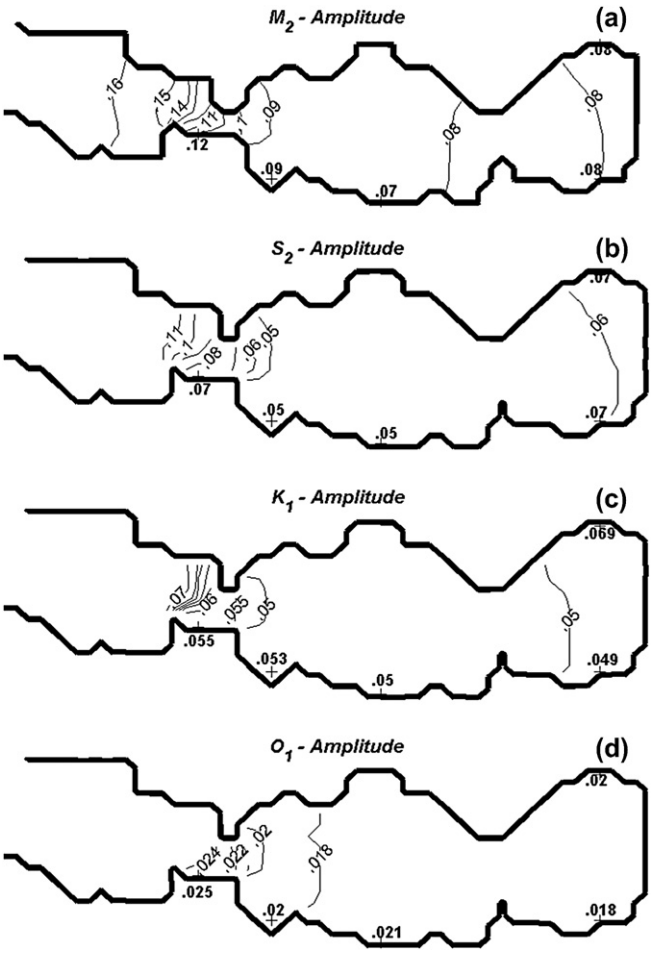

Fig. 4. (a–d) Model derived tidal amplitudes for major tidal constituents (best fit). Data in ''bold'' show amplitude from observations at Stns P-1 to P-5.

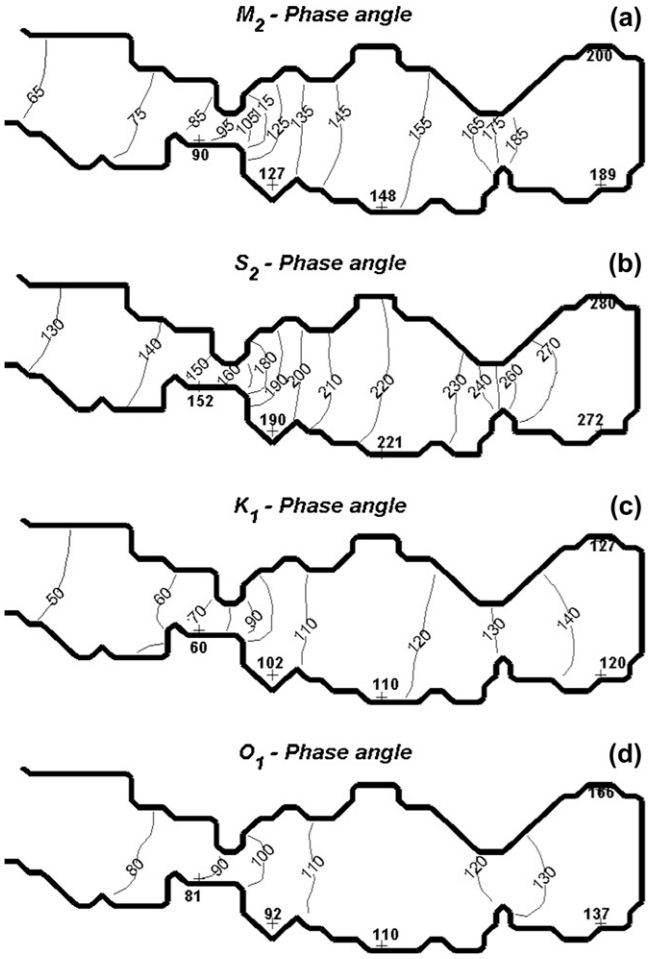

Fig. 5. (a–d) Model derived tidal phase angles for major tidal constituents (best fit). Data in ''bold'' show phase angles from observations at Stns P-1 to P-5.

The open boundary condition was specified using a synthetic sea level derived from harmonic analysis, carried out on the oceanic tide (Wijeratne, 2003), in which the major tidal components (M_2, S_2, O_1 and K_1) at the oceanic border were included. The development of the seasonal mean sea level as evaluated from Kalpitiya (Stn P-1) was added to the curve. Model calibration was made by comparing tidal ranges and phases of the major components generated by the model, with those derived from harmonic analysis of the tide gauge data within the lagoon. A single bottom drag coefficient, C_d, was used throughout, as tuning parameter. For calibration we employed data from Period I and, for validation, data from Period II to III, then using the constant C_d. For validation, we also compared phase differences between tidal elevation and currents, Δg, at Kalpitiya.

For calibration, based on Period I data, several model runs with different values of C_d, ranging from 0 to 0.006, were carried out. These runs showed that larger C_d values produce gradually smaller tidal ranges and larger phase lags compared to observed values. Model runs with $C_d = 0$ produces a tidal range, twice as large as the observed, with less than half the phase lag. A value of $C_d = 0.0032$ gave best fit with the observations. Co-amplitude and co-phase charts for M_2, S_2, K_1 and O_1 derived from the model validations are shown in Figs. 4a–d and 5a–d, respectively. Tidal ranges and phase lags for the different constituents are also shown in Table 2. Simulations were also made with a variable mean sea level. A decrease in mean depth by 30 cm (seasonal range is 25–30 cm, see below for further details) resulted in 15% decrease of tidal amplitudes and an increase of the phase lag.

6. Modelling of tidal wave progression, wind set-up and circulation

For simulations of tidal velocities all variables, including sea levels, velocities and winds, were initially set to zero, and the model was forced at the open boundary by specifying the sea level as earlier. For the wind simulations, the model was run for few tidal cycles from its initial state without wind, in order to reproduce the normal tidal oscillation. Then a steady wind was introduced, after which the model was run for another couple of tidal cycles before reaching steady state.

Phase differences between tidal elevations and currents, Δg obtained from the model with $C_d = 0.0032$, are shown for the four major constituents (M_2, S_2, O_1 and K_1) in Fig. 6a–d. By

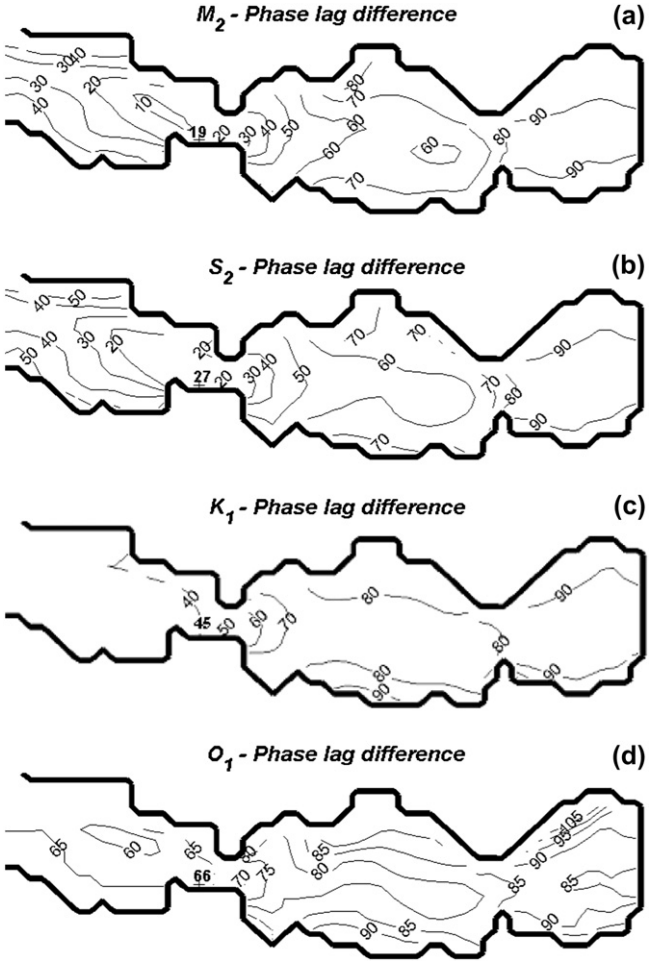

Fig. 6. (a–d) Phase differences between tidal sea levels and currents, Δg derived from model simulations. Numbers in "bold" are derived from observations of currents and sea levels at Kalpitiya, Period II, 1996.

comparing the data from observations at Kalpitiya (inserted in Fig. 6) with model data, it is obvious that the model behaves quite well also in this case. For semidiurnal tides (M_2 and S_2), Δg is small, 10–40° from the ocean to Kalpitiya, 50–70° in the central, Etalai Basin, but between 80° and 90° in the innermost Puttalam Basin. Thus, the semidiurnal tide is mainly progressive in the outer end, partially progressive in the central basin and of almost standing wave nature in the inner basin. For the diurnal components, the tides in the outer region as well as in the middle basin are partially progressive ($40° < \Delta g < 90°$), but basically standing in the inner basin. Lines of equal Δg are more or less parallel to the coast; particularly for diurnal tides, the Δg values are small in the centre but increasing towards the coast. A larger Δg near to the coastal boundaries indicates the effect of wave reflection. A minimum Δg appears near Kalpitiya for all constituents. It is clear that the tidal wave in this region is almost purely progressive.

Model runs were performed with different wind speed and directions. Set-up caused by a mean wind of 4 m s^{-1} from NE is about 8 cm at the head and 1–2 cm at Kalpitiya (with a corresponding set-down for SW winds). Steady winds from SW of 8 m s^{-1} were found to dry out some grid cells in the shallow parts of the lagoon. Set-up (and set-down) is stronger during neap than spring. Fig. 3 indicates some few occasions when the sea level is deviating from its normal range, sometimes indicating the effects of the wind. Such sea level variations contain both short-periodic standing waves and (presumably) long periodic (80–120 h) surface response to internal Kelvin wave (Wijeratne, 2003). However, the ranges rarely exceed 10 cm. Simulations, showing current patterns with and without wind stress forcing (in this case for NE/SW wind, 4 m s^{-1}), are shown in Fig. 7a–f. The current pattern is considerably changed due to winds, particularly near to the shallow coastal boundaries, where the tendency for the flow to follow the direction of the wind is obvious. The figures, showing the current patterns 3 h after high and low water, respectively, indicate considerable changes also in the slack water time.

7. Modelling of residence times

Prior to dispersion simulations, the model was run for 152 days to obtain time series velocities at grid points. Runs were made with and without wind. The first five days of spin up were not included in the velocity matrix. In the next step calculations were made for the residence time (see Appendix 2), i.e. the time for a water parcel to exit the lagoon. Groups of neutrally buoyant conservative particles were released in the grid domain, and the time required for each particle to be flushed out of the lagoon was calculated. Calculations using $C_d = 0.0032$ gave turbulent diffusion coefficients (see Appendix 2) with maximum values of $K_x = 0.06$ m^2 s^{-1} and $K_y = 0.001$ m^2 s^{-1}, respectively. Tracking runs were done repeatedly for different tidal phases: low water, 3 h after low water, high water and 3 h after high water. Tracking indicated a net inward displacement on the western side and a net outward on the eastern side, due to Coriolis force (Fig. 8; see below).

Residence times for tidal forcing alone are shown in Fig. 8a. The figure shows that residual circulation due to tides is insignificant in the innermost part of the lagoon and that the residence times are more than 125 days for particles released in this basin. In the region north of Kalpitiya, which is more efficiently ventilated because of the progressive nature of the tidal wave, the residence times are mainly below 20 days. A mean residual inflow on the western side (as mentioned above) is seen in this figure as considerably longer residence times for particles released on that side compared to particles released on the eastern side. The average residence time for waters inside Kalpitiya is just about 100 days. Model runs with NE wind, 4 m s^{-1}, shown in Fig. 8b, indicate that the residence times decrease by some 10–20% in the inner parts of the lagoon. On the other hand, there is an increase in the outer end, and the average residence time inside Kalpitiya, with tides and NE wind of 4 m s^{-1} is about 90 days. While NE winds have a relatively minor effect on the residence times, the effect is more substantial for SW winds. A mean wind of 4 m s^{-1} reduces the mean residence time to about 60 days (Fig. 8c).

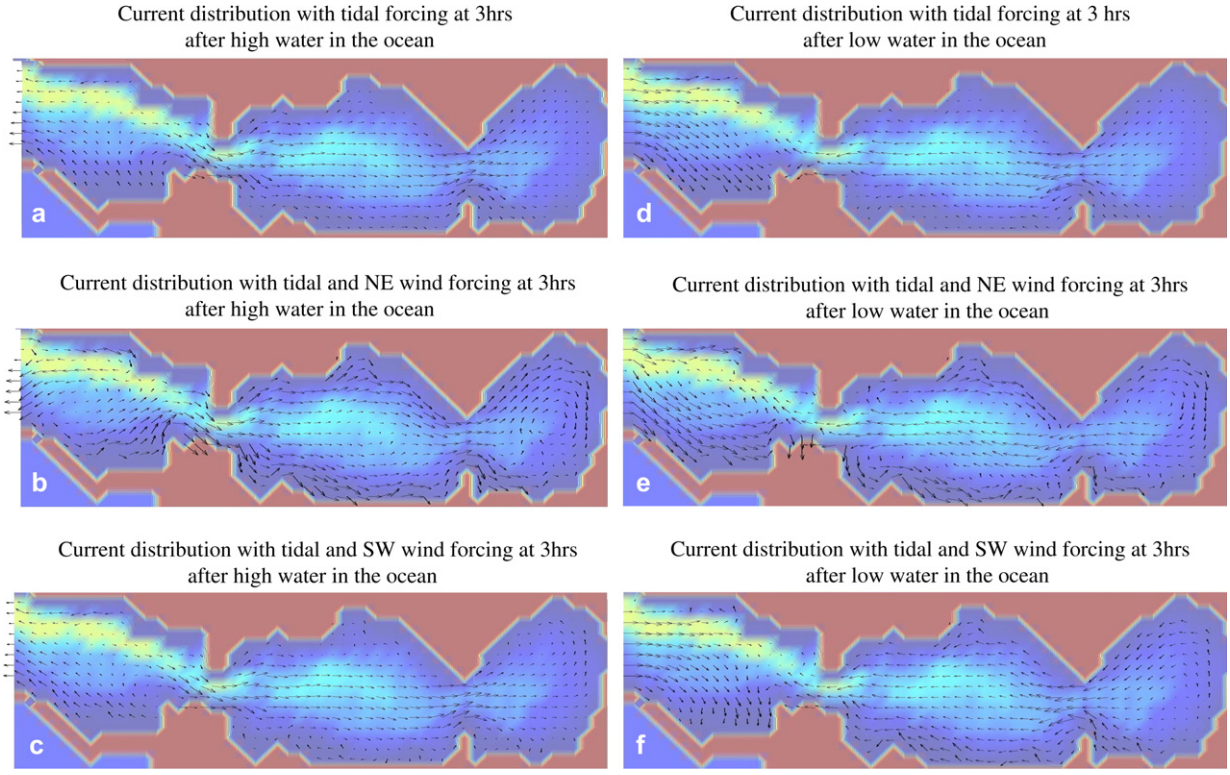

Fig. 7. (a–f) Modelled velocity distribution during flood (plates a and b) and ebb (plates d–f), respectively. Plates a and c show velocities for tidal forcing alone, plates b and d for tidal forcing and, in addition, a NE wind of 4 m s^{-1}, plates c and f, finally for tidal forcing and a SW wind of 4 m s^{-1}.

8. Discussion and conclusions

Tidal co-oscillation and related hydrodynamic phenomena in Puttalam Lagoon have been investigated by means of field measurements and a 2D numerical model. Model derived amplitudes and phase angles (Figs. 4 and 5) were used to calibrate the model. Phase differences between tides and currents (Fig. 6) were determined for validation and model runs agree quite well with data. Because of the small tidal range, and therefore moderate frictional effects, there is no total extinction of the tide, although the length $L \approx L_f$ (see Section 1). Instead, there is a combination of progressive and standing waves. In the innermost part, the tides behave close to standing waves, and the range is similar in Etalai and Puttalam Basins (Tables 1–3; Fig. 6). In the outer part, i.e. the Dutch Bay including Kalpitiya Narrows, the tides are nearly progressive, whereas in the central basin the tidal waves are partly progressive and partly standing. Interesting comparison can be made with two other lagoons, The Fleet (Robinson et al., 1983) and Laguna San Ignacio (Winant and Gutiérrez de Velasco, 2003) both of similar size, but with mean depths of about 1 and 5 m, respectively. In the former, the tide is purely progressive, and total extinction occurs, in the latter the tide is standing, with an even larger range at the head.

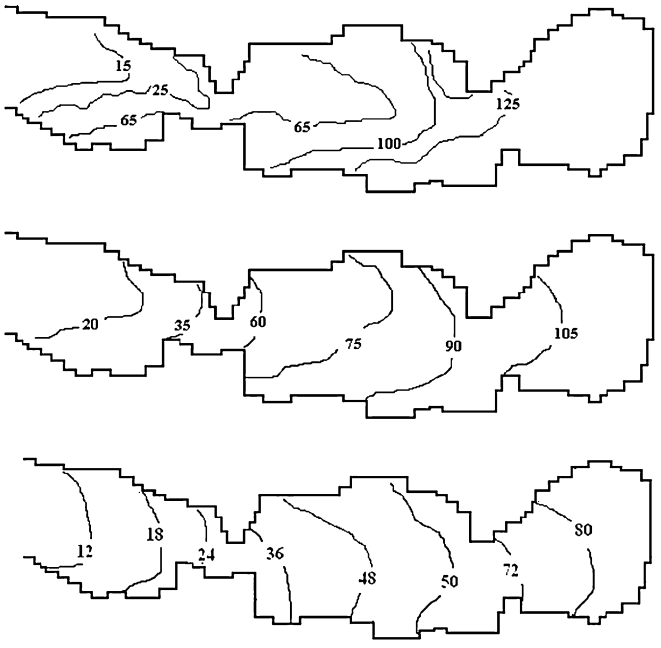

Fig. 8. (a–c) Model derived residence times in days, Plate a show residence time for tidal forcing alone, plate b for tidal forcing and, in addition, a NE wind of 4 m s^{-1}, plate c for tidal forcing with SW wind of 4 m s^{-1}.

8.1. Frictional set-up: results from observations

The observations indicated larger phase lags at low water than at high water (Table 1). Ebb periods are also somewhat longer than flood periods. Thus, there is a finite amplitude effect (although small) on the tidal wave propagation (Aubrey and Speer, 1985). Longer ebb than flood periods imply an elevated mean sea level. A frictional set-up is expected during spring (and a corresponding set-down during neap), because of

higher (lower) velocities. As pointed out, e.g. by Hill (1994), this set-up will give rise to a fortnightly tide. In Puttalam Lagoon, the range of M_f is 2 cm at Kalpitiya, compared to 6–7 cm at the head (Table 2). Differences in phase age between the ocean and the lagoon also indicate the existence of enhanced fortnightly tide. The phase age is 38 h on the west coast of Sri Lanka (Wijeratne, 2003) but increases to almost 100 h at the head, as calculated from the harmonic analysis (Table 3). Robinson et al. (1983) found a similar change in phase age from the ocean to the head of the Fleet, but because of relatively less friction with an aspect ratio of $\varepsilon = \eta_0/D \approx 0.06$, there is no tide extinction.

As mentioned, the ebb periods are somewhat longer than flood periods and the lagoon is slightly flood-dominant. It is obvious that in a frictionless channel the wave crest tends to move faster than the trough. The crest of the tide may partly overtake the trough (e.g. Friedrichs and Madsen, 1992). In a frictionally dominated shallow lagoon, the asymmetry is expected to be even more pronounced (Zimmerman, 1981; Speer and Aubrey, 1985). The asymmetric behaviour is represented by the shallow water constituents. However, harmonic analysis indicated that the shallow water tides are small, in general, with a maximum range of $MS_4 \leq 2$ cm (data not shown).

8.2. Circulation and residence times: model results

Model simulations in combination with Lagrangian tracking for tidal forcing alone indicate average residence times inside Kalpitiya of about 100 days, with large lateral variations (Fig. 7a). When a steady wind is added, the mean sea level increases towards the head of the lagoon for NE winds and decreases for SW winds. Moderate winds from NE of 4 m s^{-1} contribute to a decrease in residence times (Fig. 7b), which is most pronounced in the inner end (10–20%), but small or even opposite in the outer end. The set-up is 8 cm at the head, but 1 cm only, at Kalpitiya. Winds from SW of the same strength reduce the residence times much more efficiently, and throughout the lagoon (Fig. 7c). While the average residence time, inside Kalpitiya decreases from 100 to 90 days for a NE, 4 m s^{-1} wind, it is reduced to about 60 days for a SW wind of similar strength. Fig. 8a–f shows in details how winds affect the tidal circulation. The large difference between the different wind directions is notable, but in accordance with the study of Geyer (1997). We also found that the wind has relatively stronger influence on sea levels during neap than during spring because tidal velocities are low during neap. However, this makes no difference to the residence times, which are long compared to the spring/neap cycle. With some few exceptions (rare visits of tropical cyclones) the monsoon winds are weak. As mentioned, during the peak SWM mean winds may reach 6 m s^{-1}, whereas the residence times could be even somewhat shorter. However, mean NEM winds are hardly larger than 4 m s^{-1} on the west coast.

Model simulations carried out with variable depths (during calibration and validation) showed that a decrease in the sea level by 30 cm would reduce the tidal amplitudes by about 15% and increase the phase lag by 15–20 min from the entrance to the head. The oceanic seasonal range is typically 25–30 cm around Sri Lanka, mainly due to variations in salinity and temperature (Wijeratne, 2003). During the period of observations the decrease of the mean sea level was about 15 cm, basically from Period II to III. This decrease had some effects on ranges and phase lags (Table 1), and we realise that the relatively large seasonal variations in sea level will also have some effect on the residence times.

9. Conclusions

Puttalam Lagoon is hypersaline during the main part of the year (Fig. 2), indicating long periods of inverse estuarine circulation, but also in between the periods of low salinities and normal estuarine circulation. One might expect such conditions to result in a less efficient water exchange, particularly, because stages of weak forcing are likely to appear several times per year. This is also what is suggested for ''near neutral estuaries'' by Largier et al. (1997). However, this is not obvious from Puttalam Lagoon; modelling of tides indicates an average residence time of about 100 days. Wind forcing with moderate winds (± 4 m s^{-1}) decreases residence times to 60–90 days; depending on wind force *and* direction, whereas freshwater forcing (also weak; q_f is typically ± 10 m^3 s^{-1}) in addition, as calculated from volume and salt conservation, indicates residence times of between 40 and 80 days. Presumably, this is because the lagoon is very shallow, and high evaporation and occasional rainfall create strong horizontal gradients, typically up to 0.5 psu/km, and also high velocities (Fig. 2). In addition, estuarine circulation will become strong during slack water, respectively, and also during neap when tidal velocities are too weak to mix the waters from surface to bottom (Linden and Simpson, 1988; Nunes-Vaz et al., 1989; Zhou, 1998). And, of course, also wind forcing plays an important role here. Wind force is also strong, if evaluated per unit volume. More detailed interpretations (i.e. Scully et al., 2005) may also indicate how winds act on stratification to effect residual circulation. Or even to what extent very shallow lagoons like Puttalam are actually shaped by the combination of forces involved as discussed by Prandle (2004).

Acknowledgments

Field measurements were conducted under SIDA/SAREC/NARA Coastal Ecological Program with assistance of the Oceanography Division staff at the National Aquatic Resources Research and Development Agency (NARA). We also thank an unknown reviewer for several important and helpful comments and Ms Agneta Malm for help with the drawings.

Appendix 1. Numerical scheme

A staggered grid system was chosen used to represent the numerical form of the depth-averaged Eqs. (1)–(3). Velocity and sea level grid points are separated according to Fig. 2 such that no sea level points are located on the coastal boundary. The existing velocities are perpendicular to the boundary.

The grid points are indexed by j in the x-direction and k in the y-direction, where the shortest distance between the same variable in the x-direction is Δx and in the y-direction Δy. An index m in superscript was used for time. Forward and backward differences were used to treat the linear space and time derivatives in Eqs. (1)–(3), without wind stress. The non-linear acceleration terms were treated according to the upwind–downwind approximation (see Kowalik and Murty, 1993). Thus, the finite difference representations of Eqs. (1)–(3) are as follows:

$$\begin{aligned}\frac{u_{j,k}^{m+1}-u_{j,k}^{m}}{\Delta t}-f\overline{v}_{j,k}^{m,u}=&\frac{-g}{\Delta x}\left(\eta_{j+1,k}^{m}-\eta_{j,k}^{m}\right)\\&-\frac{\left(u_{j,k}^{m}+\left|u_{j,k}^{m}\right|\right)\left(u_{j,k}^{m}-u_{j+1,k}^{m}\right)}{2\Delta x}\\&-\frac{\left(u_{j,k}^{m}-\left|u_{j,k}^{m}\right|\right)\left(u_{j+1,k}^{m}-u_{j,k}^{m}\right)}{2\Delta x}\\&-\frac{\left(\overline{v}_{j,k}^{u,m}+\left|\overline{v}_{j,k}^{u,m}\right|\right)\left(u_{j,k}^{m}-u_{j,k-1}^{m}\right)}{2\Delta y}\\&-\frac{\left(\overline{v}_{j,k}^{u,m}-\left|\overline{v}_{j,k}^{u,m}\right|\right)\left(u_{j,k+1}^{m}-u_{j,k}^{m}\right)}{2\Delta y}\\&-C_{\mathrm{d}}\frac{\sqrt{\left(u_{j,k}^{m}\right)^{2}+\left(\overline{v}_{j,k}^{u,m}\right)^{2}}u_{j,k}^{m}}{D_{u,j,k}^{m}}\end{aligned}\tag{4}$$

$$\begin{aligned}\frac{v_{j,k}^{m+1}-v_{j,k}^{m}}{\Delta t}+f\overline{u}_{j,k}^{v,m}=&\frac{-g}{\Delta y}\left(\eta_{j,k+1}^{m}-\eta_{j,k}^{m}\right)\\&-\frac{\left(\overline{u}_{j,k}^{v,m+1}+\left|\overline{u}_{j,k}^{v,m+1}\right|\right)\left(v_{j,k}^{m}-v_{j-1,k}^{m}\right)}{2\Delta x}\\&-\frac{\left(u_{j,k}^{v,m+1}-\left|\overline{u}_{j,k}^{v,m+1}\right|\right)\left(v_{j+1,k}^{m}-v_{j,k}^{m}\right)}{2\Delta x}\\&-\frac{\left(v_{j,k}^{m}+\left|v_{j,k}^{m}\right|\right)\left(v_{j,k}^{m}-v_{j,k-1}^{m}\right)}{2\Delta x}\\&-\frac{\left(v_{j,k}^{m+1}-\left|v_{j,k}^{m}\right|\right)\left(v_{j,k+1}^{m}-v_{j,k}^{m}\right)}{2\Delta x}\\&-C_{\mathrm{d}}\frac{\sqrt{\left(\overline{u}_{j,k}^{v,m}\right)^{2}+\left(v_{j,k}^{m}\right)^{2}}v_{j,k}^{m}}{D_{v,j,k}^{m}}\end{aligned}\tag{5}$$

$$\begin{aligned}\frac{\eta_{j,k}^{m+1}-\eta_{j,k}^{m}}{\Delta t}=&-\frac{\left(u_{j,k}^{m+1}D_{u,j,k}^{m}-u_{j-1,k}^{m+1}D_{u,j-1,k}^{m}\right)}{\Delta x}\\&-\frac{\left(v_{j,k}^{m+1}D_{v,j,k}^{m}-v_{j,k-1}^{m+1}D_{v,j,k-1}^{m}\right)}{\Delta y}\end{aligned}\tag{6}$$

Here, the u velocities at v-velocity grid points, u^v and v velocities at u-velocity grid points, v^u were obtained from arithmetic averages of the surrounding values according to:

$$\overline{u}^{v,m}=\frac{u_{j,k}^{m}+u_{j,k+1}^{m}+u_{j+1,k+1}^{m}+u_{j+1,k}^{m}}{4}\tag{7}$$

$$\overline{v}^{u,m}=\frac{v_{j,k}^{m}+v_{j-1,k}^{m}+u_{j-1,k-1}^{m}+u_{j,k-1}^{m}}{4}\tag{8}$$

The lagoon was divided into 109 and 35 sections in longitudinal and cross-axis, respectively, with Δx of 450 m and Δy of 425 m. The full 2D grid net consists of 108×34 sea levels, 109×34 u-velocity points and 108×35 v-velocity points. In the 2D grid net, the tide gauge Stns P-1 to P-5 are located at grid points of (35,13), (46,4), (68,2), (102,6) and (102,28), respectively. The depths of grid points in the model (sea level points, u- and v-velocity points) were obtained by interpolating the bathymetric map of National Hydrographic Office. Harmonic tidal constants were used to specify the open boundary conditions (Table 2). Zero fluxes are specified for close boundaries as boundary condition. We also assumed zero cross-axis velocities, v at the open boundary in the model. The initial distribution of velocities and sea levels were taken to be zero. The net freshwater flux was neglected because it is very small as compared to the tidal fluxes. The time interval, Δt was chosen to be 30 s, which satisfies model stability.

The grid net of Puttalam Lagoon: Sea level points are denoted by ., longitudinal velocity (u) grid points are denoted by − and cross-axis velocity points (v) are denoted by |.

Appendix 2. Lagrangian tracking method

Groups of neutrally buoyant conservative particles are released in the grid domain, recording the time required for each particle to be flushed out of the lagoon. Modelled velocities and turbulent diffusion are forced to move the particles with a time step, $\Delta t = 30$ s. The particle displacement at

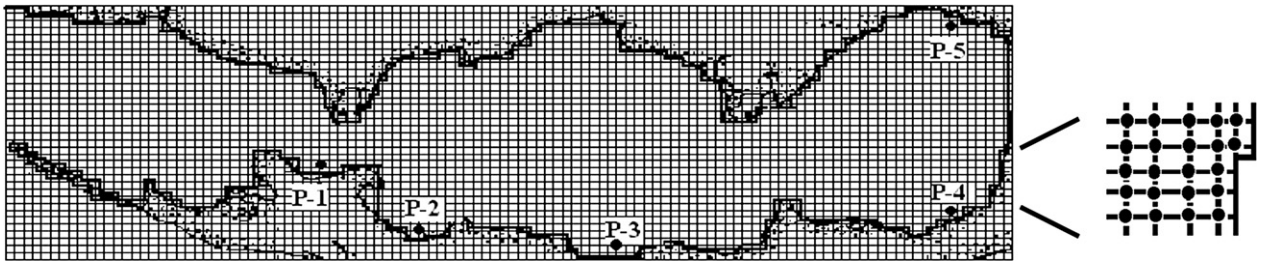

a single time step in the longitudinal, x-direction is $\Delta x = u\Delta t \pm (2\,K_x(u)\Delta t)^{1/2}$ and in the transverse y-direction $\Delta y = v\Delta t \pm (2\,K_y(v)\Delta t)^{1/2}$. The turbulent diffusion coefficient, K_x, depends on the velocity, u and the mixing depth, d_m. Following Fischer et al. (1979), $K_x(u) = C_d^{1/2} u k d_m$, where C_d is the calibrated bottom drag coefficient and $k = 0.4$, is von Karman's constant. The mixing depth, d_m, is taken equal to the total depth D. Particles are free to move between the grid points. Therefore, the velocity computed by the model was linearly interpolated for the instantaneous particle positions prior to integration. Tracking runs were done repeatedly for different tidal phases: at low water, 3 h after low water, high water and 3 h after high water.

References

Amarasinghe, U.A., Mutuwatta, L., Sakthivadivel, R., 1999. Water Scarcity Variations Within a Country: A Case Study of Sri Lanka. Research Report 32. Colombo, Sri Lanka.

Arulananthan, K., 2004. Hydrography, Coastal Water Circulation and Classification of Sri Lankan Lagoons. Ph.D thesis. Göteborg University Ser. C62. Earth Science Centre.

Arulananthan, K., Rydberg, L., Cederlöf, U., Wijeratne, E.M.S., 1995. Water exchange in a hypersaline tropical estuary, the Puttalam Lagoon, Sri Lanka. Ambio 24, 438–443.

Aubrey, D.G., Speer, P.E., 1985. A study of non-linear tidal propagation in shallow inlet/estuarine systems, part 1: observations. Estuarine, Coastal and Shelf Science 21, 185–205.

Björk, G., Liungman, O., Rydberg, L., 2000. Net circulation and salinity variations in an open-ended Swedish fjord system. Estuaries 23, 367–380.

Bolin, B., Rodhe, H., 1973. A note on the concepts of age distribution and transmit time in natural reservoirs. Tellus 25, 58–62.

Bowers, D.G., Lennon, G.W., 1990. Tidal propagation in a near-resonant system – a case study from South Australia. Estuarine, Coastal and Shelf Science 30, 17–34.

Dronkers, J.J., 1969. Tidal computations for rivers, coastal areas and seas. Journal of Hydraulics Division 95, 44–77.

Friedrichs, C.T., Aubrey, D.G., 1988. Non-linear tidal distortion in shallow well-mixed estuaries: a synthesis. Estuarine, Coastal and Shelf Science 27, 521–545.

Geyer, W.R., 1997. Influence of wind on dynamics and flushing of shallow estuaries. Estuarine, Coastal and Shelf Science 44, 713–722.

Fischer, H.B., List, E.G., Koh, R.C.Y., Imberger, J., Brooks, N.H., 1979. Mixing in Inland and Coastal Waters. Academic Press, New York, NY, 483 pp.

Friedrichs, C.T., Madsen, O.S., 1992. Nonlinear diffusion of the tidal signal in frictionally dominated embayments. Journal of Geophysical Research 97, 5637–5650.

Hansen, D.V., Rattray Jr., M., 1965. Gravitational circulation in straits and estuaries. Journal of Marine Research 23, 104–122.

Hill, A.E., 1994. Fortnightly tide in a lagoon with variable choking. Estuarine, Coastal and Shelf Science 38, 423–434.

Jayasiri, H.B., Rajapaksha, J.K., Rydberg, L., Cederlof, U., 1998. The Mundal Lake estuarine system, Sri Lanka: possible measures to avoid extreme salinity and sea level variations. Ambio 27, 745–751.

Kowalik, Z., Murty, T.S., 1993. Numerical modelling of ocean dynamics. In: Advanced Series on Ocean Engineering, vol. 5. World Scientific, Singapore, New Jersey, London, Hong Kong, 481 pp.

Largier, J.L., Hollibaugh, J.T., Smith, S.V., 1997. Seasonally hypersaline estuaries in Mediterranean climate regions. Estuarine, Coastal and Shelf Science 45, 779–787.

Le Blond, P.H., 1978. On tidal propagation in shallow rivers. Journal of Geophysical Research 83, 4717–4721.

Li, C., Valle-Levinson, A., 1999. A two-dimensional analytical tide model for a narrow estuary of arbitrary lateral depth variation: the intra-tidal motion. Journal of Geophysical Research 104, 23525–23543.

Li, C., O'Donnell, J., 2005. The effect of channel length on the residual circulation in tidally dominated channels. Journal of Physical Oceanography 35, 1826–1840.

Linden, P.F., Simpson, J.E., 1988. Modulating mixing and frontogenesis in shallow seas and estuaries. Continental Shelf Research 8, 1107–1127.

Liungman, O., Rydberg, L., Göransson, C.-G., 2001. Modelling and observations of deep water renewal and entrainment in a Swedish sill fjord. Journal of Physical Oceanography 31, 3401–3419.

Luff, R., Pohlmann, T., 1995. Calculation of water exchange times in the ICES-boxes with a Eulerian dispersion model using a half-life time approach. Deutsche Hydrographische Zeitschrift 47, 287–300.

Műnchow, A., Garvine, R.W., 1991. Nonlinear barotropic tides and bores in estuaries. Tellus 43A, 246–256.

Nunes-Vaz, R.A., Lennon, G.W., Bowers, D.G., 1990. Physical behaviour of a large, negative or inverse estuary. Continental Shelf Research 10, 277–304.

Nunes-Vaz, R.A., Lennon, G.W., de Silva Samarasinghe, J.R., 1989. The negative role of turbulence in estuarine mass transport. Estuarine, Coastal and Shelf Science 28, 361–377.

Officer, C.B., Kester, D.R., 1991. On estimating the non-advective tidal exchanges and advective gravitational circulation exchanges in an estuary. Estuarine, Coastal and Shelf Science 32, 99–103.

Prandle, D., 1984. A modeling study of the mixing of 137C in the seas of the European continental shelf. Philosophical Transactions of the Royal Society of London A310, 407–436.

Prandle, D., 1985. On salinity regimes and the vertical structure of residual flows in narrow tidal inlets. Estuarine, Coastal and Shelf Science 20, 615–633.

Prandle, D., 2004. How tides and river flows determine estuarine bathymetries. Progress in Oceanography 61, 1–26.

Robinson, I.S., Warren, L., Longbottom, J.E., 1983. Sea level fluctuations in the Fleet, an English tidal lagoon. Estuarine, Coastal and Shelf Science 16, 651–668.

Samuelsson, M., Stigebrandt, A., 1996. Main characteristics of the long-term sea level variability in the Baltic Sea. Tellus 48A, 672–683.

Scully, M.E., Friedrichs, C.T., Brubaker, J.M., 2005. Control of estuarine stratification and mixing by wind-induced straining of the estuarine density field. Estuaries 28, 321–326.

Shen, J., Lin, J., 2006. Modelling study on the influences of tide and stratification on age of water in the tidal James River. Estuarine, Coastal and Shelf Science 68, 101–112.

Signell, R.P., Butman, B., 1992. Modeling tidal exchange and dispersion in Boston Harbor. Journal of Geophysical Research 97, 15591–15606.

Simpson, J.H., Williams, E., Brasseur, L.H., Brubaker, J.M., 2005. The impact of tidal straining on the cycle of turbulence in a partially stratified estuary. Continental Shelf Research 25, 51–64.

Souto, C., Gilcoto, M., Fariña-Busto, L., Pérez, F.F., 2003. Modeling the residual circulation of a coastal embayment affected by wind-driven upwelling: circulation of the Ria de Vigo (NW Spain). Journal of Geophysical Research 108, 3340–3357.

Speer, P.E., Aubrey, D.G., 1985. A study of non-linear tidal propagation in shallow inlet/estuarine systems, part II: theory. Estuarine, Coastal and Shelf Science 21, 207–224.

Stommel, H., Farmer, H.G., 1953. Control of salinity in an estuary by a transition. Journal of Marine Research 12, 13–20.

Wijeratne, E.M.S., Cederlöf, U., Rydberg, L., Arulananthan, K., 1995. The tidal response of Puttalam Lagoon, Sri Lanka: a large shallow tropical lagoon. Ambio 24, 444–447.

Wijeratne, E.M.S., 2003. Tidal Characteristics and Modeling of Tidal Wave Propagation in Shallow Lagoons of Sri Lanka, Ser. C51. Earth Science Centre, Gothenburg University.

Winant, C.D., Gutiérrez de Velasco, G., 2003. Tidal dynamics and residual circulation in a well-mixed inverse estuary. Journal of Physical Oceanography 33, 1365–1379.

Wolanski, E., 1986. An evaporation-driven salinity maximum zone in Australian tropical estuaries. Estuaries, Coastal and Shelf Science 22, 415–424.

Zimmerman, J.T.F., 1981. Dynamics, diffusion, and geomorphological significance of tidal residual eddies. Nature 290, 549–555.

Zhou, M., 1998. Influence of bottom stress on the two-layer flow induced by gravity currents in estuaries. Estuarine, Coastal and Shelf Science 46, 811–825.

Available online at www.sciencedirect.com
ScienceDirect
Estuarine, Coastal and Shelf Science 74 (2007) 709–721
ESTUARINE COASTAL AND SHELF SCIENCE
www.elsevier.com/locate/ecss

Assessment of water exchange between a discharge region and the open sea – A comparison of different methodological concepts

Kristofer Döös [a,*], Anders Engqvist [b]

[a] Department of Meteorology, Stockholm University, SE-10691 Stockholm, Sweden
[b] Husö Biological Station, Åbo Akademi University, FIN-20500 Turku, Finland

Received 21 June 2006; accepted 9 May 2007
Available online 16 July 2007

Abstract

Two different methods of estimating the water exchange through the Baltic coastal region of Laxemar have been used, consisting of particle trajectories and passive tracers. Water is traced from and to a small discharge region near the coast. The discharge material in this region is treated as zero-dimensional particles or tracers with neutral buoyancy. The real discharge material could be a leakage of radio-nuclides through the sea floor from an underground repository of nuclear waste.

Water exchange rates between the discharge region and the model domain are estimated using both forward and backward trajectories as well as passive tracers. The Lagrangian trajectories can account for the time evolution of the water exchange while the tracers give one average age per model grid box. Water exchange times such as residence time, age and transient times have been calculated with trajectories but only the average age (AvA) for tracers. The trajectory calculations provide a more detailed time evolution than the tracers.

On the other hand the tracers are integrated ''on-line'' simultaneously in the sea circulation model with the same time step while the Lagrangian trajectories are integrated ''off-line'' from the stored model velocities with its inherent temporal resolution, presently 1 h. The sub-grid turbulence is parameterised as the Laplacian diffusion for the passive tracers and with an extra stochastic velocity for trajectories. The importance of the parameterised sub-grid turbulence for the trajectories is estimated to give an extra diffusion of the same order as the Laplacian diffusion by comparing the Lagrangian dispersions with and without parameterisation. The results of the different methods are similar but depend on the chosen diffusivity coefficient with a slightly higher correlation between trajectories and tracers when integrated with a lower diffusivity coefficient.

Keywords: Lagrangian trajectories; passive tracers; residence time; Baltic Sea; radio-nuclides; Lagrangian dispersion

1. Introduction

Radioactive nuclide particles emanating from a planned underground repository may via geospheric pathways enter into the coastal waters of Laxemar (Figs. 1 and 2). This location is one of the twoareas chosen by the Swedish Nuclear Fuel and Waste Management Co. (SKB) as possible sites for long-term storage of nuclear waste. In order to guarantee sufficient barriers (in addition to geological barriers) between the radioactive material and the biosphere, all aspects of the biosphere (e.g. surface hydrology, terrestrial, limnic and marine ecosystems) are being considered in order to assess the potential fate and distribution of radio-nuclides in the environment and exposure and risk to humans.

Should a radioactive particle enter into the water through the bottom of the coastal section, then from the entry point a long transport phase is instigated that in geological times most likely will eventually end in the bottom sediments of the world oceans with the passage through the Baltic Sea as an intermediary link.

* Corresponding author.
E-mail address: doos@misu.su.se (K. Döös).

0272-7714/$ - see front matter © 2007 Published by Elsevier Ltd.
doi:10.1016/j.ecss.2007.05.022

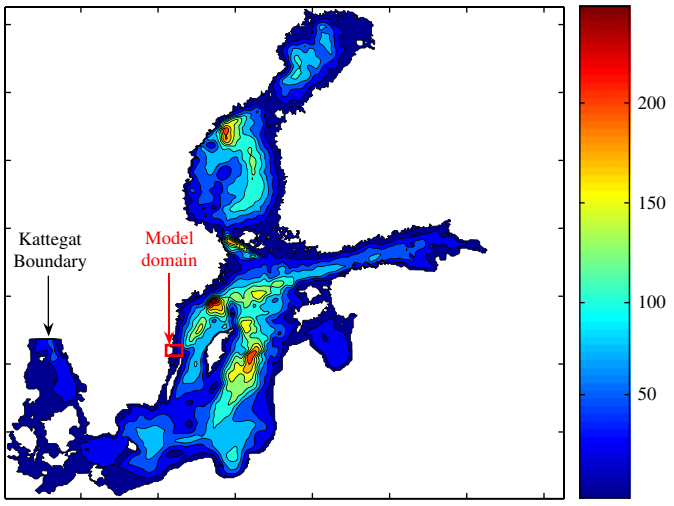

Fig. 1. Baltic model bathymetry in meters.

On a shorter time frame, advective and diffusive processes will determine the passage through the near-shore coastal region, possibly interrupted by incorporation into the biosphere or sequestration into the sediments for some period of time. The present scope is restrained to the water-borne transport phase and entails investigation of the fate of radio-nuclides in the event of leakage from the future repository. This study will employ a 3D-circulation model in order to compute residence times and water exchange statistics making use of both passive tracers and Lagrangian trajectories.

Water exchange of the coastal zone varies both in time and space. In order to being able to communicate such intricate patterns, one needs to reduce the complexity into more comprehensible concepts. We will in the present study use two different methods to trace the water movements: (1) passive tracers, which are integrated in the 3D-circulation model and (2) Lagrangian trajectories, which are calculated from the 3D model velocity field off-line, i.e. after the model has been integrated. Both passive tracers and trajectories are advected by the velocity fields but the sub-grid turbulence is parameterised differently. Furthermore the tracer is integrated in the model and has the advantage of using the correct velocity fields while the trajectories use hourly averages. The passive tracers on the other hand have a numerical diffusion due to the finite-difference approximation error.

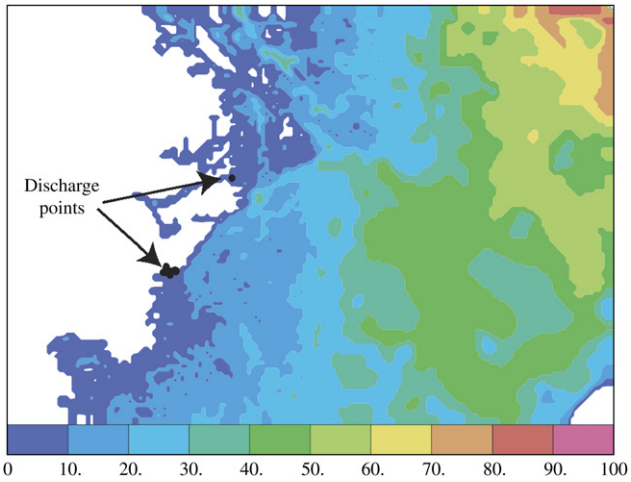

Fig. 2. The model bathymetry in meters of the Laxemar coastal region. The nuclei leakage or discharge positions are marked with black dots from where the trajectory particles and tracers are released. The area between land and the black line is referred to as the reduced study area.

The purpose of this study is not to designate which method is superior, but to assess the differences between the methods and their corresponding results. The study will, however, be an indictor of which sort of field experiment with for example floats would be necessary to validate the methods qualitatively and quantitatively in the future.

An outline of the present paper is that first a description of the 3D model and the Lagrangian trajectory and passive tracer techniques are presented in Section 2. The results of the intercomparisons between tracers, average age and trajectories are presented in Section 3, followed by a discussion and conclusions in Section 4.

2. Methodology

2.1. Sea circulation model AS3D

The numerical 3D model used in the present study was first formulated by Andrejev and Sokolov (1989). It is time-dependent with a free surface and based on the basic set of the primitive hydrodynamical equations together with the equation of state formulation of Millero and Kremling (1976). The model has 39 vertical levels with monotonically increasing layer thickness towards the bottom. The governing equations are used in flux form to ensure that a number of integral constraints (Blumberg and Mellor, 1987) are maintained. The finite-difference numerical approximations are constructed by integrating the model equations over the C-grid cell volume (Mesinger and Arakawa, 1976). The time step was split up, as suggested by Liu and Leendertse (1978). All vertical derivatives as well as the bottom friction are treated implicitly. The mode-splitting technique (Simons, 1974) was employed, where the two-dimensional (2D) equation for the volume transport (viz. the external mode) was obtained by vertical summation of the finite-difference approximations of the 3D momentum equations. Before the 3D finite-difference equations corresponding to the internal mode can be resolved, the sea surface elevation must be calculated from the volume transport equation and from the vertically integrated equation of continuity. The frictional stress at the bottom is also calculated using an iterative procedure. The 2D and 3D momentum equations are thus solved repeatedly until the absolute value of the maximum difference between the bottom velocities for subsequent iterations becomes smaller than an *a priori* prescribed minute positive number. This adjustment process permits the use of an alternating direction implicit method for solving the volume transport equation (Liu and Leendertse, 1978; Andrejev and Sokolov, 1989). It also allows usage of the same time step for all the 2D and the 3D elements of the model. These

equations are solved employing Gaussian elimination methods. Vertical convection must be parameterised since the 3D-models use the hydrostatic approximation. The study of the main circulation of the Baltic Sea was the main motive of Andrejev and Sokolov (1989) to develop the AS3D sea circulation model employed in this study.

In recent times this model has been involved in several Baltic hydrographic studies (Andrejev et al., 2004a,b). An encompassing testing of this model in relation to the measured data was performed by Engqvist and Andrejev (2003) along an interface to a model area comprising the Stockholm archipelago. It was found that the measured salinity and temperature profiles were acceptably well reproduced, with the main difference being a constant offset in salinity. For the purpose of validating the cascade model approach, salinity profiles along the interfacial boundary between these models were sampled from a ship navigating along this interface. These data were compared to independently computed model data for corresponding points in space and time. The outcome of this comparison was qualitatively convincingly similar, except for an offset average salinity of less than 1 unit in the PSU scale, most likely due to a deviation of the same magnitude in the initial salinity fields of the model. This validation increased considerably the confidence of the realism of the boundary data provided by the AS3D-model.

In the present study two sets of grids were used: one for the entire Baltic with an open boundary in Kattegat (Fig. 1) with a horizontal resolution of 2 nautical miles, and one sub-model for the Laxemar region (Fig. 2) with a horizontal resolution of 0.1 nautical miles (185 m). The horizontal eddy diffusivity was set to 30 m^2/s for the Baltic model. For the Laxemar version two simulations were done, one with 5 m^2/s and one with 20 m^2/s. The models were integrated with realistic atmospheric forcing over a 1-year cycle of the year of 1981, selected for being average concerning local temperature and fresh water discharge.

2.2. Passive tracers

The first type of a conceptual exchange measure concerns a tracer substance discharged as a fully controlled source. This can be performed both in reality and in a numerical model. An ideal tracer should be fully water-soluble, lack state transitions and at the same time be detectable in very low concentrations. The equation of the passive tracer C is

$$\frac{\partial C}{\partial t} + \mathbf{V}\cdot\nabla C = K_H \nabla_H^2 C + \frac{\partial}{\partial z}\left(K_V \frac{\partial C}{\partial z}\right) + F_C \qquad (1)$$

where K_H and K_V are the eddy diffusivity coefficients in the horizontal and the vertical direction, respectively. The former is set constant as mentioned earlier but the latter varies with depth and is made dependent on the local vertical shear and buoyancy forces according to Marchuk (1980). $\mathbf{V}$ is the velocity vector and F_C the tracer source term. The discharge points of a tracer representing a contaminant are indicated in Fig. 2. The finite-difference approximations of these equations were constructed by integrating them over a C-grid. The finite-differences are centered and hence with a truncation error of the second order.

2.3. Age tracers

The second type of a conceptual exchange measure is a time-oriented method, based on computing the age of water parcels in a reservoir defined by a close surface boundary that separates the interior from exogenous water outside. Eriksson (1971) was the first to strictly formulate a reservoir theory. In the same paper were also formulated the statistical properties that material distributed in a reservoir in steady-state must fulfil. Since the 1970s when ecological concerns instigated debates about harmful materials and their circulation through the environment, this line of statistically based analysis has had many sequels in applied sciences. The scientific debate, however, suffered from loose definitions. Bolin and Rodhe (1973) attempted to sharpen the distinction between different types of retention time concepts in order to mitigate misunderstandings. They pursued their analysis in a general way with the focus on unevenly distributed materials borne in a flowing medium, and defined the two concepts of average age (AvA) and average transit residence time (ATR), but these acronyms are of a later date. The first concept denotes the average time an ensemble of individual particles, present at a given instant inside a predefined domain, has spent inside this domain. The average should be taken over this simultaneously present ensemble. The time measurement begins for each particle as it enters the domain. This is computed by integrating Eq. (1) with the tracer source to one ($F_C = 1$) in the model domain and setting the values of the tracer to zero ($C = 0$) on the open boundaries to the north, east and west of the model domain (Fig. 2).

The time that the same particle remains in the reservoir is defined as its residence time. The average over the same simultaneously present ensemble is denoted as AvR-time. The sum of corresponding AvR- and the AvA-times for a particle gives the average transit residence time (ATR). This nomenclature was suggested by Delhez et al. (2004). The relationship between the two latter measures in steady-state conditions is given by Björkström (1978). Note that all these concepts are defined relative to a specified boundary that separates the particles or water parcels belonging to the domain from those being outside, which are referred to as being exogenous. Any relationship between these time-based measures and water exchange expressed as volume flow is only valid during steady conditions so that stable equilibrated distributions can be established. If parts of a domain are exempted from exchange for a period, such as by water being moved back and forth or by entering a secluded pathway, the AvA of these parts will increase monotonously during this time.

In a special issue dedicated to articles on time-based tracers, it may seem presumptuous to present a literature review since many more encompassing such reviews are likely to appear, such as the one presented by Monsen et al. (2002). A few highlights of the present authors' points of view can, however, be

motivated. Deleersnijder et al. (2001) presented a theoretical framework for which AvA of a set of particles subjected to advection, diffusion and destruction are accounted for using mass-weighted averages. This makes it possible to distinguish between the transporting medium (i.e. normally water or air), passive tracers and active tracers such as decaying radioactive material and/or biologically reactive constituents. Delhez et al. (2004) extended this framework to also cover ATR-times for non-stationary flow. Regarding ventilation of coastal waters, focus can naturally be placed on the renewal of the flowing medium *per se* (i.e. sea water) and not on its particle contents. An early contribution based on the ATR-time concept was given by Pilson (1985) using box-models. In this context ATR is often referred to as hydraulic residence time (Hagy et al., 2000). The AvA concept, originally defined for a single reservoir, was independently adapted to water circulation models by introducing its volume-specific counterpart (England, 1995; Engqvist, 1996), by denoting the length of time a particular water parcel (or parts thereof) on average has spent within a specified connected body of water. Applications seem to have been intensified since 2000. Several recent studies (Engqvist and Andrejev, 2003; Andrejev et al., 2004a,b) apply the original method, while Gustafsson (2000) and Khatiwala et al. (2001) restrict the active age tracers to the ones that also have been in contact with a boundary of the domain, starting the counting of age from these events. These latter approaches are based on the assumption that the employed model is capable of distinguishing the different kinds of water, a method which bears a resemblance to trajectory analysis. This can be accomplished by an additional scalar tracer marker representing the fraction of contained water type in each subcompartment. The AvA dynamics scheme should then only be applied to one particular fraction of the contents of a compartment at a time so that the corresponding AvA values represent the residence time only of this fraction. This method also expands the applicability to cover residence time of fresh water (Dettman, 2001; Sheldon and Alber, 2002), which also may be treated as exogenous water with initial age set to zero at its discharge point. Monsen et al. (2002) introduced the concept of exposure time that stands for particles that enter and leave the residential domain multiple times without having their time-based scalar measure reset to zero on exiting. This approach certainly demands a computational domain that is sufficiently greater than the studied residence domain. Various aspects of the Baltic circulation were analysed by Meier (2005) using the standard AvA method.

2.4. Lagrangian trajectories

The Lagrangian trajectories in the present study have been calculated with the trajectory model TRACMASS, which is based on Döös (1995) and Blanke and Raynaud (1997) presented in Appendix A. A selection of three trajectories calculated with sub-grid turbulence parameterisation taking highly disparate paths is presented in Fig. 3. They enter the model domain through the open boundaries, flowing into the discharge regions and then eventually exit the model domain through the open boundaries.

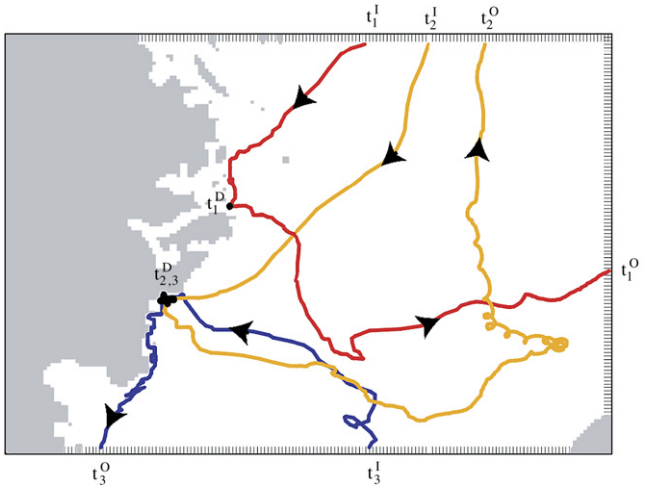

Fig. 3. A selection of three trajectories entering the model domain through the open boundaries at the times t_1^I, t_2^I, t_3^I. The discharge regions are reached at the times t_1^D, t_2^D, t_3^D. They eventually exit the model domain through the open boundaries at the times t_1^O, t_2^O, t_3^O.

The trajectory solutions obtained by Eqs. (9)–(13) in the Appendix A, only include the implicit large scale diffusion due to along-trajectory changes of temperature and salinity, and by the models parameterisation of turbulent mixing in the momentum equations. These trajectories do not, however, explicitly represent sub-grid scale turbulence. There are several ways to incorporate a sub-grid scale turbulence. One way is to add a random displacement to the trajectories (Levine, 2005). We have here chosen another method, consisting instead of adding a random turbulent velocity u' to the circulation model's saved velocity field U for each trajectory and each model grid wall. This enabled us to use the TRACMASS code as it is but with a velocity field that is somewhat shaken, resulting in stirred trajectory particles. The new velocity from which the transport is calculated in Eq. (9) is now $u = U + u'$. The amplitude of the random turbulent velocity is set to the same size as the circulation model velocity U, so that $u' = RU$, where R is a random number uniformly distributed between $-a$ and a. Best results were obtained for $a = 1$ and all the results in the present study are made with these. New random turbulent velocities were generated every time step for each trajectory.

The effect of this superimposed sub-grid turbulence is clearly visible by just plotting the trajectory positions every hour for a particle cluster released in the discharge area at a particular moment (at 1:00 on 15th June 1981) in Fig. 4. The parameterised turbulence smoothes the trajectory positions and spreads them more evenly. The stirred particles in Fig. 4b fill visibly regions where no particles were present without sub-grid turbulence in Fig. 4b.

The mean position of the trajectory cluster is defined as

$$\overline{x_i(t)} \equiv \frac{1}{N}\sum_{n=1}^{N} x_i^n(t) \tag{2}$$

where t is the time, N is the total number of trajectories contained in the cluster and i the spatial coordinate index, i.e. the zonal, meridional or vertical position of the n-th trajectory

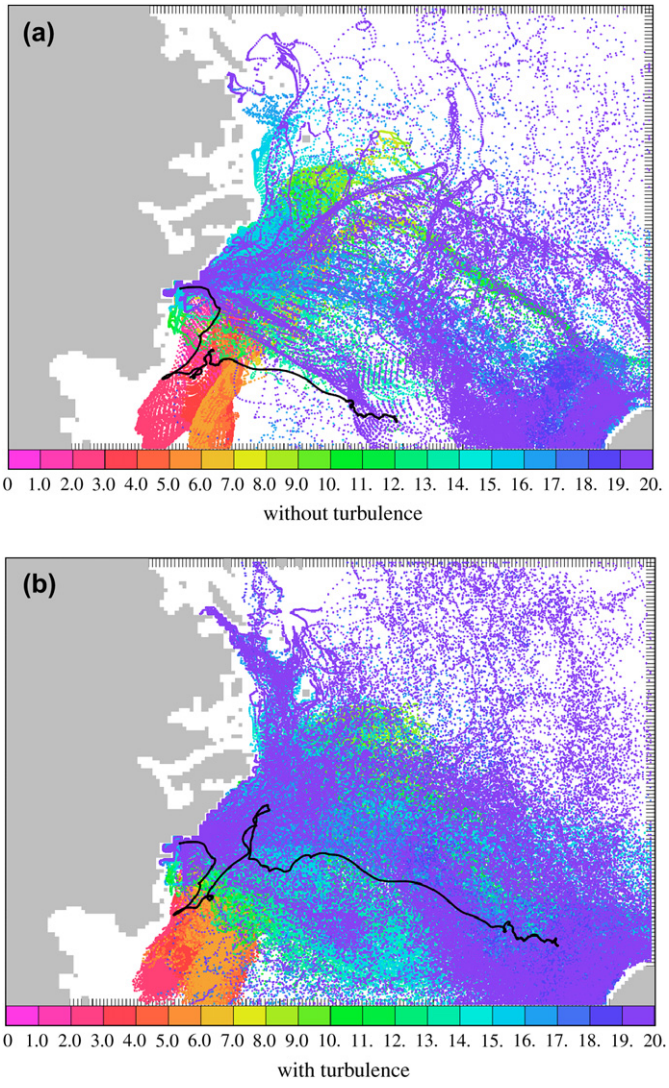

Fig. 4. 1823 Lagrangian trajectories released from the discharge regions the 15th June 1981 and followed until they exit the model domain. The trajectories' positions are plotted as colour dots every hour. The colour indicates the day during the first 20 days. The black line is the mean position of the trajectory cluster as it evolves in time. (a) Without, and (b) with sub-grid turbulence parameterisation.

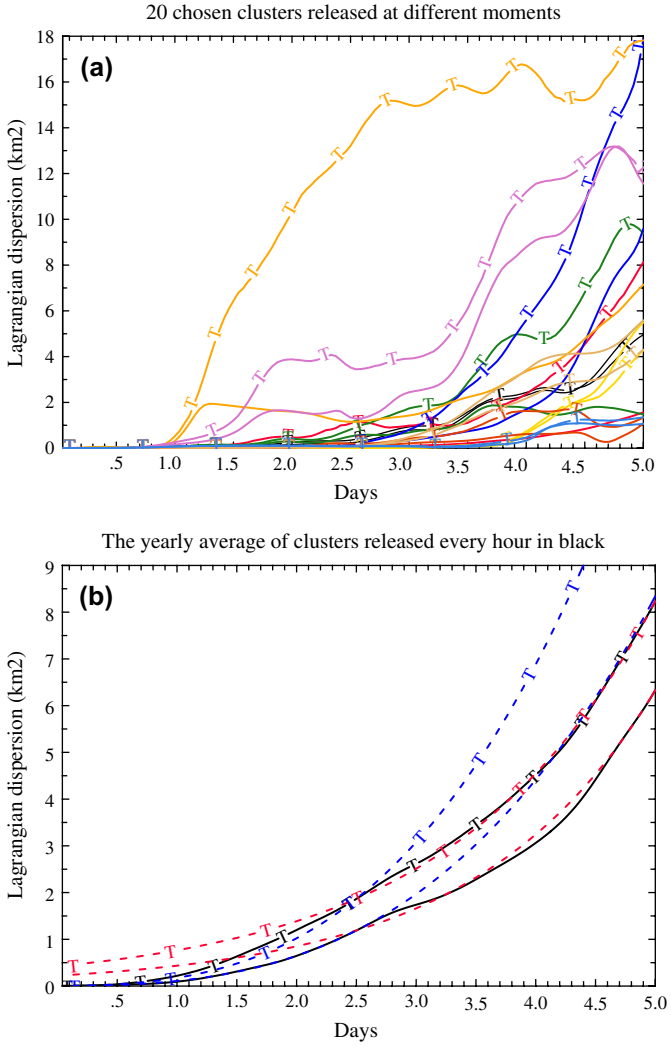

Fig. 5. The time evolution of the Lagrangian dispersion in km^2 of trajectory clusters. The lines with "– T –" are with sub-grid turbulence parameterisation and the solid lines are without. (a) Twenty chosen clusters released at different moments from the discharge area illustrating the large variety in the growth rate of the dispersion. (b) The yearly average of clusters released every hour. The Kraichnan–Richardson's dispersion growth law in dashed blue, which fits best during the first 2.5 days and the Lin's law in dashed red, which fits best for the last 2.5 days.

$x_i^n(t)$. In the present study, we will only consider the horizontal dispersion. The vertical dispersion is, however, an important measurement of the vertical mixing in the ocean but beyond the scope of the present study. The mean position is illustrated by the solid black line in Fig. 4 and shows that it is noticeably affected by the inclusion of sub-grid turbulence parameterisation.

A statistical evaluation of the effects of the parameterised sub-grid turbulence can be obtained by calculating the horizontal Lagrangian dispersion defined as the mean square displacement of the trajectories relative to the time-evolving mean position

$$D^2(t) \equiv \frac{1}{N}\sum_{i=1}^{2}\sum_{n=1}^{N}\left(x_i^n(t) - \overline{x_i(t)}\right)^2 \tag{3}$$

Fig. 5a shows the Lagrangian dispersion as a function of time for 20 clusters released at different moments from the discharge area with and without sub-grid turbulence. The time evolutions of the dispersion growth are all very different but are greater for almost all the clusters with added sub-grid turbulence. The yearly average of the Lagrangian dispersion evolution is shown by the black lines in Fig. 5b, where new clusters of trajectories have been released every hour from the discharge area during the whole year. The dispersion, which is often called the r.m.s of the separation distance of particles, is a well studied theoretical field in both two- and three-dimensional turbulence. The dispersion growth can follow two different laws. One is the Kraichnan–Richardson's law (Richardson, 1926; Kraichnan, 1966, 1967)

$$D^2(t) = \left(D^{2/3}(t_1) + c(t - t_1)\right)^3 \quad \text{for } D \gg D_I \tag{4}$$

where c is a constant and D_I is the forcing injection scale which is according to Ollitrault et al. (2005) equal to the internal Rossby radius in the case of the ocean. The second one is the Lin's law (Lin, 1972), which implies exponential growth

$$D^2(t) = D^2(t_0)\exp[2(t-t_0)/\tau] \quad \text{for } D \ll D_I \tag{5}$$

where τ is the e-folding growth time. Both these dispersions' growths have been observed in the ocean by floats (Ollitrault et al., 2005). They also apply to this model study, where we have plotted them together with the yearly average of the dispersion growth in Fig. 5b, the Kraichnan–Richardson's law in blue and the Lins's law in red for the best fitted constants. The constants were obtained by setting $t_0 = 0$ and $t_1 = 2.5$ days and are for the non-turbulent case $c = 0.016\ \mathrm{m^2/s^3}$ and $\tau = 72$ days and with turbulence $c = 0.019\ \mathrm{m^2/s^3}$ and $\tau = 81$ days.

The extra dispersion obtained after 5 days with the parameterised sub-grid turbulence is on an average $1.9\ \mathrm{km^2}$. This average slope of $4.4\ \mathrm{m^2/s}$ is the extra injected parameterised turbulence and can be compared to the Laplacian diffusion coefficients of $5\ \mathrm{m^2/s}$ and $20\ \mathrm{m^2/s}$ that were used for the passive tracers in the present study.

TRACMASS makes it possible to calculate Lagrangian trajectories both forwards and backwards between any sections or regions in the ocean. The Lagrangian trajectories correspond to the passive advection of a zero-dimension particle by the velocity fields from a 3D-circulation model. The main difference between passive tracers and Lagrangian trajectories is that the trajectories do not include the diffusion term as in the tracer equation. This diffusion term is included in the tracer equation for two reasons: (1) to parameterise the sub-grid motion that will mix the tracer between the model grid cells and (2) to stabilise numerically the circulation model. It is generally for this second reason the horizontal diffusion coefficient is set to a greater value than would be required to parameterise the sub-grid scale motion. In the present study, we have tried two different coefficients since there is no obvious choice: one as low as possible, which is $5\ \mathrm{m^2/s}$ and one somewhat greater, $20\ \mathrm{m^2/s}$.

By associating each trajectory with a transport it is possible to calculate the water mass transport. The method was applied to the Baltic by Döös et al. (2004) and Jönsson et al. (2004), where residence times were calculated for the Bay of Gdansk. These studies made use of the trajectory method's capability of keeping a record of all released water particles, which in turn makes it possible to perform statistical analysis of for instance the particles' different ages. It is hence possible to calculate the residence time R in the model domain for a particular trajectory particle, which is released in the discharge area, by integrating the trajectory forward in time so that the residence time of this trajectory can be expressed as

$$R_n = t_n^{\mathrm{O}} - t_n$$

where n is the considered trajectory, t_n^{O} is the time when trajectory n flows out through the open boundary and leaves the model domain and t_n when it is released from the discharge area. See Fig. 3 for the time indexing of the trajectories.

The average residence time, AvR, in the discharge area released at time t is then obtained by making an average over all simultaneously released particles so that

$$\mathrm{AvR}(t) = \frac{1}{N}\sum_{n=1}^{N}\left(t_n^{\mathrm{O}} - t_n\right) \tag{6}$$

where N is the total number of trajectories.

The Average age, AvA, of the trajectory particles is obtained similarly but by integrating them backward in time so that

$$\mathrm{AvA}(t) = \frac{1}{N}\sum_{n=1}^{N}\left(t_n - t_n^{\mathrm{I}}\right) \tag{7}$$

where t_n^{I} is the time when the n-th trajectory flows in through the open boundary into the model domain.

The average transit residence time ATR is simply obtained by summing each matching pair of particles of forward and backward trajectories so that

$$\mathrm{ATR}(t) = \frac{1}{N}\sum_{n=1}^{N}\left(t_n^{\mathrm{O}} - t_n^{\mathrm{I}}\right) \tag{8}$$

Note that the definition of ATR only uses the times when the trajectories enter and exit the model area but will all flow through the discharge area at the time t, since they are calculated from this spatially and temporally specified location both backward and forward in time.

A convenient way of representing the long-term circulation is to use the Lagrangian stream function, presented in Fig. 6, which is calculated by summing over selected trajectories describing the paths that one wants to study. This method was first introduced by Blanke et al. (1999). In this way one can isolate a particular water mass by following a set of trajectories between a specific initial section and a final section (see Appendix B).

The trajectory calculations in the present study all originate from the discharge points marked in Fig. 2. There are in total 1823 discharge points distributed over nine model grid cells. The trajectory particles are to mimic radio-nuclides exiting through the bottom of the sea floor. These positions correspond to where radio-nuclides would exit the sea floor due to accidental leakage of radio-nuclides from a deep repository for radioactive waste (Lindgren et al., 2001). The discharge points are therefore unevenly distributed, with most of them (1803) projected over eight adjacent grid cells in the southern area of Fig. 2. The remaining 20 discharge points are located further north in one single grid cell.

The trajectories are released every hour during the year. In total we therefore calculate 43752 [1823×24 (hours per day) $\times$ 365 (days per year) $\times$ 2 (backward and forward)] trajectories during 1 year to obtain relevant statistics for each model integration. The travel time of these trajectories was as individual as their paths. In this view, it is possible to attribute a spectrum of ages even to one singular grid cell. It is therefore necessary to calculate a large number of trajectories so that

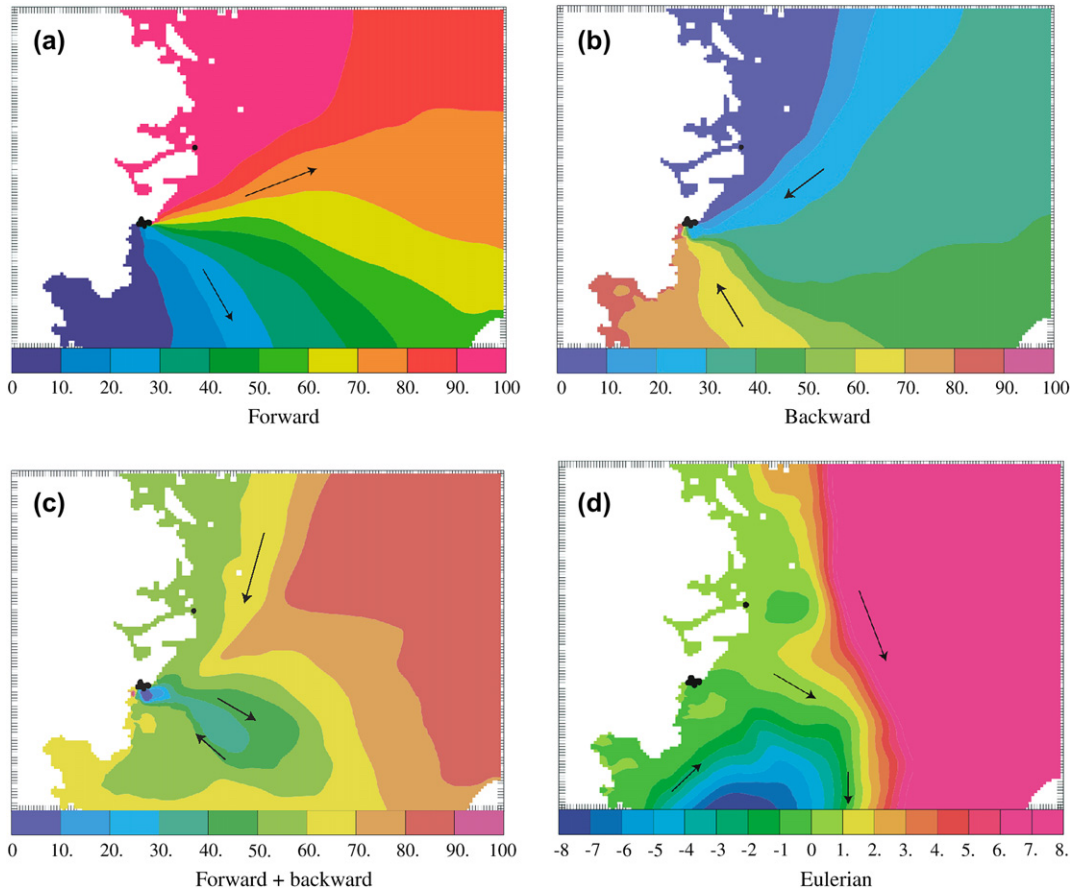

Fig. 6. The yearly averaged Lagrangian barotropic stream function calculated with (a) forward trajectories in time from the release positions until they exit the model domain, (b) backward in time trajectories, corresponding to water flowing from the open boundary to the the discharge area, (c) the sum of both the forward and the backward trajectories in previous two sub-figures, corresponding to the water flowing into the model domain through the open boundary to the discharge area and then out again through the open boundary. Units in percent of total amount of released materials. (d) The yearly averaged Eulerian barotropic stream function directly calculated from the model velocity fields. Units in 100 m^3/s.

the integrated quantities such as the Lagrangian stream function or the average particle concentrations converge and the results do not change by adding extra Lagrangian trajectories.

3. Results

The Lagrangian stream functions make it possible to isolate the mean paths from and to the discharge points near the coast. The Eulerian barotropic stream function, which shows the total mean flow through the model domain, also presented in Fig. 6, illustrates that there is a mean southward flow in the Laxemar region and a clockwise circulation in the southern part. The Lagrangian stream functions show that there is a flow from and to the discharge area from all directions, which is due to the high temporal variability in the region enabling all sorts of different circulation during the year but with a greater amplitude for water flowing from the north-east and which, after flowing through the discharge region continues towards the south-east.

The tracer concentration can be directly compared with trajectory particle concentration. Their inter-comparison is presented for a yearly average in Fig. 7. The main difference between the two categories is that the trajectory particle distribution has more fine structures than the passive tracer and that its concentration decays faster with the distance from the discharge region. The tracer simulations also differ depending on the chosen eddy diffusivity coefficient. The tracer concentration decreases more rapidly with lower eddy diffusivity and hence becomes closer to the trajectory particle concentration. The tracer concentration is also unfortunately affected by the open boundary conditions the tracer equation is integrated with, which explains why the concentration drops towards zero near the open boundary.

The tracer and particle concentrations vary, however, in time, and in order to illustrate this we have integrated the tracer and particle concentrations over the model domain and show this as a function of time in Fig. 8a. The units are in percent of maximum trajectory concentration, which happens to occur at the end of the year. The temporal variability is visibly high in Fig. 8a, with a standard deviation of 20–22% of the maximum integrated particle/tracer concentration. This can be explained by fluctuating currents that sweep away the water from the coastal area into the open Baltic Sea. The total particle/tracer concentration has lower values during

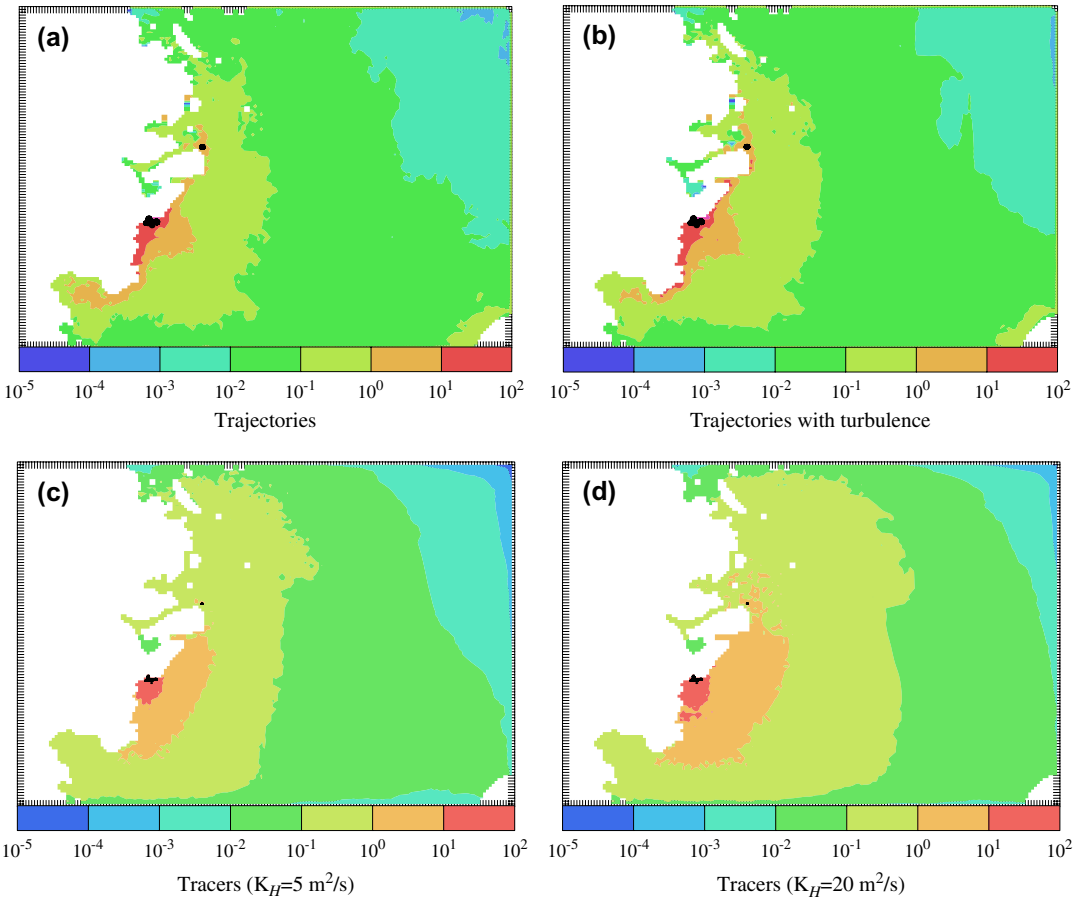

Fig. 7. A comparison of the one-year average depth integrated trajectory particle and tracer concentrations. Units in percent of maximum concentration.

the autumn and winter, due to the stronger winds during this period. There are, however, even during this period occasional high values, such as the one at the end of the year. The standard deviation, the correlation and the root mean square difference between the tracers and particles of Fig. 8a are presented in Table 1 and show that the best agreement is obtained between trajectory particles with sub-grid parameterisation of the turbulence and the tracer simulation with the lower eddy diffusion.

The tracer average age (AvA) was computed for all grid cells in the study area following the procedure described in Section 2.3. Twice a month the resulting AvA values were saved for the discharge area defined as the black dots in Fig. 2. The time evolution of the AvA is presented in Fig. 8b for both the simulation with low diffusion (red line) and high diffusion (orange line). The trajectory AvA was also calculated with trajectories by releasing them every hour from all the discharge grid cells and following them backward until they ''enter'' the study area. AvA is hence the average time, these trajectories have resided inside the study area. AvA is plotted in Fig. 8b with (blue line) and without (black line) sub-grid turbulence parameterisation.

The main difference between the tracer and trajectory average ages is that the tracer AvA is about half as big as the trajectory AvA. A possible explanation for this is that the tracer average age is subject to a Laplacian diffusion, which eliminates the extremes when constructing only one single age per grid box volume. The trajectory AvA on the other hand is an average of a whole spectrum of different trajectory ages, where some particles are several months old. The correlation is on the other hand good between the two methods. The age evolution with sub-grid parameterisation of the turbulence gives a better correlation but at the same time a higher RMS error. The corresponding statistics are presented in Table 2.

As explained in Section 2.4, it is possible to keep track of the time of all the individual trajectories and it is hence possible to calculate the time evolution of the water exchange in detail. The time decay of the number of trajectory particles in the model domain, which have been released in the discharge region and followed until they exit the model area is presented in Fig. 9a. This decay rate is equivalent to the average residence time (AvR).

With trajectories, it is possible to keep track of the full time evolution from the moment they are released until they exit the model domain or are stopped. Statistics are obtained by summing over specific trajectories, which have already been calculated and stored. The tracer on the other hand, which is integrated within the circulation model, has only a time evolution as a scalar in each model grid cell but the trajectories consist of an ensemble of many particles. The residence time

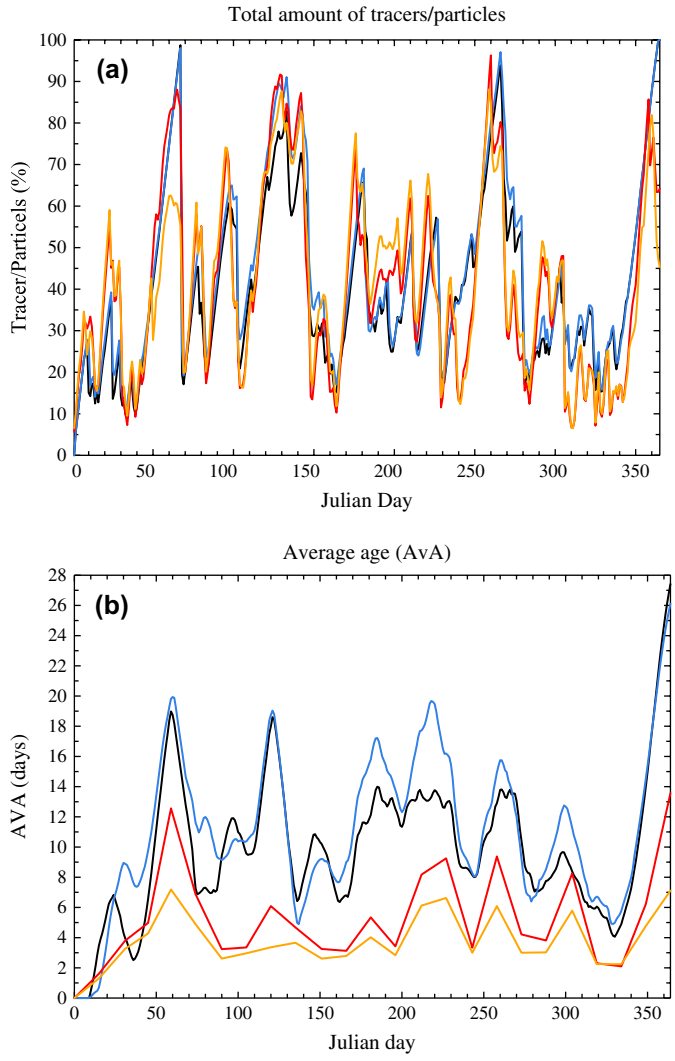

Fig. 8. Time evolution of (a) the total amount of tracers/particles, (b) average age (AvA) as a function of Julian day. The tracer/age simulation in red ($K_H = 5$ m^2/s) and orange ($K_H = 20$ m^2/s). The trajectory particles/age with sub-grid turbulence parameterisation in blue and without in black. Units in percent of maximum concentration for the integrated particles/tracers and the average age (AvA) in days. Corresponding statistics are presented in Tables 1 and 2.

evolution has been calculated for each trajectory particle cluster released every hour during the year making a total of 8760 (24×365) clusters. A selection of 20 of these clusters have been plotted in Fig. 9a–c, showing the vast variety of possible time evolution decays.

Table 1
Statistics of the time evolution of the trajectory particles and tracers integrated over the model domain, which is shown in Fig. 8a. The standard deviation(σ), the correlation and root mean square (RMS) difference between between particles and tracers. The standard deviation for the trajectories is 22% with sub-grid turbulence parameterisation and without 21%

K_H [m^2/s]	σ [%]	Correlation		RMS [%]	
		With turbulence	Without turbulence	With turbulence	Without turbulence
5	22	0.85	0.84	12	13
20	20	0.79	0.77	14	14

Table 2
Statistics of the the average age (AvA) time evolution shown in Fig. 8b of the trajectory particles and tracers integrated over the model domain. The standard deviation(σ), the correlation and root mean square (RMS) difference between between trajectory particles and tracers. The standard deviation for the trajectories is 5.0 days with sub-grid turbulence parameterisation and without 4.6 days

K_H [m^2/s]	σ [days]	Correlation		RMS [days]	
		With turbulence	Without turbulence	With turbulence	Without turbulence
5	2.6	0.85	0.78	6.7	5.6
20	1.5	0.82	0.70	8.2	7.1

Initially 100% of the particles released at a certain time are in the discharge area and thus present in the model domain as well. The number of particles is then gradually reduced as they eventually exit the model domain through the open boundaries. But already after a few hours or a day the fastest particle trajectories will have found their way out of the model domain. The large differences between the 20 lines illustrate the high temporal variability of the residence times. The residence time for a particle can hence only be a few days if it is trapped and advected by strong currents, typically occurring during the autumn when the winds are stronger. During the summer when the weather is calmer the exchange rate is often much slower, which is illustrated by the curves that decay slower and for which, 10% of the discharge can still be in the model domain after several months.

The age evolution obtained in a similar way but with trajectories integrated instead backward in time from the discharge region to where they have entered the model domain is presented in Fig. 9b. This is the equivalence of the average age (AvA) that can be calculated with age tracers but with the difference that we have a full time evolution since there is not one single age as for AvA. There is hence a decay of number of particles in time expressed in percent since the water is not one single body mass. The decay structure is similar to the forward trajectory particle evolution in Fig. 9a. The difference in the time evolution of the backward and forward particles is simply due to that the flow from the open boundary into the discharge area does not have the same structure as the flow from the discharge area to the open boundary.

By adding the forward and backward times for each matching pair of trajectories, it is possible to calculate the time evolution of the total time spent in the model domain for trajectories that have passed at least once through the discharge area. This is transient time evolution (equivalence of ATR) presented in Fig. 9c. It corresponds to the total time the particles spend in the model domain from the moment they enter through the open boundary until they exit provided they pass through the discharge region.

The yearly averages of the 8760 clusters of which a selection is shown in Fig. 9a–c have been calculated and are presented in Fig. 9d. This shows an average and therefore a smoothed time evolution of the water exchange but still much more detailed than the classic single value approach of AvR, AvA and ATR. The e-folding decays show that the

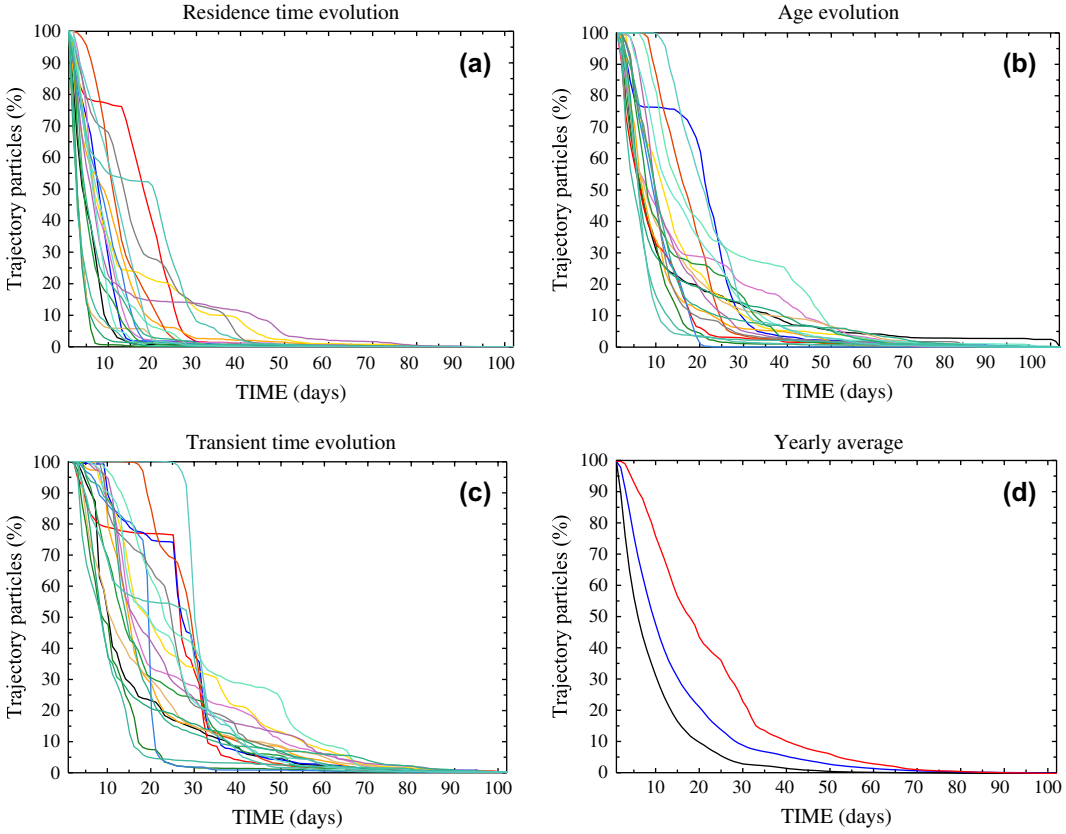

Fig. 9. Time evolution of the decay of number of trajectory particles in the model domain, which have been released in the discharge areas and followed with Lagrangian trajectories until they exit the model area. Each line corresponds to the time evolution of a particular cluster released in one single moment. Only a selection of 20 clusters have been plotted in a–c out of the 8760 (24×365) clusters that have been released during the year. (a) Residence time evolution calculated with trajectories integrated forward in time (equivalence of AvR). (b) Age evolution calculated with trajectories integrated backward in time (equivalence of AvA). (c) Transient time evolution corresponding to trajectories going from the open boundary to the release points and back to the open boundary, which is the sum of the time evolution in the two previous sub-figures (equivalence of ATR). (d) The yearly average of the time evolutions of all the 8760 clusters. The average residence times of subfigure a in black, the average age evolution of subfigure b in blue and the average transient time evolution for subfigure c in red.

number of trajectories in the model domain decay exponentially in time with an e-folding time. Note that the transient time evolution is the sum of each pair of forward and backward trajectories but not for the forward and backward distributions, which explains why the yearly mean residence time evolution (black curve in Fig. 9d) plus the yearly mean age evolution (blue line in Fig. 9d) do not add up exactly to the yearly mean of transient time (red line in Fig. 9d).

4. Discussion and conclusions

The two methods of estimating the water exchange through the Baltic coastal region of Laxemar, which have been used in the present study, show both a typical coastal region with fluctuating currents. The discharge tracers or particles are sometimes rapidly swept away in a few days and sometimes slower in a month or two, depending on the currents.

The tracer and trajectory methods both have in common that the studied water mass is advected passively with the currents and is at the same time subject to a parameterised mixing due to unresolved sub-grid scales. The tracer is integrated as a scalar simultaneously within the circulation model with the same time step. The trajectories on the other hand are calculated off-line, i.e. from the all ready calculated and stored averaged velocity fields over a longer time step (1 h in the present study).

The tracer and trajectory methods do not produce exactly the same quantities. All the tracer quantities have, however, their equivalence with Lagrangian trajectories. We have thus been able to construct the following quantities for both methods, which are directly comparable:

- tracer/particle concentrations as a function of space (Fig. 7);
- the total amount of tracers/particles in the model domain as a function of time (Fig. 8a);
- the average age of the tracers/particles (Fig. 8b).

With the trajectory method it is possible in addition to these quantities to derive some additional ones, which do not have their equivalence with the tracer method.

- The Lagrangian barotropic stream functions (Fig. 6), which cannot be calculated with passive tracers since it is not possible to isolate the velocity of a particular tracer.
- The time evolution of the residence time, the average age and the transient time averaged over an extended study

period, whereas the tracer method only gives one single value of the average age for a particular time.

The Lagrangian trajectories can hence provide a more detailed view of the exchange times and mechanisms than the tracers. This is due to that the trajectories treat the studied water mass as the sum of many particles, which one keeps record of, while the tracer is an Eulerian scalar with only one value per model grid box. These advantages in the diagnostics does not by any means imply that the trajectory method by itself is more accurate and physically realistic than the tracer method.

There are some differences in the results of the two methods. It is for instance not obvious why the average age is about half as long with tracers. A plausible explanation is that the tracer average age is subjected to the Laplacian diffusion, which eliminates the extremes when constructing only one singe age per grid box volume. The trajectory average age on the other hand is an average of a whole spectrum of different trajectory ages, where some particles remain in the basin for several months and some only a few hours.

The main difference in the present modelling aspect is how the sub-grid turbulence is parameterised. The trajectory method parameterises the sub-grid turbulence by adding a random component to the linearly interpolated flow fields that are interpolated from the advective fluxes at the sides of each grid cell in the model.

Even without sub-grid parameterisation of the turbulence the Lagrangian trajectories and tracers include an effect of dispersion since the velocity field is three-dimensional and time-dependent (in contrast to two-dimensional stationary velocity fields where the stream lines are parallel to the trajectories). The Lagrangian dispersion was quantified in the present study by calculating the dispersion rate of clusters, i.e. how fast particles diverge as they are advected by the mean current and subject to the parameterised sub-grid turbulence.

The usual time evolution of the dispersion of a cluster would have been that it complies better with Lin's law before the cluster has grown in size and then when the cluster is larger with the Kraichnan–Richardson's law. In our study it is just the opposite, for the reason that the clusters were released near the coast where the Rossby radius is close to zero, since the depth is less than 10 m and the stratification is weak there. This explains why the exponential growth of Kraichnan–Richardson's law fits best the trajectory dispersion during the first days. The cluster then moves east where the sea is deeper and stratified, resulting in an increase of Rossby radius. Although the cluster grows considerably in size after a few days it will be relatively smaller compared to the Rossby radius after a few days and will then fit the Lin's law. If the clusters had been followed further out in the Baltic, then they would most likely have followed the Kraichnan–Richardson's law once again.

The sub-grid parameterisation of the turbulence is included in the tracer equation by integrating it with the Laplacian diffusion and a chosen corresponding coefficient (K_H). There are two reasons to include this, one is physical and one is numerical.

- The physical reason is that the model needs to parameterise the sub-grid motion. This is why it is often referred to the eddy diffusivity but with a horizontal resolution of 185 m in the present study, it is not only the eddies that are not resolved but also finer scales due to, e.g. short surface gravity waves such as the swell or sub-grid scales due to unresolved bathymetry.
- The numerical reason is that 3D-circulation models generally need some diffusion and viscosity to remain numerically stable in order to dissipate energy or to eliminate numerical noise due to the truncation errors in the numerical schemes. In the present study we have presented results from the model integrated with $K_H = 20\ m^2/s$ and $K_H = 5\ m^2/s$.

If the tracer equation could be integrated with a $K_H = 0\ m^2/s$ then the tracer would be advected passively as the Lagrangian trajectories without sub-grid parameterisation of the turbulence and the differences in the results would be reduced to (1) the numerical diffusion due truncation errors in the numerical schemes of the tracer equation and (2) to that the trajectories are integrated off-line, i.e. with currents that are updated every hour while the tracer is integrated on line with the general circulation model time step of a few minutes.

There are several ways to investigate these methods further but must fall beyond the scope of the present study. One challenge would be to integrate the circulation model with a higher horizontal resolution. Finer scales are then included and one can reduce the diffusion coefficient even further since the model will resolve instead of parameterise these finer scales, which were on the sub-grid scale with a coarser model. However, new problems arise with finer resolution. If the horizontal scale begins to approach the vertical scale, the hydrostatic approximation is no longer valid and one needs to use a non-hydrostatic model, which is possible by for example employing the MIT-general circulation model by Marshall et al. (1997). Furthermore a short surface wave model could be incorporated since the wave orbital motion acts as a dispersion. This extra dispersion could be incorporated in the sub-grid turbulent approach of the Lagrangian trajectories. The tides in the Baltic are negligible but if the study would have been done in a coastal region in the world ocean then the tides would have to be included.

Finally the methods will need to be validated against observations in the future. The true amplitude of the Lagrangian dispersion could be estimated by releasing clusters of subsurface floats, which would also be a severe test to verify both tracer and trajectory dispersion, which would also make it possible to calculate the most realistic eddy diffusivity coefficient for the tracers and how to set the amplitude of the extra random component of the velocity added for the trajectories.

Acknowledgements

We thank Swedish Nuclear Fuel and Waste Management Co. (SKB) for financing the present work and Oleg Andrejev for helpful discussions and for the Baltic circulation model AS3D.

Appendix A. The trajectory model TRACMASS

Velocities calculated by the sea circulation model AS3D are known on the sides of the C-grid boxes. From these velocities, volume transports are derived. The volume transport through the eastern wall of the *ijk* grid box is given by

$$F_{i,j,k} = u_{i,j,k}\Delta y \Delta z_k \tag{9}$$

in which i, j, k denote the discretised longitude, latitude and depth, respectively; u is the zonal velocity; and $\Delta y \Delta z_k$ defines the meridional–vertical area. Meridional transports are defined analogously, while vertical transports simply follow from the non-divergency of the velocities. Inside a grid box, volume transports are obtained by interpolating linearly between the values of the opposite walls. For the zonal direction, for example, using $r = x/\Delta x$, one obtains

$$F(r) = F_{i-1,j,k} + (r - r_{i-1})\left(F_{i,j,k} - F_{i-1,j,k}\right) \tag{10}$$

Local transport and position are related by $F = \mathrm{d}r/\mathrm{d}s$, where the scaled time variable $s \equiv t/(\Delta x \Delta y \Delta z_k)$, where the denominator is the volume of the particular grid box. The approximation in Eq. (10) can now be written in terms of the following differential equation

$$\frac{\mathrm{d}r}{\mathrm{d}s} + \alpha r + \beta = 0 \tag{11}$$

with $\alpha \equiv F_{i-1,j,k} - F_{i,j,k}$ and $\beta \equiv -F_{i-1,j,k} - \alpha r_{i-1}$. Using the initial condition $r(s_0) = r_0$, the zonal displacement of the trajectory inside the considered grid box can be solved analytically and is given by

$$r(s) = \left(r_0 + \frac{\beta}{\alpha}\right)\mathrm{e}^{-\alpha(s-s_0)} - \frac{\beta}{\alpha} \tag{12}$$

The time s_1 when the trajectory reaches a zonal wall can be determined explicitly

$$s_1 = s_0 - \frac{1}{\alpha}\log\left[\frac{r_1 + \beta/\alpha}{r_0 + \beta/\alpha}\right] \tag{13}$$

where $r_1 = r(s_1)$ is given by either r_{i-1} or r_i. With the use of Eq. (9), the logarithmic factor can be expressed as $\log[F(r_1)/F(r_0)]$. For a trajectory reaching the wall $r = r_i$, for instance, the transport $F(r_1)$ must necessarily be positive, so in order for Eq. (13) to have a solution, the transport $F(r_0)$ must then be positive also. If this is not the case, then the trajectory either reaches the other wall at r_{i-1} or the signs of the transports are such that there is a zero zonal transport somewhere inside the grid box that is reached exponentially slow. For the meridional and vertical directions, similar calculations of s_1 are performed determining the meridional and vertical displacements of the trajectory, respectively, inside the considered grid box. The smallest transit time $s_1 - s_0$ and the corresponding r_1 denote at which wall of the grid box the trajectory will exit and move into the adjacent one. The exact displacements in the other two directions are then computed using the smallest s_1 in the corresponding Eq. (12). The entire procedure is then repeated for as long as is desired. The above considerations can easily be translated into an efficient numerical algorithm. The differential Eq. (11) is strictly only valid for stationary velocity fields. Vries and Döös (2001) developed a code for time-dependent velocities. It is, however, possible to use the present code with negligible loss of accuracy by simply changing the velocity fields at regular time intervals, which in our case is every hour, since the sea circulation model AS3D output data are stored at this frequency.

Appendix B. Lagrangian stream function

Each trajectory, with the index n, is associated with a volume transport (T_n) in m^3/s determined by the velocity and the area of the initial section as well as the number of trajectories initiated per grid box. All the trajectories are traced from an initial section to final section during which they conserve their volume transport. There is hence no volume sinks or sources between the initial and final sections. The corresponding velocity or transport fields is therefore non-divergent, which allows us to calculate stream functions.

The volume transport of each trajectory is inversely proportional to the number of trajectories that are calculated from their initial section. This might be regarded as the "Lagrangian resolution", which should be high enough to ensure that the Lagrangian stream function does not change by further increasing the number of trajectories. The trajectories are summed up on the model grid, so that every time a trajectory passes a grid wall it is registered. In this way one obtains a non-divergent three-dimensional field that corresponds to the volume transport for these trajectories. Every trajectory that enters a model grid box will also leave this grid box. Hence the transport field exactly satisfies the following relation:

$$T^x_{i,j,k,n} - T^x_{i-1,j,k,n} + T^y_{i,j,k,n} - T^y_{i,j-1,k,n} + T^z_{i,j,k,n} - T^z_{i,j,k-1,n} = 0$$

where $T^x_{i,j,k,n}$, $T^y_{i,j,k,n}$ and $T^z_{i,j,k,n}$ are the volume transports associated with the trajectories in the zonal, meridional and vertical directions, respectively, and i, j and k are the zonal, meridional and vertical indices. By integrating vertically over the transports and over the trajectories one obtains the Lagrangian barotropic stream function $\Psi^{\mathrm{LB}}_{i,j}$

$$\Psi^{\mathrm{LB}}_{i,j} - \Psi^{\mathrm{LB}}_{i-1,j} = \sum_k \sum_n T^y_{i,j,k,n} \quad \text{or} \quad \Psi^{\mathrm{LB}}_{i,j} - \Psi^{\mathrm{LB}}_{i,j-1} = -\sum_k \sum_n T^x_{i,j,k,n}$$

References

Andrejev, O., Sokolov, A., 1989. Numerical modelling of the water dynamics and passive pollutant transport in the Neva inlet. Meteorologica i Hydrologa 12, 78–85.

Andrejev, O., Myrberg, K., Lundberg, P., 2004a. Age and renewal time of water masses in a semi-enclosed basin – application to the Gulf of Finland. Tellus. Series A: Dynamic Meteorology and Oceanography 56, 548–558.

Andrejev, O., Myrberg, K., Alenius, P., Lundberg, P., 2004b. Mean circulation and water exchange in the Gulf of Finland – a study based on three-dimensional modelling. Boreal Environment Research 9, 1–16.

Blanke, B., Raynaud, S., 1997. Kinematics of the Pacific Equatorial Undercurrent: a Eulerian and Lagrangian approach from GCM results. Journal of Physical Oceanogrpahy 27, 1038–1053.

Blanke, B., Arhan, M., Madec, G., Roche, S., 1999. Warm water paths in the equatorial Atlantic as diagnosed with a general circulation model. Journal of Physical Oceanography 29, 2753–2768.

Blumberg, A., Mellor, G., 1987. A description of a three-dimensional coastal ocean circulation model. Coastal and Estuarine Sciences 4, 116.

Bolin, B., Rodhe, H., 1973. A note on the concepts of age distribution and transit term in natural reservoirs. Tellus 25, 58–62.

Björkström, A., 1978. A note on the relation between average age and average transit time in natural reservoirs. Tellus 30, 185–188.

Deleersnijder, E., Campin, J.-M., Delhez, E., 2001. The concept of age in marine modelling I. Theory and preliminary model results. Journal of Marine Systems 28, 229–267.

Delhez, E., Heemink, A., Deleersnijder, E., 2004. Residence time in a semi-enclosed domain from the solution of an adjoint problem. Estuarine, Coastal and Shelf Science 61, 691–702.

Dettman, E.H., 2001. Effect of water residence time on annual export and denitrification of nitrogen in estuaries: a model analysis. Estuaries 24, 481–490.

Döös, K., 1995. Interocean exchange of water masses. Journal of Geophysical Research 100 (C7), 13499–13514.

Döös, K., Meier, M., Döscher, R., 2004. The Baltic haline conveyor belt or the overturning circulation and mixing in the Baltic. Ambio 23 (4–5), 261–266.

England, M.H., 1995. The age of water and ventilation timescales in a global ocean model. Journal of Physical Oceanography 25, 2756–2777.

Engqvist, A., 1996. Long-term nutrient balances in the eutrophication of the Himmerfjärden estuary. Estuarine, Coastal and Shelf Science 42, 483–507.

Engqvist, A., Andrejev, O., 2003. Water exchange of the Stockholm archipelago – a cascade framework modeling approach. Journal of Sea Research 49, 275–294.

Eriksson, E., 1971. Compartment models and reservoir theory. Annual Review of Ecology and Systematics 2, 67–84.

Gustafsson, B., 2000. Time-dependent modeling of the Baltic Entrance area. 1. Quantification of circulation and residence times in the Kattegat and the straits of the Baltic sill. Estuaries 23 (2), 231–252.

Hagy, J.D., Boynton, W.R., Sanford, L.P., 2000. Estimation of net physical transport and hydraulic residence times for a coastal plain estuary using box models. Estuaries 3, 328–340.

Jönsson, B., Lundberg, P., Döös, K., 2004. Baltic sub-basin turnover times examined using the Rossby Centre Ocean model. Ambio 23 (4–5), 2257–2260.

Khatiwala, S., Visbeck, M., Schlosser, P., 2001. Age tracers in an ocean GCM. Deep Sea Research. Part I: Oceanographic Research Papers 48, 1423–1441.

Kraichnan, R.H., 1966. Dispersion of particle pairs in homogeneous turbulence. Physics of Fluids 9, 1937–1943.

Kraichnan, R.H., 1967. Inertial ranges in two-dimensional turbulence. Physics of Fluids 10, 1417–1423.

Lin, J.T., 1972. Relative dispersion in the enstrophy-cascading inertial range of homogeneous two-dimensional turbulence. Journal of the Atmospheric Sciences 29, 394–396.

Lindgren, M., Pettersson, M., Karlsson, S., 2001. Project SAFE – Radionuclide Release and Dose from the SFR Repository. SKB Report R-01-18. Swedish Nuclear Fuel and Waste Management Co., Stockholm.

Levine, R.C., 2005. Changes in Shelf Waters Due to Air–Sea Fluxes and Their Influence on the Arctic Ocean Circulation as Simulated in the OCCAM Global Ocean Model. Ph.D. thesis, University of Southampton, Faculty of Engineering Science and Mathematics, School of Ocean and Earth Science, 225 pp.

Liu, S.-K., Leendertse, J., 1978. Multidimensional numerical modeling of estuaries and coastal seas. Advances in Hydroscience 11, 95–164.

Marchuk, G.I., 1980. Numerical Mathematical Methods. Nauska, Moscow, 536 pp. (in Russian).

Marshall, J., Hill, C., Perelman, L., Adcroft, A., 1997. Hydrostatic, quasi-hydrostatic, and nonhydrostatic ocean modeling. Journal of Geophysical Research 102 (C3), 5733–5752.

Meier, M., 2005. Modeling the age of Baltic seawater masses: quantification and steady state sensitivity experiments. Journal of Geophysical Research 110, C02006. doi:10.1029/2004JC002607.

Mesinger, F., Arakawa, A., 1976. Numerical Methods Used in Atmospheric Models. GARP Publications Series 17, I, 64 pp.

Millero, F., Kremling, I., 1976. The densities of the Baltic Sea deep waters. Deep Sea Research 23, 611–622.

Monsen, N.E., Cloern, J.E., Lucas, L., 2002. A comment on the flushing time, residence time, and age as transport time scales. Limnology and Oceanography 47 (5), 1545–1553.

Ollitrault, M., Gabillet, C., Colin de Verdire, A., 2005. Open ocean regimes of relative dispersion. Journal of Fluid Mechanics 533, 381–407. doi:10.1017/S0022112005004556.

Pilson, M.E.Q., 1985. On the residence time of water in Narragansett Bay. Estuaries 8, 2–14.

Richardson, L.F., 1926. Atmospheric diffusion on a distance-neighbour graph. Proceedings of the Royal Society of London-Series A 110, 709–737.

Sheldon, J.E., Alber, M., 2002. A comparison of residence time calculations using simple compartment models of the Altamaha river estuary, Georgia. Estuaries 25, 1304–1317.

Simons, T.J., 1974. Verification of numerical models of Lake Ontario, Part 1. Circulation in spring and early summer. Journal of Physical Oceanography 4, 507–523.

de Vries, P., Döös, K., 2001. Calculating Lagrangian trajectories using time-dependent velocity fields. Journal of Atmospheric and Oceanic Technology 18 (6), 1092–1101.

Available online at www.sciencedirect.com
ScienceDirect
Estuarine, Coastal and Shelf Science 74 (2007) 722–731
ESTUARINE COASTAL AND SHELF SCIENCE
www.elsevier.com/locate/ecss

Hydrodynamic modeling of flushing time in a small estuary of North Bay, Florida, USA

Wenrui Huang

Civil Engineering Department, FAMU-FSU College of Engineering, 2525 Pottsdamer Street, Tallahassee, FL 32310-6046, USA

Received 18 July 2006; accepted 9 May 2007
Available online 19 July 2007

Abstract

Freshwater fraction method is popular for cost-effective estimations of estuarine flushing time in response to freshwater inputs. However, due to the spatial variations of salinity, it is usually expensive to directly estimate the long-term freshwater fraction in the estuary from field observations. This paper presents the application of the 3D hydrodynamic model to estimate the distributions of salinity and thus the freshwater fractions for flushing time estimation. For a case study in a small estuary of the North Bay in Florida, USA, the hydrodynamic model was calibrated and verified using available field observations. Freshwater fractions in the estuary were determined by integrating freshwater fractions in model grids for the calculation of flushing time. The flushing time in the North Bay is calculated by the volume of freshwater fraction divided by the freshwater inflow, which is about 2.2 days under averaged flow conditions. Based on model simulations for a time series of freshwater inputs over a 2-year period, a power regression equation has been derived from model simulations to correlate estuarine flushing time to freshwater inputs. For freshwater input varying from 12 m^3/s to 50 m^3/s, flushing time in this small estuary of North Bay changes from 3.7 days to 1.8 days. In supporting estuarine management, the model can be used to examine the effects of upstream freshwater withdraw on estuarine salinity and flushing time.

Keywords: flushing time; freshwater fraction; salinity; estuary; hydrodynamics; modeling

1. Introduction

North Bay is a small estuary system located in the north portion of the St. Andrew Bay (Fig. 1) in Florida, USA. It is about 12 km along the estuarine axis with the average width about 2 km, with the average depth is about 3 m. The bay receives freshwater input from the small rivers and rainfall runoff from the adjacent coastal watershed. Approximately 95% of the freshwater inputs are from the Deer Point Lake reservoir in the Econfina Creek watershed. According to Shermyen (1991), water withdrawals in Bay County totaled about 307 million gallons per day (MGD) in 1985. Groundwater contributes 12 MGD in total, and surface freshwater was about 30 MGD and surface saline water was about 265 MGD. During 1985 the total public supply water use was calculated to be 32 MGD. In recent years, population increase in the Panama City area has caused the increase of demand of water withdrawals from Deer Point Lake, which will result in the decrease of fresh water to the bay. Flushing time is an important index for the assessment of estuarine mixing and water quality in the North Bay. It is defined as the rate at which river freshwater is flushed out of an estuary, and therefore can be used to estimate the rate of removal of a pollutant carrying by the freshwater (Thomann and Muller, 1987). Long flushing time means that it would take long time to flush pollutant out of the bay. The report by Mills et al. (1985) at the U.S. Environmental Protection Agency (USEPA) suggested that flushing time should be examined for surface water quality analysis.

There are several approaches that have been used by researchers in estimating estuarine flushing times in estuaries

E-mail address: whuang@eng.fsu.edu

0272-7714/$ - see front matter © 2007 Elsevier Ltd. All rights reserved.
doi:10.1016/j.ecss.2007.05.016

Fig. 1. North Bay and St. Andrew Bay area.

(Lauff, 1967; Miller and McPherson, 1991; Huang and Spaulding, 1995; Tartinville et al., 1997; Chan Hilton et al., 1998; Dettmann, 2001; Kaul and Froelich, 1984). Among different approaches, the freshwater fraction method has been used by many researchers in estuaries since it was introduced by Lauff (1967). The flushing time is defined by the freshwater volume divided by the freshwater input. For estuarine applications, the freshwater volume and freshwater input are often approximated as the average values over several tidal cycles or a longer period of time (Dyer, 1973). Based on signal processing theory (Papoulis, 1977), diurnal tidal component with 24 hour period can be filtered out by a 24-h filter or by simple 48-h moving averages. The freshwater method has been used for estuarine flushing time analysis applications by many researchers for unsteady flow and tidal conditions using weekly or monthly averaging techniques to filter out tidal and unsteady flow effects for quasi-steady state analysis, for example, Asselin and Spaulding (1993) for flushing time experimental study in Providence River estuary, Pilson (1985) for Narragansett Bay, Alber and Sheldon (1999) for estuaries in Georgia, Swanson and Mendelsohn (1996) for Mt. Hope Bay, Chan Hilton et al. (1998) for Boston Inner Harbor, Hagy et al. (2000) for Patuxent River Estuary, Huang and Spaulding (2002) for Apalachicola Bay, and Sheldon and Alber (2002) for Altamaha River Estuary. Chan Hilton et al. (1998) used an exponential filter with flushing time as one of its parameters to average discharge over varying time periods and compared this to the simple averaging method. When the filtering and simple averaging methods were applied to Boston's inner harbor they yielded very similar results. Due to the spatial variations of salinity in estuaries, one of major difficulties in applying the freshwater fraction method in experimental studies for estimating flushing time is to adequately determine the freshwater volume. Fortunately, with the application of the 3D estuarine hydrodynamic model, freshwater volume in the estuary can be effectively calculated by summing freshwater volumes in subdivided model grid cells based on the model simulations of spatial distributions of salinity for a specified period.

For the study in North Bay, the freshwater fraction method was selected for flushing time analysis because of its long historical applications in estuarine research which is favored by collaborative biologists, and the availability of the 3D

hydrodynamic model for estimating freshwater volume. In the following sections, the applications a 3D hydrodynamic model to the North Bay is presented. The model was calibrated and verified to describe the mixing and transport process in the bay. The calibrated model was then used to determine the freshwater fraction and flushing time in the bay.

2. Description of hydrodynamic model

In order to investigate the circulation in the North Bay, the Princeton Ocean Model (POM, Blumberg and Mellor, 1987) was applied to Northern St. Andrew Bay. It is semi-implicit, finite-difference model that can be used to determine the temporal and spatial changes of surface elevation, salinity, temperature, and velocity in response to wind, tide, buoyancy, and Coriolis forces. The model solves a coupled system of differential, prognostic equations describing conservation of mass, momentum, heat and salinity at each horizontal and vertical location determined by the computational grid. This model incorporates a second-order turbulence closure sub-model that provides eddy viscosity and diffusivity for the vertical mixing (Mellor and Yamada, 1982). The model has a history of successful applications in other estuaries (http://www.aos.princeton.edu/WWWPUBLIC/htdocs.pom/publications.htm); for example, Oey et al. (1985a,b,c) for the Hudson-Raritan estuary, Blumberg and Goodrich (1990) for Chesapeake Bay, Galperin and Mellor (1990a,b) for Delaware Bay, River and adjacent continental shelf, Blumberg and Galperin (1990) for New York Bight, Huang et al. (2002) and Huang and Spaulding (2002) for Apalachicola Bay. In all of these studies, the model performance was assessed via comparisons with data and a confidence has been established that the model realistically reproduces the predominant physics. The model is capable of simulating the estuarine responses to time-dependent wind and multiple river inputs. Details of model descriptions were discussed by Blumberg and Mellor (1987), and the enhanced version of the curvilinear coordinate formulation is given by Blumberg and Galperin (1990). Major governing equations used in the model are given below.

Continuity equation:

$$\frac{\partial}{\partial\zeta_1}\left(h_2 \mathrm{U}_1\right)+\frac{\partial}{\partial\zeta_2}\left(h_1 \mathrm{U}_2\right)+h_1 h_2\frac{\partial \mathrm{W}}{\partial z}=0, \tag{1}$$

Momentum equation (U_1 direction):

$$\begin{aligned}&\frac{\partial}{\partial t}\left(h_2 \mathrm{U}_1\right)+\frac{1}{h_1}\frac{\partial}{\partial\zeta_1}\left[\left(h_2 \mathrm{U}_1\right)\mathrm{U}_1\right]+\frac{1}{h_2}\frac{\partial}{\partial\zeta_2}\left[\left(h_2 \mathrm{U}_1\right)\mathrm{U}_2\right]\\&\quad+\frac{\partial}{\partial z}\left[\left(h_2 \mathrm{U}_1\right)\mathrm{W}\right]+\mathrm{U}_2\left(\frac{2\mathrm{U}_1}{h_1}\frac{\partial h_1}{\partial\zeta_2}-\frac{\mathrm{U}_1}{h_2}\frac{\partial h_2}{\partial\zeta_2}-\frac{\mathrm{U}_2}{h_1}\frac{\partial h_2}{\partial\zeta_1}\right)-\mathrm{U}_2 f h_2\\&\quad=-\frac{1}{\rho_0}\frac{h_2}{h_1}\frac{\partial P}{\partial\zeta_1}+\frac{\partial}{\partial z}\left[\overline{-\left(h_2 \mathrm{u}_1\right)\mathrm{w}}\right]+\mathrm{F}_1 h_2\end{aligned} \tag{2}$$

U_1 and U_2 are the horizontal velocities and W is the vertical velocity calculated from continuity. ζ_1 and ζ_2 are horizontal curvilinear orthogonal coordinates, z is the vertical coordinate, h_1 and h_2 are metric coefficients, P_{atm} is the atmospheric pressure, and f is the Coriolis parameter. Spatial varying grids can be used in the model grid system. The term F_1 is related to the horizontal mixing processes and is parameterized as horizontal diffusion terms. The Reynolds stresses $\overline{u_1'w'}$ and $\overline{u_2'w'}$ are evaluated using the level $2^1/_2$ turbulence closure model of Mellor and Yamada (1982) modified by Galperin et al. (1988) to determine turbulent mixing.

Salinity and temperature equations:

$$\begin{aligned}&\frac{\partial(S,T)}{\partial t}+\frac{\partial \mathrm{U}_1(S,T)}{\partial\zeta_1}+\frac{\partial \mathrm{U}_2(S,T)}{\partial\zeta_2}+\frac{\partial \mathrm{W}(S,T)}{\partial z}\\&=\mathrm{A}_H\left[\frac{\partial^2(S,T)}{\partial\zeta_1^2}+\frac{\partial^2(S,T)}{\partial\zeta_2^2}\right]+\frac{\partial}{\partial z}\left[\mathrm{K}_v\frac{\partial(S,T)}{\partial z}\right]\end{aligned} \tag{3}$$

where S is the salinity and T is the temperature. K_v is the eddy diffusivity for salt and temperature, which is calculated from a second order turbulent model (Mellor and Yamada, 1982). Density is a function of temperature and salinity calculated from the equation of state as described in Blumberg and Mellor (1987). The horizontal viscosity and diffusivity coefficients A_H are calculated according to the Smagorinsky (1963) formulation where the coefficient c is set to 0.04 after sensitivity studies:

$$\mathrm{A_m}, \mathrm{A}_H = c\Delta x\Delta y\left[\left(\frac{\partial \mathrm{U}_1}{\partial\zeta_1}\right)^2+\left(\frac{\partial \mathrm{U}_2}{\partial\zeta_2}\right)^2+\frac{1}{2}\left(\frac{\partial \mathrm{U}_1}{\partial\zeta_1}+\frac{\partial \mathrm{U}_2}{\partial\zeta_2}\right)^2\right]^{1/2}. \tag{4}$$

3. Data sets for model calibration and verification

Two independent data sets are required for model calibration and verification. The data sets should consist of all external boundary conditions for model simulations, and observations at selected stations in the bay for model calibration and verification for the same model simulation period. To support model calibration and verification, a field data collection program was conducted by Northwest Florida Water Management District. Based on the limited fund available for the field data observation, field stations have been designed to characterize the spatial variations of salinity and water levels in this small estuary (about 12 km × 2 km) with minimum number of stations. Data collections include wind speed and directions, water levels, and salinity in several stations in North Bay.

The location of the field station is shown in Fig. 2. S593 is a wind monitoring station located on Deer Point Dam Causeway at CR 2321. For such a small estuary, one wind station would be sufficient to represent the wind condition in the bay. S594 is a tide station in eastern section of North Bay between SR 77 bridge and CR 2321 bridge. S595, S596, S598 are stations for salinity measurements to examine freshwater effects. All salinity measurement instruments were installed near the bottom to avoid damage by boats. Direct observations of freshwater input to the bay are not available. Alternatively, the freshwater discharge to the bay is approximated from the hydrological model (SWMM model, Rossman, 2005) simulations of rainfall runoff from the upstream

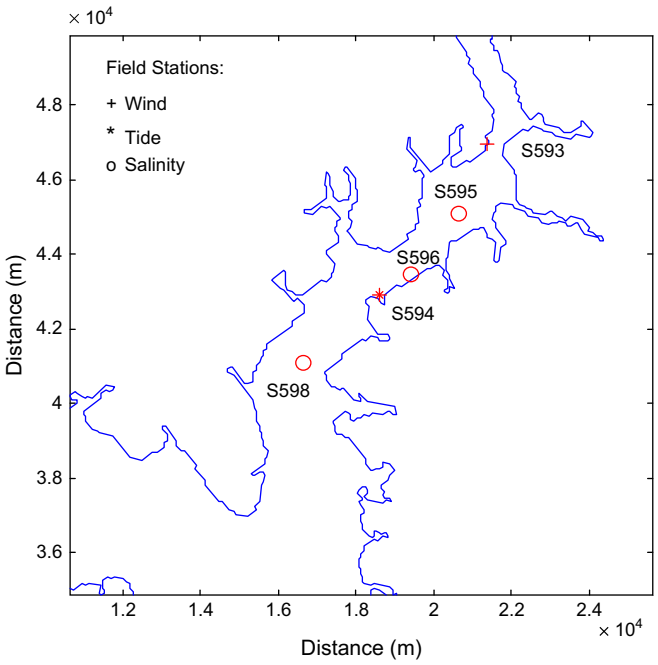

Fig. 2. Locations of field data collection stations in North Bay.

watershed and water budget calculation based on water withdraw in the upstream Deer Lake Reservoir (Fig. 3a). Observed water levels in the ocean boundary at Panama City was obtained from NOAA station near Panama City Beach given in Fig. 3b, and observed wind is presented in Fig. 3c.

Observations of water levels and salinity in North Bay are given in Fig. 4. Because of only about 15 km distance between tidal station S594 in North Bay and the open tidal boundary station (Fig. 5), tidal fluctuations in S594 are in a similar pattern as those in the model open tidal boundary. In other words, tidal variations in North Bay are mainly controlled by boundary tidal forcing. Time series of tidal variations indicate effects of both harmonic and non-harmonic signals. Salinity measurements indicate that salinity variations are small in the bay, which may partially due to the general low flow about 25 m^3/s and small tidal fluctuations (about 0.5 m range). Because of late delivery of salinity measurement instruments, salinity observations for the first 35 days were missed in Stations S596 and S598. On day 35, freshwater input and wind speed are low, the sudden drop in salinity in S595 and S596 on day 35 are thus not resulted from freshwater input and wind to the bay. Instead, it may be the result of an unrecorded sudden lease of water from the upstream reservoir. The observation data is divided into two data sets. The first data set of 40 days for the period of 10/9/2002–11/18/2002 is used for model calibration, while the 2nd data set of 30 days for the period of 11/19/2002–12/19/2002 is used as model verification.

4. Model calibration and verification

4.1. Model grid system

A horizontal grid system of three difference grid sizes has been developed for North Bay as shown in Fig. 5. The largest grids are used in the West Bay area (400 m × 200 m). Middle-size grids (200 m × 200 m) are used in the lower part of the bay. For the North Bay area, which is the focus of this study, high resolutions of smallest grids (200 m × 100 m) are used for better accuracy in salinity predictions. The employment of the mixed grid system allows efficient computations for long-term simulations, while keeping high resolution in the North Bay area. Considering small freshwater inputs and salinity fluctuations in this shallow estuary with the average depth about 3 m, five sigma layers were used to describe the water column in the vertical direction. This is consistent to

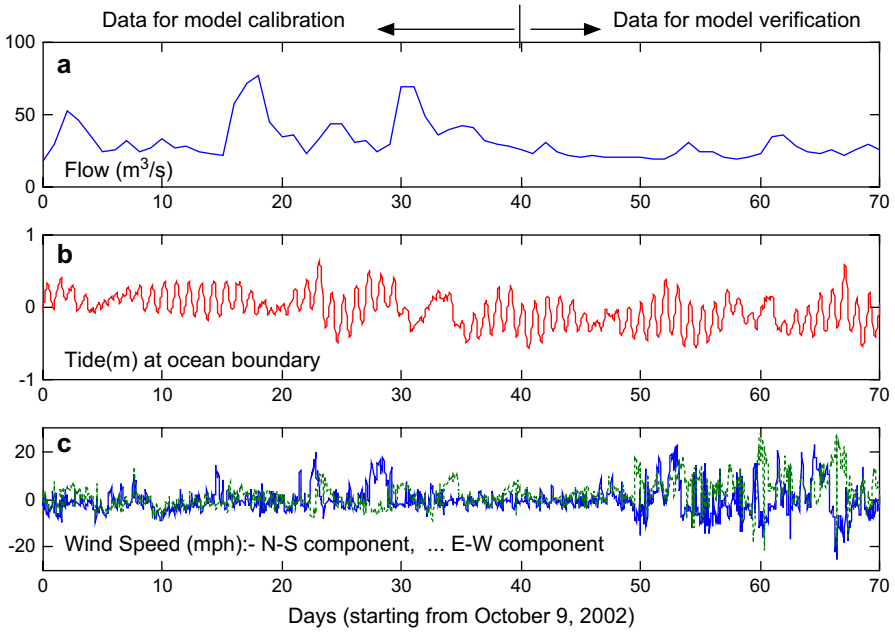

Fig. 3. Time series of freshwater input, water levels, and winds used as mode boundary conditions.

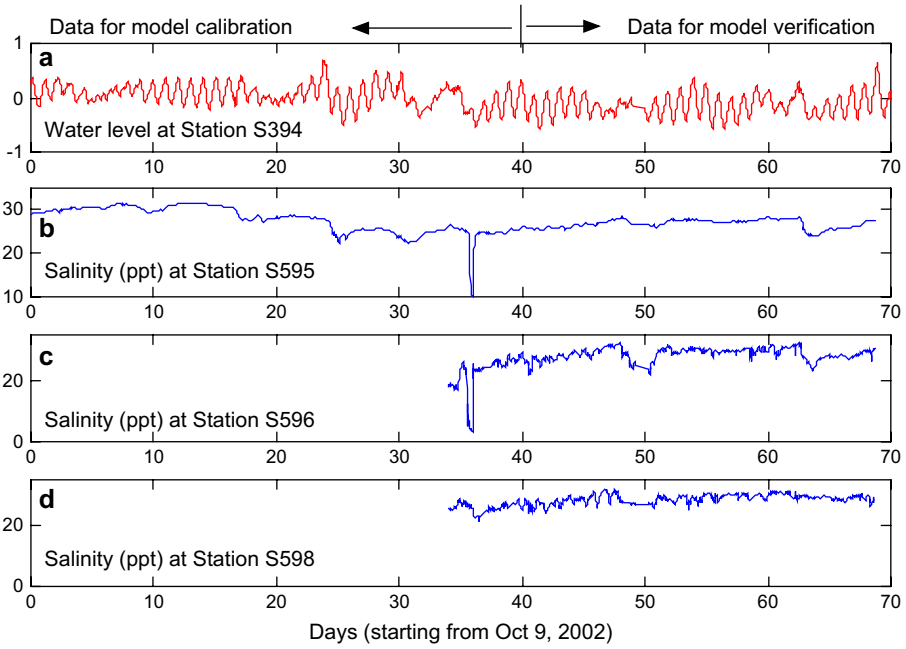

Fig. 4. Observations of water levels and salinity in North Bay.

Huang and Spaulding's (2002) and Huang et al.'s (2002) successful applications of the POM hydrodynamic model to a similar shallow estuary of Apalachicola Bay in Florida.

4.2. Boundary conditions

Observations at ocean boundary indicate that salinity at flood tide is about 34 ppt due to the dominant ocean water moving into the bay from the Gulf of Mexico. Therefore, at tidal boundary close to the Gulf of Mexico, constant 34 ppt was specified at flood tide. At ebb tide, the POM hydrodynamic model employs an advanced free flux algorithm (Blumberg and Mellor, 1987) using upstream salinity for model simulation without the needs of boundary salinity. The free flux method has been widely used in estuarine modeling (http://www.aos.princeton.edu/WWWPUBLIC/htdocs.pom/index.html).

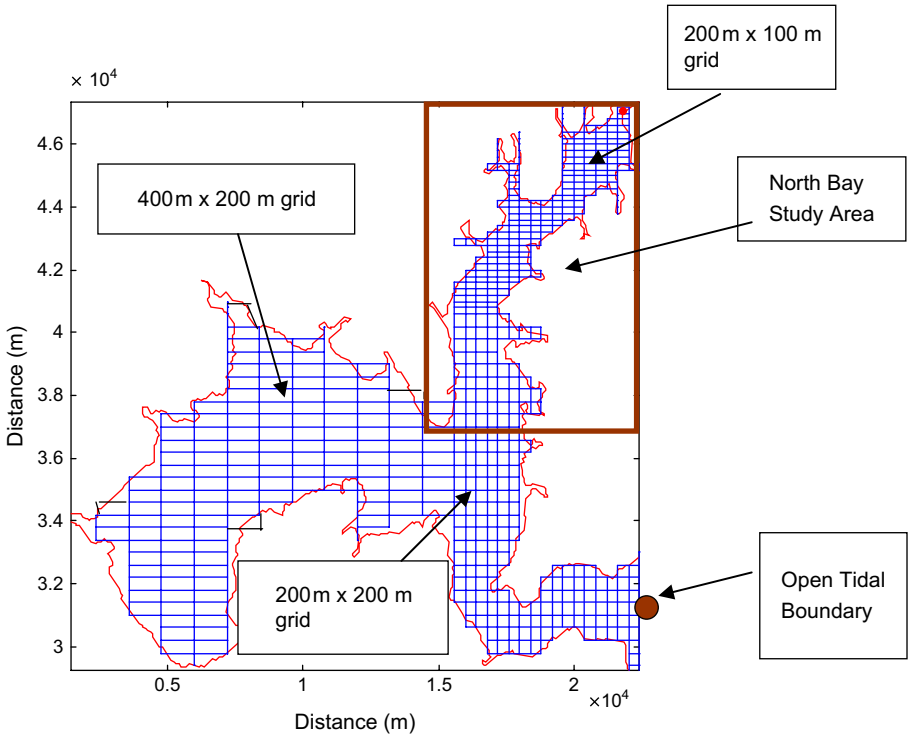

Fig. 5. The model grid system for North Bay.

Observed hourly water levels from NOAA were specified at tidal boundary. Observed hourly wind direction and speeds were used for surface boundary, and hourly freshwater inputs were specified in upstream river flow boundary. As shown in Fig. 3, tides variations range is about from −0.5 m to 0.5 m, river flow changes from 20 m^3/s to 75 m^3/s.

4.3. Model calibrations and verifications

The hydrodynamic model was calibrated and verified using field observations of water levels. The first data set for the period between October 9 and November 19 was used for model calibrations. The initial salinity was set by a 30 day model spin-up simulation. After a series of model sensitivity simulations for several bottom friction coefficients, bottom friction coefficient was selected as 0.0025 that provides the best agreement between model predictions and observations of water levels. For the model verification period of November 19 to December 19, the model coefficients determined from model calibration are kept unchanged. Excellent agreement between model predictions of water levels and observations during the verification period indicates that the model is capable of predicting water levels in other period too. During the model simulation period, water levels consist of both tidal and non-tidal signals. As shown in Fig. 6, the model satisfactorily predicts both tidal variations and those non-tidal sea level changes. The root-mean-square error between model predictions and observations is 0.011 m, and the correlation coefficient value is 0.96.

The model was also calibrated with salinity observations (Fig. 7) using a data set for the period between October 9 and November 19. As described above, the POM hydrodynamic model employed a 2nd order turbulence model to automatically calculate turbulent mixing that has shown successful applications in many estuaries (e.g. Huang et al., 2002). The only parameter that can be adjusted is the coefficient in the horizontal diffusion equation (eq. 4). After a series of sensitivity study, a value of 0.04 was used for the c coefficient in eq. (4). As shown in Fig. 7, model predictions of salinity reasonably follow the general trend of salinity observations. However, there is a short pulse of salinity drop at Station S595 and S596 on day 36, which the model was unable to reproduce such an event. However, an examination of model boundary data as shown in Fig. 3 indicates that freshwater inputs and wind speeds are constantly low on day 36. Therefore, the sudden drop in salinity observation show in Fig. 7 may be caused by an accidental release of fresh water in the Deer Point Lake Dam, which was unable to account in the freshwater input from the watershed hydrological model.

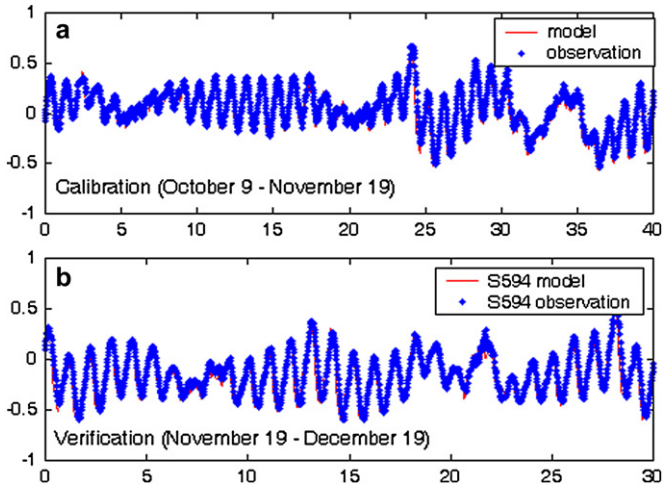

Fig. 6. Comparison of model predicted water levels (m) with observations at Station S594: (a) calibration (10/9–11/19), and (b) verification (11/19–12/19).

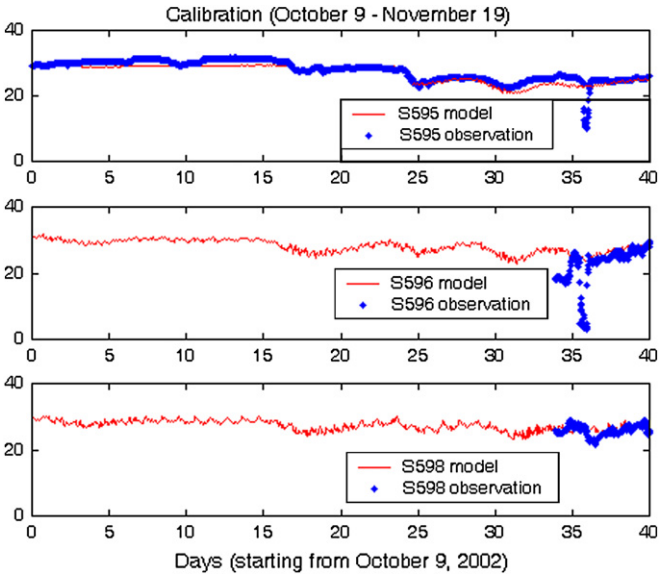

Fig. 7. Comparison of salinity (ppt) between model predictions and observations for the model calibration period (October 9 to November 19).

The calibrated model was verified using another independent data set for the period November 19 to December 19. Keeping the model coefficients determined in model calibration phase, model predictions of salinity were compared to observations. As shown in Fig. 8, model predictions of salinity reasonably match the general trend of salinity at all three stations. Considering limited available data with gaps and very small salinity fluctuations corresponding to the small river flow during the observation period, the difference of mean salinity was used as the indicator to examine the model performance. The difference of mean salinity between model predictions and observations is −1.01 ppt, 1.38 ppt, and 1.78 ppt for Station S595, S596, and S598, respectively.

4.4. Characteristics of tidal currents and salinity field

The calibrated and verified model was used to characterize tidal currents and salinity fields in the bay. As shown in Fig. 9, stronger ebb currents mainly move from upper North Bay to the Gulf ocean boundary. In the West Bay area, currents are relatively weaker than those in the North Bay area. Strongest ebb currents are about 0.5 m/s near the tidal boundary, and weakest currents are in the area of West Bay. At flood tide,

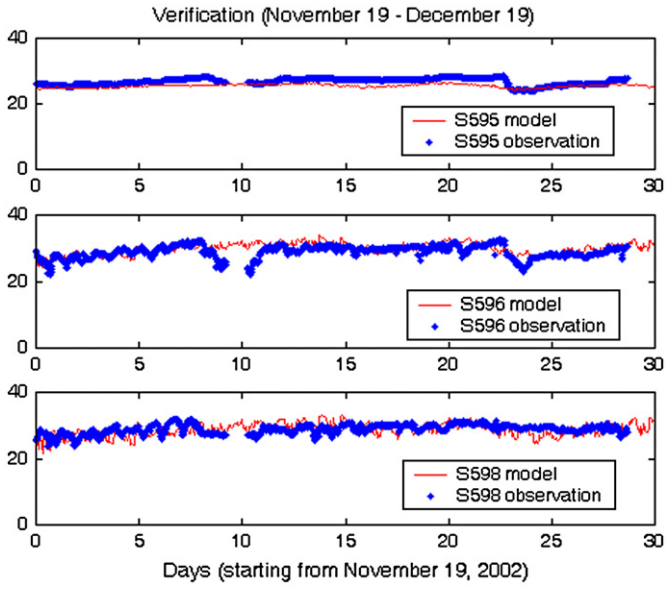

Fig. 8. Comparison of salinity (ppt) between model predictions and observations for the model verification period (November 19 to December 19).

saline water moves into the bay and spreads into the North Bay and the West Bay.

Due to the low fresh water discharge into the North Bay, salinity value in the North Bay is generally high, ranging from 30 ppt to 33 ppt in the flood tide, and about 28 ppt to 31 ppt in the ebb tide. Salinity variation between low and high tide is not significant because of the small tidal amplitude in the study area. Salinity field (Fig. 10) at flood tide indicates salinity intrusion and the result of fresh and saline water mixing through estuarine advection and dispersion. The spatial variation of salinity indicates the advantage of the hydrodynamic model for better estimation of freshwater volume in the estuary. Because the estuary was divided into small grid cells as shown in Fig. 5, freshwater volume in each grid cell can be calculated, and total freshwater volume in the estuary can then be obtained by the summation of freshwater volume in all grids.

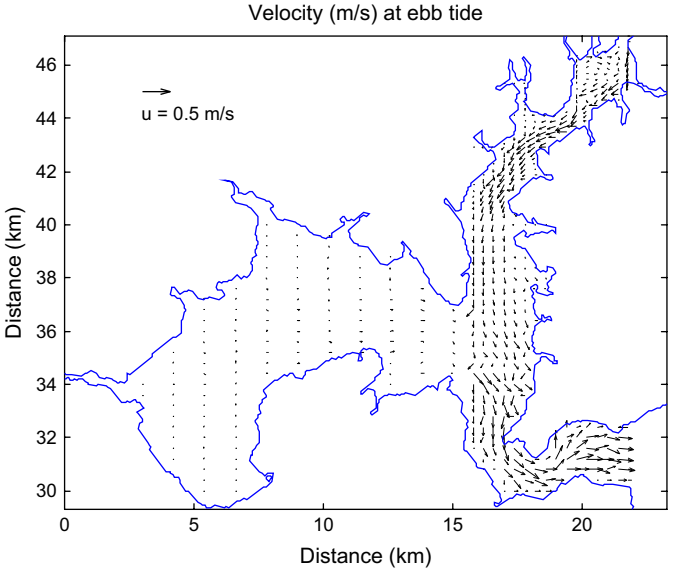

Fig. 9. Model simulated bottom currents at ebb tides in North Bay of St. Andrew Bay Estuary.

5. Flushing time determined by freshwater fraction method

Based on the hydrodynamic model simulations of temporal and spatial salinity distributions, flushing time in the North Bay can be conveniently determined by the freshwater fraction approach (Lauff, 1967; Dyer, 1973; Huang and Spaulding, 2002) which can be determined from salinity distributions. This technique provides an estimation of the time scale over which contaminants or other material released in the estuary are removed from the system. Residence time in an estuary by freshwater fraction method can be expressed by:

$$T = \frac{F}{Q} = \frac{\int_{\text{vol}} f \mathrm{d}(V)}{Q} \tag{5}$$

where F is the accumulated freshwater volume in the estuary, which can be calculated by integrating the freshwater volume $\mathrm{d}(V)$ in all the sub-divided model grids over a period of time. In estuaries with unsteady river flow and tidal variations, F and Q are approximate average freshwater volume and average freshwater input over several tidal cycles or a period of time such as a week or a month (Lauff, 1967; Dyer, 1973; Chan Hilton et al., 1998). The term f is the freshwater content or the freshwater fraction which is described by:

$$f = \frac{S_0 - S}{S_0} \tag{6}$$

where S_0 is the salinity in the ocean, and S is the salinity at the study location.

Model simulations were conducted to examine flushing time responding to various freshwater inputs. In order to examine flushing time responses under different river inflow for a longer time scale, a baseline flow scenario of daily freshwater inputs has been derived from the rainfall-runoff hydrological model based on historical rainfall data and water withdraw from the upstream reservoir over a 2-year period between 1/1/2000 and 12/31/2002. Using a similar averaging approach as described by Chan Hilton et al. (1998) to derive quasi-steady condition for studying estuarine time, freshwater input is averaged over 7 days for a 2-year period (Fig. 11a) for studying flushing time responding to freshwater inputs. The corresponding model simulated salinity is also averaged over a 7-day period to remove tidal effects. Because periods of dominant tidal harmonic components are about 24 h or less, 7-day averaging is sufficient to remove tidal effects, which generally require only 48-h moving averaging filtering (Wong and Wilson, 1984; Chan Hilton, 1998). During the 2-year simulation period, river flow varies from 12 m^3/s to 50 m^3/s. Model simulations were conducted under no-wind

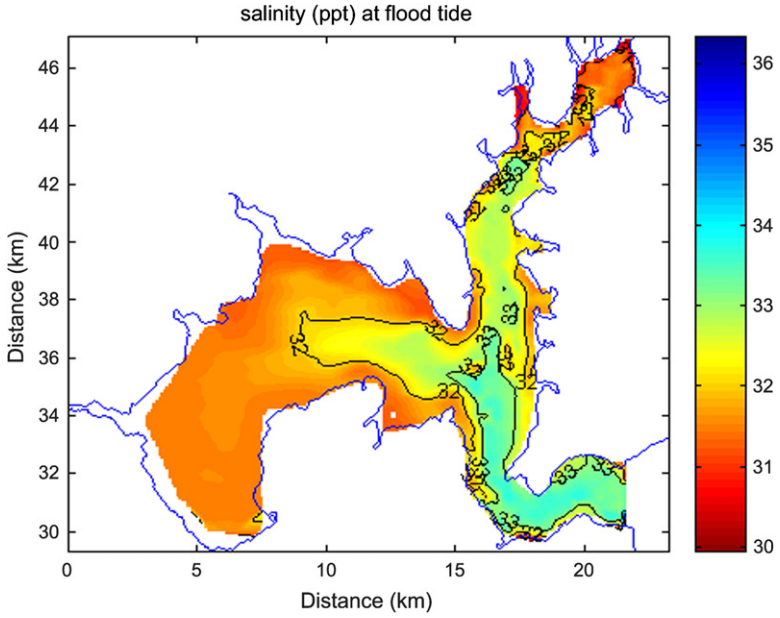

Fig 10. Model simulated bottom salinity at flood tides in North Bay of St. Andrew Bay Estuary.

condition. Tidal open boundary was specified using the dominant harmonic components based on tidal harmonic analysis of the tidal data. Salinity at open ocean boundary was specified as constant 34 ppt at flood tide. At ebb tide, the hydrodynamic model employed free flux algorithm without the usage of the boundary salinity (Blumberg and Mellor, 1987). Model prediction of salinity was averaged over 7-day period. Applying eqs. (6) and (5), flushing time corresponding to the variations of freshwater input is shown in Fig. 11b. In general, flushing time decreases as the increase of freshwater inputs. Maximum flushing time is about 3.8 days while the minimum is about 1.8 days.

Model simulated flushing time was plotted against river flow in Fig. 12. Least square regression fitting was conducted by using the following two functions:

(a) Fitting by exponential function:

$$T = 4.7613 \cdot e^{-0.0284 \cdot Q} \quad \left(R^2 = 0.9341\right) \tag{7}$$

(b) Fitting by power law:

$$T = 18.347 Q^{-0.6572} \quad \left(R^2 = 0.9647\right) \tag{8}$$

The first empirical function was fitted by an exponential function (Eq. 7). With the correlation $R^2 = 0.934$, the exponential empirical equation shows good statistical correlations between flushing time and river flow in North Bay. However, the exponential expression (7) together with eq. (5) results in a freshwater volume which at first increases then unreasonably decreases as Q increases. The 2nd empirical function was fitted by a power law as shown in eq. (8). With higher correlation

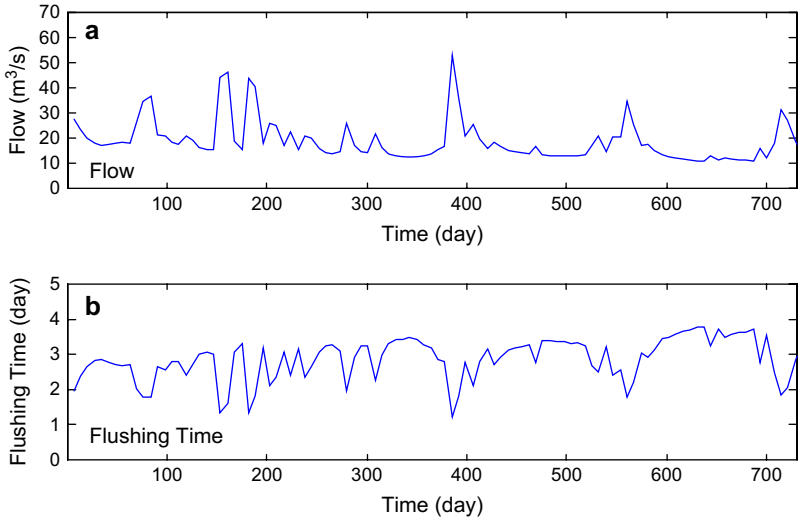

Fig. 11. Time series of 7-day-averaged freshwater inputs (m^3/s) and the corresponding flushing time (day) during 1/1/2000-12/31/2002 in North Bay.

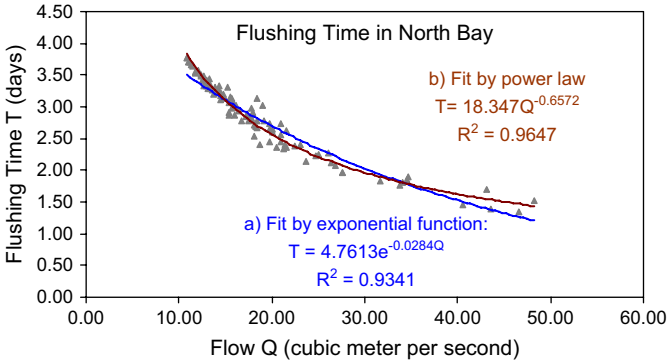

Fig. 12. Regression between flushing time and freshwater input.

value $R^2 = 0.965$, the power law statistically fits better with the data, especially in the low flow end and high flow end. In addition, the power law shows more reasonably physical characteristics between freshwater fraction and freshwater flow. Combining eq. (8) and eq. (5), the estuarine freshwater fraction can be derived, which increases as the increase of the freshwater inputs. Therefore, the power law (eq. 8) is finally selected for characterizing the flushing time and freshwater input in the North Bay.

The result of 7-day averaged flushing time was compared to a model simulation of a steady-state condition of an averaged constant flow of 25 m^3/s. Under the steady flow of 25 m^3/s condition, flushing time obtained from freshwater fraction method is 2.20 days, while it is 2.34 days from the exponential equation (eq. 7), and 2.21 days from the power expression (eq. 8). The result from the 7-day averaging of unsteady flow is close to that obtained from the steady flow condition using the corresponding averaging flow rate.

6. Conclusion

The application of the Princeton Ocean Model (POM) to characterize hydrodynamics and flushing in a small estuary of North Bay on the Florida coast has been presented in this paper. The POM hydrodynamic model has a long history of successful applications in estuaries that can be found in many journal publications (http://www.aos.princeton.edu/WWWPUBLIC/htdocs.pom/publications.htm). Using available data, model sensitivity studies have been conducted to reasonably calibrate the model with appropriate bottom friction coefficient and parameters in the horizontal diffusion equation (eq. 5). For flushing time estimation in the North Bay, the freshwater fraction method is used to examine estuarine response to freshwater inputs for a baseline flow scenario for the period 1/1/2000–12/31/2002. Because field data collections of salinity are generally easier than other water quality data collections (e.g. dye release), using hydrodynamic modeling and the freshwater fraction approach is an effective way to determine estuarine flushing time. Under time varying flow conditions, regression analysis of model results indicate that flushing time is correlated to freshwater inputs, which can be described by a power regression equation. For the 7-day averaged flow ranging from 10 m^3/s to 50 m^3/s for the North Bay area, corresponding flushing time varies from 3.7 days to 1.8 days.

One of the concerns for water resource management is the potential impact of increasing freshwater amounts being withdrawn from the reservoir upstream that would result in the reduction of fresh water to the bay. The hydrodynamic and flushing time model calibrated for North Bay can be used to examine different freshwater withdraw scenarios to support estuarine water resource planning and management. The empirical regression equation (eq. 8) also shows that flushing time may significantly increase if freshwater reduction occurs in the low flow condition.

7. Websites

Princeton Ocean Model (POM) Website: http://www.aos.princeton.edu/WWWPUBLIC/htdocs.pom/index.html.

Publications related to the applications of the POM model: http://www.aos.princeton.edu/WWWPUBLIC/htdocs.pom/publications.htm.

References

Alber, M., Sheldon, J.E., 1999. Use of a date-specific method to examine variability in the flushing times of Georgia estuaries. Estuarine, Coastal and Shelf Science 49, 469–482.

Asselin, S., Spaulding, M.L., 1993. Flushing times for Providence River based on tracer experiments. Estuaries 16 (4), 830–839.

Blumberg, A.F., Galperin, B., 1990. On the summer circulation in New York Bight and contiguous estuarine waters. In: Cheng, R.T. (Ed.), Coastal and Estuarine Studies, vol. 38, Residual Currents and Long-term Transport. Springer, New York Inc.

Blumberg, A.F., Goodrich, D.M., 1990. Modeling of wind-induced destratification in Chesapeake Bay. Estuaries 13, 3.

Blumberg, A.F., Mellor, G.L., 1987. A description of a three-dimensional coastal ocean circulation model. In: Heaps, N.S. (Ed.), Three-dimensional Coastal Ocean Models. Coastal and Estuarine Sciences, vol. 4. E.D., AGU, Washington, pp. 1–16.

Chan Hilton, A.B., McGillivary, D.L., Adams, E.E., 1998. Residence time of freshwater in Boston's Inner Harbor. Journal of Waterway, Port, Coastal, and Ocean Engineering. ASCE 124 (2), 82–89.

Dettmann, E.H., 2001. Effect of water residence time on annual export and denitrification of nitrogen in estuaries: a model analysis. Estuaries 24 (4), 481–490.

Dyer, K.R., 1973. Estuaries: A Physical Introduction. John Wiley and Sons, New York.

Galperin, B., Kantha, L.H., Hassid, S., Rosati, A., 1988. A quasi-equilibrium turbulent energy model for geophysical flows. Journal of Atmospheric Science 45, 55–62.

Galperin, B., Mellor, G.L., 1990a. A time-dependent, three-dimensional model of the Delaware Bay and River. Part 1: Description of the model and tidal analysis. Estuarine, Coastal and Shelf Science 31, 231–253.

Galperin, B., Mellor, G.L., 1990b. A time-dependent, three-dimensional model of the Delaware Bay and River. Part 2: Three-dimensional flow fields and residual circulation. Estuarine, Coastal and Shelf Science 31, 255–281.

Hagy, J.D., Boynton, W.R., Sanford, L.P., June 2000. Estimation of net physical transport and hydraulic residence times for a coastal plain estuary using box models. Estuaries 23 (3), 328–340.

Huang, W., Spaulding, M., 1995. Numerical modeling of CSO-induced pollutant transport in Mt. Hope Bay. Journal of Environmental Engineering. ASCE 12 (7), 492–498.

Huang, W., Spaulding, M., 2002. Modeling residence time response to freshwater input in Apalachicola Bay, Florida. USA. International Journal of Hydrological Processes 16, 3051–3064.

Huang, W., Jones, W.K., Wu, T., 2002. Modeling surface wind effects on subtidal salinity in Apalachicola Bay. Journal of Estuarine, Coastal and Shelf Science 55, 33–46.

Kaul, L.W., Froelich Jr., P.N., 1984. Modeling estuarine nutrient geochemistry in a simple system. Geochimica et Cosmochimica Acta 48, 1417–1433.

Lauff, G., 1967. Estuaries. American Association For the Advancement of Science. Publication No. 83. Washington, DC.

Mellor, G., Yamada, T., November 1982. Development of a turbulent closure model for geophysical fluid problems. Review of Geophysics and Space Physics 20 (4), 851–875.

Miller, R.L., McPherson, B.F., 1991. Estimating estuarine flushing and residence times in Charlotte Harbor, Florida, via salt balance and a box model. Limnology and Oceanography 36, 602–612.

Mills, W.B., Porcella, D.B., Ungs, M.J., Gherini, S.A., Summers, K.V., Mok, L., Rupp, G.L., Bowie, G.L., Haith, D.A., 1985. Water Quality Assessment: A Screening Procedure for Toxic and Conventional Pollutants in Surface and Ground Water–Part II (Revised 1985). Environmental Research Laboratory, Office of Research and Development, U.S. Environmental Protection Agency, Athens, GA. EPA/600/6–85/002b.

Oey, L.-Y., Mellor, G.L., Hires, R.I., 1985a. A three-dimensional simulation of the Hudson-Raritan estuary. I: Description of the model and model simulations. Journal of Physical Oceanography 15, 1676–1692.

Oey, L.-Y., Mellor, G.L., Hires, R.I., 1985b. A three-dimensional simulation of the Hudson-Raritan estuary. III: Salt flux analyses. Journal of Physical Oceanography 15, 1711–1720.

Oey, L.-Y., Mellor, G.L., Hires, R.I., 1985c. Tidal modeling of the Hudson-Raritan estuary. Estuarine, Coastal and Shelf Science 20, 511–527.

Papoulis, A., 1977. Signal Analysis. McGraw-Hill, 431 pp.

Pilson, M.E.Q., 1985. On the residence time of water in Narragansett, Bay. Estuaries 8, 2–14.

Rossman, L.A., 2005. Storm Water Management Model (SWMM), EPA/600/R-05/040, Revised October 2005. http://www.epa.gov/ednnrmrl/models/swmm/index.htm.

Sheldon, J.E., Alber, M., 2002. A comparison of residence time calculations using simple compartment models of the Altamaha River Estuary, Georgia. Estuaries 25 (6B), 1304–1317.

Shermyen, A.H. (Ed.), 1991. Florida Statistical Abstract 1991. Bur. Econ. Bus. Res. Coll. Bus. Adm., Univ. Florida, Univ. Press of Florida, 736 pp.

Smagorinsky, J., 1963. General circulation experiments with the primitive equations: I. The basic experiment. Monthly Weather Review 91, 99–164.

Swanson, J.C., Mendelsohn, D., 1996. BAYMAP, A simplified embayment flushing and transport model. In: Spaulding, M., Cheng, R. (Eds.), Proceedings of the Fourth International Conference on estuarine and Coastal Modeling, October 26–28, 1995, San Diego, CA.

Tartinville, B., Deleersnijder, E., Rancher, J., 1997. The water residence time in the Mururoa atoll lagoon: sensitivity analysis of a three-dimensional model. Coral Reefs 16, 193–203.

Thomann, R., Muller, J., 1987. Principle of Surface Water Quality Modeling and Control. Harper & Row Publishers, 621 pp.

Wong, K.C., Wilson, B., 1984. Observation of low-frequency variability in Great South Bay and relations to atmospheric forcing. Journal of Physical Oceanography 14, 1893–1900.

Available online at www.sciencedirect.com
ScienceDirect
Estuarine, Coastal and Shelf Science 74 (2007) 732–741
ESTUARINE COASTAL AND SHELF SCIENCE
www.elsevier.com/locate/ecss

On the coupling of uncoupled flow and transport solvers

Fahmi Naifar [a,*], Peter Wilders [a], Arnold W. Heemink [a], Guus S. Stelling [b]

[a] Delft Institute of Applied Mathematics, Faculty of Electrical Engineering, Mathematics and Computer Science, Delft University of Technology, Mekelweg 4, 2628 CD Delft, The Netherlands
[b] Faculty of Civil Engineering and Geosciences, Delft University of Technology, Post Box 5048, 2600 GA Delft, The Netherlands

Received 3 April 2006; accepted 9 May 2007
Available online 19 July 2007

Abstract

The coupling of flow and transport solvers we are dealing with in this paper represents a whole intermediate processing step taking place between the two. We develop new techniques to ensure mass conservation of the transport while using totally different numerical schemes in the flow and in the transport solvers. We also present a method which allows the use of larger time steps for the transport computation than the one used for the flow leading therefore to faster computations and considerable reduction in disk space for the storage of flow data. These techniques are applied and tested in the numerical application of 2D and 3D problems.

Keywords: flow; transport; constancy condition; time-integrated data

1. Introduction

The transport of pollutant in water bodies like rivers, estuaries or coastal regions is governed by the advection–diffusion equation. This equation, which incorporates the two mechanisms through which a tracer is transported, involves some hydrodynamic parameters, namely velocities and water depths. In general, these parameters are the output of a flow solver and they need to be readily available in order to be able to solve the transport problem. Two techniques are then possible to use. The first consists of coupling the flow and the transport solvers. In this case, the flow and transport modules run concurrently, either within the same computer code or in two separate codes running simultaneously and linked through their input and output. At each time step, the required parameters are taken from the flow output and directly input to the transport solver. The second technique consists of decoupling both the solvers. The complete flow computation is achieved first and the required output is stored on a disk for subsequent use by the transport solver.

The literature review shows that both the techniques are commonly used. As expressed in Martin and McCutcheon (1999), both approaches have advantages and disadvantages, which primarily result from tradeoffs between computer storage and computational time. Uncoupled flow and transport computations have the advantage that the flow computations do not need to be repeated, for example, when simulating different scenarios of pollutant propagation under the same flow conditions. The disadvantage is, however, the large amount of data to be computed and stored beforehand.

In the present work, we are interested in uncoupled transport simulations. However, no matter whether the selected approach was towards coupled or uncoupled computations, there are a number of conditions to be satisfied in order to obtain satisfactory transport results. The essence of these conditions results from a monotonicity requirement which states that an initially uniform scalar field remains uniform in the absence of source and sinks in the equation. This requirement is called the constancy condition in Gross et al. (2002) and the references therein. In Dawson et al. (2003), a scheme which satisfies the constancy condition is said to be zeroth-order

* Corresponding author.
E-mail addresses: f.naifar@ewi.tudelft.nl (F. Naifar), p.wilders@ewi.tudelft.nl (P. Wilders), a.w.heemink@ewi.tudelft.nl (A.W. Heemink), g.s.stelling@ewi.tudelft.nl (G.S. Stelling).

0272-7714/$ - see front matter © 2007 Elsevier Ltd. All rights reserved.
doi:10.1016/j.ecss.2007.05.021

accurate. The violation of this condition expresses the fact that some purely artificial sources and sinks are generated by the discretization, which may even lead to instabilities in the calculations. In short, we aim to state a clear definition of the conditions necessary to fulfill in order to obtain positive and mass conservative results, which is a very important aspect in any transport simulation.

We also present a technique aiming to improve the computational aspect of the uncoupled flow-transport models. This technique, which consists of using "time-integrated flow data" can be an efficient tool to speed up the computations and reduce the required storage.

This paper is organized as follows: in Sections 2 and 3, we present relevant details on the flow solver and the transport solver to be coupled. In Section 4, we go in detail through the conditions necessary to satisfy for linking the uncoupled flow and transport computations. Section 5 presents technique based on the use of time-integrated flow data which allows the use of larger time steps for the transport computation and which, in turn, results in faster computation and reduction of disk storage requirement. Finally, Section 6 is reserved for the numerical application and Section 7 for the conclusions.

2. Flow computation

Shallow water equations are commonly used to model the oceanographic circulation and the tidal fluctuations. These depth-averaged (or 2-DH) equations basically describe the conservation of mass and momentum of water in movement.

$$\begin{aligned}
&\frac{\partial Hu}{\partial t}+\frac{\partial Hu^2}{\partial x}+\frac{\partial Huv}{\partial y}-fHv+gH\frac{\partial \eta}{\partial x}=\tau_u^{\mathrm{w}}-\tau_u^{\mathrm{b}}\\
&\frac{\partial Hv}{\partial t}+\frac{\partial Huv}{\partial x}+\frac{\partial Hv^2}{\partial y}+fHu+gH\frac{\partial \eta}{\partial y}=\tau_v^{\mathrm{w}}-\tau_v^{\mathrm{b}}\\
&\frac{\partial \eta}{\partial t}+\frac{\partial Hu}{\partial x}+\frac{\partial Hv}{\partial y}=0.
\end{aligned} \tag{1}$$

The unknowns in this equation are the depth-averaged velocities u and v, the water depth H and the water level η. The other coefficients are τ_v^{w} and τ_v^{w} representing the wind stress components, τ_u^{b} and τ_v^{b} are the bottom stress components, f is the Coriolis parameter, and g is the gravitational constant. The turbulent viscosity and the baroclinic pressure terms are omitted. An extended discussion on the shallow water equations and the mathematical modeling of flows can be found, for example in Vreugdenhil (1995). Basically, the last equation of system (1), the mass conservation equation, is of interest for our transport computations since the conservation of the transported substance is closely related to that of water.

In the frame of the present work, the software package WAQUA/TRIWAQ of the Rijkswaterstaat has been used to carry out the flow computations. Rijkswaterstaat, or RWS, is the Directorate-General for Public Works and Water Management in the Netherlands. This software is also one of the oldest and most commonly used computation models at the National Institute for Coastal and Marine Management (RIKZ).

WAQUA is a 2D hydrodynamic model which computes water levels and currents in open water and TRIWAQ is its 3D version. Physical domains are represented by a staggered type of grid in which a modelled system can be regarded as consisting of a large number of linked, column shaped quadrilateral volumes of water. Fig. 1 reproduced from EDS (2000) gives an impression of the staggered grid principle.

The corners of the volumes correspond to the grid depth points, the central points, and to the water level points, see Fig. 2. Water flows through the sides of the volumes, called faces, satisfying the conservation principle:

storage = input − output.

WAQUA solves the system of shallow water equation (1) using an ADI staggered time integration method over two half time steps. A detailed description of this method can be found in Stelling (1983). For a cell of quadrilateral shape, the discretized form of the continuity equation in (1) resulting from the ADI method reads as follows:

$$\begin{aligned}
H_{\mathrm{cell}}^{n+1}-H_{\mathrm{cell}}^{n}=\frac{\tau}{A}\Bigg(&\frac{H_1^{n+1}V_1^{n+1}+H_1^{n}V_1^{n}}{2}l_1+\frac{H_2^{n+1}V_2^{n+1}+H_2^{n}V_2^{n}}{2}l_2\\
&+H_3^{n+1/2}U_3^{n+1/2}l_3+H_4^{n+1/2}U_4^{n+1/2}l_4\Bigg).
\end{aligned} \tag{2}$$

In this equation, H_{cell} is the total water depth at the central point of a cell. U_e and V_e, $e=1,\ldots4$, are the normal velocities at the midpoint of the faces as presented in Fig. 2. l_e, $e=1,\ldots4$, are the lengths of the faces and n is the time

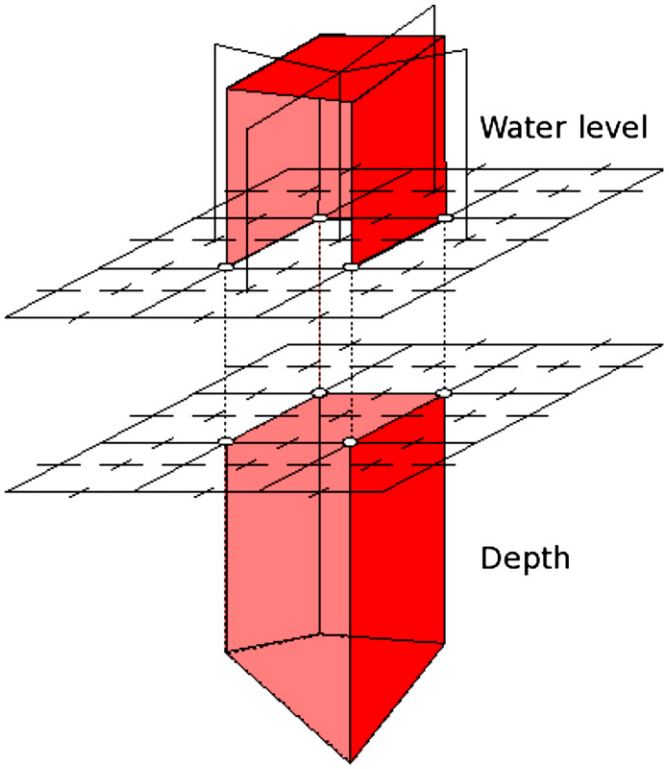

Fig. 1. Definition of the unit volume in WAQUA.

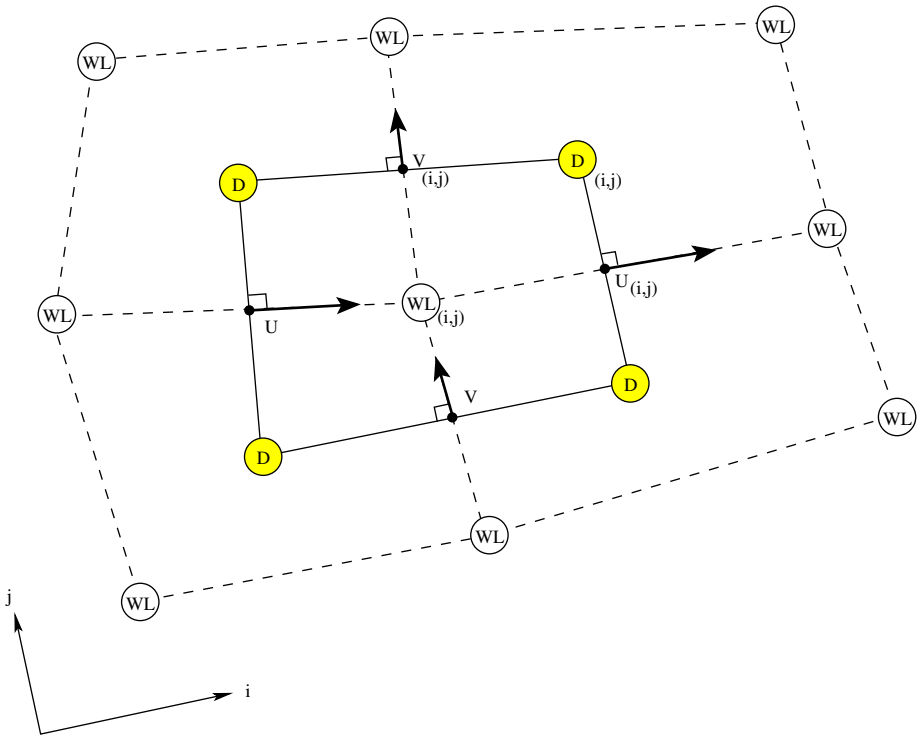

Fig. 2. Staggered grid in WAQUA. WL: water level point; D: depth point; u, v: velocity points.

index. H_e, $e = 1,\ldots4$, are the total water depths at the midpoint of the faces. n is the time index.

3. Transport solver

3.1. Governing equation

In case of negligible density changes, the concentration of a single phase miscible tracer obeys the general 3D advection–diffusion equation (or transport equation):

$$\frac{\partial c}{\partial t}+\frac{\partial uc}{\partial x}+\frac{\partial vc}{\partial y}+\frac{\partial \mathrm{w}c}{\partial z}=\frac{\partial}{\partial x}\left(D_\mathrm{h}\frac{\partial c}{\partial x}\right)+\frac{\partial}{\partial y}\left(D_\mathrm{h}\frac{\partial c}{\partial y}\right)+\frac{\partial}{\partial z}\left(D_\mathrm{v}\frac{\partial c}{\partial z}\right)+S, \tag{3}$$

where c (x, y, z, t) is the concentration of the tracer, (u, v, w) is the velocity vector, and S is the external source and sink term per volume. D_h and D_v are the horizontal and vertical diffusion coefficients. We assume that these two coefficients represent the transport by dispersion as well as the less important transport due to molecular diffusion. We still call Eq. (3) as the advection–diffusion equation since the mathematics of diffusion is used.

In case of a 2D approach, Eq. (3) can be integrated over the total water depth to obtain a depth-averaged equation. Let $\boldsymbol{u}$ represent the depth-averaged velocity vector. Assuming that the correlation terms resulting from the integration of Eq. (3) over the vertical are diffusion-like terms to be represented also by D_h, the depth-averaged transport equation can then be written under the so-called 2-DH formulation:

$$\frac{\partial H\overline{c}}{\partial t}+\nabla\cdot(H\boldsymbol{u}\overline{c})=\nabla(HD_\mathrm{h}\nabla\overline{c})+HS. \tag{4}$$

This partial differential equation is a conservation law, the coefficients of which are functions of the flow parameters.

3.2. Finite volume formulation

Finite volume methods are a class of discretization schemes that have proven highly successful in solving a large variety of conservation law systems. A general introduction to this class of methods can be found, for example in Randall (2002) and Wesseling (1992). The first step in the finite volume formulation consists of choosing a grid to represent the physical domain. It is already a very good idea to choose the same grid as for the flow solver. In fact, the use of different grids results in general in the necessity of further interpolations to get the parameters at the required locations. This is not always appreciated because the flow conservation becomes difficult to ensure.

We keep therefore the grid formed by quadrilateral shaped elements used for the flow. The horizontal area of one element is denoted by A and the boundary ∂A is composed of four elements e of length l_e. Let $\boldsymbol{f} = H\boldsymbol{u}c$ and $\boldsymbol{g} = HD_\mathrm{h}\nabla c$ Eq. (4) then becomes:

$$\frac{\partial Hc}{\partial t}+\nabla\cdot\boldsymbol{f}=\nabla\cdot\boldsymbol{g}+HS. \tag{5}$$

Integrating Eq. (5) over one grid cell and applying Green's divergence theorem, we get:

$$\int_A \frac{\partial Hc}{\partial t}\,\mathrm{d}A + \sum_{e\in\partial A}\left(\int_e \boldsymbol{f}\cdot\boldsymbol{n}_e\,\mathrm{d}\sigma\right) = \sum_{e\in\partial A}\left(\int_e \boldsymbol{g}\cdot\boldsymbol{n}_e\,\mathrm{d}\sigma\right) + \int_A HS\,\mathrm{d}A, \tag{6}$$

where $\boldsymbol{n}_e$ denotes the outward unit normal vector to the cell edge e and the discrete sum is calculated over the edges surrounding the cell. The edge integrated advective fluxes $\int_e \boldsymbol{f}\cdot\boldsymbol{n}_e\,\mathrm{d}\sigma$ and $\int_e \boldsymbol{g}\cdot\boldsymbol{n}_e\,\mathrm{d}\sigma$ are approximated by $f_e l_e$ and $g_e l_e$, where f_e and g_e are the advective and diffusive numerical fluxes, respectively. Now, we can write:

$$A\frac{\Delta Hc}{\tau} + \sum_e (f_e l_e) = \sum_e (g_e l_e) + AHS, \tag{7}$$

where τ is the time step. The numerical approximation of the fluxes is such that the second order accuracy in space is ensured. For further details concerning this aspect, the reader is referred to Naifar (2006) and Wilders and Fotia (2000). Now, we want to move directly to the time integration step which is of interest for our subject. The time integration of Eq. (7) is achieved with second order accuracy using the linearly implicit trapezoidal rule, which results in the following difference equation:

$$A\frac{H^{n+1}_{\mathrm{cell}}c^{n+1} - H^{n}_{\mathrm{cell}}c^{n}}{\tau} = -\frac{1}{2}\sum_e H^{n+1}_e u^{n+1}_e l_e c^{n+1}_e - \frac{1}{2}\sum_e H^{n}_e u^{n}_e l_e c^{n}_e + \frac{1}{2}\sum_e g^{n+1}_e l_e + \frac{1}{2}\sum_e g^{n}_e l_e + \frac{1}{2}AH^{n+1}S^{n+1} + \frac{1}{2}AH^{n}S^{n}. \tag{8}$$

We have chosen to compute the increment of concentration $(c^{n+1} - c^n)$ at each time step instead of the new concentration c^{n+1} itself. By slightly manipulating Eq. (8), we end up with the following equation, limited here for convenience to the advection terms:

$$\frac{A}{\tau}H^{n+1}_{\mathrm{cell}}\left(c^{n+1} - c^{n}\right) + \frac{1}{2}\sum_e H^{n+1}_e u^{n+1}_e \left(c^{n+1}_e - c^{n}_e\right) l_e = -A\frac{H^{n+1}_{\mathrm{cell}} - H^{n}_{\mathrm{cell}}}{\tau}c^{n} - \sum_e \frac{H^{n+1}_e u^{n+1}_e + H^{n}_e u^{n}_e}{2} l_e c^{n}_e. \tag{9}$$

Here, H_{cell} represents the total water depth at the cell centers. Since the flow solver is totally decoupled from the transport solver, the hydrodynamic coefficients H_{cell} and u_e at time levels n and $n+1$ are both available during the computation of the solution at time level n. In order to prepare for the data processing to be presented in Section 4, we propose to change the time level in the last term of the rhs as follows:

$$\frac{A}{\tau}H^{n+1}_{\mathrm{cell}}\left(c^{n+1} - c^{n}\right) + \frac{1}{2}\sum_e H^{n+1}_e u^{n+1}_e \left(c^{n+1}_e - c^{n}_e\right) l_e = -A\frac{H^{n+1}_{\mathrm{cell}} - H^{n}_{\mathrm{cell}}}{\tau}c^{n} - \sum_e H^{n}_e u^{n}_e c^{n}_e l_e. \tag{10}$$

Our computations show that this last change do not affect the properties of the numerical scheme and that mass conservation is automatically ensured as will be shown later in Section 4.

4. Constancy condition and data preprocessing

When solving our advection–diffusion equation, it is important not to end up with numerical 'wiggles' in the concentration profile. If monotonicity is ensured, the numerical scheme produces no artificial extrema as time progresses (Wesseling, 1992). A minimal monotonicity requirement is that an initially uniform scalar field remains uniform in the absence of sources and sinks in the equation. This is the so-called *constancy condition*. Any occurrence of changes in the concentration profile would mean that some sources and sinks have been artificially added and in such cases, instabilities can arise (Gross et al., 2002).

In practice, we found out that we need to ensure three major issues in order to satisfy the constancy condition. These are the following:

- the computed flow data have to satisfy exactly the discrete flow continuity equation up to machine accuracy,
- a consistency must exist between the flow and the transport schemes, and
- when drying and wetting are present in the simulation, special attention must be paid to the way of implementing the dry–wet procedure in both solvers.

In the following, we go into the details of these three issues.

4.1. Conservative flow computations

In Section 2, we mentioned that flow coefficients are computed using the package WAQUA/TRIWAQ which solves the system of shallow water equations using an ADI scheme.

These computed coefficients are supposed to satisfy Eq. (2) up to a given accuracy. However, a check of some actual computations shows that, for a number of cells in the domain, this is not always the case. This is generally due to the fact that the maximum number of iterations of some iterative procedures is reached without obtaining the required accuracy of the solution, usually when the geometry of the bottom is highly distorted (EDS, 2000). Although a correction technique is already implemented in WAQUA/TRIWAQ in order to ensure mass conservation, it is highly important that the flow coefficients satisfy the discrete continuity equation up to machine accuracy. In fact, this directly affects the transport conservative properties.

In order to ensure this conservation without having to intervene on the flow solver, we propose two correction procedures. The first consists of computing a new total water depth denoted by $\tilde{H}^{k}_{\mathrm{cell}}$ (with the superscript k indicating the time level), as follows:

$$\begin{cases} \tilde{H}^0_{\text{cell}} = H^0_{\text{cell}} \\ \tilde{H}^{n+1}_{\text{cell}} = \tilde{H}^n_{\text{cell}} + \dfrac{\tau}{A}\left(\dfrac{H_1^{n+1}V_1^{n+1} + H_1^n V_1^n}{2} l_1 + \dfrac{H_2^{n+1}V_2^{n+1} + H_2^n V_2^n}{2} l_2 \right. \\ \qquad \left. + H_3^{n+1/2} U_3^{n+1/2} l_3 + H_4^{n+1/2} U_4^{n+1/2} l_4 \right). \end{cases} \tag{11}$$

Using $\tilde{H}_{\text{cell}}$ instead of H_{cell}, it can be easily verified that Eq. (2) is now exactly verified. This correction in fact affects a limited number of locations and $\tilde{H}_{\text{cell}}$ is not expected to differ much from H_{cell}, which is verified in the numerical application.

The second type of correction uses a slightly different method. Here, for the computation of the solution at time level $n+1$, the transport model reads the required velocities and elevations at time step n and uses these values to compute H^{n+1}_{cell} according to Eq. (2) instead of reading H^{n+1}_{cell} from the input. In the next time level $n+2$, H^{n+1}_{cell} does not have the value previously computed but it is read again from the input files and it is with respect to this latter point that the procedure differs from the first type of correction. This method ensures that Eq. (2) is satisfied up to machine accuracy everywhere in the domain. However, this also means that the water depth H_{cell} may occasionally have a discontinuous profile in time. Our computations showed that this has basically no effect on the accuracy of the results.

4.2. Consistency

In order to satisfy the constancy condition, consistency must hold between the discretization of the flow computations and the discretization of the transport computation (Naifar and Wilders, 2004). The following definition is given in Gross et al. (2002) and the references therein: *A discretization of the advection equation is consistent with continuity if, given a spatially uniform scalar field as an initial datum, and a general flow field, the discretized scalar advection equation reduces to the discretized continuity equation.*

The issue of consistency between flow and transport computations was addressed by a number of authors. For example, Lin and Rood (1996) working on the modeling of tracer transport in the atmosphere realized that the inconsistency between the tracer continuity equation and the underlying equation of continuity of the air can be deleterious especially for long integrations. Leveque (1996) formulated a condition to be satisfied by the flow parameters. This condition which fits with his numerical transport scheme is a flow continuity equation under a given required discrete form. He mentioned a number of numerical flow schemes for which consistency is automatically obtained. If different schemes were to be used, further velocity projections are needed to make the velocity field divergence free. Taking care that the flow solver is consistent with the transport solver is also a technique proposed by Bonaventura et al. (2004). Dawson (2000) proposed to add extra correction term to the discrete transport equation to overcome the non-conservative velocity field and ensure local conservation. Deleersnijder (2001) also proposed to apply a velocity correction to enforce the continuity equation.

In general terms, it can be concluded that two methods are generally used to overcome the problem of inconsistency: either selecting the flow numerical scheme and the transport numerical scheme in such a way that they are consistent with each other, e.g. Leveque (1996) and Bonaventura et al. (2004), or applying corrections, e.g. Dawson (2000) and Deleersnijder (2001). In our case, different approaches and numerical schemes are used to solve flow and transport problems.

We propose a new simple method to ensure consistency between the two. The idea is to compute new flow parameters to be used by the transport solver in such way that consistency is ensured. In fact, we have the advantage that our original velocity field is not arbitrary and we know exactly how it was computed. According to the definition in the beginning of Section 4, our scheme (10) has to reduce to (2) in case of a uniform scalar field. Taking for example a uniform concentration in Eq. (10), we obtain for a quadrilateral cell:

$$\begin{aligned} H^{n+1}_{\text{cell}} - H^n_{\text{cell}} &= -\frac{\tau}{A}\sum_e H^n_{es} u^n_{es} l_e \\ &= -\frac{\tau}{A}\left(H^n_{s_1} u^n_{s_1} l_1 + H^n_{s_2} u^n_{s_2} l_2 + H^n_{s_3} u^n_{s_3} l_3 + H^n_{s_4} u^n_{s_4} l_4 \right). \end{aligned} \tag{12}$$

We use the index s in the rhs to distinguish between the coefficients of the flow solver and the coefficients to be used by our solver. We need to choose the proper water depths and velocities in such a way that (Naifar and Wilders, 2004) remains satisfied. Looking at Eqs. (2) and (12), one can satisfy the consistency with the continuity equation if the following system of equations holds:

$$\begin{cases} H^n_{1s} u^n_{1s} l_1 = \dfrac{H_1^{n+1}V_1^{n+1} + H_1^n V_1^n}{2} l_1 \\ H^n_{2s} u^n_{2s} l_2 = \dfrac{H_2^{n+1}V_2^{n+1} + H_2^n V_2^n}{2} l_2 \\ H^n_{3s} u^n_{3s} l_3 = H_3^{n+1/2} U_3^{n+1/2} l_3 \\ H^n_{4s} u^n_{4s} l_4 = H_4^{n+1/2} U_4^{n+1/2} l_4 \end{cases}. \tag{13}$$

One possible choice which satisfies Eq. (13) is the following:

$$\begin{cases} H^n_{1s} = H^n_1; \quad u^n_{1s} = \dfrac{H_1^{n+1}V_1^{n+1} + H_1^n V_1^n}{2H_1^n} \\ H^n_{2s} = H^n_2; \quad u^n_{2s} = \dfrac{H_2^{n+1}V_2^{n+1} + H_2^n V_2^n}{2H_2^n} \\ H^n_{3s} = H^n_3; \quad u^n_{3s} = \dfrac{H_3^{n+1/2}U_3^{n+1/2}}{2H_3^n} \\ H^n_{4s} = H^n_4; \quad u^n_{4s} = \dfrac{H_4^{n+1/2}U_4^{n+1/2}}{2H_4^n} \end{cases}. \tag{14}$$

Notice that other choices of H and u which satisfy Eq. (13) are also possible. Looking at the way they were computed, the new coefficients will automatically satisfy the required consistency condition. We note finally that the computation of these new parameters is a laborious preprocessing step required before proceeding with the transport computation.

4.3. Drying and wetting

Since we are dealing with transport in coastal regions, some parts of the domain change from wet to dry and vice versa following the tidal movements. Here, we do not provide many details on this issue, but we need to emphasize on the fact that it may cause violation of the constancy condition if not considered carefully. Essentially, since the flow and transport computations are decoupled from each other, we have to make sure that the definition of the wet or dry status of a given cell is consistent between the two solvers. The reader is referred to Naifar (2006) for further details.

5. Time-integrated flow data

Flow and transport phenomena have different time scales and therefore it would be very desirable if different time steps can be used for each of them. Particularly interesting for the case of uncoupled computations, the possibility of using larger time steps for the transport would contribute not only to speed up the computations but also to reduce the required flow data storage. In the present section, we present a technique which consist in using a new set of data called ''time-integrated flow data'' and which will allow the use of different time steps for the flow and for the transport.

Section 4.2 emphasized the need for consistency between the flow and transport solvers and presented a method to compute flow coefficients. This method requires the adoption of the same time step as used for the flow computation. The idea behind the time-integrated flow data consists of computing, out of the available small time step data, some new flow coefficients at larger time steps while ensuring at the same time the consistency condition and the conservation property (Naifar and Wilders, 2004).

We can write Eq. (11) for p successive time steps of the flow model:

$$H_{\text{cell}}^{n+1}-H_{\text{cell}}^{n}=\frac{\tau}{A}\left\{\frac{H_1^{n+1}V_1^{n+1}+H_1^{n}V_1^{n}}{2}l_1+\frac{H_2^{n+1}V_2^{n+1}+H_2^{n}V_2^{n}}{2}l_2+H_3^{n+1/2}U_3^{n+1/2}l_3+H_4^{n+1/2}U_4^{n+1/2}l_4\right\}$$

$$H_{\text{cell}}^{n+2}-H_{\text{cell}}^{n+1}=\frac{\tau}{A}\left\{\frac{H_1^{n+2}V_1^{n+2}+H_1^{n+1}V_1^{n+1}}{2}l_1+\frac{H_2^{n+2}V_2^{n+2}+H_2^{n+1}V_2^{n+1}}{2}l_2+H_3^{n+3/2}U_3^{n+3/2}l_3+H_4^{n+3/2}U_4^{n+3/2}l_4\right\}$$

$$\vdots$$

$$H_{\text{cell}}^{n+p}-H_{\text{cell}}^{n+p-1}=\frac{\tau}{A}\left\{\frac{1}{2}\left(H_1^{n+p}V_1^{n+p}+H_1^{n+p-1}V_1^{n+p-1}\right)l_1+\frac{1}{2}\left(H_2^{n+p}V_2^{n+p}+H_2^{n+1}V_2^{n+p-1}\right)l_2+H_3^{n+p-1/2}U_3^{n+p-1/2}l_3+H_4^{n+p-1/2}U_4^{n+p-1/2}l_4\right\}.$$

Summing these equations all together and rearranging, we get:

$$\begin{aligned}H_{\text{cell}}^{n+p}-H_{\text{cell}}^{n}&=H_{\text{cell}}^{N+1}-H_{\text{cell}}^{N}\\&=\frac{\tau}{A}\left\{\left(\frac{H_1^{n}V_1^{n}}{2}+H_1^{n+1}V_1^{n+1}+\ldots+H_1^{n+p-1}V_1^{n+p-1}+\frac{H_1^{n+p}V_1^{n+p}}{2}\right)l_1\right.\\&\quad+\left(\frac{H_2^{n}V_2^{n}}{2}+H_2^{n+1}V_2^{n+1}+\ldots+H_2^{n+p-1}V_2^{n+p-1}+\frac{H_2^{n+p}V_2^{n+p}}{2}\right)l_2\\&\quad+\left(H_3^{n+1/2}U_3^{n+1/2}+H_3^{n+3/2}U_3^{n+3/2}+\ldots+H_3^{n+p-1/2}U_3^{n+p-1/2}\right)l_3\\&\quad\left.+\left(H_4^{n+1/2}U_4^{n+1/2}+H_4^{n+3/2}U_4^{n+3/2}+\ldots+H_4^{n+p-1/2}U_4^{n+p-1/2}\right)l_4\right\},\end{aligned}\tag{15}$$

where N is the new counter of the transport time step. Obviously, the new transport time step T has to be a multiple of the flow time step; here, $T=p\tau$. In analogy to Eq. (12), we can make the following choices in order to ensure consistency:

$$\begin{cases}H_{S_1}=H_1^{n}\\U_{S_1}=\dfrac{1}{H_{S_1}}\dfrac{1}{p}\left(\dfrac{H_1^{n}V_1^{n}}{2}+H_1^{n+1}V_1^{n+1}+\ldots+H_1^{n+p-1}V_1^{n+p-1}+\dfrac{H_1^{n+p}V_1^{n+p}}{2}\right)\\H_{S_2}=H_2^{n}\\U_{S_2}=\dfrac{1}{H_{S_2}}\dfrac{1}{p}\left(\dfrac{H_2^{n}V_2^{n}}{2}+H_2^{n+1}V_2^{n+1}+\ldots+H_2^{n+p-1}V_2^{n+p-1}+\dfrac{H_2^{n+p}V_2^{n+p}}{2}\right)\\H_{S_3}=H_3^{n}\\U_{S_3}=\dfrac{1}{H_{S_3}}\dfrac{1}{p}\left(H_3^{n+1/2}U_3^{n+1/2}+H_3^{n+3/2}U_3^{n+3/2}+\ldots+H_3^{n+p-1/2}U_3^{n+p-1/2}\right)\\H_{S_4}=H_4^{n}\\U_{S_4}=\dfrac{1}{H_{S_4}}\dfrac{1}{p}\left(H_4^{n+1/2}U_4^{n+1/2}+H_4^{n+3/2}U_3^{n+3/2}+\ldots+H_4^{n+p-1/2}U_4^{n+p-1/2}\right).\end{cases}\tag{16}$$

The coefficients computed in this manner satisfy the following new continuity equation written for the new time step T:

$$H_{\text{cell}}^{N+1}-H_{\text{cell}}^{N}=-\frac{T}{A}(H_{S_1}U_{S_1}l_1+H_{S_2}U_{S_2}l_2+H_{S_3}U_{S_3}l_3+H_{S_4}U_{S_4}l_4).\tag{17}$$

The storage space required for the new coefficients is only $1/p$ times the original space, a considerable reduction. The computational CPU time is also approximately divided by p.

The use of this technique in the 3D case becomes almost a necessity. In fact, unless special computers with exceptional storage capacity are used, a 3D problem of an average size becomes simply too heavy for a normal PC. The transport

equation for a uniform concentration gives the condition which needs to be satisfied by the flow coefficients in the 3D case:

$$\frac{A}{\tau}\left(H_{\text{cell}}^{n+1}-H_{\text{cell}}^{n}\right)=-\sum_{e}H_{e}^{n}U_{e}^{n}l_{e}-A[\omega^{n}]_{z_k}^{z_{k-1}}, \tag{18}$$

where ω is the vertical velocity relative to the layer interface and z_k is the elevation of the horizontal interface number k. If we want to use a time step T multiple of τ, we need therefore to satisfy:

$$\frac{A}{T}\left(H_{\text{cell}}^{N+1}-H_{\text{cell}}^{N}\right)=-\sum_{e}H_{e}^{N}U_{e}^{N}l_{e}-A\left[\omega^{N}\right]_{z_k}^{z_{k-1}}. \tag{19}$$

In the special case when WAQUA/TRIWAQ is used as flow solver, the procedure for computing time-integrated flow data can be made easier using some special output variables from this software called ''time integrals''. These are *WPINT*, *DISUNT*, *DISVNT*, *UPINT*, and *VPINT*, defined as follows:

$$\begin{aligned} DISUNT_{k}^{t+T}&=\int_{t}^{t+T}U_{k}H_{k}\,\mathrm{d}t \quad DISVNT_{k}^{t+T}=\int_{t}^{t+T}V_{k}H_{k}\,\mathrm{d}t\\ UPINT_{k}^{t+T}&=\int_{t}^{t+T}U_{k}\,\mathrm{d}t \qquad VPINT_{k}^{t+T}=\int_{t}^{t+T}V_{k}\,\mathrm{d}t\\ WPINT_{k}^{t+T}&=\int_{t}^{t+T}\omega_{k}\,\mathrm{d}t, \end{aligned} \tag{20}$$

where T is such that the time level $N+1$ in Eq. (19) corresponds to $t+T$.

For a given element, these variables satisfy the following mass conservation equation:

$$\frac{A}{T}\left(H_{\text{cell}}^{N+1}-H_{\text{cell}}^{N}\right)=\sum_{e}\frac{DISUNT^{N+1}}{T}l_{e}+\sum_{\text{top,bottom}}A\frac{WPINT^{N+1}}{T}. \tag{21}$$

In this equation, *DISUNT* may also be *DISVNT* depending on the direction of the face. By making a correspondence between Eqs. (19) and (21), the following choice for the flow parameters ensures the required conservation property:

$$H_{e}^{N}=\frac{DISUNT^{N+1}}{UPINT};\quad U_{e}^{N}=\frac{UPINT^{N+1}}{T};\quad \omega^{N}=\frac{WPINT^{N+1}}{T}. \tag{22}$$

6. Numerical application

6.1. The 2D case

We propose to apply the new rules developed to link the flow and transport solvers in a numerical simulation of a real-life case. The proposed application considers the domain known as the Kuststrookmodel, representing a strip of about 400 by 60 km of the North Sea along the Dutch coast. This domain is represented by a grid originating from the RIKZ and contains 20,175 cells, see Fig. 3.

First, we proceed with the flow simulation and the check of the mass conservation of the obtained data, conservation in the sense of the ADI scheme used for their computation. The check shows that a correction on the total water depth is required, and for this purpose, the technique proposed in Eq. (11) is used. Our computation shows that indeed $\tilde{H}_{\text{cell}}$ is only very slightly different from H_{cell}.

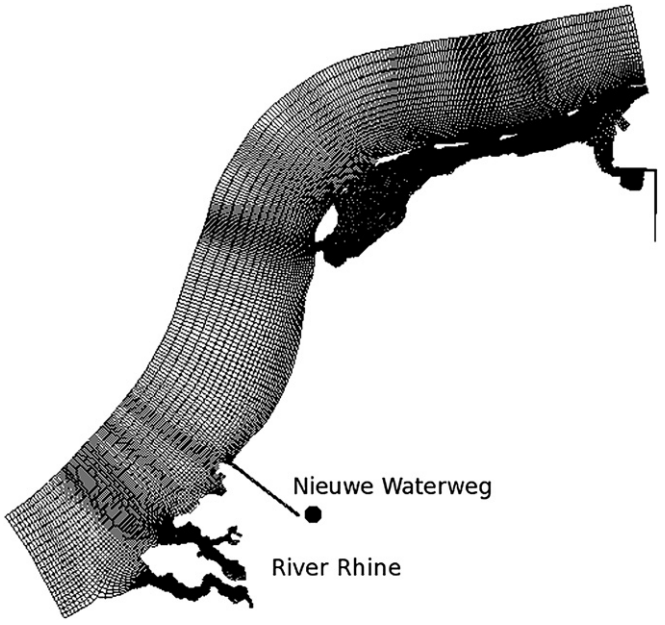

Fig. 3. Grid of the Dutch coastal region.

The next step consists of computing a new flow data set according to Eq. (14). Hydrodynamic coefficients are time-dependent variables and therefore have to be available for every computational time step and for the whole simulation period. Once the data set is ready, we proceed to the verification of the constancy condition. We set the initial concentration equal to 1 for the whole domain as well as for the inflows to the domain through the open boundaries. No source term is added to the system. The simulation over a period of two months showed that the concentration does not change confirming therefore that the constancy condition is satisfied.

Then, we simulate a continuous release of a dissolved pollutant at the upstream boundary of the Nieuwe Waterweg. This location is shown by a black dot in Fig. 3. Using the same time step of 1 min as for the flow, Fig. 4 shows the propagation of

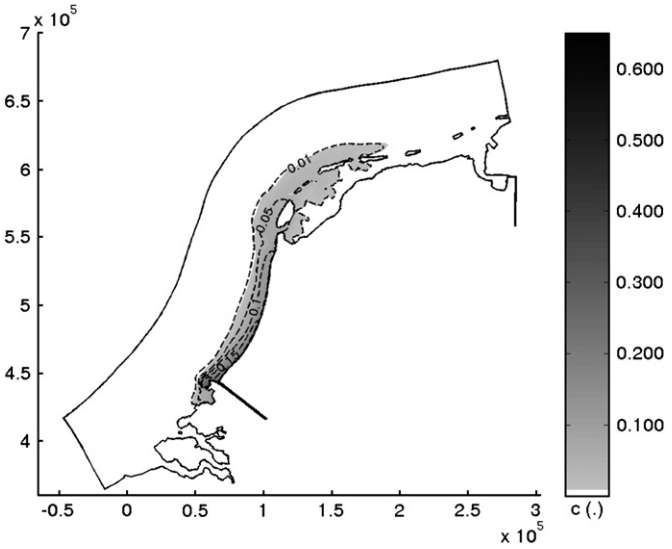

Fig. 4. Spreading after 62.5 days (90,000 time steps of 1 min).

the pollutant after 90,000 time steps (62.5 days). We can see that the contaminated area extends along the coastline towards the north and reaches the fragile northern coast, called the Waddenzee, around two months after the beginning of the release. This behavior is relatively known, see for example de Blois (1993), Salomons et al. (1989) or Stijnen (2002), but has also been proven by the results we have obtained from the transport module of WAQUA.

Now, we want to evaluate the efficiency of the technique of using time-integrated flow data presented in Section 5 through its application to the Kuststrookmodel. Then, we process the available 1-min data set from WAQUA according to Eq. (16) to produce a new set with time intervals of 15 min. The required storage space is already reduced by a factor of 1/15. Next, we check for the constancy condition for this new time step, which proves to be satisfactory. The same experiment of pollutant release in the river Rhine is now performed using the 15-min time step. A comparison between the resulting plots shows that the extent of the contaminated region is almost identical for both time steps.

Table 1, comparing the results obtained in both cases, also shows very similar figures. In particular, the total mass of pollutant present in the system at 62.5 days and computed using the obtained concentrations shows that the use of time-integrated data keeps the same mass conservation property as in the original case of 1-min data. We can therefore conclude that the use of integrated time steps is an efficient way to render the computations faster and less cumbersome.

6.2. The 3D case

The techniques of coupling flow and transport solvers and using time-integrated flow data can be even more interesting in the 3D case because this latter involves much more data. The numerical application considers a simpler case which consists of a stretch of river 500 m long and 100 m wide with a bed presenting some deformations and irregularities as shown in Fig. 5. In the vertical direction, the domain was subdivided into 10 layers of equal thickness. The flow simulation using TRIWAQ was carried out for a duration of 3 h 20 min with a time step of 0.6 s. The boundary conditions consisted of imposing a constant discharge of 5.9 m^3/s at the upstream boundary and a periodical water level at the downstream boundary according to a sine function. The bottom friction was estimated using Chezy formula with a coefficient equal to 70.

As stated earlier, we perform directly the simulations using the time-integrated flow data because of the large amount of data. For their preparation, we used the TRIWAQ time integrals presented in Eq. (20) to produce data at time step of 5 s. The check of the mass conservation of the flow was performed according to the second technique presented in Section 4.1.

Table 1
Comparison of the results of the time-integrated flow data

	$\tau = 1$ min	$\tau = 15$ min
Minimum concentration	0	-1.910^{-8}
Cells with negative concentration	0	1
Maximum concentration	0.5612	0.5612
Total mass of pollutant	3.63×10^9	3.62×10^9

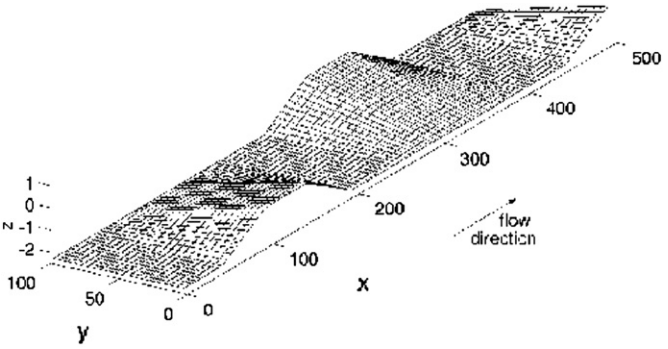

Fig. 5. Grid of the test case.

The numerical experiments started with the check for the constancy condition. Using the time step of 5 s, the run performed showed that this constancy condition was perfectly satisfied. The concentration remained perfectly equal to the chosen constant value, in our case $c = 1$, up to machine accuracy.

A continuous release of a miscible pollutant was then simulated. The release point was located at the upstream boundary of the stretch, halfway between the right and left banks and was assumed to take place at the water surface (layer 1). The computation started with a concentration equal to zero throughout the domain. The diffusion coefficients were estimated at 0.01 m^2/s for the horizontal direction and 0.001 m^2/s for the vertical direction.

Fig. 6 shows for each of the 10 layers a top view of the horizontal concentration profile. Three contour lines represent concentrations 0.05, 0.5 and 1 (when applied). Fig. 7 shows a 3D representation of the iso-value $c = 0.25$.

As in the 2D case, the concentration profile was compared with the one obtained from the transport module of TRIWAQ and very good correspondence was found. This confirms that the techniques used for coupling the flow and transport solvers are also applicable to a 3D problem. Fig. 8 shows the total mass of tracer present in the domain, computed based on the resulting concentration profile. The dashed straight line represents the total mass released, which in our case is linear in time corresponding therefore to a constant release. This figure shows a very good conservation of mass during the first 15 min of the simulation. After that, the solute starts leaving the domain from the right boundary and of course the two curves start deviating from each other. This result confirms among others that the correction applied to the flow output does not affect the mass conservation.

7. Conclusions

In this paper, we studied the issue of linking flow and transport models. It is known that the use of an arbitrary hydrodynamic data set would immediately lead to a loss of mass conservation. Previous works recommended either the use of

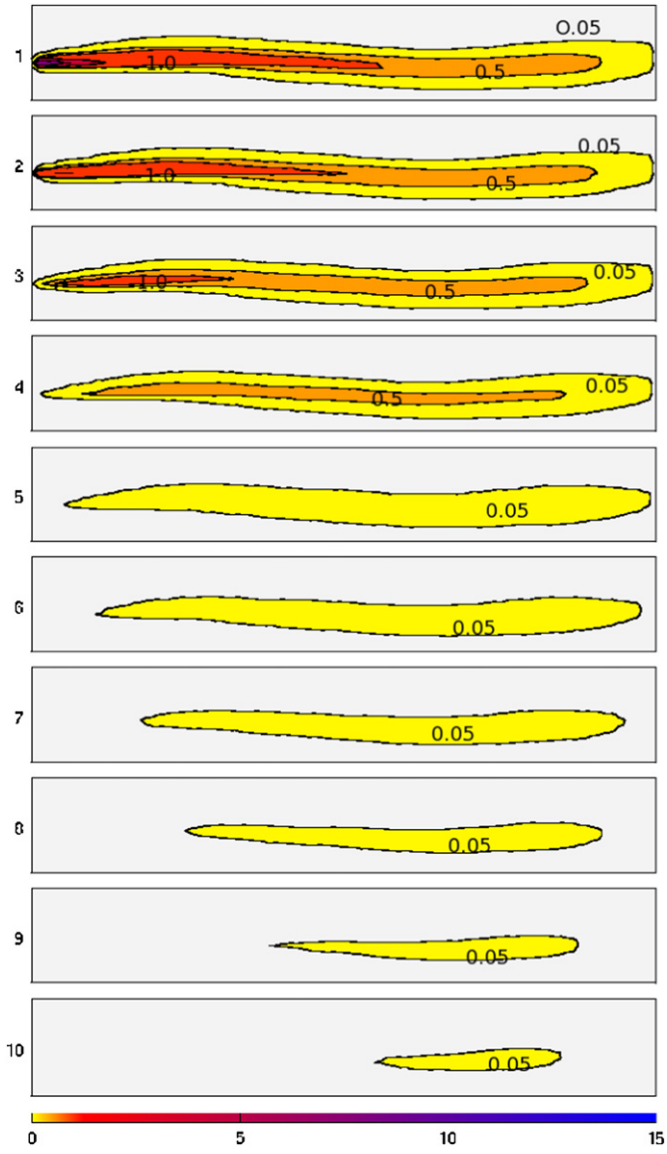

Fig. 6. Top view of the concentration at different layers after 16 min.

compatible schemes for the flow and the transport or to apply corrections in such a way local conservation is ensured. Here, we proposed a new method to link a finite volume based transport solver to a flow model using an ADI scheme. It consists in computing new velocity and water depth parameters in such a way consistency is ensured. We also proposed a new

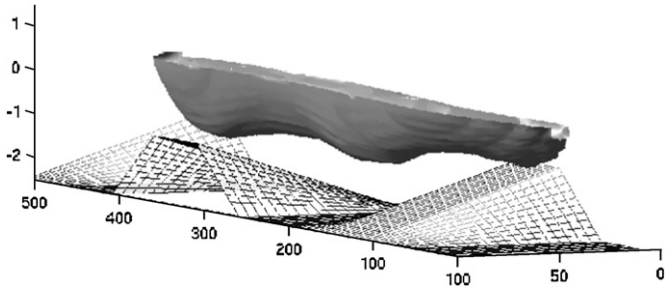

Fig. 7. 3D representation of the iso-value 0.25 after 16 min.

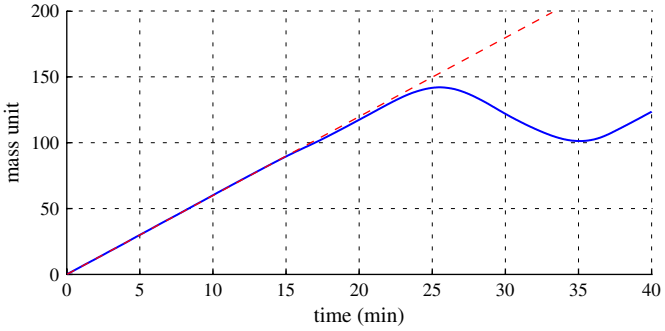

Fig. 8. Total mass in the computational domain.

technique based on the generation of time-integrated flow data set allowing at the same time the use of a larger time step for the transport solver than the one used for the flow and the reduction of the disk storage requirement. The techniques developed were applied for practical 2D and 3D cases. The results were compared with the results obtained with the transport modules of WAQUA/TRIWAQ and good correspondence was found. The check for the mass conservation also showed that the developed techniques were indeed efficient.

Acknowledgment

We would like to acknowledge the National Institute for Coastal and Marine Management in the Netherlands (RIKZ) for allowing to use their software package SIMONA and associated data.

References

de Blois, C., March 1993. Rhine Transport Model, Dynamic Pollutant Transport Modeling for Policy Evaluation in the Rhine Basin. Technical Report. Delft University of Technology, The Netherlands.

Bonaventura, L., Kornblueh, L., Giorgetta, M.A., Roeckner, E., Heinze, T., Majewski, D., Ripodas, P., Ritter, B., Ringler, T., Baudisch, J., 2004. The ICON Shallow Water Model: Scientific Documentation and Benchmark Tests. Technical Report. Max Planck Institut für Meteorologie, Hamburg, Germany.

Dawson, C., 2000. Conservative, shock-capturing transport methods with non conservative velocity approximations. Computational Geosciences 3, 205–228.

Dawson, C., Sun, S., Wheeler, M.F., 2003. Compatible algorithms for coupled flow and transport. Computer Methods in Applied Mechanics and Engineering 193, 2565–2580.

Deleersnijder, E., 2001. Enforcing the continuity equation in numerical models of geophysical fluid flows. Applied Mathematics Letters 14, 867–873.

EDS, April 2000. User's Guide WAQUA, General Information. Technical Report. Ministry of Transport, Public Works and Water Management/ Directorate-General for Public Works and Water Management, Leidschendam.

Gross, E.S., Bonaventura, L., Rosatti, G., 2002. Consistency with continuity in conservative advection schemes for free-surface models. International Journal for Numerical Methods in Fluids 38, 307–327.

Leveque, R.J., 1996. High-resolution conservative algorithms for advection in incompressible flow. SIAM Journal on Numerical Analysis 33 (2), 627–665.

Lin, S.J., Rood, R.B., 1996. Multidimensional flux-form Semi-Lagrangian transport schemes. Monthly Weather Review 124, 2046–2070.

Martin, J.L., McCutcheon, S.C., 1999. Hydrodynamics and Transport for Water Quality Modeling. Lewis, Boca Raton, Florida.

Naifar, F., 2006. A Finite Volume Solver for the Simulation of Transport Processes. Ph.D. thesis, Delft University of Technology.

Naifar, F., Wilders, P., July 2004. Towards a conservative and positive computation of pollutant transport. In: Neittaanmaki, P., Rossi, T., Majava, K. (Eds.), Fourth European Congress on Computational Methods in Applied Sciences and Engineering, Jyväskylä, Finland, ISBN 951-39-1868-8, pp. 1–21. CDRom Proceedings.

Randall, R.J. 2002. Finite Volume Methods for Hyperbolic Problems. Cambridge, United Kingdom.

Salomons, W., Bayne, B.L., Duursma, E.K., Forstner, U., 1989. Pollution of the North Sea. An Assessment. Springer-Verlag.

Stelling, G.S., 1983. On the Construction of Computational Methods for Shallow Water Flow Problems. Rijkswaterstaat Communications, No. 35/1984, The Hague. Also appeared as a thesis at the TUDelf.

Stijnen, J.W., 2002. Numerical Methods for Stochastic Environmental Models. Ph.D. Thesis, Delft University of Technology.

Vreugdenhil, C.B., 1995. Numerical Methods for Shallow-water Flow. Taylor & Francis, New Palm Beach, Florida.

Wesseling, P., 1992. An Introduction to Multigrid Methods. Wiley, New York.

Wilders, P., Fotia, G., 2000. A positive spatial advection scheme on Unstructured Meshes for Tracer Transport. Journal of Computational and Applied Mathematics 140, 809–821.

Available online at www.sciencedirect.com
ScienceDirect
Estuarine, Coastal and Shelf Science 74 (2007) 742–755
ESTUARINE COASTAL AND SHELF SCIENCE
www.elsevier.com/locate/ecss

Embayment characteristic time and biology via tidal prism model

Mohamed A. Abdelrhman

United States Environmental Protection Agency, Office of Research and Development, National Health and Environmental Effects Research Laboratory, Atlantic Ecology Division, 27 Tarzwell Drive, Narragansett, RI 02882, USA

Received 1 July 2006; accepted 9 May 2007
Available online 25 June 2007

Abstract

Transport time scales are often offered by scientists, and accepted by ecologists, as qualitative indicators of the susceptibility of ecological components within an embayment. However, rigorous quantitative methods were never presented to confirm this intuition. Transport time scales in water bodies are classically based on their physical and chemical aspects rather than their ecological and biological character. The direct connection between a physical time scale and an ecological effect has to be investigated in order to quantitatively relate a transport time scale to ecology. This concept is presented here with some general guidelines and clarifying examples. To be able to relate physical time scales to biological processes, a simple tidal prism model is developed that calculates temporal changes in concentration and the related exposure. This approach provides a quick method to calculate the characteristic time for transport in a large number of embayments, which can also help in classification endeavors.

Keywords: embayment; tidal prism model; characteristic time; concentration; threshold; biology; exposure

1. Introduction

This paper deals with the relationship between transport time scale of an embayment and biological processes. This context was discussed before by Abdelrhman (2005, 2006). The reader is encouraged to refer to these publications and the references therein for detailed explanations; however, a general and brief review is presented below. This paper is non-traditional as it pertains to developing a new understanding of the concept of physical transport time scale and its relevancy to biology. This understanding was obtained by simplifying (or bypassing) many details in both physics and biology, without compromising the scientific integrity of the paper. Idealized examples are offered to clarify the general definitions and relationships. Applications to real situations are also presented to demonstrate the practical uses and benefits of this approach.

The general concept of a ''transport time scale'' has been used in aquatic studies for decades. Most recently, three related measures of this time have been emphasized in the aquatic literature, i.e., ''flushing time,'' ''age,'' and ''residence time'' (Monsen et al., 2002). According to Monsen et al., flushing time is the ratio of the total mass of a constituent (or water) in a water body to its overall rate of renewal, age is the time a water parcel at a specified location has spent in the water body since entering it, and residence time is the time until a water parcel at a specified location leaves the water body. In addition, the ''transit time'' is another time scale that considers the total time spent by a molecule from entering until leaving the embayment (Bolin and Rodhe, 1973; Zimmerman, 1976; Takeoka, 1984), and the ''turnover time'' is the time needed to exchange all the material in the embayment with new material. All these time scales originate from physical properties of the water body (e.g., volume, tidal forcing, freshwater inflow, mixing, exchange) and chemical properties of constituents (e.g., concentration or mass, decay, partitioning). They focus on the movement, exchange, and mixing of

E-mail address: abdelrhman.mohamed@epa.gov

0272-7714/$ - see front matter © 2007 Elsevier Ltd. All rights reserved.
doi:10.1016/j.ecss.2007.05.008

water and its constituents, and not on how these relate to the ecology of a system and its biological components.

When dealing with biological components (endpoint beneficiary of the above-mentioned time scales), one may raise the following essential questions: Is there a direct quantitative relationship between these transport time scales and biology? What is this relationship? How can we obtain this relationship? To answer these questions the analysis should include biological components of interest then proceed to define the relevant and appropriate transport time scale(s). The main objective of this paper is to present simple model to address the above questions. The specific objective is to identify the effect of constituent loading patterns and the relevant transport times on the exposure of a biological component in an embayment (or suite of embayments).

2. Model

In a numerical model, it is customary to start with fine scale temporal variations in loading and spatial delineations of an embayment, and then proceed through a simulation to calculate concentration variations. This approach is very meticulous in defining spatial and temporal changes in concentration and it is highly recommended when expertise and resources are available. However, it may not match the biological responses of interest, which may function on coarser spatial scales and longer time periods. Meanwhile, management decisions sometimes favor simpler and less sophisticated approaches that can be applied rapidly to suites of embayments (i.e., classes). The approach presented here falls in this category. It is based on tidal prism analysis (e.g., Sanford et al., 1992; Luketina, 1998) with modifications to accommodate temporal variability in tidal forcing and loading and to produce time-varying concentration. It should be emphasized, however, that this tidal prism model is not designed to resolve details on time scales less than a tidal phase (flood or ebb) or spatial scales less than the size of the embayment.

The following simplifying assumptions are made to illustrate the method in an idealized embayment (Fig. 1): volume of freshwater inflow is assumed negligible relative to the volume of water in the embayment; the embayment is well mixed with negligible estuarine circulation; semidiurnal tides (as in the northeastern continental USA) exist throughout the year. The constituent can be any conservative nutrient, chemical, contaminant, etc. To simplify the analysis, details about the constituent's kinetics, sources, sinks, and partitioning are not included. The model preserves not only diurnal variations in tidal ranges and phase duration, but also changes due to spring–neap cycles throughout the year.

During the two phases of any tidal cycle (flooding and ebbing, Fig. 1a) the constituent will be loaded to and/or flushed out from the embayment. The conservation of a tracer mass requires that:

$$\frac{dM}{dt} = m_{in} - m_{out} \tag{1}$$

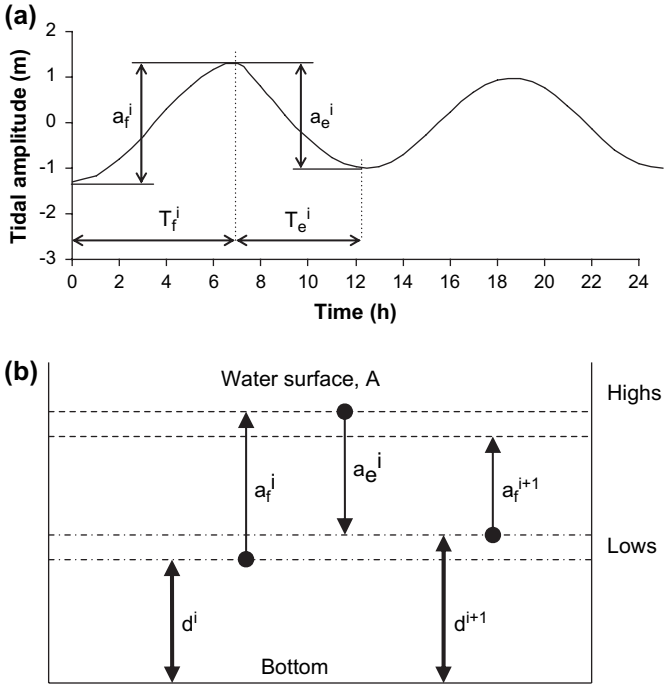

Fig. 1. Sketches of the idealized setting: (a) typical semi-diurnal tide (e.g., as in northeastern USA) with varying flood–ebb periods ($T_f^i \neq T_e^i$) and ranges ($a_f^i \neq a_e^i$), (b) embayment with variable tidal prism ($a_f^i \neq a_e^i$). Double headed arrows indicate the time-varying water depth and single headed arrows illustrate the time-varying range of the water surface, which starts from the level marked by the dot and ends at the level of the arrow head.

where M is the total mass (kg) of the tracer inside the embayment, m_{in} is the rate of mass (kg h^{-1}) entering the embayment, m_{out} is the rate of mass (kg h^{-1}) leaving the embayment, and t denotes time. The change in mass for each tidal phase (flood or ebb) can be calculated by numerically integrating Eq. (1) through the time period for each tidal phase (e.g., Luketina, 1998). To preserve the effect of tidal changes, the method used here tracks the conservation of mass for each tidal phase as well as the concentration at the end of that phase (i.e., at peak flood and at dip ebb). The total change in mass throughout a full tidal cycle is the sum of changes during these two phases which can be expressed by:

$$\Delta M = M^{i+1} - M^i = M^i_{\text{in-flood}} + M^i_{\text{in-ebb}} - M^i_{\text{out-ebb}} \tag{2}$$

where M^i is the mass at the beginning of flooding phase for the ith tidal cycle. The superscript represents the tidal cycle and the subscripts identify masses entering or exiting during flooding and ebbing periods.

During the flooding period, T_f (Fig. 1a), loading from the watershed and seaward open boundary of the embayment causes mass of the constituent to increase inside the embayment by:

$$M^i_{\text{in-flood}} = nT^i_f + M^i_{\text{entering}} \tag{3}$$

where n (kg h^{-1}) is the mass of the constituent loaded to the embayment from the watershed per hour, T_f (h) is the flooding period of a general cycle, and M_{entering} is the mass entering

through the open boundary, as described below. For simple dilution, the mean concentration in the embayment at peak elevation of the flooding phase is given by:

$$C_{\mathrm{f}}^{i}=\frac{M^{i}+M_{\text{in-flood}}^{i}}{\left(d_{\mathrm{f}}^{i}+a_{\mathrm{f}}^{i}\right)A} \tag{4}$$

where d_{f} (m) is the water depth in the embayment at the beginning of the flooding phase, a_{f} (m) is range of flooding tide inside the embayment (Fig. 1b), and A (m^2) is mean surface area of the embayment.

During the ebbing period, T_{e} (Fig. 1a), loading from the watershed will continue but that from the seaward open boundary will cease (assuming unidirectional flow at the open boundary at all times). The loaded mass of the constituent would be:

$$M_{\text{in-ebb}}^{i}=nT_{\mathrm{e}}^{i} \tag{5}$$

The volume of water that leaves the embayment during the ebbing phase, $a_{\mathrm{e}}A$ (Fig. 1b), would remove a total constituent mass:

$$M_{\text{out-ebb}}^{i}=C_{\mathrm{f}}^{i}\left(a_{\mathrm{e}}^{i}A\right)+M_{\text{in-ebb}}^{i}\frac{a_{\mathrm{e}}^{i}}{d_{\mathrm{f}}^{i}+a_{\mathrm{f}}^{i}} \tag{6}$$

where a_{e} is the range of the ebbing phase (in general $a_{\mathrm{e}}\neq a_{\mathrm{f}}$) and C_{f} is the concentration as given by Eq. (4). The first term on the right side is for the residing mass that exited during ebb tide and the second is for that portion of the mass loaded and departed during the same ebbing phase. Substituting Eqs. (3), (5), and (6), into Eq. (2), the new constituent mass at the end of the ebbing phase of the ith tidal cycle (beginning of the following flooding phase) can be calculated from:

$$M^{i+1}=M^{i}+\left\{nT_{\mathrm{f}}^{i}+M_{\text{entering}}^{i}\right\}+nT_{\mathrm{e}}^{i}-\left\{C_{\mathrm{f}}^{i}\left(a_{\mathrm{e}}^{i}A\right)+nT_{\mathrm{e}}^{i}\frac{a_{\mathrm{e}}^{i}}{\left(d_{\mathrm{f}}^{i}+a_{\mathrm{f}}^{i}\right)}\right\} \tag{7}$$

The average concentration at dip ebb would be:

$$C_{\mathrm{e}}^{i}=\frac{M^{i+1}}{\left(d_{\mathrm{f}}^{i}+a_{\mathrm{f}}^{i}-a_{\mathrm{e}}^{i}\right)A} \tag{8}$$

Eqs. (7) and (8) identify the net mass and water depth in the embayment at the end of the ith tidal cycle. These values also define the starting mass and depth for the succeeding $(i+1)$ tidal cycle when water depth is $d_{\mathrm{f}}^{i+1}=d_{\mathrm{f}}^{i}+a_{\mathrm{f}}^{i}-a_{\mathrm{e}}^{i}$ (see denominator of Eq. (8)). The calculation can be repeated for any number of successive tidal cycles until quasi-steady state concentrations are achieved. However, initial values have to be identified.

Mass entering the embayment through the open boundary, M_{entering} (Eq. (3)), consists of two main components, i.e.:

$$M_{\text{entering}}^{i}=M_{\text{returning}}^{i}+M_{\text{in-ambient}}^{i} \tag{9}$$

where $M_{\text{returning}}$ represents the mass that exited during the previous $(i-1)$ tidal cycle and returned during the ith cycle. The returning mass is calculated from the following equation:

$$M_{\text{returning}}^{i}=b^{i}M_{\text{out-ebb}}^{i-1} \tag{10}$$

where b is a factor (≤ 1) representing the fraction of water leaving during ebb and returning during the following flood (see below). In addition, ambient concentrations cause additional mass to enter the embayment through the open boundary as:

$$M_{\text{in-ambient}}^{i}=C_{o}\left(Aa_{\mathrm{f}}^{i}-bAa_{\mathrm{e}}^{i-1}\right) \tag{11}$$

Where $M_{\text{in-ambient}}$ represents ambient mass that entered the embayment and C_{o} ($\mathrm{kg\,m^{-3}}$) is concentration at the seaward side of the open boundary, away from the exiting plume. In Eq. (11), the term between the brackets is the net volume of the new ambient water that enters the embayment during the flooding phase. Eqs. (10) and (11) embed values from the previous $(i-1)$ tidal cycle needed to obtain the solution for the ith tidal cycle. The starting (initial) mass for the analysis is assumed to match ambient conditions outside the embayment with concentration C_{o} both in embayment water ($M^{i-1}=C_{\mathrm{o}}Ad_{\mathrm{f}}^{i-1}$) and in the entering water (i.e., $M_{\text{entering}}^{i-1}=C_{\mathrm{o}}Aa_{\mathrm{f}}^{i-1}$).

The return flow factor, b, depends on the relative conditions in the receiving water with respect to tidal phase, strength of the coastal flow, and degree of mixing (Sanford et al., 1993). A graphical relationship (Sanford et al., 1993 − their Fig. 5) was presented for b in terms of a parameter (denoted here by E^{i}) representing the intensity of lateral diffusion outside the embayment. This parameter is simplified here as:

$$E^{i}=\frac{\sqrt{0.05}(UHT)^{1.5}}{\pi P^{i-1}} \tag{12}$$

where U is amplitude of the coastal tidal current, H is the water depth in the coastal area outside the embayment (default value $H=d_{\mathrm{f}}^{i}$), T is the tidal period in the coastal area (default value $T=T_{\mathrm{f}}^{i}+T_{\mathrm{e}}^{i-1}$), and $P^{i-1}=Aa_{\mathrm{e}}^{i-1}$ is the tidal prism that left the embayment in the previous ebb. Validity of the presented relationship requires that flow and coastal currents covary (are in phase), and that the plume exiting the embayment hugs the coast, which are common to many embayments. This graphical relationship is approximated here by the three logarithmic equations (Fig. 2):

$$b^{i}=-0.1002\ln\left(E^{i}\right)+0.7451\left(r^{2}=0.8687\right)\quad 0.1\leq E^{i}<1 \tag{13a}$$

$$b^{i}=-0.3043\ln\left(E^{i}\right)+0.7345\left(r^{2}=0.987\right)\quad 1\leq E^{i}\leq 5 \tag{13b}$$

$$b^{i}=-0.072\ln\left(E^{i}\right)+0.3605\left(r^{2}=0.87\right)\quad 5<E^{i}\leq 100 \tag{13c}$$

where r^2 values are in reference to digitized estimates from the above-mentioned graphical relationship at 0.1 increments of b. The minimum return flow factor is set at 0.0289 when $E^{i}>100$, and the maximum value is fixed at 0.9758 when $E^{i}<0.1$. It is worth mentioning that both E and b can change with time.

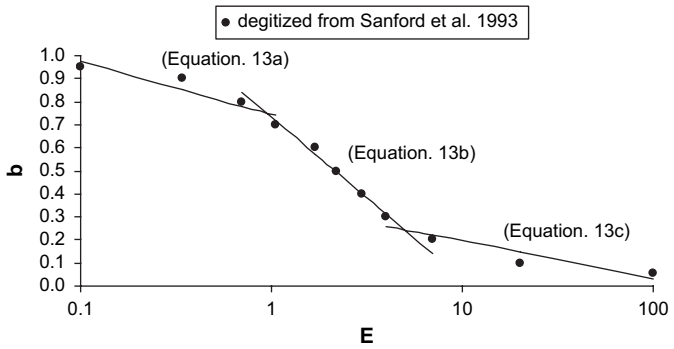

Fig. 2. Approximated relationships for the return flow factor, b, from simplification of the methods in Sanford et al. (1992) (their Fig. 5 is presented here by the dots). See text for details.

At this stage the simple model to calculate the transport time and concentration has been established. The spreadsheet (EXCEL) formulation for the above equations is presented in Table A (see Appendix).

3. Characteristic time and concentration

The above model was used to obtain temporal changes in concentration from the estimated yearly load of the constituent, N (kg y^{-1}), which can be calculated from watershed and land-use analysis of the watershed (e.g., for nitrogen, Valiela et al., 1997). A continuous load on a shorter time scale (e.g., tide cycle, day, or month) that defines variability on the scale of biological processing can be calculated after employing relevant and adequate assumptions. For example, knowing that each year has 8766 h, the average hourly load is $n = N/8766$ kg h^{-1}.

In theory, the constituent that enters the embayment in one tidal cycle will exit a few cycles later – based on the overall residence time of the embayment. Thus, continued loading at the same rate would result equilibrium concentration after a period of time. It is assumed that steady-state concentration is reached after a period of time when the relative change in concentration is less than some tolerance, i.e.:

$$\left|\frac{C_e^{i+1} - C_e^i}{C_{\text{equilibrium}} - C_{\text{initial}}}\right| \le \varepsilon \qquad (14)$$

where ε is a non-dimensional tolerance. While the numerator defines the change of concentration between two successive tide cycles, the denominator defines the total change in concentration between the starting value, C_{initial}, and the succeeding steady-state value, $C_{\text{equilibrium}}$. It is worth mentioning that as a result of the reduced dilution volume within the embayment during the ebbing phase, ebb concentrations (Eq. (8)) are always greater than flood concentrations (Eq. (4)). To be on the conservative side for a harmful contaminant, Eq. (14) and all the following analyses use ebb concentrations. (In the case of a useful nutrient, flood concentrations would be more conservative.) The tolerance, ε, can be defined from the vulnerability of the biological component of interest to the concentration (e.g., as in tapering of concentration from an instantaneous dump). In the following applications, it is assumed that the steady state for increasing or decreasing concentrations would be achieved when $\varepsilon \le 10^{-6}$. Some approaches, e.g., for the case of residence time with decreasing values, assume that the time scale is achieved when concentration (or mass) reaches a pre-specified ratio from its initial value, e.g., the e-folding value ($1/e = 0.37$), or 50% and 5% (Miller & McPherson, 1991).

Assuming an idealized embayment with physical parameters as presented in Table 1, a simple spreadsheet exercise was conducted (Appendix) to model tidal flushing. It was assumed that n and C_o are constant throughout the whole year (other time-varying scenarios are presented later). To obtain clear cause–effect relationships, the return flow factor, b, was fixed at 0.05. Effects of this parameter are presented later. Starting with ambient concentration ($C_o = 0.005$ kg m^{-3}) inside the embayment, curve AB in Fig. 3a presents the change in concentration due to an arbitrarily chosen annual load of $N = 10^8$ kg y^{-1} ($n = 11{,}408$ kg h^{-1}). Steady-state concentration of $\sim$0.0125 kg m^{-3} was reached after 47 tidal cycles. Termination of loading at any instant in time (e.g., cycle 100, point B in Fig. 3a) caused the concentration inside the embayment to recede (i.e., curve BC in Fig. 3a) to the ambient value, imposed by the concentration at the open boundary, in the same time period of 47 cycles. It is clear that, between the two limiting values 0.005 kg m^{-3} and 0.0125 kg m^{-3}, time periods to reach steady-state concentrations are the same for increasing or decreasing concentrations. Other tests indicated that for any instantaneous perturbation (increase or decrease in loading); the embayment needs the same time period (47 cycles) to reach a steady-state concentration. Changing the annual load, N, or the outside concentration, C_o, to other values did not affect this time period; it only affected the value of the equilibrium concentration inside the embayment. Replacing ebb concentrations in Eq. (14) with flood concentrations did not affect the value of CT. Indeed, this time period (47 tide cycle) defines the transport time scale for the idealized embayment (Table 1) and it is referred to as the "*Characteristic Time*" (CT) of the embayment.

Nonetheless, effects of the CT on the concentration may not be evident when temporal changes in loading happen faster than the CT of the embayment. For example, assuming that the load can change randomly between $\pm n$ in each tidal cycle, a temporal variation in concentration as depicted in Fig. 3b is obtained. Although the mean concentration has the same value (0.0125 kg m^{-3}) for the steady state in curve 1 (Fig. 3a), its

Table 1
Physical parameters for an idealized embayment

Parameter and unit	Value
Surface area, A (m^2)	10^7
Tidal ranges ($a_f = a_e$) (m)	2
Tidal phases ($T_f = T_e$) (h)	6.21
Ambient concentration at open boundary, C_o (kg m^{-3})	0.005
Water depth at start, d (m)	6
Annual load, N (kg y^{-1})	10^8
Return flow factor, b (for $U = 28.3$ m s^{-1})	0.05

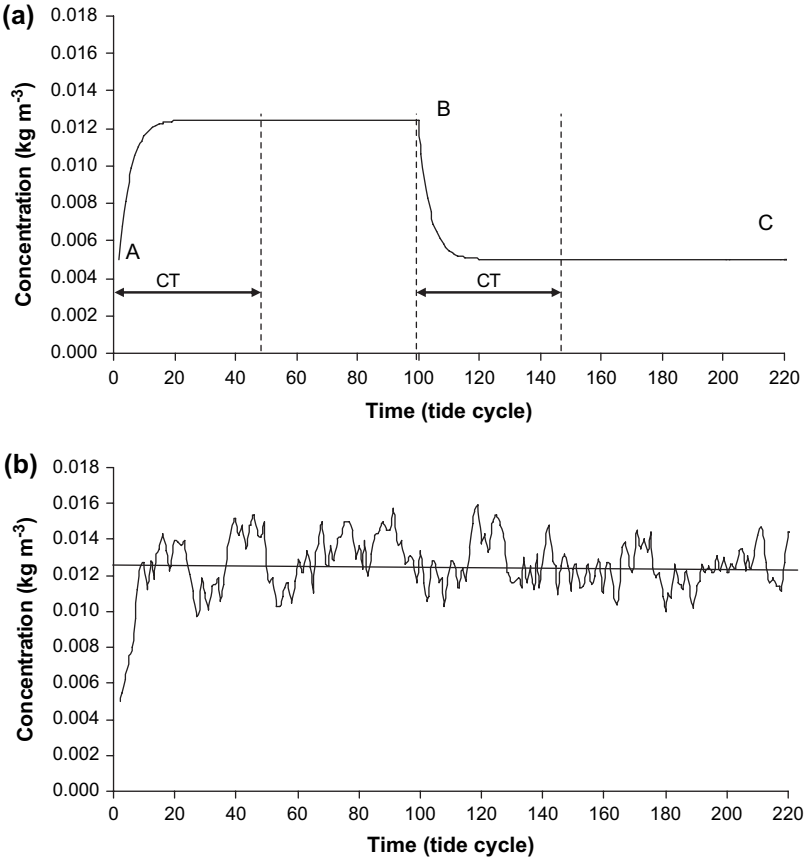

Fig. 3. Examples of temporal behavior of overall average concentration for the idealized embayment (Table 1): (a) concentration due to two loading scenarios: the curve from A to B representing loading from the watershed (10^8 kg y^{-1}) and the open boundary ($C_o = 0.005$ kg m^{-3}), and the curve from B to C following the cessation of watershed loading after 100 cycles; (b) effect of a random load from watershed (between 0 and $2n$, average $= n$) every tidal cycle. Note that any perturbation needs a CT (47 cycles) to reach steady state with relative change in concentration $\varepsilon < 10^{-6}$.

instantaneous values are different. Each single load that is delivered to the embayment in a tidal cycle would need to persist for at least a CT ($\sim$47 tidal cycles) to produce a steady-state concentration in the embayment, but the rapid change in loading from one cycle to the next does not accommodate this response. Thus, the CT may not be manifested explicitly in the concentration record, but it can shape the temporal behavior of concentration to some degree. Accordingly, it is hypothesized that not only CT, but also temporal changes in loading constitute governing factors for the concentration. This was also acknowledged by Pilson (1985) for residence times in Narragansett Bay.

Water depth and tidal range have direct effects on concentration because they define the dilution volume within the embayment. They also impact the embayment's CT. For the idealized embayment (Table 1) with tidal range $a_f = a_e = 2$ m, Fig. 4a indicates that CT has a one-to-one relationship with the water depth, d. This is expected because the larger the volume of the water body, the longer it would take to remove the constituent by tidal flushing. On the other hand, for the same embayment with water depth $d = 6$ m, CT shows an inverse power relationship with tidal range (assuming $a_f = a_e = a$) (Fig. 4b). This is also expected because as the volume of the tidal prism increases, more material would leave the embayment during ebbing tide, which leads to a shorter flushing time. Tidal range is used to produce various exposure scenarios in the idealized embayment.

4. Exposure

It is a well-established fact that organisms respond to the concentration of a constituent in their vicinity. Thus, it is essential to identify not only temporal changes in concentration of a specified constituent, but also a threshold concentration for vulnerability of a specified biological component. As commonly practiced (e.g., Thomann and Mueller, 1987– page 426), emphasis is placed on the role of constituent concentration and other factors (e.g., temperature, light, etc.) are abridged. Only the concentration threshold of the biological component is included here, other biological factors and effects are beyond the scope of this work.

Temporal variations in tidal forcing and loading during a year can cause a biological component to experience contrasting CTs within the same embayment. This is examined by utilizing the idealized example (but with $C_o = 0.0$ kg m^{-3}) to generate a suite of contrasting environments for a biological component with a hypothetical threshold concentration of 0.007 kg m^{-3}. The power relationship in Fig. 4b was used to generate 10 scenarios for CTs with values between 20 and

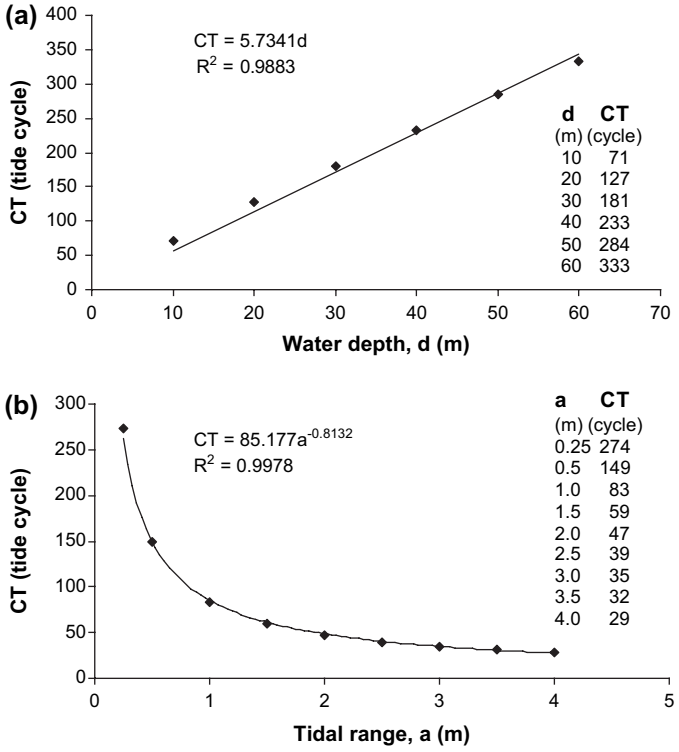

Fig. 4. Effect of embayment characteristics on CT for the idealized embayment (Table 1): (a) effect of mean water depth, and (b) effect of tidal range.

200 cycles (Table 2). The same total yearly load ($N = 10^8$ kg y^{-1}, Table 1) was used for each scenario; however, it was delivered to the embayment in increments with non-loading periods in between from 10 to 80 cycles (Table 3). A full year simulation of the overall concentration in the embayment with a known CT was generated for every loading scenario. The percent exposure was calculated from the number of cycles per year when concentration exceeded the threshold value divided by the total number of tidal cycles per year (i.e., 706 cycles, for semidiurnal tide).

The complex relationship between biology, loading, and CT is presented in a three-dimensional graph (Fig. 5). It should be emphasized that this graph represents a biological component with a known threshold concentration for vulnerability (0.007 kg m^{-3}). The four corner regions (A, B, C, and D) on the surface highlight this relationship. Region A marks long exposure times for the biological component when fast loading exists in an embayment with slow flushing. In contrast, slow loading in an embayment with fast flushing can cause short exposure (region C) for that biological component. When loading and flushing are both relatively fast, moderate-low exposure (region B) can occur. Also, when loading and flushing are both relatively slow, moderate-high exposure (region D) can take place. Notice that the quantitative values of exposure for these regions can be calculated for a specific embayment with known physical and tidal characteristics, loading behavior of a chemical of interest, and a biological component with known threshold of vulnerability to that chemical (see Section 7 for more comments). Exposure in real situations is presented below.

Two mechanisms can affect concentration and exposure: tidal variations and loading behavior. These mechanisms depend on the geographical location of the embayment and also on the time of the year. Fig. 6a presents tidal changes for the year 2005 in northeastern USA. It indicates that significant tidal variations can exist in tidal ranges and flood–ebb periods during spring–neap cycles. Fig. 6b presents temporal variations in concentration inside the idealized embayment when subjected to these tidal changes. It is clear that concentrations are lower during spring tides than neap tides. This is

Table 2
Selected CT values and the relevant tidal ranges in the idealized embayment

CT (tide cycle)	a[a] (m)
20	5.94
40	2.53
60	1.54
80	1.08
100	0.82
120	0.66
140	0.54
160	0.46
180	0.40
200	0.35

[a] $a_e = a_f = a$, calculated from the power relationship in Fig. 4b, $a = (85.177/\mathrm{CT})^{(1/0.8132)}$.

Table 3
Selected loading frequencies and relevant loading increment in the idealized embayment

Interval between loading events (tide cycle)	Loading increment[a] (kg)
10	123,905
20	236,878
30	350,167
40	447,436
50	575,275
60	671,154
70	805,384
80	894,872

[a] Total load $N = 10^8$ kg y^{-1} (Table 1).

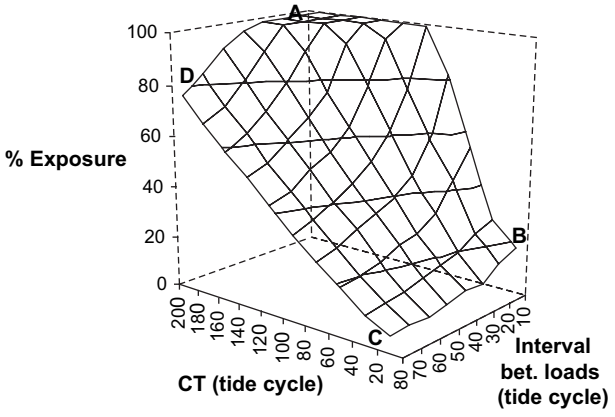

Fig. 5. Three-dimensional display of a typical relationship between CT, loading frequency, and percentage exposure throughout a full year for a biological species with a threshold limiting concentration of 0.007 kg m^{-3} in the idealized embayment (Table 1). A range of CTs was reproduced from changes in tidal ranges using the power relationship in Fig. 4b (Table 2).

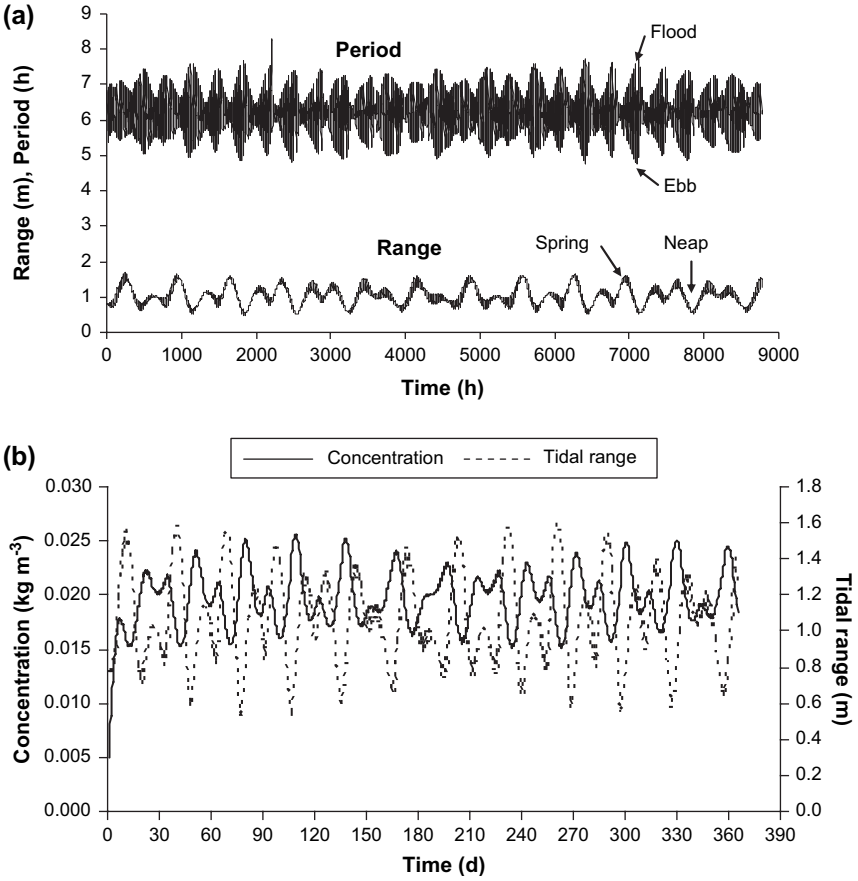

Fig. 6. Effect of tidal changes on concentration in the idealized embayment (Table 1): (a) spring–neap changes in tidal range and flood–ebb periods (using 2005 tide predictions at Newport, RI, USA from (http://tbone.biol.sc.edu/tide/tideshow.cgi), and (b) temporal changes in concentration; notice that concentration is a 180° out of phase with tidal range (To simplify the tidal trace, ranges of flooding phase are presented after smoothing with a 3-point moving average to suppress diurnal variations.). Units on time axis accommodate tidal variations.

expected due to the larger dilution volumes inside the embayment during spring tides.

Most embayments have time-varying loading. The main loading sources to an embayment are through atmospheric deposition, watershed delivery, open boundary exchange, and benthic release. To illustrate the role of CT, emphasis is put here on loading from the watershed and exchange through the open boundary of a conservative constituent. The main mechanism that delivers the constituent from the watershed to the embayment is precipitation, as manifested through surface or subsurface pathways of water. Although time lags may take place and losses may happen along these pathways, the temporal behavior of the overall delivery would be highly correlated with the temporal behavior of precipitation or riverine input. For example, Fig. 7 shows the average weights of typical variations in the daily flow rates of streams around Narragansett Bay, RI, USA. The annual load for the idealized embayment (10^8 kg y^{-1}, Table 1) was redistributed throughout the year according to these weights. Fig. 8a presents concentrations in the idealized embayment when subjected to this variable loading. Concentrations showed short-term variability and did not exhibit any plateaus with steady values (e.g., Fig. 3a). Moreover, including tidal variations (i.e., Fig. 6a) added more variability to concentration and caused low values

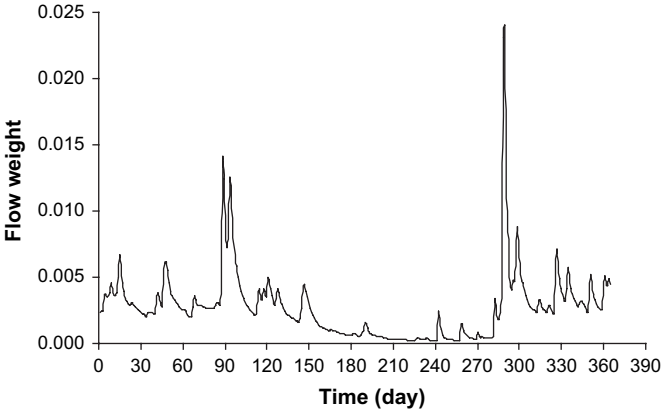

Fig. 7. Average weight of flow as a surrogate for daily loads from the watershed of Narragansett Bay, RI, USA, during 2005. The average weight is calculated from river flows of six rivers: Ten Mile River, Pawtucket River, Hunt River, Pawtuxet River, Blackstone River, and Wading River, USA; USGS stations #01109403, 01118500, 01117000, 01116500, 01112500, and 01109000, respectively, available from http://waterdata.usgs.gov/nwis/rt. Each river flow is normalized by the total yearly flow to produce an integrated value equal to one. The average of these normalized values represents the average weight of the flow.

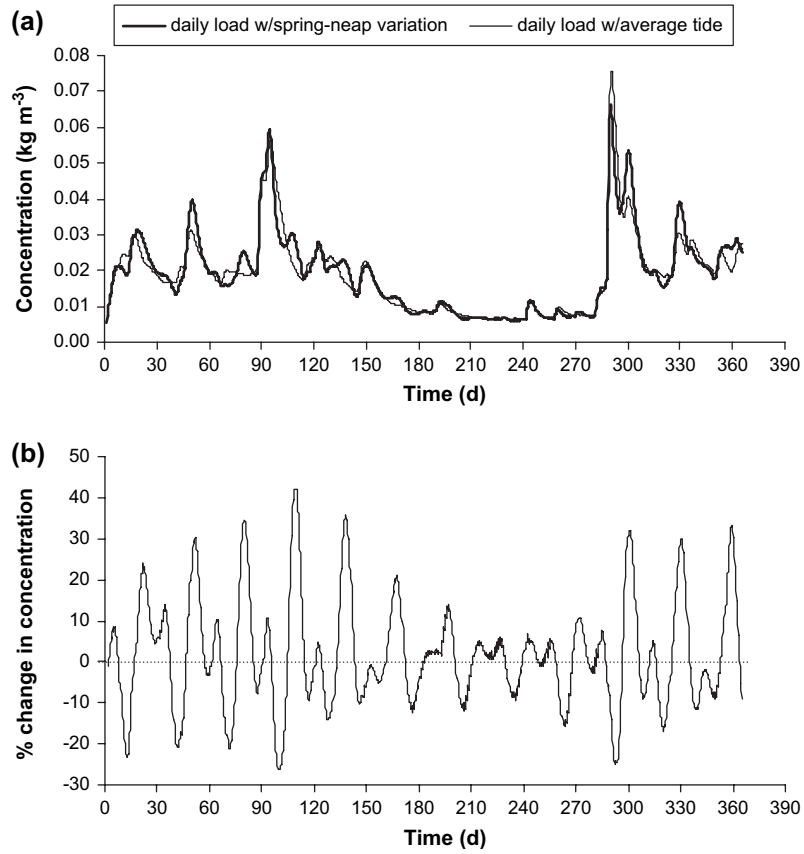

Fig. 8. Temporal variations of concentration in the idealized embayment: (a) daily loading (weighted by flow from Fig. 7) with average tide (thin line) and with spring–neap tidal variations from Fig. 6a (bold line); and (b) percent change in concentration due to spring–neap tidal variations. Units on time axis accommodate tidal variations.

to decrease by up to −20% and high values to increase by up to +40% (Fig. 8b).

5. Application

As a practical example, the above methodology was applied to 18 embayments on the northeastern coast of USA to simulate tidal flushing of nitrogen and calculate the exposure of phytoplankton to levels greater than those in the open sea. Based on field measurements in the open sea of this region concentration of nitrogen was 2.2×10^{-5} kg m^{-3} in surface water, which produced 0.001 kg dry weight phytoplankton m^{-3} (personal communications: John Kiddon, U.S. EPA, Atlantic Ecology Division, Narragansett, RI, USA). Thus, a threshold for nitrogen concentration was arbitrarily set at twice this value, i.e., 4.4×10^{-5} kg m^{-3}, which is expected to enhance phytoplankton concentration. As stated above, adverse biological effects and biomass calculations are beyond the scope of this work.

The 18 embayments are located within Narragansett Bay, RI, USA and they experience the same tidal forcing that is predicted at New Port, near the open entrance to the bay (Fig. 9). Tidal variations for 2005 (Fig. 6) were used in these applications. Yearly loads of nitrogen were obtained from watershed analysis for embayments in this region (Latimer et al., 2006). Variations in the daily loads were based on weights extracted from variations in the daily flow rates from nearby flow stations as shown in Fig. 7. Table 4 summarizes the physical parameters and yearly loads of total nitrogen for these embayments.

The predicted exposure of phytoplankton cells to concentrations of nitrogen above the specified threshold (4.4×10^{-5} kg m^{-3}) is presented in the last column of Table 4. Exposure values ranged from 0% to 97%. Closer examination of the results reveals interesting information. For example, although the three embayments Allen Harbor (# 25), Greenwich Bay (# 34) and Kickamuit River (# 36) are not in the same proximity (Fig. 9) and have very contrasting physical properties and loading values (Table 4), they all exhibit ∼30% to 40% exposure of phytoplankton to nitrogen levels above the specified threshold. Also, embayments with similar loads (e.g., Apponaug Cove (# 26) and Easton Bay (# 30) with ∼40,000 kg N y^{-1}) did not exhibit the same exposure values due to the contrast in physical properties (Table 4). The general relationship between N-loading and exposure in all 18 systems is presented in Fig. 10. It is clear that there is a logarithmic trend ($r^2 = 0.71$) between exposure and N-loading in this region. Similar relationship (not shown) existed when the threshold was three times that in the open sea (i.e., 6.6×10^{-5} kg m^{-3}). The validity of this relationship for other regions can be confirmed in future studies. Tide and precipitation (loading behavior) are the two main regional factors that can impact such relationship.

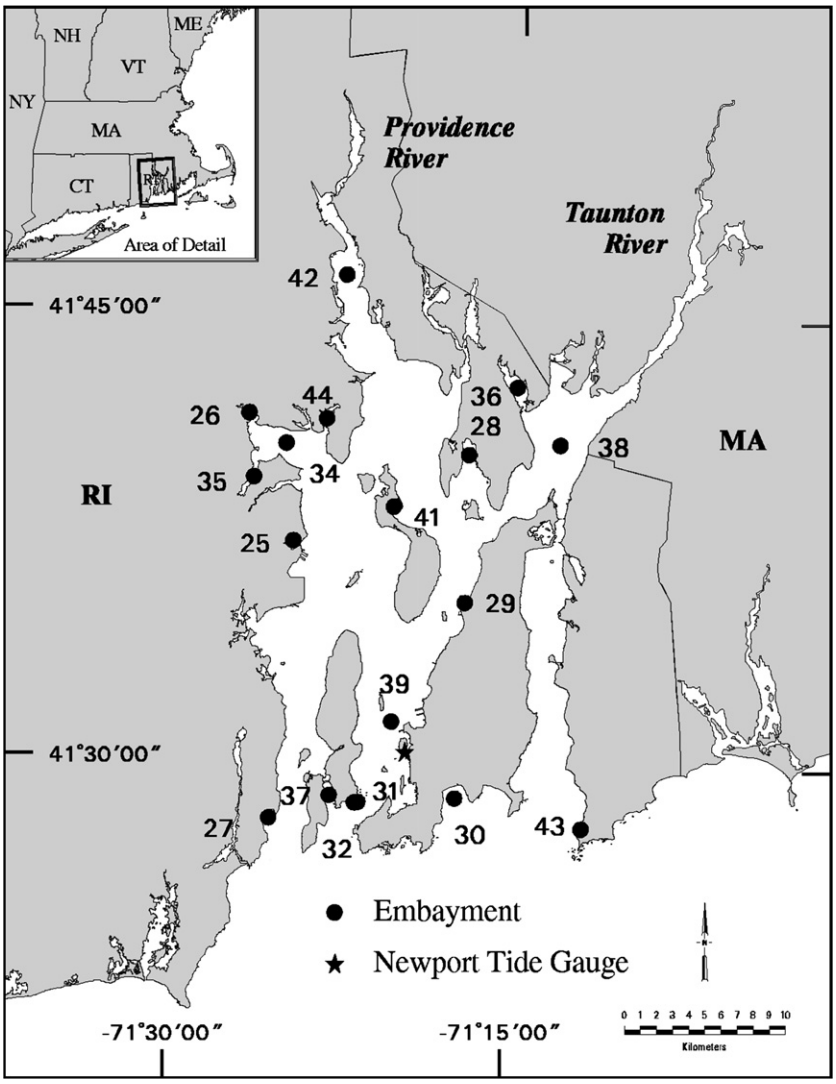

Fig. 9. Eighteen embayments located within Narragansett Bay, RI, USA. Embayment ID numbers are as set in previous studies (e.g., Abdelrhman, 2005; Latimer et al., 2006).

Table 4
Physical characteristics, N-loading, and exposure in 18 embayments in RI, USA

ID[a]	Embayment	Area (m^2)	Depth (m)	N-load ($kg\ y^{-1}$)	% Exposure
25	Allen Harbor	313,864	2.91	4209	38.10
26	Apponaug Cove	426,737	1.25	39,296	83.71
27	Bonnet Shores	688,090	4.54	7350	23.23
28	Bristol Harbor	2,062,489	4.10	102,643	72.24
29	Coggeshall Point Harbor	52,334	3.60	117	0.57
30	Easton Bay	2,002,794	4.06	42,152	58.92
31	Fort Wetherill Cove – West	17,865	7.75	38	0.0
32	Fort Wetherill Cove-East	24,396	7.05	106	1.56
34	Greenwich Bay	12,043,644	2.47	136,589	30.45
35	Greenwich Cove	751,782	1.81	23,942	68.41
36	Kickamuit River	2,236,940	1.96	28,538	34.70
37	Mackerel Cove	860,582	5.25	2471	0.71
38	Mount Hope Bay	51,046,904	4.63	1,276,085	64.59
39	Narragansett Bay	411,474,400	8.32	7,338,662	62.18
41	Potter Cove	399,095	2.09	988	0.99
42	Providence-Seekonk River	23,837,646	4.15	4,284,889	97.17
43	Sakonnet Harbor	98,448	2.06	345	1.70
44	Warwick Cove	564,639	1.46	11,579	56.23

[a] Embayment ID is based on previous studies (e.g., Latimer et al., 2006; Abdelrhman, 2005).

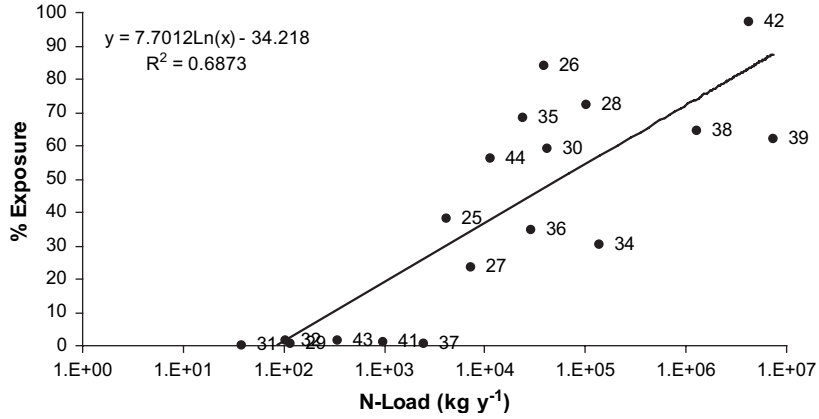

Fig. 10. Relationship between N-loading and exposure in 18 embayments in Narragansett Bay, RI, USA.

Concentrations of phytoplankton were measured in the vicinity of some of the above embayments (personal communication: Darryl Keith, U.S. EPA, Atlantic Ecology Division, Narragansett, RI) (Table 5). Visual comparisons between exposure and chlorophyll-*a* concentrations indicate that, in general, as exposure to nitrogen increases, phytoplankton concentration increases (Fig. 11). However, this may not always be the case because other factors (e.g., light, temperature) can affect phytoplankton growth and concentration. It is worth mentioning that although the presented systems are located within the inner (upper) region of Narragansett Bay, they have contrasting physical properties, N-loading magnitudes, exposure values, and phytoplankton concentrations. This is especially pronounced by the very low phytoplankton concentration and N-exposure in Potter Cove (# 41) compared to the other three embayments.

6. Return flow

In the above analysis and applications, the return flow factor (Eq. (10)) was limited to 5% to minimize its effect. When conditions are favorable in the receiving water, the return flow can have a major effect on concentration inside the embayment. As indicated by Eqs. (12) and (13), the returning mass varies with time. The main parameter that controls this returning mass is the amplitude of the coastal tidal current, U. As U decreases, lateral diffusion parameter, E (Eq. (12)), decreases and the return flow factor, b, increases (Fig. 2) causing more mass to return to the embayment. Fig. 12a shows the effect of this parameter on the total mass that enters from the open boundary.

Table 5
Concentration of chlorophyll-*a* (mg m^{-3}) from three surveys in the vicinity of four embayments (ID# 42, 28, 34, and 41) in Narragansett Bay, RI, USA; in 2005 on July 21, August 30, and October 31

ID	Location	Phytoplankton concentration (mg m^{-3}) on			% Exposure
		7/21/2005	8/30/2005	10/31/2005	
42	Providence River	18.65 ± 1.83	10.56 ± 0.78		97.17
28	Bristol Harbor		4.11 ± 0.72	1.34 ± 0.25	72.24
34	Greenwich Bay	12.5 ± 0.66	7.76 ± 1.26	1.25 ± 0.8	30.45
41	Potter Cove		3.24 ± 0.08	0.86 ± 0.33	0.99

This mass has two components (Eq. (9)): mass returning to the embayment and mass entering from the ambient water outside the embayment. Both masses level at high values of U; the former tapers off and the latter reaches the maximum ambient mass that can enter from the seaward boundary. For the idealized embayment, the maximum ambient mass that can enter is equal to ~40% of the load from the watershed. Nevertheless, when U decreases (e.g., to 1 m s^{-1}) the returning portion constitutes most of the entering mass. For the idealized embayment, returning mass is equivalent to approximately threefold the mass from the watershed. This added mass elevated concentration inside the embayment and lengthened its CT.

The effect of return flow on CT is presented in Fig. 12b for the idealized embayment. As the amplitude of the coastal current increases, CT decreases as in the shown power relationship ($r^2 = 0.8348$). This relationship is very sensitive to low values of U, when more of the exiting water returns to the embayment causing increase not only in CT, but also in concentration. Fig. 12c shows the impact of return flow on concentration: when $U = 3$ m s^{-1} instantaneous concentrations show up to 50% increase and when $U = 2$ ms^{-1} this increase reaches approximately 100%; but as U drops to 1 m s^{-1}, concentration values increase by up to 400%.

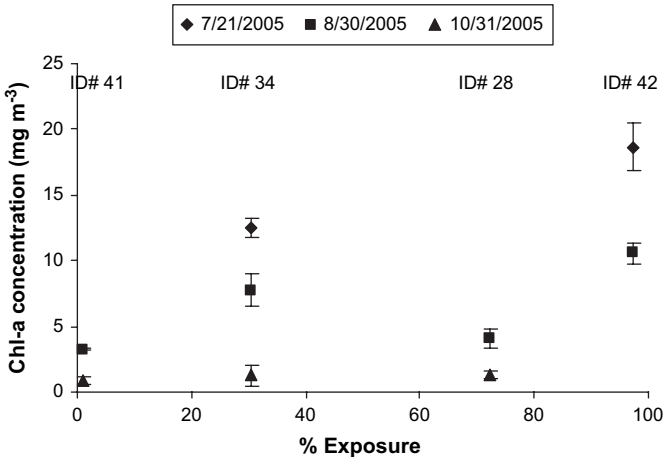

Fig. 11. Relation between calculated exposures and measured phytoplankton concentrations during various seasons in four embayments (ID# 41, 34, 28, and 42) in Narragansett Bay, RI, USA (Table 5).

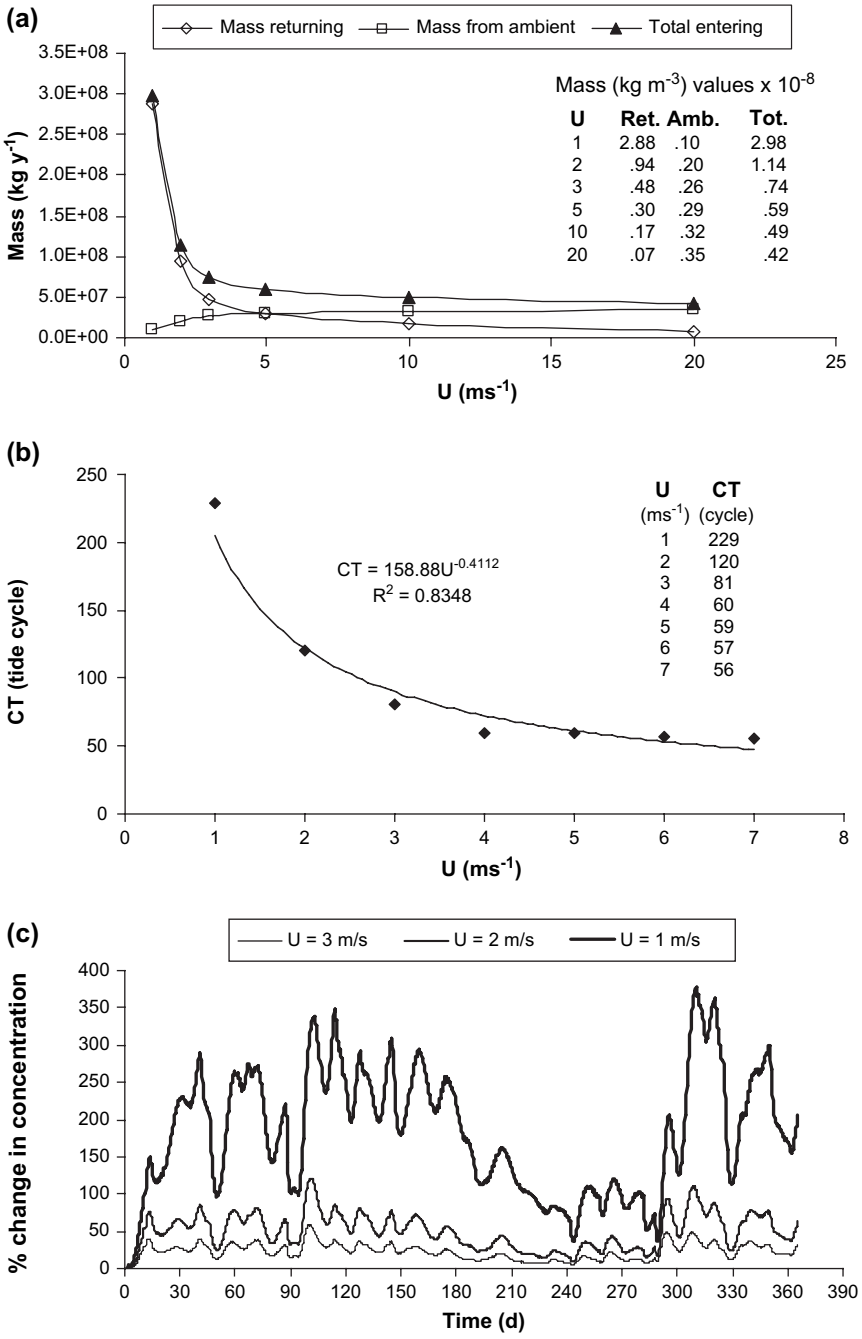

Fig. 12. Effect of U (a surrogate for return flow) on mass, CT, and concentration in the idealized embayment: (a) effect of U on returning and ambient mass entering the embayment, (b) relation between U and CT, (c) effect of U on percent change in concentration relative to the values with spring–neap tidal variations (Fig. 8a). Units on time axis accommodate tidal variations.

It should be emphasized that amplitudes of coastal currents experience spring–neap changes, and that neap periods (with lower currents and less lateral diffusion) are expected to cause higher concentration and longer CT inside the embayment. These currents act as a boundary forcing to the model and have to be estimated by the user.

7. Discussion

The presented methodology related the embayment's CT to biology as demonstrated in Fig. 5. The relationship was based on a concentration threshold that defined the vulnerability of the biological component to the constituent. The effect of CT on concentration was governed by the temporal resolution of the changes in loading (i.e., frequency and magnitude of loading events). In general, the temporal variability in tidal forcing, loading pattern, and return flow factor would prohibit the explicit manifestation of the effect of CT on concentration (e.g., Fig. 8). The regions of exposure in Fig. 5 are qualitatively defined to visually relate the general paradigm of biological exposure to physical parameters (tidal forcing, embayment characteristics, and loading behavior). For contrast,

only the four corners (A, B, C, and D) are discussed, but the shown surface is continuous and encompasses more than these corner values. The exact values for such regions will change according to the threshold concentration and the mentioned physical parameters. They can be identified by the researcher to serve the scientific inquiry at steak. (For example, a researcher may choose to define regions as: $0 < \text{low} \leq 10\%$, $10 < \text{medium-low} \leq 20\%$, $20\% < \text{medium-high} \leq 40\%$, and $\text{high} > 40\%$; or any other choices.) It is worth mentioning that a biological component with known threshold value in an embayment with known physical characteristics and loading behavior is presented by a spot (point, patch, or a strip) on the three-dimensional surface in Fig. 5. This paradigm of exposure is innovatively presented here to stimulate the imagination, but it is left to the researcher to decide the relevant exposure criteria and the position on this paradigm for the studied embayment.

To elucidate the relationship between biology and CT, emphasis was placed on exposure. Instantaneous concentrations, however, showed changes up to 40% (Fig. 8b) due to spring–neap variations, and exacerbation up to 400% due to return flow (Fig. 12b). Such high concentrations can cause traumatic effects on biology especially during sensitive seasons of reproduction and growth. With the help of the presented simple model, it is possible to identify such periods of elevated concentrations throughout the year for comparison with seasonal changes in the biological component of interest.

It should be emphasized that this approach uses approximations and assumptions (e.g., a well-mixed embayment) that can be less accurate than the more rigorous numerical approaches. For example, Abdelrhman (2006) related movement of water and its associated constituents to the ecological processes of a system using numerical methods and a relevant local time scale, referred to as "local effect time" (LET). The LETs were also based on concentration thresholds for biological components and were more appropriate and relevant to ecological components with limited or no mobility (e.g., sea grass or benthic organisms). LETs were used to quantitatively define areas susceptible to changes within an embayment.

The presented biological examples and physical settings are based on the general trends of biology, climate, and tides in the northeastern USA. Other regions can be treated similarly when these major regional factors are identified. Moreover, classification of embayments based on these regional physical factors can be enhanced by the presented simple model which provides quick and efficient means to calculate exposure in a large number of embayments. Although effects from other loading mechanisms (e.g., bottom sediment) and source/sink terms were beyond the scope of this work, they could be easily included into the developed model.

In summary, the connection between a physical transport time scale and ecological effects was investigated. As biology relates to concentration, the "characteristic time" (CT) was identified as the appropriate transport time scale for an embayment. However, natural changes in tidal forcing, constituent loading, and return flow seldom allow this time scale to manifest explicitly; instead, a complex relationship exists (Fig. 5). Although it is usually hypothesized that embayments with shorter transport times would exhibit better water quality than those with longer times, Fig. 5 demonstrates that this is not always true because loading behavior is a governing factor in this relationship. Thus, caution should be exercised when these time scales are offered as indicators of the well being of ecology.

Acknowledgments

The author thanks the reviewers of this manuscript, including Drs. Wayne Munns, Dan Campbell, William Nelson (USEPA-AED), and two anonymous reviewers for their technical reviews, insights, and constructive comments. Although the research described here has been funded by the U.S. Environmental Protection Agency, it has not been subject to Agency-level review and therefore does not necessarily reflect the views of the Agency, nor does mentioning trade names or commercial products endorse or recommend them. This manuscript is contribution no. AED-06-067 of USEPA Office Research and Development, National Health and Environmental Effects Research Laboratory, Atlantic Ecology Division.

Appendix. Model (RAHMAN-TP1)

This Appendix describes a simple spreadsheet (EXCEL) model (see Table A) that can be established by any user with very elementary knowledge.

The model occupies 26 columns (A–Z) and extends for a number of rows equal to the simulated number of full tidal cycles (e.g., 706 for a full year of semidiurnal tide). The first row is reserved for the column title; it is taken as row #10 in the spreadsheet. The second row (#11) is for the initial conditions of the simulation in the first tidal cycle. The third row (#12) contains the full formulation for the model and can be dragged downward to as many rows as needed to cover the time period of the simulation (in tidal cycles).

The following seven cells at the top of column B contain the main model parameters that have to be provided by the user (see values in Table 1 for the idealized embayment):

B1 = threshold concentration for biological vulnerability;
B2 = amplitude of coastal current, U ($\mathrm{m\,s^{-1}}$) (default = $100\ \mathrm{m\,s^{-1}}$ for minimum $b = 2.89\%$);
B3 = embayment surface area, A ($\mathrm{m^2}$);
B4 = concentration in the outside water, C_o ($\mathrm{kg\,m^{-3}}$), (default = $0.0\ \mathrm{kg\,m^{-3}}$);
B5 = starting water depth, d (m) (default = mean depth at mean low water level);
B6 = constituent load per year, N ($\mathrm{kg\,y^{-1}}$);
B7 = tolerance value for steady-state condition, ε, (default = 10^{-6}).

The first five columns (A–E) contain tidal information that has to be provided by the user, available from http://tbone.biol.sc.edu/tide/tideshow.cgi by entering the station name

(e.g., Newport, RI, USA) and requesting a tabular list of the predicted tidal highs and lows during a specified simulation period. Columns including date, time, and height (above MLLW) will be generated and can be copied to EXCEL spreadsheet. Flood and ebb periods and tidal ranges can be calculated by simple subtraction of successive values, using consistent and proper units for time and height.

Column J includes weights of loading from the watershed, which should also be provided by the user for each tidal cycle (i.e., each row) as hourly values (for example, the hourly weight for a yearly load that is distributed uniformly is $1/8760\ h^{-1}$). The sum of weights in the year should equal one. Multiplying this weight by the yearly load (e.g., $N = 10^8\ kg\ y^{-1}$) gives the loading rate (in our example: loading rate $= (1/8766) \times 10^8 = 11{,}408\ kg\ h^{-1}$). Multiplying the loading rate in a specific day by the flood and ebb periods (h) in that day (see column Z) and summing throughout the whole year (e.g., 706 cycles) should be equal to the specified annual load ($N\ kg\ y^{-1}$). A small margin of error (usually $<1\%$) can exist due to synchronization of hourly and daily loads with the variable tide periods and using the end of each tidal cycle as a pointer to the daily weight.

Columns AA and AB are not part of the model, but they provide lookup information to calculate watershed loads from daily records of annual riverine flow through the full simulation period (e.g., one year, 365 days): column AA has the ID# for the Julian day (i.e., 1–365) and column AB has the loading weight per hour. The LOOKUP command to include this information in the model is in column J with the range of data exactly matching that in columns AA and BB. Surface water flow can be obtained from http://waterdata.usgs.gov/nwis/rt) by choosing the data category as real-time for the

Table A
Model description, structure, and spreadsheet (EXCEL) formulation

Col.	Title (row 10)	Description	Initial values[c] (row 11)	Other/predicted values [a, c] (row 12 and higher)
A	Tidal cycle	Counter of cycles	1	=A11 + 1
B	T_f (h)	Flood period	[Provide][f]	[Provide]
C	a_f (m)	Flood range	[Provide]	[Provide]
D	T_e (h)	Ebb period	[Provide]	[Provide]
E	a_e (m)	Ebb range	[Provide]	[Provide]
F	d (m)	Water depth	=B5	=F11 + C11 − E11
G	Time (h)	Time in h from start	=B11 + D11	=B12 + D12 + G11
H	Time (days)	Time in days from start	=G11/24	Same[b]
I	Day ID#	ID# for Julian day	=ROUND(H11,0)	Same
J	Selected WT (h^{-1})	Loading weight in an hour	=LOOKUP(I11,AA$11:AA$375,AB$11:AB$375)[d]	Same
K	$M_{in\text{-}flood}$ (kg)	Mass in during flood	=R11	=X12 * B12 + R12
L	$M_{in\text{-}ebb}$ (kg)	Mass in during ebb	[Leave L11 blank]	=X12 * D12
M	$M_{out\text{-}ebb}$ (kg)	Mass out during ebb	[Leave M11 blank]	=S12 * E12 * B$3 + L12 × E12 / (F12 + C12)
N	E	Diffusion parameter	[Leave N11 blank]	=(SQRT(0.05) * B$2^1.5 * ((B12 + D11) * 60 * 60)^1.5 * F12^1.5)/ (3.141592654 * B$3 * E11)
O	b	Return flow factor	[Leave O11 blank]	=IF(N12>100,0.0289,IF(N12 > 5,−0.072 * LN(N12) + 0.3605,IF(N12 > 1,−0.3043 * LN(N12) + 0.7345,IF(N12 > 0.1,−0.1002 * LN(N12) + 0.7451,IF(N12 < 0.1,0.9758)))))
P	$M_{returning}$ (kg)	Returning mass	[Leave P11 blank]	=O12 * M11
Q	$M_{in\text{-}ambient}$ (kg)	Mass in from ambient	[Leave Q11 blank]	=B$4 * (B$3 * C12 − O12 * B$3 * E11)
R	$M_{entering}$ (kg)	Mass entering mouth	=B$4 * B$3 * C11	=P12 + Q12
S	C_f ($kg\ m^{-3}$)	Concentration at peak flood	[Leave S11 blank]	=(W11 + K12) / (B$3 * (F12 + C12))
T	C_e ($kg\ m^{-3}$)	Concentration at dip ebb	[Leave T11 blank]	=W12/(B$3 * (F12 + C12−E12))
U	CT_{flood} (cycle)	CT from flood concentration	[Leave U11 & U12 blank]	=IF(ABS(S13 − S12)/ABS(S13 − S$12)<B$7,A12,0)
V	CT_{ebb} (cycle)	CT from ebb concentration	[Leave V11 & V12 blank]	=IF(ABS(T13 − T12)/ABS(T13 − T$12)<B$7,A12,0)
W	M (kg)	Total mass inside	=B$4 * B$3 * F11	=W11 + K11 + L11 − M11
X	Load rate ($kg\ h^{-1}$)	Load per hour in a day	=B$6 * J11	Same
Y	Exposure	=1, if C_e > Threshold; otherwise = 0	=IF(T11 > B$1,1,0)	Same
Z	Cycle load (kg)	Load per cycle	=X11 * (B11 + D11)	Same
AA	Julian day	Day ID#	1	=AA11 + 1
AB	Load weight	Weight per hour in a day[e]	[Provide]	[Provide]

[a] Formulations in columns Q and R start from row #13 instead of row #12.
[b] "Same" means formulation as in row 11 (i.e., drag cell 11 through higher rows).
[c] [ ] Include special instructions to user.
[d] Range for LOOKUP command has to match that for columns AA and AB.
[e] Weights added through the year (365 days) and multiplied by 24 (h/d) should equal one.
[f] Provide values (see values in Table 1 for the idealized embayment).

geographic location (e.g., Rhode Island) and highlighting the USGS station(s) of interest on the map (e.g., Pawtuxet River, #01116500, or other stations) with the option of time series for daily data to be provided in separated table during the specified period (e.g., 01/01/2005 to 31/12/2005). This data can be copied to the spreadsheet and loading weights calculated by dividing each daily value by the total value for the whole period. These daily weights have to be further divided by 24 h/days to obtain the required hourly weights.

If data are available, loading rate from bottom sediment can be treated in a similar fashion and added to that from the watershed. Also, time-varying values for U and C_o can be accommodated with slight modifications to the model.

Model output includes the time trace (by tidal cycle) of the embayment average concentration during peak flood and dip ebb (C_f and C_e) in columns S and T, respectively. The characteristic time, CT, is meaningful only for simulations with steady loading during a uniform (sinusoidal) tide, otherwise it should be ignored. CT is marked by the *first non-zero value in columns U and V* for flood and ebb concentrations, respectively. Other values in these two columns are irrelevant and should be ignored. Exposure is calculated by dividing the number of tidal cycles when concentrations are above the threshold value (marked by 1 in column Y) by the total number of simulated tidal cycles (e.g., 706). The relation between any combination of the various types of mass in the embayment can be inspected by comparing columns K, L, M, P, Q, R, and W for mass from watershed during flood, mass from watershed during ebb, total exiting mass during ebb, reentering mass during ebb, ambient mass entering from outside during ebb, total mass entering from mouth during ebb, and total mass in the embayment at the end of the tide cycle, respectively. Temporal variation in the return flow factor, b, can be found in column O.

References

Abdelrhman, M.A., 2005. Simplified modeling of flushing and residence times in 42 embayments in New England, USA, with special attention to Greenwich Bay, Rhode Island. Estuarine, Coastal and Shelf Science 62 (1–2), 339–351.

Abdelrhman, M.A., 2006. A method to incorporate ecology into residence time: local effect time (LET). Journal of Integrated Environmental Assessment and Management 2 (3), 247–252.

Bolin, B., Rodhe, H., 1973. A note on the concept of age distribution and transit time in natural reservoirs. Tellus XXV (1), 58–62.

Latimer, J.S., Rego, S., Cicchetti, G., Dettmann, E.H., McKenney, R., Charpentier, M., 2006. The Relationship Between Land-based Loading and Eelgrass Extent for Embayments in Southern New England: Initial Model Construction and Application to Effects-Based Criteria Development for Estuaries. Report No. AED-05–107. USEPA/ORD/NHEERL/Atlantic Ecology Division, Narragansett, RI.

Luketina, D., 1998. Simple tidal prism models revisited. Estuarine, Coastal and Shelf Science 46, 77–84.

Miller, R.L., McPherson, B.F., 1991. Estimating estuarine flushing and residence times in Charlot Harbor, Florida, via salt balance and a box model. Limnology and Oceanography 36 (3), 602–612.

Monsen, N.E., Cloern, J.E., Lucas, V., 2002. A comment on the use of flushing time, residence time, and age as transport time scales. Limnology and Oceanography 47 (5), 1545–1553.

Pilson, M.E.Q., 1985. On the residence time of water in Narragansett Bay. Estuaries 8, 2–14.

Sanford, L.P., Biocourt, W.C., Rives, S.R., 1992. Model for estimating tidal flushing of small embayments. ASCE Journal of Waterway, Port, Coastal and Ocean Engineering 118 (6), 635–655.

Takeoka, H., 1984. Fundamental concepts of exchange and transport time scales in a coastal sea. Continental Shelf Research 3 (3), 311–326.

Thomann, R.V., Mueller, J.A., 1987. Principles of Surface Water Quality Modeling and Control. Harper Collins Publishers, New York, NY, 644 pp.

Valiela, I., Collins, G., Kremer, J., Lajtha, K., Geist, M., Seely, B., et al., 1997. Nitrogen loading from coastal watersheds to receiving estuaries: new method and application. Ecological Applications 7 (2), 358–380.

Zimmerman, J.T.F., 1976. Mixing and flushing of tidal embayments in the western Dutch Wadden Sea part I: distribution of salinity and calculation of mixing time scales. Netherlands Journal of Sea Research 10 (2), 149–191.

Available online at www.sciencedirect.com
ScienceDirect
Estuarine, Coastal and Shelf Science 74 (2007) 756–765
ESTUARINE COASTAL AND SHELF SCIENCE
www.elsevier.com/locate/ecss

Geochemical and hydrodynamic constraints on the distribution of trace metal concentrations in the lagoon of Nouméa, New Caledonia

Christophe Migon [a,*], Sylvain Ouillon [b], Xavier Mari [b], Emmanuel Nicolas [a]

[a] *UMR 7093 (CNRS-UPMC), Observatoire d'Océanologie de Villefranche (OOV), Laboratoire d'Océanographie de Villefranche (LOV), La Darse, BP 8, 06238 Villefranche-sur-Mer Cedex, France*
[b] *UR 103 (IRD), Centre IRD de Nouméa, BP A5, 98848 Nouméa Cedex, New Caledonia*

Received 10 April 2006; accepted 9 May 2007
Available online 3 August 2007

Abstract

Seawater samples were collected in the lagoon of Nouméa (southwest New Caledonia) along two transects from eutrophic coastal bays to the oligotrophic barrier reef. Land-based emissions to the lagoon were measured with dissolved and particulate concentrations of chromium (Cr) and nickel (Ni), used as tracers of both terrigenous and industrial (Ni ore treatment) activities, as well as dissolved and particulate concentrations of zinc (Zn), used as a tracer of urban effluents. The spatial variability of metal concentrations was related to geochemical and hydrodynamic conditions, i.e., respectively: (1) natural and anthropogenic emission sources, and chemical processes occurring in the water column; and (2) water residence times. The parameter used to describe the residence time of water masses was the local e-flushing time, i.e. the time required for a tracer mass contained within a given station to be reduced by a factor $1/e$. High metal concentrations were found in coastal areas (up to 9000 ng dissolved Ni L^{-1}), and steeply decreased with distance from the coast (down to 101 ng dissolved Ni L^{-1} near the barrier reef) to reach levels similar to those found in remote Pacific waters, suggesting a rapid renewal of waters close to the barrier. Distributions of metals in the lagoon are controlled upstream by land-based emission sources and later chemical processes. Then hydrodynamics constrain metal distributions, as shown by the observed relationship between local e-flushing times and the spatial variability of metal concentrations. In addition, a change in the direction of prevailing winds yielded a decrease of dissolved metal concentrations at the same site by a factor of 2.5 (Cr and Ni) and 2.9 (Zn). It is suggested that the residence time is a key parameter in the control of elemental concentrations in the lagoon waters, as much as land-based emission sources.

Keywords: trace metals; geochemistry; hydrodynamics; residence time; coastal waters; New Caledonia

1. Introduction

Soils in southern New Caledonia are developed on ultramafic rocks (peridotites) that degrade into residues (laterite and saprolite layers) highly enriched by weathering in nickel (Ni) and chromium (Cr), either adsorbed onto iron oxides or incorporated into their mineral lattice (Becquer et al., 2001; Quantin et al., 2002). These enriched layers are subjected to intense mining extraction and strong soil erosion due to tropical rainfall. The combination of these processes results in the potential mobilisation of high amounts of terrigenous fine particles, likely to affect coastal waters by aeolian and river transports.

Consequently, coastal waters are presumably enriched in trace metals, mainly cobalt, iron, Ni and Cr (Bustamante et al., 2003), which may affect the coral reef food webs (Monniot et al., 1994). The release of dissolved metals from land-based emission sources may be a significant process for coastal waters in the lagoon, particularly for the case of Ni, owing to the mineral input from New Caledonian soils (Ambatsian et al., 1997; Fernandez et al., 2006). In addition, coastal areas are subjected to anthropogenic influences in the vicinity of

* Corresponding author.
E-mail address: migon@obs-vlfr.fr (C. Migon).

0272-7714/$ - see front matter © 2007 Elsevier Ltd. All rights reserved.
doi:10.1016/j.ecss.2007.05.048

the city of Nouméa: industrial activities, chiefly linked to the treatment of lateritic and saprolitic Ni ores (Doniambo factory, Nouméa), are superimposed upon wastewater and urban effluents.

Because Ni mining plays a significant and increasing economic role in New Caledonia, a scientific program has been devoted since 1996 to the impact of its anthropogenic and terrigenous loads on the 2000 km^2 southwest lagoon around Nouméa, where about half of the island population lives. Several researches have been conducted on the functioning of this lagoon, including hydrodynamics and suspended matter transport modelling (Douillet et al., 2001; Ouillon et al., 2004), biogeochemical cycling modelling (Pinazo et al., 2004), hydrological variability (Ouillon et al., 2005) and geochemical analysis of the sediment (Fernandez et al., 2006). Global and local residence times of water masses were also calculated for the lagoon so as to bring additional tools in the analysis of its biological functioning (Jouon et al., 2006; Mari et al., 2007; Torréton et al., 2007).

In that context, this paper presents a complementary study devoted to the measurements of metal concentrations in the water column from the coast to the barrier reef and to their analysis against the magnitude of the incoming metal inputs and the physical forcing of the water circulation (wind, tide, residence time).

2. Study area

2.1. Characteristics of the lagoon

The lagoon of New Caledonia, located 1500 km east of Australia, covers a total area of 23,400 km^2 (Fig. 1). The New Caledonia Reef is the second widest tropical reef system in the world after the Australian Great Barrier Reef. The southwest lagoon of New Caledonia, around Nouméa, is a nearly enclosed, relatively shallow site (on average 17.5 m deep), surrounded by oligotrophic oceanic water and connected to the ocean by narrow passes through the reef.

Two major factors control circulation in the southwest lagoon of New Caledonia: tide and wind (Douillet, 1998). The most frequently encountered wind regime is the southeasterly trade wind (average speed 8 m s^{-1}, direction 110°, more than 2/3 of the yearly wind occurrence). A description of the resulting current regime is given in Douillet et al. (2001). Under trade wind forcing, swell penetration into the lagoon is negligible, and wind–wave growth is limited by a fetch of a few tens of kilometres.

2.2. Adjacent land use

The near-shore environment is subjected to terrestrial inputs and, especially in the bays around the city of Nouméa, to both industrial and urban inputs that increase general productivity in these areas. Industrial emission sources (treatment of Ni ores) are likely to introduce Cr and Ni in the lagoon waters. Urban emission sources presumably give off amounts of zinc (Zn), which is an ubiquitous urban tracer (Migon, 2005).

Grande Rade (from station D01) is overall characterised by urban and industrial activities (Doniambo factory). Sainte-Marie Bay (from station N04) is mostly affected by wastewater and urban effluents, but not under the influence of industrial inputs (Mari et al., 2007). Its main terrigenous Cr and Ni incoming fluxes are due to the Coulée River loads, owing to Cr and Ni ore deposits comprised in its watershed (Fernandez et al., 2006).

3. Methods

3.1. Sampling

Seawater samples (2.5 L) were collected using a Teflon pump along two transects from the coast to the barrier reef in the southwest lagoon of New Caledonia (Fig. 1). Samples were collected at 5 m depth at six stations, along the two transects, during two sampling campaigns: 22 November 2004 (D01, D08, D22, M05, M10 and M41, from Grande Rade to the outer edge of the coral reef) and 29 November 2004 (N04, N12, N33, M33, M10 and M41, from Sainte-Marie Bay to the outer edge of the coral reef). Eutrophication in the bay of Grande Rade is mainly of industrial origin, due to the close proximity of a large Ni smelt, while in the bay of Sainte-Marie, eutrophication is mostly due to wastewater outfalls from the Sainte-Marie area (i.e., urban origin). Conductivity, Temperature and Depth (CTD) profiles were recorded using a SeaBird SBE 19 probe at each sampling station.

Hydrological and chemical characteristics during the two sampling campaigns are summarised in Table 1.

3.2. Metal analysis

Seawater samples were filtered on cellulose acetate membranes (Sartorius 11107-025 N, diameter 25 mm, porosity 0.2 μm). Dissolved and particulate concentrations of Cr, Ni and Zn were measured. Exchangeable metallic forms in the dissolved phase were fixed on Chelex (Bio-Rad) resins in mini-chromatographic columns (Bio-Rad). The chemical forms fixed on the resin were eluted with 10 mL HNO_3 2.5 M and stored in Teflon PFA bottles. The quality of the exchange on the resin was checked with 10 mL more of the same acidic solution (resin blank). Dissolved samples were UV-irradiated according to the protocol proposed by Sander and Koschinsky (2000) to turn all Cr in its oxidised from Cr(VI): 50 μL H_2O_2 and 20 μL HCl were added to 10 mL of sample to increase the oxidation potential prior to the irradiation. The irradiation was carried out during 1 h at 85 °C using a 707 UV-Digester (Metrohm). This procedure guaranteed that all H_2O_2, likely to interfere with the voltammetric analysis of Cr, was removed. The particulate phase was mineralised as follows: the organic matrix was destroyed with an oxidizing attack (HNO_3), and mineral aluminosilicate matrixes were destroyed with HF. The sample was freeze-dried in 7 mL Teflon flasks, used for the mineralisation. The mineralisation protocol was:

(1) Nine hundred microlitres HNO_3 65% were added to each flask. These flasks were sealed and put into larger Teflon

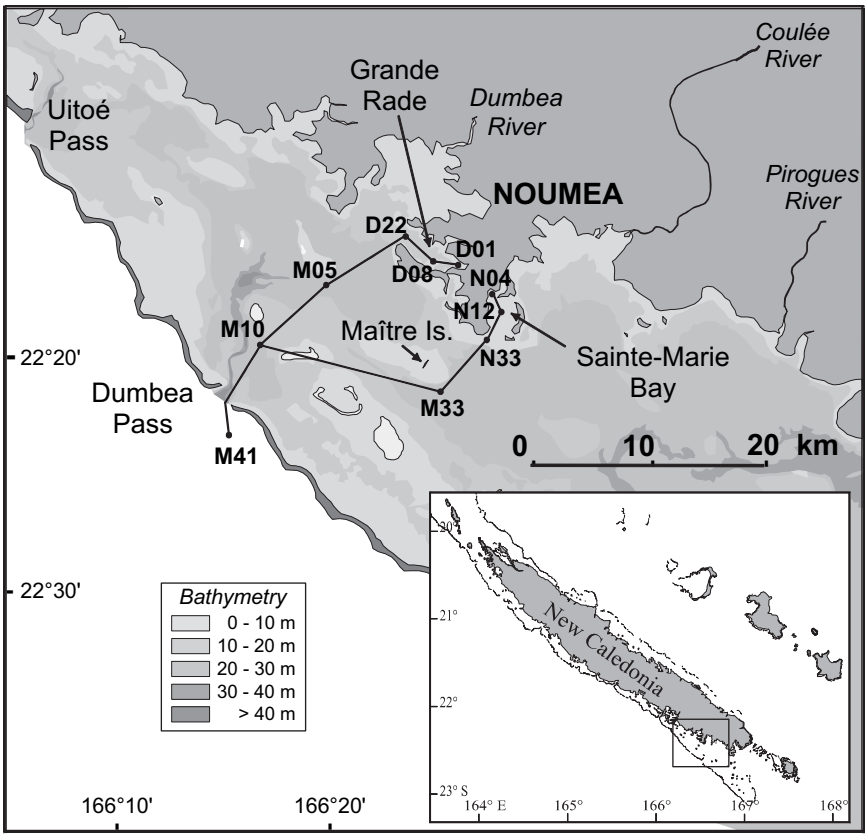

Fig. 1. Sampling stations in the southwest lagoon of New Caledonia.

bottles (60 ml) that act as expansion cells, overcome acidic evaporation by leaks and help to prevent contamination. This apparatus was left 2–3 h in an oven at 60 °C, and then 3–4 h at 150 °C, after which bottles and flasks were brought to room temperature and left open under laminar flow hood until a black dry residue remained.

(2) Two hundred microlitres HNO_3 65% and 200 μL HF 40% were added to the remainder. The flasks and bottles were closed and put in an oven 2–3 h at 60 °C, and then 3–4 h at 150 °C, prior to open evaporation at room temperature under laminar flow hood, until a white dry residue was obtained. This residue was ultrasonically dissolved in 1 mL HNO_3 1 N. The samples were then made up with Milli-Q water (resistivity: 18 MΩ cm) to 10 mL.

It was assumed that Cr(III) in particulate samples was oxidised during the mineralisation procedure, due to the use of HNO_3. Blanks for voltammetric analysis were irradiated following the same protocol. Zn samples were analysed by differential pulse anodic stripping voltammetry with a hanging mercury drop electrode. The instrumental sensitivity (i.e., smallest legible signal, arbitrarily evaluated to 1 mm) was 20 ng L^{-1}, using a standard electrolysis time of 5 min. Nickel was analysed by adsorptive cathodic stripping voltammetry. Nickel measurements were performed by adding a complexing agent (dimethylglyoxime 5×10^{-4} M) and buffering at pH 9.16. The limit of detection was 3 ng L^{-1}, with a standard electrolysis time of 5 min. This analytical technique has been described in detail by Van den Berg (1986). Chromium was analysed by adsorptive cathodic stripping voltammetry. Chromium measurements were performed by adding a complexing agent (diethylenetriaminepentaacetic acid 0.015 M) and buffering at pH 5.2. This analytical technique has been described in detail by Sander and Koschinsky (2000).

For each metal, three standard additions were used to determine the metal concentrations. Measurements were performed with an EG&G Princeton Applied Research 264A polarographic analyser in conjunction with a 303A static Hg drop electrode. A medium Hg drop electrode was used as the working electrode (1.6 mm^2 surface area). The auxiliary electrode was a Pt wire and the Ag/AgCl reference electrode was filled with a saturated solution of ultrapure KCl. The analytical procedure was checked using open ocean seawater reference material (NASS-4) provided by the National Research Council, Canada. The results were within the quoted standard deviation intervals. Reagent/manipulation blanks were always under the detection limits. Measurement reproducibility was always <5%. The preparatory manipulations of samples and voltammetric measurements were carried out in Class 100 laminar airflow benches located in a clean room. All reagents were provided by Merck (Darmstadt, Germany), quality Suprapur.

3.3. Dynamical and meteorological parameters

In order to gain understanding of the interaction between hydrodynamics and geochemistry, one must first identify the

Table 1
Hydrological and chemical characteristics during the two sampling campaigns. Local e-flushing times (LeFT) are given by Jouon et al. (2006)

Date	Stations	Temperature (°C)	Salinity	Tide regime	Wind speed ($m\,s^{-1}$)	Wind direction (Degree)	Rain the week prior to sampling (mm)	LeFT (days)
22/11/2004: Between 09:00 and 10:00 AM	D01	24.8	36.1	Low tide at 10:20 AM (0.65 m), high tide at 04:29 AM (1.20 m)	8.4 ± 1.1	113.8 ± 11.3	2.2	46.9
	D08	25.1	36.1					40.8
	D22	24.6	36.0					31.0
	M05	24.1	35.8					5.6
	M10	24.1	35.8					0.4
	M41	23.6	35.7					0.0
29/11/2004: Between 09:00 and 10:00 AM	N04	24.7	36.1	High tide at 09:38 AM (1.55 m), low tide at 03:46 PM (0.70 m)	9.9 ± 0.2	118.8 ± 3.4	7.8	17.1
	N12	24.7	36.2					12.9
	N33	24.6	36.0					12.4
	M33	24.0	35.8					0.5
	M10	23.6	35.8					0.4
	M41	23.0	35.7					0.0

hydrodynamic processes likely to affect the spatio-temporal distribution of elemental concentrations in the lagoon, and define parameters to quantify these processes.

The velocity field is relevant when the same water mass is studied at different stages from a Lagrangian point of view. In that case, and in association with hydrological measurements, it can be used to study the dilution factor of dissolved elements or the transport of suspended matter (e.g., Naudin et al., 1997). The velocity field is less relevant to compare different water masses. In that case, parameters deriving from hydrodynamics enable to analyse the kinetics of biological reagents or the moving of organisms with respect to the water masses (see a review in Jouon et al., 2006).

Several global and local transport time scales have been defined (e.g., Deleersnijder et al., 2001; Monsen et al., 2002). Each of these hydrodynamic parameters is associated to a unique calculation method which involves either the computation of input and output fluxes, the computation of the transport equation for a dissolved tracer, or the computation of series of trajectories. In their paper, Jouon et al. (2006) have compared different methods and listed the names of the associated time scale parameters found in the literature.

In the present work, the concentrations of dissolved and particulate metals are analysed against a typical scale for the renewal of a given water column, namely the local e-flushing time, expressed in days, as defined by Jouon et al. (2006). This parameter indicates the time required for a tracer mass contained within a given station (control volume) to be reduced by a factor $1/e$. It is variously called in the literature "flushing time" (Monsen et al., 2002), "residence time" (Shen and Haas, 2004; Wang et al., 2004) or "e-folding time" (Delhez et al., 2004). The local e-flushing time was calculated for all the sampling stations from a 3D hydrodynamic model adapted to the topographic, tidal and meteorological constraints of the Nouméa lagoon (Jouon et al., 2006). Fig. 2 presents the resulting field of the local e-flushing times calculated for trade wind rate (constant southeastern wind 110°, 8 $m\,s^{-1}$) and a periodic tide evolution resulting from M2 and S2 harmonics that are the major tidal constituents within the lagoon (Douillet, 1998). This modelling exercise provides estimates of the renewal rates of the water masses in the lagoon (i.e., local e-flushing times), which can be regarded as mean values, considering that the initial parameters used in the model are annual averages of wind conditions.

Wind speed and direction were continuously recorded at a meteorological station located on the Maître Island, situated between the two transects, close to the sampling station M33 (see location in Fig. 1, wind data in Fig. 3). Fig. 3 and Table 1 show that the wind conditions that prevailed during the two sampling days were trade wind conditions close to the average situation. The local e-flushing times presented in Fig. 2 are thus supposed applicable to the two sampling campaigns.

4. Results and discussion

4.1. Spatial distributions

Concentrations of dissolved and particulate Ni, Cr and Zn at all sampling stations are presented in Table 2. Two major features appear as following: (1) metal concentrations are significantly different along the transect D01–M10 and along the transect N04–M10; and (2) metal concentrations steeply decrease from the bays to the barrier reef.

The variation of metal concentrations along the two transects is shown in Fig. 4. The concentrations of dissolved metals strongly decrease from the coastal stations to the barrier reef: although the lagoon stretches over only 20 km from the bays to the barrier reef, concentrations decrease as steeply as, e.g., from 9000 down to 101 ng Ni L^{-1} from D01 to M41. The steepest decrease is found for Ni. The decrease of particulate metal concentrations exhibits the same trend, although it is less marked than that of the dissolved phase. Similar patterns have been already observed in the superficial sediment of the lagoon, with a more important decrease from the bays to the barrier reef for Ni, compared, for example, with Cr (Ambatsian et al., 1997). Dissolved and particulate concentrations of Ni are

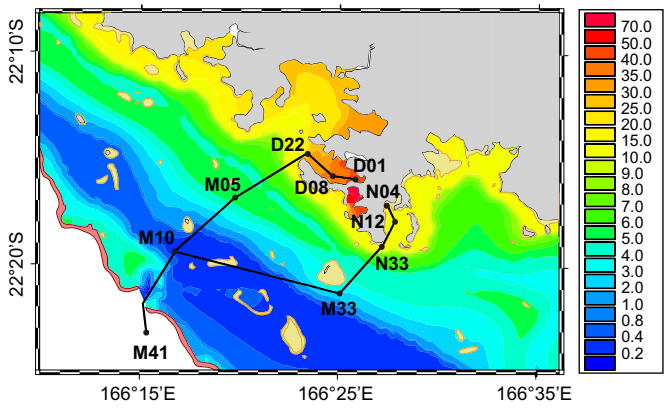

Fig. 2. Local e-flushing time distribution around Nouméa. The control volume considered for calculation is the southwest lagoon of New Caledonia as defined in Jouon et al. (2006). Local e-flushing times are expressed in days.

higher than those of Cr or Zn by a factor ranging between 2 and 45, approximately.

Dissolved Cr and Ni concentrations measured close to the barrier reef (e.g., at stations M10 and M41) are comparable to those encountered in the surface waters of the Pacific Ocean (Table 3), i.e. among the lowest values reported in the Southern Hemisphere (Apte et al., 1998).

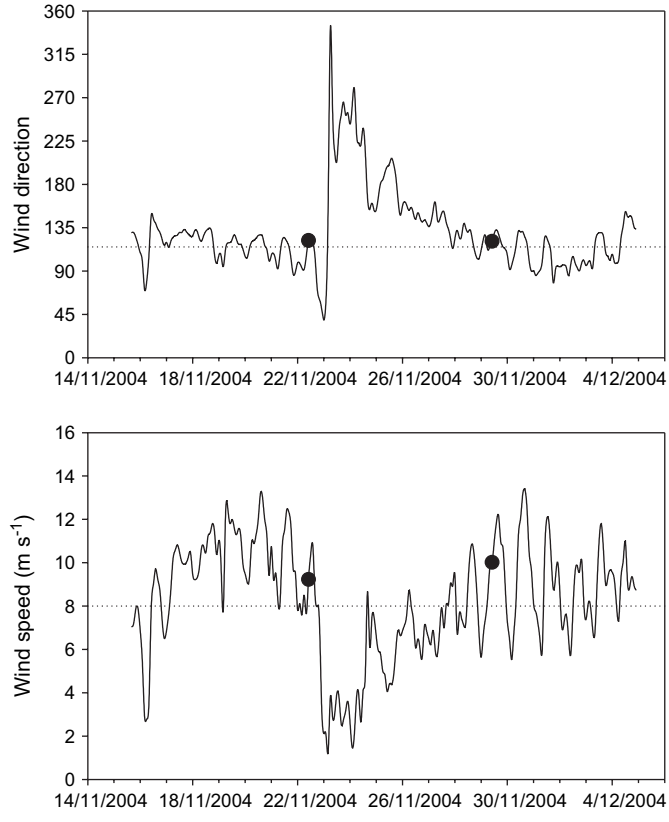

Fig. 3. Wind direction (a) and speed (b) at Maître Island during the field campaigns. Wind direction is expressed in degrees and a 0° wind comes from north.

4.2. Natural and anthropogenic emission sources

Concentrations of dissolved Ni (and, to a lesser extent, of Cr) are significantly higher in Grande Rade, under the influence of the Doniambo factory, than in Sainte-Marie Bay, where urban influences prevail (9000 ng Ni and 587 ng Cr L^{-1} at D01 vs 1800 ng Ni and 142 ng Cr L^{-1} at N04), while Zn exhibits very similar dissolved concentrations at the two sites D01 and N04: 538 and 522 ng L^{-1}, respectively (Table 2). Zinc is greatly enriched in urban runoff, compared with other metals transported by the sewerage network (Angelidis, 1995; Wiesner et al., 1998). For the specific case of New Caledonia, another significant source of Zn may be the weathering of Zn sheet roofs by tropical rainfall (J.M. Fernandez, personal communication). This probably explains that the Zn inputs to the two bays are very similar, contrarily to Cr and Ni.

Dissolved Zn concentrations in the barrier reef area are significantly higher than those found in remote Pacific areas (Table 2). This metal is mainly of urban origin, among which a great part is linked to motor vehicle use, owing to tyre wear (Wiesner et al., 1998; Migon, 2005) and, therefore, it is spread over the lagoon waters, to a large extent, by the atmospheric transport route. It is hypothesized that most of Zn loads are emitted from the southward region of Nouméa, relative to the transects, and atmospherically transported and spread over the lagoon. Aeolian inputs of Cr and Ni are relatively less important because under the influence of prevailing winds, plumes from the Dumbea factory do not significantly affect the transect area, which is only subjected to terrigenous aeolian inputs, therefore.

4.3. Geochemical processes

The difference between D01 (industrial) and N04 (urban) is even higher for particulate Ni concentrations (5818 and 505 ng L^{-1}, respectively, i.e. a factor of ~11.5). Nickel is significantly released from the sediment to the lagoon waters and then does not coprecipitates with ambient calcium carbonate ($CaCO_3$), the remaining fraction of particulate Ni being associated with iron oxides (Ambatsian et al., 1997). It is believed that the availability of iron oxides is significantly higher in the industrial loads of Grande Rade, compared with the natural inputs of the Coulée River watershed. As a result, the trapping of Ni onto iron oxides might be less efficient in Sainte-Marie Bay. Conversely, particulate Cr concentrations are slightly lower in D01 than in N04 (130 and 186 ng L^{-1}, respectively, i.e. a factor of ~0.7), despite supposedly higher emission sources of total Cr in D01. This might be due to sorption processes. Chromium is known to adsorb onto various surfaces, such as:

(1) Iron oxides and hydroxides (Eary and Rai, 1987; Sander and Koschinsky, 2000).
(2) Organic matter. The reduced form of Cr, Cr(III), commonly found in marine environments together with the oxidised species Cr(VI), is believed to significantly adsorb onto particulate organic matter, which process may be

Table 2
Dissolved and particulate concentrations of Ni, Cr and Zn at all stations, in ng L^{-1}

Sampling site	Ni		Cr		Zn	
	Dissolved	Particulate	Dissolved	Particulate	Dissolved	Particulate
M41 – 22/11/04	101		163.0	4.3		
M41 – 29/11/04	174	14.2	69.3	27.9	117.0	15.9
M10 – 22/11/04	651	50.7	166.0	4.5	370.0	33.0
M10 – 29/11/04	260	37.3	69.0	29.6	127.0	19.3
M05	470	42.0	113.5	2.2	454	95.0
D22	1800	267.4	317.0	6.0	176	64.3
D08	4000	2106.5	520.0	26.3	715	285.4
D01	9000	5818.0	587.0	129.7	538	368.0
M33	442	51.7	115.6	47.0	176	27.0
N33	755	53.8	114.0	108.0	51	34.8
N12	1300	616.1	258.0	147.6	310	149.0
N04	1800	504.5	142.0	185.8	522	226.0

enhanced in seawater because of alkaline pH (Kerndorff and Schnitzer, 1980; Poulton et al., 1988). On the one hand, in more or less oxidised surface waters, at seawater pH, the main Cr species are oxyanions in the Cr(VI) form such as CrO_4^{2-}, $HCrO_4^-$ and $Cr_2O_7^{2-}$ (Sadiq, 1992) and the concentration of Cr(III) is very low. On the other hand, the oxidation of Cr(III) to Cr(VI) is very slow in natural marine environments, and Cr(III) is involved in the faster sorption processes (Richard and Bourg, 1991). Significant amounts of Cr(III) have been found in hydrothermal plumes in Pacific waters (North Fiji Basin), supposedly stabilised by organic complexation (Sander and Koschinsky, 2000), and in open surface waters (Van den Berg et al., 1994).

(3) $CaCO_3$ surfaces. However, it is a common consensus that such surfaces play a minor role in the adsorption of Cr, particularly at seawater pH (Poulton et al., 1988; Zachara et al., 1988).

Taking into account the diversity of sorption processes for Cr, as well as the numerous factors that control these processes, the present data set does not enable to explain the different behaviours of particulate Cr in Grande Rade and Sainte-Marie Bay, compared with, e.g., Ni.

Concentrations of particulate Zn are comparable in D01 and in N04 (368 and 226 ng L^{-1}, respectively, i.e. a factor of ~1.6), which is consistent with the environmental characteristics of Grande Rade and Sainte-Marie Bay as well as with the ubiquitous character of Zn.

Distributions of trace metals in seawater are largely controlled by the biota (Bruland et al., 1991; Mackey et al., 2002). However, biological uptake and remineralisation at depth are not taken into account in the observed metal concentration variations in the present data. Except in the close vicinity of the barrier reef, metal concentrations are not of the same order of magnitude as the requirements of algal growth or bioaccumulation in plankton. It is assumed that such processes do not significantly affect the metal concentrations in the lagoon, where the prevailing causes of spatio-temporal variability of Cr, Ni and Zn are local geochemistry and hydrodynamics.

4.4. Role of hydrodynamics

The very low concentration levels of dissolved Ni and Cr close to the barrier reef (Table 2) indicate that the processes occurring in the coastal margin (atmospheric or riverine inputs, coastal effluents) are of negligible importance in determining Cr and Ni concentrations in the barrier reef area. Indeed, taking into account: (1) the significance of land-based emission sources of Cr and Ni derived from terrigenous erosion and mining activities; and (2) the relatively short distance from the bays to the barrier reef (~20 km), the concentrations at the barrier reef are unexpectedly low, and similar to open ocean values.

What is the specific influence of hydrodynamics on the spatio-temporal variability of metal concentrations? The low concentration of dissolved metals at the barrier reef and the strong concentration gradient from the coast to the barrier suggest a rapid renewal of waters close to the barrier reef, with the input of oceanic waters along the barrier. The relationship between the residence time of water masses (described by computed e-flushing times) and the spatial variability of metal concentrations (Fig. 5) confirms the role of hydrodynamics on the distributions of metal concentrations. A similar relationship between e-flushing times and other biogeochemical parameters has been previously evidenced at the same sampling sites (Mari et al., 2007; Torréton et al., 2007).

Regression lines between total concentrations and residence times give the following correlation coefficients (R^2): 0.743, 0.881 and 0.553 for Ni, Cr and Zn, respectively, for the 12 sampling stations (Fig. 5). These results show that the water renewal explains a significant part of the variance of metal concentrations in the water column. This part is very significant for Ni and Cr, but much less for Zn, which is in agreement with the peculiarities of Zn emission and transport discussed above, i.e., the significance of diffuse urban sources and of medium-range aeolian transport. For total Ni and Cr concentrations, Fig. 5 clearly shows that two sub-sets of data may be distinguished, one corresponding to the enriched and slowly renewed waters that include stations D01, D08, D22,

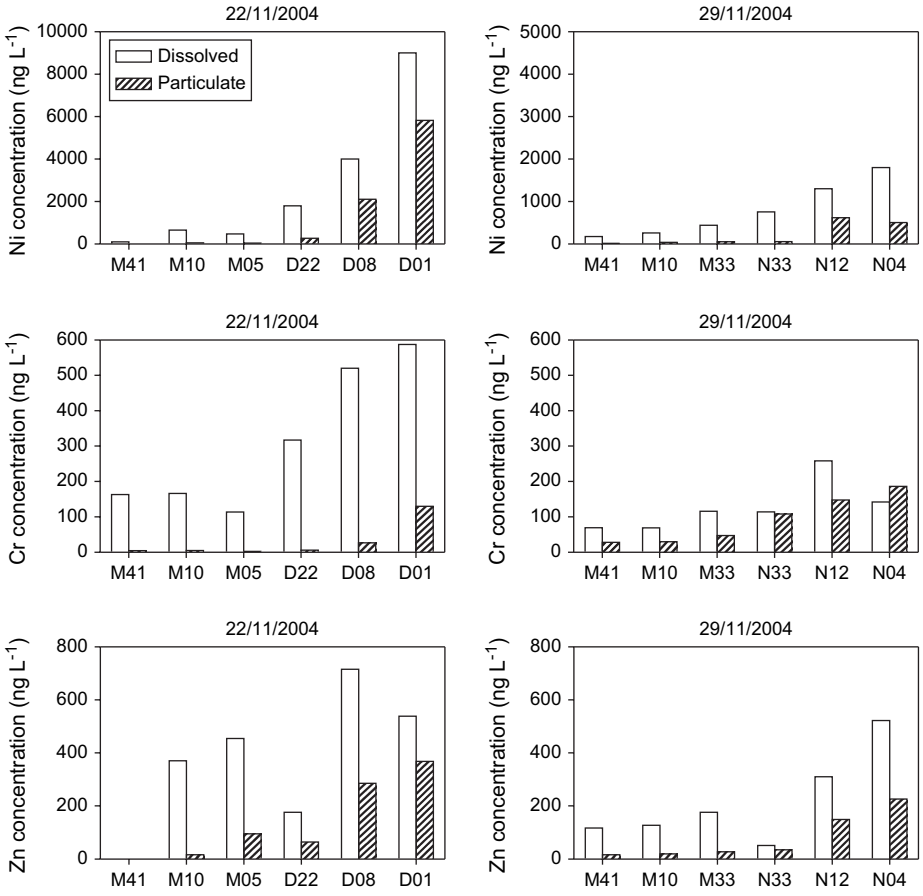

Fig. 4. Metal concentration variation from the bays to the barrier reef.

N04, N12 and N33, and the other corresponding to the rapidly renewed waters, as explained in Section 3.3.

Although no measurements of fluxes entering the bays are available, the account of local potential sources of metal emission clearly shows that the highest loads are emitted in Grande Rade, in the vicinity of the Doniambo factory and in the zone of ore ship discharge, close to the station D01. The highest residence times are found in this area. Even if it is difficult to precisely quantify the respective contributions of the intensity of inputs and hydrodynamic processes, it is clear that the combination of these two factors controls to a large extent the distribution of metals.

A comparison of the respective contributions of residence time and distance between the stations and the emission sources showed that, although usually believed a major regulating parameter of the distribution of metal concentrations, the distance was of minor importance. Fig. 6 shows that local e-flushing times explain to a large extent the variability of

Table 3
Mean dissolved Cr, Ni and Zn concentrations at stations M10 (inside edge of the lagoon) and M41 (outside edge of the lagoon), compared with other sheltered Pacific values (all expressed in ng L^{-1}). For New South Wales coastal waters, Apte et al. (1998) have hypothesized that fluvial inputs or processes occurring in the coastal margin were of limited importance in determining trace metal concentrations

Metal	Present work	Apte et al. (1998)[a]	Mackey et al. (2002)[b]	Noriki et al. (1998)[c]	Sander et al. (2003)[d]	Ellwood (2004)[d]	Nakayama et al. (1981)[e]
Cr	M10: 116 M41: 116.15	–	–	–	<200	–	480
Ni	M10: 260 M41: 137.5	180	117	70–622	–	–	–
Zn	M10: 248.5 M41: 117	<2	–	–	–	0.4–0.9	–

[a] New South Wales coastal waters.
[b] Western open Pacific.
[c] Equatorial Pacific.
[d] Sub-Antarctic Pacific (offshore New Zealand).
[e] Pacific Ocean.

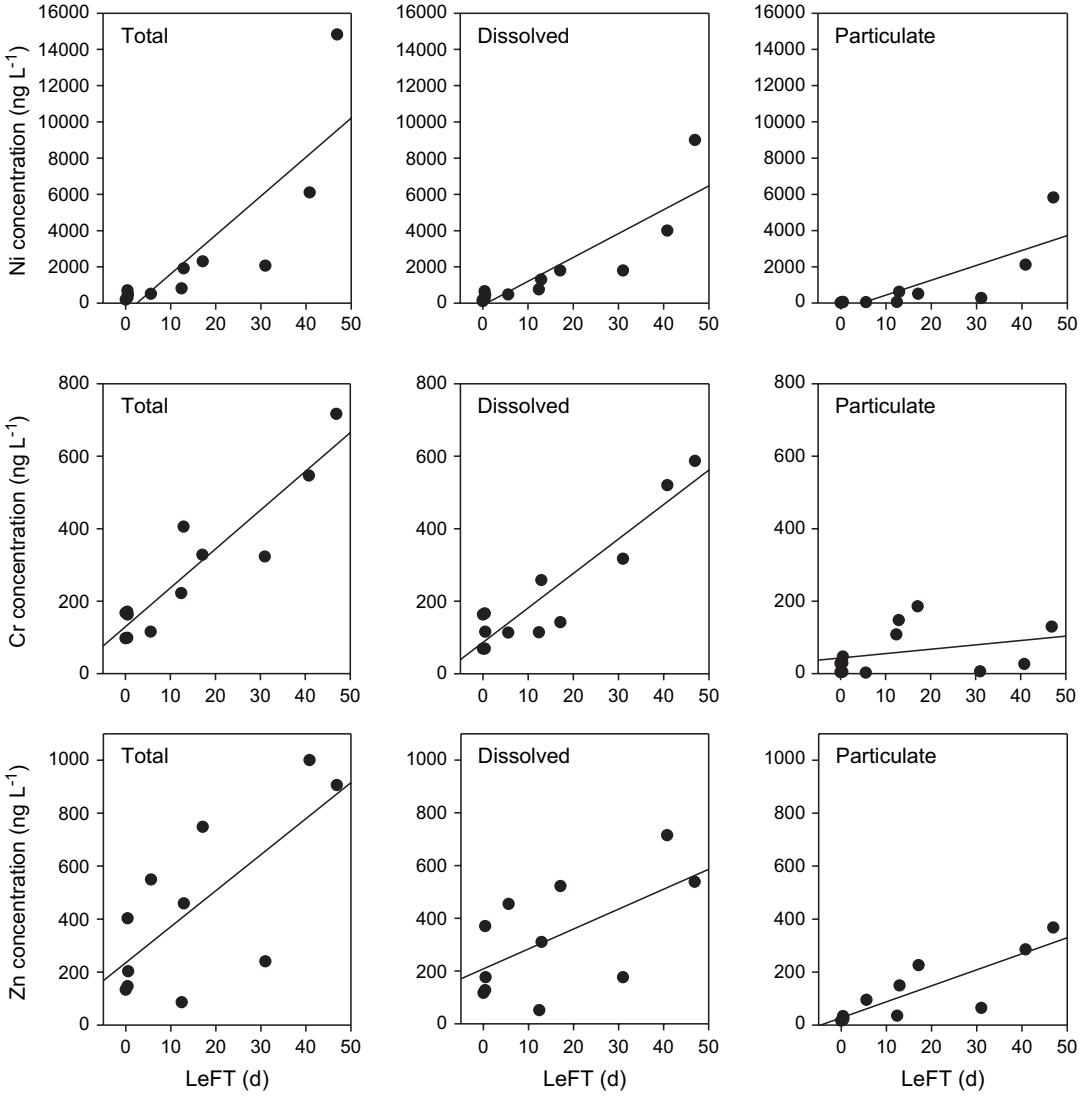

Fig. 5. Total, dissolved and particulate metal concentrations as a function of the local e-flushing time (LeFT).

metal concentrations, while the influence of the distance from the sources is very low (except for particulate Cr). This suggests that, basically, the decrease of concentrations with distance from the emission source is strongly driven by local e-flushing times. This may also explain why the decrease of Ni concentration from the bays to the barrier reef area is steeper than that of Cr: as far as one moves away from the emission source, the local e-flushing time prevails over the decreasing of metal concentrations with distance. As a result, the observed decrease of concentrations may be independent on the nature of the metal, as well as on its initial concentration level in the bays.

The correlation between concentrations and residence times is overall better for dissolved metals than for particulate metals (0.792 against 0.672 for Ni, 0.882 against 0.103 for Cr, but 0.394 against 0.749 for Zn). Dissolved concentrations are better correlated with residence times because e-flushing times are computed from the local evolution of the concentration of a dissolved tracer.

Seawater was sampled twice at two different dates at only two stations (M41 and M10), with contrasted meteorological configurations, 22 November was characterised by constant trade wind rate, while 29 November followed a change into western winds of variable strength (Fig. 3). It is likely that this change yielded an incoming flux of metal-depleted oceanic water. This flux is believed to come from west and from the outer edge of the reef. As a result, dissolved metal concentrations were significantly different at M10 between 22 and 29 November: 166–69 ng L^{-1} (Cr), 651–260 ng L^{-1} (Ni) and 370–127 ng L^{-1} (Zn). At M41, dissolved Cr concentrations fell from 163 down to 69.3 ng L^{-1}. Surprisingly, Ni dissolved concentrations increased (from 101 up to 174 ng L^{-1}). This might be the result of an analytical contamination, but the sampling station M41 is located out of the lagoon, where waters are already very depleted in metals, hence it is probably less (or not) sensitive to the impact of incoming oceanic water. Dissolved Zn concentrations were not measured at M41 on 22 November.

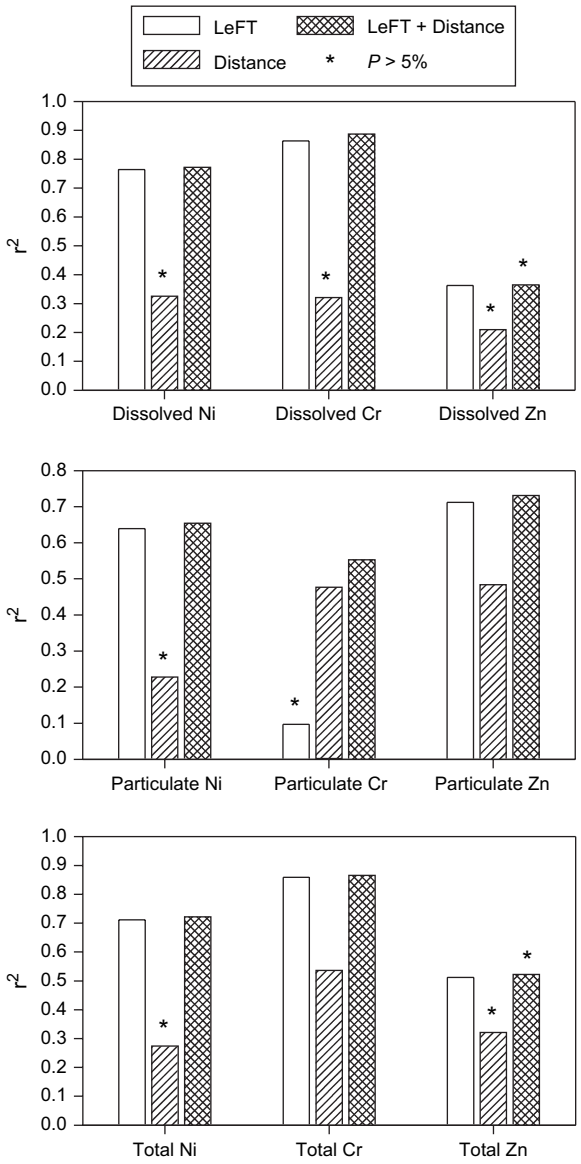

Fig. 6. Correlation coefficients of simple linear regressions for metal concentration vs local e-flushing times, and vs distance from the emission source, and multiple linear regression for metal concentration vs local e-flushing times and distance from the emission source. Taking into account the low impact of river loads, the ''mean'' emission source is assumed as the centre of Nouméa. LeFT means local e-flushing time.

As well, particulate Ni and Zn concentrations slightly decreased at M10 (50.7–37.3 and 33.0–19 ng L^{-1}, respectively). Particulate Cr concentrations were very low at M10 (4.5 ng L^{-1}). In trade wind rate, M10 is sheltered from wind waves by islands (Fig. 1) and from swell that does not penetrate into the lagoon. On the contrary, when western winds prevail, swell and water masses from the outer edge of the reef may contribute to local sediment remobilisation. Owing to the low metal concentrations at M10, it is likely that sediment mobilisation driven by incoming water masses became the most important process and yielded an increase of particulate Cr concentrations on 29 November (29.6 ng L^{-1}).

5. Conclusions

The magnitude and variability of Cr, Ni and Zn concentrations in the lagoon are controlled upstream by land-based emission sources: industrial (Grande Rade) and terrigenous (Sainte-Marie Bay) are superimposed upon a common urban source from the city of Nouméa. The raw metal loads then undergo a variety of chemical processes (sorption, precipitation, dissolution, release from sediment, etc.). However, owing to the specific circulation of the lagoon, the fate of dissolved and particulate metal concentrations is strongly constrained by hydrodynamics. The residence times of water masses point out their rapid renewal in the vicinity of the barrier reef. This is likely to counterbalance the high loads of Cr and Ni that enter the lagoon waters, and actually results in unexpectedly low concentration levels in waters close to the barrier reef. Except for Zn, of which the atmospheric input is believed to be spread over the whole surface of the lagoon, the peculiar combination of prevailing winds and lagoon hydrodynamics in the region of Nouméa finds here expression in a possible ''cleaning'' of surface waters with the rapid flushing of water masses.

As pointed out by the present data set, the fitting of metal concentrations on hydrodynamic models is difficult because of the combined influence of other parameters such as the location and strength of emission sources, and geochemical processes. The analysis may be improved by additional sampling at the same stations, for the same metals, during various episodes of wind forcing, in particular during episodes of low wind forcing. The analysis of episodes of nonsteady and aperiodic atmospheric forcing will require to adapt the methods of computation of local residence times.

Acknowledgements

We thank the crew of the R/V Coris for their assistance during sampling. Thanks are due to P. Douillet for his help in preparing the figures. This research was supported by the French National Research Agency (ANR-ECCO programme) and by the French Research Institute for Development (IRD).

References

Ambatsian, P., Fernex, F., Bernant, M., Parron, C., Lecolle, J., 1997. High metal inputs to close seas: the New Caledonia lagoon. Journal of Geochemical Exploration 59, 59–74.

Angelidis, M.O., 1995. The impact of urban effluents on the coastal marine environment of Mediterranean islands. Water Science and Technology 32 (9–10), 85–94.

Apte, S.C., Batley, G.E., Szymczak, R., Rendell, P.S., Lee, R., Waite, T.D., 1998. Baseline trace metal concentrations in New South Wales coastal waters. Marine and Freshwater Research 49 (3), 203–214.

Becquer, T., Pétard, J., Duwig, C., Bourdon, E., Moreau, R., Herbillon, A.J., 2001. Mineralogical, chemical and charge properties of Gerric Ferralsols from New Caledonia. Geoderma 103, 291–306.

Bruland, K.W., Donat, J.R., Hutchins, D.A., 1991. Interactive influences of bioactive trace metals on biological production in oceanic waters. Limnology and Oceanography 36 (8), 1555–1577.

Bustamante, P., Garrigue, C., Breau, L., Caurant, F., Dabin, W., Greaves, J., Dodemont, R., 2003. Trace elements in two odontocete species (*Kogia*

breviceps and *Globicephala macrorhynchus*) stranded in New Caledonia (South Pacific). Environmental Pollution 124 (2), 263–271.

Deleersnijder, E., Campin, J.M., Delhez, E.J.M., 2001. The concept of age in marine modeling. I. Theory and preliminary model results. Journal of Marine Systems 28, 229–267.

Delhez, E.J.M., Heemink, A.W., Deleersnijder, E., 2004. Residence time in a semi-enclosed domain from the solution of an adjoin problem. Estuarine, Coastal and Shelf Science 51, 691–702.

Douillet, P., 1998. Tidal dynamics of the south-west lagoon of New Caledonia: observations and 2D numerical modelling. Oceanologica Acta 21, 69–79.

Douillet, P., Ouillon, S., Cordier, E., 2001. A numerical model for fine suspended sediment transport in the southwest lagoon of New Caledonia. Coral Reefs 20, 361–372.

Eray, L.E., Rai, D., 1987. Kinetics of chromium(III) oxidation to chromium(VI) by reaction with manganese dioxide. Environmental Science and Technology 21, 1187–1193.

Ellwood, M.J., 2004. Zinc and cadmium speciation in subantarctic waters east of New Zealand. Marine Chemistry 87 (1–2), 37–58.

Fernandez, J.M., Ouillon, S., Chevillon, C., Douillet, P., Fichez, R., Le Gendre, R., 2006. A combined modelling and geochemical study of the fate of terrigenous inputs from mixed natural and mining sources in a coral reef lagoon (New Caledonia). Marine Pollution Bulletin 52, 320–331.

Jouon, A., Douillet, P., Ouillon, S., Fraunié, P., 2006. Calculations of hydrodynamic time parameters in a semi-opened coastal zone using a 3D hydrodynamic model. Continental Shelf Research 26, 1395–1415.

Kerndorff, H., Schnitzer, M., 1980. Sorption of metals on humic acid. Geochimica et Cosmochimica Acta 44, 1701–1708.

Mackey, D.J., O'Sullivan, J.E., Watson, R.J., Dal Pont, G., 2002. Trace metals in the western Pacific: temporal and spatial variability in the concentrations of Cd, Cu, Mn and Ni. Deep Sea Research Part I Oceanographic Research Papers 49, 2241–2259.

Mari, X., Rochelle-Newall, E., Torréton, J.P., Pringault, O., Jouon, A., Migon, C., 2007. Water residence time: a regulatory factor of the DOM to POM transfer efficiency. Limnology and Oceanography 52 (2), 808–819.

Migon, C., 2005. Trace metals in the Mediterranean Sea. In: Saliot, A. (Ed.), Chemistry of the Mediterranean Sea, The Handbook of Environmental Chemistry. Springer-Verlag, The Netherlands, pp. 151–176.

Monniot, F., Martoja, R., Monniot, C., 1994. Cellular sites of iron and nickel accumulation in ascidians related to the naturally and anthropic enriched New Caledonian environment. Annales de l'Institut Océanographique 70 (2), 205–216.

Monsen, N.E., Cloern, J.E., Lucas, L.V., Monismith, S.G., 2002. A comment on the use of flushing time, residence time, and age as transport time scales. Limnology and Oceanography 47, 1545–1553.

Nakayama, E., Tokoro, H., Kuwamoto, T., Fujinaga, T., 1981. Dissolved state of chromium in seawater. Nature 290, 768–769.

Naudin, J.J., Cauwet, G., Chrétiennot-Dinet, M.J., Deniaux, B., Devenon, J.L., Pauc, H., 1997. River discharge and wind influence upon particulate transfer at the land–ocean interaction: case study of the Rhône River plume. Estuarine, Coastal and Shelf Science 45, 303–316.

Noriki, S., Arashitani, Y., Minakawa, M., Harada, K., Tsunogai, S., 1998. Vertical cycling of Cu and Ni in the western North and Equatorial Pacific. Marine Chemistry 59 (3/4), 211–218.

Ouillon, S., Douillet, P., Andréfouët, S., 2004. Coupling satellite data with in situ measurements and numerical modeling to study fine suspended sediment transport: a study for the lagoon of New Caledonia. Coral Reefs 23, 109–122.

Ouillon, S., Douillet, P., Fichez, R., Panché, J.Y., 2005. Enhancement of regional variations in salinity and temperature in a lagoon, New Caledonia. Comptes Rendus Geoscience 337, 1509–1517.

Pinazo, C., Bujan, S., Douillet, P., Fichez, R., Grenz, C., Maurin, A., 2004. Impact of wind and freshwater inputs on phytoplankton biomass in the coral reef lagoon of New Caledonia during the summer cyclonic period: a coupled 3D biogeochemical modelling approach. Coral Reefs 23, 281–296.

Poulton, D.J., Simpson, K.J., Barton, D.R., Lum, K.R., 1988. Trace metals and benthic invertebrates in sediments of nearshore Lake Ontario and Hamilton Harbour. Journal of Great Lakes Research 14, 52–65.

Quantin, C., Becquer, T., Berthelin, J., 2002. Mn-oxide: a major source of easily mobilisable Co and Ni under reducing conditions in New Caledonia Ferralsols. Comptes Rendus Geoscience 334, 273–278.

Richard, F.C., Bourg, A.C.M., 1991. Aqueous geochemistry of chromium: a review. Water Research 25, 807–816.

Sadiq, M., 1992. Toxic Metal Chemistry in Marine Environments. Environmental Science and Pollution Control Series 1. Marcel Dekker, Inc., New York, USA, 390 pp.

Sander, S., Koschinsky, A., 2000. Onboard-ship redox speciation of chromium in diffuse hydrothermal fluids from the North Fiji Basin. Marine Chemistry 71, 83–102.

Sander, S., Koschinsky, A., Halbach, P., 2003. Redox speciation of chromium in the oceanic water column of the Lesser Antilles and offshore Otago Peninsula, New Zealand. Marine and Freshwater Research 54 (6), 745–754.

Shen, J., Haas, L., 2004. Calculating age and residence time in the tidal York River using three-dimensional model experiments. Estuarine, Coastal and Shelf Science 61, 449–461.

Torréton, J.P., Rochelle-Newall, E., Jouon, A., Faure, V., Jacquet, S., Douillet, P., 2007. Correspondence between the distribution of hydrodynamic time parameters and the distribution of biological and chemical variables in a semi-enclosed coral reef lagoon. Estuarine, Coastal and Shelf Science 74 (4), 667–677.

Van den Berg, C.M.G., 1986. The determination of trace metals in sea water using cathodic stripping voltammetry. The Science of the Total Environment 49, 89–99.

Van den Berg, C.M.G., Boussemard, M., Yokoi, K., Prartono, T., Campos, M.L.A.M., 1994. Speciation of aluminium, chromium and titanium in the NW Mediterranean. Marine Chemistry 45, 267–282.

Wang, C.F., Hsu, M.H., Kuo, A.Y., 2004. Residence time of the Danshuei River estuary, Taiwan. Estuarine, Coastal and Shelf Science 60, 381–393.

Wiesner, M.R., Characklis, G.W., Brejchova, D., 1998. Metals and colloids in urban runoff. In: Allen, H.E., Garrison, A.W., Luther III, G.W. (Eds.), Metals in Surface Waters. Ann Harbor Press, Chelsea, USA, pp. 23–35.

Zachara, J.M., Cowan, C.E., Schmidt, R.L., Ainsworth, C.C., 1988. Chromate adsorption by kaolinite. Clays and Clay Minerals 36, 317–326.

Available online at www.sciencedirect.com
ScienceDirect
Estuarine, Coastal and Shelf Science 74 (2007) 766–776
ESTUARINE COASTAL AND SHELF SCIENCE
www.elsevier.com/locate/ecss

Correspondence between the distribution of hydrodynamic time parameters and the distribution of biological and chemical variables in a semi-enclosed coral reef lagoon

Jean-Pascal Torréton [a,*], Emma Rochelle-Newall [a], Aymeric Jouon [a], Vincent Faure [b], Séverine Jacquet [a], Pascal Douillet [a]

[a] *IRD, Nouméa Center, BP A5, NC-98848 Nouméa, New Caledonia*
[b] *Centre d'Océanologie de Marseille, Station Marine d'Endoume, 13007 Marseilles, France*

Received 10 February 2006; accepted 9 May 2007
Available online 27 June 2007

Abstract

Hydrodynamic modeling can be used to spatially characterize water renewal rates in coastal ecosystems. Using a hydrodynamic model implemented over the semi-enclosed Southwest coral lagoon of New Caledonia, a recent study computed the flushing lag as the minimum time required for a particle coming from outside the lagoon (open ocean) to reach a specific station [Jouon, A., Douillet, P., Ouillon, S., Fraunié, P., 2006. Calculations of hydrodynamic time parameters in a semi-opened coastal zone using a 3D hydrodynamic model. Continental Shelf Research 26, 1395–1415]. Local e-flushing time was calculated as the time requested to reach a local grid mesh concentration of 1/e from the precedent step. Here we present an attempt to connect physical forcing to biogeochemical functioning of this coastal ecosystem. An array of stations, located in the lagoonal channel as well as in several bays under anthropogenic influence, was sampled during three cruises. We then tested the statistical relationships between the distribution of flushing indices and those of biological and chemical variables. Among the variables tested, silicate, chlorophyll *a* and bacterial biomass production present the highest correlations with flushing indices. Correlations are higher with local e-flushing times than with flushing lags or the sum of these two indices. In the bays, these variables often deviate from the relationships determined in the main lagoon channel. In the three bays receiving significant riverine inputs, silicate is well above the regression line, whereas data from the bay receiving almost insignificant freshwater inputs generally fit the lagoon channel regressions. Moreover, in the three bays receiving important urban and industrial effluents, chlorophyll *a* and bacterial production of biomass generally display values exceeding the lagoon channel regression trends whereas in the bay under moderate anthropogenic influence values follow the regressions obtained in the lagoon channel. The South West lagoon of New Caledonia can hence be viewed as a coastal mesotrophic ecosystem that is flushed by oligotrophic oceanic waters which subsequently replace the lagoonal waters with water considerably impoverished in resources for microbial growth. This flushing was high enough during the periods of study to influence the distribution of phytoplankton biomass, bacterial production of biomass and silicate concentrations in the lagoon channel as well as in some of the bay areas.

Keywords: hydrodynamics; flushing time; plankton; secondary production; nutrients; coastal lagoon; Pacific; New Caledonia

1. Introduction

As pointed out by Monsen et al. (2002), in aquatic systems, planktonic biomass and nutrients are carried in a fluid medium and it is therefore essential to understand the hydrodynamic processes that transport water and its constituents. Since Vollenweider's work showing the link between the biogeochemical

* Corresponding author. Present address: Institut de Recherche pour le Developpement, ECOLAG, UMR 5119, CNRS Université Montpellier II, Université Montpellier II, Case 093, 34095 Montpellier Cedex 05, France.
E-mail address: torreton@mpl.ird.fr (J.-P. Torréton).

0272-7714/$ - see front matter © 2007 Elsevier Ltd. All rights reserved.
doi:10.1016/j.ecss.2007.05.018

processing of phosphorus in lakes and the residence time of waters (Vollenweider, 1976), several studies on estuaries have shown relationships between variable water retention or flushing indices and the distribution of phytoplankton blooms (Doering et al., 1994; Lucas et al., 1999), phytoplankton community composition (Ferreira et al., 2005), bacterioplankton abundance (Painchaud et al., 1996) and community composition (Crump et al., 2004).

In coral reef areas, Andrews and Muller (1983) proposed that in a lagoonal patch reef of the Great Barrier Reef, a part of the variance of nutrient concentrations could be explained by tidal movements. Moreover, using literature values from several coral reef lagoons, Delesalle and Sournia (1992) revealed a negative relationship between phytoplankton biomass and estimates of exchange rates between these lagoons and the open ocean. In the Tuamotu Archipelago (French Polynesia), the size of the aperture connecting atoll lagoons to the ocean was shown to be one of the key parameters defining nutrient regime (Dufour et al., 2001) and trophic status (Torréton et al., 2002).

These studies reporting the link between potential flushing of semi-enclosed atolls and the biological or chemical properties of those atolls demonstrate the importance of water circulation in determining the distribution of chemical and biological variables in coral reef environments. However, none of these studies focused on this link at local scales, i.e. none have attempted to relate flushing rates and the distribution of biogeochemical variables on an array of stations within the same water body.

Nutrient concentrations and plankton biomass and activities are higher in the South West lagoon of New Caledonia than in the surrounding ocean and are not uniformly distributed (Bourguet et al., 2003; Briand et al., 2004; Jacquet et al., 2006). Apart from local eutrophication in the bays near Noumea City, differences are also observed in the main lagoon channel. The southern part, which is closer to oceanic inputs flushing the lagoon, usually had lower nutrient concentrations and plankton biomass and activity than in the northern part (Jacquet et al., 2006).

A recent paper focused on computations of hydrodynamic time parameters in the South West lagoon of New Caledonia using a 3D hydrodynamic model (Jouon et al., 2006). In an attempt to connect physical forcing to biogeochemical functioning of the SW lagoon of New Caledonia, the aim of this study was to test the statistical relationships between the distribution of flushing indices determined on an array of stations in the SW lagoon of New Caledonia (Jouon et al., 2006) and the distribution of biological and chemical variables acquired during three oceanographic campaigns in the same lagoon.

2. Material and methods

2.1. Study site

New Caledonia is surrounded by a 23,400-km^2 lagoon. Noumea City (home to ~60% of the total population of New Caledonia) is located on the south-west coast. The surrounding lagoonal area is known as the South West Lagoon of New Caledonia. It has an average depth of 17.5 m and varies in width from 5 km (northern limit) to 40 km (southern limit). It is separated from the open ocean by a barrier reef, bisected by three main passes (Fig. 1). Around Nouméa City, four bays were sampled. The Sainte-Marie Bay receives urban waste waters from the Sainte-Marie area. The Grande Rade and Koutio Bay also receive urban effluent, as well as industrial effluents originating from the nickel smelt. In contrast, the Dumbéa Bay is under the terrigenous influence from the Dumbéa River and receives neither urban sewage nor industrial effluents.

2.2. Hydrodynamics

The flushing lag (in days) indicates the minimum time required for a particle entering the southwest lagoon of New Caledonia (open ocean) to reach the station in question. More precisely, assuming that lagoon water presents a concentration of a passive tracer of 1 and that incoming waters from outside of the lagoon present a concentration of 0, the flushing lag represents the time required to decrease the local grid mesh concentration by 5% (Jouon et al., 2006). This value is selected to minimize the importance of computation errors. Local e-flushing time represents the time needed to attain a local grid mesh concentration of 1/e from the precedent step where numerical drogues present a concentration of 0.95. Both flushing lag and local e-flushing time at the different stations were computed from MARS3D, a hydrodynamic model implemented over the study area. The accuracy of the time scales is guaranteed by the validation of the advection dispersion of dissolved tracers in the model (Lazure and Salomon, 1991a,b; Douillet et al., 2001; Plus et al., 2003; Ouillon et al., 2004). The computation methods used are the same as those of other readily used computation methods (Thomann and Mueller, 1987; Delhez et al., 2004) which inherently take into account the significance of the time scales used (Jouon et al., 2006).

This model was adapted to compute the free surface elevation, the 3D currents, the transport of suspended particulate matter (Douillet, 1998; Douillet et al., 2001; Ouillon et al., 2004) and the hydrodynamic time parameters (Jouon et al., 2006) under tide and wind forcing in the Southwest lagoon of New Caledonia. MARS3D is a finite difference model in σ coordinates. The computation grid is of the Arakawa C type modified as described in Lazure and Salomon (1991a). The horizontal grid spacing is 500 m. 10 σ levels (Blumberg and Mellor, 1987) are used to discretize the vertical dimension. The top and bottom boundary conditions are ''slip conditions'' (Blumberg and Mellor, 1987; Deleersnijder et al., 1992) with wind friction at the top of the surface σ level and friction on the bottom of the deepest σ level. The turbulence model used is of the Pacanowsky and Philander (1981) type. The advection scheme is a Total Variation Diminishing (TVD) scheme (e.g. Sweby, 1984).

2.3. Sampling

Lagoon water was collected during three campaigns performed in September 2000 (cold season; 91 stations), June

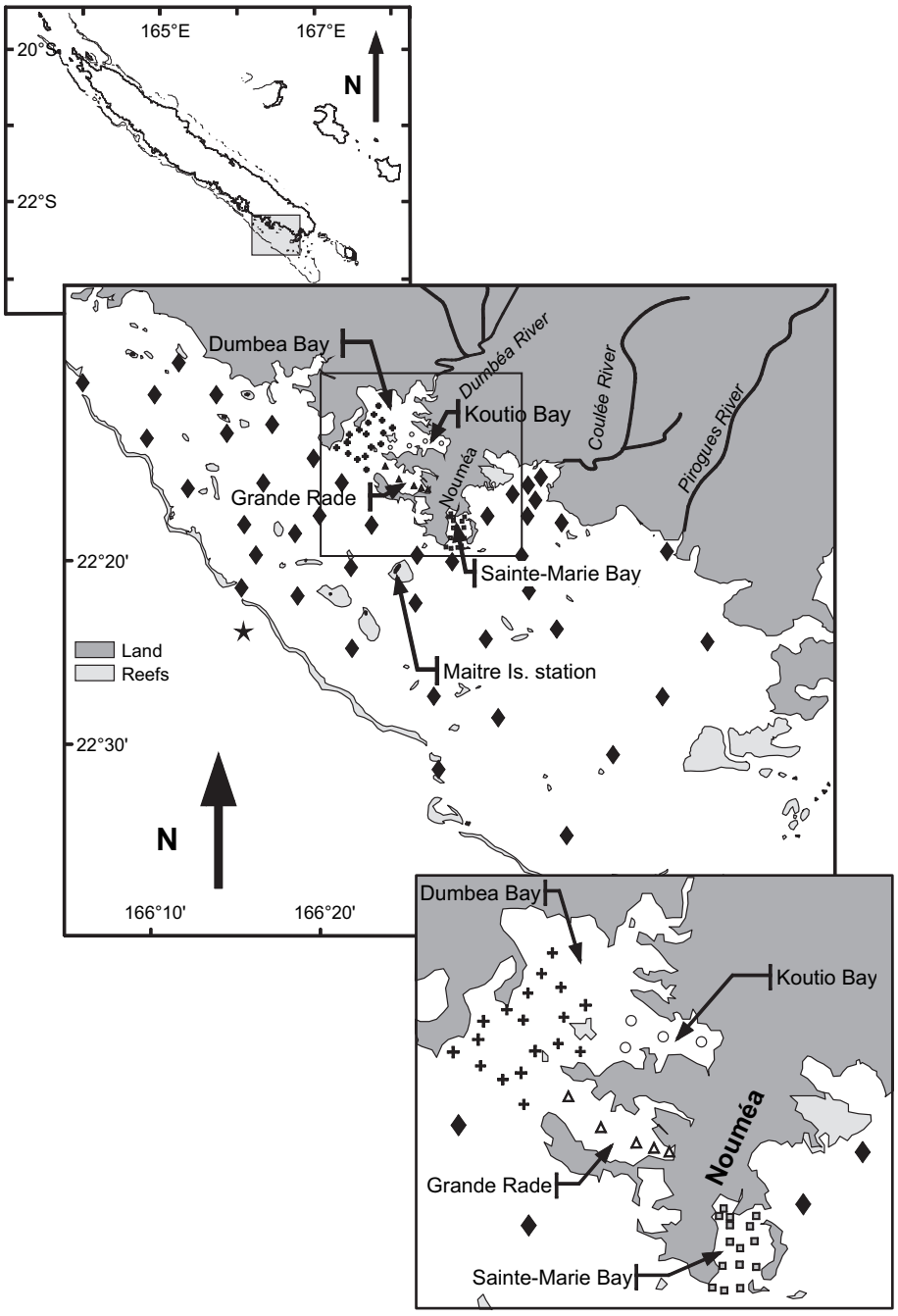

Fig. 1. The South West lagoon of New Caledonia and the sampling sites. Large grey symbols represent lagoon channel stations. Small dark symbols figure bay stations. Black star represents oceanic station. The weather station at Maitre Is. is indicated.

2003 (cold season; 79 stations) and October 2004 (dry season; 83 stations) using the R/Vs *Alis* and *Louis Hénin*. Conductivity, temperature, *in vivo* fluorescence and turbidity profiles were simultaneously recorded using a SeaBird SBE 19 profiler and Seapoint Fluorometer and Turbidity Meter, respectively. Water samples were collected at 3 m depth and were immediately processed on board.

2.4. Chlorophyll a and nutrients

Chlorophyll *a* (Chl-*a*) was analyzed fluorometrically on methanol extracts (Holm-Hansen et al., 1965) following filtration onto Whatman GF/F filters of replicate 300 ml samples. Ammonium was fluorometrically determined on a Turner TD-700 immediately after collection on three unfiltered 40 ml replicates, using the *o*-phthaldialdehyde method (Holmes et al., 1999). Unfiltered replicate samples (40 ml each) were immediately frozen until nitrate + nitrite ($NO_3 + NO_2$), phosphate (PO_4) and silicate analyses. Nitrates were reduced to nitrites and $NO_3 + NO_2$ concentrations were determined according to Raimbault et al. (1990) on a Bran+Luebbe Autoanalyzer III. Phosphates and silicates (dissolved and colloidal) were determined according to Grasshoff et al. (1983) on the same autoanalyzer.

2.5. Bacterial abundance and production

Water samples (1.5 ml) for bacterial enumeration were preserved with 7.5 µl glutaraldehyde (Sigma Grade II) and stored in liquid nitrogen. Heterotrophic bacteria were enumerated on a FACScan flow cytometer (Becton Dickinson) equipped with an air-cooled laser providing 15 mW at 488 nm and with a standard filter setup after SYBR green coloration (Marie et al., 1997). Bacterial production of biomass was determined from thymidine incorporation as in Briand et al. (2004). The biomass production rates were computed using the average of empirically determined conversion factors (2.9×10^{18} cells mol^{-1} of thymidine, unpublished data) and 12.4 fg C $cell^{-1}$ (Fukuda et al., 1998).

3. Results

3.1. Meteorological conditions

During the three oceanographic cruises, wind was recorded on Maître Island in the middle of the southwest lagoon of New Caledonia (see location on Fig. 1 and wind data on Fig. 2). In September 2000, wind intensity and direction remained relatively constant (mean trade wind, 110°, 8 m s^{-1}) prior to as well as during the cruise. In June 2003, wind intensity varied more than during the preceding campaign with an average of 5 m s^{-1} and more elevated values at the beginning and at the end of the cruise. Wind direction remained that of mean trade wind (110°) during most of the cruise. In October 2004, wind had generally the same direction (110°); however, its intensity varied widely with higher values a few days before and during the beginning of the cruise (average ± SD 10.2 ± 2.8 m s^{-1}) and lower values (5.1 ± 3.3 m s^{-1}) during the latter part of the cruise. This last part of the cruise was also characterized by large diel variations in wind intensity. On average, wind velocity was 7.2 m s^{-1} during this campaign.

In summary, although wind intensity and direction varied slightly around the mean trade wind (110°, 8 m s^{-1}), the deviations persisted for only short periods. The mean trade wind was thus relevant to force the numerical simulations providing the hydrodynamic time parameters that were then compared to the biological and chemical parameters measured during the cruises.

3.2. Flushing indices

The estimated flushing lags of the water masses at the sampling stations vary from ~0.1 day for the southernmost sector of the lagoon up to 48 days at the head of the Grande Rade under the combined influences of a typical periodic tide (components M2 and S2; see tide analysis in Douillet, 1998) and a uniform SE trade wind (110°) of 8 m s^{-1}. Under the same forcing conditions, the local e-flushing times at the sampling stations vary from a few minutes for the southernmost sector of the lagoon up to 47 days at the head of the Grande Rade (Fig. 3).

3.3. Physico-chemical characteristics and nutrients

The physico-chemical characteristics varied little among stations. Salinity averaged 35.21 (range 34.69–35.36), 35.32 (range 34.19–35.57) and 35.90 (range 35.54–36.31) in September 2000, June 2003 and October 2004, respectively. Temperature averaged 22.9 °C (range 22.2–23.4), 22.7 °C (range 22.1–23.5) and 23.3 °C (range 22.5–25.0) in September 2000, June 2003 and October 2004, respectively.

Dissolved inorganic nitrogen (DIN) concentrations varied widely among stations and averaged 0.10 µM (range 0.01–2.85), 0.12 µM (range 0.01–1.27), and 0.16 µM (range 0.01–6.17) during the three campaigns. Maximum values were recorded at the heads of the bays subject to urban and industrial effluents whereas minimum values occurred in the main lagoon channel. Dissolved inorganic phosphorus concentrations generally followed the same distribution as DIN and averaged 0.09 µM (range 0.03–0.57), 0.04 µM (range 0.00–0.45), and 0.06 µM (range 0.00–0.66) during the three campaigns.

3.4. Phytoplankton biomass and bacterial production of biomass

Chlorophyll *a* (Chl-*a*) values varied widely among stations and averaged 0.42 µg L^{-1} (range 0.13–1.98), 0.52 µg L^{-1} (range 0.13–3.64), and 0.47 µg L^{-1} (range 0.11–3.54) during the three campaigns. Bacterial abundance varied far less spatially with 0.76×10^6 ml^{-1} (range 0.43–1.46), 0.70×10^6 ml^{-1} (range 0.37–0.98), and 0.47×10^6 ml^{-1} (range 0.24–1.18) during the three campaigns. Bacterial production of biomass displayed considerable variation between stations with whole campaign averages of 0.26 µg C L^{-1} h^{-1} (range 0.02–1.64), 0.27 µg C L^{-1} h^{-1} (range 0.02–2.02), and 0.37 µg C L^{-1} h^{-1} (range 0.08–2.86) in September 2000, June 2003 and October 2004, respectively. In general, Chl-*a*, bacterial abundance and bacterial production (BP) values were distributed similarly to nutrient concentrations, i.e. values were maximal at the heads of the bays receiving urban and industrial effluents, and decreased down to lagoon channel values at the mouth of the bays. However, BP varied more between stations (36- to 114-fold) than phytoplankton biomass (16- to 31-fold), and bacterial abundance (3- to 5-fold) did.

3.5. Relationships between biological variables and local e-flushing times in the lagoon channel

Statistical relationships were generally significant between biological and chemical variables and local e-flushing time when all sampling sites were considered (Table 1). However, as most enrichment in the lagoon originates from the heads of the bays, where local e-flushing times are considerably higher than in the main lagoon channel, there could be an artificial increase in the significance of statistical relationships. We therefore determined the statistical linear relationships between biological and chemical variables and local e-flushing time only in lagoon channel stations (Table 2). In the bays the

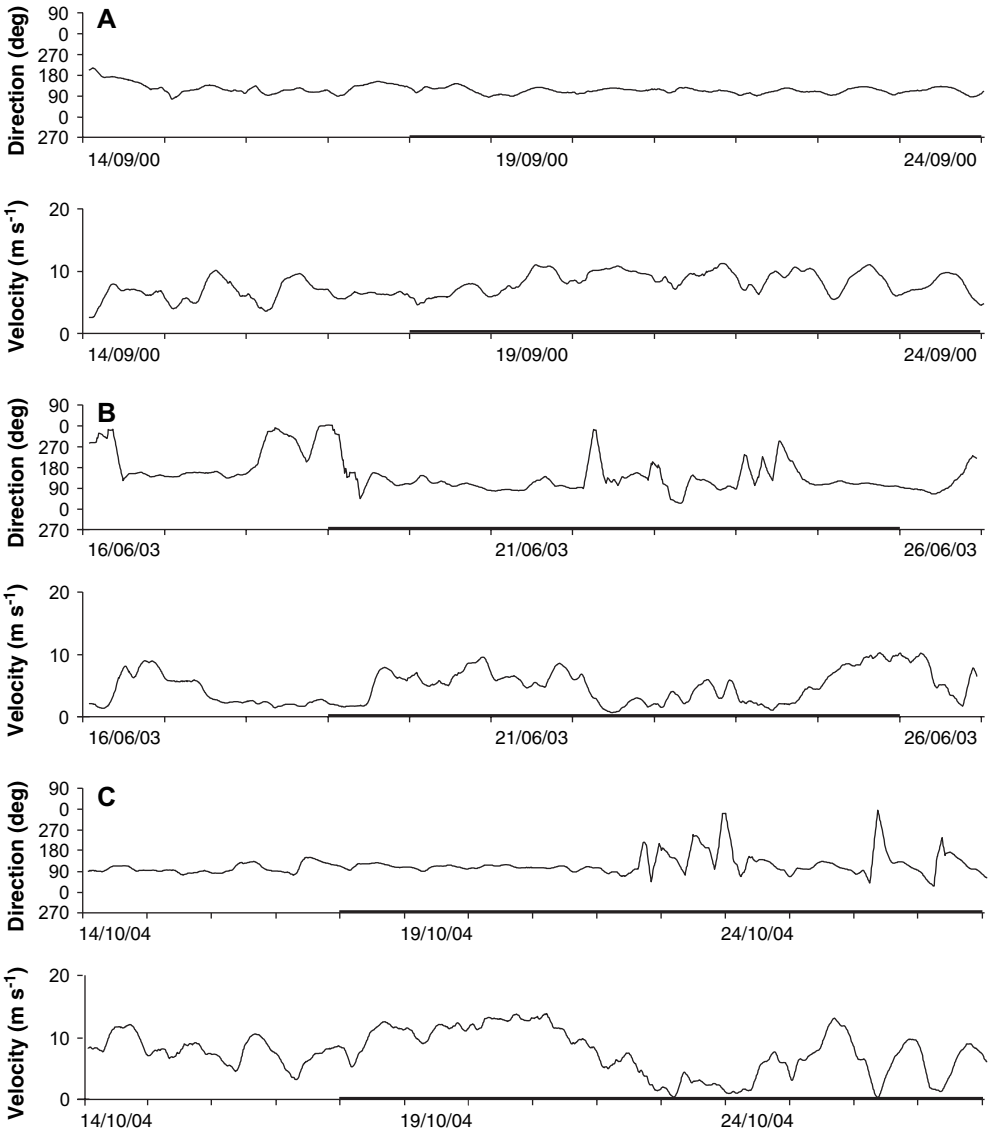

Fig. 2. Wind measurements during and before the three oceanographic cruises in (A) September 2000, (B) June 2003, and (C) October 2004. Cruises dates are indicated by wider bars.

distribution of biological and chemical variables vs. local e-flushing time can be compared to the linear relationships in the channel in Fig. 4.

Chemical variables showed generally non significant relationships with local e-flushing time in the main lagoon channel (not shown). Silicate was the only nutrient displaying significant relationships with flushing indices over the three cruises (Table 2). This is probably due to the fact that silicate (Si) is not a limiting nutrient for primary production (Jacquet et al., 2006). Indeed, as the Si:DIN ratio is always much higher than 1, we can therefore expect the turnover time of silicate to be low compared to other nutrients.

Among biological variables, Chl-*a* and BP generally displayed highly significant correlations with local e-flushing times in lagoon channel stations (Fig. 4, Table 2). For example, during the September 2000 cruise, the southernmost part of the lagoon displayed a bacterial production rate of (average ± SE) 0.07 ± 0.01 μg C L^{-1} h^{-1}, with local e-flushing times corresponding to 0.021 ± 0.016 day. BP was slightly higher (0.15 ± 0.04 μg C L^{-1} h^{-1}) in the lagoon channel facing Nouméa City (6 stations, Fig. 1) with local e-flushing times corresponding to 0.81 ± 0.20 day. Finally, BP in the northern part was nearly 3-fold higher than in the southernmost stations with 0.19 ± 0.02 μg C L^{-1} h^{-1} for local e-flushing times averaging 5.2 ± 1.7 days. BP in the oceanic waters that flush the lagoon was 3.5-fold lower than in the Southern lagoon with on average 0.0019 ± 0.002 μg C L^{-1} h^{-1} (unpublished data).

3.6. Relationships between biological variables and local e-flushing times in the bays

In Sainte-Marie, Dumbea and Koutio Bays, silicate displayed values above the lagoon channel regression lines (Fig. 4). The only exception occurred in June 03, when atypically elevated

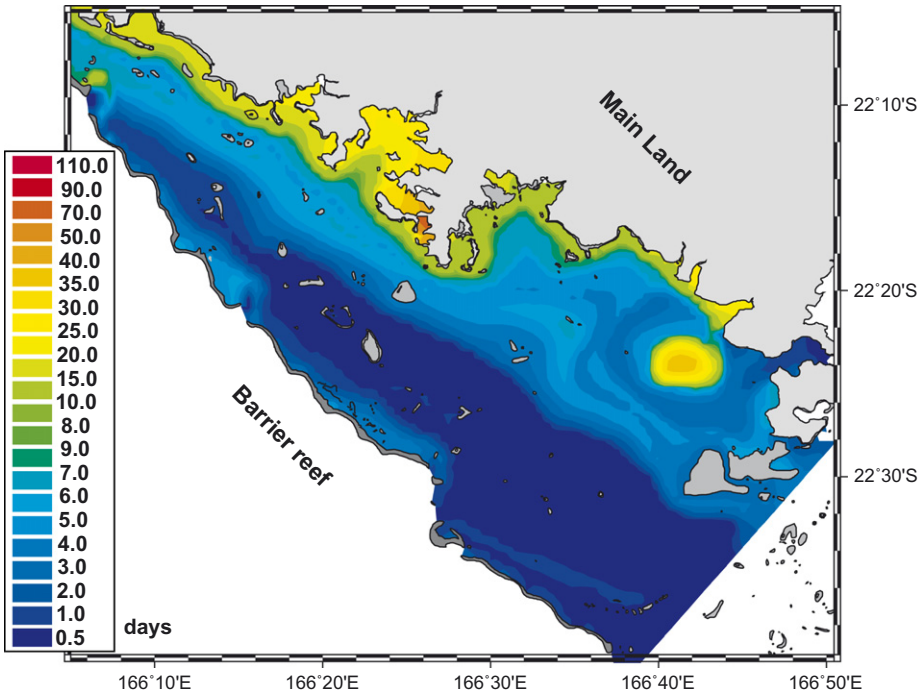

Fig. 3. Local e-flushing times determined under medium tide and 110° and 8 m s^{-1} Trade Winds in the SW lagoon of New Caledonia.

values were observed in the lagoon channel. Conversely, in the Grande Rade, silicate concentration generally fitted well with the lagoon channel relationships. Chl-*a* and BP values exhibited similar distributions versus local e-flushing times, with Dumbea Bay values sitting along the lagoon channel regression lines and Sainte-Marie Bay and Koutio Bay values falling well above the regression line (Fig. 4).

Scatter plots of biological or chemical variables as a function of flushing lags or as a function of the sum of flushing lags and local e-flushing times followed similar trends in the

Table 1
Significance of the linear relationships between biological or chemical variables and local e-flushing times in different areas of the SW lagoon channel of New Caledonia. Chl-*a*, chlorophyll *a*; BP, bacterial production; Si, silicate concentrations; *r*, correlation coefficient; *P*, significance level; *n*, number of points. *$P < 0.10$; **$P < 0.05$; ***$P < 0.01$; ****$P < 0.0001$; otherwise not significant

		September 2000			June 2003			October 2004		
		r	*P*	*n*	*r*	*P*	*n*	*r*	*P*	*n*
Chl-*a*	Channel	0.42	***	46	0.34	**	48	0.27	*	49
	Sainte-Marie Bay	0.56	**	15	0.55	*	10	0.84	***	10
	Grande Rade	0.89	**	5	0.85	*	5	0.63		5
	Koutio Bay	0.74		4	0.63		4	0.71		4
	Dumbea Bay	0.67	***	18	0.55	**	15	0.56	**	15
	Channel and Dumbea	0.70	****	64	0.51	****	63	0.47	****	64
	All stations	0.49	****	88	0.41	****	82	0.40	****	83
BP	Channel	0.32	**	46	0.29	**	47	0.44	***	50
	Sainte-Marie Bay	0.68	**	10	−0.12		9	0.79	***	10
	Grande Rade	0.92	**	5	0.41		5	0.57		5
	Koutio Bay	0.45		4	0.70		4	0.70		4
	Dumbea Bay	0.35		17	0.11		15	0.38		15
	Channel and Dumbea	0.52	****	63	0.41	****	62	0.73	****	64
	All stations	0.48	****	82	0.65	****	80	0.64	****	84
Si	Channel	0.58	****	49	0.33	**	41	0.34	**	50
	Sainte-Marie Bay	0.32		15	−0.44		10	0.66	**	10
	Grande Rade	0.87	*	5	0.60		5	0.62		5
	Koutio Bay	0.95	*	4	−0.99	**	4	0.82		4
	Dumbea Bay	0.54	**	18	0.04		15	0.54	**	15
	Channel and Grande Rade	0.79	****	54	0.80	****	53	0.70	****	55
	All stations	0.59	****	91	0.69	****	75	0.57	****	84

Table 2
Model II linear relationships between biological and chemical variables and local e-flushing times (days) in the SW lagoon channel of New Caledonia. Si, silicate (μM); Chl-*a*, chlorophyll *a* (μg L^{-1}); BP, bacterial production (μg C L^{-1} h^{-1}); NS, not significant

Cruise	Variable	Slope ± SE	Intercept ± SE	*r*	*P*	*n*
Sept. 00	Chl-*a*	0.010 ± 0.001	0.160 ± 0.010	0.412	0.004	46
Sept. 00	BP	0.011 ± 0.002	0.043 ± 0.012	0.318	0.031	46
Sept. 00	Si	0.106 ± 0.013	1.092 ± 0.094	0.576	0.000	49
June 03	Chl-*a*	0.021 ± 0.003	0.195 ± 0.018	0.344	0.015	48
June 03	BP	0.015 ± 0.002	0.091 ± 0.012	0.287	0.050	47
June 03	Si	0.275 ± 0.042	2.438 ± 0.236	0.330	0.035	48
Oct. 04	Chl-*a*				NS	49
Oct. 04	BP	0.013 ± 0.002	0.079 ± 0.013	0.439	0.001	50
Oct. 04	Si	0.079 ± 0.011	1.292 ± 0.078	0.341	0.015	50

channel, with comparable or slightly lower significance levels. In the bays, deviations from these trends were also similar to those observed with local e-flushing times.

4. Discussion

4.1. Underlying assumptions for the link between local e-flushing times and spatial distributions of nutrients and biological variables

Technically, local e-flushing time is the time required for the concentration (initially set to 1 throughout the whole control volume) in a grid cell to drop down to 1/e × 0.95 from the

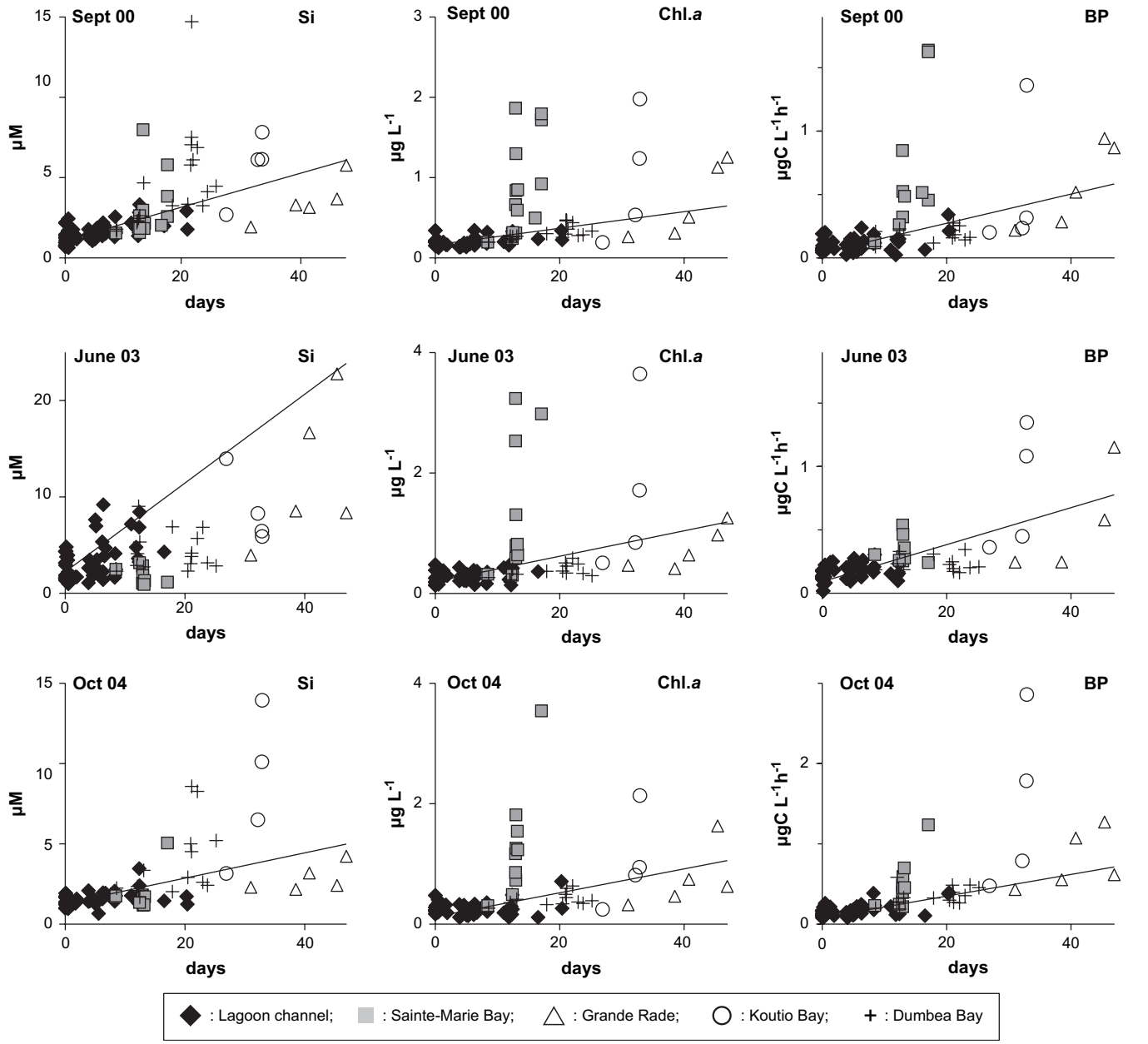

Fig. 4. Scatter plot of silicate, chlorophyll *a* and bacterioplankton production vs. local e-flushing times in the SW lagoon of New Caledonia. Symbols are the same as in Fig. 1. Solid lines indicate model II linear relationships only including lagoon channel data. Although not significant, regression of Chl-*a* vs. local e-flushing times in Oct. 04 is shown for comparison.

moment it has reached 0.95. The concentration in each grid cell decreases as more water coming from outside the control volume reaches the mentioned grid cell. Local e-flushing time is meant to quantify the replacement process of water in a grid cell. The choice of the advection scheme and size of grid space discretization as well as horizontal and vertical parameterizations of turbulence are of crucial importance for the results of the Hydrodynamic Time parameters (HTs) computations. These various choices will influence the conservation of the front formed between the incoming 0 concentration water and the 1 concentration water initially inside the control volume. The better the front is conserved, the shorter the local e-flushing time will tend to be, with all other parameters being equal elsewhere. However, these choices do not have a major influence on the relative distribution of local e-flushing time, nor on the relationship between e-flushing time and biological or chemical variables as is the main focus of this study.

The version of MARS 3D used in the present study does not solve the heat transport equations and thus the simulation does not reproduce stratification. The lack of stratification amplifies the impact of vertical turbulence. This results in an evolution of the concentration front that is similar in the bottom and surface sigma-layers of the model, leading to identical computed HTs in these two layers of the simulated area.

4.2. Representativeness of 3-m deep samples compared to the whole water column

HTs are therefore considered to be representative of the whole water column (Jouon et al., 2006); however, biological and nutrient data were collected from 3-m deep samples during the three cruises. Whether or not the 3-m deep samples can be considered as representative of the whole water column can be assessed by comparing chlorophyll *in vivo* fluorescence at 3 m to water column average. On average, 3-m deep samples were 87% (±3%; 95% confidence limits) of water column means with no significant differences between the cruises. If we assume that the vertical distribution of nutrients and other biological variables in this generally well mixed water column follows the same distribution as phytoplankton, then it can be considered that the 3-m deep samples give a reasonable approximation of the whole water column.

4.3. Relationships between nutrient concentrations or biological variables and local e-flushing times in the lagoon channel

Several attempts have been made to relate biological or chemical properties of different water bodies to flushing rates (Delesalle and Sournia, 1992; Dufour et al., 2001; Torréton et al., 2002). Most of these studies, especially in coral reef areas, performed these correlations on the scale of the entire water body. One important aspect of this work is that we determined these relationships on local scales, i.e. on a vast array of stations within the same water body.

Linking biological or chemical variables to flushing by oceanic waters implicitly assumes that these variables are continuously supplied at a similar rate over the area considered. It can be argued that these assumptions may not be correct for chemical or biological variables of a terrestrial or riverine origin, such as silicate. However, in this system, Si values decrease sharply with distance from the river mouth and quickly reach values very similar to lagoon channel averages (Fig. 5). This suggests that, at least during the periods examined, flushing by oceanic waters was high enough, relative to freshwater inputs, to verify this assumption.

Similarly, resources (nutrients and organic carbon) for phytoplankton and bacterioplankton growth are supplied at higher rates in the bays receiving important urban and industrial effluents (Grande Rade, Sainte-Marie Bay). However, as with the distribution of silicate, Chl-*a* and BP both decrease drastically along coast–lagoon channel transects and values at the mouth of the bays are generally very similar to lagoon channel averages (Fig. 6). This again suggests that, over the three campaigns, flushing with oceanic waters was important enough compared to organic and inorganic anthropogenic inputs to make this assumption sustainable.

4.4. Relationships between nutrient concentrations or biological variables and local e-flushing times in the bays

In this study silicate concentrations display significant relationships with local e-flushing times in the main lagoon channel. Sainte-Marie Bay, Dumbea Bay and Koutio Bay, characterized by significant freshwater inputs, display Si values well above the regression line of Si vs. local e-flushing times for the main lagoon channel (Fig. 4). The only exception is the June 2003 cruise where atypically elevated Si values were observed in the lagoon channel. However, as these silicate

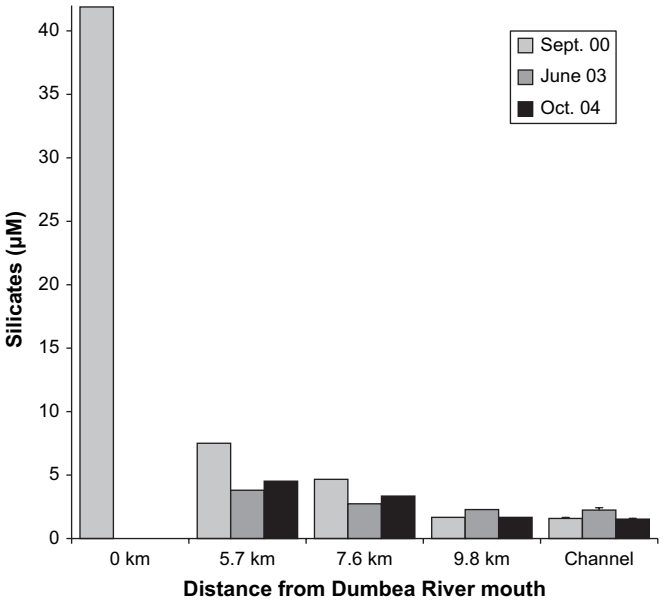

Fig. 5. Silicate concentrations (µM) along a coast-lagoon transect in Dumbea bay during the three cruises. "Channel" denotes average values in the lagoon channel. Bars figure standard errors of the mean for lagoon channel stations.

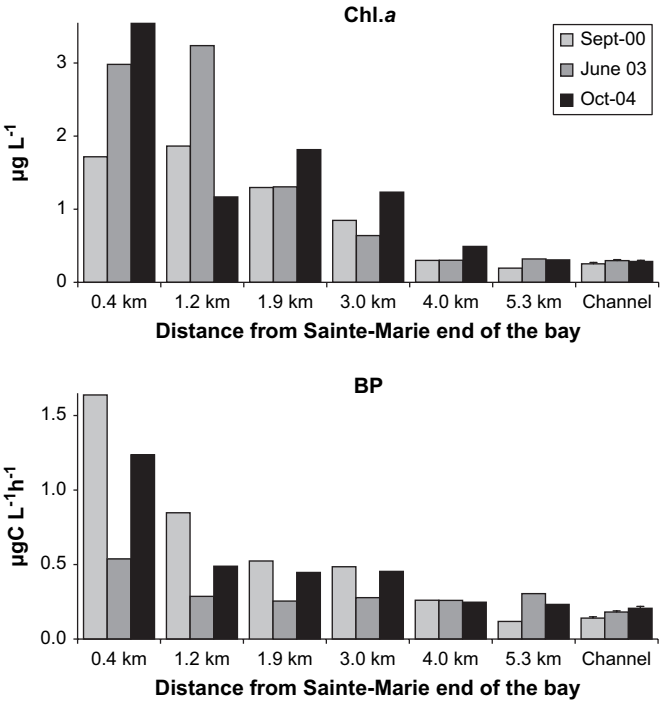

Fig. 6. Chlorophyll *a* (µg L^{-1}) and bacterial production (µg C L^{-1} h^{-1}) along a coast-lagoon transect in Sainte-Marie Bay during the three cruises. "Channel" denotes average values in the lagoon channel. Bars figure standard errors of the mean for lagoon channel stations.

measurements were determined on only one sample, sample contamination cannot be ruled out. In contrast to the other bays, Si concentrations in the Grande Rade, characterized by almost insignificant freshwater inputs, generally fit well within the main lagoon channel relationship. Moreover, when the two sites are combined, the correlation coefficients are higher than if the relationships are examined separately (Table 1).

Bacterial abundance (BA) presents almost no significant relationship with e-flushing times (not shown). This could be due to the severe top-down pressure (i.e. grazing) generally exerted on BA. Whereas BA varied by only 3-fold at the most during each cruise, BP varied by a factor of 100, yielding a pattern similar to that reported by White et al. (1991) who commented that BA generally varies by 2 orders of magnitude less than BP. Phytoplankton biomass, as assessed by Chl-*a* concentrations, varied more extensively (16- to 31-fold) among stations than bacterial biomass during the three cruises. The cross-channel gradients also varied as much as the bay-to-channel gradients, showing decreasing trends persisting at all seasons (Jacquet et al., 2006). Additionally, bacterial abundance is generally determined with a lower precision (10% on average, not shown) than BP or Chl-*a* (3% on average, not shown).

In contrast to BA, bacterial production of biomass presents significant relationships with local e-flushing times. BP may be considered as a sensitive index of resources available for microbial growth (Ducklow, 1990) and values differ widely within the lagoon environment. Thus while the actual concentrations of nutrients are not well correlated with local e-flushing times, the impact of those nutrients on BP is well correlated. Moreover, in the bays, the scatter plots of bacterial production rates vs. e-flushing times deviated from the relationships in the lagoon channel in a different way than silicate concentrations vs. e-flushing times did. Indeed, Grande Rade, Sainte-Marie Bay and Koutio Bay, which are characterized by important urban and industrial effluents, generally display values well above the regression trends (Fig. 4). Conversely, Dumbea Bay stations present BP values that fit well with the regression lines. The difference between the Si and BP relationships for the Grande Rade is probably due to two factors: heterotrophic bacteria do not require Si, and Grande Rade is not subject to riverine influences. Similarly, the difference in relationship between the lagoon channel and the Dumbea Bay for BP and Si is also due to the fact that while the Dumbea River is an important source of Si to the system, it is relatively poor, in comparison to the other bays, in terms of bioavailable resources for bacteria. Moreover, those sites with both important riverine influences as well as high concentrations of available resources for bacterial growth (Sainte-Marie Bay and Koutio Bay) show the same distributions for Si and BP relative to the lagoon channel transect (i.e. higher than the regression line).

Analogous patterns can be observed for Chl-*a* distributions across the lagoon channel, while in the bays, deviations from the lagoon channel regressions lines are comparable to those observed for BP.

The South West lagoon of New Caledonia can be viewed as a coastal mesotrophic ecosystem flushed by oligotrophic oceanic waters that replace lagoon waters with water considerably impoverished in resources for microbial growth. This flushing was high enough during the periods of study to shape the distribution of phytoplankton biomass, bacterial production of biomass and silicate concentrations in the lagoon channel as well as in some of the bay areas.

4.5. Limits

Hydrodynamic timescales are sensitive to hydrodynamic forcing conditions. Tartinville et al. (1997), Geyer (1997) and Deleersnijder et al. (1998) have demonstrated that hydrodynamic time scales can be rather sensitive to wind stress. In this lagoon, hydrodynamic timescales are computed assuming the wind to be constant for periods of time up to 90 days, an assumption that is unlikely to occur in this system.

Constant wind is of course a simplification and local e-flushing time has to be considered as a time and space varying quantity. However, taking a constant wind frees us from the sensitivity of local e-flushing time to the time variation of the wind field. In addition to this, the averaging of results over 12 different runs starting at each hour of a tidal cycle further frees us from the sensitivity of local e-flushing time to the phase of the tide at which the simulation is started. These two strategies remove the time varying property of computed local e-flushing time. Undoubtedly, the development of an inverse model (Delhez et al., 2004) would have been the best way to undertake HTs computation conserving the time varying aspect of the HTs. However, without having to develop an inverse model, one could have an idea of the effect of the variation of wind conditions on the local e-flushing time

distribution by conducting a sensitivity analysis on wind variation effects.

It is important to recognize that although local e-flushing time does explain some of the variance in the biological and chemical parameters, it does not explain all. For example, in Table 1 we show that local e-flushing time sometimes only explains around 16% of the variability on the whole SW lagoon. However, given that the biological and chemical parameters used are generally considered non-conservative parameters, this is perhaps not surprising and further highlights the importance of large scale physical processes on controlling biological and chemical parameters. Alternatively, it can be argued that a more simple method of estimating these relationships would be to use mixing diagrams (Rochelle-Newall and Fisher, 2002). However, one of the caveats of using mixing diagrams is the need to have correctly defined, non-varying endmembers, at least on the time scale of the measurement (Cifuentes et al., 1990). In the SW lagoon, although we have a clearly identifiable, effectively constant oceanic endmember, this is not the case for the coastal endmember where we have several coastal sources that are relatively heterogeneous both spatially and temporally. Moreover, the lack of significant salinity gradient in this system means that another index would need to be used, such as distance from the coast. We therefore tested the correlations between chemical and biological parameters and distance. We found that while the correlations between the parameters and distance were generally significant for the bays viewed separately, this was not the case for the lagoon channel (data not shown). This lack of correlation in the lagoon channel is due to the fact that while local e-flushing time is approximately linear with distance inside each bay, there is no correlation between distance and local e-flushing time either in the lagoon channel, or between local e-flushing time and distance when the entire data set is considered. Thus, in summary, although local e-flushing time does not describe all of the variance of the parameters, it does provide a relatively robust way to predict the distribution of biological and chemical variables, at least in this system.

5. Conclusion

This study demonstrates the pertinence of using flushing indices determined from hydrodynamic modeling to explain the distribution of planktonic and chemical variables at the scale of the SW lagoon of New Caledonia. Our flushing indices were calculated for dominant meteorological conditions (i.e. 110° trade winds averaging 8 m s^{-1} and average tides). Wind and tide driven circulation of water is undoubtedly of critical importance for the rate and distribution of planktonic processes in this coastal ecosystem. It is also probable that flushing will also exert a significant influence on short-term temporal variations of planktonic processes. Indeed, an annual survey at two stations in the SW lagoon showed that short-term (1–2 weeks) variations of bacterioplankton and phytoplankton biomass and production are of the same order of magnitude as seasonal variations (unpublished data). The next step will be to assess local variations of flushing lags over this annual cycle in order to determine their importance in constraining biological processes in this ecosystem characterized by moderate seasonal variations of physical variables.

Acknowledgments

This work was supported by the Institut Français de Recherche pour le Développement (IRD), grants from the Programme National Environnement Côtier (PNEC) and a grant from the ZoNéCo program. We express our gratitude to the crews of the IRD RV *Alis* and the New Caledonia RV *Louis Hénin* for their efficient help during sample collection.

References

Andrews, J.C., Muller, H., 1983. Space-time variability of nutrients in a lagoonal patch reef. Limnology and Oceanography 28, 215–227.

Bourguet, N., Torréton, J.-P., Galy, O., Arondel, V., Goutx, M., 2003. Specific and sensitive radiometric assay for microbial lipase activities in marine water samples: application to samples from the lagoon of Nouméa. Applied and Environmental Microbiology 69, 7395–7400.

Blumberg, A.F., Mellor, G.L., 1987. A description of a three-dimensional coastal ocean circulation model. In: Heaps, N.S. (Ed.), Three-dimensional Coastal Ocean Models. AGU, Washington, DC, pp. 1–16.

Briand, E., Pringault, O., Jacquet, S., Torréton, J.-P., 2004. The use of oxygen microprobes to measure bacterial respiration for determining bacterioplankton carbon growth efficiency along trophic gradients in a coral reef lagoon. Limnology and Oceanography: Methods 2, 406–416.

Cifuentes, L.A., Schemel, L.E., Sharp, J.H., 1990. Qualitative and numerical analyses of the mixing effects of river inflow variations on mixing diagrams in estuaries. Estuarine, Coastal Shelf Science 30, 411–417.

Crump, B.C., Hopkinson, C.S., Sogin, J.E., 2004. Microbial biogeography along an estuarine salinity gradient: combined influences of bacterial growth and residence time. Applied and Environmental Microbiology 70, 1494–1505.

Deleersnijder, E., Norro, A., Wolanski, E., 1992. A three-dimensional model of the water circulation around an island in shallow water. Continental Shelf Research 12, 891–906.

Deleersnijder, E., Wang, J., Mooers, C.N.K., 1998. A two-compartment model for understanding the simulated three-dimensional circulation in Prince William Sound, Alaska. Continental Shelf Research 18, 279–287.

Delesalle, B., Sournia, A., 1992. Residence time of water and phytoplankton biomass in coral reef lagoons. Continental Shelf Research 12, 939–949.

Delhez, E.J.M., Heemink, A.W., Deleersnijder, E., 2004. Residence time in a semi-enclosed domain from the solution of an adjoint problem. Estuarine, Coastal and Shelf Science 61, 691–702.

Doering, P.H., Oviatt, C.A., McKenna, J.H., Reed, L.W., 1994. Mixing behavior of dissolved organic-carbon and its potential biological significance in the Pawcatuck River estuary. Estuaries 17, 521–536.

Douillet, P., 1998. Tidal dynamics of the south-west lagoon of New Caledonia: observations and 2D numerical modelling. Oceanologica Acta 21, 69–79.

Douillet, P., Ouillon, S., Cordier, E., 2001. A numerical model for fine suspended sediment transport in the southwest lagoon of New Caledonia. Coral Reefs 20, 361–372.

Ducklow, H.W., 1990. The biomass, production and fate of bacteria in coral reefs. In: Dubinsky, Z. (Ed.), Coral Reefs. Elsevier, Amsterdam, pp. 265–289.

Dufour, P., Andréfouët, S., Charpy, L., Garcia, N., 2001. Atoll morphometry controls lagoon nutrient regime. Limnology and Oceanography 46, 456–461.

Ferreira, J.G., Wolff, W.J., Simas, T.C., Bricker, S.B., 2005. Does biodiversity of estuarine phytoplankton depend on hydrology? Ecological Modelling 187, 513–523.

Fukuda, R., Ogawa, H., Nagata, T., Koike, I., 1998. Direct determination of carbon and nitrogen contents of natural bacterial assemblages in marine environments. Applied and Environmental Microbiology 64, 3352–3358.

Geyer, W.R., 1997. Influence of wind on dynamics and flushing of shallow estuaries. Estuarine, Coastal and Shelf Science 44, 713–722.

Grasshoff, K., Eherhardt, M., Kremling, K., 1983. Methods of Seawaters Analysis, second ed. Verlag Chemie, Weinheim, RFA, 419 pp.

Holmes, M.R., Aminot, A., Kérouel, R., Hooker, B.A., Peterson, B.J., 1999. A simple and precise method for measuring ammonium in marine and freshwater ecosystems. Canadian Journal of Fisheries and Aquatic Sciences 56, 1801–1808.

Holm-Hansen, O., Lorenzen, C.J., Holmes, R.W., Strickland, J.D.H., 1965. Fluorimetric determination of chlorophyll. Journal du Conseil Permanent International pour l'Exploration de la Mer 30, 3–15.

Jacquet, S., Delesalle, B., Torréton, J.-P., Blanchot, J., 2006. Response of phytoplankton communities to increased anthropogenic influences (southwestern lagoon, New Caledonia). Marine Ecology Progress Series 320, 65–78.

Jouon, A., Douillet, P., Ouillon, S., Fraunié, P., 2006. Calculations of hydrodynamic time parameters in a semi-opened coastal zone using a 3D hydrodynamic model. Continental Shelf Research 26, 1395–1415.

Lazure, P., Salomon, J.C., 1991a. Coupled 2-D and 3-D modelling of coastal area. Oceanologica Acta 14, 173–180.

Lazure, P., Salomon, J.C., 1991b. Etude par modèles mathématiques de la circulation marine entre Quiberon et Noirmoutier. Oceanologica Acta 14 (SP), 93–99.

Lucas, L.V., Koseff, J.R., Cloern, J.E., Monismith, S.G., Thompson, J.K., 1999. Processes governing phytoplankton blooms in estuaries. I: The local production-loss balance. Marine Ecology Progress Series 187, 17–30.

Marie, D., Partensky, F., Jacquet, S., Vaulot, D., 1997. Enumeration and cell cycle analysis of natural populations of marine picoplankton by flow cytometry using the nucleic acid stain SYBR Green I. Applied and Environmental Microbiology 63, 186–193.

Monsen, N.E., Cloern, J.E., Lucas, L.V., Monismith, S.G., 2002. A comment on the use of flushing time, residence time, and age as transport time scales. Limnology and Oceanography 47, 1545–1553.

Ouillon, S., Douillet, P., Andréfouët, S., 2004. Coupling satellite data with in situ measurements and numerical modeling to study fine suspended sediment transport: a study for the lagoon of New Caledonia. Coral Reefs 23, 109–122.

Painchaud, J., Lefaivre, D., Therriault, J.C., Legendre, L., 1996. Bacterial dynamics in the upper St. Lawrence estuary. Limnology and Oceanography 41, 1610–1618.

Plus, M., Chapelle, A., Lazure, P., Auby, I., Levavasseur, G., Verlaque, M., Belsher, T., Deslous-Paoli, J.-M., Zaldívar, J.-M., Murray, C.N., 2003. Modelling of oxygen and nitrogen cycling as a function of macrophyte community in the Thau lagoon. Continental Shelf Research 23, 1877–1898.

Raimbault, P., Slawyk, G., Coste, B., Fry, J.C., 1990. Feasibility of measuring an automated colorimetric procedure for the determination of seawater nitrate in the 0 to 100 nM range: examples from field and culture. Marine Biology 104, 347–351.

Rochelle-Newall, E.J., Fisher, T.R., 2002. Chromophoric dissolved organic matter and dissolved organic carbon in Chesapeake Bay. Marine Chemistry 77, 23–41.

Sweby, P.K., 1984. High resolution schemes using flux limiters for hyperbolic conservation laws. SIAM Journal of Numerical Analysis 21, 995–1011.

Tartinville, B., Deleersnijder, E., Rancher, R., 1997. The water residence time in the Mururoa Atoll Lagoon: sensitivity analysis of a three dimensional model. Coral Reef 16, 193–203.

Thomann, R.V., Mueller, J.A., 1987. Principles of Surface Water Quality Modelling and Control. Harper Collins, New York.

Torréton, J.-P., Pagès, J., Talbot, V., 2002. Relationship between bacterioplankton and phytoplankton biomass, production and turnover rate in Tuamotu atoll lagoons. Aquatic Microbial Ecology 28, 267–277.

Vollenweider, R.A., 1976. Advances in defining critical loading levels for phosphorus in lake eutrophication. Memorie dell'Istituto Italiano di Idrobiologia 33, 53–83.

White, P.A., Kalff, J., Rasmussen, J.B., Gasol, J.M., 1991. The effect of temperature and algal biomass on bacterial production and specific growth rate in freshwater and marine habitats. Microbial Ecology 21, 99–118.

Available online at www.sciencedirect.com
ScienceDirect
Estuarine, Coastal and Shelf Science 74 (2007) 777–780
ESTUARINE COASTAL AND SHELF SCIENCE

Contents of Volume 74

NUMBER 1–2 AUGUST 2007

Research Papers

NUMBER 3 1 SEPTEMBER 2007

NUMBER 4 15 SEPTEMBER 2007

Special Issue

Timescale- and tracer-based methods for understanding the results of complex marine models
Eric Deleersnijder and Eric J.M. Delhez (Guest Editors)